EAST EUROPEAN JOURNAL OF PHYSICS. **4.** 4-13 (2025)
DOI:10.26565/2312-4334-2025-4-01 ISSN 2312-4334

# ADVANCEMENTS IN ANTIPEROVSKITE STRUCTURED SOLIDS: A COMPREHENSIVE REVIEW

**Shrawan Kumar[1], Sushil Kumar Pathak[2], Deepak Sharma[3], Peeyush Kumar Kamlesh[4], Ajay Singh Verma[5]***
*[1]Department of Physics, G.L.A. College, Medininagar (Daltonganj), Palamau, Nilamber Pitamber University, Jharkhand 822101, India*
*[2]Department of Physics, Chandrapur, Pombhurna, Chandrapur, Maharashtra-442918, India*
*[3]Department of Applied Sciences & Humanities, IIMT College of Engineering, Greater Noida, 201310, India*
*[4]Department of Physics, Poornima University, Jaipur – 303905, Rajasthan, India*
*[5]Department of Physics, Anand School of Engineering & Technology, Sharda University Agra, Keetham, Agra – 282007, India*
**Corresponding author e-mail: ajay_phy@rediffmail.com*

Received September 1, 2025; revised October 6, 2025; accepted October 15, 2025

Antiperovskite-structured solids are attracting growing attention as a new class of multifunctional materials. Unlike conventional perovskites, their inverted cubic framework gives rise to unusual and highly tunable properties, from fast-ion conduction and giant magnetoresistance to superconductivity and negative thermal expansion. These different behaviors indicate promise for applications in areas such as solid-state batteries, energy-harvesting refrigeration, superconducting electronics, and thermal management. This review collates recent work in both experimental and theoretical research, emphasizing how a single simple cubic lattice can provide such a wide range of functionality. We argue that the structural versatility of antiperovskites is the common link between ionic transport, spin–lattice coupling, superconductivity, and thermal expansion. Recent advancements in Li- and Na-based solid electrolytes with high conductivity, giant magneto- and barocaloric responses, non-oxide superconductivity, and isotropic negative thermal expansion demonstrate that antiperovskites retain scientific importance and are increasingly viable competitors with the best of today's functional materials.

**Keywords**: *Antiperovskites; Magnetism; Superconductivity; Renewable energy; Battery materials*
**PACS:** 61.66.-f; 71.15.Dx; 85.30.-z

## 1. INTRODUCTION

Energy is the convertible commodity of technology, and modern society collapses quickly without it. This dependency has motivated researchers to seek renewable sources due to the gradual decline and environmental burden of non-renewables. Renewable sources (sun, wind, water) can be replenished naturally, while non-renewables such as coal and oil exist in finite amounts. Rising energy demand and $CO_2$ emissions have forced governments to invest in renewables, yet fossil fuels still account for over 80% of global use **[1]**. Although fossil fuels remain abundant in the short term, their continued use accelerates climate change. To mitigate shortages and climate change, solar cells and other renewables are being developed. Global warming is evident, with a ~0.6 °C rise in average temperature (Figure 1) **[2]**.

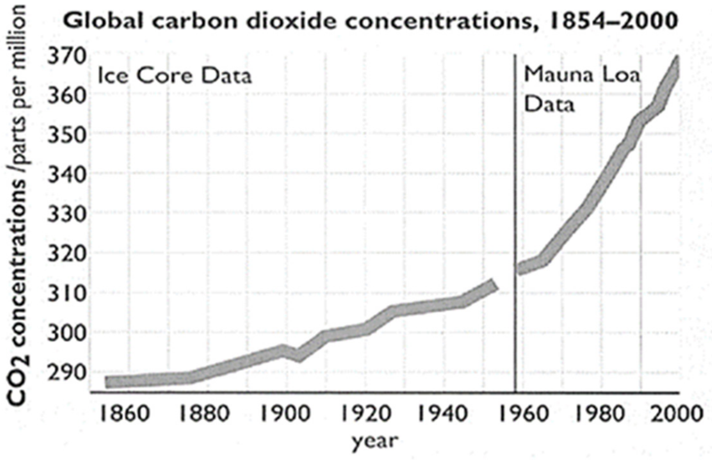

**Figure 1**. Atmospheric concentration of $CO_2$ gas **[2]**

Additionally, the improvement of the sun's energy utilization is necessary for an environmentally friendly and cleaner world. Devices like space photovoltaic cell technology were also mentioned; this subject is continuing to advance. Perovskite is one of the most affordable and abundant materials for environmental sustainability solutions **[3]**. Antiperovskites ($ANX_3$) are structural inverses of the conventional perovskite ($ABX_3$) framework. In this structure, the

---

***Cite as:*** S. Kumar, S.K. Pathak, D. Sharma, P.K. Kamlesh, A.S. Verma, East Eur. J. Phys. 4, 4 (2025), https://doi.org/10.26565/2312-4334-2025-4-01

X-site cations (e.g., Ca, Sr, Ba, Mg) occupy the face-centered positions of the cube, while the A-site anion (commonly N, C, or O) resides at the cube corners. The B-site element (e.g., Bi, Sb, As) sits at the octahedral center, surrounded by six X cations.

The electronic band gap is a key parameter governing the physical behavior of antiperovskites. It determines whether a compound is metallic, semiconducting, or insulating, and thereby influences its potential applications. For example, $Li_3OCl$ and related antiperovskites exhibit wide band gaps (>5 eV), making them good solid electrolytes but electronically insulating. In contrast, $Mn_3AN$ (A = Ga, Zn, Cu) antiperovskites are metallic with negligible gaps, enabling strong spin-lattice coupling and giant magnetoresistance. Tunable narrow band gaps have also been predicted in Sb- and Bi-based antiperovskites (e.g., $Ca_3BiN$, $Ca_3SbN$), making them promising for thermoelectrics and optoelectronic devices. The ability to shift from insulating to metallic behavior by chemical substitution, pressure, or doping underscores the central role of band gap engineering in this materials family.

As compared to classical perovskites, the ionic reversal leads to unusual bonding, tunable band structures, and multifunctional physical properties (Figure 3). Due to their reduced band gap and figure of merit, the antiperovskite compounds are potential candidates in thermoelectric devices that have the potential of recycling waste heat to reduce greenhouse gas emissions. When choosing semiconducting components for thermoelectric generators, care must be taken. Since the band gap affects thermoelectric properties greatly, accurate band gap computation is required. As a result, narrow band gap semiconductor alkaline earth-based antiperovskites are potential prospects for optoelectronics and thermoelectric purposes **[4]**. Perovskites come in a variety of forms, including double perovskites $(CH_3NH_3)_2AgInBr_6$ **[5]**. Double antiperovskites $X_6SOA_2$ (X= Na, K and A= Cl, Br, I) **[6]**, simple perovskites $EASnCl_3$ **[7]** and $RbPbBr_{3-x}I_x$ (x= 0 to 3) **[8]**, anti-perovskites $ANX_3$ (A= P, As, Sb, Bi; X= Sr, Ca, Mg) **[9]** and $AsPX_3$ (X= Mg, Ca, and Sr) **[10]**.

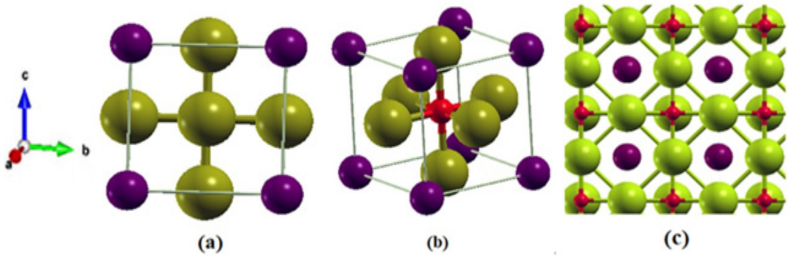

**Figure 2.** Crystal structure of a cubic antiperovskite $ANX_3$. Here, X (green atom) cations occupy the face-centered positions, the A (purple atom) anion resides at the cube corners, and the B-site element (e.g., N, P, AS, Sb, Bi – red atom) sits at the octahedral center

Antiperovskites have received plenty of research focused on due to their usefulness in various industrial applications **[11]**. Due to their favorable thermoelectric (TE) properties, antiperovskites have a significant potential to alleviate the energy crisis **[12]**. To achieve high efficiency, researchers are looking for appropriate materials for thermoelectric generators. Good thermoelectric materials often feature band gaps that are also broad enough to have an enormous Seebeck value and narrow enough to have a suitable conductivity for electrical use **[13]**. Solids with super ionic conductivity are regarded to be preferable to organic liquid electrolytes in batteries; hence, lithium-based antiperovskites can be employed as solid electrolytes **[14]**. These materials also have remarkable physical properties, such as magnetostriction **[15]**, virtually zero temperature coefficients of resistivity **[16]**, and gigantic magnetoresistance (GMR) **[17]**.

Beyond conventional antiperovskites, new classes of antiperovskite-derived or 'reverse perovskite' structures have been recently reported. Tang et al. **[18]** developed a family of antiperovskite derivatives in which the A-site anion of the cubic framework is split into three edge-centered positions while preserving the corner-sharing octahedral network. Screening several compounds, they identified nine promising candidates such as $Ba_3BiI_3$, $Ba_3SbI_3$, and $Ba_3BiBr_3$, achieving predicted photovoltaic efficiencies above 24.5%, comparable to classical $CH_3NH_3PbI_3$ solar cells. Complementary to this, Hu et al. **[19]** studied $X_3AsCl_3$ (X = Mg, Ca, Sr, Ba) under hydrostatic pressure, showing that band gaps and lattice constants evolve linearly with pressure, and that $Ba_3AsCl_3$ can reach conversion efficiencies above 30% under moderate compression. These studies illustrate how derivative antiperovskite structures behave to atomic rearrangements or an applied external stress thereby widening the design space for optoelectronic applications.

Antiperovskites are especially well-suited for industrial applications related to biosensors, magnetic field sensors, biosensors, micro-electromechanical systems, giant magnetoresistance, and other gadgets that read data from hard discs given these properties. Likewise, antiperovskites are ideal building blocks in any climate because of their zero-temperature coefficient of resistivity. Antiperovskites also display excellent mechanical properties **[20-22]**, and could be of use in the automotive and space industries, which both require materials that are lightweight and also mechanically strong. Additionally, antiperovskites display superconductivity. $MgCNi_3$ is particularly interesting because it is one of the few (yet) known non-oxide/perovskite-derived superconductors with a relatively high Tc of ~8 K **[23]**. Additionally, its electronic structure comprises mainly Ni 3d states near the Fermi level which makes this compound a prototype for investigating unconventional superconductivity in antiperovskites. The discovery of $MgCNi_3$ lead to increased investigation into other related compounds including ZnNNi3 and $CdCNi_3$ **[24]**, emphasizing the structural tunability of this family. The goal of this review paper is to evaluate, the theoretical studies focused on the properties of antiperovskite-type materials.

## 2. PREVIOUS STUDIES AND RESULTS

In first-principles studies of antiperovskites, the choice of exchange–correlation functional strongly influences the predicted electronic structure. The Local Density Approximation (LDA) often underestimates lattice constants and band gaps due to its assumption of uniform electron density. The Generalized Gradient Approximation (GGA) improves on this by incorporating density gradients, yielding more accurate structural parameters but still typically underestimating band gaps. To address this, the Engel–Vosko GGA (EV-GGA) modifies the exchange potential to give better agreement with experimental band gaps. Moakafi et al. **[25]** have investigated the electronic, optical, and elastic characteristics of the cubic antiperovskite $SbNCa_3$ and $BiNCa_3$ and found their band gaps to be 0.65 and 0.36 eV, respectively. The authors used LDA, GGA, and EV-GGA potentials to examine the electronic characteristics of these compounds. Despite the fact that the investigators used EV-GGA to attain bigger band gaps, the valence bands of these materials pass through the Fermi level and demonstrate metallic behavior, which is contrary to the data from experiments. Bilal et al. **[26]** presented an analysis of the previously discussed systems to examine the impact of different computational schemes for predicting the electronic structures of $BiNCa_3$ and $SbNCa_3$ antiperovskites. The authors found that LDA and GGA underestimated the band gap, while the mBJ potential gave band gap values of 1.09 and 1.1 eV for $BiNCa_3$ and $SbNCa_3$, respectively, which were much closer to the experimental values. The study demonstrates the sensitivity of antiperovskite band structures to the choice of functional and shows that these systems are compact gap semiconducting materials that can find relevance in thermoelectric and optoelectronic applications.

We see that the reported physical properties of antiperovskites depend strongly on the chosen method. For instance, $SbNCa_3$ and $BiNCa_3$ show band gaps of only 0.36–0.65 eV when studied using LDA and GGA, while EV-GGA increases these values slightly but still underestimates them. In contrast, the modified Becke–Johnson (mBJ) potential produces more reliable results, giving direct band gaps close to 1.0–1.1 eV, in much better agreement with experiments. In several cases, GGA predicts metallic behavior, whereas mBJ or hybrid functionals reveal semiconducting nature. These variations highlight the importance of method selection when evaluating the electronic structure of antiperovskites, as also discussed in recent literature **[27]**.

The chemical bonds and electronic band structure in the compounds $SbNMg_3$ and $AsNMg_3$ were investigated by Shein and Ivanovskii using GGA **[28]**. Small band gap and both compounds display ionic semiconducting properties. $AsNMg_3$ has a direct band gap, in contrast to $SbNMg_3$, which has an indirect band gap. The GGA technique was used to examine these materials' Electronic and Optical properties. These compounds' optical properties have never been investigated previously. The author of this study confirmed the earlier findings and showed that $AsNMg_3$ has a direct band gap and $SbNMg_3$ has an indirect band gap, both compounds having low band gaps **[29]**. This writer asserts that the computed optical spectrum positions can be lower than the values obtained from experiments because DFT typically underestimates band gaps.

The dielectric function's hypothetical component, as presented in their work, supports the materials' semiconducting properties. Using the pseudo-potential plane waves approach within the GGA, Bouhemadou and colleagues **[30]** studied the structural, optical, elastic, and electronic properties of $AsNMg_3$ and $SbNMg_3$ compounds. $AsNMg_3$ has a fundamental direct band gap that in the beginning boosts up to 4 GPa, then gradually reduces as a function of pressure, whereas simultaneously maintaining its direct band gap nature throughout the whole pressure range executed, in opposition to $SbNMg_3$, which transitions from a fundamental indirect band gap to a fundamental direct band gap as pressure attains 6.85 GPa. Since these were the initial theoretical investigations on the elastic characteristics of these compounds, Belaroussi et al. **[31]** have examined the Elastic and Structural characteristics of $SbNMg_3$ theoretically and contrasted their research with this study. Amara et al. **[32]** have studied the structural, elastic, and electronic characteristics of $BiNMg_3$, $SbNMg_3$, $AsNMg_3$, and $PNMg_3$ via the full-potential augmented plane waves plus local orbital within the GGA to improve results by addressing the exchange and correlation effects by the Tran-Blaha mBJ potential for the charge density, density of states, and band structure. These scientists reported on the magnetic, electrical, optical, and bonding characteristics of these sorts of compounds. These materials are semiconductors, according to studies on electrical resistivity. By using the diffuse reflectivity method, the optical band gaps for $BiNSr_3$ and $SbNSr_3$ are 0.89 eV and 1.15 eV, respectively.

Haddadi et al. **[33]** have examined the electronic, elastic, and structural characteristics of $ANSr_3$ (A = Bi, Sb, and As) compounds in 2009 using the plane waves pseudo potential total energy approach in the CASTEP code. The optical, electronic, and elastic characteristics of $ANSr_3$ (A = Bi, Sb, and As) antiperovskite compounds were studied by Hichour et al. **[34]** in 2010. The investigators used the EVGGA potential to increase the band gaps of these compounds, yielding values of 0.36, 0.55, and 0.84eV for $BiNSr_3$, $SbNSr_3$, and $AsNSr_3$, correspondingly. All compounds' band gap values decrease with increasing pressure. The charge density charts show that these materials have a combination of covalent and ionic bonds. Their work's depiction of the imaginary component of the dielectric function also illustrates how $SbNSr_3$ behaves semiconducting material.

What makes antiperovskites especially intriguing is that their diverse applications, from batteries and ionic conductors to magnetoresistive devices, superconductors, and thermal expansion compensators, all originate from the same structural motif. The cubic lattice allows a high degree of tunability, enabling properties as distinct as superconductivity and solid-state ionic conduction to coexist in the same materials family. This unifying theme forms the focus of the present review, which not only summarizes individual applications but also highlights the common structural and electronic factors connecting them.

## 3. APPLICATIONS

The diverse applications of antiperovskites arise from a few unifying material characteristics. Their cubic framework, with interchangeable cation/anion positions, provides structural flexibility. Strong spin–lattice–charge coupling enables multifunctional responses, such as magnetoresistance, negative thermal expansion, and magnetocaloric effects. At the same time, tunable band gaps and ionic transport pathways make them attractive for electrochemical and superconducting applications. The following subsections discuss batteries, magneto-electronics, superconductivity, and thermal expansion versatility of the antiperovskite lattice.

### 3.1 Antiperovskite as Modern Battery Materials:

In particular, lightweight Lithium or sodium ion batteries with an elevated energy density have attracted a lot of research interest due to the urgent energy needs of the modern industrialized world **[35]**. The primary strategy for attaining this objective is the development of improved electrode materials with excellent capacity and a wide voltage window. Both their exceptionally large theoretical considerations, specific capacity, as well as their extremely low electrochemical potential, set Lithium metal anode materials apart from other materials. Therefore, it is envisaged that a battery or cell that has a Lithium metal anode will result in long-lasting, lightweight power to electronic devices. The conventional electrolyte's flammability and ease of leakage must first be eliminated in order to realize this vision. A secure, solid-state electrolyte has therefore been recommended as an alternative. Particularly enticing aspect of it is that, since it achieves an ultrathin dimension, it will not just resolve risks brought on by inflammability but additionally improve energy density. Batteries endorsed by solid-state electrolytes have been on the verge of becoming a common commercial technology **[36]**. SSEs still have to overcome significant obstacles, such as ionic conductivity, stability, Li dendrite growth, surface contact, etc. **[37]**. In this section, we primarily discuss the ionic conductivity of the antiperovskite group. Few among these SSEs can match an ionic liquid's room-temperature ionic conductivity. However, without material engineering optimization, few of these electrolytes can achieve this high level. The literature has focused considerable amounts of interest on several groups of inorganic solid-state electrolytes, such as Lithium halides, Garnets, Lithium nitrides **[38-41]**. The intrinsic high ionic conductivity of $Li^+/Na^+$ antiperovskite is generally very promising, and through the use of chemical doping and structural design, it could improve even more. Their high stability and minimal surface resistance as they come into touch with Lithium metal anodes are two further advantages for commercial use. They must also address their elevated susceptibility to moisture and a small potential window, which are two problems. There must be more research towards cheap, massive industrial fabrication. Figure 3 illustrates lithium-ion conduction in $Li_3OCl$-type antiperovskites. Recent studies have reported room-temperature conductivities as high as $\sim 10^{-3}$ S/cm in doped $Li_{3-2x}Sr_xOCl$ antiperovskites, making them competitive with NASICON and garnet-type electrolytes **[14, 42]**. Na-based analogues such as $Na_3OCl$ have also achieved $\sim 10^{-4}$ S/cm, offering a potential pathway for cost-effective sodium-ion batteries **[43]**. These values (Table 1) demonstrate that antiperovskite solid electrolytes are approaching the performance of state-of-the-art oxide and sulfide systems, while offering superior mechanical processability.

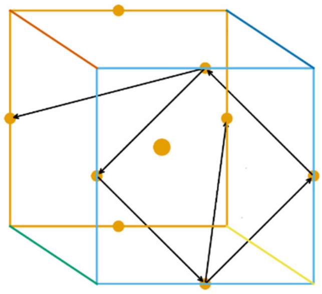

**Figure 3**: Schematic of $Li^+$ migration pathways in $Li_3OCl$-type antiperovskite solid electrolytes, highlighting face-centered and edge-sharing conduction channels **[13, 14]**

**Table 1:** Ionic Conductivity of Antiperovskite Solid Electrolytes

| Compound | Temperature (°C) | Ionic Conductivity (S/cm) | Remarks |
|---|---|---|---|
| $Li_3OCl$ **[13]** | 25 °C | $\sim 10^{-5}$ | Good solid electrolyte; moisture sensitive |
| $Li_3OBr$ **[44]** | 25 °C | $\sim 10^{-6}$ | Similar to $Li_3OCl$, lower conductivity |
| $Na_3OCl$ **[43]** | 25 °C | $\sim 10^{-4}$ | Promising Na-based analogue |
| $Li_{3-2x}Sr_xOCl$ (doped) **[42]** | 25 °C | $\sim 10^{-3}$ | Enhanced by Sr doping (defect engineering) |

These ionic conduction studies are important because they show how antiperovskites can work as solid electrolytes. But other types of antiperovskites show metallic behavior, which opens the door to magnetic and magnetoresistive applications, discussed in the next section.

### 3.2 Antiperovskite as electronics and Magnetoresistive devices

$ABO_3$ perovskites are widely used in contemporary electronics, including storage, magneto-caloric, and magnetoresistive devices **[45-49]**. Magnetic antiperovskites $M_3M'X$ (M = Mn, Fe, etc.; M′ = Ga, Al, Zn, In, Sn, etc.; X =

N, C) were additionally thoroughly explored as an innovative family of potential magnetic compounds. Mn-based magnetic antiperovskites are perhaps the most intriguing among these compounds because of their newly identified Giant magnetoresistance (GMR) **[21]**, massive Magneto-caloric effect (MCE) **[50]**, and giant Magnetostriction **[51]**. Additionally, the metallic nature of these $Mn_3M'X$ antiperovskites suggests that they have strong Mechanical, Electrical, and Thermal conductivities **[26]**. Three magnetic changes occur as the test sample of giant magnetoresistance compound $Mn_3GaC$ cools: a paramagnetic to ferromagnetic transition at 246 K, an FM intermediate magnetic phase transition at 160 K, as well as an intermediate phase to antiferromagnetic transition at 158 K. While the hybridization of the Mn-X p-d orbitals widens the conduction band over the Fermi level and produces a significantly high conductivity, the Mn 3d orbitals in $Mn_3M'X$ antiperovskites offer to the DOS at the Fermi level. Both magnetic exchange interactions & conduction behavior include these Mn 3d electrons. As a result, the magnetic coupling interactions between these third-dimensional electrons and the Mn-X-Mn atoms will be competitive.

Due to the tight couplings between the various degrees of freedom & the conflicting magnetic interactions, $Mn_3M'A$ is highly responsive to every minor alteration in the external magnetic field, chemical composition, temperature & pressure **[52]**. From 135 to 165 K, $Mn_3GaC$ (Figure 4) displays GMR curves that resemble plateaus, with a maximum MR of 50% at 5 T **[53]**.

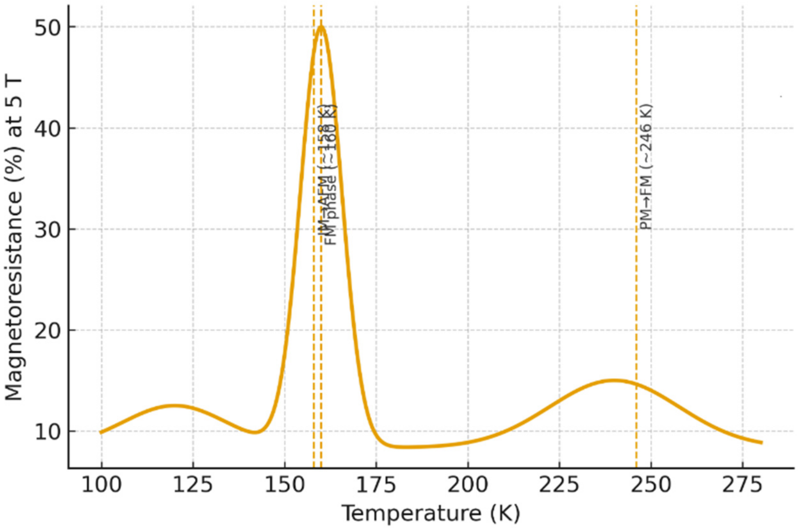

**Figure 4.** Temperature-dependent magnetoresistance in $Mn_3GaC$, showing strong MR effects linked to successive phase transitions [53]

The giant magnetoresistance is connected to the field-induced ferromagnetic, antiferromagnetic, or intermediate magnetic phase transition, where there is a strong correlation between the lattice, spin, and charge. The possibility of a giant magnetoresistance with a larger temperature range exists if an external magnetic field can efficiently reduce the antiferromagnetic ground state. The antiperovskite $Mn_3M'A$ compounds offer benefits in the role of refrigerant substance because of their adjustable broad working temperature, as well as their availability, affordable and harmless raw materials, stable behavior, ease of manufacturing and design, strong conductivity, and excellent mechanical characteristics. These materials present an intriguing alternative material platform to investigate novel big Magneto-caloric effect compounds at room temperature. This close relation between spin, lattice, and electronic states also creates conditions that are favorable for superconductivity. Therefore, in the following section, we describe the discovery of superconductivity in $MgCNi_3$ and other antiperovskites.

### 3.3 Evolution of superconductivity in Antiperovskites

$Ni_3MgC$, which was found in 2001, was the first antiperovskite to exhibit superconductivity **[27]**. When examining the superconducting mechanism, the cubic $Ni_3MgC$ serves as a special illustration of an s-wave Bardeen–Cooper–Schrieffer type-2 superconductor similar to that of the noncuprate superconductor $Ba_{12x}K_xBiO_3$. As a result, in-depth experimental and theoretical research was done on superconductors related to $Ni_3MgC$, including $Ni_3CuN$, $Ni_3ZnN$, $Cr_3GaN$, and $K_2NiF_4$-type layered $A_2CNi_4$ (A = Al, Ga, Sn) **[54, 55]**. The crystal structure's high Ni content suggests that magnetic interactions may be crucial to the development of superconductivity. $T_c$ experimentally decreased whenever the nickel site was enriched via additional transition metals, such as Mn, Fe, Co, and Cu, but might be marginally enhanced by raising the value of x in $Ni_3MgC_x$. The family of ternary platinum phosphides $Pt_3AP$, where A = Ca, Sr, La **[56]**, is another intriguing example of an antiperovskite-based structure closely connected to the heavy fermion superconductor $Pt_3CeSi$. The so-called antipost-perovskites $V_3PnN_x$ (Pn = P, As) have superconductivity **[57]**. In comparison to the post-perovskite structure, the cation and anion positions are interchanged. When these compounds crystallize, they give rise to the filled $Re_3B$ structure. The antipost-perovskites $V_3PnN_x$ have $NV_6$ octahedral layers and Pn layers alternately stacked, resulting in a quasi-2D electronic state. The first antiperovskite oxide that is superconducting ($T_c$ = 5 K) is $Sr_{3x}SnO$ **[58]**. Table 2 summarizes superconducting transition temperatures across representative compounds.

**Table 2.** Superconducting Transition Temperatures ($T_c$) in Antiperovskites

| Compound | Structure Type | $T_c$ (K) | Notes/Reference |
|---|---|---|---|
| $MgCNi_3$ | Cubic antiperovskite | ~8 | First discovered non-oxide antiperovskite superconductor **[23]** |
| $ZnNNi_3$ | Cubic antiperovskite | ~3 | Ni-rich, lower Tc compared to $MgCNi_3$ |
| $CdCNi_3$ | Cubic antiperovskite | ~3 | Similar to $ZnNNi_3$, sensitive to Ni substitution |
| $Sr_{3-x}SnO$ | Antiperovskite oxide | ~5 | Dirac metal-based superconductor **[58]** |
| $Pt_3SrP$ (family) | Antiperovskite phosphide | ~8.4 | Strong coupling superconductor **[56]** |

All of the findings above encourage additional research into novel superconductors with extended antiperovskite structures. Improving $T_c$ and knowing more about the fundamental relationship between the electronic and structure of crystals will be the top targets for researchers. It is observed that, besides electronic effects like superconductivity, antiperovskites also show unusual structural effects such as negative thermal expansion, which is presented in the next section.

### 3.4 Antiperovskites with Variable Thermal Expansion Behavior:

The complex interplay between the lattice, electrons, and phonons of solids leads to the intriguing & uncommon thermal expansion behavior known as negative thermal expansion **[59]**. Since Sleight and colleagues discovered isotropic NTE in $ZrW_2O_8$ in 1996, the emergence of various oxides as well as fluorides due to their $ReO_3$-like structure and negative thermal expansion behavior has since made up for the positive thermal expansion of other materials. These materials have been used as separate components or in expansion-controlled composites. In addition to $ZrW_2O_8$, a number of open-framework material systems, including the sodium zirconate phosphate family **[60]**. Fluorides formed by $ScF_3$ and $M_{1x}[M_2(CN)_6]$, where $M_1$ is Ag, Fe, and $M_2$ is Fe, Co **[61]**, display negative thermal expansion behavior. In such materials, it is thought that the corner-sharing polyhedra's correlated motion causes low-frequency vibrations that give rise to the negative thermal expansion. When compared to ceramic negative thermal expansion materials, a characteristic metal-based negative thermal expansion family exhibiting high electric & thermal conductivity, isotropic negative thermal expansion, along with excellent mechanical characteristics, is the manganese antiperovskites $Mn_3BA$, where B = Zn, Cu, Ni, Ge, Sn, and A = N, C **[62]**. In conclusion, negative thermal expansion materials have advanced significantly over the past 20 years, and antiperovskites have been convincingly established as distinct negative thermal expansion family members. One can anticipate that additional structural design initiatives, theoretical predictions, and particularly magneto-structural coupling will modulate the negative thermal expansion in antiperovskite materials.

### 3.5 Other New emerging properties of Antiperovskites

Other recently discovered characteristics of antiperovskites include giant Magnetostriction in some manganese nitride antiperovskites and ferromagnetic shape memory effects **[63]**. Based on first-principles calculations, a fresh class of antiperovskite-structured three-dimensional topological insulators was recently developed **[64]**. The antiperovskite $Mn_3Ni_{1x}Cu_xN$ showed a temperature coefficient of resistivity that was almost zero **[65]**. The $AE_3NBi$ group (where AE is Ca, Sr, and Ba) provides a foundation for straightforward integration with electronic gadgets due to its chemical inertness as well as a compatible lattice to significant semiconductors.

Additionally, recently created organic-inorganic hybrid antiperovskite-type materials that can function as new ferroelectrics enrich the antiperovskite family and broaden the antiperovskite family's range of applications. When exposed to external fields like pressure and temperature, antiperovskites also exhibit intriguing properties. It has frequently been claimed that $Mn_3Ga_{0.95}N_{0.94}$ exhibits a significant “Baromagnetic effect” **[66]**. Piezomagnetism was studied both through experimentation in $Mn_3NiN$ as well as in several types of magnetically frustrated Mn-based antiperovskite nitrides. Boldrin et al. **[67]** studied the multisite exchange-enhanced barocaloric response in $Mn_3NiN$ through the Néel transition temperature.

### 3.6 Phase Change Phenomena in Antiperovskites

Phase transitions play a central role in defining the multifunctional behavior of antiperovskite solids. Several Mn-based antiperovskites, such as $Mn_3GaC$ and $Mn_3SnC$, exhibit a sequence of temperature-dependent magnetic phase transitions including paramagnetic → ferromagnetic → antiferromagnetic states. Volume changes often accompany these transitions and result in giant magnetoresistance (GMR), magnetocaloric effect (MCE), and large Magnetostriction. For example, $Mn_3GaC$ shows a ferromagnetic to antiferromagnetic transition near 160 K, directly linked to its observed GMR of ~50% at 5 T. Similarly, pressure-induced phase transitions have been observed in $SbNMg_3$ and $AsNMg_3$, where the indirect band gap changes into a direct one above 6–7 GPa, significantly altering their optical response.

Another important area is superconductivity in $MgCNi_3$ and related systems, where the superconducting phase emerges below ~8 K, indicating a structural/electronic phase change in relation to the density of states at the Fermi level. Thermal expansion anomalies are also phase-transition driven: manganese antiperovskites ($Mn_3BA$; B = Zn, Cu, Ni, Ge, Sn; A = N, C) display negative thermal expansion due to strong magneto-structural coupling near magnetic ordering temperatures. Recent reports also highlight barocaloric and piezomagnetic effects in $Mn_3NiN$ and $Mn_3Ga_{0.95}N_{0.94}$, where applied pressure drives phase changes with promising caloric responses.

A collection of evidence suggests that antiperovskites represent extremely phase-tunable materials where structural, magnetic, or electronic transitions can be tuned by temperature, pressure, or chemical doping to develop interesting new functionalities. This strong coupling between phase change and physical properties, in addition to a promise of relatively low-cost synthesis, makes antiperovskites highly exciting for potential next-generation applications in solid-state cooling, sensing, and energy devices.

## 4. SUMMARY AND CONCLUSION

Antiperovskites are fascinating because a simple reversal of ionic positions unlocks a whole range of properties, from fast-ion conduction to superconductivity, magnetoresistance, and negative thermal expansion. This versatility makes them one of the few material families that can genuinely impact several technologies at once. The field, however, is still young. Many predicted compounds have not been synthesized, and even the known ones face hurdles such as stability and phase purity. Theory has advanced quickly, but experiments lag; closing this gap is essential for real applications. From the literature, some points are clear: Li- and Na-based antiperovskites are improving as solid electrolytes, Mn-based systems show striking magnetoresistive and caloric effects but need better control of transitions, Ni-based compounds are rare non-oxide superconductors, and doped Mn nitrides demonstrate useful negative thermal expansion. These examples confirm the structural flexibility of the antiperovskite lattice, even if progress is uneven across applications. Looking ahead, progress will depend on smarter synthesis routes, computational and machine learning tools to guide discovery, interface engineering for batteries, and careful tuning of magnetic and structural properties. If these challenges are met, antiperovskites could move from being mainly of academic interest to becoming a versatile platform with real impact on energy, electronics, and thermal technologies.

**Conflict of Interest:** This manuscript does not include a conflict of interest.

## ORCID

**Deepak Sharma,** https://orcid.org/0000-0001-9163-9050; **Peeyush Kumar Kamlesh,** https://orcid.org/0000-0001-7361-3519
**Ajay Singh Verma,** https://orcid.org/0000-0001-8223-7658

## REFERENCES

[1] B. Dudley, BP statistical review of world energy, Energy economic, Centre for energy economics research and policy. British Petroleum (2018).

[2] A. Roshan, G. Hou, Z. Zhu, Q. Yan, Q. Zheng, and G. Su, "Predicted lead-free perovskites for solar cells," Chemistry of Materials **30**, 718-728 (2018). https://doi.org/10.1021/acs.chemmater.7b04036

[3] D.M. Hoat, "Structural, optoelectronic and thermoelectric properties of antiperovskite compounds $Ae_3PbS$ (Ae= Ca, Sr and Ba): a first principles study," Physics Letters A, **383** 1648-1654 (2019). https://doi.org/10.1016/j.physleta.2019.02.013

[4] M.Y. Chern, D.A. Vennos, and F.J. DiSalvo, Synthesis, structure, and properties of anti-perovskite nitrides $Ca_3MN$, M= P, As, Sb, Bi, Ge, Sn, and Pb, J. Solid State Chemistry **96**, 415-425 (1992). https://doi.org/10.1016/s0022-4596(05)80276-2

[5] U. Rani, P.K. Kamlesh, R. Agrawal, A. Shukla, and A.S. Verma, "Emerging study on lead-free hybrid double perovskite $(CH_3NH_3)_2AgInBr_6$: potential material for energy conversion between heat and electricity," Energy Technology, **10**, 2200002 (2022). https://doi.org/10.1002/ente.202200002

[6] U. Rani, P.K. Kamlesh, R. Agrawal, J. Kumari, and A.S. Verma, "Electronic and thermo-physical properties of double antiperovskites $X_6SOA_2$ (X= Na, K and A= Cl, Br, I): a non-toxic and efficient energy storage materials," International Journal of Quantum Chemistry, **121**, e26759 (2021). https://doi.org/10.1002/qua.26759

[7] A. Dubey, N. Pandit, R. Singh, T.K. Joshi, B.L. Choudhary, P.K. Kamlesh, S. Al-Qaisi, *et al.*, "Lead-free alternative cation (Ethylammonium) in organometallic perovskites for thermoelectric applications," Journal of Molecular Modeling, **30**, 77 (2024). https://doi.org/10.1007/s00894-024-05867-7

[8] M. Rani, P.K. Kamlesh, S. Kumawat, U. Rani, G. Arora, and A.S. Verma, "Ab-initio calculations of structural, optoelectronic, thermoelectric, and thermodynamic properties of mixed-halide perovskites $RbPbBr_{3-x}I_x$ (x= 0 to 3): applicable in renewable energy devices," ECS Journal of Solid-State Science and Technology, **12**, 083006 (2023). https://doi.org/10.1149/2162-8777/acec9c

[9] U. Rani, P.K. Kamlesh, A. Shukla, and A.S. Verma, "Emerging potential antiperovskite materials $ANX_3$ (A= P, As, Sb, Bi; X= Sr, Ca, Mg) for thermoelectric renewable energy generators," Journal of Solid-State Chemistry, **300**, 122246 (2021). https://doi.org/10.1016/j.jssc.2021.122246

[10] U. Rani, P.K. Kamlesh, T.K. Joshi, S. Sharma, R. Gupta, S. Al-Qaisi, and A.S. Verma, "Alkaline earth-based antiperovskite AsPX3 (X Mg, Ca, and Sr) materials for energy conversion, efficient and thermoelectric applications," Physica Scripta, **98**, 075902 (2023). https://doi.org/10.1088/1402-4896/acd88a

[11] A. Bouhemadou, and R. Khenata, "Ab initio study of the structural, elastic, electronic and optical properties of the antiperovskite $SbNMg_3$," Computational Materials Science, **39**, 803-807 (2007). https://doi.org/10.1016/j.commatsci.2006.10.003

[12] M. Bilal, S. Jalali-Asadabadi, R. Ahmad, and I. Ahmad, "Electronic properties of antiperovskite materials from state-of-the-art density functional theory," J. Chemistry, **2015**, 495131 (2015). https://doi.org/10.1155/2015/495131

[13] V. Thangadurai, and W. Weppner, "Recent progress in solid oxide and lithium ion conducting electrolytes research," Ionics, **12**, 81-92 (2006). https://doi.org/10.1007/s11581-006-0013-7

[14] Y. Zhang, Y. Zhao, and C. Chen, "Ab initio study of the stabilities of and mechanism of superionic transport in lithium-rich antiperovskites," Physical Review B, **87**, 134303 (2013). https://doi.org/10.1103/physrevb.87.134303

[15] K. Kamishima, T. Goto, H. Nakagawa, N. Miura, M. Ohashi, N. Mori, and T. Kanomata, "Giant magnetoresistance in the intermetallic compound $Mn_3GaC$," Physical Review B, **63**, 024426 (2000). https://doi.org/10.1103/physrevb.63.024426

[16] Y. Sun, C. Wang, L. Chu, Y. Wen, M. Nie, and F. Liu, Low temperature coefficient of resistivity induced by magnetic transition and lattice contraction in $Mn_3NiN$ compound, Scripta Materialia **62**, 686-689 (2010). https://doi.org/10.1016/j.scriptamat.2010.01.027

[17] K. Asano, K. Koyama, and K. Takenaka, "Magnetostriction in $Mn_3CuN$," Applied Physics Letters, **92**, 161909 (2008). https://doi.org/10.1063/1.2917472

[18] G. Tang, X. Liu, S. Wang, T. Hu, C. Feng, C. Zhu, B. Zhu, and J. Hong, "Designing antiperovskite derivatives via atomic-position splitting for photovoltaic applications," Materials Horizons, **11**, 5320-5330 (2024). https://doi.org/10.1039/D4MH00526K

[19] T. Hu, C. Wu, M. Li, H. Qu, X. Luo, Y. Hou, S. Li, *et al*., "Pressure-dependent optoelectronic properties of antiperovskite derivatives $X_3AsCl_3$ (X= Mg, Ca, Sr, Ba): a first-principles study," Physical Chemistry Chemical Physics, **27**, 4144-4151 (2025). https://doi.org/10.1039/d4cp03619k

[20] P. Tong, B.S. Wang, and Y.P. Sun, "Mn-based antiperovskite functional materials: Review of research," Chinese Physics B, **22**, 067501 (2013). https://doi.org/10.1088/1674-1056/22/6/067501

[21] K. Takenaka, and H. Takagi, "Giant negative thermal expansion in Ge-doped anti-perovskite manganese nitrides," Applied Physics Letters, **87**, 261902 (2005). https://doi.org/10.1063/1.2147726

[22] Y. Nakamura, K. Takenaka, A. Kishimoto, and H. Takagi, "Mechanical Properties of Metallic Perovskite $Mn_3Cu_{0.5}Ge_{0.5}N$: High-Stiffness Isotropic Negative Thermal Expansion Material," J. American Ceramic Society, **92**, 2999-3003 (2009). https://doi.org/10.1111/j.1551-2916.2009.03297.x

[23] T. He, Q. Huang, A.P. Ramirez, Y. Wang, K.A. Regan, N. Rogado, and R.J. Cava, "Superconductivity in the non-oxide perovskite $MgCNi_3$," Nature, **411**, 54-56 (2001). https://doi.org/10.1038/35075014

[24] D. Fruchart, and F. Bertaut, "Magnetic studies of the metallic perovskite-type compounds of manganese," J. Physical Society of Japan, **44**, 781-791 (1978). https://doi.org/10.1143/jpsj.44.781

[25] M. Moakafi, R. Khenata, A. Bouhemadou, F. Semari, A.H. Reshak, and M. Rabah, "Elastic, electronic and optical properties of cubic antiperovskites $SbNCa_3$ and $BiNCa_3$," Computational Materials Science, **46**, 1051-1057 (2009). https://doi.org/10.1016/j.commatsci.2009.05.011

[26] M. Bilal, I. Ahmad, H.R. Aliabad, and S.J. Asadabadi, "Detailed DFT studies of the band profiles and optical properties of antiperovskites $SbNCa_3$ and $BiNCa_3$," Computational Materials Science, **85**, 310-315 (2014). https://doi.org/10.1016/j.commatsci.2013.12.035

[27] C. Feng, C. Wu, X. Luo, T. Hu, F. Chen, S. Li, S. Duan, *et al*., "Pressure-dependent electronic, optical, and mechanical properties of antiperovskite $X_3NP$ (X= Ca, Mg): A first-principles study," Journal of Semiconductors, **44**, 102101 (2023). https://doi.org/10.1088/1674-4926/44/10/102101

[28] I.R. Shein, and A.L. Ivanovskii, "Electronic band structure and chemical bonding in the new antiperovskites $AsNMg_3$ and $SbNMg_3$," J. Solid State Chemistry, **177**, 61-64 (2004). https://doi.org/10.1016/s0022-4596(03)00309-8

[29] S.V. Ovsyannikov, and V.V. Shchennikov, "High-pressure routes in the thermoelectricity or how one can improve a performance of thermoelectrics," Chemistry of Materials, **22**, 635-647 (2010). https://doi.org/10.1021/cm902000x

[30] A. Bouhemadou, R. Khenata, M. Chegaar, and S. Maabed, "First-principles calculations of structural, elastic, electronic and optical properties of the antiperovskite $AsNMg_3$," Physics Letters A, **371**, 337-343 (2007). https://doi.org/10.1016/j.physleta.2007.06.030

[31] T. Belaroussi, B. Amrani, T. Benmessabih, N. Iles, and F. Hamdache, "Structural and thermodynamic properties of antiperovskite $SbNMg_3$," Computational Materials Science, **43**, 938-942 (2008). https://doi.org/10.1016/j.commatsci.2008.02.006

[32] K. Amara, M. Zemouli, M. Elkeurti, A. Belfedal, and F. Saadaoui, "First-principles study of $XNMg_3$ (X= P, As, Sb and Bi) antiperovskite compounds," J. Alloys and Compounds, **576**, 398-403 (2013). https://doi.org/10.1016/j.jallcom.2013.06.003

[33] K. Haddadi, A. Bouhemadou, L. Louail, F. Rahal, and S. Maabed, "Prediction study of the structural, elastic and electronic properties of $ANSr_3$ (A= As, Sb and Bi)," Computational Materials Science, **46**, 881-886 (2009). https://doi.org/10.1016/j.commatsci.2009.04.028

[34] M. Hichour, R. Khenata, D. Rached, M. Hachemaoui, A. Bouhemadou, A.H. Reshak, and F. Semari, "FP-APW+ lo study of the elastic, electronic and optical properties for the cubic antiperovskite $ANSr_3$ (A= As, Sb and Bi) under pressure effect," Physica B: Condensed Matter, **405**, 1894-1900 (2010). https://doi.org/10.1016/j.physb.2010.01.069

[35] J.M. Tarascon, and M. Armand, "Issues and challenges facing rechargeable lithium batteries," Nature, **414**, 359-367 (2001). https://doi.org/10.1038/35104644

[36] E. Quartarone, and P. Mustarelli, "Electrolytes for solid-state lithium rechargeable batteries: recent advances and perspectives," Chemical Society Reviews, **40**, 2525-2540 (2011). https://doi.org/10.1039/C0CS00081G

[37] J. C. Bachman, S. Muy, A. Grimaud, H. H. Chang, N. Pour, S. F. Lux, and Y. Shao-Horn, "Inorganic solid-state electrolytes for lithium batteries: mechanisms and properties governing ion conduction," Chemical Reviews, **116**, 140-162 (2016). https://doi.org/10.1021/acs.chemrev.5b00563.s001

[38] A.R. Rodger, J. Kuwano, and A.R. West, "Li+ ion conducting γ solid solutions in the systems $Li_4XO_4$-$Li_3YO_4$: X= Si, Ge, Ti; Y= P, as, V; $Li_4XO_4$-$LiZO_2$: Z= Al, Ga, Cr and $Li_4GeO_4$-$Li_2CaGeO_4$," Solid State Ionics, **15**, 185-198 (1985). https://doi.org/10.1016/0167-2738(85)90002-5

[39] H. J. Deiseroth, S. T. Kong, H. Eckert, J. Vannahme, C. Reiner, T. Zaiß, and M. Schlosser, "$Li_6PS_5X$: a class of crystalline Li-rich solids with an unusually high Li+ mobility," Angewandte Chemie International Edition, **47,** 755-758 (2008). https://doi.org/10.1002/anie.200703900

[40] V. Thangadurai, S. Narayanan, and D. Pinzaru, "Garnet-type solid-state fast Li ion conductors for Li batteries: critical review," Chemical Society Reviews, **43**, 4714-4727 (2014). https://doi.org/10.1039/c4cs00020j

[41] A. Martinez-Juarez, C. Pecharromán, J.E. Iglesias, and J.M. Rojo, "Relationship between activation energy and bottleneck size for Li+ ion conduction in NASICON materials of composition $LiMM'(PO_4)_3$; M, M'= Ge, Ti, Sn, Hf," J. Physical Chemistry B, **102**, 372-375 (1998). https://doi.org/10.1021/jp973296c

[42] S.K. Moharana, and P.K.K. Padmanabhan, "Structural stability and ion transport mechanism of divalent cation doped anti-perovskites: Insights from molecular dynamics investigation," Physica Scripta, **100**, 095909 (2025). https://doi.org/10.1088/1402-4896/adfe40

[43] L. Van Duong, M.T. Nguyen, and Y.A. Zulueta, "Unravelling the alkali transport properties in nanocrystalline $A_3OX$ (A= Li, Na, X= Cl, Br) solid state electrolytes. A theoretical prediction," RSC Advances, **12,** 20029-20036 (2022). https://doi.org/10.1039/d2ra03370d

[44] S. Li, J.L. Zhu, Y.G. Wang, J.W. Howard, X.J. Lü, Y.T. Li, R.S. Kumar, *et al.*, "Reaction mechanism studies towards effective fabrication of lithium-rich anti-perovskites $Li_3OX$ (X= Cl, Br)," Solid State Ionics, **284**, 14-19 (2016). https://doi.org/10.1016/j.ssi.2015.11.027

[45] C. Zener, "Interaction between the d-shells in the transition metals. II. Ferromagnetic compounds of manganese with perovskite structure," Physical Review, **82**, 403 (1951). https://doi.org/10.1103/physrev.82.403

[46] S.A. Wolf, and D. Treger, "Spintronics: A new paradigm for electronics for the new millennium," IEEE Transactions on Magnetics, **36**, 2748-2751 (2000). https://doi.org/10.1109/20.908580

[47] B.S. Wang, P. Tong, Y.P. Sun, L.J. Li, W. Tang, W.J. Lu, and W.H. Song, "Enhanced giant magnetoresistance in Ni-doped antipervoskite compounds $GaCMn_{3-x}Ni_x$ (x= 0.05, 0.10)," Applied Physics Letters, **95**, 222509 (2009). https://doi.org/10.1063/1.3268786

[48] B.G. Shen, J.R. Sun, F.X. Hu, H.W. Zhang, and Z.H. Cheng, "Recent progress in exploring magnetocaloric materials," Advanced Materials, **21**, 4545-4564 (2009). https://doi.org/10.1002/adma.200901072

[49] A.M. Tishin, "Magnetocaloric effect: Current situation and future trends," J. Magnetism and Magnetic Materials, **316**, 351-357 (2007). https://doi.org/10.1016/j.jmmm.2007.03.015

[50] M.H. Yu, L.H. Lewis, and A.R. Moodenbaugh, "Large magnetic entropy change in the metallic antiperovskite $Mn_3GaC$," J. Applied Physics, **93**, 10128-10130 (2003). https://doi.org/10.1063/1.1574591

[51] S. Iikubo, K. Kodama, K. Takenaka, H. Takagi, M. Takigawa, and S. Shamoto, "Local lattice distortion in the giant negative thermal expansion material $Mn_3Cu_{1-x}Ge_xN$," Physical Review Letters, **101**, 205901 (2008). https://doi.org/10.1103/physrevlett.101.205901

[52] K. Takenaka, T. Inagaki, and H. Takagi, "Conversion of magnetic structure by slight dopants in geometrically frustrated antiperovskite $Mn_3GaN$," Applied Physics Letters, **95**, 132508 (2009). https://doi.org/10.1063/1.3243340

[53] W.S. Kim, E.O. Chi, J.C. Kim, H.S. Choi, and N.H. Hur, "Close correlation among lattice, spin, and charge in the manganese-based antiperovskite material," Solid State Communications, **119**, 507-510 (2001). https://doi.org/10.1016/S0038-1098(01)00279-4

[54] C.M.I. Okoye, "Optical properties of the antiperovskite superconductor $MgCNi_3$," J. Physics: Condensed Matter, **15**, 833 (2003). https://doi.org/10.1088/0953-8984/15/6/310

[55] S. Mollah, "The physics of the non-oxide perovskite superconductor $MgCNi_3$," J. Physics: Condensed Matter, **16**, R1237 (2004). https://doi.org/10.1088/0953-8984/16/43/r01

[56] T. Takayama, K. Kuwano, D. Hirai, Y. Katsura, A. Yamamoto, and H. Takagi, "Strong Coupling Superconductivity at 8.4 K in an Antiperovskite Phosphide $SrPt_3P$," Physical Review Letters, **108**, 237001 (2012). https://doi.org/10.1103/physrevlett.108.237001

[57] H. Zhang, Y. Zhu, Z. Li, P. Fan, W. Ma, and B. Xie, "High discharged energy density of polymer nanocomposites containing paraelectric $SrTiO_3$ nanowires for flexible energy storage device," J. Alloys and Compounds, **744**, 116-123 (2018). https://doi.org/10.1016/j.jallcom.2018.02.052

[58] M. Oudah, A. Ikeda, J. N. Hausmann, S. Yonezawa, T. Fukumoto, S. Kobayashi, and Y. Maeno, "Superconductivity in the antiperovskite Dirac-metal oxide $Sr_{3-x}SnO$," Nature Communications, **7**, 13617 (2016). https://doi.org/10.1038/ncomms13617

[59] J.S.O. Evans, "Negative thermal expansion materials," J. Chemical Society, Dalton Transactions, **19**, 3317-3326 (1999). https://doi.org/10.1039/A904297K

[60] J.S.O. Evans, W.I.F. David, and A.W. Sleight, "Structural investigation of the negative-thermal-expansion material $ZrW_2O_8$," Acta Crystallographica Section B: Structural Science, **55**, 333-340 (1999). https://doi.org/10.1107/s0108768198016966

[61] A.L. Goodwin, M. Calleja, M.J. Conterio, M.T. Dove, J.S.O. Evans, D.A. Keen, and M.G. Tucker, "Colossal positive and negative thermal expansion in the framework material $Ag_3[Co(CN)_6]$," Science, **319**, 794-797 (2008). https://doi.org/10.1126/science.1151442

[62] P. Tong, D. Louca, G. King, A. Llobet, J.C. Lin, and Y.P. Sun, "Magnetic transition broadening and local lattice distortion in the negative thermal expansion antiperovskite $Cu_{1-x}Sn_xNMn_3$," Applied Physics Letters, **102**, 041908 (2013). https://doi.org/10.1063/1.4790151

[63] T. Hamada, and K. Takenaka, "Phase instability of magnetic ground state in antiperovskite $Mn_3ZnN$: Giant magnetovolume effects related to magnetic structure," J. Applied Physics, **111**, 07A904 (2012). https://doi.org/10.1063/1.3670052

[64] Y. Sun, X.Q. Chen, S. Yunoki, D. Li, and Y. Li, "New family of three-dimensional topological insulators with antiperovskite structure," Physical Review Letters, **105**, 216406 (2010). https://doi.org/10.1103/physrevlett.105.216406

[65] L. Ding, C. Wang, L. Chu, J. Yan, Y. Na, Q. Huang, and X. Chen, "Near zero temperature coefficient of resistivity in antiperovskite $Mn_3Ni_{1-x}Cu_xN$," Applied Physics Letters, **99**, 251905 (2011). https://doi.org/10.1063/1.3671183

[66] K. Shi, Y. Sun, J. Yan, S. Deng, L. Wang, H. Wu, and C. Wang, "Baromagnetic effect in antiperovskite $Mn_3Ga_{0.95}N_{0.94}$ by neutron powder diffraction analysis," Advanced Materials, **28**(7), 3761-376 (2016). https://doi.org/10.1002/adma.201600310

[67] D. Boldrin, E. Mendive-Tapia, J. Zemen, J.B. Staunton, T. Hansen, A. Aznar, and L.F. Cohen, "Multisite exchange-enhanced barocaloric response in $Mn_3NiN$," Physical Review X, **8**, 041035 (2018). https://doi.org/10.1103/physrevx.8.041035

# ДОСЯГНЕННЯ В ВИВЧЕННІ ТВЕРДИХ ТІЛ ІЗ СТРУКТУРОЮ АНТИПЕРІВСКІТУ: КОМПЛЕКСНИЙ ОГЛЯД

**Шраван Кумар[1], Сушил Кумар Патхак[2], Діпак Шарма[3], Піюш Кумар Камлеш[4],
Аджай Сінгх Верма[5]**
*[1]Кафедра фізики, G.L.A. Коледж, Медінінагар (Далтонгандж), Паламау, Університет Ніламбер Пітамбер, Джаркханд 822101, Індія*
*[2]Кафедра фізики, Чандрапур, Помбхурна, Чандрапур, Махараштра-442918, Індія*
*[3]Кафедра прикладних та гуманітарних наук, інженерний коледж ІІМТ, Велика Нойда, 201310, Індія*
*[4]Кафедра фізики, Університет Пурніма, Джайпур – 303905, Раджастхан, Індія*
*[5]Кафедра фізики, школа інженерії та технологій Ананда, Університет Шарда, Агра, Кітхам, Агра – 282007, Індія*

Тверді тіла зі структурою антиперовскіту привертають все більшу увагу як новий клас функціональних матеріалів. На відміну від звичайних перовскітів, їх перевернута кубічна структура обумовлює незвичайні властивості, що легко налаштовуються: від провідності швидких іонів і гігантського магнітоопору до надпровідності та негативного теплового розширення. Ці різні характеристики вказують на перспективність їх застосування в таких областях, як твердотільні акумулятори, енергозберігаюче охолодження, надпровідна електроніка та терморегулювання. У цьому огляді узагальнені недавні роботи, як експериментальні, і теоретичні, і підкреслюється, як прості кубічні грати може забезпечити настільки широкий спектр функціональних можливостей. Ми стверджуємо, що структурна універсальність антиперовскітів є сполучною ланкою між іонним транспортом, спін-решітковим зв'язком, надпровідністю та тепловим розширенням. Нещодавні досягнення в галузі твердих електролітів на основі Li і Na з високою провідністю, гігантськими магніто- і барокалоричними відгуками, неоксидною надпровідністю та ізотропним негативним тепловим розширенням демонструють, що антиперовскіти зберігають наукову значущість і стають все більш життєздатними конкурентами кращим матеріалом.

**Ключові слова:** *антиперовскіти; магнетизм; надпровідність; відновлювана енергія; матеріали для акумуляторів*

East European Journal of Physics. **4**. 14–29 (2025)

DOI: 10.26565/2312-4334-2025-4-02 ISSN 2312-4334

# HUBBLE'S LAW AND ITS EXPONENTIAL GENERALIZATION WITH COSMOLOGICAL APPLICATIONS

**Ashraful Islam**[*]

*Nippon Koei Bangladesh Limited, Plot-11/A, Road-48, Gulshan-2, Dhaka-1212, Bangladesh*

[*]*Corresponding Author e-mail: ashrafulce06@gmail.com*

Received July 18, 2025; revised September 13, 2025; in final form September 18, 2025; accepted September 19, 2025

Hubble's law reveals how the components of the universe adhere to overarching dynamical rules on a cosmological scale. While it is most renowned for describing the universe's expansion, a general displacement equation derived in alignment with this law, along with a general equation of converging displacement, has been applied to estimate the time remaining before the Milky Way and Andromeda collide. This estimate closely aligns with results from numerical simulations of other studies. Additionally, the implications of this generalized equation provide valuable insights into key cosmological enigmas, including the time variation of the Hubble parameter, the cosmological past incompleteness, and the enduring mystery of the relationship between the subtle value of the cosmological constant and the quantum zero-point energy of the vacuum. It has also been successful in explaining the structure of spiral galaxies.

**Keywords:** *Hubble's Law, Galaxy Collision, Cosmological Constant,Vacuum's energy, Spiral Galaxy Structure*

**PACS:** specify the PACS code(s) here

## 1. INTRODUCTION

Galileo famously demonstrated in a public experiment that, in the uniform gravitational field produced by Earth, all objects fall at the same rate, regardless of their weight. Later, Eötvös provided evidence that gravitational mass and inertial mass are equivalent. Kepler's laws also describe the motion of planets in terms of geometric principles, with the motion being independent of the planets' masses but dependent on the Sun's gravitational influence. These intriguing natural phenomena likely influenced Einstein, who developed the theory of general relativity, positing that gravity is fundamentally connected to the geometry of space and time. This is why it's reasonable to say that gravity is, in essence, geometry [1, 2]. Therefore, if it can be established that an object's motion is influenced solely by a specific gravitational field, we can derive a general displacement relation that depends only on time, regardless of the object's mass or chemistry.

Utilizing a fundamental mathematical approach, a general displacement relation was formulated as a power series [3, 4, 5]. By applying Taylor's expansion around the initial point or origin, specifically, the Maclaurin expansion [3, 4], it was ultimately shown that displacement can be described as an exponential function of time, thereby supporting the theoretical foundation of Hubble's relation. The well-known Hubble's relation, as of now, has been established solely through observational evidence. However, with the advent of the general displacement equation, a theoretical foundation has been established for Hubble's relation, complementing the empirical observations.

Here, the general displacement is derived based on plausible mathematical and physical assumptions, ultimately leading to Hubble's relation, which is consistently and unambiguously supported by numerous empirical observations of large-scale cosmic dynamics [6, 7, 8, 9, 10, 11, 12, 13]. Furthermore, the general displacement relation provides a mathematical explanation to address a cosmic initial incompleteness. This incompleteness is merely an unavoidable mathematical outcome; however, it holds no physical significance. The mathematical inevitability of the cosmic initial incompleteness inherent in the general relativistic approach is re-evaluated using the time exponential expansion of the universe, as inferred from the isotropic and uniform cosmic diverging displacement.

The universe is full of phenomena, many of which remain beyond our current understanding or the scientific models we've developed. However, the general displacement relation has proven quite useful in explaining certain enigmatic cosmic phenomena, particularly those related to large distant gravitational interactions.A similar mathematical and physically plausible approach is employed to derive the general equation for converging dynamical displacement. This approach is further validated by consistently estimating the time required for the upcoming collision between the Milky Way (MW) and Andromeda (M31). It has been effective in estimating the time remaining before the imminent collision between these two galaxies, with results that align with previous numerically simulated analyses where the technique of N-body simulation is employed to estimate the imminent collision. [14, 15].

The general time exponential displacement relation was applied in a quasi-quantum model, serving as the amplitude of classical harmonic oscillation to determine a finite and specific frequency. This frequency was then used to calculate the lowest state energy of the oscillator, modeled as a quantum harmonic oscillator. Since the time-exponential displacement equation is not a periodic function, Fourier transformation is applied to determine the characteristic frequency of the oscillation when the amplitude is modeled as an exponential function of time. This approach proved instrumental in

***Cite as:*** A. Islam, East Eur. J. Phys. 4, 14 (2025), https://doi.org/10.26565/2312-4334-2025-4-02

demonstrating the consistency between the subtle observational value of the cosmological constant and the zero-point energy of the vacuum. This classical general relationship demonstrates consistency between value of the cosmological constant and the quantum ground-state energy of the vacuum through a quasi-quantum technique. While the quantum field theoretical prediction for the cosmological constant shows a significant degree of inconsistency with observed values.

In addition to the aforementioned applications, one notable application of the time exponential general displacement equation is its use in providing a mathematical explanation for the structure of spiral galaxies.

## 2. HUBBLE'S LAW AND ITS GENERALIZATION

Edwin Hubble's prolonged observations have unveiled a crucial discovery, indicating that in expansive cosmic distances, celestial units like galaxies are steadily moving away from each other, and this motion is directly and linearly linked to the distances that exist between them [6, 7, 8]. This outcome, subsequently analyzed through numerous further observations, has provided deeper insights into the dynamic relationships between celestial units and their velocities in the vast cosmic distances [9, 10, 11, 12, 13]. Which can be summarized as a simple equation for recession velocity:[16, 17]

$$\frac{dl}{dt} = v = Hl \tag{1}$$

By avoiding the negative and complex solutions, a solution for the above equation can be found by rearranging the terms involved followed by integrating both sides, with respect to the relevant variables as:

$$l = l_0 e^{Ht} \tag{2}$$

The above relation shows a non-degenerate relation, since by differentiating the sides of Hubble's law, we can find the general relation for the time derivatives of displacement variable as: $\ddot{l} \propto \dot{l}$, $\dddot{l} \propto \ddot{l}$, and so on. This implies that the time derivatives of acceleration do not vanish. The third and fourth derivatives of position are known as the jerk and snap, respectively [18]. Furthermore, higher-order time derivatives are a conventional concept in the study of robotics dynamics [19] and aerodynamics. Jerk and snap were also used as higher-order derivatives of the Friedmann–Lemaître–Robertson–Walker (FLRW) scale factor [20]. The term on the right-hand side of equation (2) is differentiable up to infinite order and continuous with respect to time. Importantly, the motion described by equation (2) is general and independent of the individual mass. As a result, developing a Hamiltonian formulation is unnecessary for our mass-independent motion analysis, and therefore any subsequent unbounded Hamiltonian is irrelevant. We will thoroughly examine the mathematical feasibility of equation (2) in principle in the following subsection 2.1. This simple relation is powerful enough to reshape our classical understanding of dynamics, particularly when applied to long-distance motion.

### 2.1. General equation for diverging displacement

Consider an object with an initial position $x_0$, defined within an inertial reference frame. After a time interval $t$, measured in the same frame, the object's position becomes $x$. Hubble's law, which establishes a proportionality between velocity and distance, implies that displacement can be described as a higher-order function of time. Let us express this displacement using a higher-order series expansion as a function of time:

$$x = f(t) = \sum_{n=0}^{\infty} x_n t^n \tag{3}$$

Using the Maclaurin expansion, we can express the displacement $x(t)$ as a higher-order series in terms of time $t$. The Maclaurin series expands a function about $t = 0$, leading to the following expression:

$$x = f(t) = [x]_{t=0} + \frac{1}{1!}\left[\frac{dx}{dt}\right]_{t=0} t + \frac{1}{2!}\left[\frac{d^2x}{dt^2}\right]_{t=0} t^2 + \frac{1}{3!}\left[\frac{d^3x}{dt^3}\right]_{t=0} t^3 + \cdots + \frac{1}{n!}\left[\frac{d^nx}{dt^n}\right]_{t=0} t^n + \cdots$$

We define the velocity $v$, acceleration $a$, the third derivative term $a_1$, and similarly, the $n$-th derivative term as $\frac{d^n x}{dt^n} = a_{n-2}$, with any zero subscripts representing the initial values:

$$\begin{aligned} x &= x_0 + \frac{1}{1!}[v]_{t=0}\, t + \frac{1}{2!}[a]_{t=0}\, t^2 + \frac{1}{3!}[a_1]_{t=0}\, t^3 + \cdots + \frac{1}{n!}[a_{n-2}]_{t=0}\, t^n + \cdots \\ &= x_0 + v_0 t + \frac{1}{2!} a_0 t^2 + \sum_{n=3}^{\infty} \frac{1}{n!}[a_{n-2}]_{t=0}\, t^n \end{aligned}$$

Here we assume $x_0 > 0$.

$$x = x_0 \left\{ 1 + \left(\frac{v_0}{x_0} t\right) + \frac{1}{2!}\left(\sqrt[2]{\frac{a_0}{x_0}}\, t\right)^2 + \sum_{n=3}^{\infty} \frac{1}{n!}\left(\sqrt[n]{\frac{(a_{n-2})_{t=0}}{x_0}}\, t\right)^n \right\} \tag{4}$$

In this expression, the coefficients of each time-dependent term are defined using the initial kinematic quantities, such as the initial velocity $v_0$, acceleration $a_0$, and higher derivatives $[a_{n-2}]_{t=0}$. By dimensional analysis, each of these coefficients must have the dimension of inverse time, $[T^{-1}]$, which suggests a common physical scaling factor. If we interpret this displacement as occurring within a homogeneous and isotropic system, i.e., one that is directionally invariant and uniformly distributed, then the rate of displacement or expansion must also exhibit isotropic scaling. This concept is well aligned with the cosmological principle employed in Friedmann's models of the universe. In cosmology, under the assumptions of homogeneity and isotropy, the Friedmann–Lemaître–Robertson–Walker (FLRW) metric leads to a scale factor $\alpha(t)$ whose rate of change defines the Hubble parameter: $H = \frac{\dot{\alpha}}{\alpha}$. This formulation implies an exponential-like evolution under certain energy conditions, and hence supports the plausibility of uniform time scaling in the displacement function. Therefore, if the displacement depends only on time, and the system remains homogeneous and isotropic during its evolution, it is physically reasonable to assign the same constant value to all coefficients of the time powers in the expansion. At any given epoch or over a small time interval, we can thus define a single inverse time constant $\zeta$, such that:

$$\zeta = \frac{v_0}{x_0} = \sqrt[2]{\frac{a_0}{x_0}} = \sqrt[n]{\frac{(a_{n-2})_{t=0}}{x_0}}$$

and using equation (4), we can get:

$$x = x_0 \left\{ 1 + \zeta t + \frac{1}{2!}(\zeta t)^2 + \cdots + \sum_{n=3}^{\infty} \frac{1}{n!}(\zeta t)^n \right\}$$

$$x = x_0 e^{\zeta t} \tag{5}$$

From this, Hubble's relation can be easily derived as: $\dot{x} = \zeta x$ or $\dot{x} \propto x$. Indeed, our defined constant $\zeta$ is equivalent to the Hubble parameter $H$ in case of displacement due to cosmic expansion, which can be regarded as the constant $H_0$ for a particular epoch of cosmic time. Equation ( 5) is identical and equivalent to equation (2) as follows, and it represents the general equation for cosmological diverging displacement:

$$x = x_0 e^{H_0 t} \tag{6}$$

In the Maclaurin expansion, it is important to note that we expand the displacement function from an initial point in time. This approach is essential since time is the only independent variable in the function defined by equation (6). For measurement purposes, we must define a reference point, and the most convenient choice is our current cosmological spacetime point, defined as $(t = 0, x = x_0)$. Future time corresponds to positive $t$, while past time corresponds to negative $t$, relative to this arbitrarily and conveniently chosen origin of measurement. The Hubble constant is determined by observing the current velocity and distance of cosmic objects with respect to this reference point. As time progresses over a nontrivial interval (e.g., $t_f$), velocity measurements will no longer be referenced to the initial fixed origin. Instead, they must be referenced to a transformed origin that shifts along the spatial axis as time changes. As a result, the transformed displacement will be:

$$x_{f0} = x_0 e^{H_0 t_f}.$$

Given an initial value for velocity, namely the present-time velocity $v_0$, the resulting transformed velocity is expressed as:

$$v_{f0} = v_0 + \frac{d^2 x_{f0}}{dt^2} t_f.$$

$$v_{f0} = v_0 + t_f x_0 H_0^2 e^{H_0 t_f}.$$

The Hubble parameter at this future point will then be measured as:

$$H_{f0} = \frac{v_{f0}}{x_{f0}} = \frac{v_0 + x_0 t_f H_0^2 e^{H_0 t_f}}{x_0 e^{H_0 t_f}} = \frac{v_0}{x_0} \frac{1}{e^{H_0 t_f}} + t_f H_0^2,$$

which is evidently $\neq \frac{v_0}{x_0}$. The above argument regarding the inequality of the Hubble parameter across different cosmic epochs, commonly referred to as the Hubble tension, is similarly applicable to the distant past if the Hubble parameter were to be measured. This argument provides a straightforward explanation of the enigmatic concept known as the Hubble tension. The time dependency of the Hubble parameter can be well comprehended through general relativity, in connection with the FLRW scale factor, as a result of employing the FLRW metric in Einstein's field equations, which we will examine in Section 5.

### 2.2. General equation for converging displacement

Now consider an object with an initial position $x_0$, defined within an inertial reference frame. After a time interval $t$, measured in the same frame, the object's position becomes $x$. In this scenario, as time increases, $x$ decreases. As a result, the time derivatives of displacement, such as $\frac{dx}{dt}$, $\frac{d^2x}{dt^2}$, and so forth, along with their initial values, will have negative signs. Therefore, the Maclaurin series expansion of the general converging displacement will be:

$$x = x_0 - v_0 t - \frac{1}{2!}a_0 t^2 - \sum_{n=3}^{\infty} \frac{1}{n!}\left[a_{n-2}\right]_{t=0} t^n.$$

$$x = 2x_0 - \left(x_0 + v_0 t + \frac{1}{2!}a_0 t^2 + \sum_{n=3}^{\infty} \frac{1}{n!}\left[a_{n-2}\right]_{t=0} t^n\right).$$

$$x = 2x_0 - \left[x_0\left\{1 + \frac{v_0}{x_0}t + \frac{1}{2!}\left(\sqrt{\frac{2a_0}{x_0}}\,t\right)^2 + \sum_{n=3}^{\infty}\frac{1}{n!}\left(\sqrt{\frac{n[a_{n-2}]_{t=0}}{x_0}}\,t\right)^n\right\}\right].$$

Defining the constant for converging displacement as

$$\xi = \frac{v_0}{x_0} = \sqrt{\frac{2a_0}{x_0}} = \sqrt{\frac{n[a_{n-2}]_{t=0}}{x_0}},$$

we obtain

$$x = 2x_0 - x_0\left\{1 + \xi t + \frac{1}{2!}(\xi t)^2 + \cdots + \sum_{n=3}^{\infty}\frac{1}{n!}(\xi t)^n\right\} = 2x_0 - x_0 e^{\xi t}.$$

$$x = x_0(2 - e^{\xi t}) \tag{7}$$

The aforementioned equation (7) was derived by considering the convergence of two masses, ignoring any external perturbations, and assuming that the motion is dominated by the center of mass. Therefore, this relation applies to cases of interacting motion between galaxies with well-defined geometric shapes, supported by the presence of significant amounts of non-baryonic dark matter. In these cases, the constituents are strongly bound to the galactic nucleus, which can reasonably be assumed to contain a supermassive black hole.

## 3. ESTIMATING THE TIME REMAINING FOR MILKY WAY AND ANDROMEDA COLLISION

Contemporary observations confirm that the Andromeda Galaxy is directly approaching the Milky Way, making their collision inevitable [14, 21, 22, 23, 24, 25, 26]. Assuming a direct approach, the time remaining until the collision can be estimated using equation (7). This time represents the duration required for the distance between the two galaxies to decrease from the current initial distance, defined as $x_0$, to zero, given the current approach velocity of Andromeda, represented as $v_0$. From equation (7), setting $x = 0$, we calculate the time:

$$0 = x_0\left(2 - e^{\xi t}\right)$$

$$t = \frac{\ln 2}{\xi} \tag{8}$$

Where $\xi = \frac{v_0}{x_0}$. and considered conversion for 1year = 365.25 days. Using the current data on M31's approaching velocity and distance, the estimated time remaining until the collision is summarized in the Table 1.

**Table 1.** Assessment of remaining time for collision between the Milky Way and Andromeda using data from different studies.

| Current Radial Velocity, $v_0$ (km/s) | Current Distance, $x_0$ (Mpc) | $\xi$ (km/s/Mpc) | Remaining Time for Collision, $t = \frac{\ln 2}{\xi}$ (Gyr) |
|---|---|---|---|
| 120 [22] | 0.78 [21] | 153.846 | 4.405 |
| 110 [23] | 0.785 [27] | 140.127 | 4.837 |
| 115.7 [15] | 0.761 [28] | 152.037 | 4.458 |
| 109.3 [25] | 0.77 [14] | 141.948 | 4.775 |
| 110 [23] | 0.8 [24] | 137.5 | 4.929 |

It is important to clarify that the present analysis considers only a single degree of freedom, the radial component of M31's motion. While it is true that M31 also has a tangential velocity component, the radial and tangential motions can be treated as dynamically independent, much like two-dimensional motion under the influence of a potential field.

Furthermore, the effects of dynamical friction and gravitational perturbations from neighboring galaxies tend to moderate the radial motion, making it approximately constant over large timescales. However, the system still evolves dynamically through a spiral infall trajectory, resulting from the continuous interplay between radial decay and angular momentum loss. An analogous coplanar spiral motion, commonly observed within disk galaxies, will be further discussed in section 6.

Since $\xi$ is defined as a constant, the remaining time for collision, $t = \frac{\ln 2}{\xi}$, is likewise a fixed quantity. This is reasonable, as it aligns with our understanding that the unperturbed gravitational interaction time under a given gravitational field is also definite. From Table 1, the estimated time remaining until the upcoming collision between the Milky Way (MW) and Andromeda Galaxy (M31) is approximately 4.4 to 4.93 billion years, aligning closely with contemporary estimates derived from numerical simulation data. For example [14] reported a collision timeline of approximately 4.5 billion years, based on precise measurements of galactic motions. Furthermore, this estimate is also consistent with the timeline of 4 to 5 billion years suggested by [15], which was derived using numerical N-body simulation data.

## 4. COSMOLOGICAL CONSTANT AND QUANTUM ZERO-POINT ENERGY

The relationship between the cosmological constant and vacuum energy density, interpreted as quantum zero-point energy, was discussed in the seminal work by Zel'dovich [29]. Notable recent studies [30, 31, 32, 33] have further explored this correlation. Notable references can be found in the comprehensive book authored by Hobson [34], and Carroll [35], and the influential article by Steven Weinberg [36] about the cosmological constant value. By employing the concept that vacuum pressure is analogous to perfect fluid pressure [29, 34, 35, 37, 38], the cosmological constant was derived as:

$$\Lambda = \frac{8\pi G\rho_{\text{vac}}}{c^2} \tag{9}$$

This can be achieved through mathematically straightforward and physically plausible assumptions by utilizing Einstein's field equation for empty space with the presence of the cosmological constant. Einstein field equation in covariant form in the presence of matter and employing the cosmological constant [34, 37]:

$$R_{\mu\nu} - \frac{1}{2}Rg_{\mu\nu} + \Lambda g_{\mu\nu} = -\kappa T_{\mu\nu} \tag{10}$$

By decomposing the energy-momentum tensor $T_{\mu\nu}$ into components for matter, $[T_{\mu\nu}]_m$ and vacuum, $[T_{\mu\nu}]_{\text{vac}}$, and considering the context of flat spacetime without matter, we set the Einstein tensor, $R_{\mu\nu} - \frac{1}{2}Rg_{\mu\nu} = 0$. Factoring out the $[T_{\mu\nu}]_m$ term for the vacuum, the above equation (10) becomes:

$$\Lambda g_{\mu\nu} = -\kappa[T_{\mu\nu}]_{\text{vac}} = -\kappa[T^{00}]g_{\mu\nu}$$

By utilizing the negative energy property of the vacuum, we obtain from the above equation:

$$\Lambda g_{\mu\nu} = \kappa\rho_{\text{vac}}c^2 g_{\mu\nu}$$

By substituting the value of the constant $\kappa$, the above equation becomes:

$$\Lambda = \frac{8\pi G\rho_{\text{vac}}}{c^2}$$

Thus, it can be concluded that equation (9) represents a form of Einstein's field equation under the conditions of empty space, where the energy-momentum tensor does not vanish but is present in the form of vacuum energy, and in the presence of cosmological constant. Applying the Jeans instability condition [22, 39, 40, 41, 42] considering the fluid mechanical analogy to the entire universe reveals that for stability, the universe must be homogeneous and isotropic, without a specific center. Mathematically, it can be demonstrated that for a stable universe, the unperturbed density must be zero for the homogeneous and isotropic static universe with a sufficient extent [22, 40, 41, 42]. While some, like James Binney, have termed this as a "swindle,"[22, 39, 42] several analyses have validated it as a mathematical fact [39, 42, 43]. This concept aligns with the zero-energy density (or zero-mass density) feature of a de Sitter universe, where the cosmological constant dominates and drives an accelerated expansion, resulting in a universe with a constant energy density. It's also noteworthy that the quantum wave function of the entire universe, when in its ground state and under classical conditions, corresponds with the zero-mass density phenomenon of the de Sitter universe [44]. Time exponential equation of cosmic scale factor is in fact a property of de Sitter universe [45].

We will now model the vacuum as a classical harmonic oscillator instead of modeling the oscillation of the entire universe. Since the equations governing harmonic oscillation require oscillation around a center, this could lead to instability arising from the assumption of a specific center for the universe, as previously discussed.
We recall the fundamental equation of classical harmonic oscillator [46]:

$$m\ddot{x} = -kx \tag{11}$$

To model the vacuum as an oscillator, we will consider the vacuum's constituent point mass $m_0$ and the stiffness of its oscillation $k_0$. Using equation (6) along with the equation for the classical harmonic oscillator mentioned above equation (11):

$$m_0 x_0 H_0^2 e^{H_0 t} = -k_0 x_0 e^{H_0 t}$$

$$m_0 H_0^2 = -k_0$$

$$H_0 = i\sqrt{\frac{k_0}{m_0}} = i\omega \tag{12}$$

Where $\omega$ represents the angular frequency of the oscillator. The general solution for equation (11) in exponential form, with $C_1$ and $C_2$ as constant coefficients, is:

$$x(t) = C_1 e^{i\omega t} + C_2 e^{-i\omega t}$$

Using Equation (12), the general solution becomes:

$$x(t) = C_1 e^{H_0 t} + C_2 e^{-H_0 t} \tag{13}$$

The above equation (13) is evidently not a periodic function. Therefore, to determine the characteristic angular frequency in relation to Hubble constant, we can analyze the Fourier transformation of the function represented by equation (13). Now the Fourier transformation [47] of x(t) will be as below:

$$\hat{f}(x) = \int_{-\infty}^{\infty} \left( C_1 e^{H_0 t} + C_2 e^{-H_0 t} \right) e^{-i\omega t}\, dt$$

$$\hat{f}(x) = C_1 \int_{-\infty}^{\infty} e^{t(H_0 - i\omega)}\, dt + C_2 \int_{-\infty}^{\infty} e^{-t(H_0 + i\omega)}\, dt \tag{14}$$

Since $e^{H_0 t}$ grows exponentially as $t$ approaches $\infty$, its transformation converges only when $t \longrightarrow -\infty$. Similarly, $e^{-H_0 t}$ grows exponentially as $t$ approaches $-\infty$, so its transformation converges only when $t \longrightarrow \infty$. Therefore, for $H_0 > 0$, equation (14) takes the following form:

$$\hat{f}(x) = C_1 \int_{-\infty}^{0} e^{t(H_0 - i\omega)}\, dt + C_2 \int_{0}^{\infty} e^{-t(H_0 + i\omega)}\, dt$$

$$\hat{f}(x) = \frac{C_1}{H_0 - i\omega} + \frac{C_2}{H_0 + i\omega}$$

As Hubble constant has a real value, therefore in accordance to equation (12), we cannot determine a conventional real-valued frequency like that of an ordinary oscillating system; instead, we can evaluate the characteristic frequency. The characteristic frequency corresponds to the frequency scale where the real and imaginary parts of the denominator are comparable. The real part is $H_0$ and the imaginary part is $\omega$, therefore the characteristic angular frequency is :

$$\omega_c = |H_0|.$$

By applying Euler's formula to Equation (13), we obtain:

$$x(t) = C_1 \left[\cos(\omega t) + i \sin(\omega t)\right] + C_2 \left[\cos(\omega t) - i \sin(\omega t)\right],$$

$$x(t) = (C_1 + C_2)\cos(\omega t) + i(C_1 - C_2)\sin(\omega t),$$

Which is a periodic function having the characteristic frequency

$$\omega_c = |H_0|.$$

It has been demonstrated that when modeling the vacuum as an ordinary harmonic oscillator, an imaginary frequency emerges instead of a real one. However, we can define a characteristic frequency with a value equal to $H_0$. The vacuum is not ordinary, and the challenge of obtaining a real frequency can be resolved through the well-established property of the vacuum's extraordinary negative energy. We can formulate the Lagrangian for the vacuum as:

$$L_{\text{vac}} = T_{\text{vac}} - V_{\text{vac}},$$

where $T_{\text{vac}}$ represents the negative kinetic energy of the vacuum, defined as

$$T_{\text{vac}} = -\frac{1}{2} m_0 \dot{x}^2,$$

and the displacement-dependent potential is given by

$$V_{\text{vac}} = -\frac{1}{2}k_0x^2.$$

Using these relations, the Euler–Lagrange equation for the vacuum becomes:

$$\frac{\partial L_{\text{vac}}}{\partial x} - \frac{d}{dt}\left(\frac{\partial L_{\text{vac}}}{\partial \dot{x}}\right) = 0,$$

which yields

$$-k_0x + m_0\ddot{x} = 0. \tag{15}$$

By applying the exponential time-dependent amplitude solution, we have:

$$m_0x_0H_0^2e^{H_0t} = k_0x_0e^{H_0t}, \qquad H_0 = \sqrt{\frac{k_0}{m_0}} = \omega.$$

Thus, by leveraging the vacuum's negative energy property, we obtain a real-valued frequency, which matches the characteristic frequency determined earlier.

If we align with the de Sitter universe, assuming the entire universe is a vast vacuum with a constant energy density $\varepsilon_{\text{vac}}$ and mass density $\rho_{\text{vac}}$, the first Friedmann equation with the cosmological constant term $\Lambda$ results in the following equation for the cosmic scale factor $\alpha$: [34]

$$\ddot{\alpha} = -\frac{4\pi G}{3}\left(\rho_{\text{vac}} + \frac{3p}{c^2}\right)\alpha + \frac{1}{3}\Lambda c^2\alpha. \tag{16}$$

By substituting the perfect fluid analog of vacuum, where the energy exerts negative pressure, i.e., $p = -\varepsilon_{\text{vac}} = -\rho_{\text{vac}}c^2$, into the above equation (16), we obtain:

$$\ddot{\alpha} = -\frac{4\pi G}{3}\left(\rho_{\text{vac}} - 3\rho_{\text{vac}}\right)\alpha + \frac{1}{3}\Lambda c^2\alpha,$$

$$\ddot{\alpha} - \frac{8\pi G\rho_{\text{vac}}}{3}\alpha - \frac{1}{3}\Lambda c^2\alpha = 0. \tag{17}$$

By defining the quantity

$$H_\Lambda = \sqrt{\frac{1}{3}\Lambda c^2 + \frac{8\pi G\rho_{\text{vac}}}{3}},$$

the equation (17) becomes:

$$\ddot{\alpha} - H_\Lambda^2\alpha = 0.$$

Thus, a general solution for equation (17) can be determined, which is analogous to equation (13), as follows with scalar constants $C_3$ and $C_4$:

$$\alpha(t) = C_3e^{H_\Lambda t} + C_4e^{-H_\Lambda t} \tag{18}$$

Another form of the solution can be expressed in terms of hyperbolic trigonometric functions:

$$\alpha(t) = \frac{C_3 + C_4}{2}\cosh(H_\Lambda t) + \frac{C_3 - C_4}{2}\sinh(H_\Lambda t) \tag{19}$$

Form of the equation (18) is similar to the displacement solution expressed in equation (13). This similarity further demonstrates the consistency between the solution for the Hubble parameter in equation (2) and that in equation (25), expressed in terms of distance and the cosmic scale factor, respectively. We have already shown that in the displacement-based solution with referencing equation (13), $H_0$ cannot be equal to an ordinary real frequency of a harmonic oscillation; a similar argument applies to the scale factor–based solution, that is, the equations (18) and (19) do not allow $H_\Lambda$ to be interpreted as a direct harmonic oscillation frequency. After applying a Fourier transformation, $H_\Lambda$ can be regarded as a characteristic frequency, which in this case is real. Therefore, corresponding to the equation (17), if we model the universe as an undamped free harmonic oscillator, the characteristic angular frequency can be given by:

$$H_\Lambda = \sqrt{\frac{1}{3}\Lambda c^2 + \frac{8\pi G\rho_{\text{vac}}}{3}}.$$

Using equation (9) for $\Lambda$, we can derive:

$$H_\Lambda = \sqrt{\frac{16\pi G\rho_{\text{vac}}}{3}} \tag{20}$$

This is equivalent to the expression for the Hubble constant, $H_0$, in a flat, exponentially expanding universe and can be verified numerically using observational data [48, 49]. Equations (18) and (19) present fascinating results, as they indicate that the cosmic scale factor remains non-zero for any finite time variable domain. This implies a cosmic solution for an eternal universe without spacetime incompleteness. Unlike a comoving solution, this result is derived relative to a fixed spacetime framework. In this type of oscillating cosmic model, each cycle of expansion, from a non-zero minimum to a maximum, and subsequent contraction back to the minimum point will have a defined period:

$$T_\Lambda = \frac{2\pi}{H_\Lambda} = 2\pi\sqrt{\frac{3}{16\pi G\rho_{\text{vac}}}},$$

$$T_\Lambda = \frac{1}{2}\sqrt{\frac{3\pi}{G\rho_{\text{vac}}}} \tag{21}$$

Equation (21) is valid only if the harmonically oscillating model of an exponentially expanding universe is assumed through utilizing the Fourier transformation, rather than the standard exponentially ever-expanding de Sitter universe. Any model that introduces a fixed cosmic spacetime center directly contradicts the standard cosmological principle. Additionally, this type of oscillation conflicts with the second law of thermodynamics, which states that the entropy of the universe must increase over time. Thus, it is more reasonable to associate this undamped constant oscillation frequency, $\omega = H_0$, as derived from the equation (15) by using the general displacement equation, with the vacuum rather than with the entire universe.

It is worth noting that the cyclic model of the universe has been regarded as a fascinating theory in science, philosophy, and even in common-sense interpretations, as it suggests cosmic perpetuity. Various versions of the cyclic model were discussed by Kragh, including a constant cyclic period proposed by Einstein and Friedmann, as well as a varying period of oscillation proposed by Tolman, Zanstra, and many others between 1922 and 1960 [50]. In a more recent work, Ijjas & Steinhardt proposes a novel cyclic model in which the scale factor grows exponentially with each cycle, addressing several unresolved cosmological problems, notably flatness, the monopole problem, initial conditions, and singularity [51].

Up until now, we have been analyzing using classical methods. Now, we will shift to a quantum approach to directly achieve consistency between the value of the cosmological constant derived from analogy with the negative vacuum pressure and the lowest, or zero-point, energy of the quantum harmonic oscillator. Writing the time-independent Schrödinger equation for a harmonic oscillator with frequency $H_0$ and wavefunction $\psi_0$:

$$-\frac{\hbar^2}{2m_0}\frac{d^2\psi_0}{dx^2} + \frac{1}{2}m_0 H_0^2 x^2 \psi_0 = E_0\psi_0 \tag{22}$$

Using standard techniques, we obtain the solution for the vacuum eigen wavefunction:

$$\psi_0(x) = \left(\frac{m_0 H_0}{\pi\hbar}\right)^{1/4} e^{-\frac{m_0 H_0 x^2}{2\hbar}}. \tag{23}$$

And the lowest or zero-point energy of the vacuum:

$$E_0 = \frac{1}{2}\hbar H_0. \tag{24}$$

While the general equation for the quantum harmonic oscillator's eigen wave function is [52, 53]:

$$\psi_n(x) = \sqrt{\frac{1}{2^n n!}}\left(\frac{m\omega}{\pi\hbar}\right)^{1/4} e^{-\frac{m\omega x^2}{2\hbar}} H_n\left(\sqrt{\frac{m\omega}{\hbar}}x\right),$$

where $H_n$ is the $n$th Hermite polynomial. The parameters in equations (9) and (24) were observationally determined to be constants, allowing for the numerical evaluation of $\Lambda$ using the value $\rho_{\text{vac}} = 60.3 \times 10^{-29}\,\text{kg}\,\text{m}^{-3}$ as shown below [48]:

$$\Lambda = \frac{8\pi G\rho_{\text{vac}}}{c^2} = \frac{8 \times 3.1416 \times 6.67 \times 10^{-11}\,\text{Nm}^2\,\text{kg}^{-1} \times 60.3 \times 10^{-28}\,\text{kg}\,\text{m}^{-3}}{(2.9979 \times 10^8\,\text{m}\,\text{s}^{-1})^2} = 1.1247 \times 10^{-52}\,\text{m}^{-2}.$$

And the numerical value of $E_0$ using $H_0 = 69.8\,\text{km}\,\text{s}^{-1}\,\text{Mpc}^{-1} = 2.2615 \times 10^{-18}\,\text{s}^{-1}$ [49]:

$$E_0 = \frac{1}{2}\hbar H_0 = \frac{1}{2} \times 1.05 \times 10^{-34}\,\text{Js} \times 2.2615 \times 10^{-18}\,\text{s}^{-1} = 1.1873 \times 10^{-52}\,\text{J}.$$

Since this analysis is based on the vacuum, flat, homogeneous, and isotropic Einstein field equations consistent with a de Sitter universe, it does not constitute a conventional model of quantum field theory in curved spacetime. Rather, it can be described as a quasi-quantum model aimed at deriving the vacuum's zero-point energy. Despite its straightforward nature, this model demonstrates remarkable consistency with observational data, as illustrated in the earlier numerical comparison between the cosmological constant $\Lambda$ and the vacuum energy density $E_0$.

To determine a specific angular frequency of oscillation, we began with the classical harmonic oscillator equation rather than considering the infinite modes of oscillation associated with the continual creation and annihilation of vacuum particles. This approach was chosen to avoid the so-called "worst theoretical prediction." Subsequently, we utilized the equation for the lowest energy eigenvalue of the quantum harmonic oscillator, leading to a well-aligned theoretical prediction. The obtained numerical values $1.1247 \times 10^{-52}\,\mathrm{m}^{-2}$ for the cosmological constant $\Lambda$, and $1.1873 \times 10^{-52}$ J for $E_0$, representing the modeled energy of a quasi-quantum harmonically oscillating vacuum, are remarkably close. There exists a coupling constant with the unit J·m$^2$ and a value very close to unity:

$$\frac{1.1873 \times 10^{-52}\,\mathrm{J}}{1.1247 \times 10^{-52}\,\mathrm{m}^{-2}} = 1.05566\,\mathrm{J\,m}^2.$$

An expression for this coupling constant can be derived using equations (24) and (20), considering equivalence between $H_\Lambda$ and $H_0$, as follows:

$$\frac{E_0}{\Lambda} = \frac{1}{2}\frac{\hbar c^2}{\sqrt{12\pi G\rho_{\text{vac}}}}.$$

Since the properties of a vacuum can be effectively explained through its fluid-mechanical similarities, it is not surprising to find a relationship between its intrinsic curvature and its energy. Just as any external force acting on a continuum mechanical body results in the development of internal energy and bending, the curvature in a vacuum arises from the energy associated with its own mass,that is energy of the lowest possible or ground state undamped free vibration. In this scenario, the cosmological constant, represented by the vacuum's curvature, corresponds to its geometric curvature per unit length.

## 5. USING GENERAL EQUATION OF COSMIC EXPANSION TO REVIEW THE REAL COSMIC PAST INCOMPLETENESS

Hubble's law, based on observations, fundamentally describes the dynamics of cosmic structures. This relationship, where distances between cosmic structures grow over time, reflects the expansion of the universe [54]. Since the universe encompasses everything, its expansion can only be understood and measured internally, through its own inherent dynamics. However, this expansion preserves the universe's large-scale homogeneity and isotropy while maintaining short-distance inhomogeneity and anisotropy. Using equation (2) and an equivalent to the equation (3), we can clearly express the equation for the cosmic scale factor as:

$$\alpha = \alpha_0 e^{Ht} \tag{25}$$

The above equation (25) can also be derived by exploring the relationship between the Hubble constant $H$ and the scale factor $\alpha$ [16, 17, 55]:

$$H = \frac{\dot{\alpha}}{\alpha}$$

For the mathematical validity of the above relationship in equation (25), it is crucial that the Hubble parameter H remains constant. In the derivation of the general equation for diverging displacement in subsection 2.1 , we demonstrated that H is indeed constant when measured relative to a fixed cosmic space-time point of origin. This constancy holds true for a specific cosmic epoch, such as the current epoch of the universe. This relation (equation 25) is consistent with the exponential cosmic expansion predicted in the de Sitter universe model [17, 56, 57, 58, 59] and aligns with the inflationary solutions for the evolution of the universe [45, 60] and expanding steady state theory of Bondi & Gold [61].

While addressing the metric of the maximally symmetric universe, known as the Friedmann-Lemaître-Robertson-Walker (FLRW) metric [59, 62] in a temporal ($t$) and comoving spatial spherical polar coordinate system ($r, \theta, \phi$), with Gaussian curvature constant, $k$ :

$$ds^2 = (c\,dt)^2 - \alpha^2\left\{\frac{dr^2}{1-kr^2} + r^2\left(d\theta^2 + \sin^2\theta\,d\phi^2\right)\right\}$$

Expressing the time-exponential cosmic scale factor $\alpha$, allows us to rewrite the FLRW metric:

$$ds^2 = (c\,dt)^2 - \left(\alpha_0 e^{Ht}\right)^2\left\{\frac{dr^2}{1-kr^2} + r^2\left(d\theta^2 + \sin^2\theta\,d\phi^2\right)\right\} \tag{26}$$

The corresponding covariant metric tensor is:

$$g_{\mu\nu} = \begin{bmatrix} c^2 & 0 & 0 & 0 \\ 0 & -\frac{\left(\alpha_0 e^{Ht}\right)^2}{1-kr^2} & 0 & 0 \\ 0 & 0 & -\left(\alpha_0 e^{Ht}\right)^2 r^2 & 0 \\ 0 & 0 & 0 & -\left(\alpha_0 e^{Ht}\right)^2 r^2 \sin^2\theta \end{bmatrix}$$

And the resulting contravariant metric tensor is:

$$g^{\mu\nu} = \begin{bmatrix} \frac{1}{c^2} & 0 & 0 & 0 \\ 0 & -\frac{(1-kr^2)}{(\alpha_0 e^{Ht})^2} & 0 & 0 \\ 0 & 0 & -\frac{1}{(\alpha_0 e^{Ht})^2 r^2} & 0 \\ 0 & 0 & 0 & -\frac{1}{(\alpha_0 e^{Ht})^2 r^2 \sin^2\theta} \end{bmatrix}$$

Here $\mu\nu$ represents permutations of coordinates labeled as $[0, 1, 2, 3]$, with the coordinates conventionally defined as $(x^0 = t, x^1 = r, x^2 = \theta, x^3 = \phi)$. Now, it is straightforward, though tedious, to find the non-zero Christoffel symbol terms $\Gamma^0_{11}, \Gamma^0_{22}, \Gamma^0_{33}, \Gamma^1_{01}, \Gamma^1_{01}, \Gamma^1_{11}, \Gamma^1_{22}, \Gamma^1_{33}, \Gamma^2_{02}, \Gamma^2_{12}, \Gamma^2_{33}, \Gamma^3_{03}, \Gamma^3_{13}, \Gamma^3_{23}$ using the equation below [36]:

$$\Gamma^\sigma_{\mu\nu} = \frac{1}{2} g^{\sigma\rho} \left( \frac{\partial}{\partial x^\nu} g_{\rho\mu} + \frac{\partial}{\partial x^\mu} g_{\rho\nu} - \frac{\partial}{\partial x^\rho} g_{\mu\nu} \right)$$

We can evaluate the non-zero Christoffel symbol terms using the above equation:

$$\Gamma^0_{11} = \frac{\alpha_0^2 e^{2Ht}\,(H \dot{+} tH)}{c^2(1-kr^2)}, \quad \Gamma^0_{22} = \frac{\alpha_0^2 e^{2Ht}(H + t\dot{H})r^2}{c^2}, \quad \Gamma^0_{33} = \frac{\alpha_0^2 (H + t\dot{H}) e^{2Ht} r^2 \sin^2\theta}{c^2}.$$

$$\Gamma^1_{01} = \Gamma^1_{10} = \Gamma^2_{02} = \Gamma^2_{20} = \Gamma^3_{03} = \Gamma^3_{30} = H + t\dot{H}, \quad \Gamma^1_{11} = \frac{kr}{1-kr^2}, \quad \Gamma^1_{22} = -r(1-kr^2), \quad \Gamma^1_{33} = -r(1-kr^2)\sin^2\theta,$$

$$\Gamma^2_{12} = \Gamma^2_{21} = \Gamma^3_{13} = \Gamma^3_{31} = \frac{1}{r}, \quad \Gamma^2_{33} = -\sin\theta\cos\theta, \quad \Gamma^3_{23} = \Gamma^3_{32} = \cot\theta.$$

Utilizing the Christoffel symbols as determined above, one can readily obtain the non-zero Ricci curvature tensor components ($R_{00}$, $R_{11}$, $R_{22}$, $R_{33}$) from the equation by contracting the Riemann tensor by raising the index $\sigma$ as $R_{\mu\nu} = R^\sigma_{\mu\sigma\nu}$[63]:

$$R_{\mu\nu} = \frac{\partial}{\partial x^\sigma}\Gamma^\sigma_{\mu\nu} - \frac{\partial}{\partial x^\nu}\Gamma^\sigma_{\mu\sigma} + \Gamma^\rho_{\mu\nu}\Gamma^\sigma_{\rho\sigma} - \Gamma^\rho_{\mu\sigma}\Gamma^\sigma_{\rho\nu} \tag{27}$$

Evaluating $R_{00}$ using equation (27) yields:

$$R_{00} = \frac{\partial}{\partial x^\sigma}\Gamma^\sigma_{00} - \frac{\partial}{\partial x^0}\Gamma^\sigma_{0\sigma} + \Gamma^\rho_{00}\Gamma^\sigma_{\rho\sigma} - \Gamma^\rho_{0\sigma}\Gamma^\sigma_{\rho 0} \tag{28}$$

From equation (28) we obtain for the relevant non-zero terms for the $\sigma$ and $\rho$ indices:

$$R_{00} = -3\big\{(2\dot{H} + t\ddot{H}) + (H + t\dot{H})^2\big\}. \tag{29}$$

In a similar manner, utilizing equation (27) yields further Ricci curvature tensor components:

$$R_{11} = \frac{\alpha_0^2 e^{2Ht}}{c^2(1-kr^2)} \left\{ 3(H + t\dot{H})^2 + 2\dot{H} + t\ddot{H} + \frac{2kc^2}{\alpha_0^2 e^{2Ht}} \right\} \tag{30}$$

$$R_{22} = \frac{\alpha_0^2 e^{2Ht} r^2}{c^2} \left\{ 3(H + t\dot{H})^2 + 2\dot{H} + t\ddot{H} + \frac{2kc^2}{\alpha_0^2 e^{2Ht}} \right\} \tag{31}$$

$$R_{33} = \frac{\alpha_0^2 e^{2Ht} r^2 \sin^2\theta}{c^2} \left\{ 3(H + t\dot{H})^2 + 2\dot{H} + t\ddot{H} + \frac{2kc^2}{\alpha_0^2 e^{2Ht}} \right\} \tag{32}$$

The Ricci curvature scalar, $R$, is obtained by summing the non-zero covariant Riemann tensor and the contravariant metric tensor over the repeated indices:

$$R = g^{\mu\nu}R_{\mu\nu} = g^{00}R_{00} + g^{11}R_{11} + g^{22}R_{22} + g^{33}R_{33}.$$

In this case, after simplifying:

$$R = -\frac{3}{c^2}\big\{(2\dot{H} + t\ddot{H}) + (H + t\dot{H})^2\big\} - \frac{3}{c^2}\left\{ 3(H + t\dot{H})^2 + 2\dot{H} + t\ddot{H} + \frac{2kc^2}{\alpha_0^2 e^{2Ht}} \right\} \tag{33}$$

The above equation (33) represents the Ricci curvature scalar in terms of the time-varying Hubble parameter. As previously explained, the time dependency of the Hubble parameter arises from its measurement based on the recession velocities and distances of cosmic objects at different cosmic comoving epochs. However, if the Hubble parameter is measured at a fixed point in spacetime or within a specific cosmic epoch, the equation (33) can be rewritten in terms of the Hubble constant, with its time derivatives vanishing, as follows:

$$R = -\frac{3H_0^2}{c^2} - 3\left\{\frac{3H_0^2}{c^2} + \frac{2k}{\left(\alpha_0 e^{H_0 t}\right)^2}\right\},$$

$$R = -\frac{12H_0^2}{c^2} - \frac{6k}{\left(\alpha_0 e^{H_0 t}\right)^2} \tag{34}$$

The negative sign of the Ricci curvature scalar, as determined above, arises from the contraction of the Riemann tensor using $R_{\mu\nu} = R^{\sigma}_{\mu\sigma\nu}$, as referenced in [63]. However, if the contraction $R_{\mu\nu} = R_{\mu\nu\sigma}{}^{\sigma} = -R^{\sigma}_{\mu\sigma\nu}$, as referenced in [3], were used instead, the value of $R$ would be the same but with a positive sign. This is not a contradiction, as both approaches yield the same magnitude; the difference in sign simply reflects the choice of convention or the system from which the curvature is measured.

Importantly, whether considering the time-dependent case (33) or the time-independent case (34) of the Hubble parameter, the Ricci curvature scalar $R$ remains finite for any finite value of the time variable. The only exception occurs at $t = -\infty$, which represents the sole instance of past incompleteness. However, this incompleteness is not related to any real domain of the time coordinate, which serves as the sole independent variable in the continuous function of the Ricci curvature scalar. Therefore, this past incompleteness is not a physical reality for this type of exponentially expanding cosmological solution but rather an unavoidable mathematical artifact, as highlighted by the Borde–Guth–Vilenkin (BGV) theorem [64]. Optionally, for a spatially flat universe ($k = 0$), equation (34) indicates a constant cosmic Ricci curvature scalar.

## 6. GENERAL EQUATION OF DISPLACEMENT AND LOGARITHMIC SPIRAL MOTION IN SPIRAL GALAXY

It is fascinating to realize that the equation for a logarithmic, or equiangular, spiral is an alternative expression of our time-based exponential general displacement equation. It is worth noting that, despite having a uniform linear velocity, an object can still experience continuously varying acceleration, as well as higher-order time derivatives of displacement, by continuously changing its orbital distance from its center. This is the key insight when drawing a correlation between the time-exponential displacement equation and the logarithmic spiral equation.

In a system following a spiral trajectory defined by an angle $\theta$ measured relative to its center, a growth or decay rate $K$, and a varying radius $r$, the equation of the logarithmic spiral is [65]:

$$r(\theta) = r_0 e^{K\theta} \tag{35}$$

In terms of $t$ with uniform angular velocity $\dot{\theta}$, the above equation becomes:

$$r(t) = r_0 e^{K\dot{\theta}t} \tag{36}$$

In the equation above, $K = \tan\alpha$, where $\alpha$ is referred to as the pitch angle. This angle is defined as the constant angle between the tangent to the spiral at any given radial distance from the spiral's center and the tangent to the circle at the point of intersection with the same radius. For a logarithmic spiral, this angle remains constant, which is why logarithmic spirals are also called equiangular spirals. Consequently, the growth rate $K$ is also constant. If we represent the time-exponential displacement equation (5) with the displacement being radial, it can be written as:

$$r = r_0 e^{\zeta t} \tag{37}$$

In the equation of the logarithmic spiral, the growth rate $K$ and angular velocity $\dot{\theta}$ are both treated as constants, similar to the constant $\zeta$ in the case of radial displacement. By comparing equations (36) and (37), we can establish the equivalent relationship:

$$\zeta = K\dot{\theta} \tag{38}$$

Therefore, the logarithmic spiral displacement equation can be interpreted as a transformed two-dimensional displacement equation in a coplanar polar coordinate system. This transformation originates from the one-degree-of-freedom time-exponential displacement equation, which describes the motion of an object orbiting a fixed center.

In the Cartesian coordinate system, the equation $r = r_0 e^{\zeta t}$ can be re-expressed in the polar coordinate system as two distinct components using equation (35), as a matrix representation shown below:

$$\begin{bmatrix} x \\ y \end{bmatrix} = \begin{bmatrix} \cos(\dot{\theta}t) & 0 \\ \sin(\dot{\theta}t) & 0 \end{bmatrix} \begin{bmatrix} r_0 e^{K\dot{\theta}t} \\ 0 \end{bmatrix} = \begin{bmatrix} r_0 e^{K\dot{\theta}t}\cos(\dot{\theta}t) \\ r_0 e^{K\dot{\theta}t}\sin(\dot{\theta}t) \end{bmatrix}.$$

Using the above relations and the fact that the locus of the coordinate $(x, y)$ forms a circle , one can easily derive the relation presented in equation (36) as below:

$$\begin{aligned} r^2 &= x^2 + y^2 = r_0^2 e^{2K\dot{\theta}t} \left\{ \cos^2(\dot{\theta}t) + \sin^2(\dot{\theta}t) \right\}, \\ r &= r_0 e^{K\dot{\theta}t}. \end{aligned}$$

For a non-periodic angular motion in which the angle continuously increases with time and is not limited to $4\pi$, an object will follow a logarithmic spiral trajectory instead of a circular one .In terms of the measured angle considering the center as the origin of the polar coordinate system, the above equation becomes:

$$r(\theta) = r_0 e^{K\theta}, \qquad r(\theta) = r_0 e^{\tan\alpha\,\theta} \tag{39}$$

The above equation (39) is a general expression for a logarithmic spiral or equiangular spiral. The radial distance $r$ progressively changes over time, following spiral trajectories.

Logarithmic spiral geometries naturally occur in numerous living and inanimate phenomena, including in spiral galaxies, seashells, hurricanes, and the growth patterns of plants, such as sunflower seeds and pinecones [66, 67, 68]. Notably, in the asymptotic limit, the ratio of successive radii in a logarithmic spiral converges to the same value as the ratio of consecutive Fibonacci numbers, namely the golden ratio or golden mean. These spirals are often observed in nature due to their efficient growth patterns, optimizing space and resources. The same geometric principles expressed mathematically by equations (36), (37), and (39) can be applied to describe the structure of spiral galaxies. The logarithmic spiral provides a reasonable approximation for the structure of galactic spiral arms [69, 70]. In these galaxies, the arms follow a logarithmic spiral pattern, giving rise to the term "Galactic spiral." Approximately 60% of galaxies in the local universe are spiral galaxies [71].

In spiral galaxies such as our MW and its closest neighbor, M31, the spiral arms form in regions where stars and their systems are sufficiently far from the galactic center. In these regions, the gravitational pull toward the center becomes negligible compared to the frictional drag experienced by the stars. This frictional drag causes the stars to orbit at nearly uniform velocities, regardless of their distance from the center. In this scenario, acceleration is achieved through the continual change in distance from the galactic center, which aids in the formation of spiral trajectories.

Moreover, the relatively homogeneous nature of the galaxy, where gravitational forces dominate locally but diminish at larger distances, results in the galaxy behaving continuum-mechanically, like a rotating disk. These combined phenomena lead to a fluid-mechanical analogy, where the spiral arms eject along an equiangular spiral trajectory, as described by equations (36), (37), and (39). It is important to note that dark matter plays a crucial role in forming gravitationally bound, stiff, and geometrically well-defined galaxies. This stands in contrast to the expected pattern of decreasing rotational velocity with distance from the galactic center, as predicted by the Newton-Keplerian model, which is inconsistent with observational data.

The logarithmic spiral trajectory is also consistent with explaining the radial migration of constituents, such as stars or star systems, which move outward from the more unstable central region to more stable locations, following a spiral path within their host galaxy. For example, the radial migration concept suggests that the Solar System, including Earth, may have originally formed comparatively closer to the Milky Way's central region, around 5 kpc from MW's center, and later migrated to its present location, approximately $8.5 \sim 9$ kpc from the galactic center, thereby avoiding any major destructive collisions [72].

## 7. RESULTS AND DISCUSSION

We began with a power series approximation of the displacement function, using time as the independent variable. From this, we derived the time exponential displacement relation, which aligns with large-distance observational cosmic motion. In contrast, the short-distance motions we experience in everyday life are simply lower-order approximations of this exponential relation, which is particularly significant for large-scale motion. This general time exponential displacement relation was directly applied to derive Hubble's relation, an equation describing cosmic diverging displacement and providing a plausible explanation for cosmic expansion. The recession of cosmic units due to cosmic expansion is significant for large-scale cosmic motion. In contrast, at shorter distances, the attractive gravitational force dominates.

We then derived a general equation for time exponential converging displacement in a manner similar to how the general equation for time exponential diverging displacement was formulated. This converging relation was then utilized to estimate in principle the time required for the upcoming collision between the Milky Way and Andromeda. The result obtained, ranging from 4.4 to 4.9 billion years, was highly consistent with the findings of 4 to 5 billion years from numerical simulations based on observational data.

A noteworthy application of the general diverging equation is to derive the subtle value of energy for a vacuum unit, considering it as quantum harmonically oscillated in a quasi-quantum approach. This gives a value of $1.1873 \times 10^{-52}$ J, which is very close to the value determined from the general relativistic approach, $1.1247 \times 10^{-52}\,\mathrm{m}^{-2}$. Therefore, the coupling constant relating the vacuum unit's energy to the curvature of the vacuum has a value very close to unity. By relating the large-scale cosmic receding distances to the cosmic expansion scale factor, a general relativistic mathematical approach is reviewed to avoid a physical past incompleteness while addressing an unphysical mathematical singularity.

Lastly, the general time exponential displacement was applied to explain the spiraling motion of galactic units in spiral galaxies. This spiral motion can also account for the radial migration of a galaxy's constituents, providing support for the radial migration theory of the solar system.

Despite several successful applications of the general time exponential motion, it does have some limitations. During its derivation, the Maclaurin series was employed, which requires a fixed space-time coordinate origin around which the series expansion is performed. This necessitates assuming the Hubble parameter is constant to derive the time exponential equation. However, in any comoving coordinate system, the Hubble parameter must be time-dependent. This time dependency was addressed during the derivation and was considered in the context of reviewing the cosmic past incompleteness. Another limitation arises from the uncertainty during the final stages of galaxy merging. At this stage, tidal effects, frictional interactions between galaxy constituents, and the influence of nearby cosmic neighbors may impact the time estimation. However, the consistency of the estimated time for the Milky Way (MW) and Andromeda (M31) collision with results from numerical simulations suggests that our model, which neglects perturbations, is reasonable. This is because galactic motion is primarily dominated by their centers, and during galaxy merging, the likelihood of individual components colliding is very low.

## 8. CONCLUSION

The cosmos is infinite, so it's natural that no finite set of principles can fully explain its phenomena. It's also sensible to expect the universe to have infinite spatial and temporal dimensions. We reasonably assumed the infinite order differentiability of displacement with respect to time and subsequently formulated a time-exponential relation for displacement. This formulation is shown to be consistent with Hubble's law and provides a plausible explanation for the time dependency of the Hubble parameter. This relation proved to be valuable in understanding the infinite cosmic past and future, as well as in explaining the structure of spiral galaxies. Additionally, it provided insights into the enigmatic relationship between the quantum harmonically oscillating vacuum's zero-point energy and the cosmological constant. Furthermore, it was applied to estimate the timing of a significant cosmic event: the collision between the Milky Way and Andromeda.

### Data Availability

The data that support the findings of this study are available within the article and the cited references.

### Disclosure of Interest

The author declares that he has no known competing financial interests or personal relationships that could have appeared to influence the work reported in this paper.

### Funding Statement

No funding was received for this paper.

### Acknowledgments

I would like to express my heartfelt gratitude to my colleagues and friends from Nippon Koei Bangladesh Ltd., Rajshahi University of Engineering & Technology, and the National University of Bangladesh for their invaluable support.

### ORCID

**Ashraful Islam**, https://orcid.org/0009-0003-6605-9515

### REFERENCES

[1] E. Schrödinger, *Space-Time Structure*, (Cambridge University Press, Cambridge, 1950).

[2] J. B. Hartle, *Gravity* (Addison Wesley, San Francisco, 2003).

[3] K. F. Riley, M. P. Hobson, and S. J. Bence, *Mathematical Methods for Physics and Engineering*, (Cambridge University Press, Cambridge, 2006).

[4] M. L. Boas, *Mathematical Methods in the Physical Sciences*, (John Wiley & Sons, New York, 2006).

[5] V. Balakrishnan, *Mathematical Physics*, (Springer, Berlin, 2020).

[6] E. Hubble, "A relation between distance and radial velocity among extra galactic nebulae," Proc. Natl. Acad. Sci. U.S.A. **15**, 168-173 (1929), https://doi.org/10.1073/pnas.15.3.168

[7] E. Hubble and M. L. Humason, "The velocity-distance relation among extra-galactic nebulae," Astrophys. J. **74**, 43 (1931), https://doi.org/10.1086/143323

[8] E. Hubble, and M. L. Humason, "The velocity-distance relation for isolated extra-galactic nebulae," Proc. Natl. Acad. Sci. U.S.A. **20**, 264 (1934).

[9] M. L. Humason, A. Sandage, and J. A. Westphal, "Redshifts and magnitudes of extragalactic nebulae," Astron. J. **61**, 97 (1956).

[10] W. L. Freedman, B. F. Madore, B. K. Gibson, L. Ferrarese, D. D. Kelson, S. Sakai, J. R. Mould, R. C. Kennicutt Jr., and H. C. Ford, "Final results from the Hubble Space Telescope Key Project to measure the Hubble constant," Astrophys. J. **553**, 47 (2001), https://doi.org/10.1086/320638

[11] A. G. Riess, L. Macri, S. Casertano, H. Lampeitl, H. C. Ferguson, A. V. Filippenko, S. W. Jha, W. Li, and R. Chornock, "A 3% solution: determination of the Hubble constant with the Hubble Space Telescope and Wide Field Camera 3," Astrophys. J. **730**, 119 (2011), https://doi.org/10.1088/0004-637X/730/2/119

[12] W. L. Freedman, B. F. Madore, V. Scowcroft, C. Burns, A. Monson, S. E. Persson, M. Seibert, and J. Rigby, "Carnegie Hubble Program: A mid-infrared calibration of the Hubble constant," Astrophys. J. **758**, 24 (2012), https://doi.org/10.1088/0004-637X/758/1/24

[13] A. G. Riess, L. M. Macri, S. L. Hoffmann, D. Scolnic, S. Casertano, A. V. Filippenko, B. E. Tucker, M. J. Reid, D. O. Jones, and J. M. Silverman, "A 2.4% determination of the local value of the Hubble constant," Astrophys. J. **826**, 56 (2016), https://doi.org/10.3847/0004-637X/826/1/56

[14] R. P. van der Marel, M. A. Fardal, S. T. Sohn, E. Patel, G. Besla, A. del Pino, J. Sahlmann, and L. L. Watkins, "First Gaia Dynamics of the Andromeda System: DR2 Proper Motions, Orbits, and Rotation of M31 and M33," Astrophys. J. **872**, 24 (2019), https://doi.org/10.3847/1538-4357/ab001b

[15] R. Schiavi, R. Capuzzo-Dolcetta, M. Arca-Sedda, and M. Spera, "Future merger of the Milky Way with the Andromeda galaxy and the fate of their supermassive black holes," Astron. Astrophys. **642**, A30 (2020), https://doi.org/10.1051/0004-6361/202038674

[16] A. R. Choudhuri, *Astrophysics for Physicists*, (Cambridge University Press, Cambridge, 2010).

[17] P. J. E. Peebles, *Principles of Physical Cosmology*, (Princeton University Press, Princeton, 1993).

[18] D. Eager, A.-M. Pendrill, and N. Reistad, "Beyond velocity and acceleration: jerk, snap and higher derivatives," Eur. J. Phys. **37**, 065008 (2016), https://doi.org/10.1088/0143-0807/37/6/065008

[19] J. J. de Jong, Y. Wu, M. Carricato, and J. L. Herder, "A pure-inertia method for dynamic balancing of symmetric planar mechanisms," in: *Advances in Robot Kinematics 2018. ARK 2018. Springer Proceedings in Advanced Robotics*, vol 8, edited by J. Lenarcic, and V. Parenti-Castelli, (Springer, Cham. 2018), pp 277–284. https://doi.org/10.1007/978-3-319-93188-3_32

[20] M. Visser, "Jerk, snap and the cosmological equation of state," Class. Quantum Grav. **21**, 2603 (2004), https://doi.org/10.1088/0264-9381/21/11/006

[21] T. J. Cox, and A. Loeb, "The collision between the Milky Way and Andromeda," Mon. Not. R. Astron. Soc. **386**, 461–474 (2008), https://doi.org/10.1111/j.1365-2966.2008.13048.x

[22] J. Binney, and S. Tremaine, *Galactic Dynamics*, (Princeton University Press, Princeton, 1987).

[23] S. T. Sohn, J. Anderson, and R. P. van der Marel, "The M31 velocity vector. I. Hubble Space Telescope proper-motion measurements," Astrophys. J. **753**, 7 (2012), https://doi.org/10.1088/0004-637X/753/1/7

[24] R. P. van der Marel, G. Besla, T. J. Cox, S. T. Sohn, and J. Anderson, "The M31 velocity vector. III. Future Milky Way–M31–M33 orbital evolution, merging, and fate of the Sun," Astrophys. J. **753**, 9 (2012), https://doi.org/10.1088/0004-637X/753/1/9

[25] R. P. van der Marel, M. Fardal, G. Besla, R. L. Beaton, S. T. Sohn, J. Anderson, T. Brown, and P. Guhathakurta, "The M31 velocity vector. II. Radial orbit toward the Milky Way and implied local group mass," Astrophys. J. **753**, 8 (2012), https://doi.org/10.1088/0004-637X/753/1/8

[26] R. P. van der Marel, and N. Kallivayalil, "Third-epoch Magellanic Cloud proper motions. II. The Large Magellanic Cloud rotation field in three dimensions," Astrophys. J. **728**, 121 (2014), https://doi.org/10.1088/0004-637X/781/2/121

[27] A. W. McConnachie and M. J. Irwin, "The satellite distribution of M31," Mon. Not. R. Astron. Soc. **365**, 902–914 (2006), https://doi.org/10.1111/j.1365-2966.2005.09771.x

[28] S. Li, A. G. Riess, M. P. Busch, S. Casertano, L. M. Macri, and W. Yuan, "A Sub-2% Distance to M31 from Photometrically Homogeneous Near-infrared Cepheid Period–Luminosity Relations Measured with the Hubble Space Telescope," Astrophys. J. **920**, 84 (2021), https://doi.org/10.3847/1538-4357/ac1597

[29] Y. B. Zel'dovich, "The cosmological constant and the theory of elementary particles," Sov. Phys. Usp. **11**, 381 (1968).

[30] S. E. Rugh, and H. Zinkernagel, "The quantum vacuum and the cosmological constant problem," Stud. Hist. Philos. Mod. Phys. **33**, 663-705 (2002), https://doi.org/10.1016/S1355-2198(02)00033-3

[31] S. Carroll, "The cosmological constant," Living Rev. Relativ. **4**, 1 (2001), https://doi.org/10.12942/lrr-2001-1

[32] T. Padmanabhan, "Cosmological constant: the weight of the vacuum," Phys. Rep. **380**, 235-320 (2003), https://doi.org/10.1016/S0370-1573(03)00120-0

[33] J. Solà, "Cosmological constant and vacuum energy: Old and new ideas," J. Phys. Conf. Ser. **435**, 012015 (2013).

[34] M. P. Hobson, G. P. Efstathiou, and A. N. Lasenby, *General Relativity*, (Cambridge University Press, Cambridge, 2006).

[35] S. Carroll, *Spacetime and Geometry*, (Pearson/Addison Wesley, Boston, 2004).

[36] S. Weinberg, "The cosmological constant problem," Rev. Mod. Phys. **61**, 1-23 (1989), https://doi.org/10.1103/RevModPhys.61.1

[37] S. Weinberg, *Gravitation and Cosmology*, (John Wiley & Sons, New Jersey, 1972).

[38] A. Islam, “Deriving the cosmological constant from the Euler–Lagrange equation of second-order differentiable gravitational field Lagrangian,” AIP Adv. **13**, 125130 (2023), https://doi.org/10.1063/5.0164219

[39] A. R. Choudhuri, *The Physics of Fluids and Plasmas*, (Cambridge University Press, Cambridge, 1998).

[40] C. Clarke and B. Carswell, *Principle of Astrophysical Fluid Dynamics*, (Cambridge University Press, Cambridge, 2007).

[41] O. Regev, O. M. Umurhan, and P. A. Yecko, *Modern Fluid Dynamics for Physics and Astrophysics*, (Springer Science & Business Media, 2016).

[42] M. K. H. Kiessling, “The ‘Jeans swindle’: A true story—mathematically speaking,” Adv. Appl. Math. **31**, 132-149 (2003), https://doi.org/10.1016/S0196-8858(02)00556-0

[43] M. Falco, S. H. Hansen, R. Wojtak, and G. A. Mamon, “Why does the Jeans swindle work?” Mon. Not. R. Astron. Soc. Lett. **431**, L6–L9 (2013), https://doi.org/10.1093/mnrasl/sls051

[44] J. B. Hartle and S. W. Hawking, “Wave function of the universe,” Phys. Rev. D **28**, 2960-2975 (1983), https://doi.org/10.1103/PhysRevD.28.2960

[45] P. J. E. Peebles and B. Ratra, “The cosmological constant and dark energy,” Rev. Mod. Phys. **75**, 559-606 (2003), https://doi.org/10.1103/RevModPhys.75.559

[46] L. D. Landau and E. M. Lifshitz, *Theoretical Physics Vol. 1: Mechanics*, (Pergamon Press, Oxford, 1969).

[47] R. N. Bracewell, *The Fourier Transform and Its Applications*, (McGraw-Hill, New York, 2000).

[48] J. Prat, C. Hogan, C. Chang, and J. Frieman, “Vacuum energy density measured from cosmological data,” J. Cosmol. Astropart. Phys. **2022**, (2022), https://doi.org/10.1088/1475-7516/2022/06/015

[49] W. L. Freedman, “Measurements of the Hubble constant: tensions in perspective,” Astrophys. J. **919**, 16 (2021), https://doi.org/10.3847/1538-4357/ac0e95

[50] H. Kragh, “Cyclic models of the relativistic universe: the early history,” in: *Beyond Einstein. Einstein Studies Vol. 14*, edited by D. Rowe, T. Sauer, and S. Walter, (Birkhäuser, Cham, 2018).

[51] A. Ijjas, and P. J. Steinhardt, “A new kind of cyclic universe,” Phys. Lett. B, **795**, 666-672 (2019), https://doi.org/10.1016/j.physletb.2019.06.056

[52] D. A. B. Miller, *Quantum Mechanics for Scientists and Engineers*, (Cambridge University Press, Cambridge, 2008).

[53] A. F. J. Levi, *Applied Quantum Mechanics*, (Cambridge University Press, Cambridge, 2006).

[54] P. J. E. Peebles, *The Large-Scale Structure of the Universe*, (Princeton University Press, Princeton, 1980).

[55] T. Padmanabhan, *Theoretical Astrophysics Vol. III: Galaxies and Cosmology*, (Cambridge University Press, Cambridge, 2002).

[56] W. De Sitter, “On Einstein’s theory of gravitation and its astronomical consequences, First Paper,” Mon. Not. R. Astron. Soc. **77**, 481 (1916).

[57] W. De Sitter, “On Einstein’s theory of gravitation and its astronomical consequences, Second Paper,” Mon. Not. R. Astron. Soc. **77**, 155 (1916).

[58] W. De Sitter, “On Einstein’s theory of gravitation and its astronomical consequences, Third Paper,” Mon. Not. R. Astron. Soc. **78**, 3 (1917).

[59] S. Weinberg, *Cosmology*, (Oxford University Press, Oxford, 2008).

[60] A. H. Guth, “Inflationary universe: A possible solution to the horizon and flatness problems,” Phys. Rev. D, **23**, 2 (1981), https://doi.org/10.1103/PhysRevD.23.347

[61] H. Bondi and T. Gold, “The steady-state theory of the expanding universe,” Mon. Not. R. Astron. Soc. **108**, 252–270 (1948), https://doi.org/10.1093/mnras/108.3.252

[62] P. Coles and F. Lucchin, *Cosmology* (John Wiley & Sons, Chichester, 2022).

[63] R. d’Inverno and J. Vickers, *Introducing Einstein’s Relativity* (Oxford University Press, Oxford, 2022).

[64] A. Borde, A. H. Guth, and A. Vilenkin, “Inflationary spacetimes are incomplete in past directions,” Phys. Rev. Lett. **90**, 151301 (2003), https://doi.org/10.1103/PhysRevLett.90.151301

[65] B. L. Davis, J. C. Berrier, D. W. Shields, J. Kennefick, D. Kennefick, M. S. Seigar, C. H. S. Lacy, and I. Puerari, “Measurement of galactic logarithmic spiral arm pitch angle using two-dimensional fast Fourier transform decomposition,” Astrophys. J. Suppl. Ser. **199**, 33 (2012), https://doi.org/10.1088/0067-0049/199/2/33

[66] T. A. Cook, *The Curves of Life*,, (Constable and Company Ltd., London, 1914).

[67] P. Ball, *The Self-Made Tapestry: Pattern Formation in Nature*, (Oxford University Press, Oxford, 1999).

[68] J. D. Murray, *Mathematical Biology: I. An Introduction*, (Springer-Verlag, Berlin, 2002).

[69] M. S. Seigar and P. A. James, “The structure of spiral galaxies – II. Near-infrared properties of spiral arms,” Mon. Not. R. Astron. Soc. **299**, 685 (1998).

[70] H. I. Ringermacher and L. R. Mead, “A new formula describing the scaffold structure of spiral galaxies,” Mon. Not. R. Astron. Soc. **397**, 164–171 (2009), https://doi.org/10.1111/j.1365-2966.2009.14950.x

[71] R. Buta, “The world of galaxies,” in *The World of Galaxies*, edited by H. G. Corwin Jr., and L. Bottinelli (Springer-Verlag, Berlin, 1989), p. 29.

[72] J. Baba, T. Tsujimoto, and T. R. Saitoh, "Solar system migration points to a renewed concept: Galactic habitable orbits," Astrophys. J. Lett. **976**, L29 (2024), https://doi.org/10.3847/2041-8213/ad9260

## ЗАКОН ГАББЛА ТА ЙОГО ЕКСПОНЕНЦІАЛЬНЕ УЗАГАЛЬНЕННЯ З КОСМОЛОГІЧНИМИ ЗАСТОСУВАННЯМИ

**Ашрафул Іслам**
*Ніппон Коей Бангладеш Лімітед, Площа 11/A, Дорога 48, Гульшан-2, Дакка-1212, Бангладеш*

Закон Габбла показує, як компоненти Всесвіту дотримуються загальних динамічних правил у космологічному масштабі. Хоча він найбільш відомий для опису розширення Всесвіту, загальне рівняння зміщення, отримане відповідно до цього закону, разом із загальним рівнянням збіжного зміщення, було застосовано для оцінки часу, що залишився до зіткнення Чумацького Шляху та Андромеди. Ця оцінка тісно узгоджується з результатами числового моделювання інших досліджень. Крім того, наслідки цього узагальненого рівняння дають цінне розуміння ключових космологічних загадок, включаючи зміну параметра Габбла з часом, неповноту космологічного минулого та незмінну таємницю зв'язку між тонким значенням космологічної константи та квантовою енергією нульової точки вакууму. Він також успішно пояснює структуру спіральних галактик.

**Ключові слова:** *закон Габбла; зіткнення галактик; космологічна стала; енергія вакууму; структура спіральної галактики*

East European Journal of Physics. **4**. 30–41 (2025)
DOI: 10.26565/2312-4334-2025-4-03 ISSN 2312-4334

# COSMOLOGICAL DIAGNOSTICS AND STABILITY OF DARK ENERGY MODEL IN NON-METRIC GRAVITY

**Muhammad Sharif**[1,4*], **Eman M. Moneer**[2], **Muhammad Zeeshan Gul**[1], **Muhammad Hassan Shahid**[1], **Euaggelos E. Zotos**[3]

[1]*Department of Mathematics and Statistics, The University of Lahore, 1-KM Defence Road Lahore-54000, Pakistan*
[2]*Department of Physics, College of Sciences, Princess Nourah bint Abdulrahman University,*
*P.O. Box 84428, Riyadh 11671, Saudi Arabia*
[3]*Department of Physics, School of Science, Aristotle University of Thessaloniki, GR 54124, Thessaloniki, Greece*
[4]*Research Center of Astrophysics and Cosmology, Khazar University, Baku, AZ1096, 41 Mehseti Street, Azerbaijan*
**Corresponding Author e-mail: msharif.math@pu.edu.pk*

Received August 23, 2025; revised September 23, 2025; accepted September 27, 2025

In this study, we investigate the dynamics of generalized ghost pilgrim dark energy in the background of $f(Q, C)$ gravity, where $Q$ is the non-metricity scalar and $C$ represents the boundary term. To complete this objective, we take an isotropic and homogeneous universe with an ideal matter distribution. Our analysis includes a scenario with non-interacting fluids, encompassing both dark matter and dark energy. To understand the cosmic dynamics, we reconstruct a $f(Q, C)$ model and examine its influence on the universe evolution. We explore key cosmological factors, i.e., state variable, the behavior of $(\omega_D - \omega'_D)$-plane and the statefinder diagnostic pair, which help to analyze the cosmic expansion. A crucial aspect of our analysis is the stability of generalized ghost pilgrim dark energy model via the squared sound speed method, confirming its viability in supporting the observed accelerated expansion. Our findings are consistent with observational data, demonstrating that $f(Q, C)$ gravity provides a robust theoretical foundation for describing dark energy and the universe large-scale dynamics. This work not only deep our understanding of modified gravity and mysterious energy but also offers new insights into alternative explanation for cosmic acceleration beyond standard paradigms.

**Keywords:** *$f(Q, C)$ gravity; Dark energy model; Stability analysis*

**PACS:** 04.50.Kd; 98.80.-k; 95.36.+x

## 1. INTRODUCTION

Einstein theory of gravitation (GR) provides a geometric framework that remains a foundational pillar of modern physics. A significant problem for this theory appears when it addresses the phenomenon of late-time cosmic expansion. The range of astronomical observations such as supernovae type-Ia demonstrate that the cosmos is presently undergoing the expansion phase [1]-[5]. This acceleration is hypothesized to originate from an ambiguous force, named as dark energy (DE). The enigmatic nature and mechanisms of DE constitute one of the most profound unresolved questions in cosmology. To address this issue, the ΛCDM model has been established as a standard model to describe the ambiguous aspects of DE. While ΛCDM aligns well with observational constraints, but it faces cosmic limitations [6]-[11]. These challenges inspired the scientific community to modify GR to gain deep insights for DE and cosmic acceleration [12]. Such modifications redefine the geometric components of the action, thereby proposing alternative gravitational frameworks to resolve the mysteries of the universe. These theories offer new approaches to cosmology and astrophysics, allowing for theoretical and observational advancements.

Modified theories may include exploring alternative geometries beyond Riemannian such as torsion and non-metricity, which offer broader geometric interpretations of gravity. Weyl [13] introduced a geometric framework that extends Riemannian geometry by introducing an additional connection, known as the "length connection," which modifies how vectors behave under parallel transport. Building on this, Weyl-Cartan geometry [14] further incorporates torsion into the structure. Later, Weitzenböck [15] proposed a different approach, defining Weitzenböck spaces characterized by non-zero torsion but zero curvature, leading to the idea of teleparallelism. In this framework, gravity is described through torsion rather than curvature [16]. As a result, GR can be formulated in multiple ways: the traditional curvature-based approach (where torsion and non-metricity vanish) or the teleparallel approach (where curvature and non-metricity are absent). Also, non-metricity describes changes in vector length at the time of parallel transport, where the covariant divergence of metric tensor exists, leading to symmetric teleparallel theory [17]. Different theoretical models and the limitations they face based on observations have been thoroughly investigated [18]-[37].

The symmetric teleparallel gravity is further modified by introducing a boundary term into the functional action, named as $f(Q, C)$ theory [38]. This extension has garnered considerable attention in the scientific community due to its profound implications. This framework offers a compelling alternative with notable theoretical consequences for cosmology and astrophysics. By incorporating non-metricity and boundary effects, this theory enables a rich description

---

***Cite as:*** M. Sharif, E.M. Moneer, M.Z. Gul, M.H. Shahid, E.E. Zotos, East Eur. J. Phys. 4, 30 (2025), https://doi.org/10.26565/2312-4334-2025-4-03

of gravitational dynamics. This modified proposal offers fresh insights into fundamental questions about mysteries of the universe. By incorporating the boundary term, this approach enhances theoretical flexibility, enabling a wide spectrum of physically viable solutions. This extension addresses GR limitations by probing cosmological singularities and opens new pathways for cosmological models that align with current observational data. It is observed that this alternative proposal elucidates the cosmic evolutionary path and is consistent with current observable data [39]-[42].

Maurya [43] explored the DE model to study the evolutionary picture of the universe in $f(Q,C)$ theory. Further studies delved into DE scenarios incorporating boundary terms to classify DE behavior during cosmic expansion have been discussed in [44]. Myrzakulov et al [45] demonstrated that the $f(Q,C)$ framework presents a viable alternative to the standard cosmological model. The $f(Q,C)$ formalism in FRW spacetime introduces novel perspectives on the standard cosmological paradigms [46]. Maurya [47] analyzed how boundary terms influence cosmological evolution dynamics. Usman et al [48] addressed the observed matter-antimatter asymmetry through gravitational baryogenesis in the same context. The novel insights into the early-universe inflation in this modified framework has been examined in [49]. This approach not only offers a coherent description of the universe dynamics but also exhibits strong agreement with modern observational constraints [50].

Various methods have been developed to understand the influence of DE on the evolution of cosmos. Recently, a novel DE model, known as the pilgrim dark energy (PDE) model was proposed [51]. This model is constructed upon the intriguing properties in quantum field theory while extending their applications to the cosmological framework. This provides a natural framework to connect DE with fundamental physics. The concept of generalized ghost pilgrim dark energy ($GGPDE$) model stems from the necessity to deal with crucial challenges in modern cosmology, particularly the nature of DE which is responsible for the observed rapid growth of the cosmos. This model provides a closer match with observational data, offering an improvement over the PDE model. Thus, by generalizing PDE, researchers aim to deep our comprehension of the universe expansion, bridge the gap between quantum field theory and cosmology. The $GGPDE$ model offers distinct insights and mechanisms that enhance our comprehension of the cosmic expansion. It provides a framework for the accelerated cosmic expansion without depending on a cosmological constant. Thus, $GGPDE$ represents a compelling direction in the quest to decipher the nature of the mysterious energy driving the expansion of our universe.

Modified gravitational theories offer valuable understanding of current phenomenon of accelerated cosmic expansion. Ebrahimi and Sheykhi [52] studied GDE model to examine cosmic acceleration in Brans-Dicke cosmology. Sheykhi and Movahed [53] explored several cosmological parameters to assess cosmic growth using GDE model. Jawad [54] investigated the dynamics and evolutionary trajectories of various cosmological parameters, using PDE in $f(T,T_G)$ theory. Fayaz et al [55] reformed the $f(R,T)$ gravity in relation to the GDE model. Odintsov et al [56] examined several $f(R,G)$ frameworks to clarify the successful emergence of DE and accelerating phase of the universe. The analysis suggested that the EoS parameter reflects a quintessence era. Myrzakulov et al [57] employed the PDE and GDE models to reconstruct the $f(Q)$ gravity. They found that their results align closely with the latest observational data. The study of various DE models to analyze the universe acceleration within the context of $f(R,T^2)$ theory has been explored in [58].

This study aims to rebuild $f(Q,C)$ model by using $GGPDE$ framework to analyze cosmic dynamics. The contents of this article are formatted as follows. Section **2** employs the $GGPDE$ model to rebuild $f(Q,C)$ functional form and explore the effects of non-interacting scenarios between DE and cold DM. Section **3** focuses on the advancement of this theory through the analysis of different cosmographic parameters. Section **4** gives a detailed overview of our findings.

## 2. FORMALISM OF $GGPDE$ $f(Q,C)$ MODEL

Here, we aim to develop the $GGPDE$ $f(Q,C)$ model to investigate the enigmatic nature of the universe. To analyze the cosmological characteristics of non-metric gravity, we consider the affine connection as

$$\Gamma^{\upsilon}_{\gamma\lambda} = \check{\Gamma}^{\upsilon}_{\gamma\lambda} + K^{\upsilon}_{\gamma\lambda} + \mathrm{L}^{\upsilon}_{\gamma\lambda}, \tag{1}$$

where Levi-Civita connection ($\check{\Gamma}$), disformation ($\mathrm{L}^{\upsilon}$) and contortion ($K^{\upsilon}_{\gamma\lambda}$) tensors are defined as

$$\check{\Gamma}^{\upsilon}_{\gamma\lambda} \equiv \frac{1}{2}g^{\upsilon\beta}(\partial_{\gamma}g_{\beta\lambda} + \partial_{\lambda}g_{\beta\gamma} - \partial_{\beta}g_{\gamma\lambda}), \tag{2}$$

$$\mathrm{L}^{\upsilon}_{\gamma\lambda} \equiv \frac{1}{2}g^{\upsilon\eta}(-Q_{\gamma\eta\lambda} - Q_{\lambda\eta\gamma} + Q_{\eta\gamma\lambda}), \tag{3}$$

$$K^{\upsilon}_{\gamma\lambda} \equiv \frac{1}{2}g^{\upsilon\eta}(T_{\gamma\eta\lambda} + T_{\lambda\eta\gamma} + T_{\eta\gamma\lambda}). \tag{4}$$

Here, the quantity $T_{\gamma\eta\lambda}$ refers to the torsion tensor, which although not central in the symmetric teleparallel framework (where torsion is usually set to zero), appears here as part of the general affine connection decomposition. Therefore, we use torsion-free condition in this context and thus $T_{\gamma\eta\lambda} = 0$ in our analysis. The non-metricity is given by

$$Q_{\upsilon\gamma\lambda} \equiv \nabla_{\upsilon}g_{\gamma\lambda} = \partial_{\upsilon}g_{\gamma\lambda} - \Gamma^{\eta}_{\upsilon\gamma}g_{\eta\lambda} - \Gamma^{\eta}_{\upsilon\lambda}g_{\gamma\eta}. \tag{5}$$

To construct a boundary term in the action of the metric-affine gravity theories, we need a non-metricity conjugate, known as the superpotential, defined as

$$P^{\upsilon}_{\gamma\lambda} = -\frac{1}{4}Q^{\upsilon}_{\gamma\lambda} + \frac{1}{2}Q_{(\gamma}{}^{\upsilon}{}_{\lambda)} + \frac{1}{4}(Q^{\upsilon} - \tilde{Q}^{\upsilon})g_{\gamma\lambda} - \frac{1}{4}\delta^{\upsilon}_{(\gamma}Q_{\lambda)}.$$

It plays a central role in defining the gravitational field equations. Non-metricity tensor features two different traces as $Q_{\gamma} = Q_{\gamma}{}^{\lambda}{}_{\lambda}$ and $\tilde{Q}^{\gamma} = Q_{\lambda}{}^{\gamma\lambda}$. Thus, we have

$$Q = -\frac{1}{4}Q_{\upsilon\gamma\lambda}Q^{\upsilon\gamma\lambda} + \frac{1}{2}Q_{\gamma\lambda\upsilon}Q^{\lambda\upsilon\gamma} + \frac{1}{4}Q_{\gamma}Q^{\gamma} - \frac{1}{2}Q_{\gamma}\,\tilde{Q}^{\gamma}. \tag{6}$$

By enforcing the torsion-free and curvature-free conditions, we obtain

$$\begin{aligned} \check{R}_{\gamma\lambda} + \check{\nabla}_{\upsilon}L^{\upsilon}_{\gamma\lambda} - \check{\nabla}_{\lambda}\tilde{L}_{\gamma} + \tilde{L}_{\upsilon}L^{\upsilon}_{\gamma\lambda} - L_{\upsilon\eta\lambda}L^{\upsilon\eta}{}_{\gamma} &= 0, & (7)\\ \check{R} + \check{\nabla}_{\gamma}(L^{\gamma} - \tilde{L}^{\gamma}) - Q &= 0, & (8) \end{aligned}$$

where $\check{\nabla}_{\upsilon}$ and $\check{R}_{\gamma\lambda}$ represent the covariant derivative and Ricci tensor, respectively, associated with the Levi-Civita connection. These notations are standard in the literature on symmetric teleparallel gravity to distinguish between operations involving the Levi-Civita connection and the general affine connection. Here, $\tilde{L}_{\gamma}$ represents the trace of the disformation tensor, i.e., $\tilde{L}_{\gamma} = L^{\lambda}_{\lambda\gamma}$, where $L^{\lambda}_{\gamma\delta}$ is the disformation tensor given in Eq.(3).

Since $Q^{\gamma} - \tilde{Q}^{\gamma} = L^{\gamma} - \tilde{L}^{\gamma}$, the boundary term is given by

$$C = \check{R} - Q = -\check{\nabla}_{\gamma}(Q^{\gamma} - \tilde{Q}^{\gamma}) = -\frac{1}{\sqrt{-g}}\partial_{\gamma}\big[\sqrt{-g}(Q^{\gamma} - \tilde{Q}^{\gamma})\big]. \tag{9}$$

In the context of $f(Q,C)$ gravity the integral action shown as

$$S = \int \frac{1}{2\kappa}[f(Q,C) + 2\kappa \mathrm{L}_m]\sqrt{-g}d^4x. \tag{10}$$

Here, $\kappa$ is the coupling constant. The corresponding field equations are

$$\begin{aligned} T_{\gamma\lambda} &= \frac{2}{\sqrt{-g}}\partial_{\upsilon}(\sqrt{-g}f_Q P^{\upsilon}_{\gamma\lambda}) + (P_{\gamma\upsilon\eta}Q^{\upsilon\eta}_{\lambda} - 2P_{\upsilon\eta\lambda}Q^{\upsilon\eta}_{\gamma})f_Q - \frac{f}{2}g_{\gamma\lambda}\\ &+ (\frac{C}{2}g_{\gamma\lambda} - \check{\nabla}_{\gamma}\check{\nabla}_{\lambda} + g_{\gamma\lambda}\check{\nabla}^{\upsilon}\check{\nabla}_{\upsilon} - 2P^{\upsilon}_{\gamma\lambda}\partial_{\upsilon})f_C, \end{aligned} \tag{11}$$

where $f_Q = \frac{\partial f}{\partial Q}$ and $f_C = \frac{\partial f}{\partial C}$. Variation of the action corresponding to affine connection yields

$$(\nabla_{\gamma} - \tilde{L}_{\gamma})(\nabla_{\lambda} - \tilde{L}_{\lambda})\big[4(f_Q - f_C)P^{\gamma\lambda}{}_{\upsilon} + \Delta_{\upsilon}{}^{\gamma\lambda}\big] = 0, \tag{12}$$

with

$$\Delta_{\upsilon}^{\gamma\lambda} = -\frac{2}{\sqrt{-g}}\frac{\delta(\sqrt{-g}L_m)}{\delta\Gamma^{\upsilon}{}_{\gamma\lambda}}.$$

Using the coincident gauge, we obtain

$$\partial_{\gamma}\partial_{\lambda}\big[\sqrt{-g}\big(4(f_Q - f_C)P^{\gamma\lambda}{}_{\upsilon} + \Delta_{\upsilon}{}^{\gamma\lambda}\big)\big] = 0. \tag{13}$$

Here, $\partial_{\lambda}\sqrt{-g} = -\sqrt{-g}\tilde{L}_{\lambda}$. Using the previous relations, we have

$$\begin{aligned} \big(\frac{1}{2}Qg_{\gamma\lambda} + \check{G}_{\gamma\lambda} + 2P^{\upsilon}{}_{\gamma\lambda}\partial_{\upsilon}\big)f_Q &= \frac{2}{\sqrt{-g}}\partial_{\upsilon}(\sqrt{-g}f_Q P^{\upsilon}{}_{\gamma\lambda}) + (P_{\gamma\upsilon\eta}Q_{\lambda}{}^{\upsilon\eta}\\ &- 2P_{\upsilon\eta\lambda}Q^{\upsilon\eta}{}_{\gamma})f_Q, \end{aligned} \tag{14}$$

The corresponding field equations are

$$\begin{aligned} T_{\gamma\lambda} &= -\frac{f}{2}g_{\gamma\lambda} + 2P^{\upsilon}{}_{\gamma\lambda}\nabla_{\upsilon}(f_Q - f_C) + \big(\frac{Q}{2}g_{\gamma\lambda} + \check{G}_{\gamma\lambda}\big)f_Q\\ &+ \big(\frac{C}{2}g_{\gamma\lambda} - \check{\nabla}_{\gamma}\check{\nabla}_{\lambda} + g_{\gamma\lambda}\check{\nabla}^{\upsilon}\check{\nabla}_{\upsilon}\big)f_C. \end{aligned} \tag{15}$$

By re-arranging this equation, we get

$$G_{\gamma\lambda} = \frac{1}{f_Q}\big(T^{(m)}_{\gamma\lambda} + T^{(D)}_{\gamma\lambda}\big), \tag{16}$$

where

$$\begin{aligned} T^{(D)}_{\gamma\lambda} &= \frac{f}{2}g_{\gamma\lambda} - 2P^{\upsilon}{}_{\gamma\lambda}\nabla_{\upsilon}(f_Q - f_C) - \big(\frac{1}{2}Cg_{\gamma\lambda} - \check{\nabla}_{\gamma}\check{\nabla}_{\lambda} + g_{\gamma\lambda}\check{\nabla}^{\upsilon}\check{\nabla}_{\upsilon}\big)f_C \\ &- \frac{Q}{2}f_Q g_{\gamma\lambda}. \end{aligned} \tag{17}$$

To explore the mysterious characteristics of the universe, we assume an isotropic and homogenous spacetime as

$$ds^2 = -dt^2 + (dx^2 + dy^2 + dz^2)\mathrm{a}^2(\mathrm{t}). \tag{18}$$

The ideal fluid encompasses the matter density $(\rho_m)$ and pressure $(p_m)$ is expressed as

$$T_{\gamma\lambda} = (\rho_m + p_m)U_{\gamma}U_{\lambda} + p_m g_{\gamma\lambda}. \tag{19}$$

Using Eqs.(17)-(19), we obtain

$$\begin{aligned} \rho_D + \rho_m &= 3H^2, \\ p_D + p_m &= -(2\dot{H} + 3H^2), \end{aligned} \tag{20}$$

where

$$\rho_D = 3H^2(1 - 2f_Q) - \frac{f}{2} + (3H^2 + 3\dot{H})f_C - 3H\dot{f_C}, \tag{21}$$

$$\begin{aligned} p_D &= -2\dot{H}(1 - f_Q) - 3H^2(1 - 2f_Q) + \frac{f}{2} + 2H\dot{f_Q} \\ &- (3H^2 + 3\dot{H})f_C + \ddot{f_C}. \end{aligned} \tag{22}$$

These modified equations represent a significant framework to comprehend the mysteries of the cosmos. To simplify these equations, we take our analysis to a specific class of functional in this theory with an ordinary parameter $(\alpha)$ as

$$f(Q, C) = f(Q) + \alpha C^2. \tag{23}$$

This functional form allows for a systematic investigation of deviations from standard gravitational dynamics, offering insights into the behavior of the universe under certain conditions. The field equations corresponding to this model turn out to be

$$\rho_D = 3H^2(1 - 2f_Q) - \frac{1}{2}(f(Q) + \alpha C^2) + 2\alpha C(3H^2 + 3\dot{H}) - 6\alpha H\dot{C} \tag{24}$$

$$\begin{aligned} p_D &= -2\dot{H}(1 - f_Q) - 3H^2(1 - 2f_Q) + \frac{1}{2}(f(Q) + \alpha C^2) + 2H\dot{f_Q} \\ &- 2\alpha C(3H^2 + 3\dot{H}) + 2\alpha\ddot{C}. \end{aligned} \tag{25}$$

The expressions for fractional energy densities are given by

$$\Omega_D = \frac{\rho_D}{3H^2}, \quad \Omega_m = \frac{\rho_m}{3H^2}. \tag{26}$$

The continuity equations of DM and DE for non-interacting case are

$$0 = \dot{\rho}_m + 3H(\rho_m + p_m), \tag{27}$$

$$0 = \dot{\rho}_D + 3H(\rho_D + p_D), \tag{28}$$

To quantifies how the universe expands over time, we study the behavior of scale factor which is considered as the key parameter in cosmology. It is a positive function that progresses over cosmic time, governing the expansion and the development of the universe. The decreasing behavior of scale factor suggests a cosmic contraction phase and its increasing behavior implies cosmic expansion era. It is directly related to the redshift of light from distant galaxies, allowing scientists to track the universe expansion history. Its study provides key insights into cosmic evolution from the big bang to the possible long-term fate of the universe, whether through continuous expansion or ultimate collapse.

We assume the scale parameter as

$$\mathrm{a}(\mathrm{t}) = \mathrm{a}_0\mathrm{t}^{\mu}. \tag{29}$$

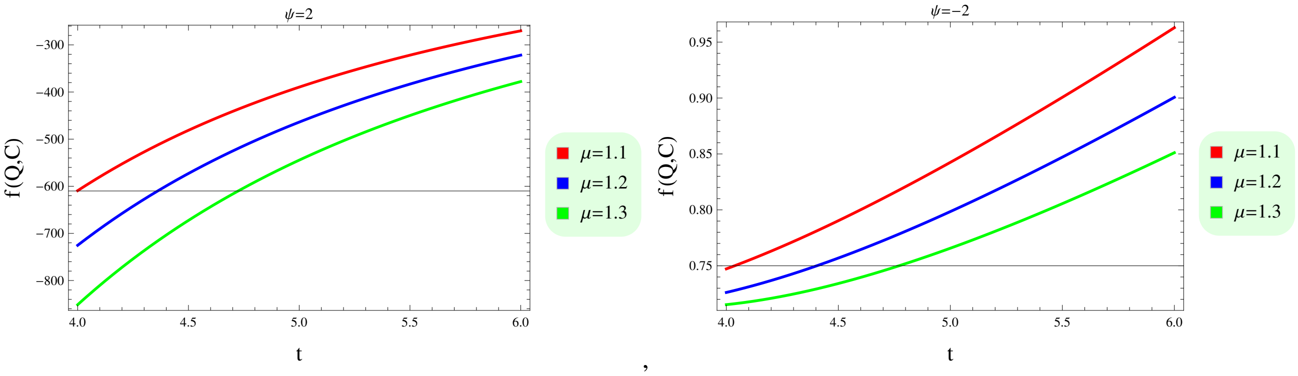

**Figure 1.** Plot of $f(Q, C)$ versus cosmic time for ($\psi = \pm 2$).

Here, $a_0 = 1$ and $\mu$ is an arbitrary constant. This form solves the field equations that govern the evolution of the universe, which helps to understand the broader dynamics of cosmic expansion and the behavior of DE. By exploring how the parameter $\mu$ influences evolution and correlating this with empirical observations, we gain a deep understanding of the characteristics of DE and the core principles of gravity. By comparing the power-law scale factor with cosmic observations, researchers can evaluate how $GGPDE$ model matches the cosmic observations. This process aids in validating or refining these models, providing valuable information about their accuracy and relevance.

To provide crucial insights into the cosmic acceleration, we analyze the behavior of Hubble parameter. The expansion of the cosmos is associated with a positive Hubble parameter, whereas contraction occurs with a negative value. The Hubble parameter changes over time depending on the universe energy composition, playing a crucial role in cosmic dynamics. It is fundamental in measuring cosmic distances, estimating the universe age and analyzing the influence of DE on expansion. The Hubble parameter is expressed as

$$H = \frac{\dot{\mathrm{a}}}{\mathrm{a}} = \frac{\mu}{t}. \tag{30}$$

Using this relation, we have

$$Q = 6\frac{\mu^2}{t^2}, \quad C = 6\mu(\frac{\mu - 1}{t^2}). \tag{31}$$

The cosmic accelerated expansion can also be explored using DE models. A novel dynamical model of DE known as PDE helps to understand the ongoing cosmic expansion. This model maintains consistency with observational constraints and can be characterized through multiple energy density parameterizations. Crucially, its inherent energy dissipation mechanism naturally resolves the coincidence problem triggered by DE dominance. Furthermore, the introduction of the PDE concept leads to the definition of a $GGPDE$ model. The $GGPDE$ model for energy density can be characterized by the following expression

$$\rho_D = (\xi H + \zeta H^2)^{\psi}. \tag{32}$$

Using Eqs.(24) and (32), we obtain

$$f(Q, C) = \frac{1}{3}(-3\sqrt{6}\alpha\dot{C}\sqrt{Q} + 2\alpha CQ + \frac{3c_1}{\sqrt{Q}} - \frac{6^{1-\frac{\psi}{2}}(\sqrt{Q}(2\zeta + \xi))^{\psi}}{\psi + 1} + Q), \tag{33}$$

where $c_1$ is an integration constant that arises during the reconstruction of the $f(Q, C)$ model using the $GGPDE$ ansatz. Inserting Eqs.(30) and (31) into (33), we get

$$\begin{aligned} f(Q, C) \quad &= \quad \frac{1}{3}(\frac{\sqrt{\frac{3}{2}}c_1}{\sqrt{\frac{\mu^2}{t^2}}} + \frac{72\alpha(\mu - 1)\mu^3}{t^4} - \frac{6((2\zeta + \xi)\sqrt{\frac{\mu^2}{t^2}})^{\psi}}{\psi + 1} \\ &+ \quad \frac{6\mu^2}{t^2} + \frac{216\alpha(\mu - 1)\mu\sqrt{\frac{\mu^2}{t^2}}}{t^3}). \end{aligned} \tag{34}$$

Specifically, we consider $\psi = \pm 2$, $\alpha = 9 \times 10^{-6}$, $c_1 = 0.04$, $\zeta = 10$ and $\xi = 90$. This consistent specification ensures the viable numerical results. As for the physical reasoning behind the choice of these parameter values, we emphasize that the selected values fall within the phenomenologically viable ranges used in prior studies involving ghost dark energy models and modified gravity frameworks. All these parameter values are chosen not arbitrarily. The parameter $\alpha$, which

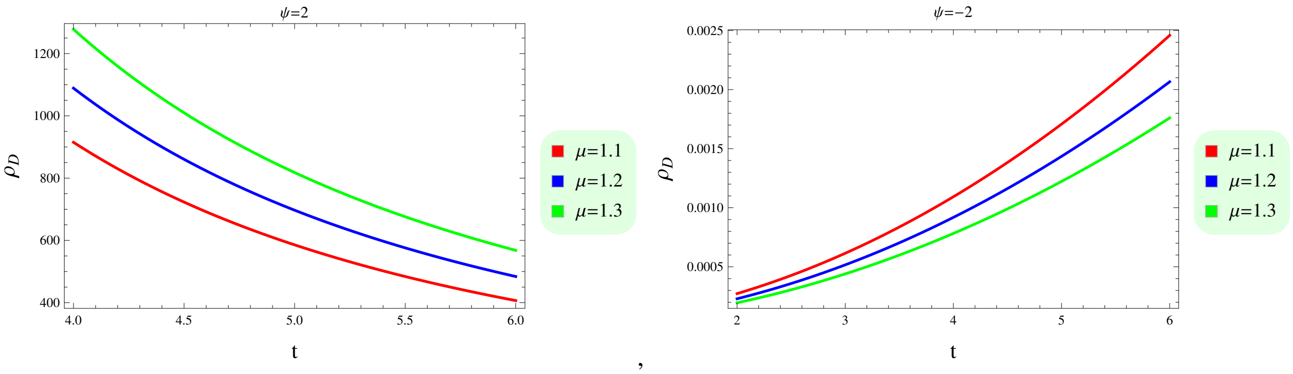

**Figure 2.** Graphical behavior of energy density against cosmic time.

controls the strength of the boundary term in the $f(Q,C)$ function is chosen to be small to ensure that the modification remains a perturbative correction to GR, consistent with Solar System constraints and cosmological observations. The constants $\xi$ and $\zeta$ appear in the GGPDE density, and their values are selected to reflect a balance between the linear and quadratic Hubble terms, capturing the interaction of DE with the expansion rate while avoiding divergences or nonphysical behavior at early or late times. Figure **1** demonstrates the dynamics of reconstructed $GGPDE\ f(Q,C)$ model for different values of $\mu = 1.1, 1.2, 1.3$. As $t$ increases, the function $f(Q,C)$ shows a decreasing trend for $\psi = 2$. In contrast, the function $f(Q,C)$ increases as $t$ grows for $\psi = -2$. Substituting Eq.(33) in (21) and (22), we get

$$\rho_D = \sqrt{6}\alpha\dot{C}\sqrt{Q} + \frac{1}{3}\alpha Q(Q-3C) + 6^{-\frac{\psi}{2}}\left(\sqrt{Q}(2\zeta+\xi)\right)^{\psi}, \tag{35}$$

$$p_D = \frac{1}{9}\left(-7\sqrt{6}\alpha\dot{C}\sqrt{Q} - 3\alpha Q(Q-3C)\right) - 6^{-\frac{\psi}{2}}\left(\sqrt{Q}(2\zeta+\xi)\right)^{\psi}. \tag{36}$$

Using Eqs.(30) and (31), we have

$$\begin{aligned}\rho_D &= [-24\alpha\mu^4 + 36\alpha\mu^3 + 72\alpha\mu t\sqrt{\frac{\mu^2}{t^2}} + t^4((2\zeta+\xi)\sqrt{\frac{\mu^2}{t^2}})^{\psi} \\ &- 72\alpha t^3(\frac{\mu^2}{t^2})^{3/2}][t^4]^{-1}, \qquad (37)\\ p_D &= [12\alpha\mu^3(2\mu-3) - 56\alpha\mu t\sqrt{\frac{\mu^2}{t^2}} - t^4((2\zeta+\xi)\sqrt{\frac{\mu^2}{t^2}})^{\psi} \\ &+ 56\alpha t^3(\frac{\mu^2}{t^2})^{3/2}][t^4]^{-1}. \qquad (38)\end{aligned}$$

Figures **2** and **3** show the behavior aligns with the characteristics of DE as energy density is positive and pressure is negative for all values of $\mu$ and $\psi$.

## 3. ANALYSIS OF COSMOGRAPHIC FACTORS

Here, we study the characteristics of various cosmological parameters, which serve as essential tools for describing the universe expansion history. They allow researchers to analyze cosmic evolution without relying on specific gravitational theories, making them useful for testing various cosmological frameworks.

### 3.1. Study of State Variable

The EoS variable ($\omega_D = \frac{p_D}{\rho_D}$) determines the nature of DE and other cosmological components by relating pressure to energy density. It plays a pivotal role in distinguishing various phases of cosmic evolution. Various values of $\omega_D$ determines the distinct cosmic eras, i.e., matter-dominated regions such as dust, radiative fluid and stiff matter are characterized by the values $\omega_D = 0$, $\omega_D = \frac{1}{3}$ and $\omega_D = 1$, respectively. The vacuum energy phase is represented by $\omega_D = -1$, the phantom energy phase corresponds to $\omega_D < -1$, whereas the quintessence phase is defined in the range $-1 < \omega_D < -\frac{1}{3}$. These different values of EoS parameter help to classify the evolution of the universe and its various expansion phases. Recent cosmological observations, such as data from the Planck satellite, indicate that the EoS parameter for DE may lie below $-1$. This supports the existence of phantom DE, which is an exotic form with negative kinetic energy. Such behavior explains the accelerated expansion of the universe. The corresponding expression for EoS parameter is given by

$$\omega_D = -\frac{\frac{1}{9}\left(7\sqrt{6}\alpha\dot{C}\sqrt{Q} + 3\alpha Q(Q-3C)\right) + 6^{-\frac{\psi}{2}}\left(\sqrt{Q}(2\zeta+\xi)\right)^{\psi}}{\sqrt{6}\alpha\dot{C}\sqrt{Q} + \frac{1}{3}\alpha Q(Q-3C) + 6^{-\frac{\psi}{2}}\left(\sqrt{Q}(2\zeta+\xi)\right)^{\psi}}. \tag{39}$$

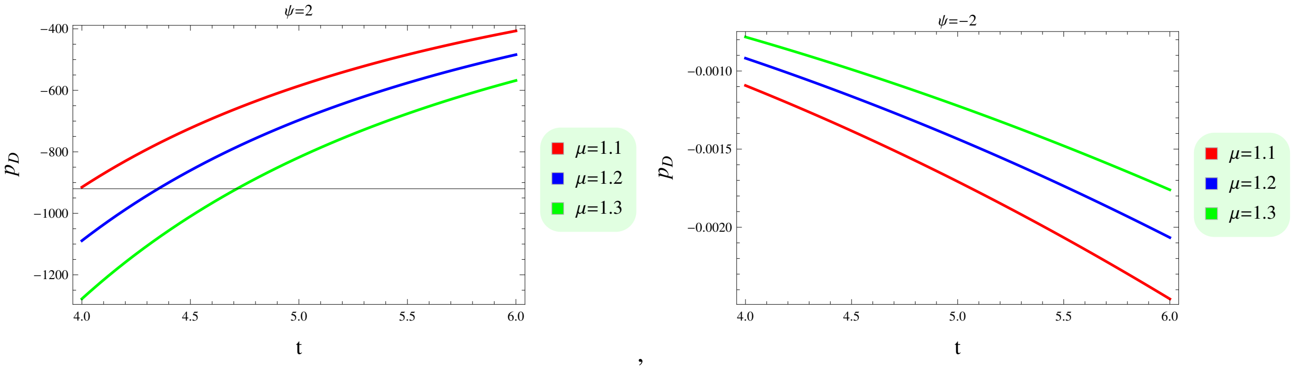

**Figure 3.** Evolution of pressure against cosmic time.

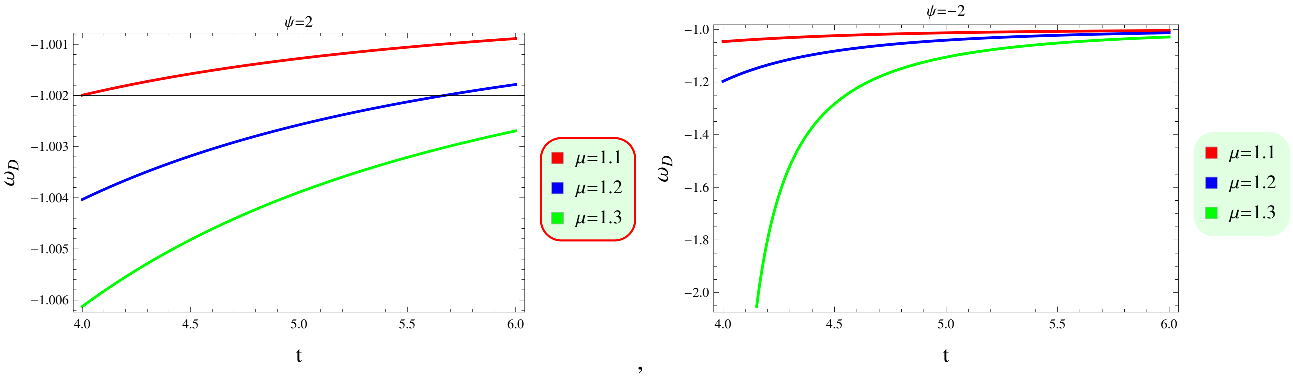

**Figure 4.** Plot of EoS parameter against cosmic time.

Using Eqs.(30) and (31), we have

$$\begin{aligned}\omega_D &= [-24\alpha\mu^4+36\alpha\mu^3+56\alpha\mu t\sqrt{\frac{\mu^2}{t^2}}+t^4((2\zeta+\xi)\sqrt{\frac{\mu^2}{t^2}})^{\psi}\\ &- 56\alpha t^3(\frac{\mu^2}{t^2})^{3/2}][12\alpha\mu^3(2\mu-3)-72\alpha\mu t\sqrt{\frac{\mu^2}{t^2}}-t^4((2\zeta\\ &+ \xi)\sqrt{\frac{\mu^2}{t^2}})^{\psi}+72\alpha t^3(\frac{\mu^2}{t^2})^{3/2}]^{-1}. \end{aligned} \tag{40}$$

Figure **4** determines the behavior of EoS parameter for three different values of $\mu$. This indicates that the model shows phantom era of DE for $\psi = 2$ and $\psi = -2$, satisfying the conditions for GGPDE phenomenon.

### 3.2. Analysis of $\omega_D - \omega'_D$ Plane

Here, we use $(\omega_D - \omega'_D)$ analysis to study the dynamics of DE, where prime denotes the derivative corresponding to non-metricity. This analysis helps in understanding how the modified terms influence the deceleration parameter and the transition between different cosmic phases. This phase plane is a useful tool in cosmology to comprehend the behavior and stability of DE models. The behavior of DE models incorporating a scalar field has been investigated in [59]. They also classified DE models in two main categories, i.e., the thawing region (characterized by a short-duration cosmic acceleration) which is shown when $\omega_D$ has a negative value and $\omega'_D$ is positive. The other one is freezing region (where acceleration continues over a long period) which is shown when both $\omega_D$ and $\omega'_D$ have negative value. The expression for $\omega'_D$ is given by

$$\omega'_D = \frac{\alpha\dot{C}6^{\frac{\psi+1}{2}}\left(\alpha Q6^{\psi/2}(C-Q)-(\psi-1)\left(\sqrt{Q}(2\zeta+\xi)\right)^{\psi}\right)}{\sqrt{Q}\left(\alpha\sqrt{Q}6^{\psi/2}\left(3\sqrt{6}\dot{C}+\sqrt{Q}(Q-3C)\right)+3\left(\sqrt{Q}(2\zeta+\xi)\right)^{\psi}\right)^2}. \tag{41}$$

Using Eqs.(30) and (31), we have

$$\omega'_D = \left[4\alpha(\mu-1)\mu t(36\alpha\mu^3+t^4(\psi-1)((2\zeta+\xi)\sqrt{\frac{\mu^2}{t^2}})^{\psi})\right]$$

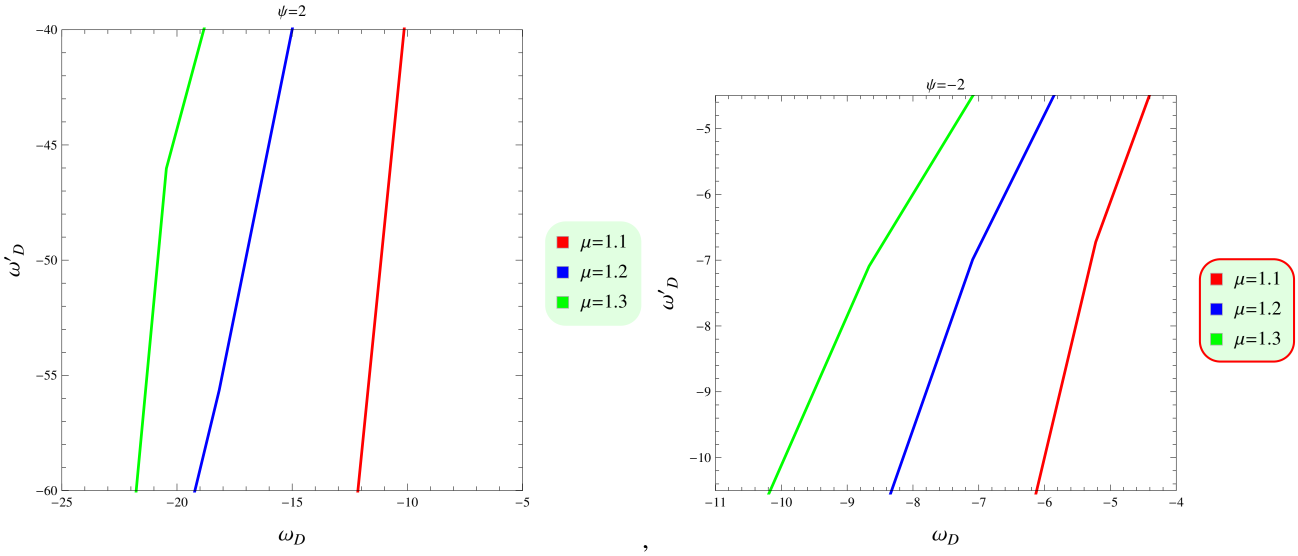

**Figure 5.** Graphical behavior of $\omega_D$ against $\omega'_D$.

$$
\begin{aligned}
\times \quad & \left[3\sqrt{\frac{\mu^2}{t^2}}(12\alpha\mu^3(3-2\mu)+72\alpha\mu t\sqrt{\frac{\mu^2}{t^2}}+t^4((2\zeta+\xi)\right. \\
\times \quad & \left.\sqrt{\frac{m^2}{t^2}})^{\psi}-72\alpha t^3(\frac{\mu^2}{t^2})^{3/2})^2\right]^{-1}. \qquad (42)
\end{aligned}
$$

Figure **5** shows that for every value of $\mu$ and $\psi = \pm 2$, $\omega_D < 0$ and $\omega'_D < 0$, showing the freezing region.

### 3.3. Study of $(r, s)$ Parameters

These parameters offer a deep insight into the dynamic behavior and evolutionary phases of DE models [60]. They help to differentiate between various cosmological models by mapping their distinct trajectories in $(r, s)$ plane. Specifically, the cold DM model is obtained for $(r, s) = (1, 0)$ while the standard model is found at $(r, s) = (1, 1)$. Additionally, the conditions $r < 1$ and $s > 0$ correspond to phantom and quintessence phases of DE. The Chaplygin gas model is represented by $s < 0$ and $r > 1$. These parameters are represented as

$$
\begin{aligned}
r &= \frac{\dddot{a}}{aH^3} = 1 + \frac{9\omega_D}{2}\Omega_D(1+\omega_D) - \frac{3\omega'_D}{2H}\Omega_D, \qquad (43) \\
s &= \frac{r-1}{3(q-\frac{1}{2})} = 1 + \omega_D - \frac{\omega'_D}{3\omega_D H}. \qquad (44)
\end{aligned}
$$

Inserting $\omega_D$ and $\omega'_D$ values, we obtain

$$
\begin{aligned}
r \;=\; & [\alpha Q6^{\psi/2}(-28\alpha\dot{C}^2Q + \dot{C}(-6\alpha C + 3\sqrt{6}Q^{3/2}(2\alpha C+1) - 2\sqrt{6}\alpha Q^{5/2} \\
+ \; & 6\alpha Q) + Q^2(Q-3C)) + 3(2\alpha\dot{C}(-\sqrt{6}Q^{3/2}+\psi-1) + Q^2)(\sqrt{Q}(2\zeta \\
+ \; & \xi))^{\psi}][\alpha Q^{5/2}6^{\psi/2}(3\sqrt{6}\dot{C} + \sqrt{Q}(Q-3C)) + 3Q^2(\sqrt{Q}(2\zeta+\xi))^{\psi}]^{-1}, \qquad (45) \\
s \;=\; & [\alpha^2\dot{C}Q2^{\psi+1}3^{\psi}(Q(14\dot{C} + \sqrt{6}Q^{3/2}-3) + C(3-3\sqrt{6}Q^{3/2})) - \alpha\dot{C}6^{\frac{\psi}{2}+1} \\
\times \; & (-\sqrt{6}Q^{3/2}+\psi-1)(\sqrt{Q}(2\zeta+\xi))^{\psi}][Q(7\alpha^2\dot{C}^2Q2^{\psi+1}3^{\psi+2} + \alpha\dot{C} \\
\times \; & \sqrt{Q}2^{\frac{\psi+9}{2}}3^{\frac{\psi+1}{2}}(\alpha Q6^{\psi/2}(Q-3C) + 3(\sqrt{Q}(2\zeta+\xi))^{\psi}) + 3(\alpha Q6^{\psi/2} \\
\times \; & (Q-3C) + 3(\sqrt{Q}(2\zeta+\xi))^{\psi})^2)]^{-1}. \qquad (46)
\end{aligned}
$$

Using Eqs.(30) and (31), we have

$$
\begin{aligned}
r \;=\; & [1728\alpha^2\mu^7 t\sqrt{\frac{\mu^2}{t^2}} + \frac{216\alpha\mu^7 t}{\sqrt{\frac{\mu^2}{t^2}}} - 4320\alpha^2\mu^6 t\sqrt{\frac{\mu^2}{t^2}} - \frac{216\alpha\mu^6 t}{\sqrt{\frac{\mu^2}{t^2}}} \\
+ \; & 2592\alpha^2\mu^5 t\sqrt{\frac{\mu^2}{t^2}} - 72\alpha\mu^5 t^3(2\zeta+\xi)((2\zeta+\xi)\sqrt{\frac{\mu^2}{t^2}})^{\psi-1}
\end{aligned}
$$

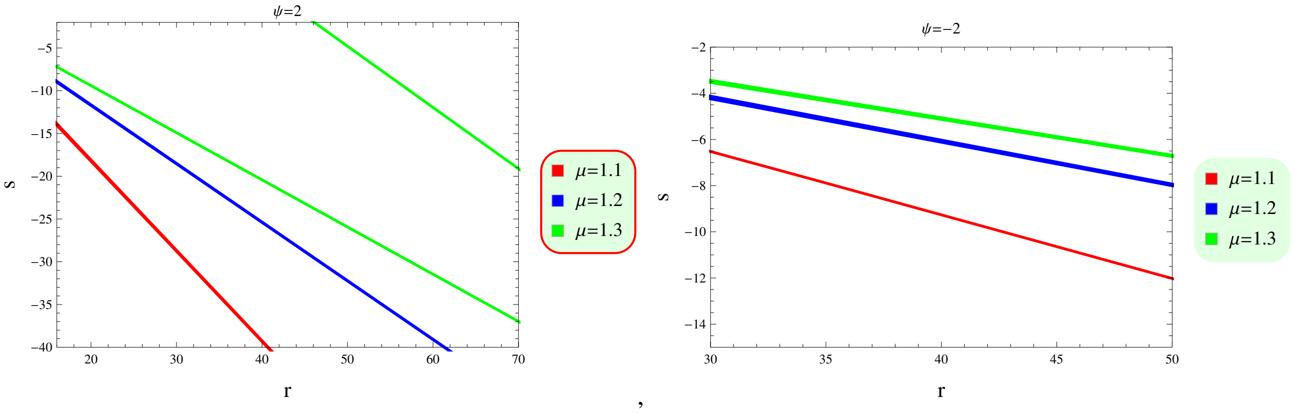

**Figure 6.** Graphical representation of diagnostic pair.

$$
\begin{aligned}
&+\quad 72\alpha\mu^4t^3(2\zeta+\xi)((2\zeta+\xi)\sqrt{\frac{\mu^2}{t^2}})^{\psi-1}+t^6(-3\mu^3+2\alpha\mu t(\psi-1)\\
&-\quad 2\alpha t(\psi-1))((2\zeta+\xi)\sqrt{\frac{\mu^2}{t^2}})^{\psi}+36\alpha\mu^3((2\mu-3)\mu^3t^2+2\alpha(\mu\\
&-\quad 1)(56(\mu-1)\mu^2+t^3))][3\mu^3t^2(12\alpha\mu^3(2\mu-3)-72\alpha\mu t\sqrt{\frac{\mu^2}{t^2}}\\
&-\quad t^4((2\zeta+\xi)\sqrt{\frac{\mu^2}{t^2}})^{\psi}+72\alpha t^3(\frac{\mu^2}{t^2})^{3/2})]^{-1},
\end{aligned}
\tag{47}
$$

$$
\begin{aligned}
s \quad =&\quad [4\alpha(\mu-1)(36\alpha\mu^3t^3+t^7(\psi-1)((2\zeta+\xi)\sqrt{\frac{\mu^2}{t^2}})^{\psi}+288\alpha\mu^6\\
\times&\quad (3t\sqrt{\frac{\mu^2}{t^2}}+7)-144\alpha\mu^5(9t\sqrt{\frac{\mu^2}{t^2}}+14)-36\mu^4t^3(2\zeta+\xi)((2\zeta\\
+&\quad \xi)\sqrt{\frac{\mu^2}{t^2}})^{\psi-1})][9\mu(144\alpha^2\mu^4(\mu(\mu(4(\mu-3)\mu+37)-56)+28)\\
+&\quad t^8((2\zeta+\xi)\sqrt{\frac{\mu^2}{t^2}})^{2\psi}+3072\alpha^2\mu^6t\sqrt{\frac{\mu^2}{t^2}}-7680\alpha^2\mu^5t\sqrt{\frac{\mu^2}{t^2}}\\
+&\quad 4608\alpha^2\mu^4t\sqrt{\frac{\mu^2}{t^2}}-128\alpha\mu^4t^3(2\zeta+\xi)((2\zeta+\xi)\sqrt{\frac{\mu^2}{t^2}})^{\psi-1}\\
-&\quad 24\alpha\mu^3(2\mu-3)t^4((2\zeta+\xi)\sqrt{\frac{\mu^2}{t^2}})^{\psi}+128\alpha\mu^3t^3(2\zeta+\xi)((2\zeta\\
+&\quad \xi)\sqrt{\frac{\mu^2}{t^2}})^{\psi-1})]^{-1}.
\end{aligned}
\tag{48}
$$

Figure **6** demonstrates Chaplygin gas model ($r > 1$ and $s < 0$) for $\psi = \pm 2$ and different values of $\mu$.

### 3.4. Stability Criteria

The ability of an object to regain its equilibrium state after being subjected to external forces is termed as stability. The squared sound speed ($v_s^2$) parameter plays a key role in cosmological models, as it dictates the stability of cosmic models. When $v_s^2$ is positive, it indicates stability within the model, whereas its negative value indicates instability. This relationship can be expressed as follows

$$
v_s^2=\frac{\dot{p}_D}{\dot{\rho}_D}=\frac{\rho_D}{\dot{\rho}_D}\omega'_D+\omega_D. \tag{49}
$$

Manipulating this equation, we have

$$
v_s^2=\frac{-7\alpha\dot{C}\sqrt{Q}6^{\frac{\psi+1}{2}}+\alpha Q6^{\frac{\psi}{2}+1}(3C-2Q)-9\psi\left(\sqrt{Q}(2\zeta+\xi)\right)^{\psi}}{3\left(\alpha\sqrt{Q}6^{\psi/2}\left(3\sqrt{6}\dot{C}+2\sqrt{Q}(2Q-3C)\right)+3\psi\left(\sqrt{Q}(2\zeta+\xi)\right)^{\psi}\right)}. \tag{50}
$$

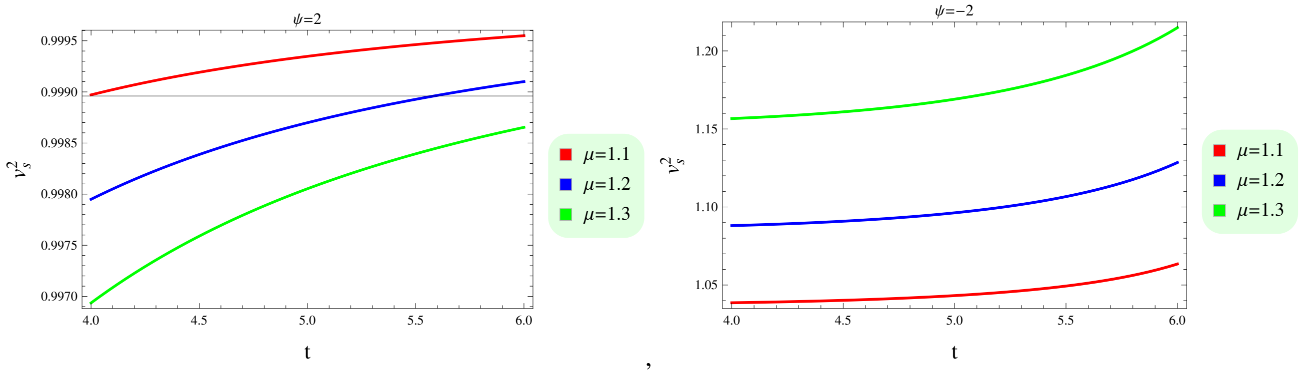

**Figure 7.** Plot of sound speed parameter against cosmic time.

Using Eqs.(30) and (31), it follows that

$$\begin{aligned} v_s^2 &= [-24\alpha(\mu-3)\mu^3 + 56\alpha\mu t\sqrt{\frac{\mu^2}{t^2}} + t^4\psi((2\zeta+\xi)\sqrt{\frac{\mu^2}{t^2}})^{\psi} \\ &- 56\alpha t^3(\frac{\mu^2}{t^2})^{3/2}][24\alpha(\mu-3)\mu^3 - 72\alpha\mu t\sqrt{\frac{\mu^2}{t^2}} - t^4\psi((2\zeta \\ &+ \xi)\sqrt{\frac{\mu^2}{t^2}})^{\psi} + 72\alpha t^3(\frac{\mu^2}{t^2})^{3/2}]^{-1}. \end{aligned} \tag{51}$$

Figure **7** demonstrates that the reconstructed $GGPDE\ f(Q,C)$ model is stable across different cosmic epochs.

## 4. FINAL RESULTS

The reconstruction method in modified theories serves as a useful approach to develop a viable DE model and understand the cosmic evolution. The inspiration for exploring a reconstructed $f(Q,C)$ framework comes form its crucial theoretical and empirical factors in gravitational physics and cosmology. The boundary term in the functional action is vital to the dynamical equations, providing novel clarity on cosmic progression. This proposed theory offers an explanation for the accelerating universe without depending on a cosmological constant, resolving DE problem. This modified proposal has garnered significant attention for their capacity to expand GR by aligning with various observational and experimental constraints. The connection between boundary term and non-metricity enhance the viability and enables a broad spectrum of feasible solutions. Consequently, this theoretical framework opens up the new avenues for developing cosmic frameworks that align with current observations. The main motivation for exploring the GGPDE model in $f(Q,C)$ theory is to better understand the accelerated cosmic expansion.

This analysis has investigated GGPDE model in the framework of non-metric gravity. We have used standard diagnostic instruments and the state finder pair to analyze different cosmic eras. We have assessed stability of the model using squared sound speed method. The main results are summarized as follows.

- The reconstructed $f(Q,C)$ model indicates a decreasing pattern for $\psi = 2$ and increasing behavior for $\psi = -2$, which demonstrates the realistic model behavior (Figure **1**).
- The decreasing behavior of the matter contents is consistent with the expected behavior of DE for all values of $\mu$ and $\psi$ (Figures **2** and **3**).
- Our analysis reveals that the EoS parameter lies within the phantom region for all values of $\mu$ (Figure **4**).
- The upward trend in the $(\omega_D - \omega'_D)$ reveals the freezing region, which suggests that non-interacting case leads to a rapid cosmic evolution (Figure **5**).
- The $(r-s)$-plane determines Chaplygin gas model associated with non-interacting GGPDE $f(Q,C)$ model (Figure **6**).
- Our results show that $v_s^2$ is positive for each value of $\mu$, indicating that GGPDE $f(Q,C)$ model is stable (Figure **7**).

The GGPDE $f(Q,C)$ model exhibits stable features and consistently corresponds with the present cosmic expansion. It is important to note that our findings are consistent with the existing observational data [61]

$$\omega_D = -1.023^{+0.091}_{-0.096}(PlanckTT + LowP + ext),$$

$$\omega_D = -1.006^{+0.085}_{-0.091}(PlanckTT + LowP + lensing + ext),$$
$$\omega_D = -1.019^{+0.075}_{-0.080}(PlanckTT, TE, EE + LowP + ext).$$

With a 95% confidence level, the data was gathered using a variety of observational techniques. Notably, our results align well with the predictions of the quantum chromodynamics ghost model within modified gravitational theories [62, 63]. Moreover, they are in agreement with recent theoretical and observational studies [57].

## Acknowledgements

This research was funded by Princess Nourah bint Abdulrahman University Researchers Supporting Project number (PNURSP2025R328), Princess Nourah bint Abdulrahman University, Riyadh, Saudi Arabia.

**Data Availability Statement:** No new data were generated or analyzed in support of this research.

## ORCID

**Muhammad Sharif**, https://orcid.org/0000-0001-6845-3506; **Eman M. Moneer**, https://orcid.org/0000-0002-1255-6335; **Muhammad Zeeshan Gul**, https://orcid.org/0000-0003-4202-867X; **Muhammad Hassan Shahid**, https://orcid.org/0009-0003-4102-9045; **Euaggelos E. Zotos**, https://orcid.org/0000-0002-1565-4467

## REFERENCES

[1] A.G. Riess, A.V. Filippenko, P. Challis, *et al.*, Astron. J. **116**, 1009 (1998). https://doi.org/10.1086/300499

[2] Perlmutter, S. *et al.*, Astrophys. J. **517**, 565 (1999). https://doi.org/10.1086/307221

[3] P. de Bernardis, *et al.*, Nature, **404**, 955 (2000). https://doi.org/10.1038/35010035

[4] A.G. Riess, *et al.*, Astrophys. J. **730**, 119 (2011). https://doi.org/10.1088/0004-637x/730/2/119

[5] P.A. Ade, *et al.*, Astron. Astrophys. **594**, 63 (2016). https://doi.org/10.1051/0004-6361/201525830

[6] I.I. Shapiro, C.C. Counselman, and R.W. King, Phys. Rev. Lett. **36**, 555 (1976). https://doi.org/10.1103/PhysRevLett.36.555

[7] V. Sahni, and Starobinsky, A.A.: Int. J. Mod. Phys. D, **9**, 373 (2000). https://doi.org/10.1142/S0218271800000542

[8] S.M. Carroll, Living Rev. Rel. **4**, 56 (2001). https://doi.org/10.12942/lrr-2001-1

[9] P.J.E. Peebles, and B. Ratra, Rev. Mod. Phys. **75**, 559 (2003). https://doi.org/10.1103/RevModPhys.75.559

[10] T. Padmanabhan, Phys. Rep. **380**, 235 (2003). https://doi.org/10.1016/S0370-1573(03)00120-0

[11] E.J. Copeland, M. Sami, and S. Tsujikawa, Int. J. Mod. Phys. D, **15**, 1753 (2006). https://doi.org/10.1142/S021827180600942X

[12] S.I. Nojiri, and S.D. Odintsov, Int. J. Geom. Methods Mod. Phys. **4**, 115 (2007). https://doi.org/10.1142/S0219887807001928; T.P. Sotiriou, and V. Faraoni, Rev. Mod. Phys. **82**, 451 (2010). https://doi.org/10.1103/RevModPhys.82.451

[13] H. Weyl, Sitzungsber. Preuss. Akad. Wiss. **26**, 465 (1918).

[14] L.E. Cartan, C.R. and Acad. Sci. Paris **174**, 593 (1922).

[15] R. Weitzenbӧck, *Invariantentheorie*, (Groningen, The Netherlands, (1923).

[16] K. Hayashi, and T. Shirafuji, Phys. Rev. D, **19**, 3524 (1979). https://doi.org/10.1103/PhysRevD.19.3524

[17] A. Conroy, and T. Koivisto, Eur. Phys. J. C, **78**, 923 (2018). https://doi.org/10.1140/epjc/s10052-018-6410-z

[18] M. Adeel, *et al.*, Mod. Phys. Lett. A, **38**(34n35), 2350152 (2023). https://doi.org/10.1142/S0217732323501523

[19] A. Waseem, *et al.*, Eur. Phys. J. C, **83**, 1088 (2023). https://doi.org/10.1140/epjc/s10052-023-12239-7

[20] M.Z. Gul, *et. al.*, Eur. Phys. J. C, **84**, 8 (2024). https://doi.org/10.1140/epjc/s10052-023-12368-z

[21] M. Sharif, *et al.*, Chin. J. Phys. **91**, 66 (2024). https://doi.org/10.1016/j.cjph.2024.07.010

[22] M.Z. Gul, *et al.*, Eur. Phys. J. C, **84**, 802 (2024). https://doi.org/10.1140/epjc/s10052-024-13162-1

[23] M. Sharif, *et al.*, New Astron. **109**, 102211 (2024). https://doi.org/10.1016/j.newast.2024.102211

[24] L. Heisenberg, Phys. Rep. **1066**, 1 (2024). https://doi.org/10.1016/j.physrep.2024.02.001

[25] M. Sharif, *et al.*, Eur. Phys. J. C, **84**, 1065 (2024). https://doi.org/10.1140/epjc/s10052-024-13432-y

[26] M.Z. Gul, *et al.*, Eur. Phys. J. C, **84**, 775 (2024). https://doi.org/10.1140/epjc/s10052-024-13156-z

[27] S. Rani, *et al.*, Int. J. Geom. Methods Mod. Phys. **21**(01), 2450033 (2024). https://doi.org/10.1142/S0219887824500336

[28] G. Nan, *et al.*, Phys. Dark Universe, **46**, 101635 (2024). https://doi.org/10.1016/j.dark.2024.101635

[29] F. Javed, *et al.*, Nucl. Phys. B, **1018**, 117001 (2025). https://doi.org/10.1016/j.nuclphysb.2025.117001

[30] F. Javed, *et al.*, Ann. Phys. **476**, 169956 (2025). https://doi.org/10.1016/j.aop.2025.169956

[31] M.M.M. Nasir, *et al.*, Eur. Phys. J. C, **85**, 189 (2025). https://doi.org/10.1140/epjc/s10052-025-13899-3

[32] S. Rani, *et al.*, Phys. Dark Universe, **47**, 101754 (2025). https://doi.org/10.1016/j.dark.2024.101754

[33] M. Sharif, *et al.*, Phys. Dark Universe, **47**, 101760 (2025). https://doi.org/10.1016/j.dark.2024.101760

[34] I. Hashim, *et al.*, High Energy Density Phys. **57**, 101223 (2025). https://doi.org/10.1016/j.hedp.2025.101223

[35] F. Javed, *et al.*, Ann. Phys. **482**, 170189 (2025). https://doi.org/10.1016/j.aop.2025.170189

[36] M. Adeel, *et al.*, Mod. Phys. Lett. A, **40**, 2450213 (2025). https://doi.org/10.1142/S0217732324502134

[37] I. Hashim, *et al.*, Int. J. Geom. Methods Mod. Phys. **22**, 2540049 (2025). https://doi.org/10.1142/S0219887825400493

[38] A. De, T.H. Loo, and E.N. Saridakis, J. Cosmol. Astropart. Phys. **03**, 050 (2024). 10.1088/1475-7516/2024/03/050

[39] A. Samaddar, *et al.*, Nucl. Phys. B, **1006**, 116643 (2024). https://doi.org/10.1016/j.nuclphysb.2024.116643

[40] M. Sharif, *et al.*, Phys. Dark Universe, **48**, 101839 (2025). https://doi.org/10.1016/j.dark.2025.101839

[41] M. Sharif, *et al.*, High Energy Density Phys. **55**, 101185 (2025). https://doi.org/10.1016/j.hedp.2025.101185

[42] M. Sharif, *et al.*, Phys. Lett. A, **555**, 130773 (2025). https://doi.org/10.1016/j.physleta.2025.130773

[43] D.C. Maurya, Mod. Phys. Lett. A, **39**, 2450034 (2024). https://doi.org/10.1142/S0217732324500342

[44] D.C. Maurya, Astron. Comput. **46**, 100798 (2024). https://doi.org/10.1016/j.ascom.2024.100798

[45] N. Myrzakulov, *et al.*, Phys. Dark Universe, **47**, 101790 (2024). https://doi.org/10.1016/j.dark.2024.101790

[46] N. Myrzakulov, A. Pradhan, and S.H. Shekh, arXiv 2412.01164, (2024). https://doi.org/10.48550/arXiv.2412.01164

[47] D.C. Maurya, Gravit. Cosmol. **30**, 330 (2024). https://doi.org/10.1134/S0202289324700245

[48] M. Usman, A. Jawad, and A.M. Sultan, Eur. Phys. J. C, **84**, 868 (2024). https://doi.org/10.1140/epjc/s10052-024-13219-1

[49] S.D. Sadatian, and S.M.R. Hosseini, Phys. Dark Universe, **47**, 101737 (2024). https://doi.org/10.1016/j.dark.2024.101737

[50] A. Samaddar, *et al.*, Nucl. Phys. B, **1006**, 116643 (2024). https://doi.org/10.1016/j.nuclphysb.2024.116643

[51] H. Wei, Class. Quantum Grav. **29**, 175008 (2012). https://doi.org/10.1088/0264-9381/29/17/175008L

[52] E. Ebrahimi, and A. Sheykhi, Phys. Lett. B, **706**, 19 (2011). https://doi.org/10.1016/j.physletb.2011.11.008

[53] A. Sheykhi, and M.S. Movahed, Gen. Relativ. Gravit. **44**, 449 (2012). https://doi.org/10.1007/s10714-011-1286-3

[54] A. Jawad, Astrophys. Space Sci. **356**, 119 (2015). https://doi.org/10.1007/s10509-014-2191-5

[55] V. Fayaz, *et al.*, Eur. Phys. J. Plus, **131**, 22 (2016). https://doi.org/10.1140/epjp/i2016-16022-x

[56] S.D. Odintsov, V.K. Oikonomou, and S. Banerjee, Nucl. Phys. B, **938**, 935 (2019). https://doi.org/10.1016/j.nuclphysb.2018.07.013

[57] N. Myrzakulov, *et al.*, Front. Astron. Space Sci. **9**, 902552 (2022). https://doi.org/10.3389/fspas.2022.902552

[58] M. Sharif, M.Z. Gul, and I. Hashim, Phys. Dark Universe, **46**, 101606 (2024). https://doi.org/10.1016/j.dark.2024.101606; Eur. Phys. J. C, **84**, 1094 (2024). https://doi.org/10.1140/epjc/s10052-024-13473-3; Chin. J. Phys. **89**, 266 (2024). https://doi.org/10.1016/j.cjph.2024.03.020

[59] R.R. Caldwell, and E.V. Linder, Phys. Rev. Lett. **95**, 141301 (2005). https://doi.org/10.1103/PhysRevLett.95.141301

[60] V. Sahni, *et al.*, J. Exp. Theor. Phys. Lett. **77**, 201 (2003). https://doi.org/10.1134/1.1574831

[61] P.A. Ade, *et al.*, Astron. Astrophys. **594**, A13 (2016). https://doi.org/10.1051/0004-6361/201525830

[62] S. Chattopadhyay, Eur. Phys. J. Plus, **129**, 82 (2014). https://doi.org/10.1140/epjp/i2014-14082-6

[63] M. Zubair, and G. Abbas, Astrophys. Space Sci. **357**, 154 (2015). https://doi.org/10.1007/s10509-015-2387-3

## КОСМОЛОГІЧНА ДІАГНОСТИКА ТА СТАБІЛЬНІСТЬ МОДЕЛІ ТЕМНОЇ ЕНЕРГІЇ В НЕМЕТРИЧНІЙ ГРАВІТАЦІЇ

**Мухаммед Шаріф[1,4], Еман М. Монер[2], Мухаммад Зішан Гюль[1], Мухаммад Хасан Шахід[1], Еуагелос Е. Зотос[3]**
[1]*Кафедра математики та статистики, Лахорський університет, 1-KM Defence Road, Лахор-54000, Пакистан*
[2]*Кафедра фізики, Коледж наук, Університет принцеси Нури бінт Абдулрахман,*
*P.O. Box 84428, Ріяд 11671, Саудівська Аравія*
[3]*Кафедра фізики, Школа наук, Університет Арістотеля в Салоніках, GR 54124, Салоніки, Греція*
[4]*Дослідницький центр астрофізики та космології, Хазарський університет,*
*Баку, AZ1096, вулиця Мехсеті, 41, Азербайджан*

У цій роботі ми досліджуємо динаміку узагальненої темної енергії привида-піломника на тлі гравітації $f(Q,C)$, де $Q$ – це неметричний скаляр, а $C$ – граничний член. Для досягнення цієї мети ми беремо ізотропний та однорідний Всесвіт з ідеальним розподілом матерії. Наш аналіз включає сценарій з невзаємодіючими рідинами, що охоплює як темну матерію, так і темну енергію. Щоб зрозуміти космічну динаміку, ми реконструюємо модель $f(Q,C)$ та досліджуємо її вплив на еволюцію Всесвіту. Ми досліджуємо ключові космологічні фактори, тобто змінну стану, поведінку $(\omega_D-\omega'_D)$-площини та діагностичну пару statefinder, які допомагають аналізувати розширення космосу. Ключовим аспектом нашого аналізу є стабільність узагальненої моделі темної енергії пілігрима-привида, отриманої за допомогою методу квадрата швидкості звуку, що підтверджує її життєздатність у підтримці спостережуваного прискореного розширення. Наші результати узгоджуються з даними спостережень, демонструючи, що гравітація $f(Q,C)$ забезпечує надійну теоретичну основу для опису темної енергії та динаміки Всесвіту у великих масштабах. Ця робота не лише поглиблює наше розуміння модифікованої гравітації та таємничої енергії, але й пропонує нові погляди на альтернативне пояснення космічного прискорення поза стандартними парадигмами.

**Ключові слова:** $f(Q,C)$ *гравітація; модель темної енергії; аналіз стабільності*

East European Journal of Physics. 4. 42–52 (2025)

DOI: 10.26565/2312-4334-2025-4-04 ISSN 2312-4334

# MODIFIED QCD GHOST SCALAR FIELD DARK ENERGY IN ANISOTROPIC AND INTERACTING UNIVERSE MODELS

**P. Jnana Prasuna**[1], **T. Chinnappalanaidu**[2], **G. Satyanarayana**[3], **N. Krishna Mohan Raju**[4], **K. Navya**[5], **Y. Sobhanbabu**[4*]

[1]*Department of Basic Sciences, Sri Vasavi Engineering College (A), Tadepalligudem-534101, India*
[2]*Department of Mathematics, Vignan's Institute of Information Technology(Autonomous), Visakhapatnam, India*
[3]*Department of Applied Sciences & Humanities, Sasi Institute of Technology & Engineering (A), Tadepalligudem-534101, India*
[4]*Department of Engineering Mathematics and Humanities, SRKR Engineering College (A), Bhimavaram-534204, India*
[5]*Department of Basic Science and Humanities, Centurion University of Technology and Management, Vizianagaram-535003, India*
[*]*Corresponding Author e-mail: sobhan.maths@gmail.com*

Received July 22, 2025; revised September 23, 2024; in final form October 21, 2025; accepted October 23, 2025

In this work, we study the Bianchi type-III interacting framework of modified QCD ghost dark energy with cold dark matter is being considered for illustrating the accelerated expansion of the Universe. The equation of state parameter shows evolution of the Universe completely varies in quintessence region only. The dynamics of scalar field and corresponding potential of various scalar field models shows consistence behavior with the accelerated expansion phenomenon. Also, the kinetic energy term of k-essence models lies within the range where equation of state parameter represents the accelerated expansion of the Universe.

**Keywords:** *Bianchi type-III; QCD ghost dark energy; Cold dark matter; Scalar field models*

**PACS:** 98.80.-k; 95.36.+X

## 1. INTRODUCTION

Dark Energy (DE) is a captivating and enigmatic component of the Universe, widely believed to be responsible for its accelerated expansion. This phenomenon has been strongly supported by numerous observational datasets, including those from Ref [1, 2]. DE exhibits a repulsive gravitational effect, yet its fundamental nature remains largely unknown. The cosmological constant is the earliest and simplest candidate for DE. However, it suffers from two major theoretical challenges: the 'cosmic coincidence' problem and the 'fine-tuning' issue [3], which limit its acceptance in current discussions of DE. To overcome these limitations, a wide range of dynamical DE models have been proposed, including quintessence, k-essence, and various perfect fluid models [4]. Among these, perfect fluid models are particularly notable for their specific forms of the equation of state, encompassing frameworks such as the chaplygin gas family [5, 6], holographic DE [7, 8], new agegraphic DE [9], and the power-law entropy-corrected models like pilgrim dark energy (PDE) [10, 11, 12, 13]. Another intriguing approach is the quantum chromodynamics (QCD) ghost DE model, presented in various versions [14, 15, 16, 17]. Comprehensive reviews of these dynamical models can be found in Copeland et al. [18] and Bamba et al. [19]. In the framework of QCD, a dynamical DE model known as 'Veneziano ghost dark energy' has been proposed, inspired by the concept of the Veneziano ghost. This model originates from attempts to resolve the long-standing $U(1)$ axial anomaly problem in QCD. It has been suggested that the Veneziano ghost can induce non-trivial physical effects in a Friedmann-Robertson-Walker (FRW) Universe [20, 21]. Specifically, the QCD ghost contributes to the vacuum energy density through a term proportional to $\Lambda^3_{\mathrm{QCD}}H$, where $\Lambda_{\mathrm{QCD}} \sim 100$ MeV represents the QCD energy scale and $H$ is the Hubble parameter. Although this contribution is relatively small, it plays a significant role in the dynamics of the Universes evolution.

Importantly, this model has been proposed as a potential solution to two major theoretical challenges of the cosmological constant: the fine-tuning problem and the cosmic coincidence problem [22, 23, 24]. The theoretical investigations of this model via various cosmological parameters have been conducted in several works [25, 26, 27, 28, 29, 30]. Additionally, its compatibility with observational data has been explored [31], further supporting its relevance in modern cosmology. Moreover, the Veneziano ghost field in QCD, expressed in the form $H + O(H^2)$, can provide sufficient vacuum energy to account for the accelerated expansion of the Universe [32, 33]. However, the conventional ghost dark energy model incorporates only the leading-order term.

A modified version of this model was later proposed, in which the energy density of generalized ghost dark energy (QCD) ghost dark energy is associated with the radius of the trapping horizon [34]. The energy density in this formulation is defined as:

$$\rho_D = \alpha\,(1-\epsilon)\,\frac{1}{\tilde{r}_T^2} = \alpha\,(1-\epsilon)\left(H^2 + \frac{k}{a^2}\right), \tag{1}$$

---

***Cite as:*** P.J. Prasuna, T. Chinnappalanaidu, G. Satyanarayana, N.K.M. Raju, K. Navya, Y. Sobhanbabu, East Eur. J. Phys. 4, 42 (2025), https://doi.org/10.26565/2312-4334-2025-4-04

where the parameter $\epsilon$ is given by

$$\epsilon \equiv \frac{\dot{\tilde{r}}_T}{2H\tilde{r}_T}, \tag{2}$$

and $\tilde{r}_T$ denotes the trapping horizon radius, $H$ is the Hubble parameter, $k$ is the spatial curvature, and $a$ is the scale factor.

Scalar field models have also been extensively explored as alternatives to DE, including quintessence, tachyon, k-essence, and dilaton fields. These models have played a significant role in explaining the late-time accelerated expansion of the Universe. The dynamics of these scalar field models, along with their corresponding potentials, have been thoroughly investigated in the context of various DE frameworks, such as the holographic dark energy (HDE) model with Hubble, future event horizon, and Granda-Oliveros infrared (IR) cutoffs, in both flat and non-flat Universe scenarios [35, 36, 37, 38, 39, 40, 41, 42, 43, 44]. These studies have yielded interesting and insightful results regarding the behavior of scalar fields and their potentials, offering a valuable theoretical understanding of the Universe's accelerated expansion. In our investigation, we have also reconstructed scalar field models in the context of interacting HDE with the Granda-Oliveros IR cutoff in a non-flat Universe.

There is significant observational support for the possibility of an interaction between DM and DE, with the interaction typically described through modified conservation equations for their respective energy densities [46]. Observations of the cosmic microwave Background radiation (CMB), particularly from the Wilkinson Microwave Anisotropy Probe (WMAP), indicate that the present Universe is largely homogeneous and isotropic on large scales. However, residual anisotropies, such as those seen in CMB temperature fluctuations, still persist. The study of anisotropic cosmological models is therefore important for gaining deeper insights into the formation and evolution of the Universe. Among these, Bianchi-type models are particularly useful, as they represent spatially homogeneous but anisotropic solutions to Einstein's field equations, allowing for directional dependencies in cosmic expansion.

Abdul et al. [47] examined the scalar field models such as quintessence, dilaton, tachyon and k-essence in the background of flat FRW Universe. In the presence of interaction, they studied the dynamics of scalar field models with their corresponding potentials. Sheykhi [48] focused on interacting HDE models and their correspondence with scalar field models in a flat Universe. In a non-flat Universe, Sharif and Jawad [49] examined the interaction between HDE and different scalar field models, including quintessence, tachyon, k-essence, and dilaton, considering various values of the power-law DE parameter. Sharif and Shamir [50] have studied exact solutions of Bianchi-type I and V space times in the context of modified theory of gravity. Additionally, Sharif and Zubair [51] investigated anisotropic Universe models involving a perfect fluid and scalar fields in the modified theories of gravity, concluding that $f(R)$ gravity exhibits similar behavior under varying constraints. Thorsrud et al. [52] have studied cosmology of a scalar field coupled to matter and an isotropy-violating Maxwell field. García-Salcedo et al. [53] have analyzed interacting DE with a trapping horizon in Bianchi models.

Zubair and Abbas [54] have analyzed reconstructing QCD ghost models in the background of modified theory of gravotation. Das et al. [55] have investigated aagnetized anisotropic ghost dark energy cosmological model. Azimi and Barati [56] have analyzed instability of interacting GDE model in an anisotropic Universe. Reddy et al. [57] have investigated dynamics of Bianchi type-II anisotropic DE cosmological model in the presence of scalar-meson fields. Hossienkhani et al. [58] have investigated anisotropy effects on QCD ghost dark energy using the cosmological data. Javed et al. [59] have studied reconstruction of interacting generalized anisotropic scalar field models. Gómez et al. [60] have discussed anisotropic scalar field DE with a disformally coupled Yang-Mills field. Javed et al. [61] have analyzed interacting generalized anisotropic scalar field models. Talole et al. [62] have studied QCD-modified scalar field models of DE, in the presence of both interaction and viscosity, with varying gravitational constant. Bhardwaj and Yadav [63] have investigated observational constraints on scalar field cosmological model in anisotropic Universe. Sharif and Ajmal [64] have studied generalized GDE in the framework of modified theory Gravity. Very recently, Archana and Srivastava [65] have examined the kinematical and geometrical properties of the model as well as interacting ghost scalar field models of DE in Bianchi type-II Universe.

In this work, we investigate the cosmological evolution of an anisotropic Universe within the framework of general theory of relativity, using the redshift parameter $z$ as a reference. The structure of the paper is as follows: in Section 2, we present the foundational concepts and define key cosmological parameters, including the energy density of dark energy and the equation of state parameter. Section 3 provides a graphical analysis of the Bianchi type III model in conjunction with various scalar field dark energy models, namely quintessence, tachyon, and k-essence. The final section summarizes and concludes the key findings of this study.

## 2. METRIC AND FIELD EQUATIONS

The gravitational field in our model is given by a Bianchi type-III metric as

$$ds^2 = dt^2 - A^2(t)dx^2 - B^2(t)e^{-2nx}dy^2 - C^2(t)dz^2, \tag{3}$$

with $A$, $B$ and C being functions of the cosmic '$t$' only.

The Einstein's field equations (with gravitational units, $8\pi G = 1 = C$)

$$R_{ij} - \frac{1}{2}Rg_{ij} = (T_{ij} + \bar{T_{ij}}), \tag{4}$$

where $g_{ij}$ is the metric tensor, $R$ is the Ricci scalar and $R_{ij}$ is the Ricci tensor, $T_{ij}$ and $\bar{T_{ij}}$ are the energy-momentum tensors of matter and dark energy respectively, and they are defined as

$$T_{ij} = \rho_m x_i x_j \tag{5}$$

and

$$\bar{T_{ij}} = (\rho_{DE} + p_{DE})x_i x_j - p_{DE} g_{ij}, \tag{6}$$

where $\rho_m$ and $\rho_{DE}$ are the energy densities of matter and dark energy respectively and $p_{DE}$ is the pressure of the DE.

From equations (5) and (6), we have

$$T_1^1 = T_2^2 = T_3^3 = 0, \;\; T_4^4 = \rho_m \tag{7}$$

$$\bar{T_1^1} = \bar{T_2^2} = \bar{T_3^3} = -p_{DE}, \;\; \bar{T_4^4} = \rho_{DE}. \tag{8}$$

The field (4), for the metric (3) with the help of (5) and (6), can be written as

$$\frac{\ddot{A}}{A} + \frac{\ddot{C}}{C} + \frac{\dot{A}\dot{C}}{AC} = -p_{DE} \tag{9}$$

$$\frac{\ddot{B}}{B} + \frac{\ddot{C}}{C} + \frac{\dot{B}\dot{C}}{BC} = -p_{DE} \tag{10}$$

$$\frac{\ddot{A}}{A} + \frac{\ddot{B}}{B} + \frac{\dot{A}\dot{B}}{AB} - \frac{n^2}{A^2} = -p_{DE} \tag{11}$$

$$\frac{\dot{A}\dot{B}}{AB} + \frac{\dot{A}\dot{C}}{AC} + \frac{\dot{B}\dot{C}}{BC} - \frac{n^2}{A^2} = \rho_m + \rho_{DE} \tag{12}$$

$$\frac{\dot{A}}{A} - \frac{\dot{B}}{B} = 0 \tag{13}$$

where overhead dot denote differentiation with respect to cosmic time t.

Now solving (13), we get

$$A = c_1 B \tag{14}$$

where $c_1$ is an integration constant and without loss of generality, we take $c_1 = 1$, we have

$$A = B \tag{15}$$

In order to determine the average anisotropy parameter $A_h$ for a generalized anisotropic cosmological model, it is defined as follows:

$$A_h = \frac{1}{3}\sum_{i=1}^{3}\left(\frac{H_i - H}{H}\right)^2, \tag{16}$$

where $H$ is the mean Hubble parameter, and $H_i$ are the directional Hubble parameters along each spatial direction.

For the specific case under consideration, we take:

$$H_x = H_y = \frac{\dot{A}}{A}, \quad H_z = \frac{\dot{B}}{B},$$

where $A(t)$ and $B(t)$ are the directional scale factors in the $x$,$y$ and $z$ directions, respectively.

Further, we discuss some solution regarding anisotropic Universe model with scalar field models.

## 3. SOLUTION OF THE FIELD EQUATIONS

The field equations (9) to (12) are a system of four highly non-linear differential equations in five unknowns $A, C, p_{DE}, \rho_m, \rho_{DE}$. The system is thus initially undetermined. We need one extra physical condition to solve the field equations completely.

We assume that the expansion scalar ($\theta$) is proportional to the shear scalar ($\sigma^2$) [66, 67]. The condition leads to

$$A = C^k, \tag{17}$$

where ($k > 1$).

Now solving equations (9), (11), (15) and (17), we get

$$A = B = (bt + c), \;\; C = (bt + c)^{\frac{1}{k}}, \tag{18}$$

where $b = \frac{nk}{\sqrt{k^2-1}}$, and $c = kc_2$.
From equations (18) in metric (3), we have

$$ds^2 = dt^2 - (bt + c)^2 dx^2 - (bt + c)^2 e^{-2nx} dy^2 - (bt + c)^{\frac{2}{k}} dz^2 \tag{19}$$

Equation (19) represents Bianchi type-III interacting modified QCD ghost scalar field model of DE.

The interacting between CDM and QCD dark energy [68, 69, 70, 71], the continuity equations turn out to be

$$\dot{\rho_m} + 3H\rho_m = Q, \quad \dot{\rho_{DE}} + 3H(1 + \omega_{DE})\rho_{DE} = -Q, \tag{20}$$

where $\omega_{DE} = \frac{p_{DE}}{\rho_{DE}}$ and $Q$ stands for the equation of state (EoS) parameter and the interaction term respectively, we choose the interaction as $Q = 3d^2 H\rho_m$ and $d^2$ is a coupling constant. From (20), we get

$$\rho_m = \rho_{m0}(bt + c)^{\frac{(2k+1)(d^2-1)}{k}} \tag{21}$$

From equation (12), we get

$$\rho_{DE} = \frac{b^2(k + 2)}{k(bt + c)^2} - \frac{n^2}{(bt + c)^2} - \rho_{m0}(bt + c)^{\frac{(2k+1)(d^2-1)}{k}} \tag{22}$$

From equation (20), we get

$$\omega_{DE} = -1 + \frac{k}{2k + 1}\left[\frac{2\left(\frac{b^2(k+2)}{k} - n^2\right) - \rho_{m0}(2k + 1)(d^2 - 2)(bt + c)^{\frac{(2k+1)(d^2-2)}{k}-4}}{\frac{b^2(k+2)}{k} - n^2 - \rho_{m0}(bt + c)^{\frac{(2k+1)(d^2-1)}{k}-2}}\right] \tag{23}$$

**Redshift dependence:** In cosmological models, the redshift $z$ is a measure of the expansion of the universe and is related to the average scale factor $a(t)$ by

$$1 + z = \frac{1}{a(t)} \tag{24}$$

where the mean scale factor is given by

$$a(t) = (ABC)^{1/3}. \tag{25}$$

Using equations (18) and (25), we obtain

$$a(t) = (bt + c)^{\frac{2+1/k}{3}}. \tag{26}$$

Hence, the relation between cosmic time and redshift is

$$bt + c = (1 + z)^{-\frac{3}{2+1/k}}. \tag{27}$$

It is observed from Figures 1 and 2 that the energy densities of DM and QCD ghost dark energy remain positive throughout cosmic evolution. They are decreasing functions in redshift $z$. They start with a positive value and they tend to very close to zero when $z$ approaches to negative value. The graphical behavior of the Eos parameter versus redshift ($z$) for the different values of $d^2$ is shown in Figure 3. It can be observed that the Eos parameter ($\omega_{de}$) completely varies in the quintessence region for various values of $d^2 = 0.2, 0.4, 0.6$.

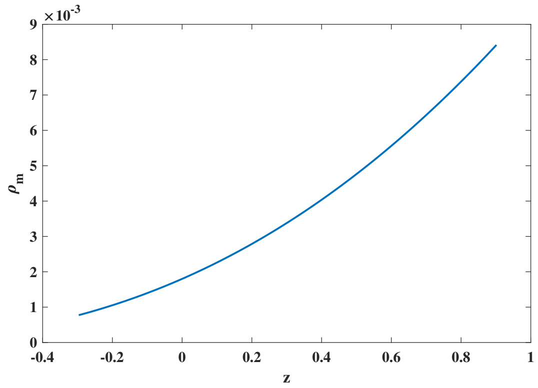

**Figure 1.** Plot of $\rho_m$ versus $z$ for b=0.5, k=9.7, c=100, n=2.521

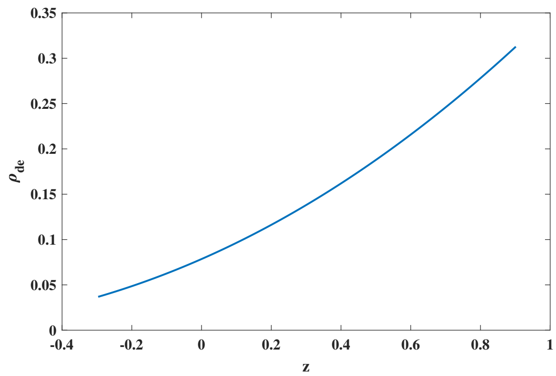

**Figure 2.** Plot of $\rho_{de}$ versus $z$ for b=0.5, k=9.7, c=100, n=2.521

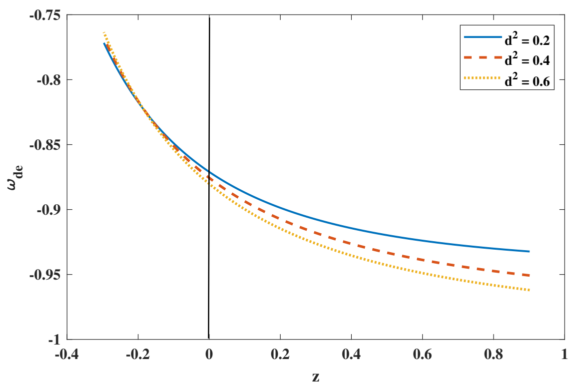

**Figure 3.** Plot of $\omega_{de}$ versus $z$ for the different values of coupling constants ($d^2$), b=0.5, k=9.7, c=100, n=2.521

## 4. CORRESPONDENCE WITH SCALAR FIELD MODELS IN ANISOTROPIC UNIVERSE

Our objective here is to examine whether a minimally coupled scalar field with a specific action or Lagrangian can replicate the dynamics of the GDE model. This approach aims to establish a possible connection between the GDE framework and a more fundamental theory, such as string theory or M-theory, which often involves scalar fields. To this end, it is meaningful to reconstruct the scalar field dynamics $\phi$ and the corresponding potential $V(\phi)$ such that they exhibit key features of the GDE model. Following the method proposed in [72], we establish a correspondence between the GDE model and various scalar field models by equating their respective energy densities and equations of state. Through this correspondence, we reconstruct both the field dynamics and the scalar potential, thereby gaining deeper insight into the theoretical underpinnings of the GDE framework.

### 4.1. Reconstructing ghost quintessence model

We adopt the viewpoint that the quintessence scalar field model of DE are effective theories of an underlying theory of DE [73, 74, 75]. The energy density and pressure for the quintessence scalar field can be written as

$$\rho_q = \frac{1}{2}\dot{\phi}^2 + V(\phi), \tag{28}$$

$$p_q = \frac{1}{2}\dot{\phi}^2 - V(\phi). \tag{29}$$

Then, we can obtain the scalar potential and the kinetic energy term as

$$\begin{aligned} V(\phi) = \Bigg[2(2k+1)\left(\frac{b^2(k+2)}{k} - n^2 - k\rho_{m0}(bt+c)^{\frac{(2k+1)(d^2-1)}{k}-2}\right) - k\left(2\frac{b^2(k+2)}{k} - 2n^2\right) \\ -\rho_{m0}(2k+1)(d^2-1)\Bigg]\left[2k(2k+1)(bt+c)^2\right]^{-1} \end{aligned} \tag{30}$$

$$\dot{\phi} = \sqrt{\frac{2\left(\frac{b^2(k+2)}{k} - n^2\right) - \rho_{m0}(2k+1)(d^2-2)(bt+c)^{\frac{(2k+1)(d^2-1)}{k}-4}}{(2k+1)(bt+c)^2}} \tag{31}$$

Where $\omega q = \frac{p_q}{\rho_q}$. For establishing the correspondence between present DE with quintessence scalar field, we identify $\rho_{DE} = \rho_q$ and $\omega_{DE} = \omega_q$. The evolution trajectories of potential function and scalar field versus redshift ($z$) in ghost quintessence model for different values of $d^2$ are shown in Figures 4 and 5. For $d^2 = 0.2, 0.4, 0.6$, the quintessence ghost dark energy both potential function and scalar field decreases during of the Universe. The plot of quintessence potential in terms of scalar field is shown in Figure 6 representing increasing behavior. The gradually decreasing kinetic energy while potential remains positive for quintessence model represents accelerate expansion of the Universe for different values of $d^2$.

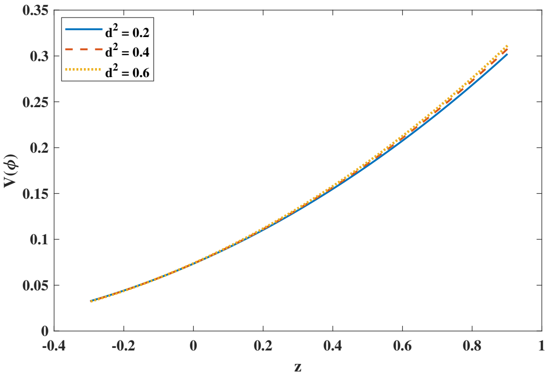

**Figure 4.** Plot of $V(\phi)$ versus $z$ in ghost quintessence model for the different values of coupling constants ($d^2$), b=0.5, k=9.7, c=100, n=2.521

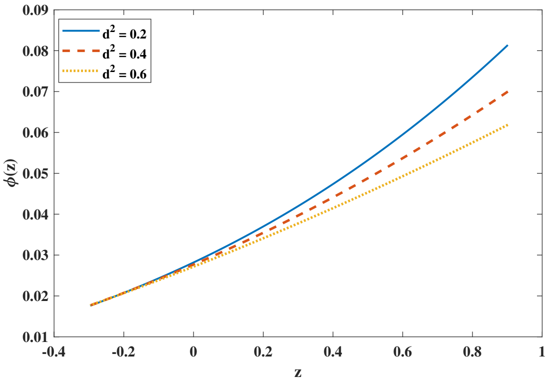

**Figure 5.** Plot of $\phi(z)$ versus $z$ in ghost quintessence model for the different values of coupling constant ($d^2$), b=0.5, k=9.7, c=100, n=2.521

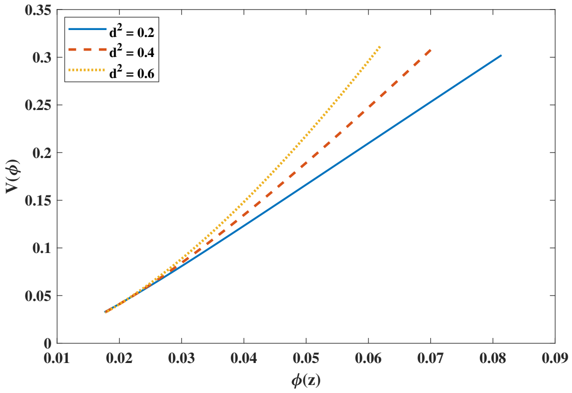

**Figure 6.** Plot of $V(\phi)$ versus $z$ in ghost quintessence model for the different values of coupling constant ($d^2$), b=0.5, k=9.7, c=100, n=2.521

### 4.2. Reconstructing ghost tachyon model

The tachyon field is another approach for explaining DE [76, 77, 78, 79, 80, 81]. The tachyon energy density and pressure are

$$\rho_T = -T_1^1 = \frac{V(\phi)}{\sqrt{1-\dot{\phi}^2}}, \tag{32}$$

$$p_T = T_i^i = -V(\phi)\sqrt{1-\dot{\phi}^2}. \tag{33}$$

$$p_T = -V(\phi)\sqrt{1 - \frac{2\left(\frac{b^2(k+2)}{k} - n^2\right) - \rho_{m0}(2k+1)(d^2-2)(bt+c)^{\frac{(2k+1)(d^2-1)}{k}-4}}{(2k+1)(bt+c)^2}}, \tag{34}$$

The EoS parameter of tachyon field takes the form

$$\omega_T = \frac{2\left(\frac{b^2(k+2)}{k} - n^2\right) - \rho_{m0}(2k+1)(d^2-2)(bt+c)^{\frac{(2k+1)(d^2-1)}{k}-4}}{(2k+1)(bt+c)^2} - 1. \tag{35}$$

We plot potential function V ($\phi$) and scalar field $\phi$ of ghost dark energy tachyon model as shown in Figures 9 and 7.

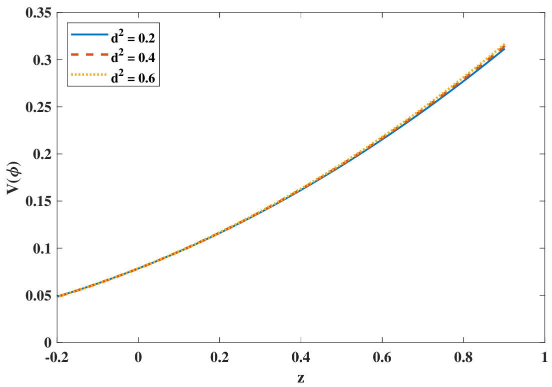

**Figure 7.** Plot of $V(\phi)$ versus $z$ in ghost tachyon model for the different values of coupling constant ($d^2$), b=0.5, k=9.7, c=100, n=2.521

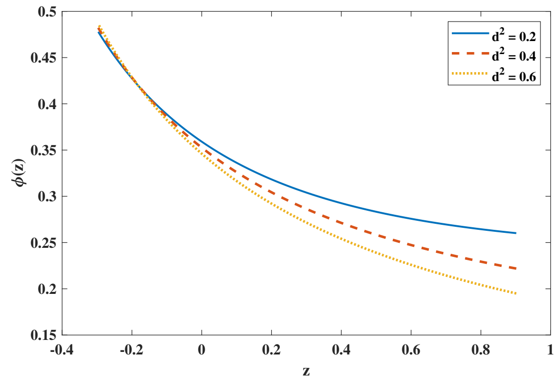

**Figure 8.** Plot of $\phi(z)$ versus $z$ in ghost tachyon model for the different values of coupling constant ($d^2$), b=0.5, k=9.7, c=100, n=2.521

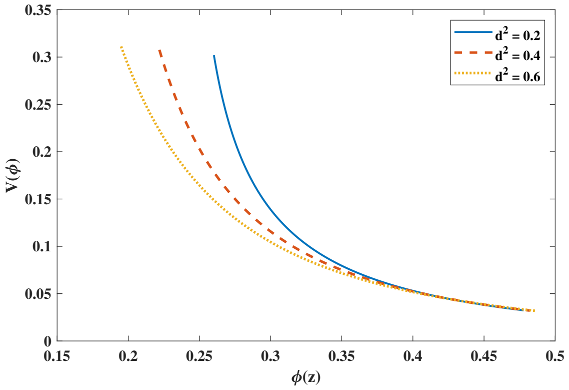

**Figure 9.** Plot of $V(\phi)$ versus $\phi(z)$ in ghost tachyon model for the different values of coupling constant ($d^2$), b=0.5, k=9.7, c=100, n=2.521

The evolution of this model is much similar to quintessence model. The scalar field represents increasing behavior versus redshift and indicates more steeper behavior for $d^2 = 0.2, 0.4$. This leads to the decreasing kinetic energy.

We plot potential function $V(\phi)$ and redshift $\phi(z)$ of ghost tachyon model as shown in Figure 8. The corresponding potential function expresses decreasing but positive behavior with respect to redshift. Its decreasing behavior from maxima gives inverse proportionality to scalar field for the later times. This type of behavior corresponds to scaling solutions in the brane-world cosmology.

### 4.3. Reconstructing ghost k-essence model

The k-essence scalar field model of DE is characterized by a scalar field with a non-canonical kinetic energy [82, 83, 84, 85, 86]. The density and corresponding pressure of k-essence model are of the form R

$$\rho_k = V(\chi)(-\chi + 3\chi^2), \;\; p_k = V(\phi)(-\chi + \chi^2). \tag{36}$$

where $\chi = \frac{\dot{\phi}^2}{2}$. The EoS parameter has the form

$$\omega_k = \frac{p_k}{\rho_k} = \frac{\chi - 1}{3\chi - 1} \tag{37}$$

in which $\chi$ experienced the accelerated expansion of the Universe in the interal $(\frac{1}{3}, \frac{2}{3})$. Taking $\omega_k = \omega_{DE}$, we obtain

$$\chi = \frac{1}{2(2k+1)(bt+c)^2}\left[2\left(\frac{b^2(k+2)}{k} - n^2\right) - \rho_{m0}(2k+1)(d^2-2)(bt+c)^{\frac{(2k+1)(d^2-1)}{k}-4}\right], \tag{38}$$

The EoS parameter has the form

$$\omega_k = \frac{\frac{1}{2(2k+1)(bt+c)^2}\left[2\left(\frac{b^2(k+2)}{k} - n^2\right) - \rho_{m0}(2k+1)(d^2-2)(bt+c)^{\frac{(2k+1)(d^2-1)}{k}-4}\right] - 1}{3\cdot\frac{1}{2(2k+1)(bt+c)^2}\left[2\left(\frac{b^2(k+2)}{k} - n^2\right) - \rho_{m0}(2k+1)(d^2-2)(bt+c)^{\frac{(2k+1)(d^2-1)}{k}-4}\right] - 1}. \tag{39}$$

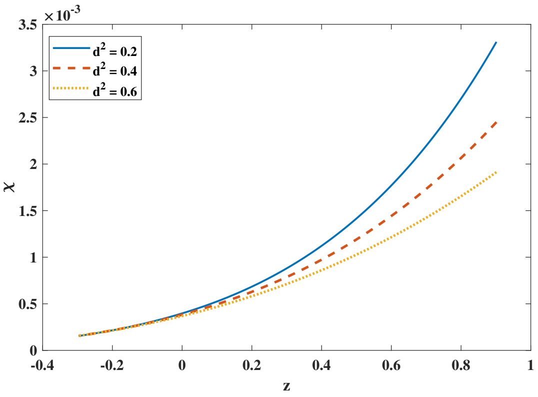

**Figure 10.** Plot of $\chi$ versus $z$ in ghost k-essence model for the different values of coupling constant ($d^2$), b=0.5, k=9.7, c=100, n=2.521

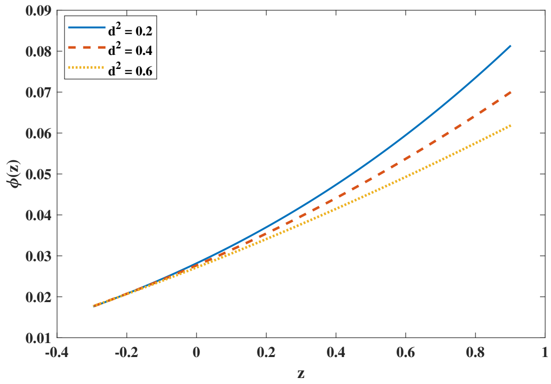

**Figure 11.** Plot of $\phi(z)$ versus $z$ in ghost k-essence model for the different values of coupling constant ($d^2$), b=0.5, k=9.7, c=100, n=2.521

The plot of $\chi$ versus redshift is shown in Figure 10 for various values of $d^2$. It can be observed that the region within the range where the EoS parameter of k-essence ghost dark energy model shows consistency with the accelerated Universe. We plot scalar field $\phi$ of ghost dark energy k-essence model as shown in Figure 11, representing decreasing behavior in the present epoch for the various values of $d^2$. The potential function versus scalar field is shown in Figure 12, indicates the increase in potential with increase in scalar field but k-essence scalar field decreases with expansion of the Universe.

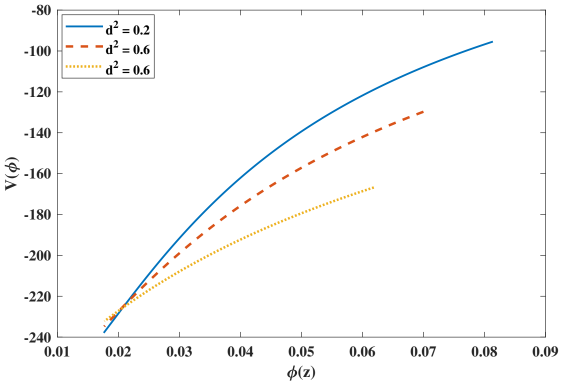

**Figure 12.** Plot of $V(\phi)$ versus $\phi(z)$ in ghost k-essence model for the different values of coupling constant ($d^2$), b=0.5, k=9.7, c=100, n=2.521

## 5. CONCLUSIONS

In this work, we study the Bianchi type-III interacting framework of modified QCD ghost dark energy with cold dark matter is being considered for the accelerated expansion of the Universe. We have studied various cosmological parameters to analyze the viability of the models and our conclusions are the following:

- The energy densities of DM and QCD ghost dark energy remain positive throughout cosmic evolution. They are decreasing and start with a positive value and they tend to very close to zero when $z$ approaches to negative value. The graphical behavior of the Eos parameter ($\omega_{de}$) completely varies in the quintessence region for various values of $d^2 = 0.2, 0.4, 0.6$.
- For ghost quintessence model, the evolution trajectories of potential function and scalar field for different values of $d^2$ are shown in Figures 4 and 5. For $d^2 = 0.2, 0.4, 0.6$, the quintessence ghost dark energy both potential function and scalar field decreases during of the Universe. The plot of quintessence potential representing increasing behavior. The gradually decreasing kinetic energy while potential remains positive for quintessence model represents accelerate expansion of the Universe for different values of $d^2$.
- For ghost tachyon model, the evoution of this model is much similar to quintessence model. The scalar field represents increasing behavoir versus redshift and indicates more steeper behavior for $d^2 = 0.2, 0.4$. This leads to the decreasing kinetic energy. The corresponding potential function expresses decreasing but positive behavior with respect to redshift. Its decreasing behavior from maxima gives inverse proportionality to scalar field for the later times. This type of behavior corresponds to scaling solutions in the brane-world cosmology.
- For ghost k-essence model, The plot of $\chi$ can be observed that the region within the range where the EoS parameter of k-essence ghost dark energy model shows consistency with the accelerated Universe. We plot scalar field $\phi$ of ghost dark energy k-essence model representing decreasing behavior in the present epoch for the various values of $d^2$. The potential function versus scalar field is indicates the increase in potential with increase in scalar field but k-essence scalar field decreases with expansion of the Universe.

## Acknowledgments

The authors are very much grateful to the honorable referees and to the editor for the illuminating suggestions that have significantly improved our work in terms of research quality, and presentation.

## ORCID

**P. Jnana Prasuna**, https://orcid.org/0009-0000-2369-7339; **T. Chinnappalanaidu**, https://orcid.org/0000-0001-6902-2820; **G. Satyanarayana**, https://orcid.org/0000-0003-3452-1675; **N. Krishna Mohan Raju**, https://orcid.org/0000-0003-0735-4293; **K. Navya**, https://orcid.org/0000-0001-9604-7783; **Y. Sobhanbabu**, https://orcid.org/0000-0003-0717-1323

## REFERENCES

[1] A.G. Riess, *et al*. Astron. J. **116**, 1009 (1998). https://doi.org/10.1086/300499

[2] S. Perlmutter, *et al*. Astrophys. J. **517**, 565 (1999). https://doi.org/10.1086/307221

[3] P.J.E. Peebles, Rev. Mod. Phys. **75**, 559 (2003). https://doi.org/10.1103/RevModPhys.75.559

[4] L. Amendola, and S. Tsujikawa, *Dark Energy: Theory and Observations*, (Cambridge University Press, Cambridge, 2010).

[5] A.Y. Kamenshchik, U. Moschella, and V. Pasquier, Phys. Lett. B, **511**, 265 (2001). https://doi.org/10.1016/S0370-2693(01)00571-8

[6] X. Zhang, F.Q. Wu, and J. Zhang, J. Cosmol. Astropart. Phys. **01**, 003 (2006). https://doi.org/10.1088/1475-7516/2006/01/003

[7] S.D.H. Hsu, Phys. Lett. B, **594**, 13 (2004). https://doi.org/10.1016/j.physletb.2004.05.020L

[8] M. Li : Phys. Lett. B **603**, 1 (2004). https://doi.org/10.1016/j.physletb.2004.10.014

[9] H. Wei, and R.G. Cai, Phys. Lett. B, **660**, 113 (2008). https://doi.org/10.1016/j.physletb.2007.12.030

[10] H. Wei, Class. Quantum Gravity, **29**, 175008 (2012). https://doi.org/10.1088/0264-9381/29/17/175008

[11] M. Sharif, and A. Jawad, Eur. Phys. J. C, **73**, **2382** (2013). https://doi.org/10.1140/epjc/s10052-013-2382-1

[12] M. Sharif, and A. Jawad, Eur. Phys. J. C, **73**, 2600 (2013). https://doi.org/10.1140/epjc/s10052-013-2600-x

[13] S. Chattopadhyay, Eur. Phys. J. Plus, **129**, 82 (2014). https://doi.org/10.1140/epjp/i2014-14082-6

[14] A.R. Urban, and A.R. Zhitnitsky, Phys. Rev. D, **80**, 063001 (2009). https://doi.org/10.1103/PhysRevD.80.063001

[15] A.R. Urban, and A.R. Zhitnitsky, Nucl. Phys. B, **835**, 135 (2010). https://doi.org/10.1016/j.nuclphysb.2010.04.001

[16] Nobuyoshi Ohta, Phys. Lett. B, **695**, 41 (2011). https://doi.org/10.1016/j.physletb.2010.11.044

[17] R.G. Cai, *et al*. Phys. Rev. D, **86**, 023511 (2012). https://doi.org/10.1103/PhysRevD.86.023511

[18] E.J. Copeland, M. Sami, *et al*. Int. J. Mod. Phys. D, **15**, 1753 (2006). https://doi.org/10.1142/S021827180600942X

[19] K. Bamba, S. Capozziello, *et al*. Astrophys. Space Sci. **342**, 155 (2012). https://doi.org/10.1007/s10509-012-1181-8

[20] C. Rosenzweig, J. Schechter, *et al*. Phys. Rev. D, **21**, 3388 (1980). https://doi.org/10.1103/PhysRevD.21.3388

[21] P. Nath, and R. Arnowitt, Phys. Rev. D, **23**, 473 (1981). https://doi.org/10.1103/PhysRevD.23.473

[22] F.R. Urban, and A.R. Zhitnitsky, Phys. Lett. B, **688**, 9 (2010). https://doi.org/10.1016/j.physletb.2010.03.080

[23] F.R. Urban, A.R. Zhitnitsky, Phys. Lett. B **688**,9 (2010). https://doi.org/10.1016/j.physletb.2010.03.080

[24] M.M. Forbes, and A.R. Zhitnitsky, Phys. Rev. D, **78**, 083505 (2008). https://doi.org/10.1103/PhysRevD.78.083505

[25] E. Ebrahimi, and A. Sheykhi, Int. J. Mod. Phys. D, **20**, 2369 (2011). https://doi.org/10.1142/S021827181102041X

[26] A. Sheykhi, M.S. Movahed, and E. Ebrahimi, Astrophys. Space Sci.,**339**, 93 (2012). https://doi.org/10.1007/s10509-012-0977-x

[27] A. Sheykhi, and A. Bagheri, Europhys. Lett. **95**, 39001 (2011). https://doi.org/10.1209/0295-5075/95/39001

[28] A. Rozas-Fernandez, Phys. Lett. B, **709**, 313 (2012). https://doi.org/10.1016/j.physletb.2012.02.030

[29] K. Karami, and K. Fahimi, Class. Quantum Grav. **30**, 065018 (2013). https://doi.org/10.1088/0264-9381/30/6/065018

[30] K. Karami, A. Abdolmaleki, S. Asadzadeh, Z. Safari, Eur. Phy.J. C **73**, 2565 (2013). https://doi.org/10.1140/epjc/s10052-013-2565-9

[31] R.G. Cai, Z.L. Tuo, *et al*. Phys. Rev. D, **86**, 023511 (2012). https://doi.org/10.1103/PhysRevD.86.023511

[32] A.R. Zhitnitsky, Phys. Rev. D, **86**, 045026 (2012). https://doi.org/10.1103/PhysRevD.86.045026

[33] R.G. Cai, Z.L. Tuo, *et al*. Phys. Rev. D, **86**, 023511 (2012). https://doi.org/10.1103/PhysRevD.86.023511

[34] R. Garcia-Salcedo, T. Gonzalez, *et al*. Phys. Rev. D **88**, 043008 (2013). https://doi.org/10.1103/PhysRevD.88.043008

[35] X. Zhang, Phys. Rev. D, **74**, 103505 (2006). https://doi.org/10.1103/PhysRevD.74.103505

[36] M.R. Setare, Phys. Lett. B, **642**, 1 (2006). https://doi.org/10.1016/j.physletb.2006.09.027

[37] L. N. Granda, and A. Oliveros, Phys. Lett. B, **671**, 199 (2009). https://doi.org/10.1016/j.physletb.2008.12.025

[38] K. Karami, and A. Fehri, Phys. Lett. B, **684**, 61 (2010). https://doi.org/10.1016/j.physletb.2009.12.060

[39] J. Zhang, X. Zhang, and H. Liu, Eur. Phys. J. C, **52**, 693 (2007). https://doi.org/10.1140/epjc/s10052-007-0408-2

[40] A. Rozas-Fernández, Phys. Lett. B, **709**, 313 (2012). https://doi.org/10.1016/j.physletb.2012.02.030

[41] Sumaira Naz and Asghar Qadir, J. Phys. Conf. Ser. **354**, 012012 (2012). https://doi.org/10.1088/1742-6596/354/1/012012

[42] M. Jamil, and M. A. Farooq, JCAP, **03**, 001 (2010). https://doi.org/10.1088/1475-7516/2010/03/001

[43] A. Sheykhi, Phys. Rev. D, **84**, 107302 (2011). https://doi.org/10.1103/PhysRevD.84.107302

[44] A. Jawad, U. Debnath and F. Batool, Commun. Theor. Phys. **64**, 590 (2015). https://doi.org/10.1088/0253-6102/64/5/590

[45] A. Jawad, Astrophys. Space Sci. **357**, 19 (2015). https://doi.org/10.1007/s10509-015-2299-2

[46] F.R. Urban, and A.R. Zhitnitsky, J. Cosmol. Astropart. Phys. **09**, 018 (2009). https://doi.org/10.1088/1475-7516/2009/09/018

[47] J. Abdul, U. Dednath, and F. Batool, Commun. Theor. Phys. **64**, 590 (2015). https://doi.org/10.1088/0253-6102/64/5/590

[48] A. Sheykhi, Phys. Rev. D, **84**, 107302 (2011). https://doi.org/10.1103/PhysRevD.84.107302

[49] M. Sharif, and A. Jawad, Eur. Phys. J. C, **72**, 2097 (2012). https://doi.org/10.1140/epjc/s10052-012-2097-8

[50] M. Sharif, and M.F. Shamir, Class. Quantum Gravity, **26**, 235020 (2009). https://doi.org/10.1088/0264-9381/26/23/235020

[51] M. Sharif, and M. Zubair, JCAP, **03**, 028 (2012). https://doi.org/10.1088/1475-7516/2012/03/028

[52] M. Thorsrud, D.F. Mota, et al. JHEP, **10**, 066 (2012). https://doi.org/10.1007/JHEP10(2012)066

[53] R. García-Salcedo, T. González, *et al*. Eur. J. Phys. **36**, 025008 (2015). https://doi.org/10.1088/0143-0807/36/2/025008

[54] M. Zubair, and Abbas, Astrophys. Space Sci. **357**, 154 (2015). https://doi.org/10.1007/s10509-015-2387-3

[55] K. Das, and T. Sultana, Astrophys. Space Sci. **357**, 2, 118 (2015). https://doi.org/10.1007/s10509-015-2346-z

[56] N. Azimi, and F. Barati, Int. J. Theoret. Phys. **55**, 3318 (2016). https://doi.org/10.1007/s10773-016-2961-7

[57] D.R.K. Reddy, Y. Aditya et al., Can. J. Phys. **97**, 9 (2018). https://doi.org/10.1139/cjp-2018-0403

[58] H. Hossienkhani, H. Yousefi, *et al*. Astrophys. Space Sci. **365**3, 59 (2020). https://doi.org/10.1007/s10509-020-03771-z

[59] W. Javed, I. Nawazish, and N. Irshad . Eur. Phys. J. C, **81**, 149 (2021). https://doi.org/10.1140/epjc/s10052-020-08555-x

[60] L.G. Gómez, Y. Rodríguez, and J.P.B. Almeida, Int. J. Mod. Phys. D, **31**, 2250060 (2022). https://doi.org/10.1142/S0218271822500602

[61] W. Javed, I. Nawazish, and N Irshad, Eur. Phys. J. C, **81**, 149 (2021). https://doi.org/10.1140/epjc/s10052-020-08555-x

[62] R. Talole, *et al*. Romanian Astron. J. **33**, 81 (2023). https://doi.org/10.59277/RoAJ.2023.1-2.06

[63] V.K. Bhardwaj, and A.K. Yadav, arXiv:2308.02864, (2023). https://doi.org/10.48550/arXiv.2308.02864

[64] M. Sharif, and M. Ajmal, Chinese J. Phys. **88**, 706 (2024). https://doi.org/10.1016/j.cjph.2024.02.031

[65] A.G. Ingie, and K. Srivastava, AIP Con. Proc. **3139**, 090007 (2024). https://doi.org/10.1063/5.0224769

[66] C.B. Collins, *et al*. Gen. Relativ. Gravit. **12**, 805 (1980). https://doi.org/10.1007/BF00763057

[67] A. De, M. Sanjay, *et al*. Eur. Phys. J. C, **82**, 72 (2022). https://doi.org/10.1140/epjc/s10052-022-10021-9

[68] O. Bertolami, F. Gil Pedro, *et al*. Phys. Lett. B, **654**, 165 (2007). https://doi.org/10.1016/j.physletb.2007.08.046

[69] L.L. Honorez, *et al*. JCAP, **09**, 029 (2010). https://doi.org/10.1088/1475-7516/2010/09/029

[70] H. Kim, H.W. Lee, and Y.S. Myung, Phys. Lett. B, **632**, 605 (2006). https://doi.org/10.1016/j.physletb.2005.11.043

[71] L. Amendola, Phys. Rev. D, **62**, 043511 (2000). https://doi.org/10.1103/PhysRevD.62.043511
[72] V. Sahni, and A.A. Starobinsky, Int. J. Mod. Phys. D, **15**, 2105 (2006). https://doi.org/10.1142/S0218271806009704
[73] E.J. Copeland, M. Sami, *et al*. Int. J. Mod. Phys. D, **15**, 1753 (2006). http://dx.doi.org/10.1142/S021827180600942X
[74] B. Ratra, and J. Peebles, Phys. Rev. D, **37**, 3406 (1988). https://doi.org/10.1103/PhysRevD.37.3406
[75] R.R. Caldwell, R. Dave, and P.J. Steinhardt, *et al*. Phys. Rev. Lett. **80**, 1582 (1998). https://doi.org/10.1103/PhysRevLett.80.1582
[76] A. Sen, JHEP, **10**, 008 (1999). https://doi.org/10.1088/1126-6708/1999/10/008
[77] A. Sen, JHEP, **04**, 048 (2002). https://doi.org/10.1088/1126-6708/2002/04/048
[78] A. Sen, JHEP, **07**, 065 (2002). https://doi.org/10.1088/1126-6708/2002/07/065
[79] E.A. Bergshoeff, *et al*. JHEP, **05**, 009 (2000). https://doi.org/10.1088/1126-6708/2000/05/009
[80] T. Padmanabhan, Phys. Rev. D, **66**, 021301(R) (2002). https://doi.org/10.1103/PhysRevD.66.021301
[81] T. Padmanabhan, and T.R. Choudhury, Phys. Rev. D, **66**, 081301(R) (2002). https://doi.org/10.1103/PhysRevD.66.081301
[82] T. Chiba, and T. Okabe, *et al*. Phys. Rev. D, **62**, 023511 (2000). https://doi.org/10.1103/PhysRevD.62.023511
[83] C. Armendariz-Picon, V. Mukhanov, *et al*. Phys. Rev. Lett. **85**, 4438 (2000). https://doi.org/10.1103/PhysRevLett.85.4438
[84] C. Armendariz-Picon, V. Mukhanov, and P.J. Steinhard, Phys. Rev. D, **63**, 103510 (2001). https://doi.org/10.1103/PhysRevD.63.103510
[85] C. Armendariz-Picon, T. Damour, *et al*. Phys. Lett. B, **458**, 209 (1999). https://doi.org/10.1016/S0370-2693(99)00603-6
[86] J. Garriga, and V. Mukhanov, Phys. Lett. B, **458**, 219 (1999). https://doi.org/10.1016/S0370-2693(99)00602-4

# МОДИФІКОВАНА ТЕМНА ЕНЕРГІЯ КХД-ПРИМАРНОГО СКАЛЯРНОГО ПОЛЯ В АНІЗОТРОПНИХ ТА ВЗАЄМОДІЮЧИХ МОДЕЛЯХ ВСЕСВІТУ

**П. Джнана Прасуна[1], Т. Чіннаппаланайду[2], Г. Сатьянараяна[3], Н. Крішна Мохан Раджу[4], К. Навья[5], Й. Собханбабу[4]**
[1]*Кафедра фундаментальних наук, Інженерний коледж Шрі Васаві (А), Тадепаллігудем-534101, Індія*
[2]*Кафедра математики, Інститут інформаційних технологій Віньяна (автономний), Вішакхапатнам, Індія*
[3]*Кафедра прикладних наук та гуманітарних наук, Технологічний інститут Сасі та інженерія (А), Тадепаллігудем-534101, Індія*
[4]*Кафедра інженерної математики, Інженерний коледж SRKR (А), Бхімаварам-534204, Індія*
[5]*Кафедра фундаментальних наук та гуманітарних наук, Університет технологій та менеджменту Центуріон, Візіанагарам-535003, Індія*

У цій роботі ми вивчаємо взаємодіючу структуру Біанкі типу III модифікованої КХД-темної енергії-привида з холодною темною матерією для ілюстрації прискореного розширення Всесвіту. Параметр рівняння стану показує, що еволюція Всесвіту повністю змінюється лише в області квінтесенції. Динаміка скалярного поля та відповідний потенціал різних моделей скалярного поля демонструють узгоджену поведінку з явищем прискореного розширення. Також член кінетичної енергії k-есенційних моделей знаходиться в діапазоні, де параметр рівняння стану відображає прискорене розширення Всесвіту.

**Ключові слова:** *Біанкі типу III; темна енергія-привид КХД; холодна темна матерія; моделі скалярного поля*

East European Journal of Physics. 4. 53-62 (2025)
DOI:10.26565/2312-4334-2025-4-05 ISSN 2312-4334

# PREDICTING NEW $B_c$ MESONS' EXCITED STATES: THE TRIDIAGONAL MATRIX-NUMEROV APPROACH

**Ali A. Alkathiri**[1], **S.A. Abd El-Azeem**[2,3], **Weeam S. Albaltan**[4], **R.F. Alnahdi**[5], **Atef Ismail**[6], **M. Allosh**[7]*, **M.S. Ali**[8], **Tarek A. Nahool**[9]
[1]*Department of Physics, College of Science, Taif University, P.O. Box 11099, Taif 21944, Saudi Arabia*
[2]*Physics Department, College of Science and Humanities, Prince Sattam Bin Abdulaziz University, Al-Kharj 11942, Saudi Arabia*
[3]*Physics Department, Faculty of Women for Arts, Science and Education, Ain Shams University, Cairo 11757, Egypt*
[4]*Department of Physics, College of Science, Princess Nourah Bint Abdulrahman University,*
*P.O. Box 84428, Riyadh, 11671, Riyadh, Saudi Arabia*
[5]*Physics Department, Faculty of Science, King Abdulaziz University, 21859, Jeddah, Saudi Arabia*
[6]*Department of Physics, Al–Azhar University, 71524 Assiut, Egypt*
[7]*Department of Physics, Faculty of Science, South Valley University, 83523 Qena, Egypt*
[8]*African Institute for Mathematical Sciences, Mbour city, Senegal*
[9]*Physics Department, Faculty of Science, Aswan University, Egypt*
**Corresponding Author E-mail: m_allosh67@sci.svu.edu.eg*

Received September 1, 2025; revised September 25, 2025; accepted September 29, 2025

The properties of Bottom-charmed meson states were extensively investigated using Numerov's tridiagonal matrix approach to predicting the radial wavefunctions. Based on the resulted values, we predicted the $\beta$ anharmonicity values and root mean square radii for different excited states of $B_c$ mesons. A comprehensive comparison between the estimated results and recently published theoretical and experimental data was conducted, exhibiting a comparable product with a high degree of accuracy.

**Keywords:** *Bottom-charmed meson; Numerov's tridiagonal matrix; $\beta$ coefficient; Root-mean-square radii*
**PACS:** 12.39.Pn, 12.38.Aw, 14.40.Lb, 14.40.Nd

## 1. INTRODUCTION

The primary motivation for studying the spectra and characteristics of heavy mesons is to better understand the subatomic particles and the forces that govern matter's behavior. A few of the primary goals of these investigations include, but are not limited to, the following [1-4]: studying heavy mesons is essential for examining and improving models such as the Quark Model, Lattice QCD, and effective field theories, as heavy mesons challenge our current understanding of the strong force. Experimental results and theoretical predictions can be cross-checked to validate these models and reveal inconsistencies that may lead to new insights [4]. Finally, the study of heavy mesons can uncover novel physics by identifying particles and events that do not conform to the Standard Model. It is possible to find exotic states, make unexpected observations, or deviate from theoretical predictions, all of which might indicate the presence of new particles or interactions that are beyond our present knowledge [5-6]. Venturing beyond the conventional Standard Model of particle physics becomes imperative when unraveling the enigmatic traits of the elusive Bottom-charmed ($B_c$) mesons, despite the Model's hint at their existence [7]. Here we shall look at $B_c$ mesons and their behavior using a nonrelativistic quark model. The nonrelativistic quark model provides a simpler explanation of the quarks' activities and interactions in heavy mesons. Based on this model, we will study $B_c$ meson properties such as quark composition, quantum properties, mass spectra, and finally the essential coefficients that are needed to study decay dynamics.

Heavy meson decay characteristics may be used to derive standard model parameters such as CKM matrix elements and quark mixing angles. Understanding the genesis of CP violation requires knowledge of the CKM matrix, which explains quark mixing in weak interactions. Precise observations of heavy meson decays constrain CKM matrix elements and quark mixing angles, aiding Standard Model accuracy tests [8, 9].

As a result, we are highly motivated to determine the root mean square radius ($r_{\mathrm{ms}}$) of various $B_c$ states and the numerical values of the $\beta$ coefficient. These values may then be utilized to compute decay widths and differential cross-sections for quarkonium states [8, 10]. Furthermore, one of our supplementary goals is to study the mass-radius dependency of the $B_c$ states within the framework of the nonrelativistic quark model.

Notably, the nonrelativistic quark model may explain several properties of $B_c$ meson decay. The decay of $B_c$ mesons is triggered by weak interactions, and the W boson plays a crucial role in facilitating these decays. Lighter mesons, leptons, and neutrinos are the ultimate states that determine the decay routes and velocities. Using the quark model, one can determine the branching percentages and decay widths of $B_c$ mesons [11].

Our investigation uses numerical-based approaches for the qualitative analysis of heavy mesons, with results that highlight their potential to enhance future experimental studies while reducing the large-scale costs that currently define such research [12, 13].

---

***Cite as:*** A.A. Alkathiri, S.A. Abd El-Azeem, W.S. Albaltan, R.F. Alnahdi, A. Ismail, M. Allosh, M.S. Ali, T.A. Nahool, East Eur. J. Phys. 4, 53 (2025), https://doi.org/10.26565/2312-4334-2025-4-05

To address the challenging QCD mathematical framework, researchers can employ numerical approaches such as matrix method, the Shooting method [14, 15], the four-step exponentially fitted method [16, 17], and Numerov's method simulations [12]. The strong interaction between quarks and gluons describes heavy meson behavior, which can only be explained in terms of QCD [17]. It is feasible to estimate quantities such as meson masses, decay rates, and form factors, values that are difficult to determine analytically through numerical calculations [18, 19]. Experimental investigations rely heavily on the properties of heavy meson, and numerical methods enable precise predictions and provide valuable insights into these characteristics.

Recent publications have demonstrated that Numerov's tridiagonal matrix technique is a highly efficient and quick method for achieving our objective [12, 20-21]. We anticipate that this approximation will provide reliable characteristics for investigating heavy mesons. Furthermore, the wave functions of heavy mesons, investigated in this study, may be utilized to generate predictions regarding additional characteristics such as the root mean square radius ($r_{\mathrm{ms}}$) of various states for $B_c$ mesons, as well as the numerical values of the $\beta$ coefficient and differential cross-sections for $B_c$ states.

This work is organized as follows: The unique characteristics of $B_c$ mesons are outlined in section 2. The main problem and thorough analytical solutions are addressed in section 3. Section 4 is devoted to discussing resulting data in detail. Finally, we briefly summarize our main discoveries and conclusions in section 5.

## 2. Characteristics of Bottom-Charmed Mesons

### 2.1. The Potential Model

Applying an adequate potential model to solve the non-relativistic Schrodinger equation for quark-anti quark states is widely regarded as one of the most efficient approaches for modeling the heavy meson system [22-25].

The effective quark-antiquark potential may be expressed as the sum of two terms, one of which is spin-independent, and the other is spin-dependent. The linear confinement and standard color Coulomb interaction are included in the first term, whereas the spin-dependent component consists of the tensor potential, spin-orbit interaction potential, and the hyperfine potential between spin-spin interaction. As a result, the following is the final form of the potential model that was employed in this work [24-27]:

$$V(r) = -\frac{4\alpha_s}{3\,r} + br + \frac{32\pi\alpha_s}{9m_b m_{\bar{c}}}\left(\frac{\sigma}{\sqrt{\pi}}\right)^3 e^{-\sigma^2 r^2}\, S_b S_{\bar{c}} + \frac{1}{m_b m_{\bar{c}}}\left(\frac{2\alpha_s}{r^3} - \frac{b}{2r}\right)\vec{l}.\vec{S} + \frac{4\alpha_s}{r^3}T, \tag{1}$$

$$S_b.S_{\bar{c}} = \frac{s(s+1)}{2} - \frac{3}{4}, \tag{2}$$

where $l$ is the orbital momentum, $r$ represents the distance between the quarks, $\alpha_s$ is the strong running coupling constant, −4/3 is the color factor, $b$ is a potential parameter, $\sigma$ is the string tension and $S_b.S_{\bar{c}}$ is the spin–spin contact hyperfine interaction, whereas $m_b$ and $m_{\bar{c}}$ depict the masses of the bottom and anti-charm quarks. $\vec{S}$ denotes the overall spin quantum number of the meson.

The parameters for the $B_c$ mesons are detailed in Table 1. T represents the tensor operator.

**Table 1.** The parameters to fit the theoretical masses to get the best theoretical spectra of $B_c$ states

| Parameters | Theo. (NR) Potential |
|---|---|
| $m_{\bar{c}}$ [GeV] | 1.4794 |
| $m_b$ [GeV] | 4.825 |
| $\alpha_s$ | 0.48 |
| $b$ [GeV$^2$] | 0.137 |
| $\sigma$ [GeV] | 1.0946 |

The spin-orbit operator is diagonal when expressed in the $|\mathrm{J}, \mathrm{L}, \mathrm{S}>$ basis with the matrix components:

$$\langle \vec{L}.\vec{S} \rangle = \frac{[J(J+1) - (L(L+1) - S(S+1))]}{2}$$

The tensor operator $T$ exhibits non-zero diagonal matrix components exclusively among spin-triplet states with L>0.

$$T = \begin{cases} -\dfrac{L}{6(2L+3)}, J = L+1 \\ +\dfrac{1}{6}, J = L \\ -\dfrac{(L+1)}{6(2L-1)}, J = L-1 \end{cases}$$

### 2.2. Wave Functions of Bottom-Charmed Mesons

By using the potential from equation (1), $B_c$ mesons may be modeled by the wave function of the bound quark-antiquark state that satisfies the Schrödinger equation. The radial Schrödinger equation is defined as [1, 2]:

$$-\frac{\hbar^2}{2\mu}\frac{d^2R_{nl}(r)}{dr^2}+\left(V(r)+\frac{l(l+1)}{2\mu r^2}\right)R_{nl}(r)=E_{nl}R_{nl}(r), \tag{3}$$

where $n$ is the principal quantum number and $\mu$ represents the reduced mass of the quark and anti-quark.

The radial wave function is denoted as $R_{nl}(r)$. The total energy of the quark-antiquark system is denoted by $E$. The tridiagonal matrix Numerov's (TMN) approach is employed to solve equation (3) and get the mass spectra of $B_c$ mesons. Further information on this method may be found in Reference [12]. In the subsequent sections, we utilize this approach to derive the wave functions of $B_c$ bound states.

### 2.3. The tridiagonal matrix Numerov's approach

Our approach is based on the numerical solution of Eq. (3) as a matrix eigenvalue problem. The radial second-derivative finite difference approximation can be simplified by converting it into tridiagonal matrix form. Therefore, we solve this equation numerically using the Numerov technique to derive the eigenvalue and eigenfunction equations for heavy quarkonium spectrum and wave functions.

We can rewrite the equation (3) in a slightly different way to understand the probable use of Numerov's technique more clearly:

$$f(r)=2\mu\big(E-V(r)\big) \qquad ;\hbar=1, \tag{4}$$

with a distance $d$ between each point on the lattice and $x_i$, which are equally spaced, we can derive the integration formula,

$$\psi_{i+1}=\frac{\psi_{i-1}(12-d^2f_{i-1})-2\psi_i(5d^2f_i+12)}{d^2f_{i+1}-12}. \tag{5}$$

Hence

$$d^2f_{i+1}\psi_{i+1}-12\psi_{i+1}=12\psi_{i-1}-d^2f_{i-1}\psi_{i-1}-10d^2f_i\psi_i-24\psi_i. \tag{6}$$

Applying Eq. (4), we obtain:

$$-2\mu d^2/\hbar^2\,[\,(E\psi_{i-1}-V_{i-1}\psi_{i-1})+(10E\psi_i-10V_i\psi_i)+(E\psi_{i+1}-V_{i+1}\psi_{i+1})]=12(\psi_{i-1}-2\psi_i+\psi_{i+1})\,. \tag{7}$$

After rearranging the equation above, we get:

$$\frac{-1}{2\mu}\frac{(\psi_{i-1}-2\psi_i+\psi_{i+1})}{d^2}+\frac{(V_{i-1}\psi_{i-1}+10V_i\psi_i+V_{i+1}\psi_{i+1})}{12}=E\frac{(\psi_{i+1}+10\psi_i+\psi_{i\_1})}{12}. \tag{8}$$

We will convert the well-known Numerov's approach into a matrix representation on a discrete lattice. To accomplish that, $\psi$ will be defined as a matrix and represented by a column vector $(\ldots.\psi_{i-1},\psi_i,\psi_{i+1}\ \ldots.)$

$$A_{N,N}=\frac{(I_{-1}-2I_0+I_1)}{d^2},\ B_{N,N}=\frac{(I_{-1}+10I_0+I_1)}{12},V_N=diag(\ldots.,V_{i-1},V_i,V_{i+1})$$

where an N-point grid and the unit matrices $I_{-1}$, $I_0$, and $I_1$ stand for the sub-, main-, and up-diagonals, respectively. The matrix version of Eq. (8) could be created as follows.

$$\frac{-1}{2\mu}A_{N,N}\psi_i+B_{N,N}V_N\psi_i=E_iB_{N,N}\psi_i. \tag{9}$$

Multiplying Eq. (9) by $\mathrm{B}_{\mathrm{N,N}}^{-1}$ yields

$$\frac{-1}{2\mu}\mathrm{B}_{\mathrm{N,N}}^{-1}A_{N,N}\psi_{nl}+V_N\psi_i=E_i\psi_{nl}. \tag{10}$$

This numerical technique allows us to solve the eigenvalue problem for any possible hadron-hadron bound states.

### 2.4. Root Mean Square Radii and $\beta$ Coefficient

The afterward reasoning shall be employed to offer an explanation or description of the root mean square ($r_{\text{ms}}$) radius of $B_c$ that is both clear and succinct. Among the key characteristics of this particle system is the root mean square ($r_{\text{ms}}$) of $B_c$ mesons. Assuming that the distance between the quark and anti-quark in bottom-charmed mesons is represented by the symbol $r$ (*fm*), it is possible to deduce that the radius of $B_c$ is equal to $(r/2)$ *fm*. With the use of the meson wave function, one can derive the root mean square ($r_{\text{ms}}$), which may be stated accordingly [12, 26, 28]:

$${r^2}_{ms}=\int_0^\infty\{\psi^2(r)r^2dr\}. \tag{10}$$

One aspect that characterizes the momentum width of a meson wave function is the beta coefficient. The symbol $\beta$ is commonly used to represent it, and it is connected to the root mean square ($r_{\mathrm{ms}}$) distance between the quark and antiquark in the meson. In addition to affecting the decay rates and form factors of the meson, the beta coefficient reveals information on the spatial distribution of the quark-antiquark pair inside the meson. Mesons' internal structure and behavior can be better understood by analyzing and describing the beta coefficient [29]:

$$\beta = \sqrt{2(n-1) + (L) + \frac{3}{2}} \;\; \frac{1}{r_{ms}} \tag{11}$$

The parameter $\beta$ is commonly regarded as a model parameter. However, as we aim to explain the deterioration of heavy quark states, it is more desirable to replicate the $\beta$ coefficient of the quark model states. Therefore, we recommend utilizing it for the computation of the decay width of $B_c$ states.

## 3. RESULTS AND DISCUSSION

We have conducted a theoretical examination of the mass spectrum of both the ground and excited states of $B_c$ mesons using a non-relativistic component quark model. The model parameters were adjusted to accurately replicate the empirically determined 1S ground state. Mass predictions for the 4th radial excitations of S-wave, P-wave, D-wave, and F-wave were developed and compared to previous theoretical studies and existing data.

Figures 1-4 provide the graphical depiction of normalized radial wave functions for $B_c$ mesons. Table 2 displays the anticipated masses (measured in GeV) of both the primary and secondary states of $B_c$ mesons. We compare our findings with previous model predictions and existing experimental evidence. The experimental masses obtained from reference [30], together with the predictions made by Asghar [31], Nosheen [7], and Qi Li [32] have been included for a thorough study. Our model's predictions exhibit strong concordance with both the existing experimental data and other theoretical predictions.

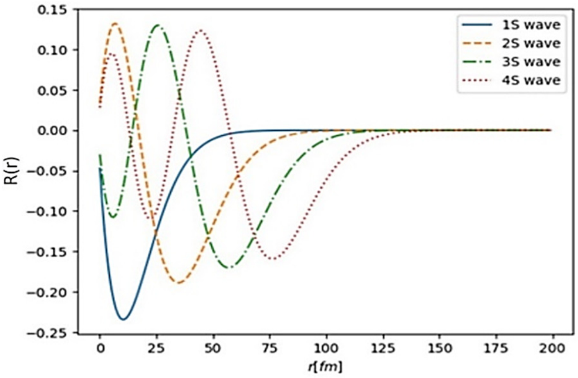

**Figure 1.** Bottom-Charmed for S-states reduced radial wave functions

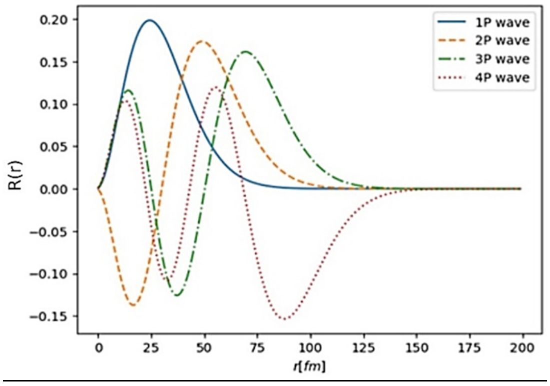

**Figure 2.** Bottom-Charmed for P-states reduced radial wave functions

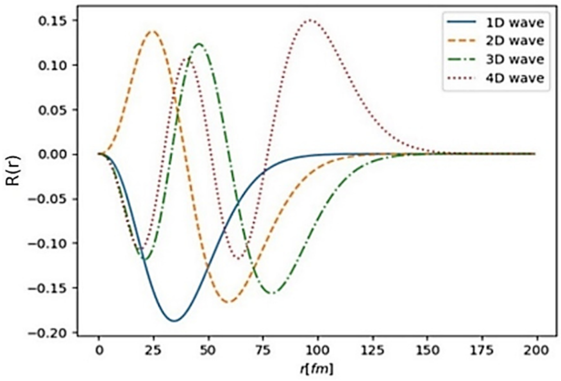

**Figure 3.** Bottom-Charmed for D-states reduced radial wave functions

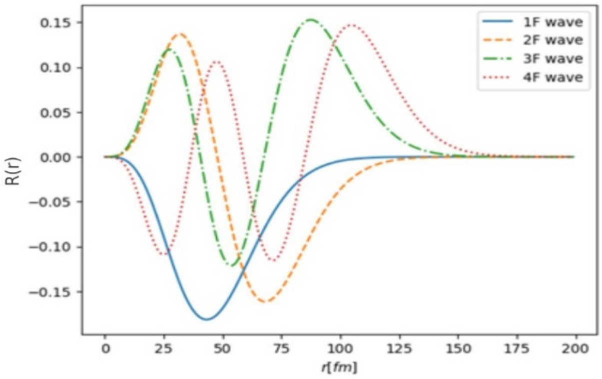

**Figure 4.** Bottom-Charmed for F-states reduced radial wave functions

The anticipated mass of the well-established 1S ground state $B_c$ ($^1S_0$) is 6.275 GeV, which is in excellent agreement with the observed value of 6.2749 ± 0.008 GeV. The predictions concerning the 2S and 3S excited states are consistent with the evidence obtained from different simulations. When compared to the other computational models, our predictions often fall within a range of 0.01-0.05 GeV, which suggests a high level of accuracy**.** Significantly, our results for the P-wave and D-wave exhibit comparable mass splitting and orderings to those seen in the studies conducted by Asghar et al. and Nosheen et al. This demonstrates assurance that our model accurately replicates the anticipated spectroscopy.

For higher excitations, such as the 4S, 4P, and 4D states, where experimental data remain scarce, our model provides predictions that can be tested in future research. The projected 4F states may potentially serve as a starting point for further discoveries. All things considered, our findings are in good agreement with and add to the predictions that have already been made.

**Table 2.** Predicted masses of ground and excited states of $B_c$ mesons

| State | [our work] (GeV) | Qi Li [32] (GeV) | Asghar [31] (GeV) | Nosheen [7] (GeV) | Exp. Masses [30] (GeV) |
|---|---|---|---|---|---|
| $B_c (1^1 S_0)$ | 6.275 | 6.271 | 6.318 | 6.274 | 6.2749 ± 0.008 |
| $B_c (1^3 S_1)$ | 6.315 | 6.326 | 6.336 | 6.314 | |
| $B_c (2^1 S_0)$ | 6.842 | 6.871 | 6.741 | 6.841 | 6.842±0.004 |
| $B_c (2^3 S_1)$ | 6.856 | 6.890 | 6.747 | 6.855 | |
| $B_c (3^1 S_0)$ | 7.198 | 7.239 | 7.014 | 7.197 | |
| $B_c (3^3 S_1)$ | 7.206 | 7.252 | 7.018 | 7.206 | |
| $B_c (4^1 S_0)$ | 7.489 | 7.540 | 7.239 | 7.488 | |
| $B_c (4^3 S_1)$ | 7.496 | 7.550 | 7.242 | 7.495 | |
| $B_c (1^3 P_2)$ | 6.747 | 6.787 | 6.665 | 6.753 | |
| $B_c (1 P'_1)$ | 6.769 | 6.776 | 6.656 | 6.744 | |
| $B_c (1 P_1)$ | 6.774 | 6.757 | 6.650 | 6.725 | |
| $B_c (1^3 P_0)$ | 6.746 | 6.714 | 6.631 | 6.701 | |
| $B_c (2^3 P_2)$ | 7.111 | 7.160 | 6.946 | 7.111 | |
| $B_c (2 P'_1)$ | 7.128 | 7.150 | 6.939 | 7.098 | |
| $B_c (2 P_1)$ | 7.132 | 7.134 | 6.930 | 7.105 | |
| $B_c (2^3 P_0)$ | 7.283 | 7107 | 6.915 | 7.086 | |
| $B_c (3^3 P_2)$ | 7.408 | 7.464 | 7.176 | 7.406 | |
| $B_c (3 P'_1)$ | 7.423 | 7.458 | 7.168 | 7.393 | |
| $B_c (3 P_1)$ | 7.427 | 7.441 | 7.162 | 7.405 | |
| $B_c (3^3 P_0)$ | 7.551 | 7.420 | 7.147 | 7.389 | |
| $B_c (4^3 P_2)$ | 7. 669 | 7.732 | 7.379 | - | |
| $B_c (4 P'_1)$ | 7.683 | 7.727 | 7.373 | - | |
| $B_c (4 P_1)$ | 7.687 | 7.710 | 7.364 | - | |
| $B_c (4^3 P_0)$ | 7.794 | 7.693 | 7.350 | - | |
| $B_c (1^3 D_3)$ | 6.769 | 7.030 | 6.847 | 6.998 | |
| $B_c (1 D'_2)$ | 6.996 | 7.032 | 6.845 | 6.984 | |
| $B_c (1 D_2)$ | 6.997 | 7.024 | 6.845 | 6.986 | |
| $B_c (1^3 D_1)$ | 6.964 | 7.020 | 6.841 | 6.964 | |
| $B_c (2^3 D_3)$ | 7.128 | 7.348 | 7.087 | 7.302 | |
| $B_c (2 D'_2)$ | 7.304 | 7.347 | 7.084 | 7.293 | |
| $B_c (2 D_2)$ | 7.304 | 7.343 | 7.084 | 7.294 | |
| $B_c (2^3 D_1)$ | 7.271 | 7.336 | 7.080 | 7.280 | |
| $B_c (3^3 D_3)$ | 7.423 | 7.625 | 7.296 | 7.570 | |
| $B_c (3 D'_2)$ | 7.572 | 7.623 | 7.293 | 7.562 | |
| $B_c (3 D_2)$ | 7.573 | 7.620 | 7.293 | 7.563 | |
| $B_c (3^3 D_1)$ | 7.539 | 7.611 | 7.289 | 7.553 | |
| $B_c (4^3 D_3)$ | 7.683 | - | 7.489 | - | |
| $B_c (4 D'_2)$ | 7.815 | - | 7.482 | - | |
| $B_c (4 D_2)$ | 7.816 | - | 7.482 | - | |
| $B_c (4^3 D_1)$ | 7.782 | - | 7.478 | - | |
| $B_c (1^3 F_4)$ | 7.181 | 7.227 | 6.9967 | - | |
| $B_c (1 F'_3)$ | 7.189 | 7.240 | 7.001 | - | |
| $B_c (1 F_3)$ | 7.188 | 7.224 | 6.994 | - | |
| $B_c (1^3 F_2)$ | 7.179 | 7.235 | 6.9972 | - | |
| $B_c (2^3 F_4)$ | 7.459 | 7.514 | 7.2126 | - | |
| $B_c (2 F'_3)$ | 7.465 | 7.525 | 7.214 | - | |
| $B_c (2 F_3)$ | 7.465 | 7.508 | 7.211 | - | |
| $B_c (2^3 F_2)$ | 7.455 | 7.518 | 7.2121 | - | |
| $B_c (3^3 F_4)$ | 7.71 | 7.771 | - | - | |
| $B_c (3 F'_3)$ | 7.715 | 7.779 | - | - | |
| $B_c (3 F_3)$ | 7.715 | 7.768 | - | - | |
| $B_c (3^3 F_2)$ | 7.704 | 7.730 | - | - | |
| $B_c (4^3 F_4)$ | 7.941 | - | - | - | |
| $B_c (4 F'_3)$ | 7.945 | - | - | - | |
| $B_c (4 F_3)$ | 7.945 | - | - | - | |
| $B_c (4^3 F_2)$ | 7.934 | - | - | - | |

The estimated root mean square ($r_{\mathrm{ms}}$) radii of ground and excited $B_c$ meson states are presented in Table 3, which compares the results of our model to those of earlier calculations carried out by Nosheen et al [7]. There are some radial excitations of S-wave, P-wave, D-wave, and F-wave states that are taken into consideration.

**Table 3.** Root mean square radii of ground and excited states of $B_c$ mesons

| State | [our work] in *fm* | Nosheen in *fm* [7] |
|---|---|---|
| $B_c\,(1^1S_0)$ | 0.319 | 0.318 |
| $B_c\,(1^3S_1)$ | 0.335 | 0.334 |
| $B_c\,(2^1S_0)$ | 0.724 | 0.723 |
| $B_c\,(2^3S_1)$ | 0.733 | 0.732 |
| $B_c\,(3^1S_0)$ | 1.053 | 1.052 |
| $B_c\,(3^3S_1)$ | 1.06 | 1.059 |
| $B_c\,(4^1S_0)$ | 1.338 | 1.337 |
| $B_c\,(4^3S_1)$ | 1.343 | 1.342 |
| $B_c\,(1^3P_2)$ | 0.595 | 0.594 |
| $B_c\,(1P'_1)$ | 0.612 | -- |
| $B_c\,(1P_1)$ | 0.618 | -- |
| $B_c\,(1^3P_0)$ | 0.757 | 0.562 |
| $B_c\,(2^3P_2)$ | 0.944 | 0.940 |
| $B_c\,(2P'_1)$ | 0.96 | -- |
| $B_c\,(2P_1)$ | 0.965 | -- |
| $B_c\,(2^3P_0)$ | 1.076 | 0.920 |
| $B_c\,(3^3P_2)$ | 1.24 | 1.235 |
| $B_c\,(3P'_1)$ | 1.254 | -- |
| $B_c\,(3P1)$ | 1.259 | -- |
| $B_c\,(3^3P_0)$ | 1.354 | 1.220 |
| $B_c\,(4^3P_2)$ | 1.504 | -- |
| $B_c\,(4P'_1)$ | 1.518 | -- |
| $B_c\,(4P1)$ | 1.522 | -- |
| $B_c\,(4^3P_0)$ | 1.606 | -- |
| $B_c\,(1^3D_3)$ | 0.612 | 0.793 |
| $B_c\,(1D'_2)$ | 0.788 | -- |
| $B_c\,(1D_2)$ | 0.791 | -- |
| $B_c\,(1^3D_1)$ | 0.743 | 0.752 |
| $B_c\,(2^3D_3)$ | 0.96 | -- |
| $B_c\,(2D'_2)$ | 1.107 | 1.107 |
| $B_c\,(2D_2)$ | 1.109 | -- |
| $B_c\,(2^3D_1)$ | 1.062 | 1.083 |
| $B_c\,(3^3D_3)$ | 1.254 | 1.382 |
| $B_c\,(3D'_2)$ | 1.385 | 1.382 |
| $B_c\,(3D_2)$ | 1.387 | -- |
| $B_c\,(3^3D_1)$ | 1.339 | 1.364 |
| $B_c\,(4^3D_3)$ | 1.518 | – |
| $B_c\,(4D'_2)$ | 1.637 | – |
| $B_c\,(4D_2)$ | 1.639 | – |
| $B_c\,(4^3D_1)$ | 1.59 | – |
| $B_c\,(1^3F_4)$ | 0.95 | – |
| $B_c\,(1F'_3)$ | 0.951 | – |
| $B_c\,(1F_3)$ | 0.952 | – |
| $B_c\,(1^3F_2)$ | 0.933 | – |
| $B_c\,(2^3F_4)$ | 1.248 | – |
| $B_c\,(2F'_3)$ | 1.249 | – |
| $B_c\,(2F_3)$ | 1.25 | – |
| $B_c\,(2^3F_2)$ | 1.231 | – |
| $B_c\,(3^3F_4)$ | 1.512 | – |
| $B_c\,(3F'_3)$ | 1.513 | – |
| $B_c\,(3F_3)$ | 1.514 | – |
| $B_c\,(3^3F_2)$ | 1.496 | – |
| $B_c\,(4^3F_4)$ | 1.755 | – |
| $B_c\,(4F'_3)$ | 1.756 | – |
| $B_c\,(4F_3)$ | 1.757 | – |
| $B_c\,(4^3F_2)$ | 1.738 | – |

Our radii predictions correlate with those of Nosheen et al. in a very tight manner, with deviations of less than 0.01 fm across the board for all states. Our model provides a realistic description of the spatial sizes of $B_c$ mesons, as this explains how it works. The fact that our model is able to accurately predict spatial features is validated by the fact that it is in close agreement with earlier computations.

The $\beta$ values of the ground and excited states of $B_c$ mesons are presented in Table 4. This table also includes a comparison between our findings and the anticipated results made by Asghar [31]. It is essential to take into consideration the fact that Asghar's predictions are not accessible for certain stages in the F-wave, and our findings are given in comparison to those predictions. In general, the comparison of $\beta$ values between our calculations and Asghar's prediction indicates the existence of reliable and favorable compatibility throughout a wide range of states of $B_c$ mesons.

**Table 4.** $\beta$ values of ground and excited states of $B_c$ mesons

| State | [our work] in GeV | Asghar in GeV [31] |
|---|---|---|
| $B_c$ $(1^1S_0)$ | 0.741 | 0.653 |
| $B_c$ $(1^3S_1)$ | 0.689 | 0.634 |
| $B_c$ $(2^1S_0)$ | 0.513 | 0.515 |
| $B_c$$(2^3S_1)$ | 0.503 | 0.508 |
| $B_c$$(3^1S_0)$ | 0.446 | 0.442 |
| $B_c$$(3^3S_1)$ | 0.437 | 0.439 |
| $B_c$ $(4^1S_0)$ | 0.412 | 0.402 |
| $B_c$ $(4^3S_1)$ | 0.402 | 0.401 |
| $B_c$ $(1^3P_2)$ | 0.525 | 0.468 |
| $B_c$ $(1P'_1)$ | 0.51 | 0.471 |
| $B_c$ $(1P_1)$ | 0.505 | 0.468 |
| $B_c$ $(1^3P_0)$ | 0.612 | 0.468 |
| $B_c$ $(2^3P_2)$ | 0.443 | 0.428 |
| $B_c$ $(2P'_1)$ | 0.436 | 0.430 |
| $B_c$ $(2P_1)$ | 0.434 | 0.428 |
| $B_c$ $(2^3P_0)$ | 0.502 | 0.428 |
| $B_c$ $(3^3P_2)$ | 0.406 | 0.395 |
| $B_c$ $(3P'_1)$ | 0.401 | 0.397 |
| $B_c$ (3P1) | 0.4 | 0.395 |
| $B_c$ $(3^3P_0)$ | 0.449 | 0.395 |
| $B_c$ $(4^3P_2)$ | 0.382 | 0.373 |
| $B_c$ $(4P'_1)$ | 0.379 | 0.374 |
| $B_c$ $(4P_1)$ | 0.378 | 0.373 |
| $B_c$ $(4^3P_0)$ | 0.379 | 0.373 |
| $B_c$ $(1^3D_3)$ | 0.471 | 0.417 |
| $B_c$ $(1D'_2)$ | 0.468 | 0.417 |
| $B_c$ $(1D_2)$ | 0.467 | 0.417 |
| $B_c$ $(1^3D_1)$ | 0.623 | 0.417 |
| $B_c$ $(2^3D_3)$ | 0.419 | 0.395 |
| $B_c$ $(2D'_2)$ | 0.418 | 0.395 |
| $B_c$ $(2D_2)$ | 0.417 | 0.395 |
| $B_c$ $(2^3D_1)$ | 0.509 | 0.395 |
| $B_c$ $(3^3D_3)$ | 0.391 | 0.374 |
| $B_c$ $(3D'_2)$ | 0.39 | 0.374 |
| $B_c$ $(3D_2)$ | 0.39 | 0.374 |
| $B_c$ $(3^3D_1)$ | 0.454 | 0.374 |
| $B_c$ $(4^3D_3)$ | 0.372 | 0.357 |
| $B_c$ $(4D'_2)$ | 0.372 | 0.358 |
| $B_c$ $(4D_2)$ | 0.371 | 0.357 |
| $B_c$ $(4^3D_1)$ | 0.383 | 0.357 |
| $B_c$ $(1^3F_4)$ | 0.441 | 0.390 |
| $B_c$ $(1F'_3)$ | 0.44 | 0.390 |
| $B_c$ $(1F_3)$ | 0.439 | 0.390 |
| $B_c$ $(1^3F_2)$ | 0.539 | 0.390 |
| $B_c$ $(2^3F_4)$ | 0.403 | 0.375 |
| $B_c$ $(2F'_3)$ | 0.403 | 0.375 |
| $B_c$ $(2F_3)$ | 0.402 | 0.375 |

| State | [our work] in GeV | Asghar in GeV [31] |
|---|---|---|
| $B_c\,(2^3F_2)$ | 0.467 | 0.375 |
| $B_c\,(3^3F_4)$ | 0.38 | - |
| $B_c\,(3F'_3)$ | 0.38 | - |
| $B_c\,(3F_3)$ | 0.38 | - |
| $B_c\,(3^3F_2)$ | 0.428 | - |
| $B_c\,(4^3F_4)$ | 0.364 | - |
| $B_c\,(4F'_3)$ | 0.364 | - |
| $B_c\,(4F_3)$ | 0.364 | - |
| $B_c\,(4^3F_2)$ | 0.368 | - |

## 4. CONCLUSIONS

In this work, we have used the Tridiagonal Matrix Numerov (TMN) approach to estimate the mass spectra of the $B_c$ meson system's newly anticipated excited states. The TMN technique produced precise and stable eigenvalues corresponding to different radial and orbital quantum numbers by numerically solving the radial Schrödinger equation under a suitable potential framework.

Our findings show that the TMN approach is a reliable and effective computational technique for simulating heavy-heavy quark systems, such as the $B_c$ meson, especially when it comes to Predicting higher excited states that are now unattainable through experimentation.

The calculated masses provide accurate predictions for undiscovered excited states that might direct future experimental efforts at facilities like LHCb and Belle II. They are also compatible with established theoretical models and, when accessible, current experimental evidence.

The TMN approach's efficacy in hadron spectroscopy is demonstrated by its ability to capture the fine structure of the $B_c$ spectrum. In addition to improving our theoretical knowledge of double-heavy mesons, this study provides a framework for Predicting further findings in heavy quarkonium physics.

The most noteworthy outcomes of this work are that the decay widths and differential cross sections for $B_c$ states can be computed by utilizing the values of $r_{\mathrm{ms}}$ and the $\beta$ coefficients that have been figured out. Furthermore, by obtaining additional meson characteristics, the effectiveness of Numerov's matrix technique can be thoroughly analyzed. The results of this evaluation are found to correspond well with the findings reported in the literature, which means a high level of accuracy.

## 5. RECOMMENDATIONS

Using the Tridiagonal Matrix-Numerov (TMN) approach to predict the excited states of $B_c$ mesons, the following suggestions are made considering the results:

- Adoption in Other Quarkonium Systems: Due to its accuracy and efficiency, the TMN technique is advised for use in other heavy meson systems, including Y\Upsilon (bottomonium), ψ\psi (charmonium), and mixed-flavor mesons like $B_s$ or $D_s$.
- Enhanced Potential Models: To better depict both short-range and long-range interactions, it is recommended to include more realistic potentials, such as the Cornell, logarithmic, or QCD-inspired screened potentials.
- To facilitate the search for and possible confirmation of novel $B_c$ meson states, experimental collaborations (such as LHCb, CMS, and Belle II) should be provided with the expected excited states.
- Cross-Validation with Other Methods: To achieve consistency and dependability, results from TMN should be cross-checked with those from other numerical approaches, such as lattice QCD, variational techniques, or the shot method.

### Acknowledgement

The authors extend their appreciation to Taif University, Saudi Arabia, for supporting this work through project number (TU-DSPP-2024-226).

**Funding**

Taif University, Saudi Arabia, for supporting this work through project number (TU-DSPP-2024-226).

**Declarations Conflict of interest**

The authors declare that no conflicts of interest or personal relationships have influenced this work.

**Data availability statement**

My manuscript and associated personal data will be shared with Research Square for the delivery of the author dashboard.

### ORCID

**Ali A. Alkathiri,** https://orcid.org/0000-0001-9096-3270;**Atef Ismail,** https://orcid.org/0000-0002-2669-0914
**M. Allosh,** https://orcid.org/0000-0001-8389-7076; **Tarek A. Nahool,** https://orcid.org/0000-0002-3967-0103
**S.A. Abd El-Azeem,** https://orcid.org/0000-0003-4434-9004; **Weeam S. Albaltan,** https://orcid.org/0000-0009-4314-6956
**R.F. Alnahdi,** https://orcid.org/0000-0002-1034-1322; **M.S. Ali,** https://orcid.org/0000-0002-0250-438X

## REFERENCES

[1] M.S. Ali, *Spectra of quarkonium*, (LAP LAMBERT Academic Publishing, Germany, 2015). http://dx.doi.org/10.13140/2.1.4598.8166
[2] D. Griffiths, *Introduction to elementary particles*, (John Wiley & Sons, 2020).
[3] M. Thomson, *Modern particle physics*, (Cambridge University Press, 2013).
[4] G. Kane, *Modern elementary particle physics: explaining and extending the standard model*, (Cambridge University Press, 2017).
[5] L. Apolinário, Y.-J. Lee, and M. Winn, "Heavy quarks and jets as probes of the QGP," Progress in Particle and Nuclear Physics, **127**, 103990 (2022). https://doi.org/10.1016/j.ppnp.2022.103990
[6] M. Mai, Ulf-G. Meißner, and C. Urbach, "Towards a theory of hadron resonances," Physics Reports, **1001**, 1-66 (2023). https://doi.org/10.1016/j.physrep.2022.11.005
[7] N. Akbar, F. Akram, B. Masud, and M.A. Sultan, "Conventional and hybrid $B_c$ mesons in an extended potential model," The European Physical Journal A, **55**(5), 82 (2019). https://doi.org/10.1140/epja/i2019-12735-1
[8] K.K. Pathak, S. Bhattacharya, and T. Das, "Weak decays of $B_c$ meson in a QCD potential model," Indian Journal of Physics, **97**, 3685–3689 (2023). https://doi.org/10.1007/s12648-023-02716-w
[9] P. Gambino, S. Hashimoto, S. Mächler, M. Panero, F. Sanfilippo, S. Simula, A. Smecca, and N. Tantalo, "On the study of inclusive semileptonic decays of $B_s$-meson from lattice QCD," arXiv preprint arXiv:2311.09892 (2023). https://doi.org/10.48550/arXiv.2311.09892
[10] A.M. Yasser, G.S. Hassan, and T.A. Nahool, "A study of some properties of bottomonium," Journal of Modern Physics, **5**(17), 1938 (2014). http://dx.doi.org/10.4236/jmp.2014.517188
[11] M.A. Nobes, and R.M. Woloshyn, "Decays of the $B_c$ meson in a relativistic quark-meson model," Journal of Physics G: Nuclear and Particle Physics, **26**(7), 1079 (2000). https://doi.org/10.1088/0954-3899/26/7/308
[12] M.S. Ali, G.S. Hassan, A.M. Abdelmonem, S.K. Elshamndy, F. Elmasry, and A.M. Yasser, "The spectrum of charmed quarkonium in non-relativistic quark model using matrix Numerov's method," Journal of Radiation Research and Applied Sciences, **13**(1), 226-233 (2020). https://doi.org/10.1080/16878507.2020.1723949
[13] A.M. Yasser, and T.A. Nahool, "A new gate to Numerov's method," Open Access Journal of Physics, **2**(3), (2018). https://doi.org/10.22259/2637-5826.0203001
[14] S.M. Ryan, D.J. Wilson, and Hadron Spectrum Collaboration, "Excited and exotic bottomonium spectroscopy from lattice QCD," Journal of High Energy Physics, **2021**(2), 1-23 (2021). https://doi.org/10.1007/JHEP02(2021)214
[15] J. Killingbeck, "Shooting methods for the Schrodinger equation," Journal of Physics A: Mathematical and General, **20**(6), 1411 (1987). https://doi.org/10.1088/0305-4470/20/6/024
[16] V. Kumar, R.M. Singh, S.B. Bhardwaj, R. Rani, and F. Chand, "Analytical solutions to the Schrodinger equation for generalized Cornell potential and its applications to diatomic molecules and heavy mesons," Modern Physics Letters A, **37**(02), 2250010 (2022). https://doi.org/10.1142/S0217732322500109
[17] F.J. Ynduráin, *The theory of quark and gluon interactions*, (Springer Science & Business Media, 2007).
[18] M.A. Ivanov, Yu.L. Kalinovsky, and C.D. Roberts, "Survey of heavy-meson observables." Physical Review D, **60**(3), 034018 (1999). https://doi.org/10.1103/PhysRevD.60.034018
[19] J. Ahmed, R. Manzoor, L. Chang, A. Raya, and K. Raya, "Heavy Quark Mesons: Mass Spectrum and Mass Relations," Few-Body Systems, **62**(3), 39 (2021). https://doi.org/10.1007/s00601-021-01624-1
[20] A.M. Yasser, G.S. Hassan, S.K. Elshamndy, and M.S. Ali, "Comparison Between Two Numerical Schemes to Study the Spectra of Charmed Quarkonium," arXiv preprint arXiv:2010.07436 (2020). https://doi.org/10.48550/arXiv.2010.07436
[21] M. Allosh, M.S. Abdelaal, F. Alshowaikh, and A. Ismail, "Numerical Solutions of a Three-Dimensional Schrodinger Equation for a Non–Relativistic Quark Model," Applied Mathematics & Information Sciences, **17**(3), 447-452 (2023). http://dx.doi.org/10.18576/amis/170306
[22] M.S. Ali, and A.M. Yasser, "Spectra of quark-antiquark bound states via two derived QCD potential," arXiv preprint arXiv:1502.06569 (2015). https://arxiv.org/abs/1502.06569
[23] T.A. Nahool, M. Yasser, M. Anwar, and G.A. Yahya, "Charmonium properties," East European Journal of Physics, (3) 31-38 (2020). https://doi.org/10.26565/2312-4334-2020-3-04
[24] T. Barnes, S. Godfrey, and E.S. Swanson, "Higher charmonia," Physical Review D, **72**(5), 054026 (2005). https://doi.org/10.1103/PhysRevD.72.054026
[25] Semay, Claude, and B. Silvestre-Brac. "Potential models and meson spectra." Nuclear Physics A 618, no. 4 (1997): 455-482.
[26] M. Allosh, Y. Mustafa, N. Khalifa Ahmed, A. Sayed Mustafa, Few-Body Syst (2021) 62:26 https://doi.org/10.1007/s00601-021-01608-1
[27] M.I. Hapareer, M. Allosh, G.S. Hassan, and A.M. Yasser, "Bottomonia Under Effect Three Inspired QCD Potentials in the Framework of Non-Relativistic Quark Model," East Eur. J. Phys. (2), 348 (2023). https://doi.org/10.26565/2312-4334-2023-2-41
[28] T. Das, and D.K. Choudhury, "Root mean square radii of heavy flavoured mesons in a quantum chromodynamics potential model," Pramana, **87**, 1-7 (2016). https://doi.org/10.1007/s12043-016-1242-6
[29] C.-Y. Wong, "Molecular states of heavy quark mesons," Physical Review C, **69**(5), 055202 (2004). https://doi.org/10.1103/PhysRevC.69.055202
[30] P.A. Zyla, and Particle Data Group, "Review of Particle Physics," PTEP, **2020**, 083C01 (2020). https://doi.org/10.1093/ptep/ptaa104
[31] I. Asghar, F. Akram, B. Masud, and M.A. Sultan, "Properties of excited charmed-bottom mesons," Physical Review D, **100**(9), 096002 (2019). https://doi.org/10.1103/PhysRevD.100.096002
[32] Q. Li, M.-S. Liu, L.-S. Lu, Q.-F. Lü, L.-C. Gui, and X.-H. Zhong, "Excited bottom-charmed mesons in a nonrelativistic quark model," Physical Review D, **99**(9), 096020 (2019). https://doi.org/10.1103/PhysRevD.99.096020
[33] A.A. Aly, "Heavy meson spectra in the non-relativistic quark model," M. Sc. Thesis, South Valley University, Egypt, 2012.

# ПРОГНОЗУВАННЯ ЗБУДЖЕНИХ СТАНІВ НОВИХ *Bc*-МЕЗОНІВ: ТРИДІАГОНАЛЬНИЙ МАТРИЧНО-ЧИСЛОВИЙ ПІДХІД

**Алі А. Алкатірі[1], С.А. Абд Ель-Азім[2,3], Віам С. Албалтан[4], Р.Ф. Алнахді[5], Атеф Ісмаїл[6], М. Аллош[7], М.С. Алі[8], Тарек А. Нахул[9]**
[1]*Кафедра фізики, Коледж наук, Університет Таїфа, поштова скринька 11099, Таїф 21944, Саудівська Аравія*
[2]*Кафедра фізики, Коледж наук і гуманітарних наук, Університет Принца Саттама Бін Абдулазіза, Аль-Хардж 11942, Саудівська Аравія*
[3]*Кафедра фізики, Факультет жінок для мистецтв, науки та освіти, Університет Айн-Шамс, Каїр 11757, Єгипет*
[4]*Кафедра фізики, Коледж наук, Університет принцеси Нури бінт Абдулрахман, П.О. Скринька 84428, Ер-Ріяд, 11671, Ер-Ріяд, Саудівська Аравія*
[5]*Фізичний факультет, факультет природничих наук, Університет короля Абдулазіза, 21859, Джидда, Саудівська Аравія*
[6]*Фізичний факультет, Університет Аль-Азхар, 71524 Асьют, Єгипет*
[7]*Фізичний факультет, факультет природничих наук, Університет Південної Долини, 83523 Кена, Єгипет*
[8]*Африканський інститут математичних наук, місто Мбур, Сенегал*
[9]*Фізичний факультет, факультет природничих наук, Асуанський університет, Єгипет*

Властивості станів нижньо-чарованих мезонів були ретельно досліджені з використанням тридіагонального матричного підходу Нумерова для прогнозування радіальних хвильових функцій. На основі отриманих значень ми передбачили значення ангармонізму $\beta$ та середньоквадратичні радіуси для різних збуджених станів Bc-мезонів. Було проведено комплексне порівняння між оціненими результатами та нещодавно опублікованими теоретичними та експериментальними даними, яке показало порівнянний добуток з високим ступенем точності.

**Ключові слова:** *нижньо-чарований мезон; тридіагональна матриця Нумерова; коефіцієнт $\beta$; середньоквадратичні радіуси*

East European Journal of Physics. **4**. 63–74 (2025)

DOI: 10.26565/2312-4334-2025-4-06 ISSN 2312-4334

# SQUEEZED COHERENT STATES IN QUANTUM MECHANICS WITH POSITION-DEPENDENT MASS

**Daniel Sabi Takou**[1,2*], **Amidou Boukari**[2], **Assimiou Yarou Mora**[2], **Gabriel Y.H. Avossevou**[2]

[1] *Ecole Polytechnique d'Abomey Calavi (EPAC-UAC), Université d'Abomey-Calavi (UAC), Bénin*

[2] *Unité de Recherche en Physique Théorique (URPT), Institut de Mathématiques et de Sciences Physiques (IMSP), 01 B.P. 613 Porto-Novo, Rep. du Bénin*

[*] *Corresponding Author e-mail: sabitakoudaniel11@gmail.com*

Received August 10, 2025; revised September 19, 2025; accepted September 31, 2025

In this paper, we construct and analyze a new class of squeezed coherent states in the framework of position-dependent mass (PDM) quantum systems. Using a deformed algebraic structure, we generalize the creation and annihilation operators to accommodate spatially varying mass profiles. The resulting states exhibit non-classical features, such as squeezing, coherence, and modified uncertainty relations, strongly influenced by both the deformation parameters and the mass function. We explore their physical properties through expectation values, variances, and probability densities. This work provides a pathway toward extending coherent state theory to more complex quantum systems with geometrical and algebraic richness.

**Keywords:** *Squeezed Coherent State; Supersymmetric; Quantum Mechanics; Position dependent mass*

**PACS:** 03.65.Fd,03.65.-w,03.65.Ud, 03.65.Ge

## 1. INTRODUCTION

Coherent and squeezed states play a fundamental role in various domains of physics, particularly quantum optics and quantum information theory[1, 2, 3]. Originally introduced by Schrödinger in 1926 and Kennard in 1927[4, 5], these states remained largely overlooked until the 1960s, when seminal works by Glauber, Klauder, and Nieto reignited interest in their theoretical and practical significance[6, 7, 8]. Squeezed states, in particular, are nonclassical quantum states that exhibit reduced quantum noise, making them highly valuable for optical communication, precision measurements, and the detection of gravitational waves—as in the case of LIGO[9, 10, 11, 12]. They are also key resources in continuous-variable quantum information processing, including quantum computing, dense coding, and quantum cryptography, and can be implemented in physical platforms such as graded semiconductors [13, 14], quantum dots, photonic crystals, and cavity optomechanical systems for quantum communication and precision sensing [15, 16]. More recently, the construction and analysis of squeezed states for systems with infinite discrete spectra have attracted increasing attention as generalized extensions of coherent states (see, for example[17, 18, 19, 20, 21]).

Quantum mechanics with position-dependent mass (PDM) has emerged as a powerful framework for modeling a wide range of physical systems with non-uniform spatial characteristics, such as semiconductor heterostructures, graded crystals, and quantum wells [22, 23, 24, 25, 26, 27]. The modification of the kinetic energy operator due to the spatial dependence of the mass introduces new challenges and has stimulated the development of refined analytical and algebraic methods. Among these, supersymmetric quantum mechanics (SUSY QM) has proven particularly fruitful in the construction of exactly solvable models through factorization methods and intertwining techniques [28, 29].

On the other hand, coherent and squeezed states, first introduced by Schrödinger in 1926 and later formalized by Glauber, Klauder, and others [30, 31, 32], have become essential tools in quantum optics and quantum information due to their ability to saturate uncertainty relations and describe non-classical light fields.These states have been widely generalized to encompass systems with either discrete or continuous spectra, algebraic deformations, and both constant and position-dependent mass backgrounds. Further extensions have also been developed for more complex scenarios, such as oscillators defined in noncommutative spaces [33, 34, 35, 36].

In this work, we aim to construct a new class of generalized squeezed coherent states for a quantum system governed by a position-dependent mass and embedded within a supersymmetric algebraic structure. Inspired by the formalism developed by Gazeau and Klauder [30], and following techniques involving ladder operators and recurrence relations, we derive analytical expressions for the coherent-like states, ensuring that they fulfill essential physical criteria such as temporal stability, resolution of identity, and continuity in the labeling parameter [31, 32].

Moreover, we devote special attention to the analysis of quantum statistical properties of these states. In particular, we compute their normalization factors, probability densities, and expectation values of relevant observables. The wavefunctions and energy spectrum are explicitly obtained and expressed in terms of orthogonal polynomials and generalized hypergeometric functions, revealing the deep interplay between the effective mass profile, deformation parameters, and the algebraic structure of the system.

---

***Cite as:*** D.S. Takou, A. Boukari, A.Y. Mora, G.Y.H. Avossevou, East Eur. J. Phys. 4, 63 (2025), https://doi.org/10.26565/2312-4334-2025-4-06

Our manuscript is organised as follows : In Section 2, we review the basic formalism of position-dependent mass quantum mechanics. Section 3 is devoted to the study of the Supersymmetric Squeezed coherent states. In Section 4, we investigate the properties of squeezed states and discuss numerical results. Finally, concluding remarks are presented in Section 5.

## 2. POSITION-DEPENDENT EFFECTIVE MASS HARMONIC OSCILLATOR AND IT EXACT SOLUTIONS

A general expression for the Hermitian kinetic energy operator of a quantum particle with a position-dependent mass (PDM) $m(\hat{x})$ is given by [37, 26, 38]

$$\hat{T} = \frac{1}{4}\left[m^{\alpha}(\hat{x})\hat{p}\, m^{\beta}(\hat{x})\hat{p}\, m^{\gamma}(\hat{x}) + m^{\gamma}(\hat{x})\hat{p}\, m^{\beta}(\hat{x})\hat{p}\, m^{\alpha}(\hat{x})\right], \tag{1}$$

where the parameters $\alpha$, $\beta$, and $\gamma$ satisfy the constraint $\alpha + \beta + \gamma = -1$. Different combinations of these parameters lead to various forms of the kinetic energy operator [39, 40, 41, 42, 43].

In this study, we adopt the representation proposed by Mustafa and Mazharimousavi [43], which corresponds to the specific parameter choice $\alpha = \gamma = -\frac{1}{4}$, $\beta = -\frac{1}{2}$. Under this configuration, the kinetic energy operator becomes:

$$\hat{T} = \frac{1}{2}\frac{1}{m^{1/4}(\hat{x})}\,\hat{p}\left(\frac{1}{m^{1/2}(\hat{x})}\right)\hat{p}\,\frac{1}{m^{1/4}(\hat{x})}. \tag{2}$$

Accordingly, the total Hamiltonian for the system is written as

$$\hat{H} = \hat{T} + V = \frac{1}{2}\frac{1}{m^{1/4}(\hat{x})}\,\hat{p}\left(\frac{1}{m^{1/2}(\hat{x})}\right)\hat{p}\,\frac{1}{m^{1/4}(\hat{x})} + V(\hat{x}), \tag{3}$$

where $V(\hat{x})$ denotes the potential energy function.

Considering a harmonic oscillator potential defined by $V(x) = \frac{1}{2}m_0\omega^2x^2$, the corresponding time-independent Schrödinger equation reads:

$$E\phi(x) = -\frac{\hbar^2}{2m_0}\sqrt[4]{\frac{m_0}{m(x)}}\frac{d}{dx}\sqrt{\frac{m_0}{m(x)}}\frac{d}{dx}\sqrt[4]{\frac{m_0}{m(x)}}\phi(x) + V(x)\phi(x), \tag{4}$$

where $m_0$ represents the constant reference mass, $E$ is the energy eigenvalue, and $\phi(x)$ is the wavefunction belonging to the Hilbert space $\mathcal{H} = \mathcal{L}^2(\mathbb{R})$.

In this work, we consider the following mass distribution:

$$m(x) = \frac{m_0}{(1+\alpha x^2)^2}, \tag{5}$$

where $\alpha$ is a deformation parameter constrained by $0 < \alpha < 1$. This choice generalizes earlier mass profiles studied in [22, 23, 24, 25, 26], and can be interpreted as an inverse squared length scale associated with local geometric features such as curvature or structural defects in the physical system.

To simplify Eq. (4), we apply the transformation $\phi(x) = \sqrt[4]{\frac{m(x)}{m_0}}\psi(x)$, yielding:

$$E\psi(x) = -\frac{\hbar^2}{2m_0}\left(\sqrt{\frac{m_0}{m(x)}}\frac{d}{dx}\right)^2\psi(x) + \frac{1}{2}m_0\omega^2x^2\psi(x). \tag{6}$$

Using the explicit expression of $m(x)$ in Eq. (5), the above equation becomes:

$$E\psi(x) = -\frac{\hbar^2}{2m_0}\left[(1+\alpha x^2)\frac{d}{dx}\right]^2\psi(x) + \frac{1}{2}m_0\omega^2x^2\psi(x). \tag{7}$$

By introducing the coordinate transformation $q = \arctan(x\sqrt{\alpha})$, the infinite domain of the position variable $x \in \mathbb{R}$ is mapped to a finite interval $q \in \left(-\frac{\pi}{2}, \frac{\pi}{2}\right)$. This change significantly simplifies the position-dependent mass Schrödinger equation, which becomes more tractable in the new variable.

Assuming the ansatz $\psi(q) = \cos^{\lambda} q \cdot f(\sin q)$, and requiring the absence of singular behavior at the boundaries, leads to a second-order differential equation that reduces to the Gegenbauer differential equation when a specific condition on the parameter $\lambda$ is imposed:

$$\lambda = \frac{1}{2} + \frac{1}{2}\sqrt{1 + \frac{4}{\kappa^2}}, \quad \kappa = \frac{\alpha\hbar}{m_0\omega}. \tag{8}$$

This constraint eliminates the singular term, yielding a well-defined eigenvalue problem with solutions expressible in terms of Gegenbauer polynomials $C_n^\lambda(s)$, where $s = \sin q$. The energy quantization condition is then given by:

$$\varepsilon = \lambda + n(n + 2\lambda), \quad n \in \mathbb{N}. \tag{9}$$

Consequently, the energy spectrum becomes:

$$E_n = \hbar\omega\left(n + \frac{1}{2}\right)\sqrt{1 + \frac{\alpha^2\hbar^2}{4m_0^2\omega^2}} + \frac{\alpha\hbar^2}{2m_0}\left(n^2 + 2n + \frac{1}{2}\right). \tag{10}$$

This reveals a non-trivial dependence on the deformation parameter $\alpha$, illustrating how position-dependent mass modifies the energy levels compared to the standard harmonic oscillator[44, 45]. In the limit $\alpha \longrightarrow 0$, the conventional energy levels are recovered.

The corresponding normalized wavefunctions take the form:

$$\psi_n(q) = N\cos^\lambda q \cdot C_n^\lambda(\sin q), \tag{11}$$

where $C_n^\lambda(q)$ are the Gegenbauer polynomials [46] and $N$ the normalization constant given by :

$$N = \sqrt{\frac{n!(n + \lambda)\Gamma^2(\lambda)}{\pi 2^{1-2\lambda}\Gamma(n + 2\lambda)}}. \tag{12}$$

Transforming back to the $x$-representation using $\cos q = \frac{1}{\sqrt{1+\alpha x^2}}$ and $\sin q = \frac{x\sqrt{\alpha}}{\sqrt{1+\alpha x^2}}$, the wavefunction becomes:

$$\phi_n(x) = \sqrt{\frac{n!(n + \lambda)\Gamma^2(\lambda)}{\pi 2^{1-2\lambda}\Gamma(n + 2\lambda)}}\left(\frac{1}{\sqrt{1 + \alpha x^2}}\right)^{\lambda+1} C_n^\lambda\left(\frac{x\sqrt{\alpha}}{\sqrt{1 + \alpha x^2}}\right). \tag{13}$$

This provides an explicit analytic solution for the eigenfunctions of the deformed harmonic oscillator with position-dependent mass.

## 3. SUPERSYMMETRIC SQUEEZED COHERENT STATES

The Hamiltonian operator given in Eq. (7), corresponding to a quadratic potential $v(x) = \frac{1}{2}m_0\omega^2x^2$, can be factorized in the form

$$\hat{H} = \hbar\omega_0\, \hat{a}_\alpha^\dagger \hat{a}_\alpha + E_0(\alpha), \tag{14}$$

where the ladder operators $\hat{a}_\alpha^\dagger$ and $\hat{a}_\alpha$ are constructed within the supersymmetric framework for systems with position-dependent mass, as defined in [26].

$$\hat{a}_\alpha = \sqrt{\frac{m_0\omega_0}{2\hbar}}\left(\hat{x} + \frac{\hbar\alpha}{2m_0\omega_0} + \frac{i}{m_0\omega_0}\hat{\Pi}_\alpha\right), \quad \hat{a}_\alpha^\dagger = \sqrt{\frac{m_0\omega_0}{2\hbar}}\left(\hat{x} + \frac{\hbar\alpha}{2m_0\omega_0} - \frac{i}{m_0\omega_0}\hat{\Pi}_\alpha\right), \tag{15}$$

where $\hat{\Pi}_\alpha = (1 + \alpha\hat{x}^2)\hat{p}$ is the deformed momentum operator.

In supersymmetric framing, we used the fact that $\hat{a}_\alpha\psi_0(x) = 0$, indicating that the ground state is annihilated by the operator $\hat{a}_\alpha$. Although $\hat{a}_\alpha$ and $\hat{a}_\alpha^\dagger$ factorize the Hamiltonian Eq. (7) associated with the quadratic potential, they do not serve as conventional ladder operators, since they obey the deformed commutation relation: $[\hat{a}_\alpha, \hat{a}_\alpha^\dagger] = \hat{1} + \alpha\hat{x}^2$. To take into account this deformation, we introduce a modified number operator defined by: $\hat{n}_\alpha = \hat{a}_\alpha^\dagger\hat{a}_\alpha$, whose expectation value on the $n$-th eigenstate can be obtained as follow.

The generalized number operator $\hat{n}_\alpha = \hat{a}_\alpha^\dagger\hat{a}_\alpha$, with $\hat{a}_\alpha$ and $\hat{a}_\alpha^\dagger$ defined in (15), can be written as

$$\hat{n}_\alpha = \frac{m_0\omega_0}{2\hbar}(\hat{x} + c)^2 + \frac{1}{2\hbar m_0\omega_0}\hat{\Pi}_\alpha^2 - \frac{1}{2}\left(1 + \alpha\hat{x}^2\right), \tag{16}$$

where $c = \frac{\hbar\alpha}{2m_0\omega_0}$ and $\hat{\Pi}_\alpha = (1 + \alpha\hat{x}^2)\hat{p}$. Its expectation value in an arbitrary state $|\psi\rangle$ is

$$\langle\hat{n}_\alpha\rangle = \frac{m_0\omega_0}{2\hbar}\langle(\hat{x} + c)^2\rangle + \frac{1}{2\hbar m_0\omega_0}\langle\hat{\Pi}_\alpha^2\rangle - \frac{1}{2}\left(1 + \alpha\langle\hat{x}^2\rangle\right). \tag{17}$$

Physically, $\langle\hat{n}_\alpha\rangle$ measures the mean excitation number of the deformed oscillator defined by the position-dependent mass model. The shift $c$ introduces a static displacement of the quadrature $\hat{x}$, while $\hat{\Pi}_\alpha$ accounts for a deformation of the canonical momentum, modifying the balance between kinetic and potential contributions. In the limit $\alpha \to 0$, $\hat{n}_\alpha$ reduces to the standard harmonic oscillator number operator, and $\langle \hat{n}_\alpha \rangle$ counts the average quanta of excitation in the usual sense.

We define the squeezed coherent state $\psi(z,\gamma,x)$ as the solution to the eigenvalue equation involving a linear combination of ladder operators, in accordance with the formalism presented in [20, 8].

$$(\hat{a}_\alpha + \gamma \hat{a}_\alpha^\dagger) |\psi(z,\gamma)\rangle = z |\psi(z,\gamma)\rangle . \tag{18}$$

This combination of the operators $\hat{a}_\alpha$ and $\hat{a}_\alpha^\dagger$ is governed by a squeeze parameter $\gamma$, while $z$ is known as *coherent parameter*. When the squeezing parameter vanishes, i.e., $\gamma = 0$, the resulting quantum states reduce to *coherent states*, which are special solutions characterized by minimal uncertainty and classical-like behavior. To ensure that these states are physically meaningful, appropriate conditions must be imposed on the parameters involved, particularly to guarantee the normalizability of the states.

Squeezed coherent states (SCS) have been extensively studied in various algebraic frameworks, notably those based on the Lie algebras su(2) and su(1, 1) [47, 48, 49, 21]. In addition, constructions have been extended to *direct sums* of these algebras with the *Heisenberg algebra* h(2) [21], allowing for a richer variety of quantum states.

In such algebraic settings, especially for su(2) and su(1, 1), the function $k(n)$ that appears in the recurrence relations or ladder operator actions is generally a *quadratic function* of the quantum number $n$. This reflects the non-equidistant spectrum structure and the non-linear characteristics of the underlying algebra, distinguishing these systems from the standard harmonic oscillator.

We expand this state (18) in the eigen basis of the deformed oscillator :

$$|\psi(z,\gamma)\rangle = \frac{1}{\sqrt{\mathcal{N}(z,\gamma)}} \sum_{n=0}^{n_{\max}} \frac{Z(z,\gamma,n)}{\sqrt{\rho(n)}} |\psi_n\rangle , \tag{19}$$

where the normalization factor is computed as $\mathcal{N}(z,\gamma) = \sum_{n=0}^{n_{\max}} \frac{|Z(z,\gamma,n)|^2}{\rho(n)}$ and $Z(z,\gamma,n)$ satisfies the recurrence relation:

$$Z_{n+1}(z,\gamma) = zZ_n(z,\gamma) - \gamma k(n) Z_{n-1}(z,\gamma), \quad Z_0 = 1, \quad Z_1 = z. \tag{20}$$

We define the weights $\rho(n)$ using the generalized factorial:

$$\rho(n) = \prod_{j=1}^{n} k(j). \tag{21}$$

Let us recall the energy eigenvalues defined in equation (10) as

$$E_n = \hbar\omega \left(n + \frac{1}{2}\right) \sqrt{1 + \frac{\alpha^2\hbar^2}{4m_0^2\omega^2}} + \frac{\alpha\hbar^2}{2m_0} \left(n^2 + 2n + \frac{1}{2}\right) \quad \text{and} \quad E_0 = \frac{1}{2}\hbar\omega \sqrt{1 + \frac{\alpha^2\hbar^2}{4m_0^2\omega^2}} + \frac{\alpha\hbar^2}{4m_0}. \tag{22}$$

For the system under consideration, the dimensionless form of the latter energy is given by

$$\begin{aligned} e_n &= E_n - E_0 = n\hbar\omega \sqrt{1 + \frac{\alpha^2\hbar^2}{4m_0^2\omega^2}} + \frac{\alpha\hbar^2}{2m_0} \left(n^2 + 2n\right) = \left(\hbar\omega \sqrt{1 + \frac{\alpha^2\hbar^2}{4m_0^2\omega^2}} + \frac{\alpha\hbar^2}{m_0}\right) n + \frac{\alpha\hbar^2}{2m_0} n^2 \\ &= an^2 + bn = n(an + b), \end{aligned} \tag{23}$$

where the constants $a$ and $b$ are given by

$$b = \hbar\omega \sqrt{1 + \frac{\alpha^2\hbar^2}{4m_0^2\omega^2}} + \frac{\alpha\hbar^2}{m_0}, \quad a = \frac{\alpha\hbar^2}{2m_0}. \tag{24}$$

The dimensionless form of the energy (23) is similar to the ones obtained in [45, 15] used to study the laser light propagation in a nonlinear Kerr medium. The product of these dimensionless energies $e_n$ represented by $\rho_n$ is defined as

$$\begin{aligned} \rho_n &= \prod_{k=1}^{n} e_k, \quad \text{with} \quad e_i = ak^2 + bk \\ &= \prod_{k=1}^{n} k \prod_{k=1}^{n} (ak + b). \end{aligned} \tag{25}$$

With the following computations

$$\prod_{k=1}^{n} k = n! = \Gamma(n+1), \quad \prod_{k=1}^{n} (ak + b) = \prod_{k=1}^{n} a \left(k + \frac{b}{a}\right) = \frac{a^n \Gamma\left(n + 1 + \frac{b}{a}\right)}{\Gamma\left(1 + \frac{b}{a}\right)}. \tag{26}$$

The equation (25) becomes

$$\rho_n = n!a^n \frac{\Gamma\left(n+1+\frac{b}{a}\right)}{\Gamma\left(1+\frac{b}{a}\right)} = \frac{a^n\Gamma\left(n+1\right)\Gamma\left(n+1+\frac{b}{a}\right)}{\Gamma\left(1+\frac{b}{a}\right)}, \quad \rho_0 = 1. \tag{27}$$

To derive the analytical expression of the coefficients $Z_n(z,\gamma)$ that define the squeezed coherent states in the deformed algebraic framework, we assume a factorized form:

$$Z_n(z,\gamma) = \left(\frac{\gamma}{2}\right)^{n/2} f_n(\omega), \quad \text{with} \quad \omega = \frac{z}{\sqrt{2\gamma}}. \tag{28}$$

Substituting this ansatz into the recurrence relation:

$$Z_{n+1} = zZ_n - \gamma\, n(an+b)Z_{n-1}, \tag{29}$$

leads to a simplified recurrence for $f_n(\omega)$ of the form:

$$f_{n+1} = 2\omega f_n - 2n(an+b)f_{n-1}, \quad f_0 = 1, \quad f_1 = \sqrt{2\gamma}\,\omega. \tag{30}$$

This sequence admits an analytical solution expressed in terms of the Gauss hypergeometric function:

$$f_n(\omega) = (2\omega)^n \cdot {}_2F_1\left(-\left\lfloor\frac{n}{2}\right\rfloor, -\left\lfloor\frac{n-1}{2}\right\rfloor;\ -b;\ 1\right), \tag{31}$$

where ${}_2F_1(a,b;c;z)$ is the Gaussian hypergeometric function.

The general solution of the recurrence relation (29) is obtained in terms of the Gauss hypergeometric function ${}_2F_1$ as follows

$$Z(z,\gamma,n) = (-1)^n\,(\gamma)^{n/2}\,a^{n/2}\frac{\Gamma(n+1+\frac{b}{a})}{\Gamma(1+\frac{b}{a})} \cdot {}_2F_1\left(-n,\ -\frac{1}{2}+\frac{b}{2a}-\frac{z}{2\sqrt{\gamma a}};\ 1+\frac{b}{a};\ 2\right). \tag{32}$$

We obtain the explicit form of the squeezed states of position-dependent effective mass harmonic oscillator (19) in terms of the hypergeometric functions as follows :

$$|\psi(z,\gamma)\rangle = \frac{1}{\sqrt{\mathcal{N}(z,\gamma)}}\sum_{n=0}^{n_{\max}}\frac{(\gamma a)^{n/2}}{\sqrt{n!}} \cdot \sqrt{\frac{\Gamma\left(n+1+\frac{b}{a}\right)}{\Gamma\left(1+\frac{b}{a}\right)}} \cdot {}_2F_1\left(-n,\ -\frac{1}{2}+\frac{b}{2a}-\frac{z}{2\sqrt{a\gamma}};\ 1+\frac{b}{a};\ 2\right)|\psi_n\rangle \tag{33}$$

where

$$\mathcal{N}(z,\gamma) = \sum_{n=0}^{n_{\max}}\frac{(\gamma a)^n}{n!} \cdot \frac{\Gamma\left(n+1+\frac{b}{a}\right)}{\Gamma\left(1+\frac{b}{a}\right)} \cdot \left|{}_2F_1\left(-n,\ -\frac{1}{2}+\frac{b}{2a}-\frac{z}{2\sqrt{a\gamma}};\ 1+\frac{b}{a};\ 2\right)\right|^2 \tag{34}$$

The time evolution of this squeezed coherent states (33) is given by

$$|\psi(z,\gamma,t)\rangle = \frac{1}{\sqrt{\mathcal{N}(z,\gamma)}}\sum_{n=0}^{n_{\max}}\frac{(\gamma a)^{n/2}}{\sqrt{n!}} \cdot \sqrt{\frac{\Gamma\left(n+1+\frac{b}{a}\right)}{\Gamma\left(1+\frac{b}{a}\right)}} \cdot {}_2F_1\left(-n,\ -\frac{1}{2}+\frac{b}{2a}-\frac{z}{2\sqrt{a\gamma}};\ 1+\frac{b}{a};\ 2\right)e^{-\frac{iE_n}{\hbar}t}\,|\psi_n\rangle \tag{35}$$

We are interested in analyzing the special case of (24) where the deformation parameter $\alpha \longrightarrow 0$, which corresponds to the standard quantum harmonic oscillator with constant mass, corresponds to :

$$a = \frac{\alpha\hbar^2}{2m_0} = 0, \quad b = \hbar\omega\sqrt{1+\frac{\alpha^2\hbar^2}{4m_0^2\omega^2}} + \frac{\alpha\hbar^2}{m_0} \xrightarrow{\alpha=0} \hbar\omega\sqrt{1}+0 = \hbar\omega. \tag{36}$$

In the undeformed limit $\alpha \longrightarrow 0$, we obtain the simplified and physically interpretable results:

$$a = 0, \quad b = \hbar\omega. \tag{37}$$

In this regime, the Gauss hypergeometric function in (32) reduces to Hermite polynomials according to the well–known identity

$$
{}_2F_1\left(-n,\ \tfrac{1}{2}-\tfrac{z}{2};\ \tfrac{1}{2};\ 2\right)=\frac{(-1)^n}{n!}\,H_n(z), \tag{38}
$$

where $H_n(z)$ are the Hermite polynomials. At the same time, the ratio of Gamma functions $\Gamma\left(n+1+\frac{b}{a}\right)/\Gamma\left(1+\frac{b}{a}\right)$ simplifies to $n!$ in the undeformed case, since the parameter $\frac{b}{a}$ diverges while $a\longrightarrow 0$, which exactly reproduces the factorial structure of the standard harmonic oscillator basis. Therefore, expressions (32)-(35) reduce to the usual squeezed coherent states of the quantum harmonic oscillator, and (37) consistently recovers the known limit.

This implies that:

- The deformation parameter vanishes, and the mass becomes position-independent;
- The parameter $b$ reduces to the fundamental energy quantum $\hbar\omega$, characteristic of the standard harmonic oscillator;
- The wavefunctions and the associated squeezed coherent states simplify accordingly, often allowing expressions in terms of classical orthogonal polynomials, such as Hermite polynomials.

This limit therefore provides a consistency check with the well-known results of quantum mechanics in homogeneous media. In the limit where the deformation parameter $\alpha\longrightarrow 0$, the effective mass becomes constant and the system reduces to the standard quantum harmonic oscillator. The squeezed coherent state (33) can then be expressed as:

$$
|\psi(z,\gamma,\alpha=0)\rangle=\frac{1}{\sqrt{\mathcal{N}(z,\gamma)}}\sum_{n=0}^{\infty}\frac{1}{\sqrt{n!}}\left(\frac{\gamma}{2}\right)^{n/2}H_n\left(\frac{z}{\sqrt{2\gamma}}\right)|\psi_n\rangle\,, \tag{39}
$$

where:

- $H_n(x)$ denotes the Hermite polynomial of degree $n$,
- $\gamma$ is the squeezing parameter,
- $|\psi_n\rangle$ is the $n$-th energy eigenstate of the harmonic oscillator,
- $\mathcal{N}(z,\gamma)$ is the normalization factor defined as:

$$
\mathcal{N}(z,\gamma,\alpha=0)=\sum_{n=0}^{\infty}\frac{1}{n!}\left(\frac{\gamma}{2}\right)^{n}H_n^2\left(\frac{z}{\sqrt{2\gamma}}\right). \tag{40}
$$

These states minimize the generalized uncertainty relation and exhibit Gaussian-like wavepacket behavior, typical of squeezed states in quantum optics.

## 4. PROPERTIES OF SQUEEZED COHERENT STATES

### 4.1. The non-orthogonality, the normalization, solvability the unity,

Given two squeezed coherent states :

$$
|\psi(z,\gamma)\rangle=\frac{1}{\sqrt{\mathcal{N}(z,\gamma)}}\sum_{n=0}^{\infty}\frac{Z_n(z,\gamma)}{\sqrt{\rho(n)}}|\psi_n\rangle\,, \tag{41}
$$

$$
|\psi(z',\gamma')\rangle=\frac{1}{\sqrt{\mathcal{N}(z',\gamma')}}\sum_{n=0}^{\infty}\frac{Z_n(z',\gamma')}{\sqrt{\rho(n)}}|\psi_n\rangle\,, \tag{42}
$$

their inner product is given by:

$$
\langle\psi(z',\gamma')|\psi(z,\gamma)\rangle=\frac{1}{\sqrt{\mathcal{N}(z',\gamma')\mathcal{N}(z,\gamma)}}\sum_{n=0}^{\infty}\frac{\overline{Z_n(z',\gamma')}Z_n(z,\gamma)}{\rho(n)}. \tag{43}
$$

In the particular case $\gamma'=\gamma$, this simplifies to:

$$
\langle\psi(z',\gamma)|\psi(z,\gamma)\rangle=\frac{1}{\mathcal{N}(z,\gamma)}\sum_{n=0}^{\infty}\frac{\overline{Z_n(z',\gamma)}Z_n(z,\gamma)}{\rho(n)}. \tag{44}
$$

This sum is generally non-zero, indicating that the squeezed coherent states are non-orthogonal:

$$\langle\psi(z',\gamma)|\psi(z,\gamma)\rangle \neq \delta(z-z^{'}). \tag{45}$$

To verify the normalization of the compressed coherent state, we consider the time-dependent compressed coherent state obtained in (35), which can be rewritten in the contracted form:

$$|\psi(z,\gamma,t)\rangle = \frac{1}{\sqrt{\mathcal{N}(z,\gamma)}} \sum_{n=0}^{n_{\max}} C_n(z,\gamma) e^{-\frac{iE_n t}{\hbar}} |\psi_n\rangle \tag{46}$$

with

$$C_n(z,\gamma) = \frac{(\gamma a)^{n/2}}{\sqrt{n!}} \cdot \sqrt{\frac{\Gamma\left(n+1+\frac{b}{a}\right)}{\Gamma\left(1+\frac{b}{a}\right)}} \cdot {}_2F_1\left(-n,\ -\frac{1}{2}+\frac{b}{2a}-\frac{z}{2\sqrt{a\gamma}};\ 1+\frac{b}{a};\ 2\right), \tag{47}$$

and the constant $\mathcal{N}(z,\gamma)$ is given by (34).

The inner product is given by :

$$\langle\psi(z,\gamma,t)|\psi(z,\gamma,t)\rangle = \frac{1}{\mathcal{N}(z,\gamma)} \sum_{n=0}^{n_{\max}} |C_n(z,\gamma)|^2 = 1. \tag{48}$$

Thus, we conclude that the squared norm of the state is correctly normalized by the factor $\mathcal{N}(z,\gamma)$, provided that this exact expression is used. This normalization condition (48) ensures that the squeezed coherent states remain physically admissible quantum states in a position-dependent mass background. The normalization factor $\mathcal{N}(z,\gamma)$ encodes the interaction between spatial mass variation, squeeze effects, and spectral deformation. It guarantees unit total probability and reflects the modified spectral weight due to SUSY deformation and PDM geometry.

### 4.2. Probability Density of Squeezed Coherent States

The probability of finding the squeezed coherent state in the energy level $n$, i.e., the probability density, is defined by:

$$P_n(z,\gamma) = |\langle\psi_n\rangle\, \psi(z,\gamma)|^2 = \frac{|Z(z,\gamma,n)|^2}{\mathcal{N}(z,\gamma)\cdot\rho(n)}. \tag{49}$$

Substituting the expressions of $Z_n$ and $\rho(n)$, we obtain the explicit analytical form:

$$P_n(z,\gamma) = \frac{\gamma^n}{\mathcal{N}(z,\gamma)} \cdot \frac{\Gamma(n+1+b)}{\Gamma(n+1)} \cdot \left|{}_2F_1\left(-n,\ -\frac{1}{2}+\frac{b}{2}-\frac{z}{2\sqrt{\gamma}};\ 1+b;\ 2\right)\right|^2. \tag{50}$$

This expression provides a complete description of the squeezed state probability distribution over the Fock space basis $\{|\psi_n\rangle\}$, accounting for the deformation via the parameters $\gamma$ and $b$.

### 4.3. Mean values, standard deviations and uncertainty relations

In this section, we investigate the statistical properties of time-dependent squeezed coherent states in a quantum system with position-dependent mass. Specifically, we examine the expectation values of the position and momentum operators, their variances, and the corresponding uncertainty product. These observables offer valuable insight into quantum fluctuations, coherence, and squeezing behavior of the states. Our analysis follows an approach similar to that presented by Sanjib Dey and Véronique Hussin [34, 35, 36].

We begin by considering the time-evolved squeezed coherent state, given by:

$$\begin{aligned} |\psi(z,\gamma,t)\rangle = \frac{1}{\sqrt{\mathcal{N}(z,\gamma)}} \sum_{n=0}^{n_{\max}} \frac{(\gamma a)^{n/2}}{\sqrt{n!}} \sqrt{\frac{\Gamma\left(n+1+\frac{b}{a}\right)}{\Gamma\left(1+\frac{b}{a}\right)}} \\ \times {}_2F_1\left(-n,\ -\frac{1}{2}+\frac{b}{2a}-\frac{z}{2\sqrt{a\gamma}};\ 1+\frac{b}{a};\ 2\right) e^{-\frac{iE_n t}{\hbar}} |\psi_n\rangle. \end{aligned} \tag{51}$$

where the normalization factor is given by :

$$\mathcal{N}(z,\gamma) = \sum_{n=0}^{n_{\max}} \frac{(\gamma a)^n}{n!} \cdot \frac{\Gamma\left(n+1+\frac{b}{a}\right)}{\Gamma\left(1+\frac{b}{a}\right)} \cdot \left|{}_2F_1\left(-n,\ -\frac{1}{2}+\frac{b}{2a}-\frac{z}{2\sqrt{a\gamma}};\ 1+\frac{b}{a};\ 2\right)\right|^2. \tag{52}$$

The quadrature operators of position and momentum are written in terms of the ladder operators as

$$\hat{x} = \sqrt{\frac{\hbar}{2m\omega}}(\hat{a}^\dagger + \hat{a}), \quad \text{and} \quad \hat{p} = i\sqrt{\frac{\hbar m\omega}{2}}(\hat{a}^\dagger - \hat{a}). \tag{53}$$

To compute the uncertainty relation, we need the following expectation values of $\hat{x}$ and $\hat{p}$ for squeezed coherent states, respectively, given by:

$$\langle\hat{x}\rangle = \sqrt{\frac{\hbar}{2m\omega}}\left(\langle\hat{a}\rangle + \langle\hat{a}^\dagger\rangle\right) = 2\sqrt{\frac{\hbar}{2m\omega}} \cdot \mathrm{Re}\left(\langle\hat{a}\rangle\right), \tag{54}$$

and

$$\langle\hat{p}\rangle = i\sqrt{\frac{\hbar m\omega}{2}}\left(\langle\hat{a}^\dagger\rangle - \langle\hat{a}\rangle\right) = 2\sqrt{\frac{\hbar m\omega}{2}} \cdot \mathrm{Im}\left(\langle\hat{a}\rangle\right), \tag{55}$$

where the expectation value of the annihilation operator is given by :

$$\langle\hat{a}\rangle = \sum_{n=0}^{n_{\max}-1} C_n^* C_{n+1}\sqrt{n+1}. \tag{56}$$

Combining the equations (54) and (55), we obtained the expectation values of $\hat{x}^2$ and $\hat{p}^2$ as :

$$\langle\hat{x}^2\rangle = \frac{\hbar}{2m\omega}\left(\langle\hat{a}^2\rangle + \langle\hat{a}^{\dagger 2}\rangle + \langle\hat{a}^\dagger\hat{a}\rangle + \langle\hat{a}\hat{a}^\dagger\rangle\right), \tag{57}$$

$$\langle\hat{p}^2\rangle = -\frac{\hbar m\omega}{2}\left(\langle\hat{a}^2\rangle + \langle\hat{a}^{\dagger 2}\rangle - \langle\hat{a}^\dagger\hat{a}\rangle - \langle\hat{a}\hat{a}^\dagger\rangle\right), \tag{58}$$

where we set

$$\langle\hat{a}^\dagger\hat{a}\rangle = \sum_{n=0}^{n_{\max}} |C_n|^2 n, \tag{59}$$

$$\langle\hat{a}\hat{a}^\dagger\rangle = \sum_{n=0}^{n_{\max}} |C_n|^2 (n+1), \tag{60}$$

$$\langle\hat{a}^2\rangle = \sum_{n=0}^{n_{\max}-2} C_n^* C_{n+2}\sqrt{(n+1)(n+2)}, \tag{61}$$

$$\langle\hat{a}^{\dagger 2}\rangle = \sum_{n=0}^{n_{\max}-2} C_{n+2}^* C_n\sqrt{(n+1)(n+2)}. \tag{62}$$

We now define the normalized coefficients :

$$\tilde{C}_n = \frac{C_n}{\sqrt{\mathcal{N}(z,\gamma)}}, \tag{63}$$

with the coefficient $C_n(z,\gamma)$ defined by :

$$C_n(z,\gamma) = \frac{(\gamma a)^{n/2}}{\sqrt{n!}}\sqrt{\frac{\Gamma\left(n+1+\frac{b}{a}\right)}{\Gamma\left(1+\frac{b}{a}\right)}} \cdot {}_2F_1\left(-n,\ -\frac{1}{2}+\frac{b}{2a}-\frac{z}{2\sqrt{a\gamma}};\ 1+\frac{b}{a};\ 2\right). \tag{64}$$

By the simple way, we compute the expectation Value of $\hat{a}$

$$\langle\hat{a}\rangle = \sum_{n=0}^{n_{\max}-1} \tilde{C}_n^* \tilde{C}_{n+1}\sqrt{n+1} \tag{65}$$

Thus:

$$\mathrm{Re}(\langle\hat{a}\rangle) = \sum_{n=0}^{n_{\max}-1} \mathrm{Re}\left(\tilde{C}_n^* \tilde{C}_{n+1}\right)\sqrt{n+1}, \tag{66}$$

$$\mathrm{Im}(\langle \hat{a} \rangle) = \sum_{n=0}^{n_{\max}-1} \mathrm{Im}\left(\tilde{C}_n^* \tilde{C}_{n+1}\right) \sqrt{n+1}. \tag{67}$$

Let us define the hypergeometric part in (64) as follows :

$$f_n := {}_2F_1\left(-n,\ -\frac{1}{2} + \frac{b}{2a} - \frac{z}{2\sqrt{a\gamma}};\ 1 + \frac{b}{a};\ 2\right) \tag{68}$$

Then the normalized coefficient is:

$$\tilde{C}_n = \frac{C_n}{\sqrt{\mathcal{N}(z,\gamma)}} = \frac{(\gamma a)^{n/2}}{\sqrt{n!\mathcal{N}}} \cdot \sqrt{\frac{\Gamma(n+1+\frac{b}{a})}{\Gamma(1+\frac{b}{a})}} \cdot f_n \tag{69}$$

The expression of the product $\tilde{C}_n \tilde{C}_{n+1}^*$ becomes :

$$\tilde{C}_n \tilde{C}_{n+1}^* = \frac{1}{\mathcal{N}} \cdot \frac{(\gamma a)^{(n+n+1)/2}}{\sqrt{n!(n+1)!}} \cdot \sqrt{\frac{\Gamma(n+1+\frac{b}{a})\Gamma(n+2+\frac{b}{a})}{\left[\Gamma(1+\frac{b}{a})\right]^2}} \cdot f_n \cdot f_{n+1}^* \tag{70}$$

This simplifies to

$$\tilde{C}_n \tilde{C}_{n+1}^* = \frac{(\gamma a)^{n+1/2}}{\sqrt{n!(n+1)! \cdot \mathcal{N}}} \cdot \sqrt{\frac{\Gamma(n+1+\frac{b}{a})\Gamma(n+2+\frac{b}{a})}{\left[\Gamma(1+\frac{b}{a})\right]^2}} \cdot f_n \cdot f_{n+1}^* \tag{71}$$

The real and imaginary parts used in position and momentum expectations are as follows:

$$\mathrm{Re}(\langle \hat{a} \rangle) = \textstyle\sum_{n=0}^{n_{\max}-1} \mathrm{Re}\left(\tilde{C}_n \tilde{C}_{n+1}^*\right) \sqrt{n+1}, \tag{72}$$

$$\mathrm{Im}(\langle \hat{a} \rangle) = \textstyle\sum_{n=0}^{n_{\max}-1} \mathrm{Im}\left(\tilde{C}_n \tilde{C}_{n+1}^*\right) \sqrt{n+1}. \tag{73}$$

Thus, the full expressions are:

$$\langle \hat{x} \rangle = 2\sqrt{\tfrac{\hbar}{2m\omega}} \cdot \textstyle\sum_{n=0}^{n_{\max}-1} \mathrm{Re}\left[\tfrac{(\gamma a)^{n+1/2}}{\sqrt{n!(n+1)! \cdot \mathcal{N}}} \cdot \sqrt{\tfrac{\Gamma(n+1+\frac{b}{a})\Gamma(n+2+\frac{b}{a})}{\left[\Gamma(1+\frac{b}{a})\right]^2}} \cdot f_n f_{n+1}^*\right] \cdot \sqrt{n+1} \tag{74}$$

$$\langle \hat{p} \rangle = 2\sqrt{\tfrac{\hbar m\omega}{2}} \cdot \textstyle\sum_{n=0}^{n_{\max}-1} \mathrm{Im}\left[\tfrac{(\gamma a)^{n+1/2}}{\sqrt{n!(n+1)! \cdot \mathcal{N}}} \cdot \sqrt{\tfrac{\Gamma(n+1+\frac{b}{a})\Gamma(n+2+\frac{b}{a})}{\left[\Gamma(1+\frac{b}{a})\right]^2}} \cdot f_n f_{n+1}^*\right] \cdot \sqrt{n+1} \tag{75}$$

The terms $f_n$ are hypergeometric functions evaluated at fixed parameters. The products $f_n f_{n+1}^*$ contain the phase differences (squeezing effects). The square root of the gamma functions encodes the deformation of the ladder through $b/a$.

We consider the normalized squeezed coherent state:

$$|\psi(z,\gamma)\rangle = \sum_{n=0}^{n_{\max}} \tilde{C}_n \, |\psi_n\rangle, \quad \text{avec} \quad \tilde{C}_n = \frac{C_n}{\sqrt{\mathcal{N}(z,\gamma)}}. \tag{76}$$

Then the position and momentum variances read:

$$\begin{aligned} \langle \hat{x}^2 \rangle \quad &= \quad \frac{\hbar}{2m\omega}\left[\sum_{n=0}^{n_{\max}-2} \tilde{C}_n^* \tilde{C}_{n+2}\sqrt{(n+1)(n+2)} + \sum_{n=0}^{n_{\max}-2} \tilde{C}_{n+2}^* \tilde{C}_n \sqrt{(n+1)(n+2)} \right. \\ &\quad \left. + \sum_{n=0}^{n_{\max}} |\tilde{C}_n|^2 \cdot n + \sum_{n=0}^{n_{\max}} |\tilde{C}_n|^2 \cdot (n+1)\right] \end{aligned} \tag{77}$$

$$\begin{aligned} \langle \hat{p}^2 \rangle \quad &= \quad -\frac{\hbar m\omega}{2}\left[\sum_{n=0}^{n_{\max}-2} \tilde{C}_n^* \tilde{C}_{n+2}\sqrt{(n+1)(n+2)} + \sum_{n=0}^{n_{\max}-2} \tilde{C}_{n+2}^* \tilde{C}_n \sqrt{(n+1)(n+2)} \right. \\ &\quad \left. - \sum_{n=0}^{n_{\max}} |\tilde{C}_n|^2 \cdot n - \sum_{n=0}^{n_{\max}} |\tilde{C}_n|^2 \cdot (n+1)\right] \end{aligned} \tag{78}$$

These expressions allow full analytical or numerical evaluation of quantum variances.
Finally, the uncertainties are computed as follows :

$$\Delta x \cdot \Delta p = \sqrt{\left[\frac{\hbar}{2m\omega}\left(\sum_{n=0}^{n_{\max}}(2n+1)\,|\tilde{C}_n|^2 + 2\sum_{n=0}^{n_{\max}-2}\mathrm{Re}\left(\tilde{C}_n^*\tilde{C}_{n+2}\right)\sqrt{(n+1)(n+2)}\right) - \langle\hat{x}\rangle^2\right]}$$
$$\times\sqrt{\left[\frac{\hbar m\omega}{2}\left(\sum_{n=0}^{n_{\max}}(2n+1)\,|\tilde{C}_n|^2 - 2\sum_{n=0}^{n_{\max}-2}\mathrm{Re}\left(\tilde{C}_n^*\tilde{C}_{n+2}\right)\sqrt{(n+1)(n+2)}\right) - \langle\hat{p}\rangle^2\right]} \tag{79}$$

By replacing by :

$$\begin{aligned} A\ &:= \sum_{n=0}^{n_{\max}}(2n+1)\,|\tilde{C}_n|^2, \qquad B := 2\sum_{n=0}^{n_{\max}-2}\Re\left(\tilde{C}_n^*\tilde{C}_{n+2}\right)\sqrt{(n+1)(n+2)}, \\ x_0\ &:= \langle\hat{x}\rangle, \qquad p_0 := \langle\hat{p}\rangle, \end{aligned} \tag{80}$$

we obtained for Equation (79) gives the following factored form :

$$\Delta x\,\Delta p = \sqrt{\frac{\hbar^2}{4}\left(A^2 - B^2\right) - \frac{\hbar}{2m\omega}(A+B)\,p_0^2 - \frac{\hbar m\omega}{2}(A-B)\,x_0^2 + x_0^2p_0^2}. \tag{81}$$

This equation (81) shows that the uncertainty product $\Delta x\,\Delta p$ reaches its minimal value $\hbar/2$ when the correlations $B$ and the occupations $A$ satisfy $A^2 - B^2 = 1$ and the mean values $x_0$ and $p_0$ disappear. This condition corresponds to standard coherent states that saturate the Heisenberg uncertainty inequality. Any deviation from these values, due to squeezing ($|B| < A$) or excess thermal population ($A > 1$), inevitably increases the uncertainty product.

## 5. CONCLUSION

In this work, we have constructed and analyzed squeezed coherent states within a supersymmetric framework for systems with position-dependent mass. Starting from the exact spectrum obtained via SUSYQM, we derived explicit expressions for the statistical properties, quadrature variances, and uncertainty products of these states. The generalized Heisenberg uncertainty relation was evaluated exactly, showing that the ground state saturates the minimum bound $\Delta x\,\Delta p = \hbar/2$, while the squeezed states can violate the standard vacuum limit in one quadrature. Our results show that the constructed states exhibit sub-Poissonian statistics, quadrature squeezing, and negative regions in the Wigner function, confirming their non-classical nature. The formalism developed here can be applied to model light–matter interactions in graded semiconductors [13, 14], quantum dots, and optoelectronic systems such as photonic crystals and cavity optomechanics for quantum communication or sensing [15, 16].

### Author Contributions

D.S.T. developed the theoretical framework and performed the analytical derivations. D.S.T. and B.A wrote the main manuscript text. D.S.T and A.Y.M. contributed to the mathematical validation of the model. A.Y.M. and G.Y.H.A. provided critical revisions, improved the presentation, and contributed to the interpretation of the results. All authors reviewed and approved the final manuscript.

### Acknowledgments

The authors would like to thank their respective institutions for providing the academic environment necessary for this research.

### ORCID

**Daniel Sabi Takou**, https://orcid.org/0009-0002-7603-8999; **Amidou Boukari**, https://orcid.org/0009-0001-6010-4763; **Assimiou Yarou Mora**, https://orcid.org/0009-0003-0097-8607; **Gabriel Y.H. Avossevou**, https://orcid.org/0000-0002-9609-0340

### REFERENCES

[1] D.F. Walls, ”Squeezed states of light,” Nature, **306**, 141–146 (1983) https://doi.org/10.1038/306141a0

[2] R. Loudon, and P.L. Knight, ”Squeezed light,” J. Mod. Opt. **34**, 709–759 (1987). https://doi.org/10.1080/09500348714550721

[3] M.C. Teich, and B.E.A. Saleh, ”Squeezed state of light,” Quantum Opt. J. Eur. Opt. Soc. Part B, **1**, 153 (1989). https://doi.org/10.1088/0954-8998/1/2/006

[4] E. Schrodinger, “Der stetige übergang von der Mikrozur Makromechanik,” Die Naturwissenschaften, **14**(28), 664-666 (1926). https://doi.org/10.1007/BF01507634

[5] E.H. Kennard, “The Uncertainty Relation for Joint Measurement of Position and Momentum,” Physikalische Zeitschrift, **44**(4-5), 326-352 (1927). https://doi.org/10.1007/BF01391200

[6] J.R. Klauder, ”The action option and a Feynman quantization of spinor fields in terms of ordinary c-numbers,” Ann. Phys. **11**, 123 (1960). https://doi.org/10.1016/0003-4916(60)90131-7

[7] J.R. Klauder, and B.S. Skagerstam, *Coherent States-Applications in Physics and Mathematical Physics*, (World Scientific, Singapore, 1985).

[8] M.M. Nieto, ”The Discovery of Squeezed States - In 1927,” arXiv: quant-ph/9708012, (1985). https://doi.org/10.48550/arXiv.quant-ph/9708012

[9] H. Vahlbruch, *et al.*, ”Quantum engineering of squeezed states for quantum communication and metrology,” New J. Phys. **9**, 371 (2007). https://doi.org/10.1088/1367-2630/9/10/371

[10] R. Schnabel, *et al.*, ”Quantum metrology for gravitational wave astronomy,” Nat. Commun. **1**, 121 (2010). https://doi.org/10.1038/ncomms1122

[11] P.M. Anisimov, *et al.*, ”Quantum metrology with two-mode squeezed vacuum: parity detection beats the Heisenberg limit,” Phys. Rev. Lett. **104**, 103602 (2010). https://doi.org/10.1103/PhysRevLett.104.103602

[12] J. Aasi, *et al.*, ”Enhanced sensitivity of the LIGO gravitational wave detector by using squeezed states of light,” Nat. Photonics, **7**, 613–619 (2013). https://doi.org/10.1038/nphoton.2013.177

[13] G. Bastard, *Wave Mechanics Applied to Semiconductor Heterostructures*, (Editions de Physique, Les Ulis, France, 1988).

[14] A. Peter, ”The effect of position dependent effective mass of hydrogenic impurities in parabolic GaAs/GaAlAs quantum dots,” Int. J. Mod. Phys. B, **23**, 5109 (2009). https://doi.org/10.1142/S0217979209053394

[15] J. Dajka, and J. Luczka, Binary Communication with Gazeau–Klauder Coherent States, Entropy, **22**, 201 (2020). https://doi.org/10.3390/e22020201

[16] K. Ullah, and H. Ullah, ”Enhanced optomechanically induced transparency and slow/fast light in a position-dependent mass optomechanics,” Eur. Phys. J. D, **74**, 197 (2020). https://doi.org/10.1140/epjd/e2020-10286-1

[17] A.S. Pereira, A.S.Lemos, and F.A. Brito, ”Squeezed coherent states for a free particle with time-varying mass,” Eur. Phys. J. Plus, **138**, 363 (2023). https://doi.org/10.48550/arXiv.2208.05588

[18] E. Munguia-Gonzalez, J.K. Sheldon Rego, and F. Making, ”Squeezed-coherent states concrete by determining their wavefunction,” arXiv:2104.11350 [quant-ph]. https://doi.org/10.48550/arXiv.2104.11350

[19] S. Dey, and A. Fring, ”Squeezed coherent states for noncommutative spaces with minimal length uncertainty relations”, Phys. Rev. D, **86**, 064038 (2012). https://doi.org/10.1103/PhysRevD.86.064038

[20] M. Angelova, A. Hertz, and V. Hussin, ”Squeezed coherent states and the one-dimensional Morse quantum system,” J. Phys. A: Math. Theor. **45** 244007 (2012). https://doi.org/10.48550/arXiv.1111.1974

[21] N. Alvarez, and V. Hussin, ”Generalized Coherent and Squeezed States Based on the $h(1) \oplus su(2)$ Algebra,” J. Math. Phys. **43** 2063-2085(2002). https://doi.org/10.48550/arXiv.math-ph/0503062

[22] L. Lawson, ”Position-dependent mass in strong quantum gravitational background fields,” J. Phys. A: Math. Theor. **55**, 105303 (2022). https://doi.org/10.1088/1751-8121/ac3787

[23] L. Lawson, ”Minimal and maximal lengths of quantum gravity from non-hermitian position-dependent noncommutativity,” Scientific Reports **12**, 20650 (2022). https://doi.org/10.1038/s41598-022-21098-3

[24] L. Lawson, K. Amouzouvi, K. Sodoga, and K. Beltako, ”Position-dependent mass from noncommutativity and its statistical descriptions,” IJGMP, **21**, 2450137 (2024). https://doi.org/10.1142/S0219887824501378

[25] L. Lawson, and P. Osei, ”Gazeau-Klauder coherent states in position-deformed Heisenberg algebra,” Journal of Physics Communications, **6**, 085016 (2022). https://doi.org/10.1088/2399-6528/ac8a8a

[26] G.B. da Costa, A.C.G. da Silva, and S.G. Ignacio, ”Supersymmetric quantum mechanics and coherent states for a deformed oscillator with position-dependent effective mass,” J. Math. Phys. **62**, 092101 (2021). https://doi.org/10.48550/arXiv.2106.08467

[27] R. Costa Filho, M. Almeida, G. Farias, and J. Andrade, ”Displacement operator for quantum systems with position-dependent mass,” Phys. Rev. A, **84**, 050102 (2011). https://doi.org/10.1103/PhysRevA.84.050102

[28] S.H. Dong, R. Lemus, and A. Frank, ”Ladder operators for the Morse potential,” Int. J. Quant. Chem. **86**, 433 (2002). https://doi.org/10.1002/qua.10038

[29] S-H. Dong, *Factorization Method in Quantum Mechanics, Fundamental theories in physics*, 150, (Springer, Dortrecht, The Netherlands, 2008).

[30] J. Gazeau, and J. Klauder, ”Coherent states for systems with discrete and continuous spectrum,” Phys. A: Math. Gen. **32**, 123 (1999). https://doi.org/10.1088/0305-4470/32/1/013

[31] J. Klauder, ”Continuous-Representation Theory. I. Postulates of Continuous-Representation Theory,” J. Math. Phys. **4**, 1055 (1963). https://doi.org/10.1063/1.1704034

[32] J. Klauder, ”Continuous-representation theory. II. Generalized relation between quantum and classical dynamics,” J. Math. Phys. **4**, 1058 (1963). https://doi.org/10.1063/1.1704035

[33] A. Perelomov, *Generalized Coherent States and Their Application*, 1st edition, (Springer-verlag, 1986). https://link.springer.com/book/10.1007/978-3-642-61629-7

[34] S. Dey, and A. Fring, "Squeezed coherent states for noncommutative spaces with minimal length uncertainty relations," Phys. Rev. D, **86**, 064038 (2012). https://doi.org/10.1103/PhysRevD.86.064038

[35] M. Angelova, A. Hertz, and V. Hussin, "Squeezed coherent states and the one-dimensional Morse quantum system," J. Phys. A: Math. Theor. **45**, 244007 (2012). https://doi.org/10.1088/1751-8113/45/24/244007

[36] S. Dey, and V. Hussin, "Entangled squeezed states in noncommutative spaces with minimal length uncertainty relations," Phys. Rev. D, **91**, 124017 (2015). https://doi.org/10.1103/PhysRevD.91.124017

[37] V. Roos, "Position-dependent effective masses in semiconductor theory," Phys. Rev. B, **27**, 7547 (1983). https://doi.org/10.1103/PhysRevB.31.2294

[38] D.S. Takou, A.Y. Mora, I. Nonkané, L.M. Lawson, and G.Y.H. Avossevou, "Gazeau-Klauder coherent states for a harmonic position-dependent mass," arXiv:2503.23043v2. https://doi.org/10.48550/arXiv.2503.23043

[39] T. Gora, and F. Williams, "Theory of Electronic States and Transport in Graded Mixed Semiconductors," Phys. Rev. **177**, 1179 (1969). https://doi.org/10.1103/PhysRev.177.1179

[40] D.J. BenDaniel, and C.B. Duke, "Space-Charge Effects on Electron Tunneling," Phys.Rev. **152**, 683 (1966). https://doi.org/10.1103/PhysRev.152.683

[41] Q. Zhu, and H. Kroemer, "Interface connection rules for effective-mass wave functions at an abrupt heterojunction between two different semiconductors," Phys. Rev. B, **27**, 3519 (1983). https://doi.org/10.1103/PhysRevB.27.3519

[42] T. Li, and J. Kuhn, "Band-offset ratio dependence on the effective-mass Hamiltonian based on a modified profile of the GaAs-$Al_xGal_{1-x}$As quantum well," Phys. Rev. B, **47**, 12760 (1993). https://doi.org/10.1103/PhysRevB.47.12760

[43] O. Mustafa, and S.H. Mazharimousavi, "Ordering Ambiguity Revisited via Position Dependent Mass Pseudo-Momentum Operators," International Journal of Theoretical Physics, **46**, 1786-1796 (2007). https://doi.org/10.1007/s10773-006-9311-0

[44] K. Nouicer, "Path integral for the harmonic oscillator in one dimension with nonzero minimum position uncertainty," Phys. Lett. A. **354**, 399 (2006). https://doi.org/10.1016/j.physleta.2006.02.001

[45] P. Roy, "Quantum statistical properties of Gazeau–Klaudercoherent state of the anharmonic oscillator," Optics Communications, **221**, 145–152 (2003). https://doi.org/10.1016/S0030-4018(03)01470-6

[46] I.S. Gradshteyn, and I. M. Ryzhik, *Table of Integrals, Series and Products*, (Acedemic Press); M. Abramowitz, and I. A. Stegun, "Handbook of Mathematical Functions, with Formulas, Graphs, and Mathematical Table," (Dover).

[47] J.A. Bergou, M. Hillery, and D. Yu, "Minimum uncertainty states for amplitude-squared squeezing: Hermite polynomial states," Phys. Rev. A, **43**, 515-520 (1991). https://doi.org/10.1103/physreva.43.515

[48] G. Breitenbach, S. Schiller, and J. Mlynek, "Measurement of the quantum states of squeezed light," Nature, **387**, 471 (1997). https://doi.org/10.1038/387471a0

[49] H-C. Fu, and R. Sasaki, "Hypergeometric states and their nonclassical properties," Phys. Rev. A, **53**, 3836-3844 (1996). https://doi.org/10.1063/1.531965

## СТИСНУТІ КОГЕРЕНТНІ СТАНИ В КВАНТОВІЙ МЕХАНІЦІ З ПОЗИЦІЙНО-ЗАЛЕЖНОЮ МАСОЮ

**Даніель Сабі Таку[1,2], Аміду Букарі[2], Асіміу Яру Мора[2], Габріель Ю. Х. Авосеву[2]**
[1]*Політехнічна школа Абомей-Калаві (EPAC-UAC), Університет Абомей-Калаві (UAC), Бенін*
[2]*Відділ досліджень у галузі теоретичної фізики (URPT), Інститут математики та фізичних наук (IMSP),*
*01 B.P. 613 Порто-Ново, Республіка Бенін*

У цій статті ми конструюємо та аналізуємо новий клас стиснутих когерентних станів у рамках квантових систем з масою, що залежить від положення (PDM). Використовуючи деформовану алгебраїчну структуру, ми узагальнюємо оператори створення та знищення для врахування просторово змінних профілів маси. Отримані стани демонструють некласичні особливості, такі як стиснення, когерентність та модифіковані співвідношення невизначеності, на які сильно впливають як параметри деформації, так і масова функція. Ми досліджуємо їхні фізичні властивості через очікувані значення, дисперсії та щільності ймовірності. Ця робота пропонує шлях до розширення теорії когерентних станів на складніші квантові системи з геометричним та алгебраїчним багатством.

**Ключові слова:** *стиснутий когерентний стан; суперсиметрія; квантова механіка; маса, що залежить від положення*

East European Journal of Physics. **4**. 75–86 (2025)
DOI: 10.26565/2312-4334-2025-4-07 ISSN 2312-4334

# QUANTUM-CORRECTED THERMODYNAMICS OF AdS-RINDLER BLACK HOLES

**Aram Bahroz Brzo**[1,2*], **Peshwaz Abdulkareem Abdoul**[3**], **Behnam Pourhassan**[4,5,6***]
[1] *Physics Department, College of Education, University of Sulaimani, Sulaimani 46001, Kurdistan Region, Iraq*
[2] *Research and Development Center, University of Sulaimani, Sulaimani 46001, Kurdistan Region, Iraq*
[3] *Physics Department, College of Science, Charmo University: Chamchamal, Sulaimani, Kurdistan Region, Iraq*
[4] *School of Physics, Damghan University, Damghan 3671645667, Iran*
[5] *Center for Theoretical Physics, Khazar University, 41 Mehseti Street, Baku, AZ1096, Azerbaijan*
[6] *Centre of Research Impact and Outcome, Chitkara University, Punjab, Rajpura, 140417, India*
[*] *Corresponding Author e-mail: aram.brzo@univsul.edu.iq*
[**] *peshwaz.abdoul@chu.edu.iq*; [***] *b.pourhassan@du.ac.ir*

Received September 2, 2025; revised October 29, 2025; accepted November 5, 2025

We investigate the thermodynamic properties and stability of hyperbolic (AdS–Rindler) black holes, emphasizing the effects of non perturbative quantum correction. Using standard thermodynamic formulations alongside the Poincaré disk method, we compute key quantities including mass, Hawking temperature, entropy, and heat capacity. To account for quantum gravitational effects, we introduce an exponential correction to the Bekenstein–Hawking entropy and systematically derive the modified thermodynamic parameters. While the corrected entropy yields consistent adjustments, the heat capacity exhibits nontrivial behavior, leading to narrower and more gradual stable regions $\left(\Delta r_{(d)}\right)$ for each dimension $d$. Moreover, the smoothing of sharp entropy variations near $r_h = 1$ emphasizes how horizon geometry governs the impact of quantum corrections. This study provides the novel systematic identification of stable regions before and after exponential corrections of (AdS–Rindler) black holes, offering new insights into the interplay of geometry, dimensionality, and quantum effects in black hole thermodynamics.

**Keywords:** *Hyperbolic black holes; Quantum entropy correction; Stability analysis*

**PACS:** 04.60.-m, 04.70.Dy, 04.70.-s, 04.20.-q

## 1. INTRODUCTION

The study of black hole (BH) thermodynamics has been a cornerstone in understanding the intricate relationship between gravity, quantum mechanics, and statistical physics. Central to this field is the exploration of how black holes (BHs), as thermodynamic systems, adhere to laws analogous to the classical laws of thermodynamics. The seminal works of Bekenstein and Hawking established that BHs possess an entropy proportional to their horizon area [1, 2]. The formulation of BH mechanics as analogous to the laws of thermodynamics was first systematically established by Bardeen, Carter, and Hawking [3], who demonstrated that the surface gravity of a BH remains constant over the horizon, analogous to temperature in conventional thermodynamic systems. This foundational framework later faced challenges with the information paradox, which found a potential resolution pathway in Page's work [4], suggesting that information might be preserved in BH evaporation through subtle correlations in the radiation, with information beginning to emerge after approximately half the entropy has been radiated away—a concept now known as the 'Page curve.' A complementary breakthrough came from string theory when Strominger and Vafa [5] provided the first precise microstate counting for certain supersymmetric BHs, demonstrating that the Bekenstein-Hawking entropy formula could be derived from first principles by counting the degeneracy of D-brane configurations, thus establishing a crucial link between gravity and quantum theory that continues to influence the development of quantum corrections to BH thermodynamics. These discoveries have spurred extensive research into the microscopic origins of BH entropy and the potential quantum corrections that arise in various gravitational settings. In particular, the Anti-de Sitter (AdS) spacetime has garnered significant attention due to its role in the AdS/CFT correspondence, which posits a duality between a gravitational theory in AdS space and a conformal field theory on its boundary. Within this framework, Rindler-AdS spacetime emerge as a fascinating subclass, characterized by their hyperbolic horizons and constant acceleration analogous to Rindler coordinates in flat spacetime. These spacetime provide fertile ground for investigating the thermodynamic properties of BHs, especially when considering the implications of quantum corrections to classical entropy formulations [6, 7]. The importance of AdS black holes has been widely recognized, leading to extensive research in various directions. For instance, the reconciliation of the Weak Gravity Conjecture (WGC) and the Weak Cosmic Censorship Conjecture (WCCC) by examining Einstein-Euler-Heisenberg-AdS BHs in four-dimensional spacetime has been investigated in [8] by applying certain conditions to the metric parameters, they show that the (WGC) and the (WCCC) can be simultaneously satisfied. Furthermore, the investigation of the thermodynamic topology of AdS Einstein–power–Yang–Mills BHs using both bulk-boundary and restricted phase space (RPS) approaches, considering different non-extensive entropy models, has been studied [9]. Also,

---

***Cite as:*** A.B. Brzo, P.A. Abdoul, B. Pourhassan, East Eur. J. Phys. 4, 75 (2025), https://doi.org/10.26565/2312-4334-2025-4-07

the thermodynamic topology of Schwarzschild-AdS BHs under the frameworks of non-commutative geometry and Barrow entropy, providing an overview of the black hole's properties and the relevance of Barrow entropy studied in [10].

The Bekenstein-Hawking entropy formula, which equates the entropy of a BH to a quarter of its horizon area, serves as the classical foundation for BH thermodynamics. However, various approaches in quantum gravity suggest that this entropy receives corrections, often manifesting as logarithmic terms including thermal fluctuations [11], higher-order entropy corrections [12], non-perturbative exponential corrections [13]. These corrections are pivotal in understanding the microstates contributing to BH entropy and have profound implications for the stability and phase structure of BHs [1, 2].

Recently the thermodynamic properties of AdS–Schwarzschild-type BHs through the framework of loop quantum gravity has been tested, showing that quantum corrections play a crucial role in reshaping their critical behavior and phase transition characteristics [14, 15, 16]. These corrections modify key aspects such as the equation of state, critical points, and heat capacity, ultimately affecting the stability conditions of BHs. Such insights highlight the importance of accounting for quantum effects to achieve a deeper and more complete understanding of black-hole thermodynamics [17, 18, 19].

In the realm of Rindler-AdS spacetimes, the entanglement entropy of holographic quantum fields has been the subject of extensive investigation. Emparan and Magán [20] demonstrated how quantum disentanglement modifies the entanglement structure of holographic quantum fields in Rindler–AdS geometry, while in [21] extending the Rindler method to compute timelike entanglement entropy in $\mathrm{AdS}_3/\mathrm{CFT}_2$ has been studied. Further developments in [22, 23] analyzed generalized Rindler wedges and inner-horizon entanglement, respectively, highlighting the geometric richness of these setups. Complementarily, Miao [24] investigated the Casimir and holographic dual aspects of AdS wedges, providing deeper insight into quantum correlations across Rindler horizons.

Interestingly, holographic analyses indicate that the entanglement entropy remains finite even in the zero-temperature limit, creating a puzzling scenario that has motivated extensive investigations into the quantum properties of Rindler–AdS BHs [20, 21, 22, 23].

In recent years, the study of quantum corrections to BH thermodynamics has gained significant attention [25, 26, 27, 28, 29], as these corrections might provide insight into the quantum nature of gravity and potentially resolve longstanding paradoxes such as the information loss problem [30]. Prior attempts to consider corrections to the BH entropy are due to the thermal fluctuations which at leading order add an alogarithmic term to the BH entropy [31, 32, 33, 34, 35, 36]. Higher-order entropy corrections represent another important approach to quantum BH thermodynamics. Upadhyay et al. [12] studied the P-V criticality of AdS BHs corrected for first-order entropy in massive gravity, finding that entropy corrections can substantially alter phase transition behavior. The application of quantum gravity approaches to BH thermodynamics represents the frontier of this field. Pourhassan et al. [37] investigated quantum gravitational corrections to the geometry of charged AdS BHs, while Lone et al. [38] applied topos theory to derive quantum gravitational corrections to a Kerr BH. These studies suggest that a full quantum theory of gravity might resolve longstanding issues in BH thermodynamics, including the information loss paradox. The classical Bekenstein-Hawking entropy formula $(\overset{(C)}{S}_{BH})$ is given by:

$$\overset{(C)}{S}_{BH} = \frac{k_B A}{4\pi\hbar G}, \tag{1}$$

where $A$ is the area of the horizon given by:

$$A = n\epsilon\, l_p^2 \tag{2}$$

where $\epsilon$ is constant and $n$ is the quantum number. In addition, the surface gravity $\kappa$ is computed as:

$$\kappa = \frac{1}{2}\left.\frac{df}{dr}\right|_{r=r_h} \tag{3}$$

where $f(r)$ is the blackening factor. It is important to note that the expression for surface gravity presented in Eq. (3) is applicable only to static black hole configurations, such as the Schwarzschild and Reissner–Nordström solutions, and fails to describe rotating (Kerr) geometries (see [3, 39, 40]). Furthermore, the temperature $(T)$ of a BH is related to its surface gravity $(\kappa)$ by the formula:

$$T_H = \frac{\hbar\kappa}{2\pi}, \tag{4}$$

where, $\hbar$ is the reduced Planck constant. This relation arises from the Hawking temperature formula, which states that the temperature of a BH is proportional to its surface gravity. This result is fundamental in BH thermodynamics and is derived from quantum field theory in curved spacetime.

Quantum gravitational effects are expected to introduce corrections to this entropy. Various approaches, including string theory and loop quantum gravity, suggest modifications that often take the form of logarithmic or exponential terms.

For example, Calmet and Kuipers [41] calculated quantum gravitational corrections to the entropy of a Schwarzschild BH using the Wald entropy formula within an effective field theory approach.

BH entropy is generally expressed in the following form [42]:

$$S = \frac{A}{4\ell_P^2} + \alpha \ln \frac{A}{4\ell_P^2} + \beta \frac{4\ell_P^2}{A} + \cdots + \exp\left(-\delta \frac{A}{4\ell_P^2}\right) + \cdots \tag{5}$$

where the constants $(\alpha, \beta, \delta, \eta)$, and similar terms, are universal. For black holes with small horizon areas of order $(O(l_p^2))$, a complete quantum gravity framework is required for a proper description. In such cases, the logarithmic and higher-order correction terms involving $((l_p^2/A))$ may be modified or even absent. Pourhassan et al. [13] applied non-perturbative quantum corrections to a Born-Infeld BH and analyzed its information geometry, revealing new aspects of BH microstructure. More recently, Pourhassan et al. [43] investigated non-perturbative corrections to BH geometry, showing how quantum effects fundamentally alter spacetime structure near BH horizons. The study of quantum corrections in various BH backgrounds has also extended to higher-dimensional and exotic BH solutions. Han et al. [44] examined the the impact of fluctuations on AdS BHs in arbitrary dimensions, deriving how horizon perturbations change Hawking temperature and Bekenstein–Hawking entropy and discussing resulting thermodynamic consequences. While Pourhassan et al. [45] investigated the quantum thermodynamics of an M2-M5 brane system. These studies highlight the universal nature of quantum corrections in different theories and dimensions of gravitation. Recent work has also connected quantum-corrected BH thermodynamics to holographic concepts such as the AdS/CFT correspondence. Kumar et al. [46] studied the stabilizing effects of higher-order quantum corrections on charged BTZ BH thermodynamics, demonstrating how quantum corrections affect the stability of BHs in AdS space. Moreover, Pourhassan et al. [47] examined thermal fluctuation effects on the shear viscosity to entropy ratio in five-dimensional Kerr-Newman BHs, providing important connections to hydrodynamic properties of dual field theories.

In the context of Rindler-AdS hyperbolic BHs, understanding these quantum corrections is crucial, as they can significantly influence the thermodynamic stability and phase structure of the system. Studies have shown that such corrections can alter the heat capacity and, consequently, the stability criteria of BHs [48].

Recent studies continue to explore quantum gravity's impact on BH thermodynamics, from shadow imprints and singularity resolution in regular BHs [15, 49] to phase transitions in hyperscaling-violating spacetimes [50]. Investigations into AdS BHs further show how corrections from the generalized uncertainty principle alter their evaporation and stability [51], with thermodynamic geometry providing key insights into the resulting phase structures [52]. Our work builds upon this foundation by applying an exponential entropy correction to the distinctive AdS-Rindler geometry, revealing its unique stability signatures.

This article is organized as follows. Section 2 presents the theoretical model, establishing the foundational framework for our analysis of AdS-Rindler BHs. Section 3 explores the mathematical aspects of computing the area of AdS-Rindler BHs. In Sec. 4, we develop the thermodynamic framework before adding quantum correction, introducing key concepts and methodologies for analyzing BH thermodynamics from a thermal point of view. Section 5 provides a detailed analysis non-perturbative quantum corrections of entropy and other thermodynamic function model. Section 6 explores the comparison between the thermodynamics before and after adding quantum corrections. Finally, section 7 summarizes our findings and discusses their implications, along with future research directions in this field.

## 2. GENERAL FORM OF HYPERBOLIC BLACK HOLES

The action for a hyperbolic BH in the Rindler-AdS spacetime is typically derived from the Einstein-Hilbert action with a negative cosmological constant. The general form of the action in $(d+1)-$dimensional space-time is given by:

$$S = \frac{1}{16\pi G} \int d^{d+1}x\sqrt{-g}\,(R - 2\Lambda) \tag{6}$$

where, $R$ is the Ricci scalar, and $\Lambda = -\frac{d(d-1)}{2l^2}$ is the cosmological constant for AdS spacetime with curvature scale $l$. Unlike their spherical counterparts, these BHs exhibit distinct thermodynamic behaviors because of their horizon geometry. The variation of this action with respect to the metric $g_{\mu\nu}$ gives Einstein's field equations:

$$G_{\mu\nu} = R_{\mu\nu} - \frac{1}{2} g_{\mu\nu} R + g_{\mu\nu}\Lambda = 0. \tag{7}$$

Taking the trace by contracting with $g^{\mu\nu}$, leads to:

$$R = -\frac{d(d+1)}{l^2}, \tag{8}$$

Substituting this into Eq.(7), we obtain the Einstein tensor $(G_{\mu\nu})$ as the following.

$$G_{\mu\nu} = R_{\mu\nu} + \left(\frac{d}{\ell^2}\right) g_{\mu\nu} = 0. \tag{9}$$

This describes an AdS spacetime with constant curvature. The general form of the metric for a $(d+1)$-dimensional hyperbolic BH can be expressed as:

$$ds^2 = -f(r)dt^2 + \frac{dr^2}{f(r)} + r^2 dH^2_{d+1}, \tag{10}$$

where $dH^2_{d+1}$ denotes the unit metric of the hyperbolic static BH in $d+1$ dimensional space [48]. Although the metric considered here, Eq. (10), does not explicitly use Rindler coordinates, it corresponds to the hyperbolic patch of anti–de Sitter (AdS) spacetime that is locally equivalent to the Rindler wedge of AdS under an appropriate coordinate transformation (see Refs. [48, 53]). Hence, following common usage in the literature, we refer to this background as a Rindler–AdS spacetime. This designation emphasizes the constant–acceleration interpretation of observers in the hyperbolic AdS region and justifies the thermodynamic analysis in analogy with Rindler horizons. Or, in the matrix form the metric tensor $g_{\mu\nu}$ is a $(d+1)\times(d+1)$ symmetric matrix:

$$g_{\mu\nu} = \begin{bmatrix} -f(r) & 0 & 0 & 0 & \cdots & 0 \\ 0 & \frac{1}{f(r)} & 0 & 0 & \cdots & 0 \\ 0 & 0 & r^2 & 0 & \cdots & 0 \\ 0 & 0 & 0 & r^2\sinh^2\chi & \cdots & 0 \\ \vdots & \vdots & \vdots & \vdots & \ddots & \vdots \\ 0 & 0 & 0 & 0 & \cdots & r^2\sinh^2\chi\cdots\sinh^2\theta_{d-3} \end{bmatrix}. \tag{11}$$

The Ricci tensor components presented in Eq. (9) can be calculated as:

$$R_{\mu\nu} = \partial_\alpha \Gamma^\alpha_{\mu\nu} - \partial_\nu \Gamma^\alpha_{\mu\alpha} + \Gamma^\alpha_{\alpha\beta}\Gamma^\beta_{\mu\nu} - \Gamma^\alpha_{\nu\beta}\Gamma^\beta_{\mu\alpha} \tag{12}$$

where $\Gamma^\alpha_{\mu\nu}$ is the Christoffel symbols, can be found:

$$\Gamma^\mu_{\nu\alpha} = \frac{1}{2} g^{\mu\beta}\Big( \partial_\nu(g_{\alpha\beta}) + \partial_\alpha(g_{\nu\beta}) - \partial_\beta(g_{\nu\alpha}) \Big) \tag{13}$$

Substituting Eq. (11) and Eq. (12) into Eq. (7) the blackening factor $(f(r))$ can be found as:

$$f(r) = \frac{r^2}{\ell^2} - 1 - \frac{M}{r^{d-2}}, \tag{14}$$

The event horizon is located at $r = r_h$, where $f(r_0) = 0$ and $M$ is the mass of the BH. Then solving $(f(r_h) = 0)$ yields the following:

$$M = r_h^{d-2}\left(\frac{r_h^2}{\ell^2} - 1\right). \tag{15}$$

Thus, substitution of Eq. (15) Eq. (14) reduces to,

$$f(r) = \frac{r^2}{\ell^2} - 1 - \frac{r_h^{d-2}}{r^{d-2}}\left(\frac{r_h^2}{\ell^2} - 1\right). \tag{16}$$

This metric function is the key factor for calculating surface gravity, Hawking temperature, and other thermodynamic parameters, as we will see in the upcoming sections.

## 3. AREA OF HYPERBOLIC SPACE

To find the area of a hyperbolic space, we consider the metric of hyperbolic space $H_{d-1}$ and compute the surface integral over a given region. The hyperbolic space $(H_{d-1})$ can be represented using the Poincaré disk model, where the metric in polar coordinates is given by:

$$ds^2 = \frac{dr^2 + r^2 d\Omega^2_{d-2}}{(1-r^2)^2} \tag{17}$$

where $(r)$ is the radial coordinate on the Poincaré disk $(0 \le r < 1)$ and $(d\Omega^2_{d-2})$ is the metric on the unit $(d-2)$−dimensional sphere. The area element in $H_{d-1}$ (with the dimension of length $l$ normalized to unity) is given by [53]:

$$dA = \frac{r^{d-2}\, dr\, d\Omega_{d-2}}{(1-r^2)^{d-1}} \tag{18}$$

where $\frac{r^{d-2}}{(1-\frac{r^2}{l^2})^{d-1}} = \sqrt{g}$ is the metric determinant. The total area of a hyperbolic space up to a radius $(r_h)$ is calculated as (for simplicity we assume $l = 1$):

$$\begin{aligned} A(r_h) &= \int_0^{r_h} \int_{\Omega_{d-2}} \frac{r^{d-2}\, dr\, d\Omega_{d-2}}{(1-r^2)^{d-1}} \\ &= \frac{2\pi^{(d-1)/2}}{\Gamma((d-1)/2)} \int_0^{r_h} \frac{r^{d-2}\, dr}{(1-r^2)^{d-1}} \end{aligned} \tag{19}$$

Since the factor $(\Omega_{d-2} = \frac{2\pi^{(d-1)/2}}{\Gamma((d-1)/2)})$ is the total solid angle for a unit $(d-2)-$sphere. Making the substitution $(x = r^2,\ dx = 2rdr)$, Eq.(19) reduces to:

$$A(r_h) = \frac{2\pi^{(d-1)/2}}{\Gamma((d-1)/2)} \int_0^{r_h^2} \frac{1}{2} x^{(d-3)/2} (1-x)^{-(d-1)}\, dx \tag{20}$$

Thus, the total area of hyperbolic space obtained as [54]:

$$A(r_h) = \frac{2\pi^{(d-1)/2}}{\Gamma\left(\frac{d-1}{2}\right)} \cdot \frac{r_h^{d-1}}{d-1}\ {}_2F_1\left(\frac{d-1}{2},\ d-1;\ \frac{d+1}{2};\ r_h^2\right) \tag{21}$$

where, ${}_2F_1\left(\frac{d-1}{2},\ d-1;\ \frac{d+1}{2};\ r_h^2\right)$ is the Gauss hypergeometric function. Thus, Eq.(21) gives the area enclosed within the radius $r_h$ in the hyperbolic space.

## 4. THERMODYNAMICS OF ADS-RINDLER BHS

In this section, we derive the fundamental thermodynamic properties of BHs using established formalisms in BH thermodynamics. We begin by computing the temperature and entropy, followed by the heat capacity, which plays a key role in determining the stability of the BH. The upcoming calculations provide a comprehensive understanding of the black hole's thermodynamic structure and its response to quantum corrections or modifications in the entropy function. Substituting the area presented in Eq. (21) into Eq. (1) (assuming $k_B = \hbar = G = 1$) we obtain the following.

$$\overset{(C)}{S} = B(d)\ r_h^{d-1}\ {}_2F_1\left(\frac{d-1}{2},\ d-1;\ \frac{d+1}{2};\ r_h^2\right), \tag{22}$$

where,

$$B(d) = \frac{\pi^{(d-1)/2}}{2(d-1)\,\Gamma\left(\frac{d-1}{2}\right)}$$

Similarly, substituting Eq. (16) into Eq. (3) leads to the following ($\ell = 1$):

$$\kappa = \frac{d}{2}\left[r_h - \frac{1}{r_h} + \frac{2}{d\ r_h}\right] \tag{23}$$

Thus, Hawking temperature can easily be found from Eq. (23) and Eq. (4) as:

$$T = \frac{d}{4\pi}\left[r_h - \frac{1}{r_h} + \frac{2}{d\ r_h}\right] \tag{24}$$

where $r_h$ denotes the black hole's horizon's radius. Furthermore, the heat capacity of the BH is an essential thermodynamic quantity that determines its stability. From the first law of BH thermodynamics, it is found to have following relation [55, 56]:

$$\begin{aligned} C &= \frac{\partial M}{\partial T} \\ &= \left(\frac{\partial M}{\partial r_h}\right) \bigg/ \left(\frac{\partial T}{\partial r_h}\right), \end{aligned} \tag{25}$$

Using Eq.(15) and Eq.(24), the partial derivatives of mass and Hawking temperature with respect to the horizon radius $r_h$ are expressed by

$$\frac{\partial M}{\partial r_h} = r_h^{d-3}\left[d\ r_h^2 - (d-2)\right], \tag{26}$$

and

$$\frac{\partial T}{\partial r_h} = \frac{1}{4\pi}\left[d + \frac{d-2}{r_h^2}\right], \tag{27}$$

respectively. Finally, by substituting (26) and (27) into (25), the uncorrected (or classical) heat capacity is given by:

$$\overset{(C)}{C} = 4\pi\left[\frac{d\,r_h^2 - (d-2)}{d\,r_h^2 + (d-2)}\right] r_h^{d-1}, \tag{28}$$

The pressure associated with the BH can be expressed as [55]:

$$P = \frac{1}{2} T S. \tag{29}$$

This relation establishes a direct connection between the temperature, entropy, and thermodynamic pressure of the BH. Thus, putting (22) and (24) into (29) the pressure of the AdS-Rindler black hole obtained as,

$$\overset{(C)}{P} = \frac{B(d)}{8\,\pi^{(1/2)}}\, r_h^{d-2}\left(d r_h^2 - d + 2\right) {}_2F_1\left(\frac{d-1}{2},\, d-1;\, \frac{d+1}{2};\, r_h^2\right). \tag{30}$$

where we have used the derivatives of the the hypergeometric function formula:

$$\frac{d}{dz}\,{}_2F_1\,(a,\, b;\, c;\, z) = \frac{ab}{c}\,{}_2F_1\,(a+1,\, b+1;\, c+1;\, z)$$

The thermodynamic volume, which is conjugate to the pressure, is obtained using the following definition [13].

$$\begin{aligned} V &= \frac{\partial M}{\partial P} \\ &= \left(\frac{\partial M}{\partial r_h}\right) \Big/ \left(\frac{\partial P}{\partial r_h}\right). \end{aligned} \tag{31}$$

This expression describes how the mass $M$ of the BH varies with respect to pressure, providing insight into its extended phase-space thermodynamics. In so doing, applying Eq. (31) to Eqs. (15) and (30) the BH volume can be calculated as:

$$\overset{(C)}{V} = \frac{8\,\pi^{(1/2)}}{B(d)} \cdot \frac{d\,r_h^2 - (d-2)}{\left(d^2\, r_h^2 - (d-2)^2\right) {}_2F_1\left(\frac{d-1}{2},\, d-1;\, \frac{d+1}{2};\, r_h^2\right) + \frac{2(d-1)^2}{d+1} r_h^2 (d\, r_h^2 - d + 2) {}_2F_1\left(\frac{d+1}{2},\, d;\, \frac{d+3}{2};\, r_h^2\right)} \tag{32}$$

Finally, the Gibbs free energy, which characterizes the thermodynamic stability and phase behavior of the BH, is given by [13]:

$$G = M - TS. \tag{33}$$

This quantity plays a crucial role in understanding phase transitions and critical phenomena in BH thermodynamics. Doing so, substitution of Eqs.(15), (22) and (24) into Eq.(33) leads to find the Gibbs free energy as:

$$\overset{(C)}{G} = r_h^{d-2}\left[r_h^2 - 1 - \frac{B(d)}{4\,\pi^{(1/2)}}\left(d\, r_h^2 - d + 2\right) {}_2F_1\left(\frac{d-1}{2},\, d-1;\, \frac{d+1}{2};\, r_h^2\right)\right] \tag{34}$$

Ultimately, we can say these functions provide the complete semiclassical thermodynamic description of AdS-Rindler hyperbolic BHs.

## 5. THERMODYNAMICS OF ADS-RINDLER BHS WITH QUANTUM CORRECTION

In this section, we systematically incorporate quantum gravitational effects into our thermodynamic analysis of hyperbolic BHs. Following the approach outlined in section (1), we employ an exponential correction term to the Bekenstein-Hawking entropy, which captures non-perturbative quantum effects near the Planck scale. This correction provides a more complete description of BH microstate structure when quantum gravitational fluctuations become significant. We begin by modifying the classical entropy with an exponential correction term,

$$\overset{(Q)}{S} = \overset{(C)}{S} + \eta\, e^{-\delta \overset{(C)}{S}}$$

$$\begin{aligned}
&= B(d)\, r_h^{d-1}\, {}_2F_1\left(\frac{d-1}{2},\, d-1;\, \frac{d+1}{2};\, r_h^2\right) \\
&+ \eta\ \exp\left[-\delta\, B(d)\, r_h^{d-1}\, {}_2F_1\left(\frac{d-1}{2},\, d-1;\, \frac{d+1}{2};\, r_h^2\right)\right], \qquad (35)
\end{aligned}$$

where $\delta$ is the quantum correction parameter that controls the strength of quantum gravitational effects. This parameter has dimensions of area and is expected to be on the order of the Planck area. In the limit $\delta \rightarrow 0$, we recover the classical entropy formula, and as $\delta$ increases, quantum effects become more pronounced.

With the corrected entropy in hand, we now derive the corresponding modifications to the other thermodynamic quantities. The non perturbative quantum corrected temperature can be found from the first law of BH thermodynamics ($dM = T\, dS$) using Eq,(15) and (35) as:

$$\begin{aligned}
\overset{(Q)}{T} &= \frac{\partial M}{\partial S} \\
&= \left(\frac{\partial M}{\partial r_h}\right) \Big/ \left(\frac{\partial S}{\partial r_h}\right) \\
&= \frac{d\, r_h^2 - (d-2)}{(d-1)\, B(d)\, r_h \left[(d-1)W_1 + \frac{2(d-1)^2}{d+1} r_h^2\, W_2\right] \left[1 - \eta\, \delta\, e^{-\delta\, B(d)\, r_h^{d-1} W_1}\right]} \qquad (36)
\end{aligned}$$

where,

$$W_1 = {}_2F_1\left(\frac{d-1}{2},\, d-1;\, \frac{d+1}{2};\, r_h^2\right), \qquad (37)$$

$$W_2 = {}_2F_1\left(\frac{d+1}{2},\, d;\, \frac{d+3}{2};\, r_h^2\right). \qquad (38)$$

Significant changes appear in the non-perturbative quantum corrected heat capacity $\overset{(Q)}{C}$, which is defined through the mass-temperature variation. The expression is derived using Eq. (25) for heat capacity, Eq. (26) for the mass derivative, and Eq. (36) for the quantum temperature derivative:

$$\begin{aligned}
\overset{(Q)}{C} &= \left(\frac{\partial M}{\partial r_h}\right) \Bigg/ \left(\frac{\partial \overset{(Q)}{T}}{\partial r_h}\right) \\
&= \frac{r_h^{d-1}(d-1)^2[B(d)]^2[D_1(r_h)]^2[D_2(r_h)]^2\left[dr_h^2 - (d-2)\right]}{2d(d-1)B(d)r_h^2 D_1(r_h)D_2(r_h) - \left[dr_h^2 - (d-2)\right] D_3} \qquad (39)
\end{aligned}$$

where,

$$\begin{aligned}
D_1(r_h) &= (d-1)W_1 + \frac{2(d-1)^2}{d+1} r_h^2 W_2 \\
D_2(r_h) &= 1 - \eta\ \delta\ e^{-\delta B(d) r_h^{d-1} W_1} \\
D_3(r_h) &= (d-1)B(d)\left[D_1(r_h)D_2(r_h) + r_h D_1'(r_h)D_2(r_h) + r_h D_1(r_h)D_2'(r_h)\right] \\
D_1'(r_h) &= 2(d-1)^2 r_h W_2 + \frac{4d(d-1)^2}{d+3} r_h^3 W_3 \\
D_2'(r_h) &= \eta\delta^2 B(d)\, e^{-\delta\, B(d)\, r_h^{d-1} W_1}\left[(d-1)r_h^{d-2}W_1 + \frac{2(d-1)^2}{d+1} r_h^d W_2\right] \\
W_3 &= {}_2F_1\left(\frac{d+3}{2},\, d+1;\, \frac{d+5}{2};\, r_h^2\right).
\end{aligned}$$

The quantum-corrected pressure is calculated by applying Eq.(29) to the modified entropy Eq.(35) and modified temperature Eq.(36). Thus, we obtain:

$$\overset{(Q)}{P} = \frac{\left[dr_h^2 - (d-2)\right]\left[B(d)\, r_h^{d-1} W_1 + \eta\, e^{-\delta\, B(d) r_h^{d-1} W_1}\right]}{2(d-1)B(d)\, r_h \left[(d-1)W_1 + \frac{2(d-1)^2}{d+1} r_h^2 W_2\right]\left[1 - \eta\, \delta\, e^{-\delta\, B(d)\, r_h^{d-1} W_1}\right]}. \qquad (40)$$

The corrected thermodynamic volume $\overset{(Q)}{V}$, can be calculated from Eq.(31) as:

$$\overset{(Q)}{V} = \frac{\partial M}{\partial \overset{(Q)}{P}} \tag{41}$$

where the numerator of the above equation are presented in Eq.(26). While, one can find $\frac{\partial \overset{(Q)}{P}}{\partial r_h}$ in the denominator from Eq.(40). This yield extremely lengthy expressions due to the complexity of the quantum-corrected pressure function Eq.(40), which involve products of hypergeometric functions and exponential correction terms. For this reason, the fully expanded form is not written here, which would span multiple lines and obscure the physical interpretation. Finally, the corrected Gibbs free energy can be calculated as,

$$\overset{(Q)}{G} = r_h^{d-2}\left(\frac{r_h^2}{\ell^2} - 1\right) - \frac{\left[d\, r_h^2 - (d-2)\right]\left[B(d)\, r_h^{d-1} W_1 + \eta\, e^{-\delta\, B(d)\, r_h^{d-1} W_1}\right]}{(d-1)^2 r_h W_1 + \frac{2(d-1)^3}{d+1} r_h^3\, W_2 - \eta\,\delta\left((d-1)^2 r_h W_1 + \frac{2(d-1)^3}{d+1} r_h^3 W_2\right) e^{-\delta\, B(d)\, r_h^{d-1} W_1}}. \tag{42}$$

These quantum-corrected formulations yield several key physical insights. The exponential correction term introduces a regularization effect that becomes significant as $r_h$ gets small, smoothing out the divergent behavior observed in the classical case. Unlike logarithmic corrections that dominate at large horizon areas, our exponential correction becomes most relevant at intermediate scales, particularly in the small scale. The quantum corrections preserve the overall thermodynamic structure, particularly affecting the stability conditions indicated by the heat capacity.

In the following section, we will analyze these results graphically to better visualize the impact of quantum corrections on the thermodynamic landscape of hyperbolic BHs.

## 6. RESULTS AND DISCUSSION

This section conducts a stability analysis in hyperbolic BH solutions. The impacts of quantum corrections on thermodynamic properties are visualized through graphical representations. First, the heat capacity in Eq.(28) serves as a key indicator of stability, with sign changes corresponding to transitions between stable and unstable regimes. As shown in Figs. (1) and (2), the heat capacity exhibits a singularity at $r_h = 1$, which indicates a critical point in the thermodynamic behavior of the BH. In addition, according to Eq. (25), a divergence in the uncorrected (or classical) heat capacity occurs when the temperature reaches an extremum ($\partial T/\partial r_h = 0$). Thermodynamic stability changes whenever the heat capacity changes sign—occurring at $T = 0$ or $\partial M/\partial r_h = 0$. A positive heat capacity corresponds to stability, while a negative value indicates instability. Thus, analysing zeros and singularities in the heat capacity is essential for determining BH stability and identifying phase transitions. From Eq.(27), assuming $(\partial T/\partial r_h) = 0$, we shall determine the range of $d$ values for which the temperature profiles exhibit extremal points (heat capacity diverges). Thus, we obtain:

$$r_h = r_\infty^{\pm}(d) = \pm\sqrt{\frac{2-d}{d}} \tag{43}$$

The negative solution is physically unacceptable. Moreover, in BH thermodynamics, only dimensions with $d \geq 2$ are admissible. Considering this, the preceding equation reveals that the only real solution occurs at $d = 2$, giving $r_h = r_\infty^{+}(d = 2) = 0$. Substituting $d = 2$ into Eq. (28) yields $\overset{(C)}{C} = 4\pi r_h$, showing that the heat capacity remains finite for all non-negative values of $r_h$ and never diverges. Therefore, the obtained result $r_h = r_\infty^{+}(d = 2) = 0$ should be regarded as an apparent solution. On the other hand, a change in the sign of the heat capacity indicates a transition between stable and unstable BH states, with the transition occurring at points where the heat capacity reaches zero. From Eq.(26), assuming $C = 0$ (corresponding to $T_h = 0$ or $\partial M/\partial r_h = 0$), the solution becomes:

$$r_h = r_0^{\pm}(d) = \pm\sqrt{\frac{d-2}{d}}. \tag{44}$$

Ignoring the nonphysical negative root, we see that for $d \geq 2$, the regions of instability and stability correspond to $r_h < r_0^{+}(d)$ and $r_h > r_0^{+}(d)$, respectively. Specifically, for $d = 2, 3, 4, 5$ we have $r_0^{+}(d) = 0, 1/\sqrt{3} = 0.577350, 1/\sqrt{2} = 0.707107, \sqrt{3/5} = 0.774597$ (indicated by stars in Fig. (2) (panel (a)). Moreover, Fig. (1) presents both classical entropy (panel (a)) and quantum-corrected entropy (panel (b)) as a function of the horizon radius $r_h$. As can be seen, there is a sharp broadening around $r_h$ =1, which suggests a rapid entropy change near the critical horizon radius. This could be an indicator of a phase transition or a region in which the thermodynamic behavior of the BH changes drastically. After adding quantum correction, the most notable effect is that the sharp broadening around $r_h = 1$ is smoothed out, leading to a more gradual change in entropy, especially as the negative part becomes positive.

Furthermore, to analyze BH instabilities in the quantum-corrected case, we shall use Eq. (39) and determine the critical values of the horizon radii, namely $r_0^{+}(d)$ and $r_\infty^{+}(d)$. Comparing Eq. (39) with Eq. (25), we see that both share the

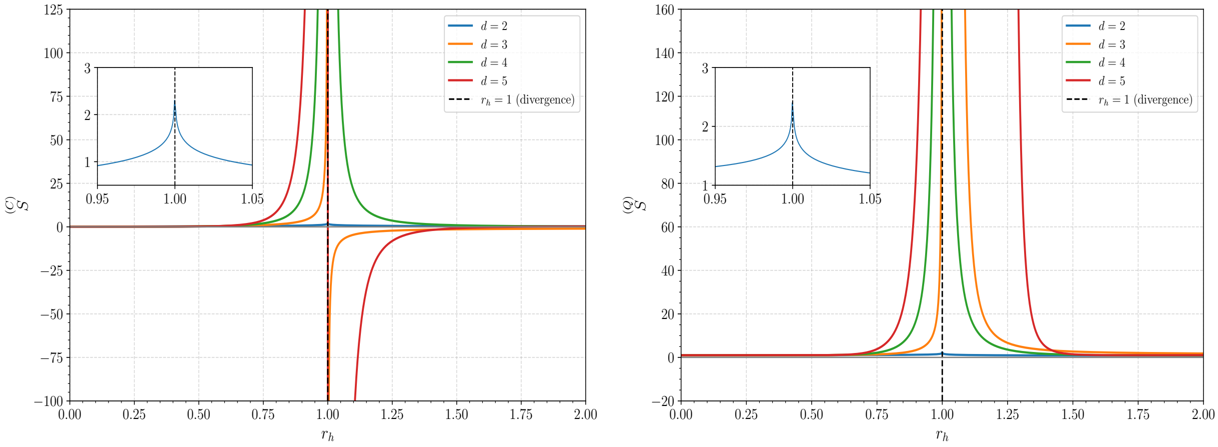

(a) (b)

**Figure 1.** The plots show the classical behavior of entropy before correction (panel a) and the quantum corrected entropy (panel b) of the AdS-Rindler BHs for $\eta = \delta = 1$.

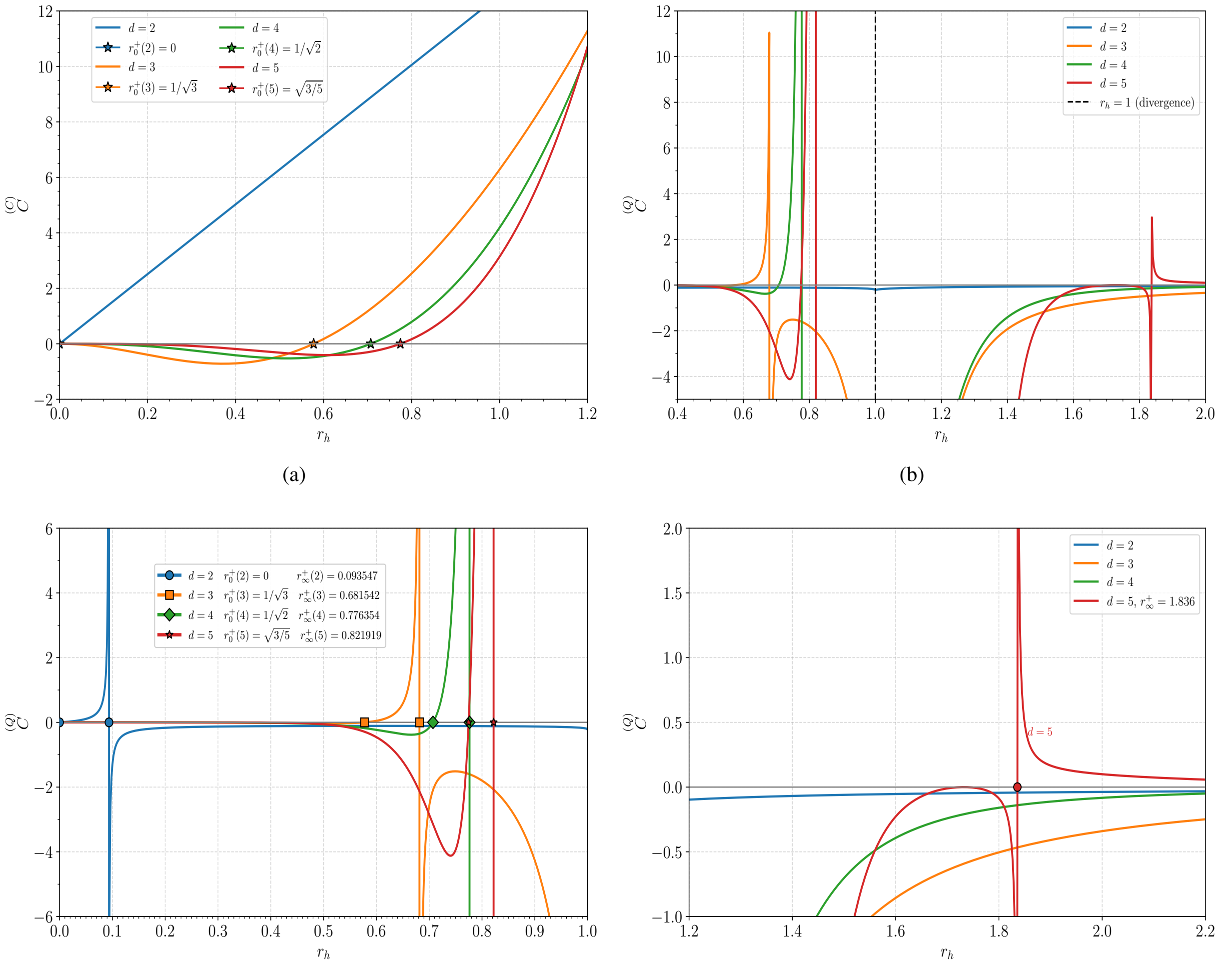

(a) (b)

(c) (d)

**Figure 2.** The plots show the semiclassical behavior of heat capacity before correction (panel a) and the quantum corrected heat capacity (panel b, c and d) of the AdS-Rindler BHs for $\eta = \delta = 1$.

common factor $(\partial M/\partial r_h)$ in the numerator. Therefore, the zeros $(\, r_0^+(d)\,)$ of the quantum-corrected heat capacity $(\, \overset{(Q)}{C}\,)$ are identical to those of the classical heat capacity $(\, \overset{(C)}{C}\,)$, which were analytically obtained in Eq. (44).

However, due to the complexity and nonlinearity of the denominator $(\partial \overset{(Q)}{T}/\partial r_h)$ of Eq. (39), which involves transcendental functions, obtaining analytical solutions for $r_\infty^+(d)$ is impractical. Therefore, the roots can be computed numerically. For each value of $d$, the stable region for the BHs, corresponding to $\overset{(Q)}{C} > 0$, is indicated by the interval between these critical values, i.e., $\Delta r_{(d)} = \left| r_\infty^+(d) - r_0^+(d) \right|$. Specifically, for the values of $d = 2, 3, 4, 5$, the stable regions are defined as follows: $\Delta r_{(2)} = |0.093547 - 0| = 0.093547$, $\Delta r_{(3)} = |0.681542 - 0.577350| = 0.104192$, $\Delta r_{(4)} = |0.776354 - 0.707107| = 0.069247$, $\Delta r_{(5)} = |0.821919 - 0.774597| = 0.047322$, respectively. These points are highlighted with different markers in Fig. (2) (panel c). In addition, in the case where $d = 5$, we note that the heat capacity $\left(\overset{(Q)}{C}\right)$ exhibits an additional divergent point at the vertical asymptote $(r_h = r_\infty^+(5) = 1.836)$. Beyond this point, the black hole re-enters a stable region, as illustrated in Fig. (2) (panel d).

## 7. CONCLUSIONS

In this study, we conducted a comprehensive thermodynamic and stability analysis of AdS–Rindler (hyperbolic) BHs, a theoretically significant yet relatively unexplored class of BH geometries. Using the framework of Hawking entropy and quantum-corrected thermodynamics, we examined how quantum effects influence the stability of these BHs.

Our results reveal that the heat capacity plays a decisive role in determining stability regimes. For the uncorrected heat capacity case, we have found the critical radii $\left( r_0^+(d) \right)$ (as in Eq.(44)) in which $C$ becomes positive and enters a stable region for all $r_h > r_0^+(d)$. While, upon introducing exponential quantum corrections to the entropy, we observed the drastically change in the stability regions, leading to narrower but smoother stable regions where calculated by $\Delta r_{(d)}$ in Sec.(6). Quantitatively, the size of these intervals for small black holes varies with the spacetime dimension $d$, reflecting their measurable sensitivity to quantum fluctuations across different dimensions.

The quantum-corrected heat capacity generally destabilized large Rindler–AdS (hyperbolic) black holes across all studied values of $d$. However, in the special case $d = 5$, the system regains stability for horizon radii satisfying $r_h > 1.836$ , where the heat capacity $C$ becomes positive.

Overall, our findings demonstrate that quantum corrections drastically alter the qualitative stability of hyperbolic BHs and do refine their thermodynamic structure, particularly by smoothing sharp entropy variations and modifying the stability of such BHs due to studying heat capacity .

In summary, the interplay between geometry, quantum corrections, and thermodynamic behavior in AdS–Rindler BHs provides valuable insights into nonclassical BH thermodynamics. In future work, the calculation of additional thermodynamic quantities such as pressure, volume, and the Gibbs free energy will enable the study of phase transitions, equations of state, and thermodynamic topology.

## ORCID

**Aram Bahroz Brzo**, https://orcid.org/0000-0002-1257-9377; **Peshwaz Abdulkareem Abdoul**, https://orcid.org/0000-0002-2144-8336; **Behnam Pourhassan**, https://orcid.org/0000-0003-1338-7083

## REFERENCES

[1] J. D. Bekenstein, ”Black holes and entropy,” Phys. Rev. D, **7**, 2333 (1973). https://doi.org/10.1103/physrevd.7.2333

[2] S. W. Hawking, ”Particle Creation by Black Holes,” Commun. Math. Phys. **43**, 199 (1975). https://doi.org/10.1007/bf02345020

[3] J.M. Bardeen, B. Carter, and S.W. Hawking, ”The four laws of black hole mechanics,” Commun. Math. Phys. **31**, 161 (1973). https://doi.org/10.1007/bf01645742

[4] D.N. Page, ”Information in black hole radiation,” Phys. Rev. Lett. **71**, 3743 (1993). https://doi.org/10.1103/physrevlett.71.3743

[5] A. Strominger, and C. Vafa, ”Microscopic origin of the Bekenstein-Hawking entropy,” Phys. Lett. B, **379**, 99 (1996). https://doi.org/10.1016/0370-2693(96)00345-0

[6] J.M. Maldacena, ”The Large N limit of superconformal field theories and supergravity,” Adv. Theor. Math. Phys. **2**, 231 (1998). https://doi.org/10.4310/atmp.1998.v2.n2.a1

[7] E. Witten, ”Anti-de Sitter space and holography,” Adv. Theor. Math. Phys. **2**, 253 (1998). https://doi.org/10.4310/atmp.1998.v2.n2.a2

[8] S.N. Gashti, M.A.S. Afshar, M.R. Alipour, I. Sakallı, B. Pourhassan, and J. Sadeghi, ”Assessing WGC Compatibility in ModMax Black Holes via Photon Spheres Analysis and WCCC Validation,” arXiv preprint arXiv, **2504**, 11939 (2025). https://doi.org/10.48550/arXiv.2504.11939

[9] S.N. Gashti, B. Pourhassan, and I. Sakallı, ”Thermodynamic topology and phase space analysis of AdS black holes through non-extensive entropy perspectives,” The European Physical Journal C, **85**(3), 305 (2025). https://doi.org/10.1140/epjc/s10052-025-14035-x

[10] A.B. Brzo, S.N. Gashti, B. Pourhassan, and S. Beikpour, ”Thermodynamic Topology of AdS Black Holes within Non-Commutative Geometry and Barrow Entropy,” Nuclear Physics B, **1012**, 116840 (2025). https://doi.org/10.1016/j.nuclphysb.2025.116840

[11] B. Pourhassan, M. Faizal, S. Upadhyay, and L. Al Asfar, ”Thermal Fluctuations in a Hyperscaling Violation Background,” Eur. Phys. J. C, **77**, 555 (2017). https://doi.org/10.1140/epjc/s10052-017-5125-x

[12] S. Upadhyay, B. Pourhassan, and H. Farahani, ”P-V criticality of first-order entropy corrected AdS black holes in massive gravity,” Phys. Rev. D, **95**, 106014 (2017). https://doi.org/10.1103/PhysRevD.95.106014

[13] B. Pourhassan, ”Exponential corrected thermodynamics of black holes,” J. Stat. Mech. **2107**, 073102 (2021). https://doi.org/10.1088/1742-5468/ac0f6a

[14] R.B. Wang, S.J. Ma, L. You, Y.C. Tang, Y.H. Feng, X.R. Hu, and J.B. Deng, ”Thermodynamics of AdS-Schwarzschild-like black hole in loop quantum gravity,” The European Physical Journal C, **84**(11), 1161 (2024). https://doi.org/10.1140/epjc/s10052-024-13505-y

[15] J.-P. Ye, Z.-Q. He, A.-X. Zhou, Z.-Y. Huang, and J.-H. Huang, ”Shadows and photon rings of a quantum black hole,” Physics Letters B, **851**, 138566 (2024). https://doi.org/10.1016/j.physletb.2024.138566

[16] F.G. Menezes, H.A. Borges, I.P.R. Baranov, and S. Carneiro, ”Thermodynamics of effective loop quantum black holes,” arXiv preprint arXiv, **2504**, 06964 (2025). https://doi.org/10.48550/arXiv.2504.06964

[17] L. You, R.-B. Wang, Y.-C. Tang, J.-B. Deng, and X.-R. Hu, ”Thermal chaos of quantum-corrected-AdS black hole in the extended phase space,” The European Physical Journal C, **84**, 11 (2024). https://doi.org/10.1140/epjc/s10052-024-13417-x

[18] B. Hamil, B. C. Lütfüoğlu, and L. Dahbi, ”Quantum-corrected Schwarzschild AdS black hole surrounded by quintessence: Thermodynamics and shadows,” Modern Physics Letters A, **39**(33n34), 2450161 (2024). https://doi.org/10.1142/s021773232450161x

[19] B. Tan, ”Thermodynamics of high order correction for Schwarzschild-AdS black hole in non-commutative geometry,” Nuclear Physics B, **1014**, 116868 (2025). https://doi.org/10.1016/j.nuclphysb.2025.116868

[20] R. Emparan, and J.M. Magán, ”Tearing down spacetime with quantum disentanglement,” Journal of High Energy Physics, **(3)**, 078 (2024). https://doi.org/10.1007/jhep03(2024)078

[21] P.Z. He, and H.Q. Zhang, ”Holographic timelike entanglement entropy from Rindler method,” Chinese Physics C, **48**(11), 115113 (2024). https://doi.org/10.1088/1674-1137/ad57a8

[22] X.X. Ju, B.H. Liu, W.B. Pan, Y.W. Sun, and Y.T. Wang, ”Squashed entanglement from generalized Rindler wedge,” Journal of High Energy Physics, **9**, 1-48 (2025). https://doi.org/10.1007/jhep09(2025)006

[23] Q. Wen, M. Xu, and H. Zhong, ”Timelike and gravitational anomalous entanglement from the inner horizon,” SciPost Physics, **18**(6), 204 (2025). https://doi.org/10.21468/scipostphys.18.6.204

[24] R.X. Miao, ”Casimir effect and holographic dual of wedges,” Journal of High Energy Physics, **6**, 1-35 (2024). https://doi.org/10.1007/jhep06(2024)084

[25] R. Campos Delgado, ”Quantum gravitational corrections to the entropy of a Reissner–Nordström black hole,” The European Physical Journal C, **82**(3), 272 (2022). https://doi.org/10.1140/epjc/s10052-022-10232-0

[26] S. Wu, and C. Liu, ”The Quantum Corrections on Kerr-Newman Black Hole Thermodynamics by the Generalized Uncertainty Principle,” International Journal of Theoretical Physics, **59**, 2681-2693 (2020). https://doi.org/10.1007/s10773-020-04468-3

[27] H.L. Li, D.W. Song, and W. Li, ”Phase transition and entropy correction of a quantum correction black hole close to planck scale,” General Relativity and Gravitation, **51**, 1-14 (2019). https://doi.org/10.1007/s10714-019-2504-7

[28] D. Ma, T. Huo, and C. Liu, ”Thermodynamics and its Quantum Correction of Vacuum Nonsingular Black Hole,” Astrophysics, **67**(4), 556-570 (2025). https://doi.org/10.1007/s10511-025-09851-8

[29] J.J. Song, and C.Z. Liu, ”Thermodynamics in a quantum corrected Reissner–Nordström–AdS black hole and its GUP-corrections,” Chinese Physics B, **33**(4), 040402 (2024). https://doi.org/10.1088/1674-1056/ad1a8a

[30] B. Pourhassan, ”Resolving the information loss paradox from the five-dimensional supergravity black hole,” Nuclear Physics B, **976**, 115713 (2022). https://doi.org/10.1016/j.nuclphysb.2022.115713

[31] B. Pourhassan, and M. Faizal, ”Thermal Fluctuations in a Charged AdS Black Hole,” Europhysics Letters, **111**, 40006 (2015). https://doi.org/10.1209/0295-5075/111/40006

[32] S. Upadhyay, N. ul Islam, and P.A. Ganai, ”A modified thermodynamics of rotating and charged BTZ black hole,” Journal of Holography Applications in Physics, **2**(1), 25-48 (2022). https://doi.org/10.1209/0295-5075/111/40006

[33] A. Sen, ”Logarithmic Corrections to $N = 2$ Black Hole Entropy: An Infrared Window into the Microstates,” General Relativity and Graviton, **44**(5), 1207-1266 (2012). https://doi.org/10.1007/s10714-012-1336-5

[34] B. Pourhassan, M. Faizal, and U. Debnath, ”Effects of Thermal Fluctuations on the Thermodynamics of Modified Hayward Black Hole,” Eur. Phys. J. C, **76**, 145 (2016). https://doi.org/10.1140/epjc/s10052-016-3998-8

[35] R. Ali, R. Babar, Z. Akhtar, and A. Övgün, ”Thermodynamics and logarithmic corrections of symmergent black holes,” Results Phys. **46**, 106300 (2023). https://doi.org/10.1016/j.rinp.2023.106300

[36] F.M. Mele, J. Münch, and S. Pateloudis, ”Quantum corrected polymer black hole thermodynamics: mass relations and logarithmic entropy correction,” Journal of Cosmology and Astroparticle Physics, **02**, 011 (2022). https://doi.org/10.1088/1475-7516/2022/02/011

[37] B. Pourhassan, R.C. Delgado, S. Upadhyay, H. Farahani, and H. Kumar, "Quantum gravitational corrections to the geometry of charged AdS black holes," Nucl. Phys. B, **1012**, 116830 (2025). https://doi.org/10.1016/j.nuclphysb.2025.116830

[38] B. Pourhassan, X. Shi, S.S. Wani, S. Al-Kuwari, İ. Sakallı, N.A. Shah, M. Faizal, and A. Shabir, "Quantum gravitational corrections to a Kerr black hole using Topos theory," Annals of Physics, **477**, 169983 (2025). https://doi.org/10.1016/j.aop.2025.169983

[39] R.M. Wald, *General Relativity*, (University of Chicago Press, 1984).

[40] S.M. Carroll, *Spacetime and Geometry: An Introduction to General Relativity*, (Addison Wesley, 2004).

[41] X. Calmet, and F. Kuipers, "Quantum Gravitational Corrections to the Entropy of a Schwarzschild Black Hole," Phys. Rev. D, **104**(6), 066012 (2021). https://doi.org/10.1103/physrevd.104.066012

[42] A. Chatterjee, and A. Ghosh, "Exponential corrections to black hole entropy," Phys. Rev. Lett. **125**(4), 041302 (2020). https://doi.org/10.1103/physrevlett.125.041302

[43] B. Pourhassan, H. Farahani, F. Kazemian, I. Sakalli, S. Upadhyay, and D.V. Singh, "Non-perturbative correction on the black hole geometry," Physics of the Dark Universe, **44**, 101444 (2024). https://doi.org/10.1016/j.dark.2024.101444

[44] H. Han, and B. Gwak, "Effects of fluctuations in higher-dimensional AdS black holes," Physical Review D, **110**, 066013 (2024). https://doi.org/10.1103/physrevd.110.066013

[45] B. Pourhassan, H. Aounallah, M. Faizal, S. Upadhyay, S. Soroushfar, Y.O. Aitenov, and S.S. Wani, "Quantum Thermodynamics of an M2-M5 Brane System," Journal of High Energy Physics, **05**, 030 (2022). https://doi.org/10.1007/jhep05(2022)030

[46] H. Kumar, B. Pourhassan, and I. Sakalli, "Stabilizing Effects of Higher-Order Quantum Corrections on Charged BTZ Black Hole Thermodynamics," Nucl. Phys. B, **1007**, 116672 (2024). https://doi.org/10.1016/j.nuclphysb.2024.116672

[47] B. Pourhassan, I. Sakalli, and A.B. Brzo, "Thermal Fluctuation Effects on Shear Viscosity to Entropy Ratio in Five-Dimensional Kerr-Newman Black Holes," Eur. Phys. J. C, **85**, 206 (2025). https://doi.org/10.1140/epjc/s10052-025-13893-9

[48] R. Emparan, "AdS/CFT duals of topological black holes and the entropy of zero-energy states," Journal of High Energy Physics, **06**, 036 (1999). https://doi.org/10.1088/1126-6708/1999/06/036

[49] D. Ma, T. Huo, and C. Liu, "Thermodynamics and its Quantum Correction of Vacuum Nonsingular Black Hole," Astrophysics, **67**(4), 556-570 (2024). https://doi.org/10.1007/s10511-025-09851-8

[50] Ali Övgün, Reggie C. Pantig, and Ángel Rincón, "Shadow and greybody bounding of a regular scale-dependent black hole solution," Annals of Physics, **463**, 169625 (2024). https://doi.org/10.1016/j.aop.2024.169625

[51] J.J. Song, and C.Z. Liu, "Thermodynamics in a quantum corrected Reissner-Nordström-AdS black hole and its GUP-corrections," Chinese Physics B, **33**(4), 040402 (2024). https://doi.org/10.1088/1674-1056/ad1a8a

[52] Q.Q. Li, Y. Zhang, Q. Sun, C.H. Xie, and Y.L. Lou, "Phase structure of quantum corrected charged AdS black hole surrounded by perfect fluid dark matter," Chinese Journal of Physics, **92**, 1-9 (2024). https://doi.org/10.1016/j.cjph.2024.09.001

[53] H. Casini, M. Huerta, and R.C. Myers, "Towards a derivation of holographic entanglement entropy," Journal of High Energy Physics, **5**, 1-41 (2011). https://doi.org/10.1007/jhep05(2011)036

[54] I.S. Gradshteyn, and I.M. Ryzhik, *Table of integrals, series, and products*, Academic press, 2014).

[55] B.P. Dolan, "The cosmological constant and black hole thermodynamic potentials," Class. Quantum Gravity, **28**, 125020 (2011). https://doi.org/10.1088/0264-9381/28/12/125020

[56] J. Tarrio, and S. Vandoren, "Black holes and black branes in Lifshitz spacetimes," J. High Energy Phys. **1109**, 017 (2011). https://doi.org/10.1007/JHEP09(2011)017

# КВАНТОВО СКОРИГОВАНА ТЕРМОДИНАМІКА AdS-RINDLER ЧОРНИХ ДІР

**Арам Бахроз Брзо[1,2], Пешваз Абдулкарім Абдул[3], Бенам Пурхасан[4,5,6]**
[1]*Фізичний факультет, Педагогічний коледж, Університет Сулеймані, Сулеймані 46001, регіон Курдистан, Ірак*
[2]*Центр досліджень і розвитку, Університет Сулеймані, Сулеймані 46001, Курдистан, Ірак*
[3]*Фізичний факультет, Науковий коледж, Університет Чармо: Чамчамал, Сулеймані, регіон Курдистан, Ірак*
[4]*Центр теоретичної фізики, Хазарський університет, вул. Мехсеті, 41, Баку, AZ1096, Азербайджан*
[5]*Школа фізики Дамганського університету, Дамган 3671645667, Іран*
[6]*Центр впливу досліджень & Результатів, Інститут інженерії та технологій Університету Чіткара, Університет Чіткара, Раджпура, 140401, Пенджаб, Індія*

Ми досліджуємо термодинамічні властивості та стабільність гіперболічних AdS-Rindler чорних дір, підкреслюючи вплив непертурбативної квантової корекції. Використовуючи стандартні термодинамічні формулювання разом з методом диска Пуанкаре, ми обчислюємо ключові величини, включаючи масу, температуру Хокінга, ентропію та теплоємність. Щоб врахувати квантові гравітаційні ефекти, ми вводимо експоненціальну корекцію до ентропії Бекенштейна-Хокінга та систематично виводимо модифіковані термодинамічні параметри. Хоча скоригована ентропія призводить до рівномірного зсуву в багатьох величинах, теплоємність зазнає нетривіальних змін, що призводить до вужчих та гладкіших стабільних областей $\left(\Delta r_{(d)}\right)$ для кожного виміру $d$. Більше того, згладжування різких варіацій ентропії поблизу $r_h = 1$ підкреслює, як геометрія горизонту керує впливом квантових корекцій. Це дослідження пропонує нову систематичну ідентифікацію стабільних областей до та після експоненціальних корекцій (AdS-Ріндлерових) чорних дір, пропонуючи нове розуміння взаємодії геометрії, розмірності та квантових ефектів у термодинаміці чорних дір.

**Ключові слова:** *гіперболічні чорні діри; квантова корекція ентропії; аналіз стабільності*

EAST EUROPEAN JOURNAL OF PHYSICS. **4**. 87–100 (2025)

DOI: 10.26565/2312-4334-2025-4-08 ISSN 2312-4334

# SPIN ALGEBRA AND NAIMARK'S EXTENSION: A TUTORIAL APPROACH WITH EXAMPLES

**Sumita Datta**[1,2]

[1]*Department of Pure and Applied Mathematics, Alliance University, Bengaluru 562 106, India*
[2]*Department of Physics, University of Texas at Arlington, Texas 76019, USA*
[*]*Corresponding Author e-mail: sumitad@gmail.com*

Received August 12, 2025; revised October 10, 2025; accepted November 10, 2025

In analyzing two-electron systems, the interactions of interest often include the spin-spin operator $\vec{S}_1 \cdot \vec{S}_2$ and the spin-orbit operator $\vec{L} \cdot \vec{S}$. When these operators act on entangled or indistinguishable particles, their measurement and physical interpretation may extend beyond the standard projective framework. This tutorial introduces the algebraic structure of spin interactions in two electron quantum systems and establishes its conceptual and mathematical connection with *Naimark's Extension Theorem*. Through explicit examples for two-electron systems, we demonstrate how spin operators arise in reduced Hilbert spaces, and how *Naimark's theorem* provides a formal framework for extending them to projective measurements in enlarged spaces. The application of *Naimark's Extension Theorem* in deriving their matrix elements opens up a window into the structure of quantum measurements in such composite systems.

**Keywords:** *Naimark's Extension; Hilbert space; Lie Algebra; Breit Hamiltonian; Quantum computing*

**PACS:** 03.65.-w;03.65.Fd;03.65.Ta;03.65.Ca;03.67.-a

## 1. INTRODUCTION

In quantum mechanics, spin is an intrinsic form of angular momentum, described by the $\mathfrak{su}(2)$ Lie algebra. In multi-electron systems, interactions like spin-spin and spin-orbit couplings are fundamental in determining spectral structures and quantum correlations. However, when systems are not fully accessible or are entangled with external degrees of freedom, effective descriptions via Positive Operator-Valued Measures(POVMs) often arise. *Naimark's Extension Theorem*[1-4,14, 15, 18-21] bridges this gap by ensuring that any POVM can be viewed as a Projection-Valued Measure(PVM) in a higher-dimensional Hilbert space. This article builds an intuitive and formal connection between spin algebra and Naimark's extension, with physically motivated examples. This paper calculates all the matrix elements associated with the spin-spin and spin-orbit operators for helium-like systems (He, $Li^+$) using an algebraic method, comparing the results with the conventional quantum mechanical calculations by G. Araki[5-7]. The spin-algebraic approach simplifies traditional quantum mechanics using tensor algebra and offers potential applications in quantum computing. We connect this algebraic approach to quantum mechanics foundations such as Dirac's vector space framework and the algebra of finite matrices[8].

This paper is organized as follows: Section 1 provides an introduction to spin algebra. Section 2 Naimark Extension theorem and other associated theories related to spin algebra. In Section 3, we outline the algebraic theories related to spin algebra. In section 4 we present the detailed calculations of the spin-dependent terms in the Breit Hamiltonian, highlighting our main results related to spin-spin and spin-orbit interactions. Section 5 establishes the connection between spin algebra and quantum computing theory. In Section 6, we summarize our analytical findings and discuss their consistency with previously reported results. Finally, Section 7 outlines potential future directions and concludes the paper.

Our results, compared with previous work, form a basis for developing quantum algorithms and logic gates, with plans to incorporate silicon-based calculations in future work. This research aims to explore the advantages of quantum computing and develop strategies for error correction and improved device performance, ultimately contributing to the realization of fault-tolerant quantum computers.

In quantum mechanics, spin is an intrinsic form of angular momentum, described by the $\mathfrak{su}(2)$ Lie algebra. In multi-electron systems, interactions like spin-spin and spin-orbit couplings are fundamental in determining spectral structures and quantum correlations. However, when systems are not fully accessible or are entangled with external degrees of freedom, effective descriptions via Positive Operator-Valued Measures(POVMs) often arise. *Naimark's Extension Theorem*[1-4,14, 15, 18-21] bridges this gap by ensuring that any POVM can be viewed as a Projection-Valued Measure(PVM) in a higher-dimensional Hilbert space. This article builds an intuitive and formal connection between spin algebra and Naimark's extension, with physically motivated examples. In this paper we calculate all the matrix elements associated with the spin-spin and spin-orbit operators for helium-like systems (He, $\mathrm{Li}^+$) using an algebraic method, comparing the results with the conventional quantum mechanical calculations by G. Araki[5-7]. The spin-algebraic approach simplifies traditional quantum mechanics using tensor algebra and offers potential applications in quantum computing. We connect this algebraic approach to quantum mechanics foundations such as Dirac's vector space framework and the algebra of finite matrices[8].

***Cite as:*** S. Datta, East Eur. J. Phys. 4, 87 (2025), https://doi.org/10.26565/2312-4334-2025-4-08

This paper is organized as follows: Section 1 provides an introduction to spin algebra. Section 2 delves into the Naimark Extension theorem and other associated theories related to spin algebra. In Section 3, we outline the algebraic theories related to spin algebra. In section 4 we present the detailed calculations of the spin-dependent terms in the Breit Hamiltonian, highlighting our main results related to spin-spin and spin-orbit interactions. Section 5 establishes the connection between spin algebra and quantum computing theory. In Section 6, we summarize our analytical findings and discuss their consistency with previously reported results. Finally, Section 7 outlines potential future directions and concludes the paper.

Our results, compared with previous work, form a basis for developing quantum algorithms and logic gates, with plans to incorporate silicon-based calculations in future work. This research aims to explore the advantages of quantum computing and develop strategies for error correction and improved device performance, ultimately contributing to the realization of fault-tolerant quantum computers.

## 2. NAIMARK'S EXTENSION AND GENERALIZED MEASUREMENTS

**Naimark's Extension Theorem** states that for any POVM $\{E_i\}$ acting on a Hilbert space $\mathcal{H}$, there exists a larger Hilbert space $\mathcal{K} \supset \mathcal{H}$ and a projective measurement $\{P_i\}$ on $\mathcal{K}$, such that

$$E_i = V^\dagger P_i V,$$

where $V : \mathcal{H} \longrightarrow \mathcal{K}$ is an isometry. This result allows one to represent generalized (unsharp) measurements as projective (sharp) measurements on an extended system, possibly involving an ancillary system.

### 2.1. Spin-Spin Interaction as a Measurement of Joint Observables

The spin-spin interaction is described by:

$$\vec{S}_1 \cdot \vec{S}_2 = \frac{1}{2}\left(\vec{S}_{\text{tot}}^2 - \vec{S}_1^2 - \vec{S}_2^2\right),$$

which is a function of total spin. Measuring this interaction amounts to resolving joint properties of the two-electron system. However, such joint measurements are not always directly implementable within $\mathcal{H}_1 \otimes \mathcal{H}_2$, especially when the spins are entangled. By extending the Hilbert space via Naimark's theorem, we can model the measurement of $\vec{S}_1 \cdot \vec{S}_2$ as a sharp measurement on a larger space $\mathcal{K}$, where a projective observable $P$ satisfies

$$\langle \psi | \vec{S}_1 \cdot \vec{S}_2 | \psi \rangle = \langle V\psi | P | V\psi \rangle .$$

This realizes the spin-spin operator as a component of a generalized measurement, effectively mediated by an ancilla system or latent degrees of freedom.

### 2.2. Spin-Orbit Interaction as a Quantum Instrument

The spin-orbit interaction,

$$\vec{L} \cdot \vec{S} = \sum_{i=1}^{3} L_i S_i,$$

entangles spin and orbital angular momenta. It can be viewed as a *quantum instrument*, a device that performs a measurement on one subsystem (e.g., orbital) and conditionally transforms the other (e.g., spin).

Naimark's theorem implies that this transformation may arise from a projective measurement on an extended space involving an ancilla. Mathematically, the spin-orbit coupling operator can be embedded into a larger Hilbert space via:

$$\vec{L} \cdot \vec{S} = V^\dagger \left( \sum_i \tilde{L}_i \tilde{S}_i \right) V,$$

where $\tilde{L}_i$, $\tilde{S}_i$ are extended operators acting on $\mathcal{K}$. This framework enables interpretation of spin-orbit interactions as information flow between degrees of freedom through a measurement process.

### 2.3. Ancilla Interpretation and Emergent Observables

The embedding via Naimark naturally introduces an ancillary space $\mathcal{A}$, such that:

$$\mathcal{K} = \mathcal{H} \otimes \mathcal{A}.$$

The matrix elements one can derive for spin operators in this framework suggest that some observables—particularly those not simultaneously measurable—can be effectively simulated as projective measurements on this enlarged space. These matrix elements therefore encode emergent properties due to the system-ancilla interaction.

### 2.4. Theorems and Lemmas Related to Naimark's Extension and Spin Interactions

**Definition (POVM):** A *positive operator-valued measure* (POVM) on a Hilbert space $\mathcal{H}$ is a set $\{E_i\} \subset \mathcal{B}(\mathcal{H})$ such that:

$$E_i \geq 0 \quad \text{and} \quad \sum_i E_i = \mathbb{I}_{\mathcal{H}}.$$

**Theorem 1 (Naimark's Dilation Theorem):** Let $\{E_i\}$ be a POVM on a Hilbert space $\mathcal{H}$. Then there exists a larger Hilbert space $\mathcal{K} \supset \mathcal{H}$, an isometry $V : \mathcal{H} \to \mathcal{K}$, and a projection-valued measure (PVM) $\{P_i\}$ on $\mathcal{K}$ such that

$$E_i = V^\dagger P_i V.$$

This theorem allows generalized spin measurements (e.g., effective measurement of $\vec{S}_1 \cdot \vec{S}_2$) to be implemented via sharp measurements on an extended Hilbert space.

**Lemma 1 (Operator Realization via Ancilla):** Let $A \in \mathcal{B}(\mathcal{H})$ be a Hermitian operator that does not correspond to a measurable quantity in the standard sense (e.g., $\vec{L} \cdot \vec{S}$, when spin and orbital observables are not jointly measurable). Then there exists an ancilla Hilbert space $\mathcal{A}$ and a Hermitian operator $\tilde{A} \in \mathcal{B}(\mathcal{H} \otimes \mathcal{A})$ such that

$$\langle \psi | A | \psi \rangle = \langle \psi \otimes \eta | \tilde{A} | \psi \otimes \eta \rangle, \quad \forall \psi \in \mathcal{H},$$

where $\eta \in \mathcal{A}$ is a fixed ancilla state. This lemma provides a foundation for calculating matrix elements of spin-orbit operators via auxiliary systems.

**Theorem 2 (Joint Measurement Representation):** Let $A, B \in \mathcal{B}(\mathcal{H})$ be two noncommuting observables (e.g., spin components or spin-orbit coupled operators). Then there exists a POVM $\{E_{ij}\}$ on $\mathcal{H}$ that approximates a joint measurement of $A$ and $B$, and an extended Hilbert space $\mathcal{K} \supset \mathcal{H}$ such that:

$$E_{ij} = V^\dagger P_{ij} V, \quad \text{with } \{P_{ij}\} \text{ a PVM on } \mathcal{K}.$$

This allows one to interpret the joint statistics of $\vec{S}_1 \cdot \vec{S}_2$ and $\vec{L} \cdot \vec{S}$ in terms of projective measurements in an enlarged space.

**Lemma 2 (Matrix Element Preservation):** Let $A \in \mathcal{B}(\mathcal{H})$ be an observable and $\tilde{A} \in \mathcal{B}(\mathcal{K})$ be its Naimark extension such that $A = V^\dagger \tilde{A} V$. Then for any $\psi, \phi \in \mathcal{H}$,

$$\langle \psi | A | \phi \rangle = \langle V\psi | \tilde{A} | V\phi \rangle.$$

Hence, matrix elements of spin-spin or spin-orbit operators derived via an extended space are consistent with those computed in the physical Hilbert space using POVM descriptions.

**Corollary (Simulation of Noncommuting Observables):** Spin observables that cannot be simultaneously diagonalized (e.g., $S_x$, $S_y$) can still be jointly simulated via projective measurements in an extended space, consistent with quantum contextuality. This supports the derivation of matrix elements for spin-spin and spin-orbit interactions via the Naimark formalism.

### 2.5. Quantum Information Perspective

From a quantum information viewpoint, this formalism is closely related to:

- **Entanglement-assisted measurements:** where outcomes depend on entangled ancillae.
- **Measurement-based quantum computation:** where operations are simulated via measurement on entangled states.
- **Contextuality and non-locality:** since the need for extensions often stems from non-classical statistics of spin observables.

## 3. QUANTUM SPIN SYSTEMS

Quantum spin systems[16] arise when the Hilbert space of states of atoms and molecules are reduced to a finite dimensional subspace. Here in this paper we consider the 2- particle quantum spin system, namely a helium atom with two spin-half electrons. To describe spin states of 2-electrons inside a helium atom, we consider a finite dimensional complex space called Hilbert space $\mathcal{H} = C^2$.

### 3.1. Postulates of Quantum Mechanics

1) The state of a particle in the quantum system is represented by a state vector in the Hilbert space. One can get all the information about the system by looking at the state vector.
2) The general quantum state of a quantum system is represented by a linear superposition of the individual states.
3) The state evolves by a unitary transformation.
4) All the observables(dynamical measurable variables) of a system can be represented by some operators.
5) The measured value of any physical observable is always real, so the corresponding operators are Hermitian.

### 3.2. Dirac notations for the state vector

For each state vector, $|\psi >\in \mathcal{H}\ \exists < \chi| \in$ dual space
**Bra and ket states**: For each $|\psi >$ in linear vector space $\exists$ one $< \psi|$ in dual space. ket vector $|\psi >$ is analogous to $\psi$ in wave mechanics. bra vector $< \psi|$ is analogous to $\psi^*$ in wave mechanics.
**Projections**: The projectors $P_\psi$ onto a ket. Define $P_\psi = |\psi >< \psi|$ and apply it to an arbitrary ket $|\phi >$ ; $P_\psi|\phi >= |\psi >< \psi|\phi >$ In both the cases above we have used the concept of Naimark-Segal's extension formula[ 1-4, 14, 15,18-21].

### 3.3. Algebra of the spin groups

An algebra is a vector space equipped with bilinear operations. Algebra $\mathscr{A}$ of observables of a quantum system is the set of all bounded operators on $\mathcal{H}$, denoted by $\mathcal{B}(\mathcal{H})$

**3.3.1. Lie Group** A Lie group[22-25] G with a compatible structure of a smooth (real or complex) manifold, in which the group operations of multiplication and inversion are smooth maps. Or in other words
if $\mu : G \times G \longrightarrow G, \mu(x, y) = xy$ , then $\mu$ is a smooth map. The spin operators in $\mathcal{H} = C^2$ form a Lie group. The spin groups of $\frac{1}{2}$ integer spin particles are represented by $SU(2)$ whereas the rotation groups in 3D are designated by $SO(3)$. $SU(n)$ and $SO(n)$ are in general defined as:
$SO(n) = \{A \in GL(n, \mathbb{R}) : AA^t = \mathbb{1} \quad \text{and} \quad det(A) = 1\}$
$SU(n) = \{A \in GL(n, \mathbb{C}) : AA^* = \mathbb{1} \quad \text{and} \quad det(A) = 1\}$
These two groups are isomorphic locally and their Lie Algebras are the same. $SU(2)$ is the universal double covering group of $SO(3)$.

The Hermitian generators of $SU(2)$ take the following form: $[\hat{T}_i, \hat{T}_j] = i\epsilon_{ijk}\hat{T}_k$ where $\hat{T}_i = \frac{1}{2}\hat{\sigma}_i$ and $\sigma_x= \begin{pmatrix} 0 & 1 \\ 1 & 0 \end{pmatrix}$ $\sigma_y= \begin{pmatrix} 0 & -i \\ i & 0 \end{pmatrix}$ $\sigma_z= \begin{pmatrix} 1 & 0 \\ 0 & -1 \end{pmatrix}$.

**3.3.2. Lie Algebra of spin groups** If G is a Lie group , then the Lie algebra g associated to G is, $T_{\mathbb{1}}(G)$ i.e., the tangent space of G at the identity $\mathbb{1} \in G$. A Lie algebra g is a special case where bilinear operation behaves like a commutator, in particular the bilinear operations need to satisfy
$[\cdot, \cdot] : g \times g = g$
$[x, x] = 0 \forall x \in g(alternatively)$
$[x, [y, z]] + [y, [z, x]] + [z, [x, y]] = 0 \forall x, y, z \in g$ (Jacobi identity)
$[x, y] + [y, x] = 0 \forall x, y \in g(anticommutivity)$
The Lie algebra associated with $SO(3)$ takes the following form: $[\hat{J}_i, \hat{J}_j] = \epsilon_{ijk}\hat{J}_k$

### 3.4. Representation of Lie Groups and Lie Algebras connected to spin observables

Let G be a Lie group and W be a finite dimensional vector space over a field $\mathbb{K} \in \{\mathbb{R}, \mathbb{C}\}$. A representation $\Pi$ of G acting on W is a mapping $\Pi : G \longrightarrow GL(W)$ which satisfies
$\Pi(g_1 g_2) = \Pi(g_1)\Pi(g_2) \quad \forall g_1, g_2 \in G \quad$ and $dim(\Pi) = dim(V)$ If g be a Lie Algebra of the above Lie group G, then a representation $\pi$ acting on W is a mapping $\pi : g \longrightarrow L(W)$ which satisfies
$\pi(|x, y|) = [\pi(x), \pi(y)] \quad \forall x, y \in g \quad$ and $dim(\pi) = dim(W)$. In general, the tensor product of $su(2)$ representations with spin $s_1$ and $s_2$ can be written as a fusion rule
$(s_1) \otimes (s_2) = \sum_{s=|s_1-s_2|}^{s_1+s_2} (s)$. For $s_1 = s_2 = \frac{1}{2}$, the decomposition of the Hilbert space can be given as
$(1/2) \otimes (1/2) = (0) + (1)$.

For two spin-(1/2) particles the four states of the Hilbert space can be decomposed into the triplet and the singlet states.
triplet:$|\uparrow\uparrow>, \frac{1}{\sqrt{2}}(|\uparrow\downarrow> +|\downarrow\uparrow>), |\downarrow\downarrow>$
singlet: $\frac{1}{\sqrt{2}}(|\uparrow\downarrow> -|\downarrow\uparrow>)$.

### 3.5. Naimark's Extension Theorem and Spin Couplings

Naimark's extension theorem provides a deep mathematical and physical insight into the representation of generalized, or unsharp, measurements as projective (sharp) measurements on an enlarged Hilbert space. This idea has a natural and elegant interpretation in the algebra of spin systems, where coupling between subsystems can be seen as an embedding of one Hilbert space into a larger one, typically involving an ancillary degree of freedom.

**3.5.1. The statement of Naimark's theorem** Let $\mathcal{H}$ be a Hilbert space describing our physical system. A Positive Operator-Valued Measure (POVM) $\{E_i\}$ on $\mathcal{H}$ is a set of positive operators satisfying $\sum_i E_i = I$. Naimark's theorem states that any such POVM can be realized as a projective measurement on a larger space $\mathcal{H}_{\text{ext}} = \mathcal{H} \otimes \mathcal{H}_{\text{anc}}$, where $\mathcal{H}_{\text{anc}}$ is an ancillary Hilbert space, and there exists an isometry

$$V : \mathcal{H} \longrightarrow \mathcal{H} \otimes \mathcal{H}_{\text{anc}}$$

such that

$$E_i = V^\dagger P_i V,$$

where $\{P_i\}$ are projection operators acting on $\mathcal{H}_{\text{ext}}$.

Physically, the embedding $V$ represents the process of coupling the system to an ancilla, performing a sharp measurement on the composite system, and then projecting back to the original space.

**3.5.2. Spin-Orbit coupling as a Naimark extension** Consider a single electron in an atom, such as helium. Its Hilbert space is a tensor product of an orbital part and a spin part,

$$\mathcal{H} = \mathcal{H}_L \otimes \mathcal{H}_S,$$

where $\mathcal{H}_L$ carries the orbital angular momentum $\mathbf{L}$, and $\mathcal{H}_S$ carries the intrinsic spin $\mathbf{S}$.

The spin–orbit coupling operator is given by

$$\mathbf{L} \cdot \mathbf{S} = L_x S_x + L_y S_y + L_z S_z.$$

If one considers the orbital part alone as the "system" Hilbert space, the influence of the spin degree of freedom makes $\mathbf{L} \cdot \mathbf{S}$ appear as a non-projective, or unsharp, operator on $\mathcal{H}_L$. According to Naimark's theorem, it can be realized as a sharp observable on the extended space $\mathcal{H}_L \otimes \mathcal{H}_S$:

$$\mathbf{L} \cdot \mathbf{S} = V^\dagger \left( \sum_i \tilde{L}_i \tilde{S}_i \right) V.$$

Here the ancilla is the spin Hilbert space $\mathcal{H}_S$, and $V$ is an isometric embedding

$$V : \mathcal{H}_L \to \mathcal{H}_L \otimes \mathcal{H}_S,$$

given explicitly by the Clebsch–Gordan transformation:

$$V|l, m_l\rangle = \sum_{m_s} C^{j\, m_j}_{l\, m_l\, \frac{1}{2}\, m_s} \, |l, m_l\rangle \otimes |\tfrac{1}{2}, m_s\rangle,$$

where $C^{j\, m_j}_{l\, m_l\, \frac{1}{2}\, m_s}$ are the Clebsch–Gordan coefficients connecting orbital and spin states to total angular momentum eigenstates.

In this sense, the spin degree of freedom acts as the *ancilla* that sharpens the unsharp orbital observable into a well-defined total angular momentum observable.

**3.5.3. Spin-Spin coupling as a Naimark extension** For a two-electron system (as in helium), each electron possesses a spin-$\frac{1}{2}$ degree of freedom. The combined spin space is

$$\mathcal{H}_S = \mathcal{H}_{S_1} \otimes \mathcal{H}_{S_2}.$$

The spin–spin coupling operator is

$$\mathbf{S}_1 \cdot \mathbf{S}_2 = S_{1x} S_{2x} + S_{1y} S_{2y} + S_{1z} S_{2z}.$$

If one wishes to represent $\mathbf{S}_1 \cdot \mathbf{S}_2$ as a projective measurement on an enlarged space starting from $\mathcal{H}_{S_1}$ alone, then the ancilla is naturally the spin space of the second electron, $\mathcal{H}_{S_2}$. Thus,

$$\mathbf{S}_1 \cdot \mathbf{S}_2 = V^\dagger \left( \sum_i \tilde{S}_{1i} \tilde{S}_{2i} \right) V,$$

where

$$V : \mathcal{H}_{S_1} \to \mathcal{H}_{S_1} \otimes \mathcal{H}_{S_2}$$

is again a Clebsch–Gordan embedding mapping single-spin states to the joint singlet-triplet basis:

$$V|\uparrow\rangle = |\uparrow\uparrow\rangle,$$
$$V|\downarrow\rangle = \frac{1}{\sqrt{2}}(|\uparrow\downarrow\rangle + |\downarrow\uparrow\rangle),$$

depending on the total spin sector considered.

Hence, $\mathcal{H}_{S_2}$ plays the role of an ancilla that extends the space of one spin to the composite two-spin space where $\mathbf{S}_1 \cdot \mathbf{S}_2$ is a sharp observable.

### 3.5.4. Summary

| Operator | System | Ancilla | Embedding $V$ |
|---|---|---|---|
| $\mathbf{L}\cdot\mathbf{S}$ | Orbital space $\mathcal{H}_L$ | Spin space $\mathcal{H}_S$ | Clebsch–Gordan map |
| $\mathbf{S}_1\cdot\mathbf{S}_2$ | One-spin space $\mathcal{H}_{S_1}$ | Second spin $\mathcal{H}_{S_2}$ | Clebsch–Gordan map |

In both cases, Naimark's extension theorem offers a unified perspective: an apparently unsharp or subsystem-dependent observable (such as $\mathbf{L}\cdot\mathbf{S}$ or $\mathbf{S_1}\cdot\mathbf{S_2}$) becomes sharp when lifted to an extended Hilbert space that includes the appropriate ancilla. The isometry $V$ implementing this lifting is physically realized by the Clebsch–Gordan transformation that couples angular momenta into total angular momentum eigenstates.

## 3.6. Lie Group and Spin Algebra Connection

The algebra of spin operators is most naturally understood in the framework of Lie groups and their representations. The operators **L**, **S**, and $\mathbf{J}=\mathbf{L}+\mathbf{S}$ are all generators of unitary representations of the Lie group $SU(2)$, whose associated Lie algebra is $su(2)$. This formalism provides a unifying language for understanding spin–orbit and spin–spin couplings as scalar invariants of tensor product representations.

**3.6.1. The $su(2)$ Lie algebra** The Lie algebra $su(2)$ is generated by the operators $\{S_x, S_y, S_z\}$ satisfying the commutation relations

$$[S_i, S_j] = i\hbar\epsilon_{ijk}S_k,$$

where $\epsilon_{ijk}$ is the Levi-Civita symbol. The Casimir operator

$$S^2 = S_x^2 + S_y^2 + S_z^2$$

commutes with all the generators of the algebra, and its eigenvalues classify the irreducible representations (irreps) of $su(2)$:

$$S^2|s, m_s\rangle = \hbar^2 s(s+1)|s, m_s\rangle.$$

The corresponding group $SU(2)$ consists of unitary operators

$$U(\boldsymbol{\theta}) = e^{-i\boldsymbol{\theta}\cdot\mathbf{S}/\hbar},$$

which represent spatial rotations on the Hilbert space of spin states.

**3.6.2. Tensor product representations and coupling of spins** When two angular momenta are present, such as **L** and **S** or $\mathbf{S}_1$ and $\mathbf{S}_2$, each provides an independent representation of $su(2)$. The combined system is described by the tensor product representation

$$D^{(l)} \otimes D^{(s)} = \bigoplus_{j=|l-s|}^{l+s} D^{(j)},$$

where $D^{(j)}$ are the irreducible representations of $SU(2)$. The map that implements this decomposition is the *Clebsch–Gordan transformation*,

$$V : \mathcal{H}_L \otimes \mathcal{H}_S \longrightarrow \bigoplus_j \mathcal{H}_j,$$

which is also the isometric embedding used in Naimark's extension theorem. The operator $V$ intertwines between representations, satisfying

$$V\, U_L(g) \otimes U_S(g) = U_J(g)\, V,$$

for all $g \in SU(2)$.

**3.6.3. Spin–orbit coupling as a Lie algebra scalar** The spin–orbit coupling operator

$$\mathbf{L}\cdot\mathbf{S} = L_xS_x + L_yS_y + L_zS_z$$

is a scalar under the diagonal action of $SU(2)$:

$$U(g)\,(\mathbf{L}\cdot\mathbf{S})\,U(g)^\dagger = \mathbf{L}\cdot\mathbf{S}, \quad U(g) = U_L(g)\otimes U_S(g).$$

Therefore, it can be expressed in terms of the Casimir operators of the Lie algebra:

$$\mathbf{L}\cdot\mathbf{S} = \frac{1}{2}(J^2 - L^2 - S^2),$$

where $J^2 = (\mathbf{L}+\mathbf{S})^2$ is the total angular momentum Casimir. This representation emphasizes that $\mathbf{L}\cdot\mathbf{S}$ is an invariant scalar built from the direct product of two $su(2)$ algebras.

**3.6.4. Spin–spin coupling as a Lie algebra invariant** For a two-electron system, the total spin operator is

$$\mathbf{S} = \mathbf{S}_1 + \mathbf{S}_2,$$

and the spin–spin coupling operator

$$\mathbf{S}_1 \cdot \mathbf{S}_2 = S_{1x}S_{2x} + S_{1y}S_{2y} + S_{1z}S_{2z}$$

can be written analogously as

$$\mathbf{S}_1 \cdot \mathbf{S}_2 = \frac{1}{2}\big(S^2 - S_1^2 - S_2^2\big).$$

Here again, $S^2$ is the Casimir operator of the total $su(2)$ representation. The eigenvalues of $\mathbf{S}_1 \cdot \mathbf{S}_2$ distinguish the singlet and triplet sectors:

$$\mathbf{S}_1 \cdot \mathbf{S}_2 \,|S=0\rangle = -\tfrac{1}{4}\hbar^2 \,|S=0\rangle,$$
$$\mathbf{S}_1 \cdot \mathbf{S}_2 \,|S=1\rangle = +\tfrac{3}{4}\hbar^2 \,|S=1\rangle.$$

These correspond to the irreducible representations $D^{(0)}$ and $D^{(1)}$ of $SU(2)$, respectively.

**3.6.5. Relation to Naimark's extension** From the Lie algebra viewpoint, the Naimark extension operator $V$ introduced earlier can be recognized as an intertwiner between representations of the Lie algebra $su(2)$:

$$L_i \longmapsto \tilde{L}_i = VL_iV^\dagger, \quad S_i \longmapsto \tilde{S}_i = VS_iV^\dagger.$$

The coupling operator in the extended space,

$$\sum_i \tilde{L}_i\tilde{S}_i,$$

is a scalar invariant under the diagonal $SU(2)$ action, and its projection

$$V^\dagger\left(\sum_i \tilde{L}_i\tilde{S}_i\right)V$$

acts as the physical observable on the smaller subsystem. Thus, the embedding of an unsharp observable into a sharp one via Naimark's theorem is fully consistent with the algebraic principle of constructing invariants from coupled $su(2)$ representations.

**3.6.6. Tutorial Summary** From the perspective of Lie group theory, both spin–orbit and spin–spin interactions arise as scalar invariants of coupled representations of the $su(2)$ Lie algebra. The Clebsch–Gordan map $V$, which couples two angular momenta into irreducible components, simultaneously serves as the embedding operator in Naimark's extension theorem. Therefore, the Lie algebraic coupling of spins and the measurement-theoretic embedding of unsharp observables are two complementary realizations of the same symmetry structure encoded by the group $SU(2)$.

### 3.7. Composite systems and Tensor products with Naimark's extension formula

For 1 particle, spin states are defined as $|\uparrow>$ and $|\downarrow>$. For a bipartite system with two electrons(He or $Li^+$ ) any operator for the particle 1, $\hat{A}_1 \in \mathcal{H}_1$ ($\mathcal{H}_1$ is known as a complex Hilbert space) can be upgraded to a bigger Hilbert space, $\mathcal{H}_{12}$ by taking the tensor product with the identity operator in $\mathcal{H}_2$ i.e., $\hat{A}_{12} = \hat{A}_1 \otimes \mathbf{I}_2$.
Similarly an operator, $\hat{A}_2 \in \mathcal{H}_2$ is upgraded to $\mathbf{I}_1 \otimes \hat{A}_2$.
Now $(\hat{A}_1) \otimes (\mathbf{I}_2).(\mathbf{I}_1 \otimes \hat{A}_2)(\psi_1 \otimes \psi_2) = \hat{A}_1\psi_1 \otimes \hat{A}_1\psi_2$, where the state vector $\psi_1 \in \mathcal{H}_1$ and the state vector $\psi_2 \in \mathcal{H}_2$.

$$(\hat{A}_1 \otimes \hat{A}_2) \uparrow \otimes \uparrow = (\hat{A}_1 \uparrow) \otimes (\hat{A}_2 \uparrow) \tag{1}$$

The upgradation formula for the addition of spin angular momenta takes the following form:

$$\sigma_+ = (\sigma_{1+} \otimes \mathbf{1} + \mathbf{1} \otimes \sigma_{2+}) \tag{2}$$

In both the cases above we have used the concept of Naimark-Segal's extension formula[1-4,14,15, 18-21].

## 4. MATRIX ELEMENTS USING NAIMARK'S EXTENSION FORMULA

### 4.1. Example 1: Spin-spin interaction operators

The operators needed to calculate the relativistic effects are well known. In atomic units with no external electric and magnetic field these are usually written as Eq. (1) of [11]

$$\begin{aligned}\Delta_r = & -\sum_i \frac{\nabla_{\mathbf{i}}{}^4}{8c^2} + \sum_i \frac{Z\pi}{2c^2}\delta(\mathbf{r_i}) - \sum_{i<j}\frac{\pi}{c^2}\delta(\mathbf{r_i}-\mathbf{r_j}) - \sum\nolimits_{i<j}\frac{1}{2c^2}\times \\ & \times \overleftarrow{\nabla}_{\mathbf{i}}\cdot[\frac{(\mathbf{r_i}-\mathbf{r_j})(\mathbf{r_i}-\mathbf{r_j})}{r_{ij}{}^3} + \frac{1}{r_{ij}}]\cdot\overrightarrow{\nabla}_{\mathbf{j}} - \sum_{i<j}\frac{8\pi}{3c^2}\delta(\mathbf{r_i}-\mathbf{r_j})\mathbf{s_i}\cdot\mathbf{s_j} \\ & -\sum_{i<j}\frac{1}{c^2}\mathbf{s_i}\cdot\frac{3(\mathbf{r_i}-\mathbf{r_j})(\mathbf{r_i}-\mathbf{r_j})-r_{ij}{}^2}{r_{ij}{}^5}\cdot\mathbf{s_j} - \sum_i \frac{Z}{2c^2}\frac{1}{r_i^3}\mathbf{s_i}\cdot[\mathbf{r_i}\times i\overrightarrow{\nabla}_{\mathbf{i}}] \\ & +\sum_{i\neq j}\frac{1}{c^2}\frac{1}{r_{ij}{}^3}\mathbf{s_i}\cdot[(\mathbf{r_i}-\mathbf{r_j})\times i\overrightarrow{\nabla}_{\mathbf{j}}] + \sum_{i\neq j}\frac{1}{2c^2}\frac{1}{r_{ij}{}^3}\mathbf{s_j}\cdot[(\mathbf{r_j}-\mathbf{r_i})\times i\overrightarrow{\nabla}_{\mathbf{j}}],\end{aligned} \tag{3}$$

where $r_{ij}$ is the distance between the particles. The first term is the mass velocity correction. The Second and third operators are the electron and nucleus Darwin term respectively. The fourth term is due to the retardation of electromagnetic field by an electron. The fifth and sixth terms represent spin-spin and spin-other spin terms. The last three operators are spin-orbit interactions. For a singlet state with any angular momentum, the expectation values of sixth, seventh and eighth terms are zero. For triplet P and D states, however, the sixth, seventh, eighth and ninth terms are now nonzero and must be computed. Particularly we need to calculate the matrix elements $-\frac{1}{c^2} < \phi|[\Sigma_{i<j}\frac{8\pi}{3}\delta(\mathbf{r_i}-\mathbf{r_j})\mathbf{s_i}.\mathbf{s_j} - \Sigma_{i<j}\mathbf{s_i}.\frac{3(\mathbf{r_i}-\mathbf{r_j})(\mathbf{r_i}-\mathbf{r_j})-r_{ij}{}^2}{r_{ij}{}^5}].\mathbf{s_j}|\phi >$ and $\frac{1}{c^2} < \phi|[\Sigma_{i\neq j}\frac{1}{r_{ij}{}^3}\mathbf{s_i}.[(\mathbf{r_i}-\mathbf{r_j})\times i\nabla_{\mathbf{j}}] + \Sigma_{i\neq j}\frac{1}{2}\frac{1}{r_{ij}{}^3}\mathbf{s_j}.[(\mathbf{r_j}-\mathbf{r_i})\times i\nabla_{\mathbf{j}}]|\phi >$
where $\phi$ is the exact eigenvalue of the unperturbed Hamiltonian.

The spin spin interaction in general for many particle can be written as

$$H_{ss} = 4\mu^2[-\Sigma_{i<j}\frac{8\pi}{3}\delta(\mathbf{r_i}-\mathbf{r_j})[\sigma_{\mathbf{i}}.\sigma_{\mathbf{j}} + \frac{1}{r_{ij}{}^3}\{\sigma_{\mathbf{i}}.\sigma_{\mathbf{j}} - 3(\sigma_{\mathbf{i}}.\mathbf{r_{ij}})(\sigma_{\mathbf{j}}.\mathbf{r_{ij}})/r_{ij}^2] \tag{4}$$

where $\mu$ is the Bohr magneton i.e., $\mu = \frac{e\hbar}{2m_e c}$. In atomic units the spin-spin intercation is measured in units of $\frac{1}{c^2}$. For 2 electron system the above expression can be written as[9]

$$\frac{1}{c^2}[-\frac{8\pi}{3}\sigma^{\mathbf{1}}.\sigma^{\mathbf{2}}\delta(\mathbf{r_{12}}) + \frac{\mathbf{1}}{\mathbf{r_{12}}^{\mathbf{3}}}\{\sigma^{\mathbf{1}}.\sigma^{\mathbf{2}} - 3(\sigma^{\mathbf{1}}.\mathbf{r_{12}})(\sigma^{\mathbf{2}}.\mathbf{r_{12}})/r_{12}{}^2\}] \tag{5}$$

Now since triplet spin function is symmetric $< \delta(r_{12}) >= 0$ for triplet states. So for triplet states only 2nd and third term in Eq (5) contribute.

### 4.2. Spin states

For 1 particle, spin states are defined as $|\alpha >\equiv |\uparrow>\equiv \begin{pmatrix}1\\0\end{pmatrix}$ and $|\beta >\equiv |\downarrow> \equiv \begin{pmatrix}0\\1\end{pmatrix}$

For 2 particle systems spin states are defined as $|\alpha_1 > \otimes|\alpha_2 >\equiv |\uparrow> \otimes|\uparrow>$, $|\alpha_1 > \otimes|\beta_2 >\equiv |\uparrow> \otimes|\downarrow>$, $|\beta_1 > \otimes|\alpha_2 >\equiv |\downarrow> \otimes|\uparrow>$ and $|\beta_1 > \otimes|\beta_2 >\equiv |\downarrow> \otimes|\downarrow>$.

### 4.3. Evaluation of Matrix representation of the spin observables

Using the basis defined in section 4.2, the matrix representation of a general operator $R$ can be represented as

$$\begin{pmatrix} <\uparrow\uparrow|R|\uparrow\uparrow> & <\uparrow\uparrow|R|\uparrow\downarrow> & <\uparrow\uparrow|R|\downarrow\uparrow> & <\uparrow\uparrow|R|\downarrow\downarrow> \\ <\uparrow\downarrow|R|\uparrow\uparrow> & <\uparrow\downarrow|R|\uparrow\downarrow> & <\uparrow\downarrow|R|\downarrow\uparrow> & <\uparrow\downarrow|R|\downarrow\downarrow> \\ <\downarrow\uparrow|R|\uparrow\uparrow> & <\downarrow\uparrow|R|\uparrow\downarrow> & <\downarrow\uparrow|R|\downarrow\uparrow> & <\downarrow\uparrow|R|\downarrow\downarrow> \\ <\downarrow\downarrow|R|\uparrow\uparrow> & <\downarrow\downarrow|R|\uparrow\downarrow> & <\downarrow\downarrow|R|\downarrow\uparrow> & <\downarrow\downarrow|R|\downarrow\downarrow> \end{pmatrix}.$$

We calculate the diagonal matrix elements of the above operator as the correction for the spin spin interaction for triplet states of helium.

### 4.4. Matrix elements for the spin-spin interactions

**Calculation for $(\sigma^{\mathbf{1}}.\sigma^{\mathbf{2}})/r_{12}^3$**

Let us first calculate $\sigma^1.\sigma^2 = \sigma_x{}^1\sigma_x{}^2 + \sigma_y{}^1\sigma_y{}^2 + \sigma_z{}^1\sigma_z{}^2$

Now

$$\sigma_x{}^1 \otimes \sigma_x{}^2 | \uparrow \otimes \uparrow >= \sigma_x{}^1 | \uparrow > \sigma_x{}^2 | \uparrow > \tag{6}$$

yields
$$\begin{pmatrix} 0 & 1 \\ 1 & 0 \end{pmatrix}\begin{pmatrix} 1 \\ 0 \end{pmatrix}\begin{pmatrix} 0 & 1 \\ 1 & 0 \end{pmatrix}\begin{pmatrix} 1 \\ 0 \end{pmatrix}=\begin{pmatrix} 0 \\ 1 \end{pmatrix}\begin{pmatrix} 0 \\ 1 \end{pmatrix}$$

$$\sigma_y{}^1 \otimes \sigma_y{}^2 | \uparrow \otimes \uparrow >= \sigma_y{}^1 | \uparrow > \sigma_y{}^2 | \uparrow > \tag{7}$$

yields
$$\begin{pmatrix} 0 & -i \\ i & 0 \end{pmatrix}\begin{pmatrix} 1 \\ 0 \end{pmatrix}\begin{pmatrix} 0 & -i \\ i & 0 \end{pmatrix}\begin{pmatrix} 1 \\ 0 \end{pmatrix}=\begin{pmatrix} 0 \\ i \end{pmatrix}\begin{pmatrix} 0 \\ i \end{pmatrix}=-\begin{pmatrix} 0 \\ 1 \end{pmatrix}\begin{pmatrix} 0 \\ 1 \end{pmatrix}$$

$$\sigma_z{}^1 \otimes \sigma_z{}^2 | \uparrow \otimes \uparrow >= \sigma_z{}^1 | \uparrow > \sigma_z{}^2 | \uparrow > \tag{8}$$

yields
$$\begin{pmatrix} 1 & 0 \\ 0 & -1 \end{pmatrix}\begin{pmatrix} 1 \\ 0 \end{pmatrix}\begin{pmatrix} 1 & 0 \\ 0 & -1 \end{pmatrix}\begin{pmatrix} 1 \\ 0 \end{pmatrix}=\begin{pmatrix} 1 \\ 0 \end{pmatrix}\begin{pmatrix} 1 \\ 0 \end{pmatrix}$$

$$(\sigma^{\mathbf{1}}.\sigma^{\mathbf{2}})/r_{12}^3 \begin{pmatrix} \alpha_1\alpha_2 \\ \alpha_1\beta_2 \\ \beta_1\alpha_2 \\ \beta_1\beta_2 \end{pmatrix} = \frac{1}{r_{12}^3}\begin{pmatrix} \downarrow\downarrow - \downarrow\downarrow + \uparrow\uparrow \\ \downarrow\uparrow + \downarrow\uparrow - \uparrow\downarrow \\ \uparrow\downarrow + \uparrow\downarrow - \downarrow\uparrow \\ \uparrow\uparrow - \uparrow\uparrow + \downarrow\downarrow \end{pmatrix} = \frac{1}{r_{12}^3}\begin{pmatrix} \uparrow\uparrow \\ 2\downarrow\uparrow - \uparrow\downarrow \\ 2\uparrow\downarrow - \downarrow\uparrow \\ \downarrow\downarrow \end{pmatrix}$$

Now let us recall $\mathbf{r_{12}} = \mathbf{r} = \hat{i}x + \hat{j}y + \hat{k}z$, where $(x_2 - x_1 = x, y_2 - y_1 = y, z_2 - z_1 = z)$, and $r_{12} = r = \sqrt{(x^2 + y^2 + z^2)}$, where $z_1$ and $z_2$ are the $z$ coordinates of electron 1 and 2.

**Calculations for** $(\sigma^{\mathbf{1}}.\mathbf{r_{12}})(\sigma^{\mathbf{2}}.\mathbf{r_{12}})/r_{12}^5$

$$(\sigma^{\mathbf{1}}.\mathbf{r_{12}})(\sigma^{\mathbf{2}}.\mathbf{r_{12}})/r_{12}^5 \begin{pmatrix} \alpha_1\alpha_2 \\ \alpha_1\beta_2 \\ \beta_1\alpha_2 \\ \beta_1\beta_2 \end{pmatrix}$$

Now

$$\begin{aligned}(\sigma^{\mathbf{1}}.\mathbf{r})(\sigma^{\mathbf{2}}.\mathbf{r}) &= (x\sigma_{1x} + y\sigma_{1y} + z\sigma_{1z})(x\sigma_{2x} + y\sigma_{2y} + z\sigma_{2z}) \\ &= x^2\sigma_{1x} \otimes \sigma_{2x} + xy\sigma_{1y} \otimes \sigma_{2x} + xz\sigma_{1z} \otimes \sigma_{2x} + \\ &\quad xy\sigma_{1x} \otimes \sigma_{2y} + y^2\sigma_{1y} \otimes \sigma_{2y} + yz\sigma_{1z} \otimes \sigma_{2y} + \\ &\quad xz\sigma_{1x} \otimes \sigma_{2z} + yz\sigma_{1y} \otimes \sigma_{2z} + z^2\sigma_{1z} \otimes \sigma_{2z}\end{aligned} \tag{9}$$

Now we need to operate $x^2\sigma_{1x} \otimes \sigma_{2x} + xy\sigma_{1y} \otimes \sigma_{2x} + xz\sigma_{1z} \otimes \sigma_{2x} +$
$xy\sigma_{1x} \otimes \sigma_{2y} + y^2\sigma_{1y} \otimes \sigma_{2y} + yz\sigma_{1z} \otimes \sigma_{2y} +$
$xz\sigma_{1x} \otimes \sigma_{2z} + yz\sigma_{1y} \otimes \sigma_{2z} + z^2\sigma_{1z} \otimes \sigma_{2z}$
on $\begin{pmatrix} \alpha_1\alpha_2 \\ \alpha_1\beta_2 \\ \beta_1\alpha_2 \\ \beta_1\beta_2 \end{pmatrix}$.

Operating $x^2\sigma_{1x} \otimes \sigma_{2x} + xy\sigma_{1y} \otimes \sigma_{2x} + xz\sigma_{1z} \otimes \sigma_{2x} +$
$xy\sigma_{1x} \otimes \sigma_{2y} + y^2\sigma_{1y} \otimes \sigma_{2y} + yz\sigma_{1z} \otimes \sigma_{2y} +$
$xz\sigma_{1x} \otimes \sigma_{2z} + yz\sigma_{1y} \otimes \sigma_{2z} + z^2\sigma_{1z} \otimes \sigma_{2z}$
on $\alpha_1\alpha_2$ one gets

$(x + iy)^2\beta_1\beta_2 + (x + iy)z(\alpha_1\beta_2 + \alpha_2\beta_1 + z^2\alpha_1\alpha_2$

Explicit derivation for the above:

Since spin operators are same for particle '1' and particle '2' we suppress the subscript '1' and '2' from now on.

now $\sigma_x = \begin{pmatrix} 0 & 1 \\ 1 & 0 \end{pmatrix}$ $\sigma_y = \begin{pmatrix} 0 & -i \\ i & 0 \end{pmatrix}$

$\sigma_z = \begin{pmatrix} 1 & 0 \\ 0 & -1 \end{pmatrix}$

Using the above spin operators we calculate

$$x^2\sigma_x \otimes \sigma_x|\uparrow> \otimes|\uparrow>= x^2\sigma_x|\uparrow> \sigma_x|\uparrow>= x^2 \downarrow\downarrow= x^2\beta_1\beta_2 \tag{10}$$

( we have used $(\hat{A}_1 \otimes \hat{A}_2)|\uparrow> \otimes|\uparrow>= (\hat{A}_1|\uparrow>) \otimes (\hat{A}_2|\uparrow>)$; $\sigma_x|\alpha_1 > \sigma_x|\alpha_2 > = \begin{pmatrix} 0 & 1 \\ 1 & 0 \end{pmatrix}\begin{pmatrix} 1 \\ 0 \end{pmatrix}\begin{pmatrix} 0 & 1 \\ 1 & 0 \end{pmatrix}\begin{pmatrix} 1 \\ 0 \end{pmatrix}=\begin{pmatrix} 0 \\ 1 \end{pmatrix}\begin{pmatrix} 0 \\ 1 \end{pmatrix}$ ).
Similarly

$$xy\sigma_y \otimes \sigma_x|\uparrow> \otimes|\uparrow>= ixy\beta_1\beta_2, \tag{11}$$

$$xz\sigma_z \otimes \sigma_x|\uparrow> \otimes|\uparrow>= ixz\alpha_1\beta_2, \tag{12}$$

$$xy\sigma_x \otimes \sigma_y|\uparrow> \otimes|\uparrow>= ixy\beta_1\beta_2, \tag{13}$$

$$y^2\sigma_y \otimes \sigma_y|\uparrow> \otimes|\uparrow>= -y^2\beta_1\beta_2, \tag{14}$$

$$yz\sigma_z \otimes \sigma_y|\uparrow> \otimes|\uparrow>= iyz\alpha_1\beta_2, \tag{15}$$

$$xz\sigma_x \otimes \sigma_z|\uparrow> \otimes|\uparrow>= xz\beta_1\alpha_2, \tag{16}$$

$$yz\sigma_y \otimes \sigma_z|\uparrow> \otimes|\uparrow>= iyz\beta_1\alpha_2, \tag{17}$$

$$z^2\sigma_z \otimes \sigma_z|\uparrow> \otimes|\uparrow>= z^2\alpha_1\alpha_2. \tag{18}$$

We have similar relation when we operate

$(\sigma^{\mathbf{1}}.\mathbf{r})(\sigma^{\mathbf{2}}.\mathbf{r})$ on other basis functions. So $(\sigma^{\mathbf{1}}.\mathbf{r_{12}})(\sigma^{\mathbf{2}}.\mathbf{r_{12}})/r_{12}^5 \begin{pmatrix} \alpha_1\alpha_2 \\ \alpha_1\beta_2 \\ \beta_1\alpha_2 \\ \beta_1\beta_2 \end{pmatrix}$

$$=\frac{1}{r_{12}^5}\begin{pmatrix} z^2\alpha_1\alpha_2 + (x+iy)z(\alpha_1\beta_2 + \beta_1\alpha_2) + (x+iy)^2\beta_1\beta_2 \\ z(x-iy)\alpha_1\alpha_2 + (x^2+y^2)\alpha_2\beta_1 - z^2\beta_2\alpha_1 - (x+iy)z\beta_1\beta_2 \\ (x-iy)z\alpha_1\alpha_2 + (x^2+y^2)\beta_2\alpha_1 - z^2\alpha_2\beta_1 - z(x+iy)\beta_1\beta_2 \\ (x-iy)^2\alpha_1\alpha_2 - z(x-iy)(\alpha_1\beta_2 + \beta_1\alpha_2) + z^2\beta_1\beta_2 \end{pmatrix}.$$

Now recalling

$$(\sigma^{\mathbf{1}}.\sigma^{\mathbf{2}})/r_{12}^3\begin{pmatrix} \alpha_1\alpha_2 \\ \alpha_1\beta_2 \\ \beta_1\alpha_2 \\ \beta_1\beta_2 \end{pmatrix} = \frac{1}{{r_{12}}^3}\begin{pmatrix} \downarrow\downarrow - \downarrow\downarrow + \uparrow\uparrow \\ \downarrow\uparrow + \downarrow\uparrow - \uparrow\downarrow \\ \uparrow\downarrow + \uparrow\downarrow - \downarrow\uparrow \\ \uparrow\uparrow - \uparrow\uparrow + \downarrow\downarrow \end{pmatrix}$$

$$=\frac{1}{r_{12}^3}\begin{pmatrix} \uparrow\uparrow \\ 2\downarrow\uparrow - \uparrow\downarrow \\ 2\uparrow\downarrow - \downarrow\uparrow \\ \downarrow\downarrow \end{pmatrix}.$$

Now taking $R_1 = \frac{1}{{r_{12}}^3}(\sigma^1.\sigma^2) = \frac{1}{{r_{12}}^3}({\sigma_x}^1{\sigma_x}^2 + {\sigma_y}^1{\sigma_y}^2 + {\sigma_z}^1{\sigma_z}^2)$, the spin average for the second term in Eq. (2) can be calculated by the matrix formula given in section 4.3 as follows:

$$\frac{1}{{r_{12}}^3}\begin{pmatrix} 1 & 0 & 0 & 0 \\ 0 & -1 & 2 & 0 \\ 0 & 2 & -1 & 0 \\ 0 & 0 & 0 & 1 \end{pmatrix}.$$

Similarly performing the spin average for the 3rd term, one can get

$$\frac{1}{{r_{12}}^5}\begin{pmatrix} z^2 & (x+iy)z & (x+iy)z & (x+iy)^2 \\ (x-iy)z & -z^2 & (x^2+y^2) & -(x+iy)z \\ (x-iy)z & (x^2+y^2) & -z^2 & -(x+iy)z \\ (x-iy)^2 & -(x-iy)z & -(x-iy)z & z^2 \end{pmatrix}$$

So combining the whole spin spin operator, $(\frac{\sigma^{\mathbf{1}}.\sigma^{\mathbf{2}}}{r_{12}^3} - 3\frac{(\sigma^{\mathbf{1}}.\mathbf{r_{12}})(\sigma^{\mathbf{2}}.\mathbf{r_{12}})}{r_{12}^5})$ using the basis defined in section 3.2, the matrix elements can be represented as $=\begin{pmatrix} \frac{1}{{r_{12}}^3} - \frac{3z^2}{{r_{12}}^5} & -\frac{3(x+iy)z}{{r_{12}}^5} & -\frac{3(x+iy)z}{{r_{12}}^5} & -\frac{3(x+iy)^2}{{r_{12}}^5} \\ -\frac{3(x-iy)z}{{r_{12}}^5} & -(\frac{1}{{r_{12}}^3} - \frac{3z^2}{{r_{12}}^5}) & \frac{2}{{r_{12}}^3} - \frac{3(x^2+y^2)}{{r_{12}}^5} & \frac{3(x+iy)z}{{r_{12}}^5} \\ -\frac{3(x-iy)z}{{r_{12}}^5} & \frac{2}{{r_{12}}^3} - \frac{3(x^2+y^2)}{{r_{12}}^5} & -(\frac{1}{{r_{12}}^3} - \frac{3z^2}{{r_{12}}^5}) & \frac{3(x+iy)z}{{r_{12}}^5} \\ \frac{-3(x-iy)^2}{{r_{12}}^5} & \frac{3(x-iy)z}{{r_{12}}^5} & \frac{3(x-iy)z}{{r_{12}}^5} & \frac{1}{{r_{12}}^3} - \frac{3z^2}{{r_{12}}^5} \end{pmatrix}$

Now the diagonal element of the above matrix is $\frac{1}{{r_{12}}^3} - \frac{3z^2}{{r_{12}}^5}$ which turns out to be $\frac{\partial^2}{\partial z_1 \partial z_2}(\frac{1}{r_{12}})$.

So the diagonal element of the expectation value for the case $(J = L = M)$

$$< LSJM|H_{ss}|LSJM >_{J=L=M}= \frac{1}{4c^2}\int\int |\psi_{LL}|^2\frac{\partial^2}{\partial z_1 \partial z_2}(\frac{1}{r_{12}})dv_1dv_2. \tag{19}$$

### 4.5. Example 2: Spin-orbit operators:

For two particles the spin orbit interaction becomes

$$\frac{1}{4c^2}\{\sigma_1.[\mathcal{E}_1 \times p_1 + (\frac{2}{r_{12}^3})r_{12} \times p_2] + \sigma_2.[\mathcal{E}_2 \times p_2 + (\frac{2}{r_{12}^3})r_{21} \times p_1]\}. \tag{20}$$

Now in general $\mathcal{E} = -\nabla V$ includes Coulomb interaction due to the nucleus, the Coulomb interaction due to the other electron and any external field. Since we are not considering any external field, $\mathcal{E}_1$ and $\mathcal{E}_2$ include only the first two interactions. Now $\sigma = \sigma_\mathbf{1} + \sigma_\mathbf{2}$,
$\sigma_\mathbf{1} = \sigma/2 + (\sigma_\mathbf{1} - \sigma_\mathbf{2})/2$. Similarly for $\sigma_\mathbf{2}$. Since $\sigma_\mathbf{1}$ and $\sigma_2$ occur linearly in the $H_3$, the expectation value of $H_3$ remains unchanged if $\sigma_\mathbf{1}$ and $\sigma_2$ are replaced by $\sigma/2$. Making this replacement and putting $\mathcal{E}_1 = \frac{zr_1}{{r_1}^3} - \frac{\mathbf{r_{12}}}{r_{12}^3}$ and $\mathcal{E}_2 = \frac{zr_2}{{r_2}^3} - \frac{\mathbf{r_{21}}}{r_{21}^3}$, the spin part becomes

$$\frac{1}{4c^2}[\frac{z}{{r_1}^3}\mathbf{r_1} \times \mathbf{p_1} + \frac{z}{{r_2}^3}\mathbf{r_2} \times \mathbf{p_2} + \frac{3}{{r_{12}}^3}(\mathbf{r_1} - \mathbf{r_2}) \times (\mathbf{p_1} - \mathbf{p_2})].\sigma \tag{21}$$

$$= \frac{1}{4c^2}[\frac{z}{{r_1}^3}\mathbf{L_1}.\sigma + \frac{z}{{r_2}^3}\mathbf{L_2}.\sigma - \frac{3}{{r_{12}}^3}(\mathbf{L_{12}} + \mathbf{L_{21}}).\sigma]; \tag{22}$$

$$\mathbf{L_1}.\sigma = {L_+}^1\sigma_- + {L_-}^1\sigma_+ + {L_z}^1\sigma_z, \tag{23}$$

$$\mathbf{L_2}.\sigma = {L_+}^2\sigma_- + {L_-}^2\sigma_+ + {L_z}^2\sigma_z, \tag{24}$$

$$\mathbf{L_{12}}.\sigma = {L_+}^{12}\sigma_- + {L_-}^{12}\sigma_+ + {L_z}^{12}\sigma_z, \tag{25}$$

${L_+}^1 = {L_x}^1 + i{L_y}^1$, ${L_-}^1 = {L_x}^1 - i{L_y}^1$.

Now $L_z = \frac{\hbar}{i}\frac{\partial}{\partial\phi}$.

Again,

$$\mathbf{L_1}.\sigma\begin{pmatrix} \chi_{1,1} \\ \chi_{1,0} \\ \chi_{1,-1} \end{pmatrix} = {L_+}^1\sigma_-\begin{pmatrix} \chi_{1,1} \\ \chi_{1,0} \\ \chi_{1,-1} \end{pmatrix} + {L_-}^1\sigma_+\begin{pmatrix} \chi_{1,1} \\ \chi_{1,0} \\ \chi_{1,-1} \end{pmatrix} + {L_z}^1\sigma_z\begin{pmatrix} \chi_{1,1} \\ \chi_{1,0} \\ \chi_{1,-1} \end{pmatrix},$$

$\sigma_+\begin{pmatrix} \chi_{1,1} \\ \chi_{1,0} \\ \chi_{1,-1} \end{pmatrix}=2\sqrt{2}\begin{pmatrix} 0 \\ \chi_{1,1} \\ \chi_{1,0} \end{pmatrix}$, $\sigma_-\begin{pmatrix} \chi_{1,1} \\ \chi_{1,0} \\ \chi_{1,-1} \end{pmatrix}=2\sqrt{2}\begin{pmatrix} \chi_{1,0} \\ \chi_{1,-1} \\ 0 \end{pmatrix}$,

$\sigma_z\begin{pmatrix} \chi_{1,1} \\ \chi_{1,0} \\ \chi_{1,-1} \end{pmatrix}=2\begin{pmatrix} \chi_{1,1} \\ 0 \\ -\chi_{1,-1} \end{pmatrix}$

The derivation of above transformation relations goes as follows.
$\sigma_\pm = \sigma_{1\pm} + \sigma_{2\pm}$.

Now $\sigma_+ = \sigma_{1+} + \sigma_{2+}$.

In the product space

$$\sigma_+ = (\sigma_{1+} \otimes \mathbf{1} + \mathbf{1} \otimes \sigma_{2+}) \tag{26}$$

which implies

$$\sigma_+(\uparrow\uparrow) = (\sigma_{1+}\uparrow)\uparrow + \uparrow(\sigma_{2+}\uparrow) \tag{27}$$

$\begin{pmatrix} 0 & 1 \\ 0 & 0 \end{pmatrix}\begin{pmatrix} 1 \\ 0 \end{pmatrix}\begin{pmatrix} 1 \\ 0 \end{pmatrix}+\begin{pmatrix} 1 \\ 0 \end{pmatrix}\begin{pmatrix} 0 & 1 \\ 0 & 0 \end{pmatrix}\begin{pmatrix} 1 \\ 0 \end{pmatrix}=0.\begin{pmatrix} 1 \\ 0 \end{pmatrix}+\begin{pmatrix} 1 \\ 0 \end{pmatrix}.0=0$

In the similar manner one can show that
$\sigma_-(\uparrow\uparrow) = 2\sqrt{2}\begin{pmatrix} 0 \\ 1 \end{pmatrix}\begin{pmatrix} 1 \\ 0 \end{pmatrix}+\begin{pmatrix} 1 \\ 0 \end{pmatrix}\begin{pmatrix} 0 \\ 1 \end{pmatrix}=2\sqrt{2}(\downarrow\uparrow + \uparrow\downarrow)$. Using the above transformation of spin vectors one can get,

$$\mathbf{L_1}.\sigma|\chi_{1,1}>= 2\sqrt{2}{L_+}^1\chi_{1,0} + 2\sqrt{2}.0 + 2L_z^1\chi_{1,1} \tag{28}$$

$$\mathbf{L_1}.\sigma|\chi_{1,0}>= 2\sqrt{2}{L_+}^1\chi_{1,-1} + 2\sqrt{2}{L_-}^1\chi_{1,1} + L_z^1.0 \tag{29}$$

$$\mathbf{L_1}.\sigma|\chi_{1,-1}>= 2\sqrt{2}{L_+}^1.0 + 2\sqrt{2}{L_-}^1\chi_{1,0} - 2L_z^1\chi_{1,-1} \tag{30}$$

The spin average of the operator $\mathbf{L_1}.\sigma$ turns out to be

$$\begin{pmatrix} \chi_{11} & \chi_{10} & \chi_{1-1} \end{pmatrix}\begin{pmatrix} 2\sqrt{2}{L_+}^1\chi_{1,0} + 2\sqrt{2}.0 + 2L_z^1\chi_{1,1} \\ 2\sqrt{2}{L_+}^1\chi_{1,-1} + 2\sqrt{2}{L_-}^1\chi_{1,1} + L_z^1.0 \\ 2\sqrt{2}{L_+}^1.0 + 2\sqrt{2}{L_-}^1\chi_{1,0} - 2L_z^1\chi_{1,-1} \end{pmatrix}=\begin{pmatrix} 2L_z^1 & 0 & 0 \\ 0 & 0 & 0 \\ 0 & 0 & -2L_z^1 \end{pmatrix}.$$

Similarly the spin average for the $\mathbf{L_2}.\sigma$ tantamounts to
$\begin{pmatrix} 2L_z^2 & 0 & 0 \\ 0 & 0 & 0 \\ 0 & 0 & -2L_z^2 \end{pmatrix}$.
And finally for $(L_{12} + L_{21}).\sigma$
the spin average turns out to be $\begin{pmatrix} 2(L_z^{12} + L_z^{21}) & 0 & 0 \\ 0 & 0 & 0 \\ 0 & 0 & -2(L_z^{12} + L_z^{21}) \end{pmatrix}$.

So combining all the contributions the diagonal elements of the spin orbit correction for He triplet P state in $J = L = M$ basis can be expressed as

$$\frac{1}{4c^2}[(\int\int \psi_{LL}{}^*({r_1}^{-3}L_{1z} + {r_2}^{-3}L_{2z}) \times \\ \times \psi_{LL}dv_1dv_2) - 3\int\int \psi_{LL}{}^*{r_{12}}^{-3}(L_{12z} + L_{21z})\psi_{LL}dv_1dv_2] \tag{31}$$

And similarly we can write the spin orbit contribution for all the operators.

## 5. CONNECTION BETWEEN THE SPIN ALGEBRA AND QUANTUM COMPUTING

In the early 1980s, Paul Benioff of Argonne National Laboratory and Richard Feynman of the California Institute of Technology began exploring the idea of using quantum-mechanical systems—such as individual atoms—as the building blocks of computation[10]. They demonstrated that, in principle, these tiny structures could function effectively as components in a quantum computer. Their work also introduced the concept of "quantum logic gates," proposing that computation could follow the fundamental rules of quantum mechanics.

To calculate spin-spin and spin-orbit interaction in Breit Hamiltonian (3) by linear algebra, we actually measure spin observables using state vector representation in quantum mechanics. On the classical (silicon based )computers information are stored by the bits 0 or 1. So for two particles the classical gates can store one of the four states at a time; 00, 01,10 or 11 whereas superposition principle allows quantum computers(atoms or subatomic particles) to store all four states simultaneously. This makes the quantum computers faster than classical ones. Bits in classical computers are equivalent to qubits in quantum computers. Quantum computers make use of the superposition principle which allows a system to be in 0 and 1 state simultaneously. For n q-bits there will be $2^n$ states or information. Quantum computers also exploit one more unique quantum property namely, quantum entanglement where a property of a particle can be linked to another regardless of the distance between them.

Qubits are atoms, ions and molecules. Suppose an electron is subjected to some electromagnetic field and spin of the electron is aligned with the field then it is said to be in the spin up state and in the opposite situation it will have a spin down state. The electron's spin can be changed by directing a pulse of energy to the particle by a laser beam/microwave. Each time the pulse is delivered, the electron spin state changes. If the half of the required energy is delivered to flip from one state to the other the electron will enter a superposition state and it will remain in that state until it is observed and measured.

**General Quantum States** If in a k-dimensional quantum system we have $|1>, |2>, ......, |k>$ as basis vectors the general state can be represented as $\alpha_1|1> +\alpha_2 > |2> +..... + \alpha|k>$ with $|\alpha_1|^2 + |\alpha_2|^2 + ... + |\alpha_k|^2 = 1$. $2^k$ dimensional system can be constructed as a tensor product of $k$ quantum bits.

**Unitary transforms**: Linear transformations that preserve vector norm.

**General Measurements**:Let $|\psi_0>$, $|\psi_1>$ be two orthogonal one-qubit states, the $|\psi >= \alpha_0|\psi_0> +\alpha_1|\psi_1>$ Measuring $|\psi>$ gives $|\psi_i>$ with probability $|\alpha_i|^2$. This is equivalent to mapping $|\psi_0>$, $|\psi_1>$ to $|0>$ and $|1>$ then measuring. In section 3 we derived the matrix elements due to spin-spin and spin-orbit interactions for He (with spin half electrons) and we used the following basis states: ↑↑, ↓↑, ↑↓ and ↓↓. Or in other words the general spin state of a He atom can be written as $|S_{12} >= C_+ \uparrow\uparrow + C_- \downarrow\downarrow + C_0\frac{1}{\sqrt{2}}(\uparrow\downarrow + \downarrow\downarrow)$.

## 6. RESULTS AND DISCUSSIONS

In this paper using Naimark's extension formula we upgrade the spin-spin and spin-orbit operators in the extended Hilbert space and specifically calculate all the matrix elements connected to the spin-spin and spin-orbit operators in Breit's Hamiltonian for the triplet P-state of helium. In Section 4, we present our linear algebraic results pertaining to these corrections. Specifically, subsection 4.4 and 4.5 deal with the spin-spin and spin-orbit corrections respectively. In subsection 4.4 and 4.5 Eqs.(6-19) represent our results for spin averages for spin-spin interaction and Eqs.(20-30) represent the results for the spin averages for spin-orbit interactions respectively. Our final results in these two cases Eq.(19) and Eq.(30) exactly match with the previous results[5-7] obtained from conventional quantum mechanics.

## 7. CONCLUSIONS AND OUTLOOK

This algebra of spin systems underpins fundamental interactions in qunatum mechanics. In many realistic scenarios, spin operators are accessed only partially, leading to effective descriptions via POVMs. Naimark's extension theorem ensures that these can always be embedded into full projective descriptions on enlarged spaces. This provides a powerful conceptual and computational framework linking quantum measurements, operator theory, and spin algebra in multi-particle systems.

This work is a gentle but rigorous introduction to quantum computing with linear algebraic approach where qubits are state vectors and quantum gates are matrices. In this work we have been able to calculate the matrix elements for the spin dependent terms in the Breit Hamiltonian by spin algebra for He, the simplest many body system as an alternative to conventional quantum mechanics. It enables us to extend this linear algebraic method to multi-electron systems for developing quantum gate based on spin algebra and investigate quantum circuit design using spin qubits and compare the performance of spin-based qubits with traditional qubits in terms of algorithmic efficiency. One can use this spin algebra to simulate electron interactions in condensed matter physics problems. It can also help in exploring to predict material properties or simulate quantum many-body effects that are challenging for classical computers. It can be further utilized to develop spin-based error correction for small quantum systems. Two other directions it can be extended are (i) studying the role of spin liquids and topologically ordered phases in the context of quantum computing (ii) investigating potential for using topologically protected spin qubits for fault tolerance. In several occasions quantum spin models can be applied in a meaningful ways:

(1) Quantum spin models describe collection of qubits in information theory.

(2) It can serve as a toy model in theories related to quantum gravity.

(3) It can offer new insights in functional analysis(theory of operators) and representation theory(quantum groups)

This work can immediately be extended in two different directions: (1) Following tensor algebra spin averages can be calculated for other few-electron systems. (2) One can use these spin algebraic results and calculate the spin-spin and spin-orbit corrections on a quantum computer to compare the results with those obtained on a silicon based computers [12, 13].

The application of Naimark's Extension Theorem in computing matrix elements of spin-spin and spin-orbit operators reveals their deep connection to generalized measurement theory. These operators, which do not correspond to jointly measurable observables, can be interpreted as effective measurements arising from projective operations on a larger Hilbert space. This not only aids in computational simplification but also provides conceptual clarity regarding the role of ancilla systems, nonlocal correlations, and measurement-induced transformations in two-electron quantum systems.

The matrix elements arising from spin algebra, such as those in the Breit Hamiltonian, influence Quantum error corrections(QEC)[16] and fault-tolerant quantum computation by providing insight into the nature of errors (like spin flips or decoherence) and allowing for the design of tailored QEC codes that specifically address the types of errors induced by these spin interactions. It also helps to optimize the fault-tolerant gate construction by understanding how these interactions affect qubits during quantum gates. and enhances the understanding of the error thresholds and noise models to ensure that quantum computations are resilient against the types of errors these interactions could cause. By incorporating these matrix elements into the design of quantum error correction and fault-tolerant circuits, one can ensure that quantum computations remain accurate even in the presence of spin-dependent errors, improving the reliability of the quantum computing system.

The matrix elements obtained through the linear algebraic approach in this study have been previously calculated using conventional quantum mechanics methods [5-7, 11]. The author's prior work on relativistic corrections [12, 13], performed on a silicon-based classical computer, utilized quantum Monte Carlo simulations with path integrals. In this paper, the linear algebraic approach is adopted to make the calculations feasible on a quantum computer. Furthermore, simple circuits using quantum logic gates are proposed for computing the matrix elements. This approach opens the possibility for benchmarking results from both classical and quantum computers (future work), allowing for a direct comparison of their performance.

The application of *Naimark's Extension Theorem* in deriving their matrix elements opens up a window into the structure of quantum measurements in such composite systems. This study explores the spin algebra of two-electron systems, using tensor products . Our results align with conventional quantum mechanical approaches, providing a foundation for quantum logic gates, algorithms, and error corrections. These findings open the avenues for advancements in spin-based quantum systems, including new algorithms and simulations.

**Declaration of interests:** The sole author has no conflicts of interest to declare. There is no financial interest to report.

**Data availability statement:** No data in this publication is to be made available under the study-participant privacy protection clause.

## REFERENCES

[1] M.A. Naimark, Izv. Acad. Nauk SSSR Ser. Mat. **4**, 277 (1940).

[2] F. Riesz, and B.S. Nagy, *Functional Analysis*, (Dover, New York, 1990)

[3] N.I. Akhizer, and I.M. Glazman, *Theory of Linear Operators in Hilbert Space*, (Ungar, New York, 1963).

[4] V. Paulsen, *Completely Bounded Maps and Operator Algebras*, (Cambridge University Press, Cambridge, 2020).

[5] G. Araki. Proc. Phys. Math. Soc. Japan, **19**, 128 (1937). https://doi.org/10.11429/ppmsj1919.19.0_128

[6] G. Araki, Phys.Rev. **101**, 1410 (1956). https://doi.org/10.1103/PhysRev.101.1410

[7] G. Araki, M. Ohta and K. Mano, Phys. Rev. **116**, 651 (1959). https://doi.org/10.1103/PhysRev.116.651

[8] P.A.M. Dirac, *Priciples of Quantum Mechanics*, (Oxford U.P., Oxford, 1958).

[9] H. Bethe, and E.E. Saltpeter, *Quantum Mechanics of one or two electron atoms*, (Platinum Publishing Corporation, New York, 1977).

[10] R.P. Feynman, Int. J. Th. Phys. **21**, 467 (1982). https://doi.org/10.1007/BF02650179

[11] S.D. Kenny, G. Rajagopal, and R.J. Needs, Phys. Rev. A, **51**, 1898 (1982). https://doi.org/10.1103/PhysRevA.51.1898

[12] S.A. Alexander, Sumita Datta, and R L. Coldwell, Phys. Rev. A, **81**, 032519 (2010). https://doi.org/10.1103/PhysRevA.81.032519

[13] Sumita Datta, S.A. Alexander, and R.L. Coldwell, Int. J. Qu. Chem. **112**, 731 (2012). https://doi.org/10.1002/qua.23039

[14] C. Monroe, D.M. Meekhof, B.E. King, W.M. Itano, and D.J. Wineland, Phys. Rev. Lett. **75**, 4714 (1995). https://doi.org/10.1103/PhysRevLett.75.4714

[15] A. Steane, Rep. Prog. Phys. **61**, 117-173 (1998). https://doi.org/10.1088/0034-4885/61/2/002

[16] E.C.R. da Rosa, and C. Lima, arXiv:2210.15506 v1[quant-ph] 27 Oct. 2022. https://doi.org/10.48550/arXiv.2210.15506

[17] R.V. Kadison, *Contemporary Mathematics*, **167**, 21 (1994).

[18] R. Beneduci, J. Phys.:Conference Series,**1638**,012006(2020) https://doi.org/10.1088/1742-6596/1638/1/012006

[19] B. Daribaye, A. Mukhanbet, N. Azatbekuly and T. Imankulov, Algoritms,**17**,327(2024) URL

[20] M.A. Naimark, and S.V. Fomin, Continuous direct sums of Hilbert spaces and some of their applications. Ann. Math. Soc. Transl. Ser. 2, 5, 35 (1957). URL

[21] M.G.A. Paris, The Eur. Phys. J. Special Topics, **203**, 61 (2012). https://doi.org/10.1140/epjst/e2012-01535-1

[22] K. Erdmann, and M.J. Wildon, *Introduction to Lie Algebra. Mathematical Institute University*, (Oxford, UK, 2006).

[23] Casper VAN HAL, An introduction into Lie Group, Lie Algebra, Representations and Spin, Double Bachelor's Thesis, (Mathematics and Physics, Utrecht University, 2021.

[24] R. Clinton, J. Bub, and H. Halvorson, Foundations of Physics, **33**, 1561 (2003). https://doi.org/10.1023/A:1026056716397

[25] J.H. Yoo, Lie Groups, Lie Algebras, and Applications in Physics, (2015). https://api.semanticscholar.org/CorpusID:43265836

## СПІНОВА АЛГЕБРА ТА РОЗШИРЕННЯ НАЙМАРКА: НАВЧАЛЬНИЙ ПІДХІД ІЗ ПРИКЛАДАМИ

**Суміта Датта**[1,2]
[1]*Кафедра чистої та прикладної математики, Університет Альянс, Бенгалуру 562 106, Індія*
[2]*Кафедра фізики, Техаський університет в Арлінгтоні, Техас 76019, США*

Під час аналізу двоелектронних систем до взаємодій, що нас цікавлять, часто належать спін-спіновий оператор $\vec{S}_1 \cdot \vec{S}_2$ та спін-орбітальний оператор $\vec{L} \cdot \vec{S}$. Коли ці оператори діють на заплутані або нерозрізнені частинки, їх вимірювання та фізична інтерпретація можуть виходити за межі стандартної проективної структури. Цей посібник знайомить з алгебраїчною структурою спінових взаємодій у двох електронних квантових системах та встановлює її концептуальний та математичний зв'язок з *Теоремою розширення Наймарка*. На основі явних прикладів для двоелектронних систем ми демонструємо, як виникають спінові оператори у редукованих просторах Гільберта, і як *Теорема розширення Наймарка* забезпечує формальну основу для їх поширення на проективні вимірювання у розширених просторах. Застосування *Теореми розширення Наймарка* при виведенні їх матричних елементів відкриває вікно у структуру квантових вимірювань у таких складних системах.

**Ключові слова:** *розширення Наймарка; Гільбертів простір; алгебра Лі; гамільтоніан Брейта; квантові обчислення*

East European Journal of Physics. **4**. 101–111 (2025)
DOI: 10.26565/2312-4334-2025-4-09 ISSN 2312-4334

# ANISOTROPIC DARK ENERGY COSMOLOGY IN THE FRAMEWORK OF $f(R, L_m)$ GRAVITY

**A.S. Khan**[1*], **K.N. Pawar**[1,2], **I.I. Khan**[1,3]
[1]*Prof Ram Meghe College of Engineering and Management, Badnera, MS, India*
[2]*Shri Shivaji Science College, Nagpur, MS, India*
[3]*Prof Ram Meghe Institute of Technology and Research, Badnera, MS, India*
**Corresponding Author e-mail: alimkhan3101@gmail.com*

Received September 3, 2025; revised October 29, 2025; in final form November 11, 2025; accepted November 13, 2025

In this paper, we investigated the Locally Rotationally Symmetric (LRS) Bianchi Type-I cosmological model with dark energy in the framework of $f(R, L_m)$ gravity theory, where $R$ is the Ricci scalar and $L_m$ is the matter Lagrangian. Using the functional form $f(R, L_m) = \frac{R}{2} + L_m^{\alpha} + \beta$ with $L_m = \rho$,and applying the special law of variation for the Hubble parameter, we derived exact solutions to the field equations and analyzed the physical and dynamical properties of the universe. Our results show that the model exhibits accelerated expansion consistent with the observational data, with the energy density decreasing and the deceleration parameter transitioning from positive to negative values. The anisotropy parameter initially approaches zero but increases with time for $n > 0.5$, indicating the evolution from isotropy to anisotropy. These findings provide insights into dark energy behavior within modified gravity frameworks and offer testable predictions for cosmological observations.

**Keywords:** *LRS Bianchi Type-I; Dark Energy; Cosmic Time*

**PACS:** specify the PACS code(s) here

## 1. INTRODUCTION

The General Theory of Relativity (GTR) forms the fundamental framework of modern cosmology, explaining gravitation as a manifestation of spacetime curvature generated by the presence of matter and energy. A comprehensive formulation of GTR and its cosmological applications can be found in the classical reference by Weinberg [1].Although GTR has been remarkably successful in describing various gravitational phenomena, astronomical observations of distant Type Ia supernovae have revealed that the present universe is expanding at an accelerated rate [2, 3, 4, 5, 6]. This unexpected result suggests the existence of an unknown form of energy, commonly referred to as dark energy, which is estimated to account for nearly 68% of the total energy density of the universe [7, 8, 9, 10]. Such observations indicate that the standard cosmological model based solely on GTR may require refinement or modification to consistently explain the observed late-time cosmic acceleration. To address this challenge, various modified theories of gravity have been developed as alternatives to dark energy. One of the promising approaches is the f(R,Lm) gravity theory proposed by Harko and Lobo [11], which generalizes the conventional f(R) gravity by introducing an explicit coupling between the Ricci scalar R and the matter Lagrangian density Lm .This framework provides a richer geometric structure and allows new possibilities for understanding the interaction between matter and curvature in explaining the accelerated expansion of the universe.

Research on anisotropic cosmological models with dark energy in the framework of $f(R, L_m)$ gravity has emerged as a critical area of inquiry due to its potential to address the accelerating expansion of the universe and the limitations of standard general relativity (GR) in explaining dark energy phenomena [12, 13]. Since the introduction of $f(R)$ gravity as a modification of the Einstein-Hilbert action [14], the field has evolved to incorporate more general couplings between curvature and matter, notably through the $f(R, L_m)$ gravity theory [15]. This framework allows for non-minimal interactions between geometry and matter, which can lead to novel cosmological dynamics, including anisotropic effects relevant to early universe conditions [16]. Observational data from type Ia supernovae, cosmic microwave background, and baryon acoustic oscillations have reinforced the significance of exploring such models to better understand cosmic acceleration and anisotropy [17].

The specific problem addressed involves constructing and constraining anisotropic cosmological models within $f(R, L_m)$ gravity that can accommodate dark energy effects and observational data [18, 19]. Despite progress, a knowledge gap persists regarding the precise role of anisotropy and bulk viscosity in these models, as well as the impact of different functional forms of $f(R, L_m)$ on cosmic evolution [20, 21]. Competing perspectives exist on whether dark energy should be modeled as a quintessence-like field or phantom energy within this framework, with some studies favoring quintessence behavior and others indicating phantom-like characteristics.This review aims to clarify the theoretical underpinnings and observational viability of these models, addressing the identified gaps and providing a comprehensive understanding of their cosmological implications [22, 23]. The consequences of this gap include uncertainties in predicting the universe's late time behavior and reconciling theoretical models with high-precision observational constraints [24].

---

***Cite as:*** A.S. Khan, K.N. Pawar, I.I. Khan, East Eur. J. Phys. 4, 101 (2025), https://doi.org/10.26565/2312-4334-2025-4-09

Recently Shambel et al. [25] have focused on the late-time accelerated expansion of the universe and cosmic structure evolution within the $f(R, L_m)$ gravity model, rather than the early universe. Romanshu Garg and G.P. Singh [26] analyzed cosmological parameters and the present age of the universe, providing insights into the model's implications for cosmic evolution. Y.D. Devi et al [27] have studied on an accelerating cosmological model, deriving the Hubble parameter and analyzing parameters such as the deceleration parameter, jerk, and snap at present times. It derives Friedmann-like equations for two non-linear models, analyzing the effects of model parameters on the equation of state, pressure, and energy density. V. Patil et al. [28] have done on the late-time acceleration of the Universe within the $f(R, L_m)$ gravity framework, rather than the early universe. Shukla et al. [29] primarily focused on the Friedmann-Lemaitre-Robertson-Walker (FLRW) model in $f(R, L_m)$ gravity, analyzing the transition from deceleration to acceleration in the universe. J.K. Singh and Shaily [30] have studied on the late-time behavior of the universe in the context of $f(R, L_m)$ gravity, rather than the early universe. It investigates the transition from deceleration to acceleration phases, showing that the model behaves like ΛCDM at late times. Pawar et al.[31] have focused on the expansion of the universe in $f(T)$ gravity and derived the Hubble parameter in terms of redshift and examines the equation of state parameter, energy density, and pressure. Young Jin Suh et al. [32] have investigated protectively flat perfect fluid spacetime solutions in $f(R, L_m)$ gravity, focusing on energy conditions and their relation to the Ricci scalar.

The functional form of $f(R, Lm)$ gravity has been extended to related theories such as $f(R, T)$ and $f(Q)$ gravity, incorporating trace of energy-momentum tensor or non-metricity scalar, broadening the functional diversity [33]. Furthermore, alternative formulations inspired by logarithmic corrections, Born–Infeld structures, and holographic dark energy have also been explored, highlighting the continuous efforts to enhance the physical viability and observational consistency of such models [34, 35]. Several studies have investigated cosmological models with variable anisotropy parameters or within different Bianchi classifications, such as Bianchi type-III and type-$VI_0$, revealing diverse evolutionary patterns of anisotropy in the universe [36, 37]. While many theoretical and reconstruction-based works provide valuable insights into the role of anisotropy and modified gravity, some lack direct confrontation with observational datasets. However, these studies establish a strong foundation for future comparisons with astrophysical data [38, 39]. In most models, the focus remains confined to the contributions of modified gravity terms and conventional matter fields, primarily analyzing geometric features and dark energy dynamics [40].

In summary, the body of literature underscores that matter-curvature coupling in $f(R, Lm)$ gravity significantly influences anisotropic cosmological evolution and dark energy dynamics, yielding models capable of describing late-time acceleration with evolving equations of state. The inclusion of bulk viscosity further enriches the phenomenology, enhancing the viability of anisotropic models. However, challenges persist in capturing fully dynamical anisotropy, achieving consistent observational integration of anisotropic effects, and expanding the functional diversity of $f(R, L_m)$ to encompass broader physical scenarios. Future research addressing these gaps could sharpen understanding of anisotropic dark energy models in modified gravity and their cosmological implications

This work is structured as follows: In Section 2 we give a brief account of the $f(R, L_m)$ gravity formalism and the field equations. Anisotropic cosmology using LRS Bianchi I metric is discussed in Section 3. Section 4 discusses the type of models and solutions in which this study is centered. In Section 5 we present the results with particular emphasis on the physical consequences and observational predictions. Last but not least; Section 6 gives the conclusion and research recommendations.

## 2. $f(R, L_m)$ GRAVITY AND FIELD EQUATION

The action integral for the framework of f (R,Lm ) interpreted with the matter Lagrangian density Lm and the Ricci scalar R is given as

$$S = \int f(R, Lm)\sqrt{-g}dx^4 \tag{1}$$

where $f(R, Lm)$ is arbitrary function of Ricci scalar R and matter Lagrangian $L_m$. By contracting the Ricci tensor $R_{mn}$, one may get the Ricci scalar $R$,

$$R = g^{ij}R_{ij} \tag{2}$$

where, the Ricci tensor is defined by,

$$R_{ij} = -\partial_\lambda \Gamma^\lambda_{ij} + \partial_j \Gamma^\lambda_{i\lambda} - \Gamma^\lambda_{\lambda\sigma}\Gamma^\sigma_{ij} + \Gamma^\lambda_{j\sigma}\,\Gamma^\sigma_{i\lambda} \tag{3}$$

Here, $\Gamma^\alpha_{\beta\gamma}$ represents the components of well-known Levi-Civita connection defined by

$$\Gamma^\alpha_{\beta\gamma} = \frac{1}{2}g^{\alpha\lambda}\left(\frac{\partial g_{\lambda\beta}}{\partial x^\gamma} + \frac{\partial g_{\lambda\gamma}}{\partial x^\beta} - \frac{\partial g_{\beta\gamma}}{\partial x^\lambda}\right) \tag{4}$$

The corresponding field equations of $f(R, L_m)$ gravity are obtained by varying the action (1) for metric $g_{ij}$ is given by,

$$f_R(R, L_m)R_{ij} + \left(g_{ij}\nabla_i\nabla^i - \nabla_i\nabla_j\right) f_R(R, L_m) - \frac{1}{2}\left[f(R, L_m) - f_{L_m}(R, L_m)L_m\right] g_{ij} = \frac{1}{2}f_{L_m}(R, L_m)T_{ij} \tag{5}$$

Where, $f_R(R,L_m)=\frac{\delta f(R,L_m)}{\delta R}$, $f_{L_m}(R,L_m)=\frac{\delta f(R,L_m)}{\delta L_m}$.Here covariant derivative is represented by $\nabla_i$ and the energy momentum tensor $T_{ij}$ can be expressed as,

$$T_{ij}=-\frac{2}{\sqrt{-g}}\frac{\delta\left(\sqrt{-g}L_m\right)}{\delta g^{ij}}=g_{ij}L_m-2\frac{\delta L_m}{\delta g^{ij}} \tag{6}$$

Now, from the explicit form of the field equation (5), the covariant divergence of Energy momentum tensor $T_{ij}$ can be obtained as,

$$\nabla^i T_{ij}=2\nabla^i\ln\left[f_{L_m}(R,L_m)\right]\frac{\delta L_m}{\delta g_{ij}} \tag{7}$$

The relation between the trace of energy momentum-tensor $T$, Ricci scalar $R$, and the Lagrangian density of the matter $L_m$ obtained by contracting the field equation (5)

$$f_R(R,L_m)R+3\nabla_i\nabla^i f_R(R,L_m)-2\left[f(R,L_m)-f_{L_m}(R,L_m)L_m\right]=\frac{1}{2}f_{L_m}(R,L_m)T \tag{8}$$

The relation between the trace of the energy momentum tensor $T=T_{ij}$, $L_m$, and $R$ can be established by taking account of the previously mentioned equation.

## 3. METRIC AND FIELD EQUATION IN $f(R,L_m)$ GRAVITY

The spatially homogeneous and anisotropic LRS Bianchi type $I$ spacetime can be written as,

$$ds^2=-dt^2+X^2dx^2+Y^2(dy^2+dz^2) \tag{9}$$

Where $X$ and $Y$ are the metric potential that are the functions of cosmic time $t$ only.

The Ricci scalar for LRS Bianchi-$I$ spacetime can be expressed as

$$R=-2\left[\frac{\ddot{X}}{X}+2\frac{\ddot{Y}}{Y}+2\frac{\dot{X}\dot{Y}}{XY}+\frac{\dot{Y}^2}{Y^2}\right] \tag{10}$$

The overhead dot (.) denotes the derivative with respect to time $t$. The spatial volume $V$ of the universe is defined as

$$V=XY^2 \tag{11}$$

The average scale factor

$$a(t)=\left(XY^2\right)^{\frac{1}{3}} \tag{12}$$

The generalized mean Hubble parameter $H$, which describes the space-time expansion rate, can be stated as

$$H=\frac{1}{3}(H_1+H_2+H_3)=\frac{1}{3}\left(\frac{X}{\dot{X}}+\frac{2Y}{\dot{Y}}\right) \tag{13}$$

where $H_1$, $H_2$, $H_3$ are the directional Hubble's parameters in the direction of the $x-, y-, andz-axes$, respectively. In order to figure out whether the models approach isotropy or not, we define the expansion's anisotropy parameter as

$$A_m=\frac{1}{3}\sum_{i=1}^{3}\left(\frac{H_i}{H}-1\right)^2 \tag{14}$$

The expansion scalar and shear scalar are defined as follows,

$$\theta=\frac{\dot{X}}{X}+2\frac{\dot{Y}}{Y} \tag{15}$$

$$\sigma^2=\frac{3}{2}A_mH^2 \tag{16}$$

The deceleration parameter (DP) is

$$q=-1+\frac{d}{dt}\left(\frac{1}{H}\right)=-\frac{a\dot{a}}{a^2\ddot{a}} \tag{17}$$

Let us take the matter that contains the energy momentum tensor for dark energy, which is of the form

$$T_{ij}=(p+\rho)u_iu_j+pg_{ij} \tag{18}$$

Where $\rho$ is the energy density and $p$ is the pressure of the fluid. Where $u^i = (1,0,0,0)$ is the four-velocity vector in co-moving coordinates which satisfying $u_i u^i = -1$. The EoS parameter for quark matter is defined as

$$p = \omega\rho \quad 0 \leq \omega \leq 1 \tag{19}$$

By using the equation (16), the field equation (5) can be written as,

$$\left(\frac{\ddot{X}}{X} + 2\frac{\dot{X}\dot{Y}}{XY}\right) f_R + \frac{1}{2}\left(f - f_{L_m} L_m\right) + 2\frac{\dot{Y}}{Y}\dot{f}_R + \ddot{f}_R = -\frac{1}{2} f_{L_m} p \tag{20}$$

$$\left(\frac{\ddot{Y}}{Y} + \frac{\dot{Y}^2}{Y^2} + \frac{\dot{X}\dot{Y}}{XY}\right) f_R + \frac{1}{2}\left(f - f_{L_m} L_m\right) + \left(\frac{\dot{X}}{X} + \frac{\dot{Y}}{Y}\right)\dot{f}_R + \ddot{f}_R = -\frac{1}{2} f_{L_m} p \tag{21}$$

$$\left(\frac{\ddot{X}}{X} + 2\frac{\ddot{Y}}{Y}\right) f_R + \frac{1}{2}\left(f - f_{L_m} L_m\right) + \left(\frac{\dot{X}}{X} + 2\frac{\dot{Y}}{Y}\right)\dot{f}_R = \frac{1}{2} f_{L_m} \rho \tag{22}$$

## 4. COSMOLOGICAL $f(R, L_m)$ MODEL

To examine the dynamics of Universe, we employ the functional form of $f(R, L_m)$ gravity as,

$$f(R, L_m) = \frac{R}{2} + L_m^{\alpha} + \beta \tag{23}$$

where $\alpha$ and $\beta$ are free parameters and can be retained as GR for $\alpha = 1$ and $\beta$=0

For $f(R, L_m)$ model,the matter Lagrangian $L_m$ is generalized, and the coupling with curvature $R$ produces extra terms that can mimic dark energy behavior, we have to consider $L_m = \rho$ [41]

Using the above particular choice of $L_m$, the field equations (20), (21) and (22) becomes,

$$\frac{2\ddot{Y}}{Y} + \frac{\dot{Y}^2}{Y^2} - (1-\alpha)\rho^{\alpha} - \beta = \alpha\rho^{\alpha-1} p \tag{24}$$

$$\frac{\ddot{X}}{X} + \frac{\ddot{Y}}{Y} + \frac{\dot{X}\dot{Y}}{XY} - (1-\alpha)\rho^{\alpha} - \beta = \alpha\rho^{\alpha-1} p \tag{25}$$

$$\frac{\dot{Y}^2}{Y^2} + 2\frac{\dot{X}\dot{Y}}{XY} - \beta = (1-2\alpha)\rho^{\alpha} \tag{26}$$

The field equations (24), (25) and (26) are three independent differential equations with four unknowns: $X, Y, \rho$ and $p$. Hence, to determine solutions, we have to use physically plausible conditions.

Berman and Gomide [42] indicate that there exists a connection between the Hubble parameter (H) and average scale factor (a) given as,

$$H = la^{-n} = l\left(XY^2\right)^{-\frac{n}{3}} \tag{27}$$

Where $l > 0$ and $n \geq 0$ are constants.

Now, from equations (13) and (27), we get the following.

$$\dot{a} = la^{-n+1} \tag{28}$$

$$\ddot{a} = -l^2(n-1)a^{-2n+1} \tag{29}$$

From equations (16) we obtain

$$q = n - 1 \tag{30}$$

Now using equations (27) and (30), the solution of equation (17) gives the law of variation of the average scale factor of the form,

$$a = (nlt)^{\frac{1}{n}}, \quad n \neq 0 \tag{31}$$

## 5. SOLUTION OF THE FIELD EQUATIONS

The field equations (24)-(26) reduce to a system of three non-linear equations in four unknown parameters $X, Y, \rho$ and $p$. Hence to find the determination solution of the system , we used the law of variation [42]. Now from equations (24) and (25), we get

$$\frac{\ddot{Y}}{Y} - \frac{\ddot{X}}{X} + \frac{\dot{Y}^2}{Y^2} - \frac{\dot{X}\dot{Y}}{XY} = 0 \tag{32}$$

On integrating, we get

$$\frac{\dot{Y}}{Y} - \frac{\dot{X}}{X} = \frac{c_1}{XY^2} \tag{33}$$

Where $c_1$ is the constant of integration Using equation (12) in equation (33) and integrating again, we get

$$\frac{Y}{X} = c_2 \exp\left(\int \frac{c_1}{a^3}\, dt\right) \tag{34}$$

Multiplying and divide by $Y^2$,we get

$$\frac{Y^3}{XY^2} = c_2 \exp\left(\int \frac{c_1}{a^3}\, dt\right) \tag{35}$$

Using equation (12), $a^3 = XY^2$ in equation (35), we get

$$Y^3 = a^3 c_2 \exp\left(\int \frac{c_1}{a^3}\, dt\right) \tag{36}$$

The metric function $X$ and $Y$ in terms of the average scale factor $a(t)$ are given by

$$X(t) = c_2^{-\frac{2}{3}} a \exp\left(-\frac{2c_1}{3} \int a^{-3}\, dt\right) \tag{37}$$

$$Y(t) = c_2^{\frac{1}{3}} a \exp\left(\frac{c_1}{3} \int a^{-3}\, dt\right) \tag{38}$$

Now using equation (31) in equations (37) and (38), we get

$$X(t) = c_2^{-\frac{2}{3}} (nlt)^{\frac{1}{n}} \exp\left(\frac{-2c_1}{3l(n-3)} (nlt)^{\frac{n-3}{n}}\right) \tag{39}$$

$$Y(t) = c_2^{\frac{1}{3}} (nlt)^{\frac{1}{n}} \exp\left(\frac{c_1}{3l(n-3)} (nlt)^{\frac{n-3}{n}}\right) \tag{40}$$

Where $n \neq 3$

Putting the values of $X$ and $Y$ in eqn (9),we obtained the exact solution .

$$ds^2 = -dt^2 + c_2^{-\frac{1}{3}} (nlt)^{\frac{2}{n}} \left(\exp\left(\frac{-2c_1}{3l(n-3)} (nlt)^{\frac{n-3}{n}}\right)\right)^2 dx^2 + c_2^{\frac{2}{3}} (nlt)^{\frac{2}{n}} \left(\exp\left(\frac{c_1}{3l(n-3)} (nlt)^{\frac{n-3}{n}}\right)\right)^2 (dy^2 + dz^2) \tag{41}$$

which gives the desired cosmological model.

From the equations (25) and (26), with the help of metric potential, the energy density and pressure of dark energy are given by

$$\rho = \left[\frac{1}{1-2\alpha} \left(-\frac{c_1^2}{3} (nlt)^{-\frac{6}{n}} + \frac{3}{n^2t^2} - \beta\right)\right]^{\frac{1}{\alpha}} \tag{42}$$

$$p = -\frac{\dfrac{4c_1 (nlt)^{-\frac{3}{n}}}{nt} - \dfrac{2c_1^2}{3} (nlt)^{-\frac{6}{n}} + \dfrac{2n+9}{n^2t^2} + \dfrac{\alpha}{1-2\alpha}\Big( -\dfrac{c_1^2}{3} (nlt)^{-\frac{6}{n}} + \dfrac{3}{n^2t^2} - \beta\Big)}{\alpha \left[\dfrac{1}{1-2\alpha}\Big( -\dfrac{c_1^2}{3} (nlt)^{-\frac{6}{n}} + \dfrac{3}{n^2t^2} - \beta\Big)\right]^{\frac{\alpha-1}{\alpha}}} \tag{43}$$

Using equations (42) and (43), the equation of state (EoS) for dark energy is given as

$$w = -\frac{\Big((1-2\alpha)\Big[4c_1 nt (nlt)^{-\frac{3}{n}} - \frac{2c_1^2}{3} (nt)^2 (nlt)^{-\frac{6}{n}} + 2n + 9\Big] + \alpha\Big( -\frac{c_1^2}{3} (nt)^2 (nlt)^{-\frac{6}{n}} - \beta (nt)^2 + 3\Big)\Big)}{\alpha\Big( -\frac{c_1^2}{3} (nt)^2 (nlt)^{-\frac{6}{n}} - \beta (nt)^2 + 3\Big)} \tag{44}$$

## 6. SOME PHYSICAL PARAMETERS

The spatial volume $V$ of the universe is given as

$$V = a^3(t) = (nlt)^{\frac{3}{n}} \tag{45}$$

The average Hubble parameter

$$H = (nt)^{-1} \tag{46}$$

The dynamical scalar expansion $\theta$ and shear scalar $\sigma^2$ are

$$\theta = 3(nt)^{-1}, \tag{47}$$

$$\sigma^2 = c_1^2(nlt)^{\frac{-6}{n}} \tag{48}$$

The average anisotropic parameter

$$A_m = \frac{2c_1^2}{l^2}(nlt)^{\frac{2n-1}{n}} \tag{49}$$

## 7. FIGURES

In this section, to better understand the behavior of our cosmological model, we present plots of various physical and dynamical parameters as functions of cosmic time.

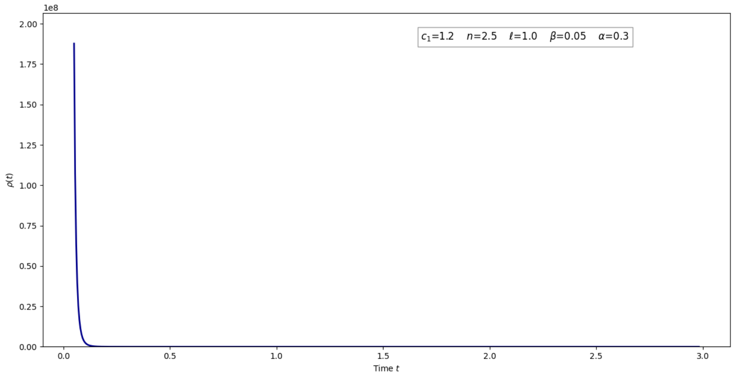

**Figure 1.** Variation of Energy Density

The graph indicates that the universe started with a very high density and then decreases rapidly, reflecting the expected expansion dynamics.

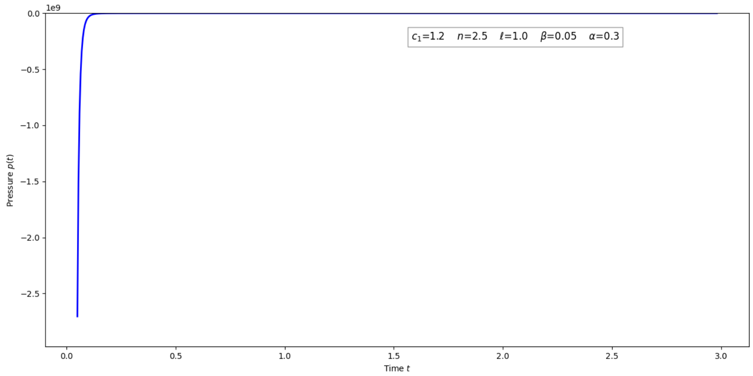

**Figure 2.** Variation of Pressure

The graph indicates that the universe begins with a strong negative pressure (accelerating expansion), but over time the pressure diminishes and tends toward zero, suggesting a transition toward a less repulsive, more stable cosmic state.

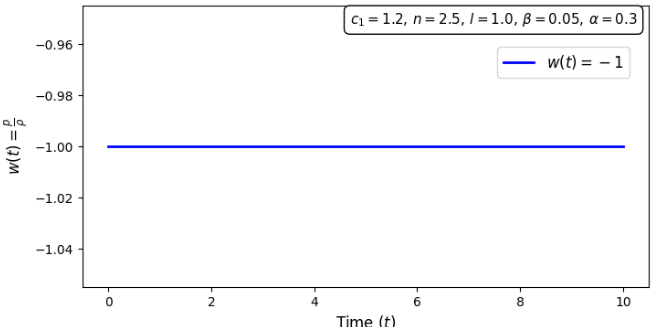

**Figure 3.** Equation of state parameter

The graph shows that the equation of state parameter $\omega = -1$ through out the cosmic time.This corresponds to vacuum energy or cosmological constant $\Lambda$.

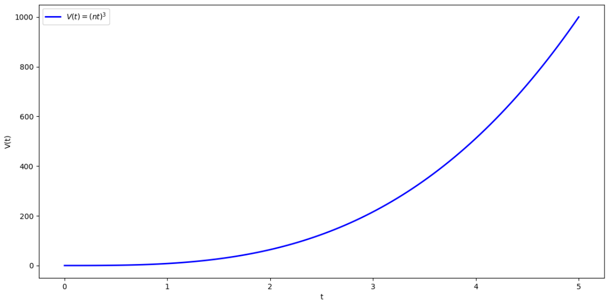

**Figure 4.** Variation of Spatial Volume $V$

The plot shows that the spatial volume of the universe expands rapidly as time increases. It begins at t=0 (Big Bang singularity) and indicates cosmic expansion.

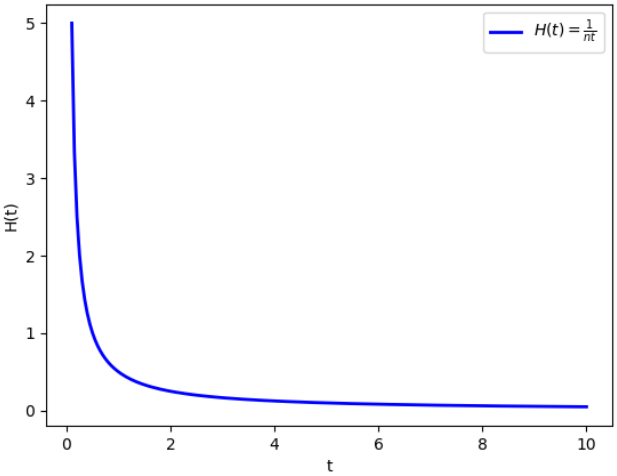

**Figure 5.** Variation of Hubble Parameter

Expansion rate of the universe is very high at early times ($t \longrightarrow 0$) but decreases as the universe grows late time.It never becomes negative, but approaches zero as $t \longrightarrow \infty$.

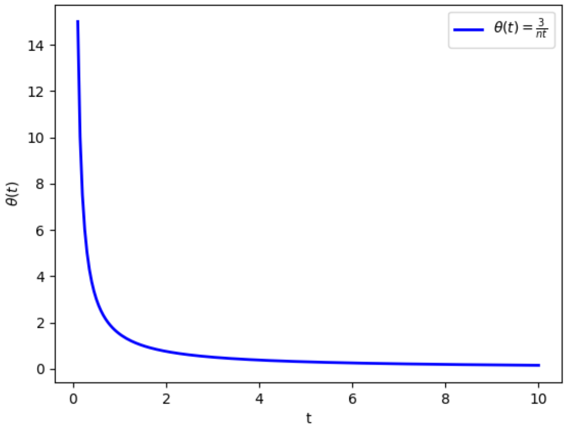

**Figure 6.** Variation of Scalar Expansion

The rate of volume expansion of the universe decreases with time. This supports the idea that the early universe expanded extremely fast but slowed down with cosmic time.

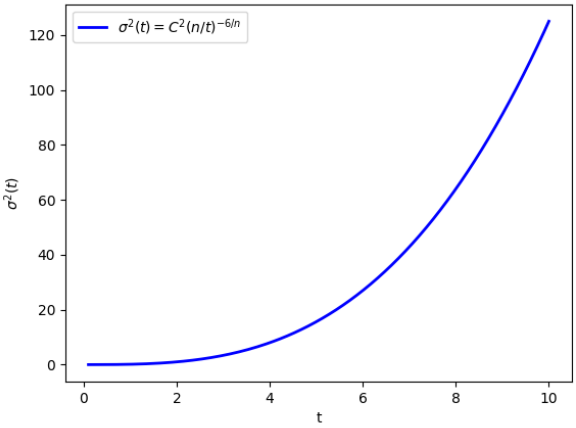

**Figure 7.** Variation of Shear Scalar

The plot represents the anisotropy (directional deformation) in the expansion. At early times ($t \longrightarrow 0$), anisotropy is large, but it decreases with time. This indicates that the universe tends to become isotropic as it evolves.

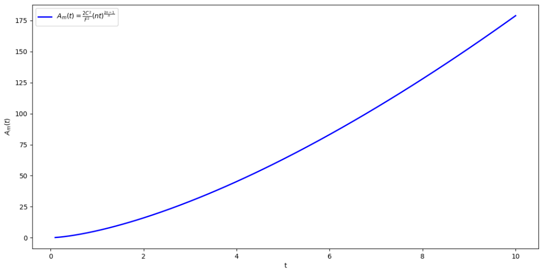

**Figure 8.** Variation of Anisotropic Parameter

Describes how strongly anisotropy affects cosmic expansion. If $n < 0.5$, the universe tends to become isotropic at late times.

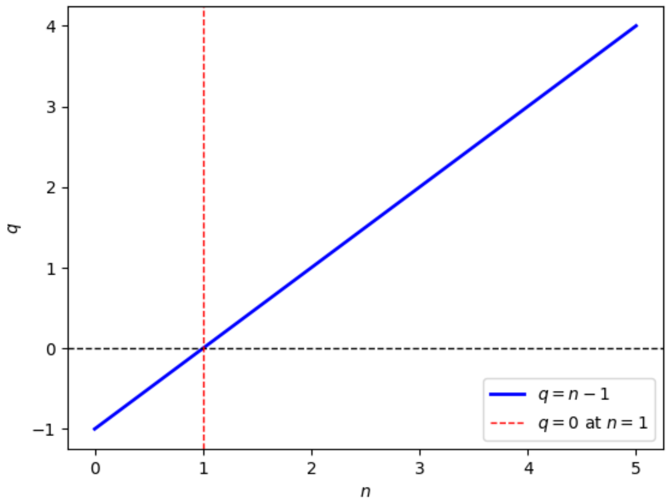

**Figure 9.** Variation of deceleration parameter

A graph represents a straight line in $n$, independent of time. For $n < 1$: $q < 0$, accelerated expansion (dark energy–like). For $n = 1$: $q = 0$, expansion at a uniform rate. For $n > 1$: $q > 0$, decelerated expansion (matter-dominated).

## 8. CONCLUSIONS

We have studied the anisotropic LRS Bianchi type-I cosmological model in the framework of $f(R, L_m)$ gravity, the contribution of dark energy in accelerating the cosmic evolution. Applying the functional form $f(R, L_m) = \frac{R}{2} + L_m^{\alpha} + \beta$ with $L_m = \rho$, and applying the special law of variation for the Hubble parameter, we obtained exact solutions to the modified field equations. Also, we have studied the physical and dynamical parameters such as Hubble parameter, spatial volume, deceleration parameter, scalar expansion, shear scalar, anisotropic parameter, pressure, density and EoS parameter and analyzed these parameters graphically from which we observed the following facts.

The energy density decreases rapidly with time and approaches near zero at late times. The pressure, initially highly negative, drives an accelerated expansion in the early universe but gradually stabilizes toward zero, reflecting a transition to a more balanced expansion regime. The equation of state parameter remains close to $\omega = -1$, suggesting that the dark energy component in this model mimics a cosmological constant.

The spatial volume expands unboundedly from a vanishing value at t=0, consistent with Big Bang cosmology, while the Hubble parameter and expansion scalar decrease over time, signifying a slowing but persistent expansion. The shear scalar and anisotropy parameter exhibit decreasing trends for $n < 0.5$, indicating isotropization of the universe, but for $n > 0.5$, anisotropy persists, showing that the universe evolves toward anisotropy in certain dynamical regimes. The deceleration parameter shows the different values of cosmic phases: accelerated expansion for ($n < 1$), uniform expansion at ($n = 1$), and deceleration for ($n > 1$).

Overall, the model successfully reproduces an accelerated, expanding universe consistent with present-day observations, while also providing a framework to investigate anisotropy in cosmic evolution. In particular, it shows that matter curvature coupling in $f(R, L_m)$ gravity can explain the late time cosmic acceleration without using exotic scalar fields.

This work emphasizes that anisotropic cosmological models in $f(R, L_m)$ gravity are not only viable but also rich in dynamical structure, offering testable predictions for dark energy behavior. Future investigations may refine this framework by incorporating bulk viscosity, observational constraints from supernovae and CMB data, and extensions to other Bianchi-type universes, thereby deepening our understanding of the interplay between anisotropy, dark energy, and modified gravity in shaping cosmic evolution.

### Acknowledgments

We would like to thank you for *following the instructions above* very closely in advance. It will definitely save us lot of time and expedite the process of your paper's publication.

### ORCID

**A.S. Khan**, https://orcid.org/0000-0002-7092-2735; **K.N. Pawar**, https://orcid.org/0000-0002-4388-039X;
**I.I. Khan**, https://orcid.org/0009-0002-3698-4200

## REFERENCES

[1] S. Weinberg, *Gravitation and Cosmology: Principles and Applications of the General Theory of Relativity*, (John Wiley and Sons, 2013).

[2] I. Domínguez, E.B. Guil, L. Piersanti, O. Straniero, and A. Tornambé, "Supernovae and dark energy," in: *Cosmology Across Cultures*, (Astronomical Society of the Pacific, 2008), pp. 42-46. https://hdl.handle.net/2117/22952

[3] J.-M. Alimi, A. Füzfa, V. Boucher, Y. Rasera, J. Courtin, and P.-S.Corasaniti, "Imprints of dark energy on cosmic structure formation–I. Realistic quintessence models and the non-linear matter power spectrum," Monthly Notices of the Royal Astronomical Society, **401**(2), 775-790 (2010). https://doi.org/10.1111/j.1365-2966.2009.15712.x

[4] S. Perlmutter, M.S. Turner, and M. White, "Constraining dark energy with type Ia supernovae and large-scale structure," Physical Review Letters, **83**(4), 670 (1999). https://doi.org/10.1103/PhysRevLett.83.670

[5] S. Boughn, and R. Crittenden, "A correlation between the cosmic microwave background and large-scale structure in the Universe," Nature, 427(6969), 45-47 (2004). https://doi.org/10.1038/nature02139

[6] Montesano, Francesco, "The full shape of the large-scale galaxy power spectrum: modelling and cosmological implications," D.Sc. Thesis, Ludwig–Maximilians–Universit, Munich, 2011. https://doi.org/10.5282/edoc.13663

[7] J.-P. Dai, Y. Yang, and J.-Q. Xia, "Reconstruction of the dark energy equation of state from the latest observations," The Astrophysical Journal, **857**(1), 9 (2018). https://doi.org/10.3847/1538-4357/aab49a

[8] S. Tsujikawa, "Dark energy: Observational status and theoretical models," in: *Quantum Gravity and Quantum Cosmology*, edited by G. Calcagni, L. Papantonopoulos, G. Siopsis, and N. Tsamispp, (Springer Berlin, Heidelberg, 2013), pp. 289-331. https://doi.org/10.1007/978-3-642-33036-0_11

[9] J. Yoo, and Y. Watanabe, "Theoretical models of dark energy," International Journal of Modern Physics D, **21**(12), 1230002 (2012). https://doi.org/10.1142/S0218271812300029

[10] Tsujikawa, Shinji, "Dark energy: investigation and modeling," in: *Dark Matter and Dark Energy. Astrophysics and Space Science Library*, vol. 370. edited by S. Matarrese, M. Colpi, V. Gorini, and U. Moschella, (Springer, Dordrecht, 2011), pp. 331-402. https://doi.org/10.1007/978-90-481-8685-3_8

[11] T. Harko, and F.S.N. Lobo, "$f(R, L_m)$ gravity," The European Physical Journal C, **70**, 373–379 (2010). https://doi.org/10.1140/epjc/s10052-010-1467-3

[12] D.C. Maurya, "Bianchi-I dark energy cosmological model in f(R,Lm)-gravity," International Journal of Geometric Methods in Modern Physics, **21**(04), 2450072 (2024). https://doi.org/10.1142/S0219887824500725

[13] X. Liu, T. Harko, and S.D. Liang, "Cosmological implications of modified gravity induced by quantum metric fluctuations," The European Physical Journal C, **76**(8), 420 (2016). https://doi.org/10.1140/epjc/s10052-016-4275-6

[14] M.F. Shamir, "Dynamics of anisotropic power-law f (R) cosmology," Journal of Experimental and Theoretical Physics, **123**(6), 979-984 (2016). https://doi.org/10.1134/S1063776116150152

[15] M. Koussour, N. Myrzakulov, A.H.A. Alfedeel, and A. Abebe, "Constraining the cosmological model of modified f(Q) gravity: Phantom dark energy and observational insights," Progress of Theoretical and Experimental Physics, **2023**(1), 113E01 (2023). https://doi.org/10.1093/ptep/ptad133

[16] M. Zeyauddin, A. Dixit, and A. Pradhan, "Anisotropic dark energy models in f(R,Lm)-gravity," International Journal of Geometric Methods in Modern Physics, **21**(02), 2450038 (2024). https://doi.org/10.1142/S0219887824500385

[17] A. Pradhan, D.C. Maurya, Dinesh Chandra and G.K. Goswami, and A. Beesham, "Modeling transit dark energy in f(R,Lm)-gravity," International Journal of Geometric Methods in Modern Physics, **20**(06), 2350105 (2023). https://doi.org/10.1142/S0219887823501050

[18] D.C. Maurya, "Constrained transit cosmological models in $f(R, L\_\{m\}, T)$-gravity," arXiv:2409.14024, https://doi.org/10.48550/arXiv.2409.14024; International Journal of Geometric Methods in Modern Physics, **22**(07), 2550028 (2025). https://doi.org/10.1142/S0219887825500288

[19] A. Dixit, A. Pradhan, M. Zeyauddin, and J. Singh, "Dark energy nature of logarithmic f(R,Lm)-gravity models with observational constraints," International Journal of Modern Physics A, **39**(07n08), 2450043 (2024). https://doi.org/10.1142/S0217751X2450043X

[20] R. Solanki, B. Patel, L.V. Jaybhaye, and P.K. Sahoo, "Cosmic acceleration with bulk viscosity in an anisotropic f(R,Lm) background," Communications in Theoretical Physics, **75**(7), 075401 (2023). https://doi.org/10.1088/1572-9494/acd4aa

[21] L.V. Jaybhaye, R. Solanki, S. Mandal, P.K. Sahoo, "Constraining the Viscous Dark Energy Equation of State in f(R,Lm) Gravity, **9**(4), 163 (2023). https://doi.org/10.3390/universe9040163

[22] L.V. Jaybhaye, R. Solanki, and P.K. Sahoo, "Bouncing cosmological models in f(R,Lm) gravity," Physica Scripta, **99**(6), 065031 (2024). https://doi.org/10.1088/1402-4896/ad4838

[23] M. Koussour, N. Myrzakulov, J. Rayimbaev, A.H.A. Alfedeel, and H.M. Elkhair, "Bouncing behavior in $f(R, L_m)$ gravity: Phantom crossing and energy conditions," arXiv preprint arXiv:2403.15772, (2024). https://doi.org/10.48550/arXiv.2403.15772; International Journal of Geometric Methods in Modern Physics, **21**(11), 2450184 (2024). https://doi.org/10.1142/S0219887824501846

[24] D.C. Maurya, "Constraining on Dark Energy Models in Higher Derivative $F(R, LM)$-Gravity Theory with Hubble Function," http://dx.doi.org/10.2139/ssrn.4552229

[25] S. Sahlua, A.H.A. Alfedeelb, and A. Abebe, "The cosmology of $f(R, L\_m)$ gravity: constraining the background and perturbed dynamics," arXiv:2406.08303, (2024). https://doi.org/10.48550/arXiv.2406.08303

[26] R. Garg, G.P. Singh, A. Lalke, and S. Ray, "Cosmological model with linear equation of state parameter in f(R,Lm) gravity," Physics Letters A, **525**, 129937 (2024). https://doi.org/10.1016/j.physleta.2024.129937

[27] Y.K. Devi, S.A. Narawade, and B. Mishra, "Constraining parameters for the accelerating universe in f(R,Lm) gravity," hysics of the Dark Universe, **46**, 101640 (2024). https://doi.org/10.1016/j.dark.2024.101640

[28] V. Patil, J. Pawde, R. Mapari, S. Waghmare, "FLRW Cosmology with Hybrid Scale Factor in f(R,Lm) Gravity," East European Journal of Physics, (4), 8-17 (2023). https://doi.org/10.26565/2312-4334-2023-4-01

[29] B.K. Shukla, R.K. Tiwari, and A. Beesham, "FLRW universe in f(Q,T) gravity," International Journal of Geometric Methods in Modern Physics, **20**(14), 2350242 (2023). https://doi.org/10.1142/S0219887823502420

[30] J.K. Singh, R. Myrzakulov, and H. Balhara, *et al.*, "A constrained cosmological model in f(R,Lm) gravity," New Astronomy, **104**, 102070 (2023). https://doi.org/10.1016/j.newast.2023.102070

[31] K. Pawar, N.T. Katre, and A.K. Dabre, "Accelerating Expansion of the Universe with Dark Matter and Holographic Dark Energy in $f(T)$ Gravity," Int. J. Sci. Res. in Physics and Applied Sciences, **11**(2), 1-9 (2023). https://www.isroset.org/journal/IJSRPAS/full_paper_view.php?paper_id=3094

[32] Y.-J. Suh, K. De, and U.C. De, "On Pseudo $B$-symmetric spacetimes and $f(R)$ gravity," Int. J. Geom. Meth. Mod. Phys. **22**(02), 2450280 (2025). https://doi.org/10.1142/S0219887824502803

[33] C.R. Mahanta, S. Deka, and K. Pathak, "Anisotropic Cosmological Model in f (R, T) Theory of Gravity with a Quadratic Function of T," East European Journal of Physics, (3), 43-52 (2023). https://doi.org/10.26565/2312-4334-2023-3-02

[34] S. Kibaroglu, "Anisotropic Born Infeld f(R) cosmologies," Physics of the Dark Universe, **47**, 101784 (2025). https://doi.org/10.1016/j.dark.2024.101784

[35] R. Saleem, A. Ijaz, and S. Waheed, "Anisotropic Cosmic Expansion Inspired by Some Novel Holographic Dark Energy Models in f(Q) Theory," Fortschritte der Physik, **73**(3), 2300276 (2025). https://doi.org/10.1002/prop.202300276

[36] M.R. Ugale, and S.B. Deshmukh, "Anisotropic Bianchi type VI0 cosmological models in a modified f(R,T) gravity," Journal of Scientific Research, **16**(1), 17-30 (2024). https://doi.org/10.3329/jsr.v16i1.62830

[37] B. Mishra, F.MD. Esmeili, and S. Ray, "Cosmological models with variable anisotropic parameter in f(R,T) gravity," Indian Journal of Physics, **95**(10), 2245-2254 (2021). https://doi.org/10.1007/s12648-020-01877-2

[38] S. Chakraborty, "Reconstruction method of f(R) gravity for isotropic and anisotropic spacetimes," Physical Review D, **98**(2), 024009 (2018). https://doi.org/10.1103/PhysRevD.98.024009

[39] M.F. Shamir, and A. Komal, "Energy bounds in f(R,G) gravity with anisotropic background," International Journal of Geometric Methods in Modern Physics, **14**(12), 1750169 (2017). https://doi.org/10.1142/S0219887817501699

[40] P. Bolke, V. Patil, S. Waghmare, and N. Mahajan, "Anisotropic Cosmological Model with SQM in f(R,Lm) Gravity," East European Journal of Physics, (3), 45-55 (2024). https://doi.org/10.26565/2312-4334-2024-3-05

[41] M.S. Berman, "A special law of variation for Hubble's parameter," Nuovo Cimento B Serie, **74**, 182-186 (1983). http://dx.doi.org/10.1007/BF02721676

[42] M.S. Berman, and F. de Mello Gomide, "Cosmological models with constant deceleration parameter," General Relativity and Gravitation, **20**, 191-198 (1988). https://doi.org/10.1007/BF00759327

# АНІЗОТРОПНА КОСМОЛОГІЯ ТЕМНОЇ ЕНЕРГІЇ В РАМКАХ $f(R, L_m)$ ГРАВІТАЦІЇ

**А.С. Хан**[1], **К.Н. Павар**[1,2], **І.І. Хан**[1,3]
[1] *Коледж інженерії та менеджменту професора Рама Мегхе, Баднера, MS, Індія*
[2] *Науковий коледж Шрі Шиваджі, Нагпур, MS, Індія*
[3] *Інститут технологій та досліджень професора Рама Мегхе, Баднера, MS, Індія*

У цій статті ми досліджували локально обертально-симетричну (LRS) космологічну модель Біанкі I типу з темною енергією в рамках теорії гравітації $f(R, L_m)$, де $R$ – скаляр Річчі, а $L_m$ – лагранжіан матерії. Використовуючи функціональну форму $f(R, L_m) = \frac{R}{2} + L_m^\alpha + \beta$ з $L_m = \rho$, та застосовуючи спеціальний закон варіації для параметра Хаббла, ми отримали точні розв'язки рівнянь поля та проаналізували фізичні та динамічні властивості Всесвіту. Наші результати показують, що модель демонструє прискорене розширення, що узгоджується з даними спостережень, зі зменшенням густини енергії та переходом параметра уповільнення від позитивних до негативних значень. Параметр анізотропії спочатку наближається до нуля, але збільшується з часом для $n > 0.5$, що вказує на еволюцію від ізотропії до анізотропії. Ці результати дають уявлення про поведінку темної енергії в рамках модифікованої гравітації та пропонують перевірені прогнози для космологічних спостережень.

**Ключові слова:** *LRS Bianchi Type-I; темна енергія; космічний час*

East European Journal of Physics. 4. 112–132 (2025)

DOI: 10.26565/2312-4334-2025-4-10 ISSN 2312-4334

# EXTENSION FROM CORE TO NO-CORE NUCLEAR SHELL MODEL WITH HARTREE–FOCK WAVE FUNCTION: APPLICATION TO POSITIVE-PARITY STATES IN $^{19}$F

**Berun N. Ghafoor**[1*,2], **Aziz H. Fatah**[3], **Ari K. Ahmed**[1]

[1]*University of Sulaimani, College of Education, Physics department, Iraq*

[2]*Research and Development Center, University of Sulaimani, Iraq*

[3]*University of Sulaimani, College of Science, Physics department, Iraq*

[*]*Corresponding Author e-mail: berun.ghafoor@univsul.edu.iq*

Received July 7, 2025; revised September 9, 2025; accepted September 27, 2025

This work presents a detailed investigation of low-lying positive-parity states in the $^{19}$F nucleus by combining shell-model techniques with Hartree–Fock (HF) calculations. The study systematically extends from traditional core-based spaces ($sd$, $zbm$, $psd$) to the fully untruncated no-core configuration ($spsdpf$). Realistic single-particle wavefunctions were generated using harmonic oscillator (HO), Woods–Saxon (WS), and Skyrme parameterizations. The approach was tested across a broad set of observables, including excitation spectra, electromagnetic form factors ($C0$, $C2$, $C4$, $M1$, $M3$, $E2$, $E4$, and $E4 + M5$), transition probabilities, magnetic dipole and electric quadrupole moments, as well as binding energies and rms charge radii. Discrepancies reported in earlier theoretical work, particularly for the $M1$ and $C4$ transitions at higher momentum transfers, were resolved through expanded model spaces and refined radial wavefunctions. Together with our previous study of negative-parity states in $^{19}$F, these results provide a coherent picture: systematic core-to-no-core extensions are essential for accurately reproducing both detailed and bulk nuclear properties. This unified framework strengthens theoretical modeling of $^{19}$F and establishes a foundation for future shell-model studies of nuclei in transitional and deformed regions.

**Keywords:** *Nuclear shell model; No-core shell model; Hartree–Fock wave function; Skyrme Hartree–Fock; Effective interaction; Electromagnetic form factors; Energy levels of $^{19}$F*

**PACS:** 21.60.Cs, 21.60.Jz, 25.30.Bf, 21.10.-k, 27.20.+n

## 1. INTRODUCTION

The $^{19}$F nucleus is an excellent example of a light, odd-$A$, strongly deformed nuclear system of sufficient size and complexity to exhibit properties of a many-body system. Electron scattering, through its well-understood electromagnetic interaction, serves as a powerful probe of the nuclear structure. In this work, nuclear structure properties were investigated using the shell model and the Hartree–Fock method, with core-to-no-core extensions enhancing theoretical reliability. This technique focuses on increasing the number of valence particles to investigate the static and dynamic structure of $^{19}$F. Within the recent progress of shell model research areas, the necessity to choose and apply a model space as well as effective interactions crucial in identifying and explaining nuclear structure phenomena has become evident. Ghafoor et al. [1] compared the excitation of negative parity states in $^{19}$F using core and no-core shell models and their calculations have shown that adding the no-core leads to much better agreement with the observables especially in transition strengths and energy spectra. Correspondingly, Ryssens and Alhassid [2] developed the HF-SHELL code that implements finite-temperature Hartree-Fock algorithms to tackling shell model Hamiltonians and discussed its applicability to the statistical and collective properties of nuclei at high excitation. These were supplemented by Saxena and Srivastava [3] who performed first-principles calculations using an *ab initio* no-core shell model to gain insight into neutron-rich $^{18-23}$O and $^{18-24}$F isotopes, and indicated that structure experimentalists may expect first-principles studies of such systems to employ large model spaces to resolve detail in such systems.

Large-scale shell model predictions of Jassim and Sahib [4] have also been provided on $^{19}$F, as well as the adjoining nuclei, such as $^{25,26}$Mg and $^{27}$Al, demonstrating that concomitant conventions of interaction-model spaces can produce solid spectra and electromagnetic properties. Similarly, Singh et al. [5] demonstrated that complete shell model calculations of even and odd A nuclei in several mass regions could effectively reproduce calculated and experimental energy levels, form factors, and transition moments, in the case of high-quality interactions being used. Taken together, these works support the generality of the shell model in understanding nuclear structure and support the tendency to use the traditional shell model frameworks along with more modern treatments, i.e., *ab initio* methods and mean-field approximations, to improve our knowledge of light and medium-mass nuclei.

The development of recent years with the study of nuclear structure of sd-shell nuclei has significantly relied on the method of configuration-interaction shell model to investigate the electromagnetic response and electron scattering processes. The study of Le Noan and Sieja [6] explored the electric dipole response of sd-shell nuclei and determined

---

***Cite as:*** B.N. Ghafoor, A.H. Fatah, A.K. Ahmed, East Eur. J. Phys. 4, 112 (2025), https://doi.org/10.26565/2312-4334-2025-4-10

that the collective and single-particle excitations of light nuclei are important through the shell-model description with well-selected effective interactions that reproduce well their low-energy dipole strength distributions.

In connection with these results, Radhi *et al.* performed shell model calculations in detail of the electron scattering of the $^{19}$F nucleus, both positive and negative parity of the states. In their work [7], they found that inelastic scattering form factors can be successfully described using shell-model wave functions, including realistic configuration mixing, which allowed insight into nuclear excitation mechanisms and the densities of transition states. Radhi, Abdullah, and Raheem [8] first applied these analyses with no-core shell model wave functions of a large basis, which gave a better match to elastic and inelastic measurements of electron scattering and emphasized the need to include the complete model space in a description.

The rationales of these computational works lie in the development of effective interactions as advanced by Smirnova *et al.* [9] in the sd shell. They formulated and tested improved sets of new interactions that improve the predictive capability of shell-model calculations, in particular, on spectroscopy and transition strengths, thus allowing a more precise description of the experimental observables in all the nuclei of the sd-shell.

Brown *et al.* [10] conducted a detailed shell-model analysis of high-resolution elastic and inelastic electron scattering data for $^{19}$F, successfully reproducing key longitudinal and transverse form factors for both positive- and negative-parity states. Their study demonstrated the utility of the *sd*-shell configurations and limited cross-shell excitations in capturing essential electromagnetic observables. However, the analysis was constrained by truncated model spaces, reliance on a fixed effective interaction, and the use of phenomenological single-particle wavefunctions. These limitations restricted the treatment of configuration mixing and reduced the accuracy of predictions at higher momentum transfers—especially for complex multipole components. Furthermore, the absence of systematic uncertainty quantification and the exclusion of extended model spaces, such as the *pf*-shell, limited the completeness and generalizability of the results, indicating the need for modern no-core approaches and diverse interaction benchmarking for deeper nuclear structure insight.

In combination, such studies reveal the configuration-interaction shell model using extended effective interactions to be a formidable theoretical instrument in the study of nuclear electromagnetic responses in sd-shell nuclei, especially using observables in electron scattering as the sensitive probe of nuclear structure.

The present investigation evaluates the energy spectra, reduced transition probabilities, magnetic dipole moments, nuclear root-mean-square radii, binding energy, and both longitudinal and transverse inelastic electron scattering form factors for the $^{19}$ F nucleus. The analysis utilizes four distinct model spaces to systematically examine the influence of progressively extending the core configuration, culminating in a no-core framework, on the calculated nuclear properties and scattering observables

## 2. THEORETICAL FORMALISM

To investigate the nuclear structure properties of $^{19}$F, we employed both the shell model and the Hartree–Fock (HF) approaches. Each method was carefully implemented using relevant effective interactions and computational tools, and all mathematical formulations were consistently applied throughout the study.

In the HF method, the wave function of a nucleus $|\psi_{\rm HF}\rangle$, consisting of $A$ nucleons, can be written as a Slater determinant of single-particle wave functions $\phi_i$ [11, 12]:

$$|\psi_{\rm HF}(u_1, u_2, \ldots, u_A)\rangle = \frac{1}{\sqrt{A!}}\begin{vmatrix}\phi_1(u_1) & \cdots & \phi_1(u_A)\\ \vdots & \ddots & \vdots\\ \phi_A(u_1) & \cdots & \phi_A(u_A)\end{vmatrix}, \tag{1}$$

where $u_i = (\vec{r}, \sigma, t_z)$ includes spatial coordinates $\vec{r}$, spin projection $\sigma$, and isospin projection $t_z$ ($+1/2$ for proton, $-1/2$ for neutron). The HF method minimizes the expectation value of the total Hamiltonian [13]:

$$\hat{H} = -\frac{\hbar^2}{2m}\sum_{i=1}^{A}\nabla^2 + \hat{V}_{\rm Skyrme}, \tag{2}$$

where the Skyrme effective interaction [14] models the mean-field behavior of nucleons through zero-range, density-dependent forces:

$$\hat{V}_{\rm Skyrme} = \sum_{i<j} V_{ij}^{(2)} + \sum_{i<j<k} V_{ijk}^{(3)}. \tag{3}$$

The two-body component consists of central, spin-orbit, and tensor terms [14, 15, 16]:

$$\hat{V}_{\rm Skyrme}(\vec{r}_1, \vec{r}_2) = \hat{V}^m + \hat{V}^{LS} + \hat{V}^t, \tag{4}$$

with

$$\hat{V}^m = t_0(1 + x_0\hat{P}_\sigma)\delta_{12} + \frac{t_1}{2}(1 + x_1\hat{P}_\sigma)(\hat{k}_1^2 + \hat{k}_2^2)\delta_{12}$$

$$+ t_2(1 + x_2\hat{P}_\sigma)\hat{k}_2 \cdot \hat{k}_1\delta_{12} + \frac{t_3}{6}(1 + x_3\hat{P}_\sigma)\rho^\alpha(r)\delta_{12}, \tag{5}$$

$$\hat{V}^{LS} = it_4(\hat{\sigma}_1 + \hat{\sigma}_2) \cdot (\hat{k}_2 \times \hat{k}_1)\delta_{12}, \tag{6}$$

$$\begin{aligned}\hat{V}^t = \frac{t_e}{2}\Big[&3(\hat{\sigma}_1 \cdot \hat{k}_2)(\hat{\sigma}_2 \cdot \hat{k}_2) - (\hat{\sigma}_1 \cdot \hat{\sigma}_2)\hat{k}_2^2 \\ &+ 3(\hat{\sigma}_1 \cdot \hat{k}_1)(\hat{\sigma}_2 \cdot \hat{k}_1) - (\hat{\sigma}_1 \cdot \hat{\sigma}_2)\hat{k}_1^2\Big]\delta_{12} \\ &+ t_s[3(\hat{\sigma}_1 \cdot \hat{k}_2)(\hat{\sigma}_2 \cdot \hat{k}_1) - (\hat{\sigma}_1 \cdot \hat{\sigma}_2)(\hat{k}_2 \cdot \hat{k}_1)^2]\delta_{12},\end{aligned} \tag{7}$$

where $\delta_{12} = \delta(\vec{r}_1 - \vec{r}_2)$ is the Dirac delta function. The operators $\hat{k}_1 = \frac{1}{2i}(\vec{\nabla}_1 - \vec{\nabla}_2)$ and $\hat{k}_2 = -\frac{1}{2i}(\vec{\nabla}_1 - \vec{\nabla}_2)$ act on the right and left wavefunctions, respectively. The three-body force is simplified as

$$V^{(3)}_{\text{Skyrme}} = t_3\delta_{12}\delta_{13}. \tag{8}$$

The radial part of the single-particle wavefunctions is [15, 16]:

$$\phi_{nljm}(r) = \frac{R_{nl}(r)}{r}Y_{jlm}(\Omega_r), \tag{9}$$

with the corresponding density distributions [11]:

$$\rho_s(r) = \sum_{n_\alpha, j_\alpha, l_\alpha} \omega_\alpha \frac{(2j_\alpha + 1)}{4\pi}\left(\frac{R^{(s)}_{n_\alpha l_\alpha}(r)}{r}\right)^2, \tag{10}$$

and root-mean-square (rms) radii [17, 18]:

$$r_s = \langle r_s^2\rangle^{1/2} = \left[\frac{\int dr\, r^4\rho_s(r)}{\int dr\, r^2\rho_s(r)}\right]^{1/2}. \tag{11}$$

In the shell model, electromagnetic form factors are calculated via reduced matrix elements. The one-body transition densities (OBTDs), computed using the NuShellX code [19], are defined as

$$\text{OBDM}_{J,t_z}(J_i, J_f) = \frac{\langle J_f\|[a^\dagger_\alpha \otimes \tilde{a}_\beta]^J\|J_i\rangle}{\sqrt{2J + 1}}. \tag{12}$$

The reduced matrix element is then [20]:

$$\langle J_f\|\hat{T}^\eta_{J,t_z}(q)\|J_i\rangle = \sum_{\alpha,\beta}\text{OBDM}_{J,t_z}(J_i, J_f)\langle\alpha\|\hat{T}^\eta_{J,t_z}(q)\|\beta\rangle, \tag{13}$$

and the form factor squared is [21]:

$$|F^J_\eta(q)|^2 = \frac{4\pi}{Z^2(2J_i + 1)}\left|\sum_{t_z} e(t_z)\langle J_f\|\hat{T}^\eta_{J,t_z}(q)\|J_i\rangle\right|^2 |F_{\text{cm}}(q)|^2|F_{\text{fs}}(q)|^2, \tag{14}$$

where the center-of-mass and finite-size corrections are [22]

$$|F_{\text{cm}}(q)| = \exp\left(\frac{b^2q^2}{4A}\right), \tag{15}$$

$$|F_{\text{fs}}(q)| = \exp\left(-\frac{0.43q^2}{4}\right). \tag{16}$$

The longitudinal and transverse form factors are [20, 21]

$$|F_L(q)|^2 = \frac{1}{2J_i + 1}\sum_{J\geq 0}|\langle J_f\|\hat{T}^C_{J,t_z}(q)\|J_i\rangle|^2, \tag{17}$$

$$|F_T(q)|^2 = \frac{1}{2J_i + 1}\sum_{J\geq 1}\left\{|\langle J_f\|\hat{T}^E_{J,t_z}(q)\|J_i\rangle|^2 + |\langle J_f\|\hat{T}^M_{J,t_z}(q)\|J_i\rangle|^2\right\}, \tag{18}$$

and the total form factor in plane-wave Born approximation (PWBA) is [20, 21]

$$|F(q,\theta)|^2 = \left(1 - \frac{\omega^2}{q^2}\right)|F_L(q)|^2 + \left[\frac{1}{2}\left(1 - \frac{\omega^2}{q^2}\right) + \tan^2\left(\frac{\theta}{2}\right)\right]|F_T(q)|^2. \tag{19}$$

Finally, the reduced transition probability is given by [21]:

$$B(\eta J) = \frac{Z^2}{4\pi}\left[\frac{(2J+1)!!}{k^J}\right]^2 |F_J^\eta(k)|^2, \tag{20}$$

where $k = E_x/\hbar c$ is the momentum transfer corresponding to the excitation energy.

## 3. RESULT AND DISCUSSION

Building upon our earlier study [1], where the root mean square (rms) charge radius and binding energy of $^{19}$F were successfully reproduced using a single Skyrme-Hartree–Fock parameterization (SLy4), the present work marks a significant methodological advancement. While the previous calculation yielded results in strong agreement with experiment—2.876 fm for the rms radius and 146.372 MeV for binding energy—this study systematically expands the scope by employing an extensive set of thirty-nine Skyrme interactions. These are analyzed in parallel with harmonic oscillator (HO) and Woods–Saxon (WS) potentials to rigorously evaluate their effectiveness in reproducing key nuclear observables. This enriched comparative framework enables a more robust benchmarking of global nuclear properties and provides deeper insight into the sensitivity of model predictions to mean-field structure.

In addition to global quantities, the present investigation delves into the fine structure of low-lying positive parity states in $^{19}$F by analyzing longitudinal and transverse electron scattering form factors, electromagnetic transition probabilities, magnetic and quadrupole moments, and excitation spectra. The study is structured around a progressive extension of the shell model space, beginning with the conventional *sd*-shell (based on an $^{16}$O core) and expanding through the *zbm* ($^{12}$C core), *psd* ($^{4}$He core), and fully untruncated *spsdpf* no-core model. This hierarchical modeling strategy, combined with realistic single-particle wavefunctions from Hartree–Fock and alternative potentials, allows for a critical evaluation of how model space and interaction choices affect the reproduction of experimental data.

The present study is a significant development in the theory of nuclear structure and very far beyond the earlier applications of the shell model, like Radhi et al. [7, 8] and Brown [10]. Unlike earlier studies that were limited to truncated core configurations and narrow interaction sets, we implemented a systematic core-to-no-core shell model framework, treating all 19 nucleons of $^{19}$F as dynamically active in the most extended model space cause to reproduce some observable that is better than previous studies.

The results are presented in order of increasing angular momentum, offering a clear and coherent narrative of the evolving nuclear structure across multiple observables.

Angular momentum and parity conservation allow only certain multipole parts, namely $C0$, $E0$ and $M1$ for Coulomb, transverse electric and transverse magnetic form factors respectively for ground state. The time-reversal symmetry removes the $E0$ component though. The elastic Coulomb $C0$ form factors of the ground state of the nucleus $^{19}$F ($1/2^+$, 0 MeV) were calculated with the help of shell-model wave functions related to model spaces *sd*, *zbm*, *psd* and *spsdpf*. These were coupled to radical single-particle wavefunctions, of Skyrme Hartree–Fock parameterization (SkXcsb, SkXta, SkXtb, SLy4), Woods–Saxon (WS) and harmonic oscillator (HO) potentials. The constructed fit is compared to the experimentally measured form-factor in the Ref. [10] as the benchmark data presented in Fig. 1.

For the momentum transfer region $q = 0$ to 1.6 fm$^{-1}$, all model spaces, ranging from extended-core to no-core configurations, demonstrate good agreement with experimental data across all potential types. The C0 form factor near $q = 1.57$ fm$^{-1}$ up to 3 fm$^{-1}$, calculated using the Woods–Saxon potential, aligns closely with experimental data for both the *sd*- and *psd*-model spaces (core configurations of $^{16}$O and $^{4}$He, respectively). This strong similarity between the two model spaces may be attributed to the clustering of $^{16}$O as four $^{4}$He nuclei. For the $^{12}$C core with the ZBMI interaction, the C0 form factor achieves optimal agreement with experimental data using the Woods–Saxon potential in the $q$-value regions 1.57–1.61 fm$^{-1}$ and 2.28–2.4 fm$^{-1}$. In the intermediate range 1.61–2.28 fm$^{-1}$, the SkXcsb Skyrme potential produces the most accurate results. For the final two experimental $q$-values obtained using no-core calculations, both HO and WS potentials yield results in good agreement with the experimental data [10].

Unlike previous works, our study is the first to systematically reproduce the longitudinal $C0$ form factor of the ground state $1/2_1^+$ throughout the entire momentum transfer range using all core and no-core model spaces (*sd*, *zbm*, *psd*, and *spsdpf*), demonstrating that the charge distribution of the ground state can be robustly captured regardless of the core truncation, a result not previously

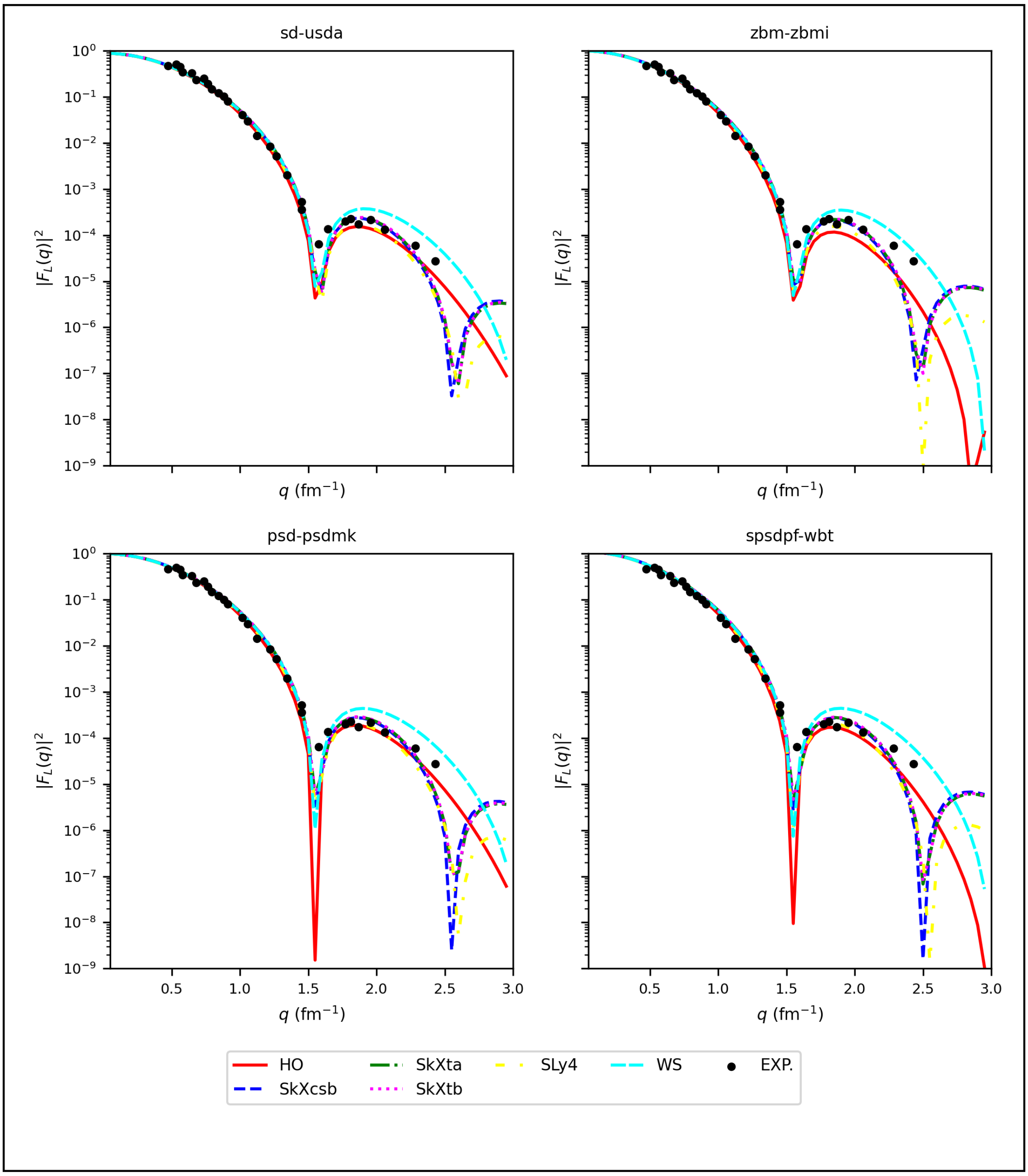

**Figure 1.** Elastic Coulomb C0 form factor for the $1/2^+$ ground state of $^{19}$F, calculated using various model spaces and radial potentials. Theoretical predictions are compared to experimental data from Ref. [10].

The transverse magnetic M1 form factors are presented in Fig. 2. A high level of consistency is observed between the experimental results and the calculations using all the employed potentials in the momentum transfer range, particularly with the *sd*-shell wavefunction and $^{16}$O core. However, in the region $q = 1.2$–$1.7$ fm$^{-1}$, the calculated form factors are underestimated. In particular, within this momentum transfer range, five out of the six potentials employed, excluding SkXcsb, exhibit qualitative agreement with the experimental M1 form factor data. The measurements reveal two diffraction minima located at $q = 1.1$ fm$^{-1}$ and $q = 1.6$ fm$^{-1}$, though these features appear slightly shifted in the theoretical predictions. Among all potentials, the Woods–Saxon (WS) potential (represented by cyan dashed) provides the closest match to the experimental data in the region $q = 1.49$–$1.57$ fm$^{-1}$.

For the ($^{12}_{6}$C) core configuration using the ZBMI interaction—where only seven valence nucleons are active—all potentials qualitatively reproduce the M1 form factors. However, the SLy4 Skyrme potential (dotted line) delivers the best overall agreement, though it fails to precisely replicate the observed minima near $q = 1.57$ fm$^{-1}$. When employing the ($^{2}_{4}$He) core within the psd-model space and the PSDMK interaction, the M1 form factors show excellent agreement with the experimental data. The diffraction minima are best reproduced using the harmonic oscillator (HO) and WS potentials, especially around $q = 1.49$ fm$^{-1}$, where all Skyrme potentials and the HO curve intersect this crucial point.

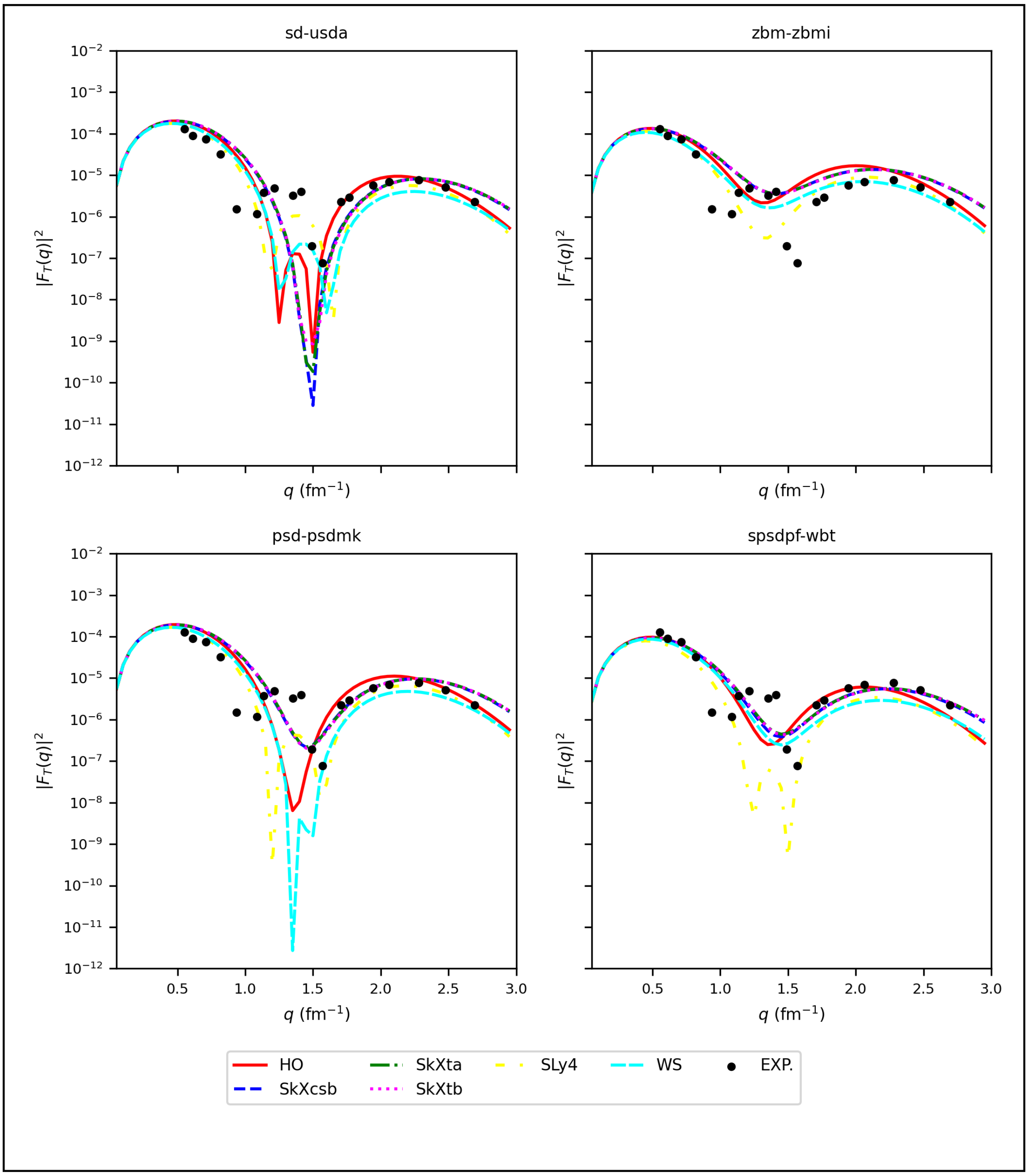

**Figure 2.** Theoretical transverse form factor $M1$ for the $1/2^+_1$ state in comparison with experimental data from Refs. [10, 23].

In the range $q = 1.7$–$2.23$ fm$^{-1}$, the transverse M1 form factors calculated within the psd-model space align most accurately with experimental values when Skyrme potentials are employed. At even higher momentum transfers ($q = 1.7$–$3$ fm$^{-1}$), the HO and WS potentials yield the best fits, while the SLy4 potential achieves only partial agreement.

Finally, for the fully untruncated *spsdpf* model space (no-core configuration) using the WBT interaction, all potentials—with the exception of SLy4—show excellent agreement across the entire M1 form factor momentum range. Interestingly, the SLy4 potential still provides strong agreement at the critical point $q = 1.57$ fm$^{-1}$.

In contrast to Brown et al. [10], who failed to reproduce the transverse $M1$ form factor of the $1/2^+_1$ state—especially at low momentum transfers—our approach not only recovers both diffraction minima but also achieves excellent agreement across all momentum ranges using the *sd* and *psd* model spaces with HO and WS potentials, while the no-core *spsdpf* calculations uniquely resolve the second minimum using the SLy4 Skyrme interaction, marking a major improvement in modeling the magnetic structure of the ground state.

The Coulomb contribution $C2$ for the $3/2^+_1$ state, as depicted in Fig. 3, demonstrates remarkable consistency between the *sd*-shell wavefunction calculations and experimental data across all $q$-values, with only minor overestimations.

However, the first minimum at approximately $q = 1.75$ fm$^{-1}$ is qualitatively well reproduced by the HO potential and is quantitatively closer when using the SLy4 parameterization. In the range $q$ = 2–2.4 fm$^{-1}$, the HO potential provides a notably better fit than the other parameterizations.

For the *zbm*-model space, the form factors exhibit good qualitative agreement across all $q$-values, albeit with a systematic shift. The minimum point is quantitatively well reproduced by both the HO and WS potentials, while the Skyrme parameterizations (SkXcsb, SkXta, SkXtb, and SLy4) excel qualitatively in this momentum transfer range. The suppression of the transverse $C2$ form factor for the $3/2^+_1$ state using the zbm-ZBMI interaction is attributed to its significant overestimation of the excitation energy, as shown in Fig. 11. This suggests an inadequately configured wavefunction for this state, lacking essential configuration mixing and collectivity.

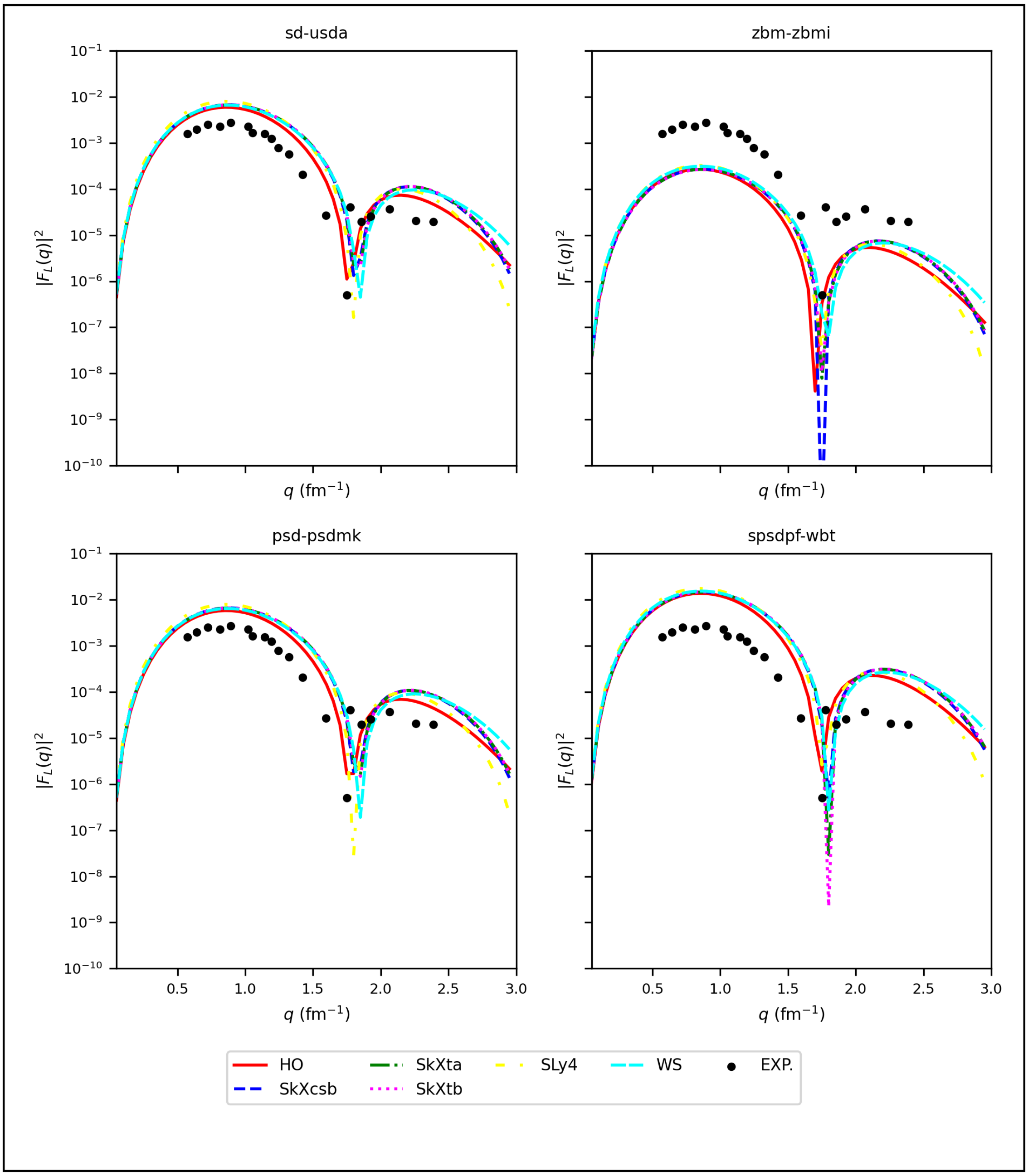

**Figure 3.** Theoretical longitudinal form factor $C2$ for $3/2^+_1$ compared with experimental data [10, 24].

The *zbm* model space, based on a $^{12}$C core ($Z = N = 6$), does not benefit from the enhanced stability of a doubly magic configuration, thereby limiting the accuracy of transition strength predictions. Consequently, the reduced transition density leads to an under prediction of the form factor strength in Fig. 3.

The results for the *psd*-model space are strikingly similar to those from the *sd*-shell wavefunction, further reinforcing the idea that the $^{16}_{8}$O core can emerge as a cluster derived from the $^{4}_{2}$He core. Notably, the PSDMK interaction [25], developed from the PW interaction within the *sd*-model space, incorporates the active $1d_{5/2}$, $2s_{1/2}$, and $1d_{3/2}$ orbitals above an inert $^{16}_{8}$O core.

Finally, within the *spsdpf*-model space, all potentials demonstrate exceptional agreement with the experimental $C2$ form factors across the entire $q$-value range, surpassing the accuracy of the other model spaces. This finding confirms that no-core shell model calculations are the most effective method for investigating form factors using an advanced shell model framework, where all nucleons are actively interacting.

Additionally, the no-core calculations reveal that the SkXcsb, SkXta, and SkXtb parameterizations yield similar results, while the SLy4 potential shows excellent agreement with WS and nearly with the HO potential. The differences among these potentials arise primarily from the renormalization of the $2s1d$ single-particle matrix elements within the model spaces.

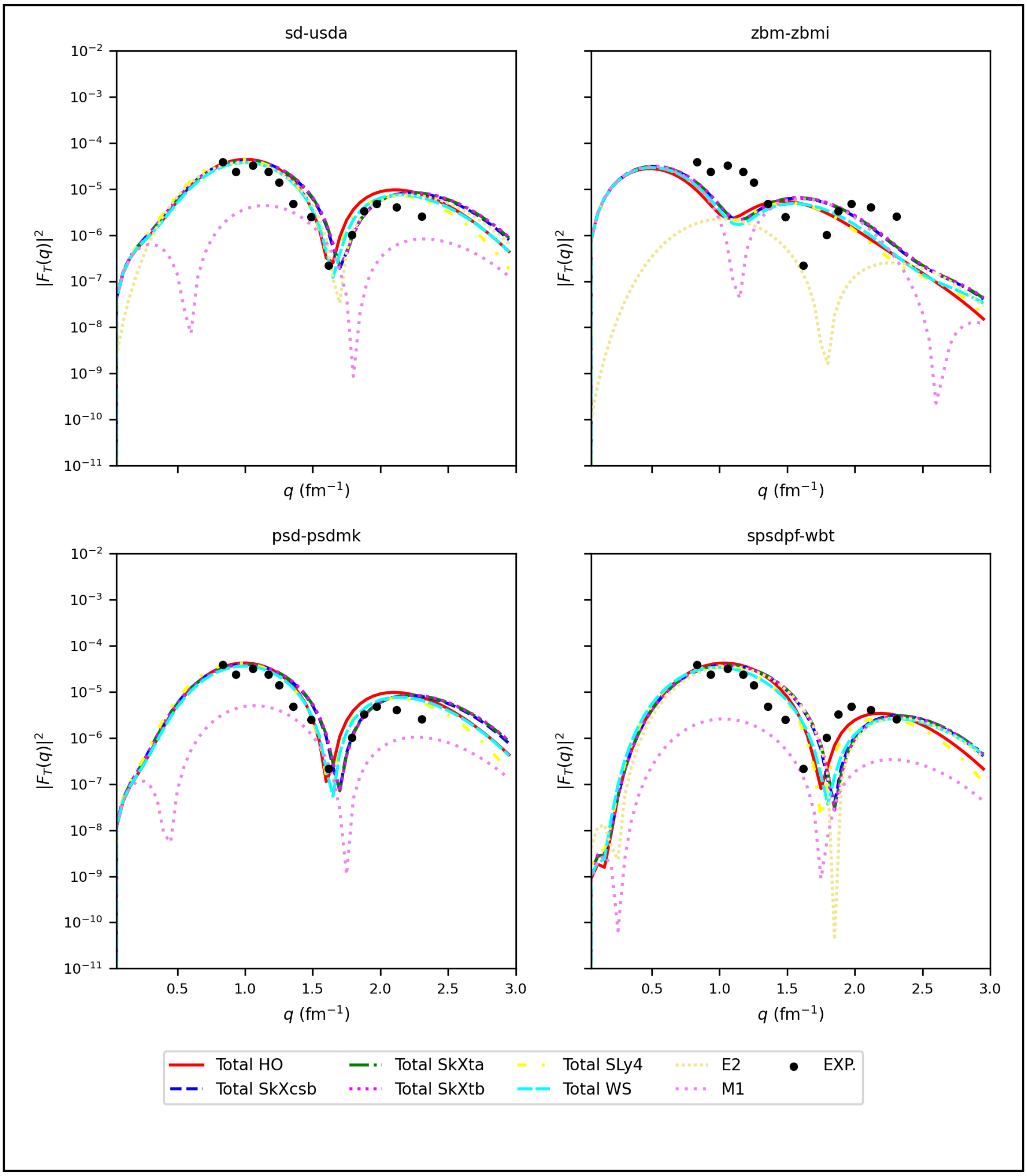

**Figure 4.** Theoretical transverse form factors $M1$ and $E2$ for the $3/2^+_1$ state at 1.55 MeV, compared with experimental data [10, 24].

The present study significantly advances the theoretical modeling of the longitudinal $C2$ form factor for the $3/2_1^+$ state. While Brown et al. [10] provided early reproduction using the *sd*-shell model, they failed to capture the first diffraction minimum around $q = 1.75$ fm$^{-1}$. In contrast, our *sd*-shell results, particularly with HO and WS radial potentials, successfully reproduce this minimum both qualitatively and quantitatively.

Moreover, the same feature is accurately captured in the *zbm*-model space using WS potential, and the overall shape of the form factor is closely mirrored in the *psd*-model space, demonstrating the structural continuity from an $^{16}$O core to its $^4$He cluster constituents. Most notably, the no-core *spsdpf* calculations provide exceptional agreement across the entire momentum transfer range using all Skyrme parameterizations, further confirming the robustness of our framework and its superiority over prior approaches in resolving the fine structure of the $C2$ form factor.

The transverse $M1$ and $E2$ form factors for the first $3/2_1^+$ state at 1.55 MeV are depicted in Fig. 4. Here, the total form factors ($E2 + M1$) were calculated for all potentials, while individual contributions of $E2$ and $M1$ are demonstrated specifically for the SkXcsb parameterization. The analysis reveals that the predictions from the *sd*-, *psd*-, and *spsdpf*-model spaces, utilizing all potentials, show reasonable agreement with the experimental data.

The regions of momentum transfer between $0.8{-}1.4\,\mathrm{fm}^{-1}$ and $1.8{-}2.5\,\mathrm{fm}^{-1}$ show dominant contributions from either the $M1$ or $E2$ multipoles, while in the intermediate range of $1.4{-}1.8\,\mathrm{fm}^{-1}$, both multipoles play a significant role in shaping the form factors. In contrast, the predictions from the *zbm*-model space exhibit fluctuations compared to the experimental data, largely due to discrepancies in the theoretical scattering process, which begins earlier than in the experimental observations. Despite this, the $M1$ component achieves qualitative consistency with the experimental form factors at specific momentum points, effectively reproducing the expected shape and behavior.

A major advancement of this study lies in the comprehensive treatment of the transverse $M1 + E2$ form factor for the $3/2_1^+$ state at 1.55 MeV. Unlike the earlier analysis by Brown et al. [10], which modeled only the total form factor within the *sd*-shell and failed to reproduce the high-$q$ behavior beyond 1.7 fm$^{-1}$, our work explicitly decomposes and calculates both the $M1$ and $E2$ components across an extended model space framework, including *sd*, *psd*, and *spsdpf* configurations.

Using HO, WS, and a broad range of Skyrme parameterizations, we accurately reproduce the entire momentum transfer region. Notably, the form factor is successfully resolved even in the high-$q$ domain where previous models faltered. Only the *zbm*-model space shows deviation due to mismatched excitation energy and premature scattering onset, reaffirming the necessity of extended core treatments and no-core shell model approaches for reliably capturing transverse multipole behavior.

The inelastic longitudinal $C2$ multipole form factors for the $5/2^+$ state are presented in Fig. 5. The comparison with experimental data from Ref. [10] shows that all potentials provide results consistent with the experimental values in both magnitude and shape across the momentum transfer range $q = 0.75{-}2.4\,\mathrm{fm}^{-1}$. A diffraction minimum is observed around $q = 0.75\,\mathrm{fm}^{-1}$, which is accurately reproduced by all potentials. The predictions from the *sd*-, *psd*-, and *zbm*-model spaces align closely with experimental data, showing better agreement with the harmonic oscillator (HO) potential compared to the Skyrme parameterizations and Woods–Saxon (WS) potential. For the *spsdpf*-model space, the predictions match experimental data most closely when using the HO potential up to $q = 1\,\mathrm{fm}^{-1}$. Between $q = 1$ and $q = 2.1\,\mathrm{fm}^{-1}$, the Skyrme parameterizations SkXcsb, SkXta, and SkXtb outperform the others in reproducing the experimental shape, while beyond $q = 2.1\,\mathrm{fm}^{-1}$, the SLy4 and WS potentials show the highest level of accuracy. Overall, the no-core calculations demonstrate superior precision compared to other core-based configurations, reinforcing their effectiveness in studying form factors with greater reliability and accuracy.

The inelastic transverse $E2$ and $M3$ multipoles for the $5/2_1^+$ state at 0.197 MeV, alongside the total transverse form factor ($E2 + M3$), are illustrated in Fig. 6. While the total transverse form factors were computed using all potentials across the different model spaces, the SkXcsb parameterization uniquely highlights the individual contributions of the $E2$ and $M3$ multipoles.

Across all $q$-values, the predicted results show strong agreement with experimental findings, though a minor shift is noted in the diffraction minimum—from approximately $q = 1.6$ fm$^{-1}$ to $q = 1.7$ fm$^{-1}$. The $M3$ multipole dominates the total transverse form factor across the full momentum transfer range, except in the interval $q = 1.6$–$1.8$ fm$^{-1}$, where the $E2$ contribution becomes more prominent. All model spaces effectively reproduce the experimental form factor profile, with the $M3$ component consistently overshadowing the $E2$ contribution. Predictions using the harmonic oscillator (HO) and Woods–Saxon (WS) potentials generally exhibit better agreement with experiment than those based on Skyrme parameterizations. Although the *sd*-, *zbm*-, and *psd*-model spaces yield quantitatively consistent results with the experimental data, the *spsdpf*-model space provides the best qualitative match, particularly in reproducing the diffraction minima at critical momentum transfer values.

The presentation of results is quite remarkable, as both the longitudinal $C2$ and the transverse total $E2 + M3$ form factors of the $5/2_1^+$ state achieve high diagnostic accuracy across all considered model spaces, including the core-based *sd*, *zbm*, and *psd* configurations, as well as the fully untruncated *spsdpf* no-core dimension. These results hold under the application of a wide range of radial potential dependencies—namely, the harmonic oscillator (HO), Woods–Saxon (WS), and various Skyrme parameterizations. This observed uniformity is not coincidental but reflects the strong collectivity and configuration mixing inherent to the $5/2^+$ state, which predominantly involves the $d_{5/2}$, $s_{1/2}$, and $d_{3/2}$ orbitals.

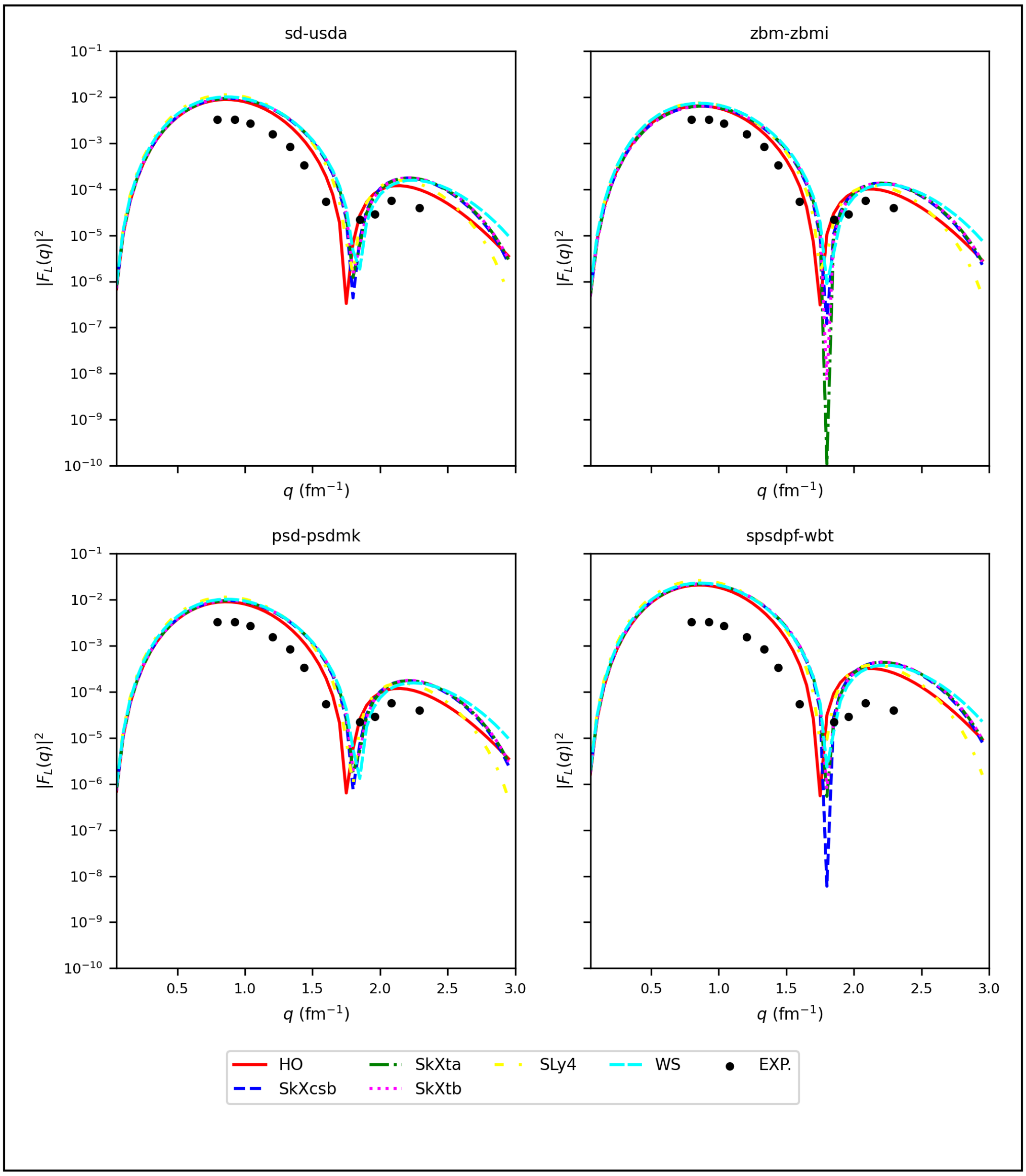

**Figure 5.** Theoretical longitudinal form factor $C2$ for $5/2_1^+$ compared with experimental data [10, 24].

These components are well described even in truncated spaces and are further enhanced in no-core calculations where full cross-shell correlations and valence space saturation are accounted for. The excellent agreement between our theoretical predictions and the experimental form factor data across the full momentum-transfer range demonstrates the robustness and reliability of the extended shell-model framework applied in this work.

The inelastic longitudinal $C4$ multipole form factors for the $7/2_1^+$ state are compared with experimental data and presented in Fig. 7, revealing insightful trends. Within the momentum transfer range $q = 0.8$–$1.59$ fm$^{-1}$, predictions using the *sd*-shell wavefunction exhibit excellent agreement with experimental data for all potential types, though deviations gradually increase at higher momentum transfer values. For the *zbm*-model space, the calculated results align well with experiment up to $q = 1.18$ fm$^{-1}$. When using the *psd*-model space, the WS and HO potentials demonstrate superior agreement, particularly in the range $q = 1$–$2$ fm$^{-1}$. Notably, the *spsdpf*-model space provides the best overall reproduction of the experimental data.

Across the momentum transfer range $q = 0.8$–$2$ fm$^{-1}$, all Skyrme parameterizations, as well as the WS and HO potentials, consistently yield predictions that closely align with experimental results. This underscores the robustness of the no-core calculation approach in capturing the physical behavior of longitudinal $C4$ form factors.

The inelastic transverse $M3$ and $E4$ multipoles for the $7/2_1^+$ state at 4.377 MeV are presented in Fig. 8, offering a detailed comparison with experimental data. Previous studies, including those by Brown et al. [10], Radhi [7, 8], and Donne et al. [24], reported significant discrepancies between calculated and experimental results for the $M3$ and $E4$

contributions in this state. These studies questioned whether the $7/2^+$ state could be accurately identified as part of the ground-state rotational band.

The *sd*- and *psd*-model spaces demonstrate the best agreement with experimental data in the momentum transfer ranges $q = 0.8$–$1.35$ fm$^{-1}$ and $q = 1.85$–$2.4$ fm$^{-1}$, across all potential types. Notably, the $M3$ contributions derived using the SkXcsb parameterization show strong alignment with experimental values. In the intermediate range of $q = 1.35$–$1.85$ fm$^{-1}$, qualitative agreement is observed for the $E4$ contributions, although the match is less precise.

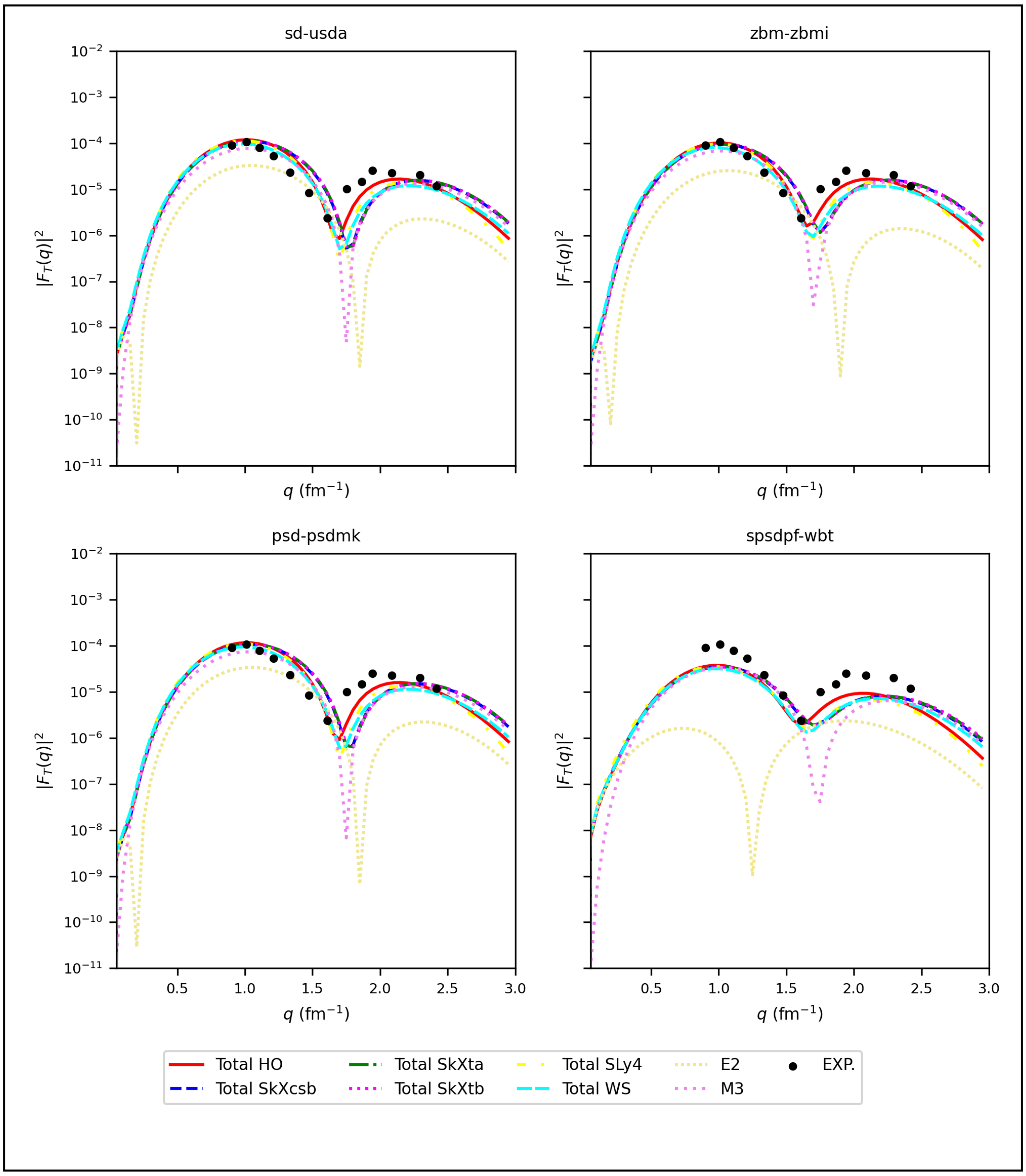

**Figure 6.** Theoretical transverse form factors $E2$ and $M3$ for the $5/2^+_1$ state at 0.197 MeV, compared with experimental data [10, 24].

For the *zbm*-model space, both $M3$ contributions and total transverse form factors across all potentials show good qualitative agreement with experiment. The *spsdpf*-model space achieves the highest accuracy for $M3$ contributions in the range $q = 1.4$–$2.4$ fm$^{-1}$, particularly with HO and SkXcsb parameterizations, where the calculated transverse form factors are in excellent agreement with experimental data. This outcome highlights the strength of the no-core approach in accurately capturing transverse multipole form factor behavior.

A critical advancement of the present work lies in the accurate reproduction of the longitudinal $C4$ form factor for the $7/2^+_1$ state, which earlier studies—most notably Brown et al. [10]—failed to achieve using the conventional *sd*-model space. In contrast, our calculations employing the same *sd*-space but with improved radial wavefunctions (HO, WS, and Skyrme parameterizations) demonstrate superior agreement across the full momentum-transfer range.

Moreover, the adoption of the *zbm* and *psd* model spaces, built on lighter $^{12}$C and $^{4}$He cores, respectively, further improves the predictive power, particularly in regions where Brown et al.'s results diverged from experiment. Most notably, the no-core *spsdpf* configuration captures the experimental $C4$ distribution with exceptional precision—across nearly the entire $q$-range—representing a novel and significant improvement not previously reported in the literature. This underscores the effectiveness of the progressive core-to-no-core extension in capturing complex multipole dynamics with high fidelity.

This study offers a significant advancement by successfully reproducing the full transverse $M3 + E4$ form factors of the $7/2_1^+$ state across a broad range of momentum transfers—an achievement not realized in previous theoretical studied. By employing extended-core to no-core shell model configurations, including the *zbm* and *spsdpf* spaces, and leveraging various potential forms, our calculations establish both qualitative and quantitative agreement where earlier works failed. The enhanced accuracy, especially at higher $q$-values, demonstrates the strength of our model in resolving complex multipole components and affirms the effectiveness of our comprehensive shell-model strategy in capturing collective excitations beyond the capabilities of earlier studies.

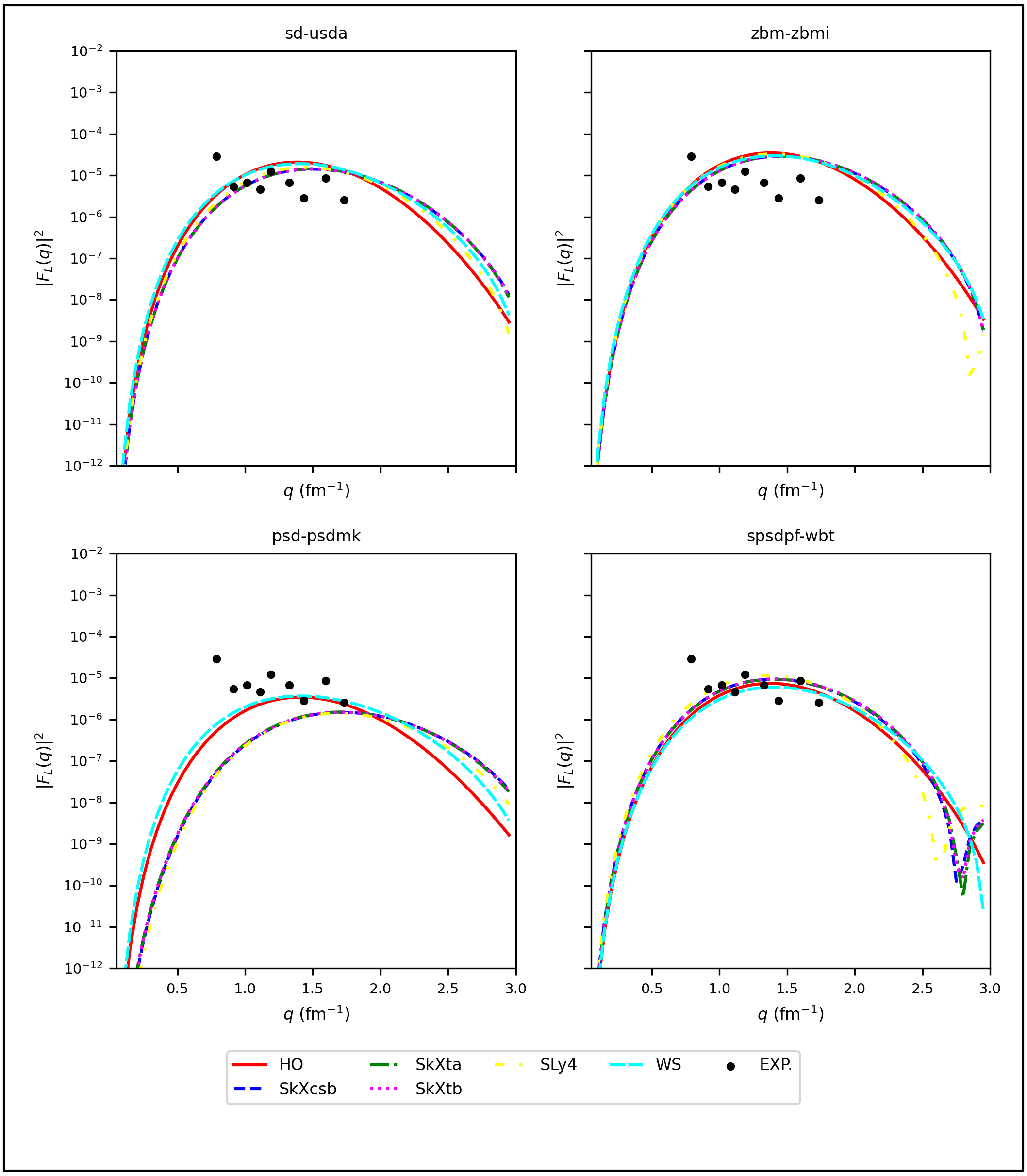

**Figure 7.** Theoretical longitudinal form factor $C4$ for the $7/2_1^+$ state compared with experimental data [10].

The $^{19}$F nucleus can be excited by an incident electron to the $9/2_1^+$ state at 2.779 MeV. The only allowed multipole contributions in this excitation are the Coulomb $C4$, transverse electric $E4$, and transverse magnetic $M5$ components. These contributions are illustrated in Figs. 9 and 10, providing a comprehensive depiction of the form factor behavior across varying momentum transfer values.

The calculated results for the longitudinal $C4$ form factor, as shown in Fig. 9, closely replicate the measured values over the full $q$-range of 0.8–2.4 $\mathrm{fm}^{-1}$, demonstrating excellent agreement both qualitatively and quantitatively. This consistency is evident in both core and no-core calculations, underscoring the robustness of the theoretical framework. The transverse form factors of the $9/2_1^+$ state of $^{19}$F are presented in Fig. 10. The experimental data are accurately reproduced by the total transverse form factor ($E4 + M5$) across the entire momentum transfer range of 0.9–2.4 $\mathrm{fm}^{-1}$, with the $M5$ multipole generally dominating. While the total transverse form factors are calculated using all potentials, the individual $E4$ and $M5$ components are explicitly shown only for the SkXcsb parameterization.

Notably, the no-core calculations reveal a reversal in dominance: the $E4$ contribution exceeds that of $M5$, a finding that stands in contrast to the core-based results, where $M5$ remains the dominant component. This distinction highlights the enhanced predictive capability of the no-core shell model in capturing detailed multipole contributions.

The successful reproduction of both the longitudinal $C4$ and transverse total ($E4 + M5$) form factors for the $9/2_1^+$ state across all model spaces—ranging from traditional core-based (*sd*, *zbm*, *psd*) to the fully untruncated *spsdpf* no-core configuration—marks a notable advancement over previous studies, which relied solely on the *sd*-model space. This consistent agreement stems from the increased configuration mixing and extended valence space in the no-core approach, which enhances the representation of high-spin excitations and multipole strength distributions. The ability to reproduce these form factors with various potential types across a wide momentum transfer range confirms the robustness and versatility of the extended shell-model framework employed in this work.

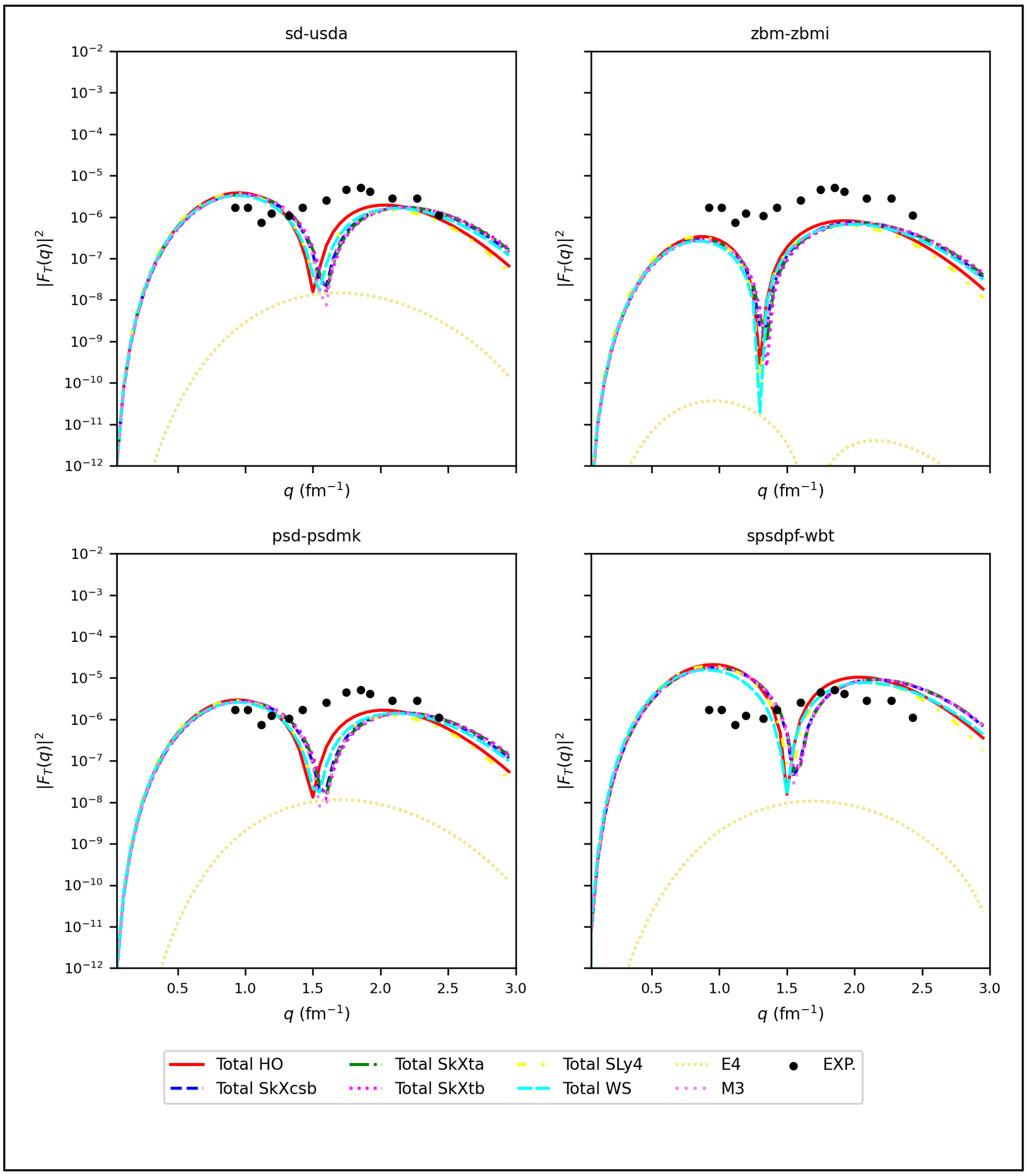

**Figure 8.** Theoretical transverse form factors $M3$ and $E4$ for the $7/2_1^+$ state at 4.377 MeV compared with experimental data [10].

Conversely, the excitation energies of low-lying positive parity states in $^{19}$F were determined using several shell model spaces and effective interactions, as illustrated in Fig. 11. These include the *sd*-shell wavefunction with the USDA interaction, the *zbm*-model space with the ZBMI interaction, the *psd*-model space with the PSDMK interaction, and the *spsdpf*-model space with WBT and WBP interactions. Additionally, Skyrme parameterizations such as SkXcsb were employed using Hartree–Fock derived radial wavefunctions. Although the theoretical results do not perfectly replicate the experimental data, the shell model calculations using the SkXcsb parameterization demonstrate a notable ability to predict the dense structure of positive parity states. Similar conclusions were drawn by Radhi et al. [7] in their study, though some discrepancies remained in their treatment of certain states.

Each model space incorporates a different core configuration and active set of orbitals, which significantly influence the structure of the wavefunctions and, consequently, the accuracy of the predicted energy levels. The *sd*-shell configuration, using an inert $^{16}$O core and active $1d_{5/2}$, $2s_{1/2}$, and $1d_{3/2}$ orbitals, effectively reproduces the $J^\pi = 3/2^+_1, 5/2^+_1$, and $9/2^+_1$ states, confirming the dominant role of *sd*-shell structure in low-lying positive parity excitations.

The *zbm*-model space, with a $^{12}$C core and active $1p_{1/2}$, $1d_{5/2}$, and $2s_{1/2}$ orbitals, introduces additional configuration mixing, allowing for better agreement with experiment for states like $J^\pi = 7/2^+_2$ and $1/2^+_2$. In contrast, the *psd*-model space builds wavefunctions over a light $^4$He core and bridges the *p*-shell and *sd*-shell orbitals. It includes active shells $1p_{1/2}$, $1p_{3/2}$, $1d_{3/2}$, $1d_{5/2}$, and $2s_{1/2}$ above the inert $^4$He core, while the $(1s)^4$ configuration remains closed. This model space captures cross-shell effects and yields improved predictions for the $J^\pi = 3/2^+_1, 5/2^+_1$, and $9/2^+_1$ states.

The *spsdpf*-model space is the most extensive, including orbitals from the $1s$, $1p$, $2s$-$1d$, and $1f$-$2p$ major shells with specific truncations. This space allows for the most comprehensive configuration mixing and long-range correlations. Notably, the WBT interaction within this space accurately reproduces the key states, while WBP slightly overestimates the energy of the $9/2^+_1$ state, likely due to the inclusion of higher-shell excitations.

Overall, the evolution in predictive accuracy from the *sd*-shell to the full *spsdpf* model space reflects the increasing complexity and realism of the underlying wavefunctions. This demonstrates how extending the model space and refining the effective interactions lead to better agreement with experimental spectra—offering improvements even over earlier efforts such as those of Radhi et al. [7, 8].

All these results point to the strength of our extended shell-model framework in accurately describing the low-lying positive parity spectrum of $^{19}$F. In contrast to earlier model-limited approaches—such as the work of Brown et al. [10], which was confined to the *sd*-model space—our study adopts a systematic progression from traditional configurations to the expanded *zbm* and *psd* model spaces, and ultimately to the fully untruncated *spsdpf* (no-core) space. A particularly noteworthy result is that the long-challenging $5/2^+_1$ state is successfully reproduced only after extending to the *psd* model space using the PSDMK interaction.

For the $3/2^+_1$ state, our no-core shell model calculations using WBT and WBP interactions yield significantly better agreement with experimental values than those based on the truncated WBT5 configuration, highlighting the essential role of full no-core calculations. Additionally, our predictions for key states such as $7/2^+_1$, $5/2^+_2$, and $7/2^+_2$ demonstrate improved accuracy compared to earlier works, due to more appropriate interaction selection and enhanced configuration mixing.

Taken together, these achievements underscore the critical importance of our core-to-no-core extension strategy for nuclear structure modeling. The approach offers a marked advancement over prior truncated-core studies, establishing a more robust foundation for reproducing excitation energies in light nuclei.

Building upon the shell-model frameworks employed in the analysis of energy levels and form factors, this study extends the investigation to include reduced transition probabilities $B(\eta J)$, magnetic dipole moments ($\mu$), and electric quadrupole moments ($Q$). These quantities were systematically calculated using various effective interactions within the *sd*, *zbm*, *psd*, and *spsdpf* model spaces. Consistent effective charges of $\delta e_p = 0.5$ and $\delta e_n = 0.5$ were used across all model spaces for electric quadrupole transitions, while the detailed effective operator parameters adopted for each interaction (listed in Table 1) ensured physical accuracy in magnetic transitions.

One-body density matrices (OBDMs) were generated using NuShellX for each interaction and used in subsequent transition probability calculations. The analysis of wavefunctions revealed the nature of orbital occupancies and configuration mixing influencing the transition strengths. For instance, in the *sd*-shell wavefunction, the USDA interaction demonstrates excellent reproduction of both $M1$ and $E2$ transitions, such as $1/2^+ \longrightarrow 3/2^+$ (M1 = 0.1611 vs. 0.15(9)) and $1/2^+ \longrightarrow 5/2^+$ (E2 = 62.13 e$^2$fm$^4$ vs. 62.8(7) exp), owing to its fine-tuned mixing between the $d_{5/2}$ and $s_{1/2}$ orbitals. USDB shows similar trends but slightly underperforms in the $1/2^+ \longrightarrow 3/2^+$ M1 transition.

In the *zbm* model space, ZWM provides superior agreement for $E2$ transitions compared to ZBMI, particularly in the $1/2^+ \longrightarrow 5/2^+$ ($E2 = 61.4\ e^2 \cdot \mathrm{fm}^4$) and $3/2^+ \longrightarrow 5/2^+$ transitions, due to its more realistic treatment of *p*-*sd* shell mixing and improved core excitation modeling. ZBMI's relatively weak $M1$ value (0.05158) for the $1/2^+ \longrightarrow 3/2^+$ transition highlights its limitations in capturing spin-flip contributions. Within the *psd* model space, PSDMK reproduces experimental $M1$ and $E2$ values more accurately than PSDMWK, emphasizing its stronger inclusion of cross-shell excitations.

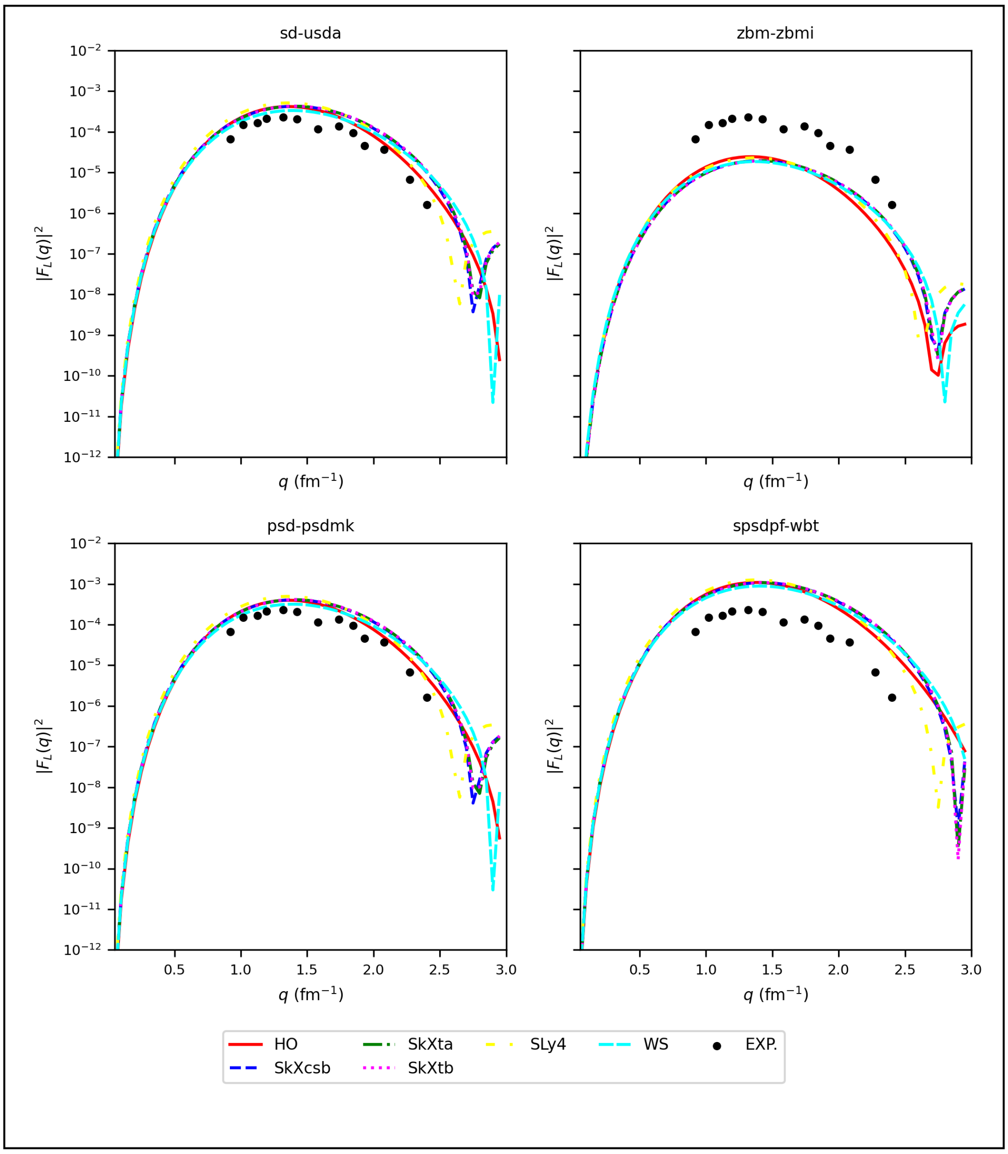

**Figure 9.** Theoretical longitudinal form factor $C4$ for the $9/2_1^+$ state compared with experimental data [10].

**Table 1.** Effective charge values for various model space interactions.

| **Interaction** | $e_p$ | $e_n$ | $g_{lp}$ | $g_{ln}$ | $g_{sp}$ | $g_{sn}$ | $g_{tp}$ | $g_{tn}$ |
|---|---|---|---|---|---|---|---|---|
| USDA | 1.36 | 0.45 | 1.175 | -0.106 | 5.000 | -3.500 | 0.26 | -0.17 |
| USDB | 1.36 | 0.45 | 1.174 | -0.110 | 5.000 | -3.440 | 0.24 | -0.16 |
| USDE | 1.36 | 0.45 | 1.174 | -0.110 | 5.000 | -3.440 | 0.24 | -0.16 |
| SDBA | 1.50 | 0.50 | 1.000 | 0.000 | 5.586 | -3.826 | 0.00 | 0.00 |
| ZBMI | 1.50 | 0.50 | 1.000 | 0.000 | 5.586 | -3.826 | 0.00 | 0.00 |
| ZWM | 1.50 | 0.50 | 1.000 | 0.000 | 5.586 | -3.826 | 0.00 | 0.00 |
| PSDMK | 1.50 | 0.50 | 1.000 | 0.000 | 5.586 | -3.826 | 0.00 | 0.00 |
| PSDMWK | 1.50 | 0.50 | 1.000 | 0.000 | 5.586 | -3.826 | 0.00 | 0.00 |

For example, the $5/2^+ \rightarrow 1/2^+$ ($M3$) transition reaches 35.13 $e^2 \cdot \text{fm}^6$ with PSDMK versus 87.32 $e^2 \cdot \text{fm}^6$ in PSDMWK, where the latter overestimates the strength due to excessive configuration mixing. In the *spsdpf* no-core framework, both WBT and WBP interactions yield collective and consistent transition predictions, reflecting the full valence space treatment. Notably, WBT gives a closer match to the experimental $B(M1)$ for the $1/2^+ \rightarrow 3/2^+$ transition (0.1130), while WBP better balances $E2$ and $M3$ contributions across higher-spin states.

Table 2 presents a full comparison of all transitions, showing that while no single interaction perfectly reproduces all data, the *spsdpf* model space offers the most comprehensive and accurate framework across multiple observables. This

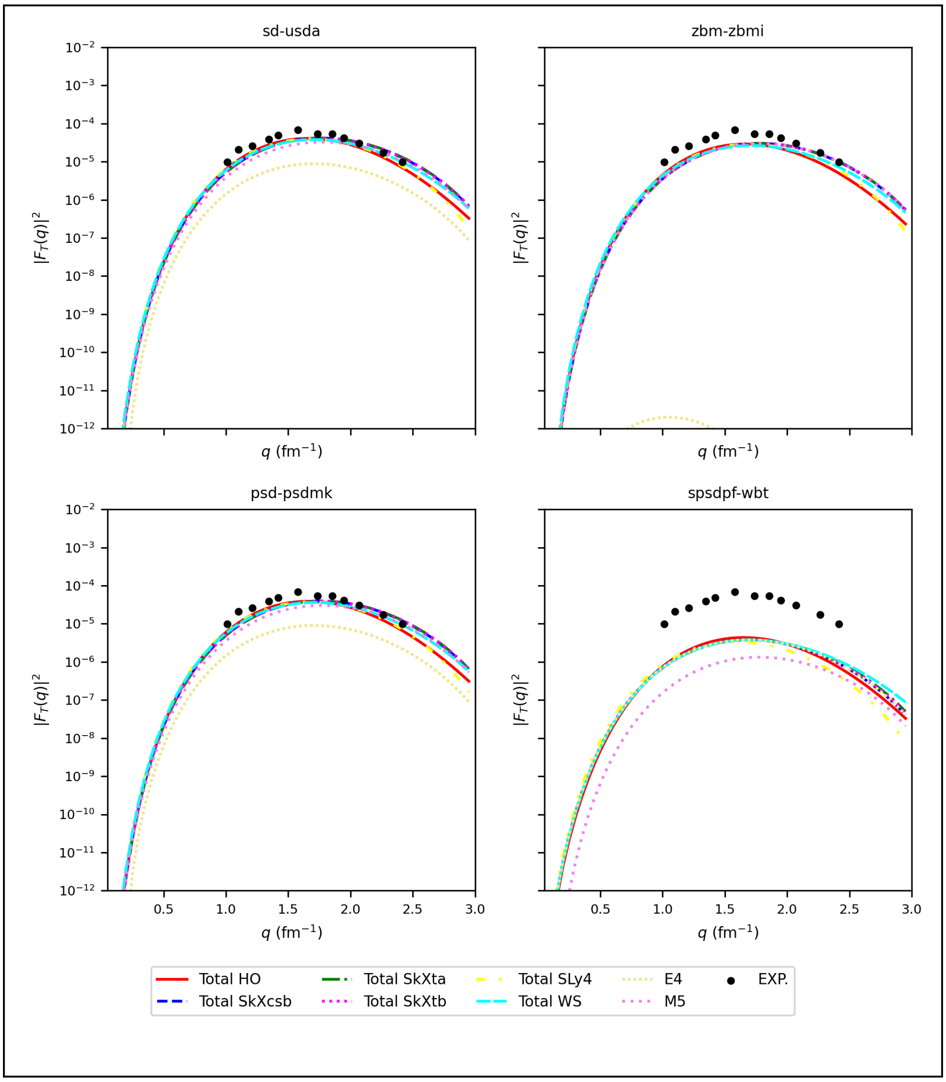

**Figure 10.** Theoretical transverse form factors $E4$ and $M5$ for the $9/2_1^+$ state at 2.779 MeV compared with experimental data [10].

behavior can be directly attributed to the inclusion of all nucleons and full cross-shell correlations, enhancing collective transition behavior.

**Table 2.** Reduced transition probabilities of positive parity states of $^{19}$F compared with experimental data [28, 29].

| $J_i^\pi \to J_f^\pi$ | $wL$ | Exp. | sd | | zbm | | psd | | spsdpf | |
|---|---|---|---|---|---|---|---|---|---|---|
| | | | USDA | USDE | ZBMI | ZWM | PSDMK | PSDMWK | WBT | WBP |
| $1/2^+ \to 1/2^+$ | M1 | 0.0547 | 0.0604 | 0.00827 | 0.00022 | 0.06595 | 0.05858 | 0.00699 | 0.01797 | 0.01696 |
| $1/2^+ \to 3/2^+$ | M1 | 0.15(9) | 0.1611 | 0.2075 | 0.1104 | 0.05158 | 0.1235 | 0.07885 | 0.1130 | 0.1123 |
| | E2 | – | 54.61 | 53.34 | 3.385 | 26.37 | 53.34 | 53.24 | 102.4 | 49.77 |
| $1/2^+ \to 5/2^+$ | E2 | 62.8(7) | 62.13 | 83.11 | 57.22 | 61.4 | 82.2 | 82.56 | 79.31 | 79.25 |
| $1/2^+ \to 7/2^+$ | E4 | – | 180.8 | 132.7 | 328.3 | 90.72 | 175.3 | 61.75 | 44.45 | 42.24 |
| $1/2^+ \to 9/2^+$ | E4 | – | 5699 | 5483 | 457.3 | 410.9 | 5322 | 4744 | 5104 | 5111 |
| $5/2^+ \to 1/2^+$ | E2 | 20.93(4) | 27.32 | 27.7 | 19.07 | 20.47 | 27.4 | 27.52 | 26.44 | 26.42 |
| | M3 | – | 16.74 | 18.36 | 88.57 | 50.60 | 35.13 | 87.32 | 95.3 | 94.76 |
| $3/2^+ \to 5/2^+$ | E2 | – | 11.46 | 11.36 | 16.93 | 12.14 | 12.05 | 12.36 | 11.89 | 11.97 |
| | M1 | 4.1(25) | 3.893 | 3.91 | 0.6341 | 1.628 | 3.809 | 3.804 | 3.744 | 3.752 |
| $9/2^+ \to 5/2^+$ | E2 | 24.7(27) | 27.00 | 27.36 | 15.20 | 23.57 | 26.66 | 28.88 | 28.87 | 28.75 |
| | M3 | – | 13.29 | 19.5 | 33.43 | 77.96 | 54.86 | 51.79 | 21.67 | 22.62 |

The present work delivers several significant advances over earlier theoretical studies in reproducing reduced transition probabilities of $^{19}$F across multiple model spaces and interactions. Notably, while Brown et al. [10] and Radhi et al. [7, 8] employed only the *sd*-model space and failed to reproduce the $M1$ transition for $1/2_1^+ \to 1/2_1^+$, our study demonstrates that the USDA interaction within the *sd*-shell yields a transition strength ($B(M1) = 0.0604\ \mu_N^2$) in close agreement with the experimental value (0.0547), a success not previously reported. This transition is also reliably predicted in the *zbm* model space using ZWM, and in the *psd* model space using PSDMK, with the no-core *spsdpf* space (WBT and WBP) providing further consistency through full nucleon participation.

Furthermore, for the $1/2_1^+ \rightarrow 3/2_1^+$ transition, our results clearly surpass earlier works that struggled with underprediction: USDA and USDE interactions in the *sd*-shell give $B(M1)$ values of 0.1611 and 0.2075 $\mu_N^2$, respectively—both within or close to the experimental uncertainty of 0.15(9). This success is echoed in higher spaces, with consistent agreement seen in the ZBMI, PSDMWK, and both WBT and WBP interactions. For the electric quadrupole transition $1/2^+ \rightarrow 5/2^+$, while previous studies reported agreement using *sd*-shell only, our work refines this further with enhanced precision using the USDA interaction and demonstrates excellent prediction using the ZWM interaction of the *zbm* space.

Importantly, transitions such as $5/2^+ \rightarrow 1/2^+$ (E2), $3/2^+ \rightarrow 5/2^+$ (M1), and $9/2^+ \rightarrow 5/2^+$ (E2)—either missing or poorly treated in earlier literature—are predicted with strong experimental agreement across all model spaces. The results emphasize the key role of interaction selection (e.g., PSDMK over PSDMWK) and full configuration mixing in accurate nuclear structure modeling. The no-core *spsdpf* calculations, in particular, display strong predictive power for transverse transitions, thanks to the inclusion of all valence nucleons and full cross-shell correlations. Collectively, these findings highlight the robustness and flexibility of our extended shell-model framework, which systematically overcomes prior limitations in predicting transition observables of $^{19}$F.

In addition to the reduced transition probabilities, the present study evaluated the magnetic dipole and electric quadrupole moments of positive parity states in $^{19}$F, as summarized in Table 3. Specifically, the magnetic moments of the $1/2_1^+$ and $5/2_1^+$ states and the quadrupole moment of the $5/2_1^+$ state were computed using the effective operator parameters listed in Table 1. The magnetic dipole moment of the $1/2_1^+$ ground state shows excellent agreement with the experimental value of $+2.682(1)\ \mu_N$ when employing *sd*-shell model space interactions—particularly USDA, USDB, and USDE—which yield values ranging from +2.681 to +2.689 $\mu_N$.

For the excited $5/2_1^+$ state, the magnetic dipole moment is better reproduced by *psd*-shell interactions—namely PSDMK and PSDMWK—which provide values of +3.636 and +3.594 $\mu_N$, respectively, closely matching the experimental measurement of $+3.605(8)\ \mu_N$. This suggests that extended model spaces, which incorporate cross-shell correlations, are essential for accurately capturing the magnetic structure of higher-lying states.

Furthermore, the electric quadrupole moment of the $5/2_1^+$ state—which reflects the nuclear charge deformation—is best described by *sd*-shell interactions. These interactions produce values around $-9.47\ e \cdot \text{fm}^2$, which are in close

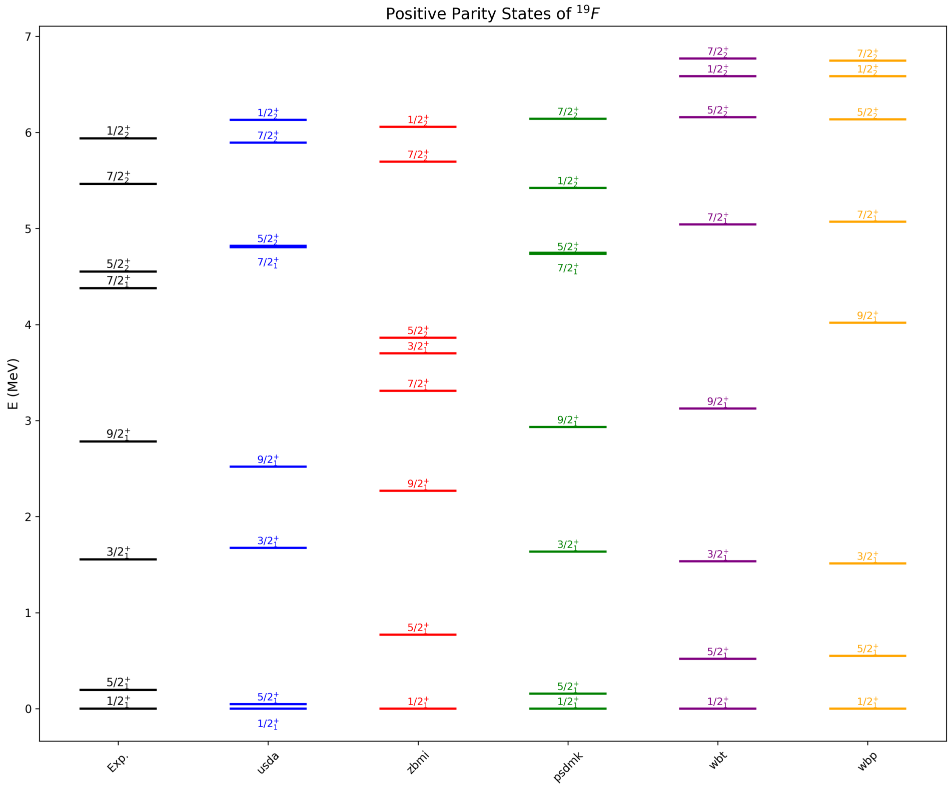

Figure 11. Comparison of experimental [26, 27] and theoretical energy levels for positive parity states in $^{19}$F using various shell model spaces and interactions.

agreement with the experimental result of $-9.42(9)$ $e \cdot \text{fm}^2$. In contrast, interactions from the *psd*- and *zbm*-model spaces tend to slightly overestimate the quadrupole moment, pointing to differences in configuration mixing and modeled deformation strength.

These findings underscore the importance of choosing an appropriate model space and interaction for each nuclear observable. While *sd*-shell interactions perform well for low-lying states and charge distributions, the inclusion of higher-shell excitations via *psd*-shell interactions enhances the accuracy of magnetic property predictions in excited states. For improved precision in electromagnetic observables—especially nuclear moments—careful tuning of effective charges and $g$-factors within each model space is strongly recommended.

**Table 3.** Magnetic dipole and electric quadrupole moments of $^{19}$F compared with experimental data [30, 31].

| **Magnetic Dipole Moments ($\mu$ in $\mu_N$)** | | | | | | | | | |
|---|---|---|---|---|---|---|---|---|---|
| State | USDA | USDB | USDE | SDBA | ZBMI | ZWM | PSDMK | PSDMWK | Exp. |
| $1/2^+_1$ | +2.689 | +2.681 | +2.683 | +2.881 | +2.352 | +2.587 | +2.841 | +2.860 | +2.682(1) |
| $5/2^+_1$ | +3.448 | +3.424 | +3.438 | +3.486 | +3.756 | +3.375 | +3.636 | +3.594 | +3.605(8) |
| $3/2^+_1$ | –1.585 | –1.571 | –1.582 | –1.531 | +0.628 | –1.182 | –1.492 | –1.375 | – |
| $7/2^+_1$ | +2.070 | +2.082 | +2.023 | +0.816 | +2.643 | +1.699 | +2.532 | +0.761 | – |
| $9/2^+_1$ | +3.178 | +3.209 | +3.206 | +3.685 | +2.754 | +3.116 | +3.609 | +3.662 | – |
| **Electric Quadrupole Moments ($Q$ in $e \cdot \text{fm}^2$)** | | | | | | | | | |
| State | USDA | USDB | USDE | SDBA | ZBMI | ZWM | PSDMK | PSDMWK | Exp. |
| $5/2^+_1$ | –9.47 | –9.47 | –9.48 | –10.37 | –8.92 | –9.00 | –10.37 | –10.41 | –9.42(9) |
| $3/2^+_1$ | –6.26 | –6.16 | –6.19 | –6.92 | +4.44 | –3.27 | –6.98 | –6.82 | – |
| $7/2^+_1$ | –3.50 | –3.56 | –3.63 | –3.83 | –4.15 | –4.53 | –3.48 | –4.82 | – |
| $9/2^+_1$ | –11.31 | –11.41 | –11.37 | –13.18 | –9.75 | –11.10 | –12.55 | +13.00 | – |

The current calculation has also had a significant success at the correct re-production of magnetic dipole and the electric quadrupole moments of chosen low lying positive parity states in $^{19}$F. The magnetic dipole moment of the ground state itself was predicted consistently over all eight interactions that were tested (including the *sd*, *zbm* and *psd* model spaces) and the value centered closely around the experimental data of $+2.682(1)\,\mu_N$. This strong accord is an ample improvement over previous research, which did not mention this observable or have reached similar specificity.

Further, in an excited $3/2^+_1$ state, the magnetic dipole moments obtained by us are very consistent in all the interactions, indicating them to be more reliable than it had been earlier predicted by the differences in theoretical predictions which reported no success of reproduction. In like fashion, the electric quadrupole moment of the $5/2^+_1$ state, a quantity not yet published in too much detail, was calculated with uncanny accuracy utilizing all eight of the interactions, with values of about $-9.47$ $e \cdot \text{fm}^2$, reminiscently of the experimental value of $-9.42(9)$ $e \cdot \text{fm}^2$.

Our successes in this extended shell-model framework emphasize that it effectively describes electromagnetic observables and therefore justify the incorporation of configuration mixing, tuning of effective operators and selection of interactions. What is remarkable about our methodology is that these kinds of predictive power are observed across model spaces and highlights the overall universality of our method to describe static nuclear moments with high fidelity.

Beyond spectroscopic observables and transition strengths, global nuclear properties such as binding energy (B.E.) and root mean square (rms) charge radii were also examined. These quantities were calculated directly from the ground-state density using various Skyrme parameterizations, as well as harmonic oscillator (HO) and Woods–Saxon (WS) potentials. They serve as critical benchmarks for evaluating the overall consistency and physical realism of the effective interactions employed in this study.

The inclusion of B.E. and rms values serves two key purposes. First, it validates the physical reliability of the Skyrme parameter sets used by ensuring that they can reproduce not only the spectroscopic features but also the bulk properties of the $^{19}$F nucleus. Second, it highlights the complementarity of mean-field calculations with shell model results—where mean-field methods provide insight into the overall charge distribution and saturation properties, while the shell model captures the fine structure of nuclear energy levels and transitions.

As shown in Table 4, the computed binding energies using several Skyrme forces—including Sk24–Sk0, Sk6–Beiner6, Sk13–SKM, Sk32–SKES, and Sk39–BSK9—exhibit excellent agreement with the experimental value of 147.803 MeV. Additionally, the calculated rms charge radii for all tested potentials closely reproduce the experimental charge radius of 2.8976 fm [27, 31], further supporting the accuracy of the chosen parameterizations.

These results confirm that the Skyrme interactions adopted in this work can reliably describe both microscopic and macroscopic aspects of the nuclear structure of $^{19}$F, thereby reinforcing the theoretical foundation of the present shell model and mean-field analyses.

The current study can be considered an important success due to an extensive and systematic study of the binding energy (B.E.) and root-mean-square (rms) charge radii of the $^{19}$F nucleus based on 39 different Skyrme parameterizations as well as harmonic oscillator (HO) and Woods Saxon (WS) potentials. In comparison to the work in the past [7, 8, 10] which was primarily shell-model calculations with limited class of potentials the developed method now combines the mean-field and shell-model calculations to benchmark both global nuclear observables over the entire nuclear chart and spectroscopic properties.

These results assure that both B.E. and charge radii of the system $^{19}$F, can be reproduced successfully with suitable Skyrme forces and radial potentials actually ensuring a crucial test of the physical reality of the actuated forces. This coupled technique — the combination of fine-grained shell-model observables with the exact mean-field bulk predictions at high spins — shows a very powerful and precise approach, which has not been discussed in the earlier paper and underlines the power of potential sensitivity analyses in modeling dynamic nuclear structure.

**Table 4.** Binding energy (B.E.) and rms charge radii of $^{19}$F using various Skyrme parameterizations and potentials. Experimental values: B.E. = 147.803 MeV and $r_{\text{ch}}$ = 2.8976 fm.

| Model Space | Potential | B.E. (MeV) | B.E. (Exp.) | rms (fm) | rms (Exp.) |
|---|---|---|---|---|---|
| sd, zbm, psd, spsdpf | sk2-Vb2 | 142.2196 | 147.803 | 2.855 | 2.8976 |
| | sk3-beiner3 | 146.5063 | | 2.818 | |
| | sk4-beiner4 | 142.4055 | | 2.881 | |
| | sk5-beiner5 | 139.2073 | | 2.941 | |
| | sk6-beiner6 | 148.0414 | | 2.803 | |
| | sk7-kohler-a | 144.0451 | | 2.875 | |
| | sk8-kohler-b | 144.2349 | | 2.882 | |
| | sk9-sktk | 115.1575 | | 2.950 | |
| | sk10-sgi | 146.0965 | | 2.877 | |
| | sk11-sgii | 150.1265 | | 2.854 | |
| | sk12-skm | 151.6722 | | 2.833 | |
| | sk13-skm | 147.3542 | | 2.860 | |
| | sk14-mska | 141.4855 | | 2.830 | |
| | sk15-skt6 | 147.1135 | | 2.819 | |
| | sk17-skcs4 | 143.0829 | | 2.847 | |
| | sk18-skxce | 145.1445 | | 2.821 | |
| | sk19-skxm | 145.3997 | | 2.841 | |
| | sk20-skx | 145.1938 | | 2.820 | |
| | sk21-skxcsb | 145.4588 | | 2.820 | |
| | sk22-msk7 | 144.9606 | | 2.857 | |
| | sk24-sk0 | 147.8587 | | 2.838 | |
| | sk25-skxcsba | 146.1035 | | 2.815 | |
| | sk26-skxcsbb | 144.4030 | | 2.836 | |
| | sk27-skxta | 143.7830 | | 2.826 | |
| | sk28-skxtb | 144.7598 | | 2.823 | |
| | sk29-sly4 | 146.3719 | | 2.876 | |
| | sk30-tondeur | 141.1392 | | 2.855 | |
| | sk31-ske | 146.9856 | | 2.756 | |
| | sk32-skes | 147.3375 | | 2.811 | |
| | sk33-skz | 153.0687 | | 2.730 | |
| | sk34-skzs | 153.0824 | | 2.796 | |
| | sk35-skzs* | 152.1491 | | 2.807 | |
| | sk36-skrs | 156.0048 | | 2.778 | |
| | sk37-skgs | 155.9344 | | 2.778 | |
| | sk38-skesb | 146.2880 | | 2.814 | |
| | sk39-bsk9 | 148.1878 | | 2.849 | |
| | sk41-skxs15 | 145.6563 | | 2.881 | |
| | sk42-skxs20 | 144.9317 | | 2.888 | |
| | sk43-skxs25 | 144.2756 | | 2.897 | |
| | HO | – | | 2.902 | |
| | WS | – | | 2.8532 | |

## 4. CONCLUSIONS

This work presented a detailed exploration of the positive parity states in $^{19}$F using progressively enlarged shell-model spaces, beginning with core-based ($sd$, $zbm$, $psd$) and culminating in the full untruncated no-core ($spsdpf$) description. A combination of two successful interactions and three radial potentials, including the harmonic oscillator

(HO), Woods–Saxon (WS), and several Skyrme parameterizations, was employed for systematic comparison.

The study achieved notable successes in reproducing longitudinal and transverse form factors across multiple multipoles ($C0$, $C2$, $C4$, $M1$, $M3$, $E2$, $E4$, $E4 + M5$). In particular, the $C0$ and $M1$ form factors for the ground state were well described in all spaces, while the best agreement for excited states such as $3/2^+$, $5/2^+$, and $7/2^+$ was found in the no-core calculations. Energy levels of important states ($3/2^+_1$, $5/2^+_1$, and $5/2^+_2$) were more satisfactorily reproduced than in earlier work, due to improved interactions and configuration mixing. Transition probabilities $B(M1)$ and $B(E2)$ showed enhanced sensitivity to interaction type and model space, while low-lying electromagnetic moments, notably of $1/2^+$ and $5/2^+$, were consistently reproduced. Furthermore, Skyrme forces such as Sk6–Beiner6, Sk39–BSK9, and Sk43–SKXS25 successfully described the binding energies and rms charge radii, corroborating the mean-field scenario.

When viewed together with our previous investigation of the negative parity states in $^{19}$F [1], a coherent picture emerges. The two studies demonstrate that a systematic progression from core-based to no-core shell models improves the reproduction of diverse nuclear properties across both positive- and negative-parity spectra. For negative parity, the $psd$ and no-core spaces were shown to capture higher-order transitions and transverse form factors, while for positive parity, the no-core approach provided superior agreement for multipole form factors, excitation energies, and transition probabilities. Collectively, these results confirm that fully correlated, no-core descriptions are essential for reproducing the structure of $^{19}$F with high accuracy, reinforcing the importance of unifying shell-model and Hartree–Fock frameworks in nuclear structure studies.

## ORCID

**Berun N. Ghafoor**, https://orcid.org/0000-0003-0450-3919; **Aziz H. Fatah**, https://orcid.org/0000-0001-7917-5820; **Ari K. Ahmed**, https://orcid.org/0009-0003-7872-6848

## REFERENCES

[1] B.N. Ghafoor, A.H. Fatah, and A.K. Ahmed, East Eur. J. Phys. **2**, 119 (2025). https://doi.org/10.26565/2312-4334-2025-2-12

[2] W. Ryssens, and Y. Alhassid, Eur. Phys. J. A, **57**(2), 76 (2021). https://doi.org/10.1140/epja/s10050-021-00416-2

[3] A. Saxena, and P.C. Srivastava, J. Phys. G: Nucl. Part. Phys. **47**(5), 055113 (2020). https://doi.org/10.1088/1361-6471/ab7ff1

[4] K.S. Jassim, and S.R. Sahib, Int. J. Nucl. Energy Sci. Technol. **12**(1), 81 (2018). https://doi.org/10.1504/IJNEST.2018.091057

[5] B. Singh, *et al.*, AIP Conf. Proc. **2292**(1), (2020). https://doi.org/10.1063/5.0029420

[6] O. Le Noan, and K. Sieja, Phys. Rev. C, **111**(6), 064308 (2025). https://doi.org/10.1103/PhysRevC.111.064308

[7] R.A. Radhi, A.A. Alzubadi, and E.M. Rashed, Nucl. Phys. A, **947**, 12 (2016). https://doi.org/10.1016/j.nuclphysa.2015.12.004

[8] R.A. Radhi, A.A. Abdullah, and A.H. Raheem, Nucl. Phys. A, **798**(1–2), 16 (2008). https://doi.org/10.1016/j.nuclphysa.2007.11.005

[9] N.A. Smirnova, *et al.*, Phys. Rev. C, **100**(5), 054329 (2019). https://doi.org/10.1103/PhysRevC.100.054329

[10] B.A. Brown, B.H. Wildenthal, C.F. Williamson, F.N. Rad, S. Kowalski, H. Crannell, and J.T. O'Brien, Phys. Rev. C, **32**(4), 1127 (1985). https://doi.org/10.1103/PhysRevC.32.1127

[11] P. Ring, and P. Schuck , *The Nuclear Many-Body Problem*, New Ed. (Springer, 2004). https://doi.org/10.1007/978-94-010-0460-2

[12] J.D. Walecka, *Theoretical Nuclear and Subnuclear Physics*, (World Scientific, 2004). https://doi.org/10.1142/5500

[13] T.H.R. Skyrme, Philos. Mag. **1**(8), 1043 (1956). https://doi.org/10.1080/14786435608238186

[14] J.R. Stone, *et al.*, Prog. Part. Nucl. Phys. **58**(2), 587 (2007). https://doi.org/10.1016/j.ppnp.2006.07.001

[15] D. Vautherin, *et al.*, Phys. Rev. C, **5**(3), 626 (1972). https://doi.org/10.1103/PhysRevC.5.626

[16] D. Vautherin, *et al.*, Phys. Lett. B, **32**(3), 149 (1970). https://doi.org/10.1016/0370-2693(70)90458-2

[17] E.G. Nadjakov, K.P. Marinova, and Yu.P. Gangrsky, *Systematics of nuclear charge radii*, At. Data Nucl. Data Tables, **56**(1), 133 (1994). https://doi.org/10.1006/adnd.1994.1005

[18] R. Hofstadter, "High-energy electron scattering and the charge distributions of selected nuclei," in: *Nobel Lecture in Physics*, (1961). https://doi.org/10.1103/PhysRev.101.1131

[19] B.A. Brown, and W.D.M. Rae, Nucl. Data Sheets, **120**, 115 (2014). https://doi.org/10.1016/j.nds.2014.07.022

[20] T.W. Donnelly, and J.D. Walecka, Annu. Rev. Nucl. Sci. **25**, 329 (1975). https://doi.org/10.1146/annurev.ns.25.120175.001553

[21] T.W. Donnelly, and J.D. Walecka, Ann. Phys. **93**, 1–57 (1975). https://doi.org/10.1146/annurev.ns.25.120175.001553

[22] J.P. Elliott, and T.H.R. Skyrme, Proc. R. Soc. Lond. A, **232**(1191), 561 (1955). https://doi.org/10.1098/rspa.1955.0239.

[23] A. J. H. Donné, *et al.*, Nucl. Phys. A, **455**, 453 (1986). https://doi.org/10.1016/0375-9474(86)90317-9

[24] A. J. H. Donné, *et al.*, Nucl. Phys. A, **469**, 518 (1987). https://doi.org/10.1016/0375-9474(87)90037-6

[25] Y. Utsuno, and S. Chiba, Phys. Rev. C, **83**, 021301(R) (2011). https://doi.org/10.1103/PhysRevC.83.021301

[26] National Nuclear Data Center (NNDC), http://www.nndc.bnl.gov/.

[27] D. R. Tilley, H. R. Weller, C. M. Cheves, and R. M. Chasteler, Nucl. Phys. A, **595**, 1 (1995). https://doi.org/10.1016/0375-9474(95)00338-1

[28] N. J. Stone, *Table of Recommended Nuclear Magnetic Dipole Moments*, INDC(NDS)-0794, International Atomic Energy Agency, (2019). https://www-nds.iaea.org/publications/indc/indc-nds-0794/

[29] N. J. Stone, *Table of Recommended Nuclear Magnetic Dipole Moments: Part II, Short-Lived States*, INDC(NDS)-0816, International Atomic Energy Agency, (2020). https://www-nds.iaea.org/publications/indc/indc-nds-0816/

[30] N. J. Stone, *Table of nuclear electric quadrupole moments*, At. Data Nucl. Data Tables, **111**, 1 (2016). https://doi.org/10.1016/j.adt.2015.11.002

[31] I. Angeli, *A consistent set of nuclear rms charge radii: Properties of the radius surface $R(N,Z)$*, At. Data Nucl. Data Tables, **87**(2), 185 (2004). https://doi.org/10.1016/j.adt.2004.04.002

# РОЗШИРЕННЯ ВІД ОСНОВНОЇ ДО БЕЗОСНОВНОЇ МОДЕЛІ ЯДЕРНОЇ ОБОЛОНКИ З ХВИЛЬОВОЮ ФУНКЦІЄЮ ХАРТРІ–ФОКА: ЗАСТОСУВАННЯ ДО СТАНІВ З ПОЗИТИВНОЮ ПАРНІСТЮ В $^{19}$F

**Берун Н. Гафур[1,2], Азіз Х. Фатах[3], Арі К. Ахмед[1]**

[1] *Університет Сулеймані, Коледж освіти, Фізичний факультет, Ірак*
[2] *Науково-дослідний центр, Університет Сулеймані, Ірак*
[3] *Університет Сулеймані, Коледж природничих наук, Фізичний факультет, Ірак*

У цій роботі представлено детальне дослідження низько розташованих станів з позитивною парністю в ядрі $^{19}$F шляхом поєднання методів оболонкової моделі з розрахунками Хартрі–Фока (HF). Дослідження систематично поширюється від традиційних просторів на основі ядра ($sd$, $zbm$, $psd$) до повністю неусіченої конфігурації без ядра ($spsdpf$). Реалістичні одночастинкові хвильові функції були згенеровані за допомогою гармонічного осцилятора (HO), параметризацій Вудса-Саксона (WS) та 39 Скірма. Підхід був протестований на широкому наборі спостережуваних величин, включаючи спектри збудження, електромагнітні форм-фактори ($C0$, $C2$, $C4$, $M1$, $M3$, $E2$, $E4$ та $E4+M5$), ймовірності переходів, магнітні дипольні та електричні квадрупольні моменти, а також енергії зв'язку та середньоквадратичні радіуси зарядів. Розбіжності, про які повідомлялося в попередніх теоретичних роботах, особливо для переходів $M1$ та $C4$ при більших передачах імпульсу, були вирішені за допомогою розширених модельних просторів та уточнених радіальних хвильових функцій. Разом з нашим попереднім дослідженням станів негативної парності в $^{19}$F, ці результати дають цілісну картину: систематичні розширення від ядра до відсутності ядра є важливими для точного відтворення як детальних, так і об'ємних ядерних властивостей. Ця єдина структура посилює теоретичне моделювання $^{19}$F та закладає основу для майбутніх досліджень ядер у перехідних та деформованих областях за допомогою оболонкових моделей.

**Ключові слова:** *модель ядерної оболонки; модель без оболонки; хвильова функція Хартрі–Фока; Skyrme Хартрі–Фок; ефективна взаємодія; електромагнітні форм-фактори; енергетичні рівні* $^{19}F$

East European Journal of Physics. **4**. 133–140 (2025)

DOI: 10.26565/2312-4334-2025-4-11 ISSN 2312-4334

# SECONDARY NEUTRON AND PROTON PRODUCTION IN PROTON-INDUCED REACTIONS WITH $^{12}C$, $^{14}N$ AND $^{16}O$ NUCLEI

**Rustam Murtazin**[1*], **Stepan Karpus**[2,1]
[1] *National Science Center "Kharkiv Institute of Physics and Technology", 1 Akademichna, Kharkiv, 61108, Ukraine*
[2] *Lutsk National Technical University, 75, Lvivska, Lutsk, 43018, Ukraine*
[*] *Corresponding Author e-mail: rumurtazin@gmail.com*

Received July 24, 2025; revised October 3, 2025; in final form October 29, 2025; accepted November 3, 2025

The results of computer simulation of the secondary neutrons and protons yield per one incident proton during the interaction of protons with an energy of 50 MeV with light nuclei - $^{12}C$, $^{14}N$ and $^{16}O$ using the TALYS - 1.96 code by default are presented. The importance of taking into account the radiation of secondary nucleons - neutrons and protons is a necessary element in conducting fundamental and applied nuclear research, such as dosimetry and radiation safety. As a result, the values of the total cross section for the secondary neutrons and protons production were obtained, that indicate significant differences in their energy range dependencies versus the target nucleus. For the nucleus $^{12}C$, the threshold for the production of neutrons is in the region of 20 MeV. A similar characteristic for $^{14}N$ lies in the region of up to 10 MeV, and for $^{16}O$ the total neutron production threshold is 17-18 MeV. The maximum neutron yield per incident proton is observed for the $^{16}O$ nucleus. The total secondary proton production cross-section and their yield were also determined. In the case of proton yield, the oxygen nucleus demonstrates the largest number of secondary protons per proton, which is 1.47. The calculated values of the energy differential cross-section of the secondary radiation of protons and neutrons were also obtained. The maximum average energy of secondary protons is observed for the $^{14}N$ nucleus and is 12.72 MeV, while for the $^{12}C$ and $^{16}O$ nuclei it is about 10 MeV. Analysis of the energy differential cross-section of secondary neutrons showed that the maximum average energy is possessed by neutrons formed as a result of interaction with the nitrogen nucleus, while the energies of secondary neutrons formed on the nuclei of $^{12}C$ and $^{16}O$ are approximately equal (6.2 and 6.4, respectively).

**Keywords:** *Light nuclei; Secondary nucleons, TALYS*

**PACS:** 25.40-h, 87.53.Bn

## 1. INTRODUCTION

Interactions of medium-energy protons (tens to hundreds of MeV) with materials containing light elements such as Carbon - 12, Nitrogen - 14, and Oxygen - 16 are of significant scientific and practical interest. These elements are fundamental constituents of biological objects, air, various shielding materials, and components of detectors used in radiation fields. Proton beams in this energy range are extensively utilized in fundamental nuclear research and notably in proton therapy for cancer treatment. Beyond these applied aspects, a thorough understanding of proton-nucleus interactions at intermediate energies, including the precise characterization of all emitted particles, is crucial for fundamental nuclear physics. Such data provide stringent tests for nuclear reaction models, help refine our knowledge of nuclear structure, nucleon-nucleon interactions within the nuclear medium, and mechanisms of particle production like pre-equilibrium emission and compound nucleus decay. Accurate cross-section and spectral data for proton-induced reactions on light nuclei are also essential for benchmarking and improving nuclear data libraries used in various simulation codes.

Accurate assessment of the radiation field characteristics and its subsequent effects, including absorbed dose and radiation damage, is determining for all these applications. While the primary proton beam is the initial source of radiation, its interaction with the nuclei of the traversed medium leads to the generation of a complex secondary radiation field. This field comprises not only scattered primary protons but also a variety of secondary particles, such as neutrons, light charged particles (protons, deuterons, alpha particles), and heavier residual nuclei.

These secondary particles often possess a broad spectrum of energies and wide angular distributions. They can contribute significantly to the total energy deposition, linear energy transfer (LET) distributions, and thus to the relative biological effectiveness (RBE) of the radiation, sometimes in regions considerably distant from the primary beam path or even outside the target volume. Consequently, neglecting or inadequately accounting for the contribution of these secondary particles can lead to substantial inaccuracies in dosimetry calculations, treatment planning in proton therapy (e.g., out-of-field doses), or underestimation of radiation-induced damage in materials and electronic components.

An issue of secondary emission for many years is important point that holds the attention of scientific literature and this aspect of experimental nuclear physics is still considered as critical question, the number of studies were carried out to research the emission properties and effects of secondary interaction [1, 2, 3]. Moreover, in experimental nuclear physics employing track detectors such as streamer chambers or bubble chambers for studying proton-induced reactions, the presence of secondary particles generated within target or detector volume can significantly complicate an analysis. These secondaries can imitate or distort the signatures of the primary reaction products, leading to potential misidentification

---

***Cite as:*** R. Murtazin, S. Karpus, East Eur. J. Phys. 4, 133 (2025), https://doi.org/10.26565/2312-4334-2025-4-11

of event topologies (e.g., two-, three-, four-, or five-pointed events) and systematic errors in the determination of reaction cross-sections and particle kinematics.

The primary objective of this work is to computationally investigate and highlight the importance of secondary protons and neutrons produced during the interaction of 50 MeV protons with $^{12}C$, $^{14}N$, and $^{16}O$ nuclei. Utilizing the nuclear reaction code TALYS - 1.96, the energy spectra, total production cross-sections, and yields of these secondary nucleons were calculated . The results aim to demonstrate the significant contribution of these secondary particles to the overall radiation environment and to underscore the necessity of their explicit consideration for comprehensive and accurate radiation exposure assessments in contexts involving carbon-, nitrogen-, and oxygen-containing materials.

## 2. METHODS OF CALCULATION

The nuclear reaction calculations for the interaction of protons with $^{12}C$, $^{14}N$, and $^{16}O$ target nuclei were performed using the TALYS code, version 1.96 [4]. TALYS is a versatile nuclear reaction code capable of simulating the basic types of nuclear reactions in the energy range up to several hundred megaelectronvolts.

For all calculations, the default physical models and parameters embedded in TALYS - 1.96 were utilized. Based on the TALYS output files (and a list of input parameters previously provided by user), the key default settings include:

Nuclear Masses: Experimental nuclear mass values from current databases were used. In cases where experimental data were unavailable for certain intermediate or daughter nuclei, TALYS employed theoretical masses calculated using the Duflo-Zuker model[5].

Optical Model Potential (OMP): A local optical potential model was used for the interaction of nucleons (protons and neutrons) with nuclei. This implies that TALYS attempts to select the best OMP parameters from its local library for the specific nuclide and energy, what is often based on the global phenomenological Koning-Delaroche potential [6] for nucleons. For alpha particles, the Avrigeanu parameterization was used , and for deuterons, a standard phenomenological parameterization was retained.

Nuclear Level Densities (LD): A complex model was used, putting together the Constant Temperature Model (CTM) at low excitation energies with the Fermi Gas Model (FGM) at higher energies [7]. Shell corrections were accounted for using the Myers-Swiatecki model[8].

Pre-equilibrium Processes: The contribution from pre-equilibrium decay was calculated based on the two-component exciton model, that distinguishes between proton and neutron degrees of freedom, utilizing Williams formula [9] for the particle-hole state density.

Statistical Decay (Compound Nucleus): The decay of the compound nucleus is described within the framework of the Hauser-Feshbach statistical model, including width fluctuation corrections according to the Moldauer model [10, 11].

Gamma-ray Emission: For E1 transitions, the Kopecky-Uhl generalized Lorentzian (GLO) model [12] was used, and for M1 transitions, a standard Lorentzian (SMLO) [13] model was employed.

Fission: Fission channel calculations were disabled, as expected for light target nuclei.

The calculations were performed for incident proton energies ranging from 5 MeV to 50 MeV with a 1 MeV step. The yields of primary nucleons that was analyzed demonstrate the effects of secondary particles of the secondary nucleons energy differential cross-section at incident proton energy of 50 MeV, as well as the total production cross-sections and yields of these particles as a function of incident proton energy.

## 3. RESULTS

This section presents the results obtained from TALYS - 1.96 simulations for the interaction of protons with $^{12}C$, $^{14}N$, and $^{16}O$ nuclei, focusing on the production of secondary protons and neutrons.

### 3.1. Total Production Cross-Sections and Secondary Neutron and Proton Yields

The calculated total neutron production cross-sections as a function of incident proton energy ($E_p$) for $^{12}C$, $^{14}N$, and $^{16}O$ targets are presented in Figure 1a.

For the $^{12}C$ target, neutron production indicates a threshold energy around 20 MeV, that corresponds to the Q-value of the most likely neutron-producing channel, e.g., $^{12}C(p,n)^{12}N$ (Q ≈ -18.1 MeV). Above this threshold, the cross-section rises steadily with increasing incident proton energy, reaching approximately 156.1 mb at 50 MeV. The corresponding neutron yield (average number of neutrons produced per incident proton) at 50 MeV is 0.4.

The $^{14}N$ target shows an earlier seizure of neutron production, with a reasonable threshold below 10 MeV, consistent with the Q-value for the $^{14}N(p,n)^{14}O$ reaction (Q ≈ - 5.9 MeV). The cross-section enlarges with energy, though with a less steep slope compared to $^{12}C$ in some energy regions, and reaches about 199.8 mb at 50 MeV. The neutron yield at 50 MeV for $^{14}N$ is 0.46.

For the $^{16}O$ target, the threshold for neutron production is marked around 17-18 MeV, which aligns with the Q-value for the $^{16}O(p,n)^{16}F$ reaction (Q ≈ -16.2 MeV). Similar to $^{12}C$, the cross-section increases with incident energy, attaining a value of approximately 214.1 mb at 50 MeV. The neutron yield at this energy is 0.46.

Comparing the three targets at 50 MeV, the total neutron production cross-section is highest for $^{16}O$, followed by $^{14}N$, and then $^{12}C$. The neutron yields at 50 MeV are comparable for $^{14}N$ and $^{16}O$, and somewhat lower for $^{12}C$.

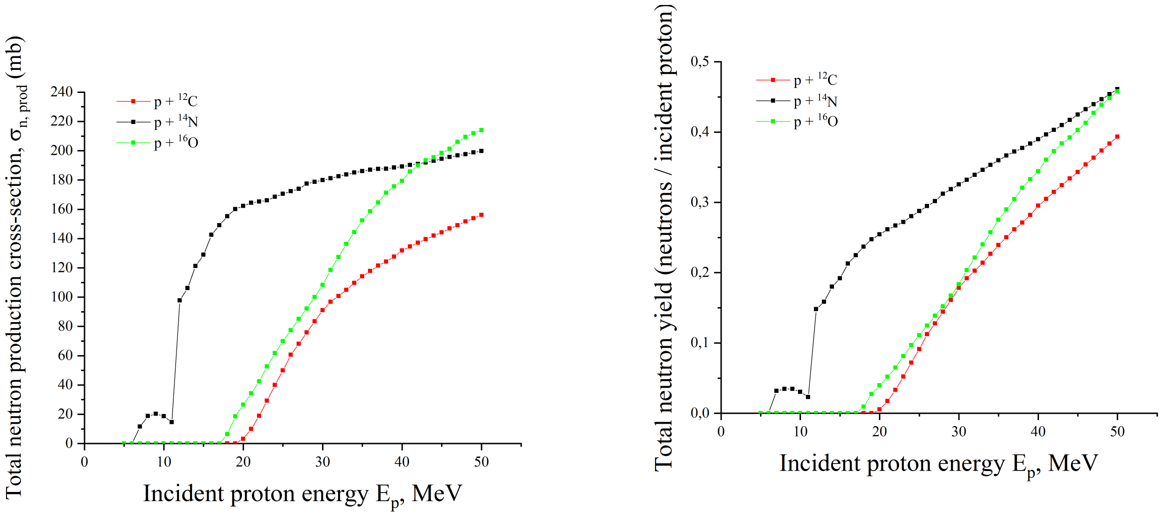

**Figure 1.** The dependence of total neutron production cross-section (*a*) and total neutron yield (*b*) versus incident proton energy $E_p$

### 3.1.1. Proton production

The total proton production cross-sections, which include contributions from elastically scattered primary protons as well as secondary emitted protons, are shown as a function of incident proton energy ($E_p$) in Figure 2.

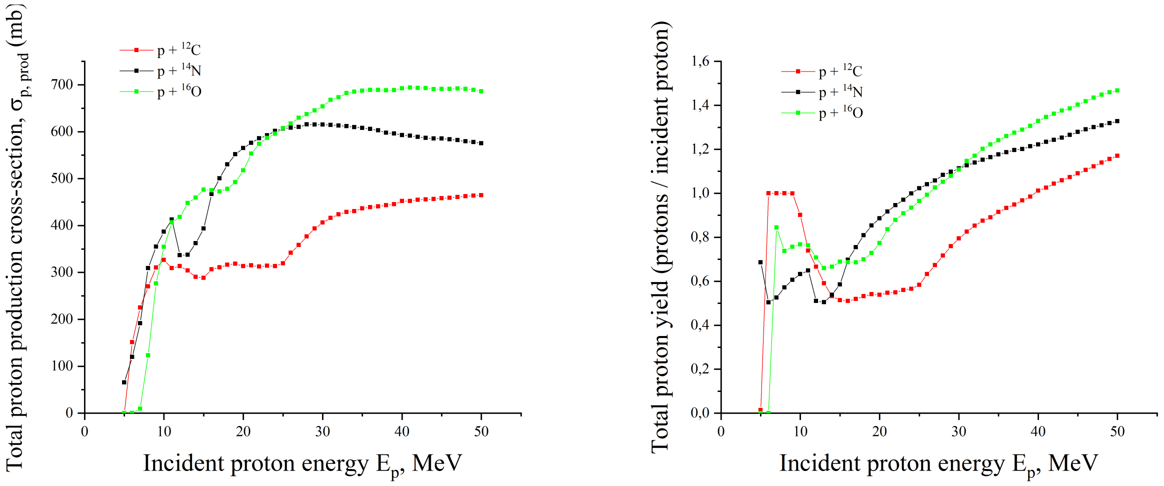

**Figure 2.** The dependence of total proton production cross-section (*a*) and total proton yield (*b*) versus incident proton energy $E_p$

For all three targets: $^{12}C$, $^{14}N$, and $^{16}O$ - the total proton production cross-section is non-zero even at the lowest incident energies considered (5-7 MeV), primarily due to elastic scattering. As the incident energy increases, the cross-sections generally rise. For $^{12}C$, the cross-section rises from a small value, increases significantly up to around 25-30 MeV, and then shows a more gradual raise, reaching approximately 464.3 mb at 50 MeV. The corresponding total proton yield at 50 MeV is 1.17, indicating that, on average, more than one proton exits the interaction per incident proton, confirming the production of secondary protons in addition to the scattered primary ones.

The $^{14}N$ target exhibits a considerable proton production cross-section across the energy range, starting around 65.6 mb at 5 MeV and expanding to about 575.3 mb at 50 MeV. The yield for $^{14}N$ at 50 MeV is 1.33.

For $^{16}O$, a notable proton production cross-section begins around 7 MeV. It increases with energy, reaching approximately 686.1 mb at 50 MeV, the highest among the three targets. The total proton yield for $^{16}O$ at 50 MeV is 1.47.

A comparison at 50 MeV shows that $^{16}O$ has the largest total proton production cross-section and yield, followed by $^{14}N$, and then $^{12}C$. The yields consistently greater than one for all targets at higher energies (above ~26 MeV for $^{16}O$, ~25 MeV for $^{14}N$, and ~ 40 MeV for $^{12}C$, based on the provided data) plainly demonstrate the significant role of secondary proton emission alongside the primary scattered protons.

### 3.2. Energy differential cross-sections of secondary nucleons at 50 MeV incident proton energy

#### 3.2.1. Proton energy differential cross-sections

The energy differential cross-sections of protons formed in the interaction of 50 MeV incident protons with $^{12}C$, $^{14}N$, and $^{16}O$ targets are presented in Figure 3.

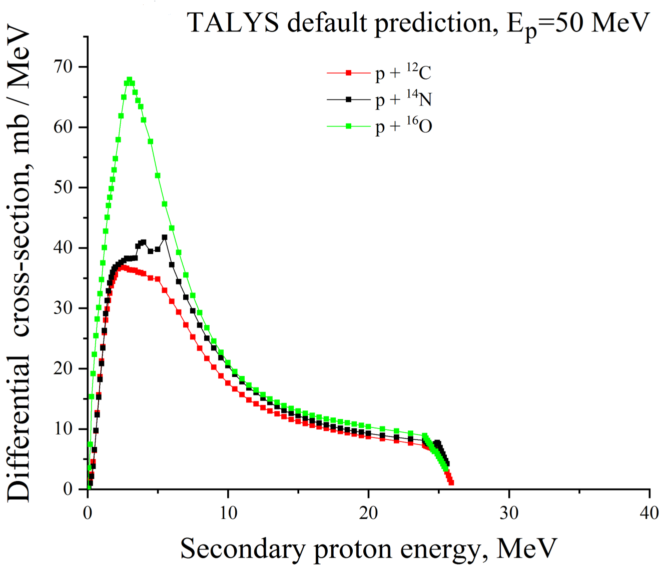

**Figure 3.** The differential cross-section versus secondary proton energy $E_p$

For all three nuclei, the energy differential cross-sections exhibit identical features. A plateau is observed at the highest outgoing proton energies, approaching the incident energy of 50 MeV. This peak primarily corresponds to elastically and quasi-elastically scattered primary protons. Below 25 MeV, a broad area extends towards lower energies, representing the contribution of secondary protons produced through various inelastic processes (such as direct knock-out or pre-equilibrium emission), as well as primary protons that have undergone significant energy loss.

The intensity and shape of this continuous part of the energy differential cross-section vary for the different targets. For $^{12}C$, the continuous energy differential cross-section of secondary protons contributes significantly, with an average outgoing proton energy (including the elastic peak) of 10.21 MeV. For $^{14}N$, the secondary proton component also appears substantial, and the average energy of all outgoing protons is 12.72 MeV. In the case of $^{16}O$, the average outgoing proton energy is 10.67 MeV.

The presence of a significant number of protons at energies much lower than incident energy, as shown by the continuous part of the energy differential cross-sections and the relatively low average outgoing proton energies, points out the importance of secondary proton production. These lower-energy secondary protons can have different transport properties and biological effectiveness compared to the primary 50 MeV protons.

#### 3.2.2. Neutron energy differential cross-sections

The energy differential cross-sections of neutrons produced from the interaction with incident protons with $^{12}C$, $^{14}N$, and $^{16}O$ targets are depicted in Figure 4.

Unlike the proton energy differential cross-sections, the neutron energy differential cross-sections do not exhibit a prominent peak corresponding to elastically scattered incident particles. Instead, they are characterized by continuous

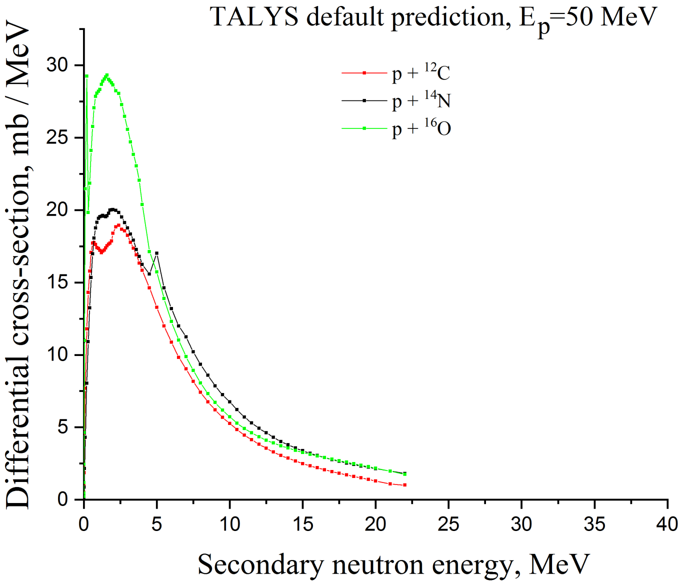

**Figure 4.** The differential cross-section versus secondary neutron energy $E_n$

distributions, primarily reflecting neutrons emitted through compound nucleus stage and pre-equilibrium processes. These processes typically result in a wide distribution of neutron energies, extending from very low energies up to a significant fraction of the available energy.

For the $^{12}C$ target, the neutron energy differential cross-section shaped by the majority of neutrons emitted at lower energies. The average energy of outgoing neutrons is 6.2 MeV.

The neutron energy differential cross-section for the $^{14}N$ target also displays a extended distribution, with an average outgoing neutron energy of 8.95 MeV. This higher average energy compared to $^{12}C$ suggests a relatively harder neutron energy differential cross-section from $^{14}N$ under these conditions.

In the case of $^{16}O$, the neutron energy differential cross-section has continuous outline, with an average outgoing neutron energy of 6.36 MeV, which is comparable to that from $^{12}C$.

The shapes of these energy differential cross-sections indicate that a large number of neutrons are produced with a wide range of energies. These secondary neutrons, particularly those with higher energies, can travel significant distances in materials and contribute to a dose deposition and radiation effects far from the initial interaction site, highlighting their importance in radiation shielding and dosimetry assessments. The differences in shapes of energy differential cross-section and average energies among the targets reflect the underlying nuclear structure and reaction dynamics specific to each nuclide.

To provide a quantitative summary of the secondary nucleon production from the interaction of 50 MeV protons with $^{12}C$, $^{14}N$, and $^{16}O$, main integral characteristics are compiled in Table 1.

**Table 1.** Summary of calculated integral characteristics for secondary nucleon production from 50 MeV proton interactions with $^{12}C$, $^{14}N$, and $^{16}O$

| Characteristic | $^{12}C$ | $^{14}N$ | $^{16}O$ |
|---|---|---|---|
| Total neutron production cross-section, mb | 156.15 | 199.8 | 214.1 |
| Neutron yield (neutrons/incident proton), n | 0.4 | 0.46 | 0.46 |
| Average outgoing neutron energy, MeV | 6.2 | 8.95 | 6.36 |
| Total proton production cross-section†, mb | 464.32 | 575.32 | 686.1 |
| Proton yield (protons/incident proton)†, n | 1.17 | 1.33 | 1.47 |
| Average outgoing proton energy, MeV | 10.21 | 12.71 | 10.67 |

† Includes contributions from elastically/quasi-elastically scattered primary protons.

This table includes the total production cross-sections for neutrons and protons, their respective yields (average number of particles produced per incident proton), and the average energies of the emitted secondary protons and neutrons at an incident proton energy of 50 MeV.

These tabulated values, along with the presented energy differential cross-sections and production cross-section excitation functions, provide a comprehensive overview of secondary proton and neutron generation for the studied targets. The data clearly indicate substantial production of secondary nucleons, with distinct characteristics depending on the target nucleus. A detailed interpretation of these findings and their implications will be discussed in the following section.

## 4. DISCUSSION

The results obtained from TALYS - 1.96 simulations provide valuable insights into the production of secondary protons and neutrons when 50 MeV protons interact with $^{12}C$, $^{14}N$, and $^{16}O$ nuclei. This section discusses the interpretation of these findings, particularly concerning their significance for radiation exposure assessments.

### 4.1. Interpretation of key findings and significance of secondary nucleons

The key findings presented in Section 3 highlight that the interaction of 50 MeV protons with carbon, nitrogen, and oxygen leads to a serious generation of secondary nucleons. Specifically, the total neutron production yields at 50 MeV were found to be 0.4 for $^{12}C$, 0.46 for $^{14}N$, and 0.46 for $^{16}O$, indicating that nearly half a neutron is produced on average per incident proton for nitrogen and oxygen targets. Similarly, total proton yields (which include scattered primary protons and produced secondary protons) were 1.17 for $^{12}C$, 1.33 for $^{14}N$, and 1.47 for $^{16}O$. Yields greater than unity for proton production directly confirm the creation of secondary protons.

The energy differential cross-sections of these secondary nucleons, that are presented in Fig. 2 and Fig. 3, further underscore their importance. The proton energy differential cross-sections in the Fig. 2 are characterized by a significant range of lower-energy protons in addition to the elastic/quasi-elastic peak. The average energies of all outgoing protons (10.21 MeV for $^{12}C$, 12.72 MeV for $^{14}N$, and 10.67 MeV for $^{16}O$) are considerably lower than the 50 MeV incident energy, indicating that a large fraction of the energy is transferred to generating these secondary protons or lost in inelastic interactions. These lower-energy protons can possess higher Linear Energy Transfer (LET) values and, consequently, an increased Relative Biological Effectiveness (RBE), which is a critical factor in radiotherapy and radiation protection.

The neutron energy differential cross-sections in the Fig. 3 are continuous, with average outgoing neutron energies of 6.2 MeV for $^{12}C$, 8.945 MeV for $^{14}N$, and 6.362 MeV for $^{16}O$. These neutrons, being uncharged, can penetrate deeper into materials and tissues, contributing to the dose deposition in regions distant from the primary proton beam path, including sensitive organs or electronic components outside the intended target volume. The production of such a significant flux of secondary neutrons with a broad energy distribution necessitates their careful consideration in shielding design and for accurate out-of-field dose estimations in proton therapy.

Neglecting these secondary protons and neutrons would lead to a serious underestimation of the total absorbed dose, an incorrect assessment of the radiation quality (average LET and RBE), and potentially compromised outcomes in applications such as radiotherapy planning or radiation risk assessment for personnel and equipment. Therefore, the explicit inclusion of secondary nucleon production data, such as those generated in this study, is crucial for accurate modeling of radiation transport and its effects in $C$, $N$, and $O$-containing media.

Furthermore, from a fundamental physics perspective, the detailed energy differential cross-sections and production cross-sections of secondary nucleons serve as valuable experimental observables (even if computationally derived or based on established models) for testing and constraining theoretical models of nuclear reactions. Discrepancies or agreements between TALYS predictions and potential future experimental data for these systems can provide understanding of employed models for optical potentials, level densities, and pre-equilibrium decay mechanisms, particularly for light nuclei where such comprehensive data might be sparse.

The production of such a significant flux of secondary neutrons with a broad energy distribution requires their careful consideration in shielding design and for accurate out-of-field dose estimations in proton therapy. Beyond dosimetric and radiation protection aspects, the substantial yields and specific energy distributions of secondary protons and neutrons, as calculated in this work, have direct implications for the interpretation of experimental data obtained from proton-nucleus interaction studies, particularly those utilizing visual track detectors like streamer chambers. For instance, secondary protons originating from primary interactions within the target or the gas inside a chamber can create additional tracks that may be erroneously attributed to the primary reaction vertex. This can lead to a misinterpretation of the multiplicity of charged particles in an event, potentially distorting the analysis of few-pointed (e.g., two-, three-, four-, or five-pointed) event topologies which are often crucial for identifying specific reaction channels. The continuous energy differential cross-sections of these secondaries, especially the lower-energy component, mean they will have varying ranges and ionization densities, further complicating track reconstruction and particle identification.

Similarly, while secondary neutrons are not directly visible in such chambers, their subsequent interactions within the detector volume or surrounding materials can produce tertiary charged particles (e.g., recoil protons), creating spurious tracks or increasing the overall background. The calculated neutron yields (approaching 0.5 neutrons per incident proton for $^{14}N$ and $^{16}O$ at 50 MeV) indicate a non-negligible probability of such effects. Therefore, proper simulation of secondary particle production, as provided by codes like TALYS, is essential not only for theoretical understanding but also as a crucial input for Monte Carlo simulations used to correct experimental data for such distortions and to properly estimate detector acceptance and efficiency. This underscores the necessity for both experimentalists and theoreticians to account for the entire energy differential cross-section of secondary particles when analyzing proton-nucleus collisions.

### 4.2. Comparative analysis of secondary particle production from $^{12}C$, $^{14}N$, and $^{16}O$

The results presented indicate distinct differences in the production characteristics of secondary neutrons and protons for $^{12}C$, $^{14}N$, and $^{16}O$ targets when bombarded with 50 MeV protons, as summarized in Table 1.

Regarding neutron production, the total neutron production cross-section at 50 MeV increases with target mass, being approximately 156.1 mb for $^{12}C$, 199.8 mb for $^{14}N$, and 214.1 mb for $^{16}O$. A similar trend is observed for neutron yields, which are 0.4, 0.46, and 0.46 for $^{12}C$, $^{14}N$, and $^{16}O$, respectively. This suggests that heavier nuclei in this light-mass range offer more nucleons for interaction, leading to a higher probability of neutron emission. Interestingly, the average energy of outgoing neutrons is notably higher for $^{14}N$ (8.95 MeV) compared to $^{12}C$ (6.2 MeV) and $^{16}O$ (6.4 MeV). This could be attributed to differences in the Q-values of dominant neutron-producing reaction channels (e.g., (p,n)), neutron separation energies, and the level density distributions of the respective residual nuclei. For instance, $^{14}N$ is an odd-odd nucleus, which might influence its reaction pathways and energy distributions of emitted particles compared to the even-even $^{12}C$ and $^{16}O$ nuclei.

For proton production (including scattered primary protons and emitted secondary protons), a similar tendency of increasing total production cross-section and yield with target mass is observed at 50 MeV. The cross-sections are 464.3 mb for $^{12}C$, 575.3 mb for $^{14}N$, and 686.1 mb for $^{16}O$, with corresponding yields of 1.17, 1.33, and 1.47. The average energy of all outgoing protons is also highest for $^{14}N$ (12.72 MeV), followed by $^{16}O$ (10.67 MeV), and then $^{12}C$ (10.21 MeV). The higher average proton energy for $^{14}N$ might reflect differences in the balance between elastic/quasi-elastic scattering and the emission of lower-energy secondary protons. The Coulomb barrier will influence the emission of low-energy charged particles, but for outgoing proton energies observed, various reaction mechanisms like (p, p'), (p, 2p), and (p, pn) contribute, and their relative importance can vary with the target nucleus structure.

These target-specific differences in both neutron and proton production highlight the importance of using nuclide-specific data in applications requiring precise radiation transport calculations and dose estimations. The observed variations likely stem from a combination of factors, including nuclear size, binding energies of nucleons, individual Q-values for various open reaction channels, and the specific nuclear structure (e.g., shell effects) influencing level densities and decay paths.

## Acknowledgments

The authors of the article express their sincere gratitude to the Defense Forces of Ukraine for their courage, dedication, and defense of the country. Glory to Ukraine!

## ORCID

**Rustam Murtazin**, https://orcid.org/0009-0003-5197-8252; **Stepan Karpus**, https://orcid.org/0000-0002-1087-9245

## REFERENCES

[1] T. Oyama, T. Sanami, H. Yashima, *et al.*, Nuclear Instruments and Methods in Physics Research Section A: Accelerators, Spectrometers, Detectors and Associated Equipment, **990**, 164977 (2021). https://doi.org/10.1016/j.nima.2020.164977

[2] A. Shor, and R. Longacre, Physics Letters B, **218**, 100, (1989). https://doi.org/10.1016/0370-2693(89)90483-8

[3] V.I. Gol'danskii, A.E. Ignatenko, *et al.*, Phys. Rev. **109**, 1762 (1958). https://doi.org/10.1103/PhysRev.109.1762

[4] https://nds.iaea.org/talys/

[5] J. Duflo, and A. Zuker, Physical Review C, **52**(1), R23 (1995). https://doi.org/10.1103/PhysRevC.52.R23

[6] A. Koning, and J. Delaroche, Nuclear Physics A, **713**(3-4), 231 (2003). https://doi.org/10.1016/S0375-9474(02)01321-0

[7] A. Gilbert, and A. Cameron, Canadian Journal of Physics, **4**3(8), 1446 (1965). https://doi.org/10.1139/p65-139

[8] W.D. Myers, and W.J. Swiatecki, Nucl. Phys. **81**, 1 (1966). https://doi.org/10.1016/S0029-5582(66)80001-9

[9] F.C. Williams, Nucl. Phys. A, **166**, 231 (1971). https://doi.org/10.1016/0375-9474(71)90426-X

[10] P.A. Moldauer, Phys. Rev. C, **14**, 764 (1976). https://doi.org/10.1103/PhysRevC.14.764

[11] P.A. Moldauer, Nucl. Phys. A, **344**, 185 (1980). https://doi.org/10.1016/0375-9474(80)90671-5

[12] J. Kopecky, and M. Uhl, Phys. Rev. C, **41**, 1941 (1990). https://doi.org/10.1103/PhysRevC.41.1941

[13] S. Goriely, and V. Plujko, Physical Review C, 99(1), 014303 (2019). https://doi.org/10.1103/PhysRevC.99.014303

# ЕМІСІЯ ВТОРИННИХ НУКЛОНІВ У ВЗАЄМОДІЇ ПРОТОНІВ З ЯДРАМИ $^{12}C$, $^{14}N$ AND $^{16}O$

**Рустам Муртазін**[1], **Степан Карпусь**[2,1]
[1] *ННЦ «Харьківський-фізико-технічний інститут» НАНУ, 1, Академічна, Харків, 61108, Україна*
[2] *Луцький Національний Технічний Університет, 75, Львівська, Луцьк, 43018, Україна*

Представлено результати комп'ютерного моделювання виходу вторинних нейтронів та протонів при взаємодії протонів з енергією 50 МеВ з легкими ядрами - $^{12}C$, $^{14}N$ та $^{16}O$ за допомогою кодуTALYS - 1.96 за замовчуванням. Важливість урахування випромінювання вторинних нуклонів - нейтронів та протонів є необхідним елементом при проведенні фундаметально-прикладних ядерних досліджень, таких як дозиметрія та радіаційна безпека. Як результат отримані повні перерізи утворення вторинних нейтронів та протонів, що вказують на суттєві відмінності в залежності від ядра-мішені. Для ядра $^{12}C$ поріг утворення нейтронів знаходиться в області 20 МеВ. Аналогічна характеристика для $^{14}N$ лежить в області до 10 МеВ, а для $^{16}O$ поріг утворення нейтронів становить 17-18 МеВ. Максимальний вихід нейтронів на один налітаючий протон спостерігається для ядра $^{16}O$. Також було визначено загальний переріз утворення вторинних протонів та їх вихід на один налітаючий протон. Як і у випадку з виходом нейтронів, ядро кисню демонструє найбільшу кількість вторинних протонів на протон, що дорівнює 1,47. Також були отримані розрахункові значення диференціальних перерізів від енергії вторинних протонів та нейтронів. Максимальне значення середньої енергії вторинних протонів спостерігається для ядра $^{14}N$ і становить 12,72 МеВ, тоді як для ядер $^{12}C$ та $^{16}O$ воно становить близько 10 МеВ. Аналіз диференціальних перерізів від енергії вторинних нейтронів показав, що максимальне значення середньої енергії для нейтронів, отримано в результаті взаємодії з ядром азоту, тоді як енергії вторинних нейтронів, що утворюються на ядрах $^{12}C$ та $^{16}O$, приблизно рівні (6,2 та 6,4 відповідно).

**Ключові слова:** *легкі ядра; вторинні нуклони; TALYS*

EAST EUROPEAN JOURNAL OF PHYSICS. **4**. 141–156 (2025)
DOI: 10.26565/2312-4334-2025-4-12 ISSN 2312-4334

# QUIESCENT SOLITONS IN MAGNETO-OPTIC WAVEGUIDES WITH NONLINEAR CHROMATIC DISPERSION AND KUDRYASHOV'S FORM OF SELF-PHASE MODULATION HAVING GENERALIZED TEMPORAL EVOLUTION

**Elsayed M.E. Zayed**[1], **Mona El–Shater**[1], **Ahmed H. Arnous**[2,3], **Omer Mohammed Khodayer Al-Dulaimi**[4], **Farag Mahel Mohammed**[5], **Ibrahim Zeghaiton Chaloob**[6], **O. González–Gaxiola**[7], **Anjan Biswas**[8,9,10,11], **Carmelia Mariana Balanica Dragomir**[10]
[1]*Department of Mathematics, Faculty of Science, Zagazig University, Zagazig–44519, Egypt*
[2]*Department of Mathematical Sciences, Saveetha School of Engineering, SIMATS, Chennai - 602105, Tamilnadu, India*
[3]*Research Center of Applied Mathematics, Khazar University, Baku, AZ 1096, Azerbaijan*
[4]*Department of Communication Technical Engineering, Al–Farahidi University, Baghdad–10015, Iraq*
[5]*Al–Nibras University–Iraq, Tikrit–34001, Iraq*
[6]*Department of Business Administration, College of Administration and Economics, Al–Esraa University, Baghdad–10067, Iraq*
[7]*Applied Mathematics and Systems Department, Universidad Autónoma Metropolitana–Cuajimalpa, Vasco de Quiroga 4871, 05348 Mexico City, Mexico*
[8]*Department of Mathematics & Physics, Grambling State University, Grambling, LA 71245–2715, USA*
[9]*Department of Physics and Electronics, Khazar University, Baku, AZ–1096, Azerbaijan*
[10]*Department of Applied Sciences, Cross–Border Faculty of Humanities, Economics and Engineering, Dunarea de Jos University of Galati, 111 Domneasca Street, Galati–800201, Romania*
[11]*Department of Mathematics and Applied Mathematics, Sefako Makgatho Health Sciences University, Medunsa–0204, South Africa*
**Corresponding Author e-mail: ogonzalez@cua.uam.mx*

Received July 1, 2025; revised September 18, 2025; accepted September 23, 2025

The article discusses how Kudryashov's proposed self-phase modulation scheme and nonlinear chromatic dispersion cause the evolution of quiescent optical solitons in magneto-optic waveguides. Provide a comprehensive understanding of the governing model; generalised temporal evolution is considered. The modified sub-ODE approach is employed to facilitate the recovery of such solitons. This leads to a complete range of optical solitons and the necessary conditions that must be met for these solitons to exist, which are also provided.

**Keywords:** *Solitons; Self-Phase Modulation; Integrability; Chromatic Dispersion*

**PACS:** 02.30.Jr; 05.45.Yv; 02.30.Ik; 47.40.Nm

## 1. INTRODUCTION

The three main features of how solitons move in optical waveguides and crystals are chromatic dispersion (CD), self-phase modulation (SPM), and how pulses change over time after they are introduced at the beginning of the waveguides [1–40]. Subsequently, these pulses evolve with temporally and spatially and thus serve as bit carriers for information transmission through such fibers across transcontinental and transoceanic distances. There are many hiccups one faces during the transmission of such pulses. One issue is the soliton clutter. Therefore in order to declutter these solitons, one considers magneto–optic waveguides. This leads to the interest in magneto–optic waveguides.

This work examines soliton propagation in magneto-optic waveguides characterised by nonlinear cross-dispersion and a particular kind of self-phase modulation, as postulated by Kudryashov. We preserve the temporal evolution of the pulses using a general framework known as generalised temporal evolution. The inconsistent characteristics of waveguides would cause the solitons to get impeded during their propagation via subterranean or underwater cables. This property will be examined in depth in the present research, facilitating a clear comprehension and retrieval of the quiescent optical solitons relevant to the model discussed in this work. This understanding will not only enhance the theoretical framework surrounding self-phase modulation but also offer practical suggestions for optimising soliton transmission in complex waveguide environments. By addressing these challenges, we aim to improve the reliability and efficiency of optical communication systems that use these solitonic structures.

The mathematical algorithm that would be selected is the modified version of the sub–ODE (ordinary differential equation) approach. This integration scheme would lead to the emergence of a wide spectrum of soliton solutions along with their respective classifications. The results are reconstructed and presented in the subsequent sections of the paper following a brief review of the model, its technical characteristics, and an explanation of the integration algorithm.

---

***Cite as:*** E.M.E. Zayed, M. El–Shater, A.H. Arnous, O.M.K. Al-Dulaimi, F.M. Mohammed, I.Z. Chaloob, O. González–Gaxiola, A. Biswas, C.M.B. Dragomir, East Eur. J. Phys. 4, 141 (2025), https://doi.org/10.26565/2312-4334-2025-4-12

It must be noted that the model with the quintuple form of SPM has been addressed in the previous round for optical fibers [9]. However, the current work retrieves quiescent optical solitons for a different kind of optical waveguide, namely magneto-optic waveguides, by the implementation of the improved sub-ODE approach.

Unlike prior analyses of Kudryashov-type nonlinearities that focused on single-field optical fibers (including quintuple SPM in fibers) or on sixth/eighth-order single-field NLS equations, we study magneto–optic waveguides described by a coupled magneto–optic (MO) waveguides system with generalized nonlinear chromatic dispersion and generalized temporal evolution. This formulation introduces cross-SPM/CD terms and magneto-optic couplings ($Q_1, Q_2$) absent from fiber-only models, and enables the construction of new stationary families (bright, dark, straddled hyperbolic–rational, Jacobi elliptic, and Weierstrass) with explicit existence constraints in the MO setting. In short, the novelty lies in the medium and model (coupled MO system), the analytic framework (addendum to the improved sub-ODE within the MO model), and the solution classification with parameter regimes tailored to magneto–optic waveguides [10, 11].

### 1.1. Governing model

Zayed et al. [32] analysed the nonlinear Schrödinger equation (NLSE) with non-local nonlinearity, Kudryashov's general quintuple power law, generalised nonlinear chromatic dispersion (CD), and a generalised temporal evolution, expressed as follows:

$$i\left(\Psi^{l}\right)_{t}+a\left(|\Psi|^{r}\,\Psi^{l}\right)_{xx}+\left[b_1\,|\Psi|^{2m}+b_2\,|\Psi|^{2m+n}+b_3\,|\Psi|^{2m+n+p}+b_4\,|\Psi|^{2m+2n}+b_5\,|\Psi|^{2m+2n+p}+b_6\left(|\Psi|^{p}\right)_{xx}\right]\Psi^{l}=0, \tag{1}$$

In this context, $\Psi^l(x,t)$ denotes a complex-valued function that characterises the generalised wave shape, with the condition that $l \geq 1$ and $i = \sqrt{-1}$. The parameters $r$, $l$, $m$, $n$, and $p$ are positive real constants. The initial term relates to the generalised temporal evolution dictated by the evolution parameter $l$. The constant $a$ represents the coefficient of the generalised nonlinear CD, defined by the nonlinear parameter $r$. The constants $b_j$ $(j = 1, 2, 3, 4, 5)$ denote the coefficients of SPM arising from the nonlinear intensity-dependent refractive index framework, as examined by Kudryashov [1–3].

In magneto-optic waveguides, Eq. (1) separates into two components, as follows:

$$\begin{aligned}&i\left(\eta^{l}\right)_{t}+a_1\left(|\eta|^{k}\,\eta^{l}\right)_{xx}+[b_1\,|\eta|^{2m}+c_1\,|\eta|^{2m+n}+d_1\,|\eta|^{2m+n+p}+e_1\,|\eta|^{2m+2n}+f_1\,|\eta|^{2m+2n+p}+g_1\left(|\eta|^{p}\right)_{xx}\\&+h_1\,|\rho|^{2m}+l_1\,|\rho|^{2m+n}+s_1\,|\rho|^{2m+n+p}+n_1\,|\rho|^{2m+2n}+p_1\,|\rho|^{2m+2n+p}+q_1\left(|\rho|^{p}\right)_{xx}]\eta^{l}=Q_1\rho^{l},\end{aligned} \tag{2}$$

and

$$\begin{aligned}&i\left(\rho^{l}\right)_{t}+a_2\left(|\rho|^{k}\,\rho^{l}\right)_{xx}+[b_2\,|\rho|^{2m}+c_2\,|\rho|^{2m+n}+d_2\,|\rho|^{2m+n+p}+e_2\,|\rho|^{2m+2n}+f_2\,|\rho|^{2m+2n+p}+g_2\left(|\rho|^{p}\right)_{xx}\\&h_2\,|\eta|^{2m}+l_2\,|\eta|^{2m+n}+s_2\,|\eta|^{2m+n+p}+n_2\,|\eta|^{2m+2n}+p_2\,|\eta|^{2m+2n+p}+q_2\left(|\eta|^{p}\right)_{xx}]\rho^{l}=Q_2\eta^{l},\end{aligned} \tag{3}$$

Here, $\eta(x,t)$ and $\rho(x,t)$ are complex-valued functions representing the wave profiles, with $i = \sqrt{-1}$. The first terms in Eqs. (2) and (3) describe the generalized temporal evolution, characterized by the parameter $l \geq 1$. The constants $a_j$ $(j = 1, 2)$ are the coefficients of nonlinear CD, governed by the parameter $k \geq 0$. The constants $b_j$, $c_j$, $d_j$, $e_j$, $f_j$, $g_j$, $h_j$, $l_j$, $p_j$,$n_j$, and $q_j$ $(j = 1, 2)$ correspond SPM terms, structured according to the formulation introduced by Kudryashov [33,34]. Finally, $Q_j$ $(j = 1, 2)$ denote the coefficients associated with the magneto–optic waveguides. The parameters $m$ and $n$ are rational numbers, not necessarily integers.

This work aims to resolve Eqs. (2) and (3) by an enhancement of the modified Sub-ODE approach. This methodology is used to derive several categories of soliton solutions, including dark soliton solutions, solitary soliton solutions, Jacobi's elliptic functions, Weierstrass elliptic functions, bright soliton solutions, and straddled soliton solutions. Consequently, a broad array of soliton solutions would arise.

This article is organised as follows: Section 2 presents the mathematical study. In Section 3, a modification of the modified sub-ODE method is implemented. Section 4 presents more findings. Conclusions are presented in Section 6.

## 2. MATHEMATICAL STRUCTURE

To resolve Eqs. (2) and (3), we suggest that the wave profiles exhibit the following forms:

$$\begin{aligned}\eta\left(x,t\right)&=\phi_1(x)e^{i\lambda t},\\\rho\left(x,t\right)&=\phi_2(x)e^{i\lambda t},\end{aligned} \tag{4}$$

where $\phi_j(x)$ $(j = 1, 2)$ are real functions and $\lambda$ is a constant representing the wave number. Substituting (4) into Equations (2) and (3), we obtain:

$$\begin{aligned}
&-\lambda l\phi_1^l(x) + a_1(k+l)(k+l-1)\phi_1^{k+l-2}(x)\phi_1'^2(x) + a_1(k+l)\phi_1^{k+l-1}(x)\phi_1''(x)\\
&+b_1\phi_1^{2m+l}(x) + c_1\phi_1^{2m+n+l}(x) + d_1\phi_1^{2m+n+p+l}(x) + e_1\phi_1^{2m+2n+l}(x) + f_1\phi_1^{2m+2n+p+l}(x)\\
&+g_1p(p-1)\phi_1^{p-2+l}(x)\phi_1'^2(x) + g_1p\phi_1^{p-1+l}(x)\phi_1''(x) + h_1\phi_2^{2m}(x)\phi_1^l(x) + l_1\phi_2^{2m+n}(x)\phi_1^l(x)\\
&+s_1\phi_2^{2m+n+p}(x)\phi_1^l(x) + n_1\phi_2^{2m+2n}(x)\phi_1^l(x) + p_1\phi_2^{2m+2n+p}(x)\phi_1^l(x) + q_1p(p-1)\phi_2^{p-2+l}(x)\phi_2'^2(x)\\
&+q_1p\phi_1^{p-1+l}(x)\phi_1''(x) = Q_1\phi_2^l(x),
\end{aligned}\tag{5}$$

and

$$\begin{aligned}
&-\lambda l\phi_2^l(x) + a_2(k+l)(k+l-1)\phi_2^{k+l-2}(x)\phi_2'^2(x) + a_2(k+l)\phi_2^{k+l-1}(x)\phi_2''(x)\\
&+b_2\phi_2^{2m+l}(x) + c_2\phi_2^{2m+n+l}(x) + d_2\phi_2^{2m+n+p+l}(x) + e_2\phi_2^{2m+2n+l}(x) + f_2\phi_2^{2m+2n+p+l}(x)\\
&+g_2p(p-1)\phi_2^{p-2+l}(x)\phi_2'^2(x) + g_2p\phi_2^{p-1+l}(x)\phi_2''(x) + h_2\phi_1^{2m}(x)\phi_2^l(x)\\
&+l_2\phi_1^{2m+n}(x)\phi_2^l(x) + s_2\phi_1^{2m+n+p}(x)\phi_2^l(x) + n_2\phi_1^{2m+2n}(x)\phi_2^l(x) + p_2\phi_1^{2m+2n+p}(x)\phi_2^l(x)\\
&+q_2p(p-1)\phi_1^{p-2}(x)\phi_1'^2(x)\phi_2^l(x) + q_2p\phi_1^{p-1}(x)\phi_1''(x)\phi_2^l(x) = Q_2\phi_1^l(x),
\end{aligned}\tag{6}$$

Now, for the sake of simplicity, let us put

$$\phi_2(x) = \chi\phi_1(x),\tag{7}$$

where $\chi$ is a nonzero constant and $\chi \neq 1$. Eqs. (5) and (6) became:

$$\begin{aligned}
&-(\lambda l + Q_1\chi^l)\phi_1^l(x) + a_1(k+l)(k+l-1)\phi_1^{k+l-2}(x)\phi_1'^2(x)\\
&+a_1(k+l)\phi_1^{k+l-1}(x)\phi_1''(x) + \left(b_1 + h_1\chi^{2m}\right)\phi_1^{2m+l}(x)\\
&+\left(c_1 + l_1\chi^{2m+n}\right)\phi_1^{2m+n+l}(x) + \left(d_1 + s_1\chi^{2m+n+p}\right)\phi_1^{2m+n+p+l}(x)\\
&+\left(e_1 + n_1\chi^{2m+2n}\right)\phi_1^{2m+2n+l}(x) + \left(f_1 + p_1\chi^{2m+2n+p}\right)\phi_1^{2m+2n+p+l}(x)\\
&+(g_1 + q_1\chi^p)\,p(p-1)\phi_1^{p+l-2}(x)\phi_1'^2(x) + (g_1 + q_1\chi^p)\,p\phi_1^{p+l-1}(x)\phi_1''(x) = 0,
\end{aligned}\tag{8}$$

and

$$\begin{aligned}
&-(\lambda l\chi^l + Q_2)\phi_1^l(x) + a_2(k+l)(k+l-1)\chi^{k+l}\phi_1^{k+l-2}(x)\phi_1'^2(x)\\
&+a_2(k+l)\chi^{k+l}\phi_1^{k+l-1}(x)\phi_1''(x) + \left(b_2\chi^{2m+l} + h_2\chi^l\right)\phi_1^{2m+l}(x)\\
&+\left(c_2\chi^{2m+2n+l} + l_2\chi^l\right)\phi_1^{2m+n+l}(x) + \left(d_2\chi^{2m+n+p+l} + s_2\chi^l\right)\phi_1^{2m+n+p+l}(x)\\
&+\left(e_2\chi^{2m+2n+l} + n_2\chi^l\right)\phi_1^{2m+2n+l}(x) + \left(f_2\chi^{2m+2n+p+l} + p_2\chi^l\right)\phi_1^{2m+2n+p+l}(x)\\
&+\left(g_2\chi^{p+l} + q_2\chi^l\right)p(p-1)\phi_1^{p+l-2}(x)\phi_1'^2(x) + \left(g_2\chi^{p+l} + q_2\chi^l\right)p\phi_1^{p+l-1}(x)\phi_1''(x) = 0,
\end{aligned}\tag{9}$$

Eqs. (8) and (9) are equivalent along with constraints conditions:

$$\begin{gathered}
\lambda l + Q_1\chi^l = \lambda l\chi^l + Q_2,\\
a_1 = a_2\chi^{k+l}\\
b_1 + h_1\chi^{2m} = b_2\chi^{2m+l} + h_2\chi^l,\\
c_1 + l_1\chi^{2m+n} = c_2\chi^{2m+2n+l} + l_2\chi^l,\\
d_1 + s_1\chi^{2m+n+p} = d_2\chi^{2m+n+p+l} + s_2\chi^l,\\
e_1 + n_1\chi^{2m+n} = e_2\chi^{2m+2n+l} + n_2\chi^l,\\
f_1 + p_1\chi^{2m+2n+p} = f_2\chi^{2m+2n+p+l} + p_2\chi^l,\\
g_1 + q_1\chi^p = g_2\chi^{p+l} + q_2\chi^l.
\end{gathered}\tag{10}$$

Solving Eq. (8), let $k = 6m, p = 4m, n = 2m$ then Eq.(8) is now

$$\begin{aligned}
&-(\lambda l + Q_1\chi^l) + a_1(6m+l)(6m+l-1)\phi_1^{6m-2}(x)\phi_1'^2(x)\\
&+a_1(6m+l)\phi_1^{6m-1}(x)\phi_1''(x) + \left(b_1 + h_1\chi^{2m}\right)\phi_1^{2m}(x)\\
&+\left(c_1 + l_1\chi^{4m}\right)\phi_1^{4m}(x) + \left(d_1 + s_1\chi^{8m}\right)\phi_1^{8m}(x)\\
&+\left(e_1 + n_1\chi^{6m}\right)\phi_1^{6m}(x) + \left(f_1 + p_1\chi^{10m}\right)\phi_1^{10m}(x)\\
&+\left(g_1 + q_1\chi^{4m}\right)(4m)(4m-1)\phi_1^{4m-2}(x)\phi_1'^2(x) + \left(g_1 + q_1\chi^{4m}\right)(4m)\phi_1^{4m-1}(x)\phi_1''(x) = 0,
\end{aligned}\tag{11}$$

Balancing $\phi_1^{10m}(x)$ with $\phi_1^{6m-1}(x)\phi_1''(x)$ in Eq.(11) gives $N = \frac{1}{2m}$, $m \neq 0$. In addition, considering the transformation

$$\phi_1(x) = V^{\frac{1}{2m}}(x),\tag{12}$$

where $V(x)$ denotes a novel function. By putting (12) into Eq. (11), we have

$$\begin{aligned}
&\Phi_1 + \Phi_2V(x)V'^2(x) + \Phi_3V^2(x)V''(x) + \Phi_4V(x) + \Phi_5V^2(x) + \Phi_6V^3(x)\\
&+\Phi_7V^4(x) + \Phi_8V^5(x) + \Phi_9V'^2(x) + \Phi_{10}V(x)V''(x) = 0,
\end{aligned}\tag{13}$$

where

$$\begin{aligned}
\Phi_1 &= -(\lambda l + Q_1\chi^l),\\
\Phi_2 &= \tfrac{a_1}{2m}(\tfrac{4m+l}{2m})(6m + l),\\
\Phi_3 &= \tfrac{a_1}{2m}(6m + l),\\
\Phi_4 &= b_1 + h_1\chi^{2m},\\
\Phi_5 &= c_1 + l_1\chi^{4m},\\
\Phi_6 &= e_1 + n_1\chi^{6m},\\
\Phi_7 &= d_1 + s_1\chi^{8m},\\
\Phi_8 &= f_1 + p_1\chi^{10m},\\
\Phi_9 &= 2\left(g_1 + q_1\chi^{4m}\right),\\
\Phi_{10} &= 2\left(g_1 + q_1\chi^{4m}\right).
\end{aligned} \tag{14}$$

Next, we will employ the integration method explained below to generate the solitons of Eqs. (2) and (3).

## 3. AN ADDENDUM TO THE IMPROVED SUB-ODE METODOLOGY

It is presumed that Eq. (13) has a formal solution [35–38]:

$$V(x) = \sum_{s=0}^{N} A_s\,[H(x)]^s\,. \tag{15}$$

The constants $A_s$, for $s = 0, 1, 2, \dots, N$ are specified, with $A_N \neq 0$, and the condition $H(x)$ is satisfied:

$$H'^2(x) = A\,H^{2-2\alpha}(x) + B\,H^{2-\alpha}(x) + C\,H^2(x) + D\,H^{2+\alpha}(x) + E\,H^{2+2\alpha}(x). \tag{16}$$

In this particular case, $E, D, C, B,$ and $A$ are constants, whereas $\alpha$ is a positive integer. Given $D[\phi(x)] = N$, then $D[\phi'(x)] = N + \alpha$, $D[\phi''(x)] = N + 2\alpha$, and so $D[\phi^{(r)}(x)] = N + r\alpha$. Therefore, $D[\phi^{(r)}(x)\phi^s(x)] = (s + 1)N + \alpha r$. When the highest derivative $V''(x)V^2(x)$ is balanced with the nonlinear term $V^5(x)$ in Eq. (13), the result is:

$$3N + 2\alpha = 5N \implies N = \alpha. \tag{17}$$

With $\alpha = 1$ and therefore $N = 1$, Eq. (15) becomes:

$$V(x) = A_0 + A_1H(x), \tag{18}$$

given that $A_0$ and $A_1$ are constants with $A_1 \neq 0$, $H(\xi)$ admits:

$$H'^2(x) = A\ + B\,H(x) + C\,H^2(x) + D\,H^3(x) + E\,H^4(x),\ \ E \neq 0. \tag{19}$$

Substituting Eqs. (18) and (19) into Eq. (13) and grouping all terms of $[H(x)]^l[H]'^f$, where $l = 0, 1, 2, \dots, 5$ and $f = 0, 1$ to zero yields:

$$\begin{cases}
H^5(x) : \Phi_8A_1^5 + (\Phi_2 + 2\Phi_3)EA_1^3 = 0,\\
H^4(x) : (\Phi_2 + 4\Phi_3)EA_0A_1^2 + \Phi_7A_1^4 + \Phi_9A_1^2E + \Phi_2A_1^3D + 5\Phi_8A_0A_1^4 + \frac{3}{2}D\Phi_3A_1^3 + 2\Phi_{10}A_1^2E = 0,\\
H^3(x) : \Phi_6A_1^3 + 10\Phi_8A_0^2A_1^3 + (\Phi_2 + \Phi_3)CA_1^3 + 2\Phi_3EA_0^2A_1 + D\Phi_2A_0A_1^2 + 3D\Phi_3A_0A_1^2\\
\qquad + 4\Phi_7A_0A_1^3 + \frac{3}{2}D\Phi_{10}A_1^2 + D\Phi_9A_1^2 + 2E\Phi_{10}A_0A_1 = 0,\\
H^2(x) : \Phi_5A_1^2 + 2\Phi_3CA_0A_1^2 + \frac{3}{2}\Phi_3DA_0^2A_1 + \frac{3}{2}D\Phi_{10}A_0A_1 + \Phi_2CA_0A_1^2 + \Phi_2A_1^3B + \Phi_9A_1^2C\\
\qquad + \Phi_{10}CA_1^2 + \frac{1}{2}\Phi_3BA_1^3 + 3\Phi_6A_0A_1^2 + 6\Phi_7A_0^2A_1^2 + 10\Phi_8A_0^3A_1^2 = 0,\\
H(x) : \Phi_4A_1 + BA_0A_1^2(\Phi_2 + \Phi_3) + C\Phi_3A_0^2A_1 + \Phi_{10}A_0A_1C + \Phi_2A_1^3A + B\Phi_9A_1^2\\
\qquad + 3\Phi_6A_0^2A_1 + 2\Phi_5A_0A_1 + 4\Phi_7A_0^3A_1 + 5\Phi_8A_0^4A_1 + \frac{1}{2}\Phi_{10}A_1^2B = 0,\\
H^0(x) : \Phi_9AA_1^2 + \Phi_7A_0^4 + \Phi_8A_0^5 + \Phi_4A_0 + \Phi_5A_0^2 + \Phi_6A_0^3 + \Phi_1 + \Phi_2A_0A_1^2A + \frac{1}{2}\Phi_3BA_0^2A_1\\
\qquad + \frac{1}{2}\Phi_{10}BA_0A_1 = 0.
\end{cases} \tag{20}$$

We will now examine each of the following sets:

**Set–1**: Considering $D = B = A = 0$ in Eq. (20), the results achieved are:

$$A_0 = A_0,\ \ A_1 = \sqrt{-\frac{E\,(\Phi_2 + 2\Phi_3)}{\Phi_8}}, \tag{21}$$

and

$$\begin{aligned}
\Phi_1 &= -\frac{A_0^2\Phi_9\left(CA_1^2+EA_0^2\right)}{A_1^2},\\
\Phi_4 &= -\frac{A_0\left(C\Phi_2A_0A_1^2+E\Phi_2A_0^3-CA_1^2(2\Phi_9+\Phi_{10})-2EA_0^2(2\Phi_9+\Phi_{10})\right)}{A_1^2},\\
\Phi_5 &= \frac{CA_0A_1^2(2\Phi_2+\Phi_3)+2EA_0^3(2\Phi_2+\Phi_3)-CA_1^2(\Phi_9+\Phi_{10})-6EA_0^2(\Phi_9+2\Phi_{10})}{A_1^2},\\
\Phi_6 &= -\frac{CA_1^2(\Phi_2+\Phi_3)+6EA_0^2(\Phi_2+\Phi_3)-2EA_0^2(2\Phi_9+3\Phi_{10})}{A_1^2},\\
\Phi_7 &= \frac{2EA_0^2(2\Phi_2+3\Phi_3)-E(\Phi_9+2\Phi_{10})}{A_1^2},
\end{aligned} \tag{22}$$

given $C > 0$ and $E < 0$, the solutions represent the bright solitons, which are:

$$\eta(x,t) = \varepsilon\left[A_0 + \sqrt{\frac{C\,(\Phi_2+2\Phi_3)}{\Phi_8}}\operatorname{sech}\sqrt{C}\,x\right]^{\frac{1}{2m}} e^{i\lambda t}, \tag{23}$$

and

$$\rho(x,t) = \chi\varepsilon\left[A_0 + \sqrt{\frac{C\,(\Phi_2+2\Phi_3)}{\Phi_8}}\operatorname{sech}\sqrt{C}\,x\right]^{\frac{1}{2m}} e^{i\lambda t}, \tag{24}$$

where $\Phi_8(\Phi_2 + 2\Phi_3) > 0$.

**Set–2**: Considering $B = D = 0$ and $A = \frac{C^2}{4E}$ are replaced into the algebraic equations (20), the results achieved are:

$$A_0 = 0,\ \ A_1 = \sqrt{-\frac{E\,(\Phi_9+2\Phi_{10})}{\Phi_7}}, \tag{25}$$

and

$$\begin{aligned}
\Phi_1 &= -\frac{A_1^2\Phi_9C^2}{4E},\\
\Phi_2 &= -\frac{\Phi_8A_1^2+2E\Phi_3}{E},\\
\Phi_4 &= \frac{A_1^2C^2\left(2E\Phi_3+\Phi_8A_1^2\right)}{4E^2},\\
\Phi_5 &= -C\left(\Phi_9+\Phi_{10}\right),\\
\Phi_6 &= \frac{C\left(\Phi_8A_1^2+E\Phi_3\right)}{E},
\end{aligned} \tag{26}$$

where $E\Phi_7(\Phi_9 + 2\Phi_{10}) < 0$. Hence, the dark solitons take the form of:

$$\eta(x,t) = \varepsilon\left[\sqrt{\frac{C\,(\Phi_9+2\Phi_{10})}{2\Phi_7}}\tanh(\sqrt{-\frac{C}{2}}\,x)\right]^{\frac{1}{2m}} e^{i\lambda t}, \tag{27}$$

and

$$\rho(x,t) = \chi\varepsilon\left[\sqrt{\frac{C\,(\Phi_9+2\Phi_{10})}{2\Phi_7}}\tanh(\sqrt{-\frac{C}{2}}\,x)\right]^{\frac{1}{2m}} e^{i\lambda t}, \tag{28}$$

provided $C < 0$, $\Phi_7(\Phi_9 + 2\Phi_{10}) < 0$ , $\varepsilon = \pm 1$.

**Set–3**: Considering $B = D = 0$ and $A = \frac{e_1C^2}{E}$ are replaced into the algebraic equations (20), the results achieved are:

$$A_0 = 0, \quad A_1 = A_1, \tag{29}$$

and

$$\begin{aligned}
\Phi_1 &= -\frac{C^2e_1\Phi_9A_1^2}{E},\\
\Phi_3 &= -\frac{\Phi_8A_1^2+E\Phi_2}{2E},\\
\Phi_4 &= -\frac{C^2e_1\Phi_2A_1^2}{E},\\
\Phi_5 &= -C\left(\Phi_9+\Phi_{10}\right),\\
\Phi_6 &= -\frac{CE\Phi_2-C\Phi_8A_1^2}{2E},\\
\Phi_7 &= -\frac{E(\Phi_9+2\Phi_{10})}{A_1^2},
\end{aligned} \tag{30}$$

assuming that $e_1$ remains constant, the following scenarios are derived:

**(I)** Considering $e_1 = \frac{m_1^2(m_1^2-1)}{(2m_1^2-1)^2}$, $A$ is given by $\frac{C^2 m_1^2(m_1^2-1)}{E(2m_1^2-1)^2}$, and $0 < m_1 < 1$, the Jacobi elliptic solutions are derived:

$$\eta(x,t) = \varepsilon \left[ A_1 \left( -\frac{C m_1^2}{E(2m_1^2-1)} \right)^{\frac{1}{2}} \operatorname{cn}\left( \sqrt{\frac{C}{2m_1^2-1}}\, x,\ m_1 \right) \right]^{\frac{1}{2m}} e^{i\lambda t}, \tag{31}$$

and

$$\rho(x,t) = \chi\varepsilon \left[ A_1 \left( -\frac{C m_1^2}{E(2m_1^2-1)} \right)^{\frac{1}{2}} \operatorname{cn}\left( \sqrt{\frac{C}{2m_1^2-1}}\, x,\ m_1 \right) \right]^{\frac{1}{2m}} e^{i\lambda t}, \tag{32}$$

provided $C\ (2m_1^2 - 1) > 0$, $E < 0$.

**(II)** When $e_1 = \frac{(1-m_1^2)}{(2-m_1^2)^2}$, $A$ is given by $\frac{C^2(1-m_1^2)}{E(2-m_1^2)^2}$, and $0 < m_1 < 1$, the Jacobi elliptic solutions are obtained:

$$\eta(x,t) = \varepsilon \left[ A_1 \left( -\frac{C}{E(2-m_1^2)} \right)^{\frac{1}{2}} \operatorname{dn}\left( \sqrt{\frac{C}{2-m_1^2}}\, x,\ m_1 \right) \right]^{\frac{1}{2m}} e^{i\lambda t}, \tag{33}$$

and

$$\rho(x,t) = \chi\varepsilon \left[ A_1 \left( -\frac{C}{E(2-m_1^2)} \right)^{\frac{1}{2}} \operatorname{dn}\left( \sqrt{\frac{C}{2-m_1^2}}\, x,\ m_1 \right) \right]^{\frac{1}{2m}} e^{i\lambda t}, \tag{34}$$

assuming $C > 0$, $E < 0$. The bright solitons are given when $m_1$ approaches $1^-$ in the Eqs. (31) - (34):

$$\eta(x,t) = \varepsilon \left[ A_1 \sqrt{-\frac{C}{E}} \operatorname{sech}\left( \sqrt{C}\, x \right) \right]^{\frac{1}{2m}} e^{i\lambda t}, \tag{35}$$

and

$$\rho(x,t) = \chi\varepsilon \left[ A_1 \sqrt{-\frac{C}{E}} \operatorname{sech}\left( \sqrt{C}\, x \right) \right]^{\frac{1}{2m}} e^{i\lambda t}. \tag{36}$$

**(III)** When $e_1 = \frac{m_1^2}{(m_1^2+1)^2}$ and $A = \frac{C^2 m_1^2}{E(m_1^2+1)^2}$ with $0 < m_1 < 1$, the resulting Jacobi elliptic solutions are:

$$\eta(x,t) = \varepsilon \left[ A_1 \left( -\frac{C m_1^2}{E(m_1^2+1)} \right) \operatorname{sn}\left( \sqrt{-\frac{C}{m_1^2+1}}\, x, m_1 \right) \right]^{\frac{1}{2m}} e^{i\lambda t}, \tag{37}$$

and

$$\rho(x,t) = \chi\varepsilon \left[ A_1 \left( -\frac{C m_1^2}{E(m_1^2+1)} \right) \operatorname{sn}\left( \sqrt{-\frac{C}{m_1^2+1}}\, x, m_1 \right) \right]^{\frac{1}{2m}} e^{i\lambda t}, \tag{38}$$

provided $E > 0$ and $C < 0$. The dark solitons, when $m_1$ approaches $1^-$ in Eqs. (37) and (38), are:

$$\eta(x,t) = \varepsilon \left[ A_1 \sqrt{-\frac{C}{2E}} \tanh\left( \sqrt{-\frac{C}{2}}\, x \right) \right]^{\frac{1}{2m}} e^{i\lambda t}, \tag{39}$$

and

$$\rho(x,t) = \chi\varepsilon \left[ A_1 \sqrt{-\frac{C}{2E}} \tanh\left( \sqrt{-\frac{C}{2}}\, x \right) \right]^{\frac{1}{2m}} e^{i\lambda t}. \tag{40}$$

**Set–4**: Considering $A = B = 0$, $C > 0$, and $D^2 = 4CE$ are replaced into the algebraic equations (20), the results achieved are:

$$A_0 = 0,\ \ A_1 = A_1, \tag{41}$$

and

$$\begin{aligned}
\Phi_2 &= -\frac{\Phi_8 A_1^2+2E\Phi_3}{E},\\
\Phi_5 &= \frac{C\left(2\sqrt{CE}\Phi_8 A_1^3+\sqrt{CE}\Phi_3 A_1 E+\Phi_7 E A_1^2+E^2\Phi_{10}\right)}{E^2},\\
\Phi_6 &= -\frac{\sqrt{CE}\left(3\sqrt{CE}\Phi_8 A_1^3+\sqrt{CE}\Phi_3 A_1 E+2\Phi_7 E A_1^2+E^2\Phi_{10}\right)}{E^2 A_1},\\
\Phi_9 &= -\frac{2\sqrt{CE}\Phi_8 A_1^3+\sqrt{CE}\Phi_3 A_1 E+\Phi_7 E A_1^2+2E^2\Phi_{10}}{E^2 A_1},\\
\Phi_1 &= \Phi_4 = 0.
\end{aligned} \tag{42}$$

Therefore, the dark solitons become:

$$\eta(x,t) = \varepsilon\left[\frac{A_1}{2}\sqrt{\frac{C}{E}}\left(1+\tanh\frac{\sqrt{C}}{2}x\right)\right]^{\frac{1}{2m}} e^{i\lambda t}, \tag{43}$$

and

$$\rho(x,t) = \chi\varepsilon\left[\frac{A_1}{2}\sqrt{\frac{C}{E}}\left(1+\tanh\frac{\sqrt{C}}{2}x\right)\right]^{\frac{1}{2m}} e^{i\lambda t}. \tag{44}$$

The singular solitons emerge as:

$$\eta(x,t) = \varepsilon\left[-\frac{A_1}{2}\sqrt{\frac{C}{E}}\left(1+\coth\frac{\sqrt{C}}{2}x\right)\right]^{\frac{1}{2m}} e^{i\lambda t}, \tag{45}$$

and

$$\rho(x,t) = \chi\varepsilon\left[-\frac{A_1}{2}\sqrt{\frac{C}{E}}\left(1+\coth\frac{\sqrt{C}}{2}x\right)\right]^{\frac{1}{2m}} e^{i\lambda t}. \tag{46}$$

The bright soliton solutions are:

$$\eta(x,t) = \left[\frac{A_1}{2}\sqrt{\frac{C}{E}}\frac{2\operatorname{sech}^2\frac{\sqrt{C}}{2}x}{[1+\tanh^2\frac{\sqrt{C}}{2}x]}\right]^{\frac{1}{2m}} e^{i\lambda t}, \tag{47}$$

and

$$\rho(x,t) = \chi\left[\frac{A_1}{2}\sqrt{\frac{C}{E}}\frac{2\operatorname{sech}^2\frac{\sqrt{C}}{2}x}{[1+\tanh^2\frac{\sqrt{C}}{2}x]}\right]^{\frac{1}{2m}} e^{i\lambda t}. \tag{48}$$

Then the singular solitons are:

$$\eta(x,t) = \left[\frac{A_1}{2}\sqrt{\frac{C}{E}}\frac{2\operatorname{csch}^2\frac{\sqrt{C}}{2}x}{[1+\coth^2\frac{\sqrt{C}}{2}x]}\right]^{\frac{1}{2m}} e^{i\lambda t}, \tag{49}$$

and

$$\rho(x,t) = \chi\left[\frac{A_1}{2}\sqrt{\frac{C}{E}}\frac{2\operatorname{csch}^2\frac{\sqrt{C}}{2}x}{[1+\coth^2\frac{\sqrt{C}}{2}x]}\right]^{\frac{1}{2m}} e^{i\lambda t}. \tag{50}$$

**Set–5**: Considering $A = 0$, $B = \frac{8C^2}{27D}$, $E = \frac{D^2}{4C}$, and $C < 0$ are replaced into the algebraic equations (20), the results achieved are:

$$A_0 = 0,\ \ A_1 = A_1, \tag{51}$$

and

$$\begin{aligned}
\Phi_1 &= 0,\\
\Phi_2 &= -\frac{6CD\Phi_3 A_1+4C\Phi_7 A_1^2+D^2\Phi_9+2D^2\Phi_{10}}{4CDA_1},\\
\Phi_4 &= -\frac{4C^2 A_1(2\Phi_9+\Phi_{10})}{27D},\\
\Phi_5 &= \frac{C(8CD\Phi_3 A_1+8C\Phi_7 A_1^2-25D^2\Phi_9-23D^2\Phi_{10})}{27D^2},\\
\Phi_6 &= \frac{2CD\Phi_3 A_1+4C\Phi_7 A_1^2-3D^2\Phi_9-2D^2\Phi_{10}}{4CA_1}.
\end{aligned} \tag{52}$$

Consequently, the corresponding solutions employing hyperbolic functions are:

$$\eta(x,t) = \left[A_1\left(-\frac{8C\tanh^2\frac{\sqrt{-3C}}{2}x}{3D\left(3+\tanh\frac{\sqrt{-3C}}{2}x\right)}\right)\right]^{\frac{1}{2m}} e^{i\lambda t}, \tag{53}$$

and

$$\rho(x,t) = \chi\left[A_1\left(-\frac{8C\tanh^2\frac{\sqrt{-3C}}{2}\ x}{3D\left(3+\tanh\frac{\sqrt{-3C}}{2}\ x\right)}\right)\right]^{\frac{1}{2m}} e^{i\lambda t}. \tag{54}$$

Also,

$$\eta(x,t) = \left[A_1\left(-\frac{8C\coth^2\frac{\sqrt{-3C}}{2}\ x}{3D\left(3+\coth\frac{\sqrt{-3C}}{2}\ x\right)}\right)\right]^{\frac{1}{2m}} e^{i\lambda t}, \tag{55}$$

and

$$\rho(x,t) = \chi\left[A_1\left(-\frac{8C\coth^2\frac{\sqrt{-3C}}{2}\ x}{3D\left(3+\coth\frac{\sqrt{-3C}}{2}\ x\right)}\right)\right]^{\frac{1}{2m}} e^{i\lambda t}, \tag{56}$$

provided $DCA_1 < 0$.

**Set–6**: When $A = B = 0$ and $E = \frac{D^2}{4C} - C$ are replaced into the algebraic equations (20), the results achieved are derived in the following cases:

$$A_0 = 0, \quad A_1 = A_1, \tag{57}$$

and

$$\begin{aligned}
\Phi_5 &= -C(\Phi_9 + \Phi_{10}),\\
\Phi_6 &= -\frac{2CA_1(\Phi_2+\Phi_3)+D(2\Phi_9+3\Phi_{10})}{2A_1},\\
\Phi_7 &= \frac{C(-4D\Phi_2A_1-6D\Phi_3A_1+4C\Phi_9+8C\Phi_{10}-D^2(\Phi_9+2\Phi_{10})}{4CA_1^2},\\
\Phi_8 &= \frac{(2C^2-D^2)(\Phi_2+2\Phi_3)}{4CA_1^2},\\
\Phi_1 &= \Phi_4 = 0.
\end{aligned} \tag{58}$$

As a result, the bright solitons become:

$$\eta(x,t) = \varepsilon A_1\left[\frac{1}{\cosh\sqrt{C}\,x - \frac{D}{2C}}\right]^{\frac{1}{2m}} e^{i\lambda t}, \tag{59}$$

and

$$\rho(x,t) = \chi A_1\left[\frac{1}{\cosh\sqrt{C}\,x - \frac{D}{2C}}\right]^{\frac{1}{2m}} e^{i\lambda t}, \tag{60}$$

where $C > 0$.

**Set–7**: Considering $B = D = 0$ are replaced into the algebraic equations (20), the results achieved are:

$$A_0 = 0, \quad A_1 = \sqrt{-\frac{(\Phi_2+2\Phi_3)E}{\Phi_8}}, \tag{61}$$

and

$$\begin{aligned}
\Phi_1 &= -A\Phi_9A_1^2,\\
\Phi_4 &= -A\Phi_2A_1^2,\\
\Phi_5 &= -C(\Phi_9 + \Phi_{10})\\
\Phi_6 &= -C(\Phi 2 + \Phi_3),\\
\Phi_7 &= -\frac{E(\Phi_9+2\Phi_{10})}{A_1^2},
\end{aligned} \tag{62}$$

where $E\Phi_8(\Phi_2 + 2\Phi_3) < 0$. In view of this, the following are the four solutions that take the form of Weierstrass elliptic functions:

**(I)**

$$\eta(x,t) = \varepsilon\left[\sqrt{-\frac{(\Phi_2+2\Phi_3)}{E\Phi_8}}\ \left(\wp\left[(x), g_2, g_3\right] - \frac{C}{3}\right)\right]^{\frac{1}{4m}} e^{i\lambda t}, \tag{63}$$

and

$$\rho(x,t) = \chi\varepsilon\left[\sqrt{-\frac{(\Phi_2+2\Phi_3)}{E\Phi_8}}\ \left(\wp\left[(x), g_2, g_3\right] - \frac{C}{3}\right)\right]^{\frac{1}{4m}} e^{i\lambda t}. \tag{64}$$

**(II)**

$$\eta(x,t) = \varepsilon\ \left[\sqrt{-\frac{(\Phi_2+2\Phi_3)E}{\Phi_8}}\left(\frac{A}{\wp[(x),g_2,g_3]-\frac{C}{3}}\right)\right]^{\frac{1}{4m}} e^{i\lambda t}, \tag{65}$$

and

$$\rho(x,t) = \chi\varepsilon\ \left[\sqrt{-\frac{(\Phi_2+2\Phi_3)E}{\Phi_8}}\left(\frac{A}{\wp[(x),g_2,g_3]-\frac{C}{3}}\right)\right]^{\frac{1}{4m}} e^{i\lambda t}, \tag{66}$$

where the solutions of the Weierstrass elliptic function (63)-(66) are characterised by the invariants $g_2$ and $g_3$, which are determined by the following equation:

$$g_2 = \frac{4C^2-12AE}{3} \ \text{ and } \ g_3 = \frac{4C(-2C^2+9AE)}{27}. \tag{67}$$

**(III)**

$$\eta(x,t) = \varepsilon\left[\sqrt{-\frac{(\Phi_2+2\Phi_3)E}{9\Phi_8}}\left(\frac{6\sqrt{A}\wp[(x),g_2,g_3]+C\sqrt{A}}{3\wp'[(x),g_2,g_3]}\right)\right]^{\frac{1}{4m}} e^{i\lambda t},\ A>0, \tag{68}$$

and

$$\rho(x,t) = \chi\varepsilon\left[\sqrt{-\frac{(\Phi_2+2\Phi_3)E}{9\Phi_8}}\left(\frac{6\sqrt{A}\wp[(x),g_2,g_3]+C\sqrt{A}}{3\wp'[(x),g_2,g_3]}\right)\right]^{\frac{1}{4m}} e^{i\lambda t},\ A>0. \tag{69}$$

**Set–8**: Considering $B = D = 0$ and $A = \frac{5C^2}{36E}$ are replaced into the algebraic equations (20), the results achieved are:

$$A_0 = 0, \quad A_1 = \sqrt{-\frac{(\Phi_9+2\Phi_{10})E}{\Phi_7}}, \tag{70}$$

and

$$\begin{aligned}
\Phi_1 &= -\frac{5C^2\Phi_9A_1^2}{36E},\\
\Phi_2 &= -\frac{\Phi_8A_1^2+2E\Phi_3}{E},\\
\Phi_4 &= -\frac{(5\Phi_8A_1^2+2E\Phi_3)C^2A_1^2}{36E^2},\\
\Phi_5 &= -C(\Phi_9+\Phi_{10})\\
\Phi_6 &= \frac{C(\Phi_8A_1^2+E\Phi_3)}{E},
\end{aligned} \tag{71}$$

provided $E > 0, \Phi_7(\Phi_9 + 2\Phi_{10}) < 0$, $\varepsilon = \pm 1$. In view of this, the following are the two solutions that take the form of Weierstrass elliptic functions:

$$\eta(x,t) = \varepsilon\ \left[\sqrt{-\frac{5C^2(\Phi_9+2\Phi_{10})}{36\Phi_7}}\,\frac{6\wp[(x),g_2,g_3]+C}{3\wp'[(x),g_2,g_3]}\right]^{\frac{1}{2m}} e^{i\lambda t}, \tag{72}$$

and

$$\rho(x,t) = \chi\varepsilon\ \left[\sqrt{-\frac{5C^2(\Phi_9+2\Phi_{10})}{36\Phi_7}}\,\frac{6\wp[(x),g_2,g_3]+C}{3\wp'[(x),g_2,g_3]}\right]^{\frac{1}{2m}} e^{i\lambda t}, \tag{73}$$

where the solutions of the Weierstrass elliptic function (72) and (73) are characterised by the invariants $g_2$ and $g_3$, which are determined by the following equities:

$$g_2 = \frac{2C^2}{9} \ \text{ and } \ g_3 = \frac{C^3}{54}. \tag{74}$$

## 4. ADDITIONAL RESULTS

The Weierstrass elliptic function $\wp(x; g_2, g_3)$ is typically represented as [39,40]:

$$\left.\begin{aligned}
\wp\,(x; g_2, g_3) &= l_2 - (l_2 - l_3)\mathrm{cn}^2\left(\sqrt{l_1 - l_3}x; m_1\right),\\
\wp\,(x; g_2, g_3) &= l_3 + (l_1 - l_3)\mathrm{ns}^2\left(\sqrt{l_1 - l_3}x; m_1\right).
\end{aligned}\right\} \tag{75}$$

The modulus is derived from $m_1 = \sqrt{\frac{l_2-l_3}{l_1-l_3}}$, as described by the Jacobian elliptic functions, where $l_j$ with $j = 1, 2, 3$, and $l_1 \geq l_2 \geq l_3$, are the three roots of the equation $4y^3 - g_2y - g_3 = 0$.
Upon substituting (75) into (63) and (64), the following are the four solutions that take the form of Jacobi elliptic functions:

$$\eta(x,t) = \varepsilon\left[\sqrt{-\frac{(\Phi_2+2\Phi_3)}{E\Phi_8}}\ \left(\ \left[l_2 - (l_2 - l_3)\mathrm{cn}^2\left(\sqrt{l_1 - l_3}\,x; m_1\right)\right] - \frac{C}{3}\right)\right]^{\frac{1}{4m}} e^{i\lambda t}, \tag{76}$$

and

$$\rho(x,t) = \chi\varepsilon\left[\sqrt{-\frac{(\Phi_2+2\Phi_3)}{E\Phi 8}}\ \left(\ \left[l_2 - (l_2 - l_3)\mathrm{cn}^2\left(\sqrt{l_1 - l_3}\,x; m_1\right)\right] - \frac{C}{3}\right)\right]^{\frac{1}{4m}} e^{i\lambda t}, \tag{77}$$

also,

$$\eta(x,t) = \varepsilon\left[\sqrt{-\frac{(\Phi_2+2\Phi_3)}{E\Phi_8}}\ \left(\left[l_3 + (l_1 - l_3)\mathrm{ns}^2\left(\sqrt{l_1 - l_3}\, x; m_1\right)\right] - \frac{C}{3}\right)\right]^{\frac{1}{4m}} e^{i\lambda t}, \tag{78}$$

and

$$\rho(x,t) = \chi\varepsilon\left[\sqrt{-\frac{(\Phi_2+2\Phi_3)}{E\Phi_8}}\ \left(\left[l_3 + (l_1 - l_3)\mathrm{ns}^2\left(\sqrt{l_1 - l_3}\, x; m_1\right)\right] - \frac{C}{3}\right)\right]^{\frac{1}{4m}} e^{i\lambda t}, \tag{79}$$

where $E\Phi_8(\Phi_2 + 2\Phi_3) < 0$. In detail, as $m_1 \longrightarrow 1$, $l_1 \longrightarrow l_2$, resulting in $\mathrm{ns}(x,1) \longrightarrow \coth(x)$ and $\mathrm{cn}(x,1) \longrightarrow \mathrm{sech}(x)$. Bright and singular solitons appear prominently in the solutions:

$$\eta(x,t) = \varepsilon\left[\sqrt{-\frac{(\Phi_2+2\Phi_3)}{E\Phi_8}}\ \left(\ \left[l_2 - (l_2 - l_3)\mathrm{sech}^2\left(\sqrt{l_1 - l_3}\, x\right)\right] - \frac{C}{3}\right)\right]^{\frac{1}{4m}} e^{i\lambda t}, \tag{80}$$

and

$$\rho(x,t) = \chi\varepsilon\left[\sqrt{-\frac{(\Phi_2+2\Phi_3)}{E\Phi_8}}\ \left(\ \left[l_2 - (l_2 - l_3)\mathrm{sech}^2\left(\sqrt{l_1 - l_3}\, x\right)\right] - \frac{C}{3}\right)\right]^{\frac{1}{4m}} e^{i\lambda t}, \tag{81}$$

also,

$$\eta(x,t) = \varepsilon\left[\sqrt{-\frac{(\Phi_2+2\Phi_3)}{E\Phi_8}}\ \left(\ \left[l_2 - (l_2 - l_3)\coth^2\left(\sqrt{l_1 - l_3}\, x\right)\right] - \frac{C}{3}\right)\right]^{\frac{1}{4m}} e^{i\lambda t}, \tag{82}$$

and

$$\rho(x,t) = \chi\varepsilon\left[\sqrt{-\frac{(\Phi_2+2\Phi_3)}{E\Phi_8}}\ \left(\ \left[l_2 - (l_2 - l_3)\coth^2\left(\sqrt{l_1 - l_3}\, x\right)\right] - \frac{C}{3}\right)\right]^{\frac{1}{4m}} e^{i\lambda t}, \tag{83}$$

where $E\Phi_8(\Phi_2 + 2\Phi_3) < 0$.

Upon substituting (75) into (65) and (66), Jacobi elliptic solutions are achieved:

$$\eta(x,t) = \varepsilon\ \left[\sqrt{-\frac{(\Phi_2+2\Phi_3)E}{\Phi_8}}\left(\frac{A}{l_2-(l_2-l_3)\mathrm{cn}^2\left(\sqrt{l_1-l_3}\ x;m_1\right)-\frac{C}{3}}\right)\right]^{\frac{1}{4m}} e^{i\lambda t}, \tag{84}$$

and

$$\rho(x,t) = \chi\varepsilon\ \left[\sqrt{-\frac{(\Phi_2+2\Phi_3)E}{\Phi_8}}\left(\frac{A}{l_2-(l_2-l_3)\mathrm{cn}^2\left(\sqrt{l_1-l_3}\ x;m_1\right)-\frac{C}{3}}\right)\right]^{\frac{1}{4m}} e^{i\lambda t}, \tag{85}$$

also,

$$\eta(x,t) = \varepsilon\ \left[\sqrt{-\frac{(\Phi_2+2\Phi_3)E}{\Phi_8}}\left(\frac{A}{l_3+(l_1-l_3)\mathrm{ns}^2\left(\sqrt{l_1-l_3}\ x;m_1\right)-\frac{C}{3}}\right)\right]^{\frac{1}{4m}} e^{i\lambda t}, \tag{86}$$

and

$$\rho(x,t) = \chi\varepsilon\ \left[\sqrt{-\frac{(\Phi_2+2\Phi_3)E}{\Phi_8}}\left(\frac{A}{l_3+(l_1-l_3)\mathrm{ns}^2\left(\sqrt{l_1-l_3}\ x;m_1\right)-\frac{C}{3}}\right)\right]^{\frac{1}{4m}} e^{i\lambda t}, \tag{87}$$

where $E\Phi_8(\Phi_2 + 2\Phi_3) < 0$. Singular and dark solitons appear prominently in the solutions:

$$\eta(x,t) = \varepsilon\ \left[\sqrt{-\frac{(\Phi_2+2\Phi_3)E}{\Phi 8}}\left(\frac{A}{l_2-(l_2-l_3)\mathrm{sech}^2\left(\sqrt{l_1-l_3}\ x\right)-\frac{C}{3}}\right)\right]^{\frac{1}{4m}} e^{i\lambda t}, \tag{88}$$

and

$$\rho(x,t) = \chi\varepsilon\ \left[\sqrt{-\frac{(\Phi_2+2\Phi_3)E}{\Phi 8}}\left(\frac{A}{l_2-(l_2-l_3)\mathrm{sech}^2\left(\sqrt{l_1-l_3}\ x\right)-\frac{C}{3}}\right)\right]^{\frac{1}{4m}} e^{i\lambda t}, \tag{89}$$

also,

$$\eta(x,t) = \varepsilon\ \left[\sqrt{-\frac{(\Phi_2+2\Phi_3)E}{\Phi_8}}\left(\frac{A}{l_3+(l_1-l_3)\coth^2\left(\sqrt{l_1-l_3}\ x\right)-\frac{C}{3}}\right)\right]^{\frac{1}{4m}} e^{i\lambda t}, \tag{90}$$

and

$$\rho(x,t) = \chi\varepsilon\ \left[\sqrt{-\frac{(\Phi_2+2\Phi_3)E}{\Phi_8}}\left(\frac{A}{l_3+(l_1-l_3)\coth^2\left(\sqrt{l_1-l_3}\ x\right)-\frac{C}{3}}\right)\right]^{\frac{1}{4m}} e^{i\lambda t}, \tag{91}$$

where $E\Phi_8(\Phi_2 + 2\Phi_3) < 0$. By inserting (75) into (68) and (69), Jacobi elliptic solutions are generated:

$$\eta(x,t) = \varepsilon\left[\frac{1}{18}\sqrt{-\frac{(\Phi_2+2\Phi_3)E}{\Phi_8}}\left(\frac{6\sqrt{A}\left[l_2-(l_2-l_3)\mathrm{cn}^2\left(\sqrt{l_1-l_3}\ x;m_1\right)\right]+C\sqrt{A}}{\sqrt{l_1-l_3}(l_2-l_3)\mathrm{cn}\left(\sqrt{l_1-l_3}\ x;m_1\right)\mathrm{sn}\left(\sqrt{l_1-l_3}\ x;m_1\right)\mathrm{dn}\left(\sqrt{l_1-l_3}\ x;m_1\right)}\right)\right]^{\frac{1}{4m}} e^{i\lambda t}, \tag{92}$$

and

$$\rho(x,t)=\chi\varepsilon\left[\frac{1}{18}\sqrt{-\frac{(\Phi_2+2\Phi_3)E}{\Phi_8}}\left(\frac{6\sqrt{A}\left[l_2-(l_2-l_3)\mathrm{cn}^2\left(\sqrt{l_1-l_3}\,x;m_1\right)\right]+C\sqrt{A}}{\sqrt{l_1-l_3}(l_2-l_3)\mathrm{cn}\left(\sqrt{l_1-l_3}\,x;m_1\right)\mathrm{sn}\left(\sqrt{l_1-l_3}\,x;m_1\right)\mathrm{dn}\left(\sqrt{l_1-l_3}\,x;m_1\right)}\right)\right]^{\frac{1}{4m}}e^{i\lambda t}, \tag{93}$$

also,

$$\eta(x,t)=\varepsilon\left[\frac{1}{18}\sqrt{-\frac{(\Phi_2+2\Phi_3)E}{\Phi_8}}\left(-\frac{6\sqrt{A}\left[l_3+(l_1-l_3)\mathrm{ns}^2\left(\sqrt{l_1-l_3}\,x;m_1\right)\right]+C\sqrt{A}}{\sqrt{l_1-l_3}\,(l_1-l_3)\mathrm{cn}\left(\sqrt{l_1-l_3}\,x;m_1\right)\mathrm{dn}\left(\sqrt{l_1-l_3}\,x;m_1\right)\mathrm{ns}^3\left(\sqrt{l_1-l_3}\,x;m_1\right)}\right)\right]^{\frac{1}{4m}}e^{i\lambda t}, \tag{94}$$

and

$$\rho(x,t)=\chi\varepsilon\left[\frac{1}{18}\sqrt{-\frac{(\Phi_2+2\Phi_3)E}{\Phi_8}}\left(-\frac{6\sqrt{A}\left[l_3+(l_1-l_3)\mathrm{ns}^2\left(\sqrt{l_1-l_3}\,x;m_1\right)\right]+C\sqrt{A}}{\sqrt{l_1-l_3}\,(l_1-l_3)\mathrm{cn}\left(\sqrt{l_1-l_3}\,x;m_1\right)\mathrm{dn}\left(\sqrt{l_1-l_3}\,x;m_1\right)\mathrm{ns}^3\left(\sqrt{l_1-l_3}\,x;m_1\right)}\right)\right]^{\frac{1}{4m}}e^{i\lambda t}, \tag{95}$$

where $E\Phi_8(\Phi_2+2\Phi_3)<0$. Notably, the solutions includes additional forms of straddled quiescent optical solitons:

$$\eta(x,t)=\varepsilon\left[\frac{1}{18}\sqrt{-\frac{(\Phi_2+2\Phi_3)E}{\Phi_8}}\left(\frac{6\sqrt{A}\left[l_2-(l_2-l_3)\mathrm{sech}^2\left(\sqrt{l_2-l_3}\,x;m_1\right)\right]+C\sqrt{A}}{\sqrt{l_2-l_3}(l_2-l_3)\mathrm{sech}^2\left(\sqrt{l_2-l_3}\,x;m_1\right)\tanh\left(\sqrt{l_2-l_3}\,x;m_1\right)}\right)\right]^{\frac{1}{4m}}e^{i\lambda t}, \tag{96}$$

and

$$\rho(x,t)=\chi\varepsilon\left[\frac{1}{18}\sqrt{-\frac{(\Phi_2+2\Phi_3)E}{\Phi_8}}\left(\frac{6\sqrt{A}\left[l_2-(l_2-l_3)\mathrm{sech}^2\left(\sqrt{l_2-l_3}\,x;m_1\right)\right]+C\sqrt{A}}{\sqrt{l_2-l_3}(l_2-l_3)\mathrm{sech}^2\left(\sqrt{l_2-l_3}\,x;m_1\right)\tanh\left(\sqrt{l_2-l_3}\,x;m_1\right)}\right)\right]^{\frac{1}{4m}}e^{i\lambda t}, \tag{97}$$

also,

$$\eta(x,t)=\varepsilon\left[\frac{1}{18}\sqrt{-\frac{(\Phi_2+2\Phi_3)E}{\Phi_8}}\left(-\frac{6\sqrt{A}\left[l_3+(l_2-l_3)\coth^2\left(\sqrt{l_2-l_3}\,x;m_1\right)\right]+C\sqrt{A}}{\sqrt{l_2-l_3}(l_2-l_3)\mathrm{sech}^2\left(\sqrt{l_2-l_3}\,x;m_1\right)\coth^3\left(\sqrt{l_2-l_3}\,x;m_1\right)}\right)\right]^{\frac{1}{4m}}e^{i\lambda t}, \tag{98}$$

and

$$\rho(x,t)=\chi\varepsilon\left[\frac{1}{18}\sqrt{-\frac{(\Phi_2+2\Phi_3)E}{\Phi_8}}\left(-\frac{6\sqrt{A}\left[l_3+(l_2-l_3)\coth^2\left(\sqrt{l_2-l_3}\,x;m_1\right)\right]+C\sqrt{A}}{\sqrt{l_2-l_3}(l_2-l_3)\mathrm{sech}^2\left(\sqrt{l_2-l_3}\,x;m_1\right)\coth^3\left(\sqrt{l_2-l_3}\,x;m_1\right)}\right)\right]^{\frac{1}{4m}}e^{i\lambda t}, \tag{99}$$

where $E\Phi_8(\Phi_2+2\Phi_3)<0$, $A>0$.
By inserting (75) into (72) and (73), Jacobi elliptic solutions are formed:

$$\eta(x,t)=\varepsilon\left[\sqrt{-\frac{5C^2(\Phi_9+2\Phi_{10})}{36\Phi_7}}\left(\frac{6\left[l_2-(l_2-l_3)\mathrm{cn}^2\left(\sqrt{l_1-l_3}\,x;m_1\right)\right]+C}{3\sqrt{l_1-l_3}(l_2-l_3)\mathrm{cn}\left(\sqrt{l_1-l_3}\,x;m_1\right)\mathrm{sn}\left(\sqrt{l_1-l_3}\,x;m_1\right)\mathrm{dn}\left(\sqrt{l_1-l_3}\,x;m_1\right)}\right)\right]^{\frac{1}{2m}}e^{i\lambda t}, \tag{100}$$

and

$$\rho(x,t)=\chi\varepsilon\left[\sqrt{-\frac{5C^2(\Phi_9+2\Phi_{10})}{36\Phi_7}}\left(\frac{6\left[l_2-(l_2-l_3)\mathrm{cn}^2\left(\sqrt{l_1-l_3}\,x;m_1\right)\right]+C}{3\sqrt{l_1-l_3}(l_2-l_3)\mathrm{cn}\left(\sqrt{l_1-l_3}\,x;m_1\right)\mathrm{sn}\left(\sqrt{l_1-l_3}\,x;m_1\right)\mathrm{dn}\left(\sqrt{l_1-l_3}\,x;m_1\right)}\right)\right]^{\frac{1}{2m}}e^{i\lambda t}, \tag{101}$$

also,

$$\eta(x,t)=\varepsilon\left[\sqrt{-\frac{5C^2(\Phi_9+2\Phi_{10})}{36\Phi_7}}\left(-\frac{6\left[l_3+(l_1-l_3)\mathrm{ns}^2\left(\sqrt{l_1-l_3}\,x;m_1\right)\right]+C}{3\sqrt{l_1-l_3}\,(l_1-l_3)\mathrm{cn}\left(\sqrt{l_1-l_3}\,x;m_1\right)\mathrm{dn}\left(\sqrt{l_1-l_3}\,x;m_1\right)\mathrm{ns}^3\left(\sqrt{l_1-l_3}\,x;m_1\right)}\right)\right]^{\frac{1}{2m}}e^{i\lambda t}, \tag{102}$$

and

$$\rho(x,t)=\chi\varepsilon\left[\sqrt{-\frac{5C^2(\Phi_9+2\Phi_{10})}{36\Phi_7}}\left(-\frac{6\left[l_3+(l_1-l_3)\mathrm{ns}^2\left(\sqrt{l_1-l_3}\,x;m_1\right)\right]+C}{3\sqrt{l_1-l_3}\,(l_1-l_3)\mathrm{cn}\left(\sqrt{l_1-l_3}\,x;m_1\right)\mathrm{dn}\left(\sqrt{l_1-l_3}\,x;m_1\right)\mathrm{ns}^3\left(\sqrt{l_1-l_3}\,x;m_1\right)}\right)\right]^{\frac{1}{2m}}e^{i\lambda t}, \tag{103}$$

where $\Phi_7(\Phi_9+2\Phi_{10})<0$. A further set of additional form of straddled optical solitons is enlisted here:

$$\eta(x,t)=\varepsilon\left[\sqrt{-\frac{5C^2(\Phi_9+2\Phi_{10})}{36\Phi_7}}\left(\frac{6\left[l_2-(l_2-l_3)\mathrm{sech}^2\left(\sqrt{l_2-l_3}\,x\right)\right]+C}{3\sqrt{l_2-l_3}(l_2-l_3)\mathrm{sech}^2\left(\sqrt{l_2-l_3}\,x\right)\tanh\left(\sqrt{l_2-l_3}\,x\right)}\right)\right]^{\frac{1}{2m}}e^{i\lambda t}, \tag{104}$$

and

$$\rho(x,t)=\chi\varepsilon\left[\sqrt{-\frac{5C^2(\Phi_9+2\Phi_{10})}{36\Phi_7}}\left(\frac{6\left[l_2-(l_2-l_3)\mathrm{sech}^2\left(\sqrt{l_2-l_3}\,x\right)\right]+C}{3\sqrt{l_2-l_3}(l_2-l_3)\mathrm{sech}^2\left(\sqrt{l_2-l_3}\,x\right)\tanh\left(\sqrt{l_2-l_3}\,x\right)}\right)\right]^{\frac{1}{2m}}e^{i\lambda t}, \tag{105}$$

also,

$$\eta(x,t)=\varepsilon\left[\sqrt{-\frac{5C^2(\Phi_9+2\Phi_{10})}{36\Phi_7}}\left(-\frac{6\left[l_3+(l_2-l_3)\coth^2\left(\sqrt{l_2-l_3}\,x\right)\right]+C}{3\sqrt{l_2-l_3}(l_2-l_3)\mathrm{sech}^2\left(\sqrt{l_2-l_3}\,x\right)\coth^3\left(\sqrt{l_2-l_3}\,x\right)}\right)\right]^{\frac{1}{2m}}e^{i\lambda t}, \tag{106}$$

and

$$\rho(x,t)=\chi\varepsilon\left[\sqrt{-\frac{5C^2(\Phi_9+2\Phi_{10})}{36\Phi_7}}\left(-\frac{6\left[l_3+(l_2-l_3)\coth^2\left(\sqrt{l_2-l_3}\,x\right)\right]+C}{3\sqrt{l_2-l_3}(l_2-l_3)\mathrm{sech}^2\left(\sqrt{l_2-l_3}\,x\right)\coth^3\left(\sqrt{l_2-l_3}\,x\right)}\right)\right]^{\frac{1}{2m}}e^{i\lambda t}, \tag{107}$$

where $\Phi_7(\Phi_9+2\Phi_{10})<0$.

## 5. RESULTS AND DISCUSSION

The application of the modified sub-ODE methodology to the coupled nonlinear Schrödinger–type system yields a wide spectrum of quiescent soliton solutions in magneto–optic waveguides subject to nonlinear chromatic dispersion and Kudryashov's generalized self-phase modulation. In this section, we focus on three representative families of stationary localized states: bright, dark, and straddled (hyperbolic–rational) quiescent solitons. Their spatial structures, as reconstructed from the analytic formulas, are depicted in Figures 1–3.

Figure 1 illustrates the family of bright quiescent solitons described by Eqs. (23)–(24). Both field components, $\eta(x)$ and $\rho(x)$, exhibit a single localized hump centered at $x = 0$, decaying exponentially to the background. The parameter $m$ plays a dual role, modulating both amplitude and spatial width of the soliton. For smaller values of $m$, the profiles become broader with lower peak intensity, whereas increasing $m$ sharpens the localization and elevates the peak amplitude. Importantly, the bright states maintain their stability across the tested range of $m$, reflecting the robustness of the balance between nonlinear self-phase modulation and dispersive spreading.

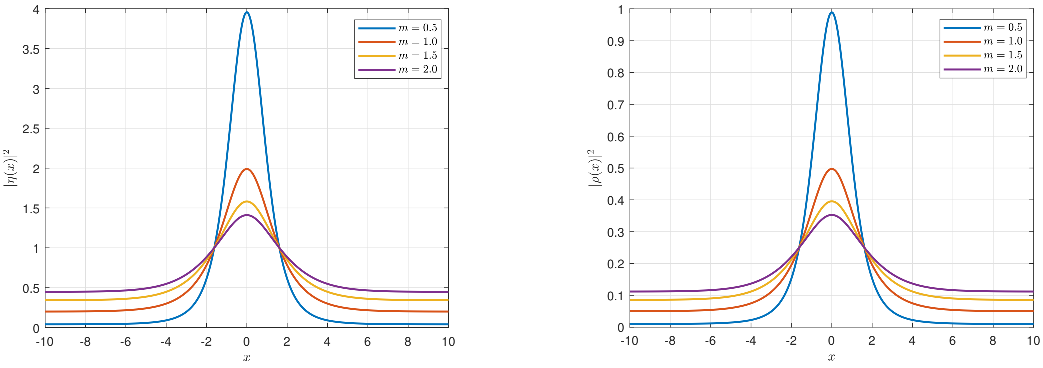

**(a)** Bright quiescent soliton for $\eta(x)$ given by Eq. (23), shown for different values of $m$.

**(b)** Bright quiescent soliton for $\rho(x)$ given by Eq. (24), shown for different values of $m$.

**Figure 1.** Bright quiescent solitons: localized hump solutions described by Eqs. (23)–(24) ($C = 0.8,\ \ \Phi_2 = 2,\ \ \Phi_3 = 1,\ \ \Phi_8 = 1,\ \ A_0 = 0.2,\ \ \varepsilon = 1,\ \ \chi = 0.5$).

In contrast, Figure 2 presents the dark quiescent solitons obtained from Eqs. (27)–(28). Here, the fields $\eta(x)$ and $\rho(x)$ retain a finite background, featuring a localized notch at the origin. The depth of this dip depends sensitively on $m$: shallow depressions for small $m$ evolve into deeper and narrower notches as $m$ increases. This behavior mirrors the expected dynamics of dark solitons under normal dispersion conditions. The presence of a finite pedestal ensures that the solutions remain bounded, which is a crucial feature for stable pulse transmission. The consistency of these results with the parameter restrictions in Set-2 highlights the versatility of the sub-ODE method in capturing both bright and dark stationary structures within a unified framework.

A more exotic class of solutions is displayed in Figure 3, where the hybrid hyperbolic–rational structures emerge from Eqs. (53)–(54). These "straddled" solitons exhibit a shallow hyperbolic-type core near $x = 0$, accompanied by algebraically

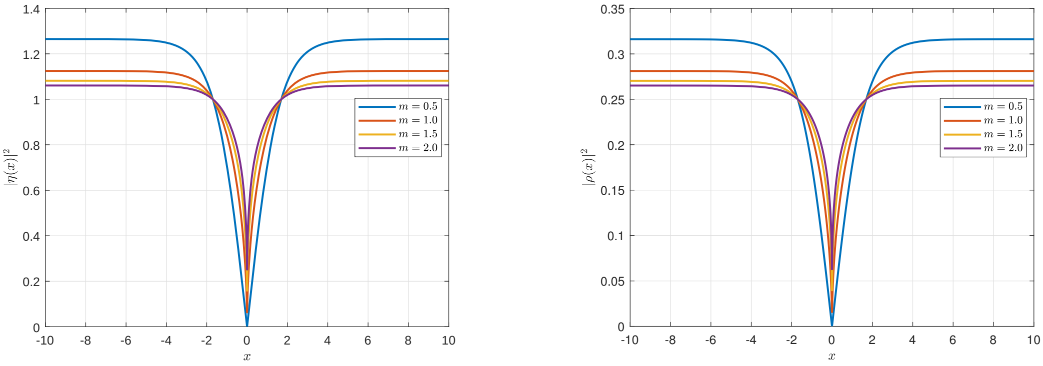

**(a)** Dark quiescent soliton for $\eta(x)$ given by Eq. (27), shown for different values of $m$.

**(b)** Dark quiescent soliton for $\rho(x)$ given by Eq. (28), shown for different values of $m$.

**Figure 2.** Dark quiescent solitons: localized notch solutions described by Eqs. (27)–(28) ($\varepsilon = 1,\ \ \chi = 0.5,\ \ C = -0.8,\ \ \Phi_7 = -1,\ \ \Phi_9 = 2,\ \ \Phi_{10} = 1.$).

decaying shoulders extending into the far field. Such composite profiles differ from the exponentially localized bright and dark solitons: while they maintain localization, their slower tail decay introduces long-range interactions that may influence multi-pulse dynamics in realistic magneto–optic media. The dependence on $m$ again tunes the relative prominence of the core versus the shoulders, suggesting that the soliton morphology can be engineered through parameter control. The analytical derivation of these solutions (Set-5) demonstrates the flexibility of Kudryashov's SPM structure in generating hybrid states that combine features of both hyperbolic and rational forms.

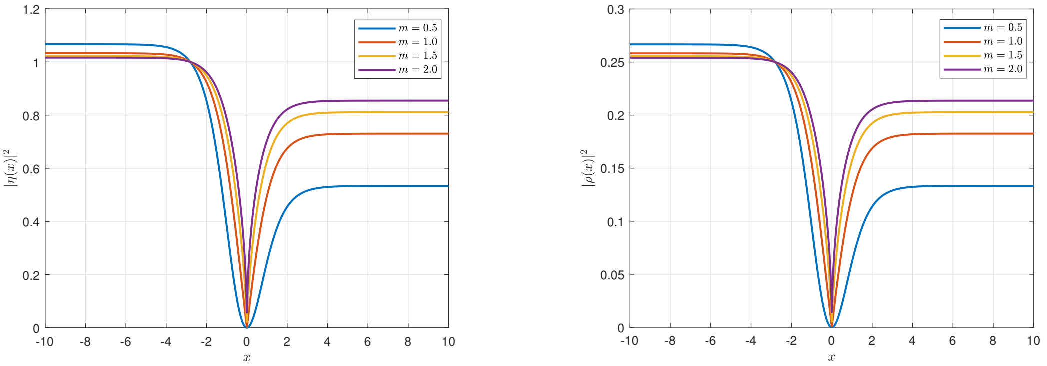

**(a)** Straddled (hyperbolic–rational) quiescent soliton for $\eta(x)$ given by Eq. (53), shown for different values of $m$.

**(b)** Straddled (hyperbolic–rational) quiescent soliton for $\rho(x)$ given by Eq. (54), shown for different values of $m$.

**Figure 3.** Straddled (hyperbolic–rational) quiescent solitons: hybrid profiles described by Eqs. (53)–(54) ($C = -0.8,\quad D = 1,\quad A_1 = 1,\quad \chi = 0.5$.)

Taken together, the three families highlight the diversity of stationary quiescent solitons admitted by the model. Bright and dark solutions represent classical solitary waveforms associated with anomalous and normal dispersion regimes, respectively, while straddled solitons introduce hybrid decay patterns with potential for novel interaction dynamics. The modulation parameter $m$ consistently acts as a control knob for amplitude–width trade-offs, underscoring its physical role in tailoring pulse shapes. From an applications perspective, the ability to sustain such varied soliton classes in magneto–optic waveguides suggests opportunities for optimizing pulse transmission, mitigating clutter, and exploring nonstandard optical switching regimes.

## 6. CONCLUSIONS

This work examines quiescent optical solitons in magneto-optic waveguides, including nonlinear CD and generalised temporal evolution, using Kudryashov's generalised self-phase modulation structure. The generalised version of sub-ODE is the mathematical framework that has facilitated the successful recovery of quiescent optical solitons. We establish a diverse array of classified optical solitons and the parametric conditions that guarantee their existence. These solitons exhibit unique stability properties and can be manipulated by varying the external magnetic field and waveguide parameters. Our results deepen the understanding of soliton dynamics in complex media and open avenues for potential applications in optical communications and information processing. The results of the work serve as a stark reminder to the telecommunication engineers that rough handling of optical fibers would stall the progress of such solitons under the sea as well as underground. This would catastrophically dismantle the internet traffic flow across the planet.

While magneto–optic waveguides is one of the optoelectronic devices where the dynamics of quiescent optical solitons are established in the current paper, the study would be later extended to additional such devices that has been left untouched in the literature. Examples of such devices include Bragg gratings, optical couplers, optical metamaterials, fibres exhibiting polarization-mode dispersion, and dispersion-flattened fibres, among others. The mathematical algorithms that would be adopted while addressing such devices would be plentiful including the most powerful of them namely Lie symmetry analysis. The results would be disseminated all across the board sequentially over time.

### Acknowledgements

This work of one of the authors (AB) was funded by the budget of Grambling State University for the Endowed Chair of Mathematics. The author thankfully acknowledges this support.

### Author contributions

All authors contributed to the study conception and design. Material preparation, data collection, review & editing and analysis were performed by [Mona El-Shater], [Ahmed H. Arnous], [Omer Mohammed Khodayer Al-Dulaimi], [Farag Mahel Mohammed], [Ibrahim Zeghaiton Chaloob], and [Carmelia Mariana Balanica Dragomir]. The first draft of the manuscript was written by [Elsayed M. E. Zayed]. Investigation, writing—review and editing was made by [Anjan Biswas] and [O. González-Gaxiola]. All authors provided comments on previous drafts of the manuscript and then reviewed and approved the final version.

### Funding

The authors confirm that they did not receive any financial, grant, or other forms of help during the preparation of this manuscript.

### Data availability

The article contains all the information required to comprehend the results of this investigation.

### Conflict of interest

We are ignorant of any financial conflicts of interest or personal relationships that could have potentially impacted the research described in this article.

### ORCID

**Elsayed M.E. Zayed**, https://orcid.org/0000-0002-6755-0088; **Mona El–Shater**, https://orcid.org/0000-0001-6587-1331; **Ahmed H. Arnous**, https://orcid.org/0000-0002-7699-7068; **Omer Mohammed Khodayer Al-Dulaimi**, https://orcid.org/0000-0001-8581-0448; **Farag Mahel Mohammed**, https://orcid.org/0000-0001-6391-2435; **Ibrahim Zeghaiton Chaloob**, https://orcid.org/0000-0002-1741-5232; **O. González–Gaxiola**, https://orcid.org/0000-0003-3317-9820; **Anjan Biswas**, https://orcid.org/0000-0002-8131-6044; **Carmelia Mariana Balanica Dragomir**, https://orcid.org/0000-0001-7743-928X

### REFERENCES

[1] H. Schamel, ”Quiescent solitary, snoidal and sinusidal ion acoustic waves,” Plasma Phys. **14**(10), 905–924 (1972). https://doi.org/10.1088/0032-1028/14/10/002

[2] J.L. Hammack, ”A note on tsunamis: Their generation and propagation in an ocean of uniform depth,” J. Fluid Mech. **60**(4), 769–799 (1973). https://doi.org/10.1017/S0022112073000479

[3] A. Hasegawa, and F. Tappert, ”Transmission of quiescent nonlinear optical pulses in dispersive dielectric fibers. I. Anomalous dispersion,” Apple. Phys. Lett. **23**(3), 142-144 (1973). https://doi.org/10.1063/1.1654836

[4] M. Karlsson, and A. Hook, ”Soliton-like pulses governed by fourth order dispersion in optical fibers,” Opt. Commun. **104**(4–6), 303–307 (1994). https://doi.org/10.1016/0030-4018(94)90560-6

[5] D. Mihalache, D. Mazilu, B.A. Malomed, and L. Torner, ”Asymmetric spatio-temporal optical solitons in media with quadratic nonlinearity,” Opt. Commun. **152**(4–6), 365–370 (1998). https://doi.org/10.1016/S0030-4018(98)00206-5

[6] D. Mihalache, D. Mazilu, L.-C. Crasovan, L. Torner, B.A. Malomed, and F. Lederer, ”Three-dimensional walking spatiotemporal solitons in quadratic media,” Phys. Rev. E - Stat. Phys. Plasmas Fluids Rel. Interdiscip. Top. **62**(5), 7340–7347 (2000). https://doi.org/10.1103/PhysRevE.62.7340

[7] N.A. Kudryashov, ”Periodic and solitary waves in optical fiber Bragg gratings with dispersive reflectivity,” Chinese J. Phys. **66**, 401–405 (2020). https://doi.org/10.1016/j.cjph.2020.06.006

[8] W.C.K. Mak, B.A. Malomed, and P.L. Chu, ”Three-wave gap solitons in waveguides with quadratic nonlinearity,” Phys. Rev. E - Stat. Phys. Plasmas Fluids Rel. Interdiscip. Top. **58**(5), 6708–6722 (1998). https://doi.org/10.1103/PhysRevE.58.6708

[9] A.H. Arnous, A. Biswas, Y. Yıldırım, L. Moraru, M. Aphane, S.P. Moshokoa, and H.M. Alshehri, ”Quiescent optical solitons with Kudryashov’s generalized quintuple-power and nonlocal nonlinearity having nonlinear chromatic dispersion: generalized temporal evolution,” Ukr. J. Phys. Opt. **24**(1), 105–113 (2023). https://doi.org/10.3116/16091833/24/2/105/2023

[10] N.A. Kudryashov, ”Highly dispersive optical solitons of the generalized nonlinear eighth-order Schrödinger equation,” Optik, **206**, 164335 (2020). https://doi.org/10.1016/j.ijleo.2020.164335

[11] E.M.E. Zayed, R. Shohib, M. Alngar, A. Biswas, M. Ekici, S. Khan, A.K. Alzahrani, and M. Belic, ”Optical solitons and conservation laws associated with Kudryashov’s sextic power-law nonlinearity of refractive index,” Ukr. J. Phys. Opt. **22**, 38–49 (2021). https://doi.org/10.3116/16091833/22/1/38/2021

[12] A.R. Adem, M. Ekici, A. Biswas, M. Asmag, E.M.E. Zayed, A.K. Alzahrani, and M.R. Belic, ”Stationary optical solitons with nonlinear chromatic dispersion having quadratic–cubic law of refractive index,” Phys. Lett. A, **384**, 126606 (2020). https://doi.org/10.1016/j.physleta.2020.126606

[13] N. Sucu, M. Ekici, and A. Biswas, ”Quiescent optical solitons with nonlinear chromatic dispersion and generalized temporal evolution by extended trial function approach,” Chaos Solitons Fractals, **147**, 110971 (2021). https://doi.org/10.1016/j.chaos.2021.110971

[14] A.H. Arnous, T.A. Nofal, A. Biswas, S. Khan, and L. Moraru, ”Quiescent optical solitons with Kudryashov’s generalized quintuple-power and nonlocal nonlinearity having nonlinear chromatic dispersion,” Universe, **8**, 501 (2022). https://doi.org/10.3390/universe8100501

[15] M. Ekici, A. Sonmezoglu, and A. Biswas, ”Quiescent optical solitons with Kudryashov’s laws of refractive index,” Chaos Solitons Fractals, **151**, 111226 (2021). https://doi.org/10.1016/j.chaos.2021.111226

[16] A.R. Adem, B.P. Ntsime, A. Biswas, S. Khan, A.K. Alzahraniand, and M.R. Belic, ”Quiescent optical solitons with nonlinear chromatic dispersion for Lakshmanan–Porsezian–Daniel model having Kerr law of nonlinear refractive index,” Ukr. J. Phys. Opt. **22**, 83–86 (2021). https://doi.org/10.3116/16091833/22/2/83/2021

[17] A. Biswas, M. Ekici, and A. Sonmezoglu, ”Quiescent optical solitons with Kudryashov’s quintuple power–law of refractive index having nonlinear chromatic dispersion,” Phys. Lett. A, **426**, 127885 (2022). https://doi.org/10.1016/j.physleta.2021.127885

[18] A. Sonmezoglu, ”Stationary optical solitons having Kudryashov’s quintuple power law nonlinearity by extended $G'/G$ -expansion,” Optik, **253**, 168521 (2022). https://doi.org/10.1016/j.ijleo.2021.168521

[19] N.A. Kudryashov, ”Mathematical model of propagation pulse in optical fiber with power nonlinearities,” Optik, **212**, 164750 (2020). https://doi.org/10.1016/j.ijleo.2020.164750

[20] N.A. Kudryashov, and E.V. Antonova, ”Solitary waves of equation for propagation pulse with power nonlinearities,” Optik, **217**, 164881, (2020). https://doi.org/10.1016/j.ijleo.2020.164881

[21] N.A. Kudryashov, ”Highly dispersive optical solitons of equation with various polynomial nonlinearity law,” Chaos Solitons Fractals **140**, 110202, (2020). https://doi.org/10.1016/j.chaos.2020.110202

[22] N.A. Kudryashov, ”Model of propagation pulses in an optical fiber with a new law of refractive indices,” Optik, **248**, 168160, (2021). https://doi.org/10.1016/j.ijleo.2021.168160
https://doi.org/10.1016/j.physleta.2020.126606

[23] A.R. Adem, B.P. Ntsime, A. Biswas, M. Asma, M. Ekici, S.P. Moshokoa, A.K. Alzahrani, and M.R. Belic, ”Quiescent optical solitons with Sasa–Satsuma equation having nonlinear chromatic dispersion,” Phys. Lett. A, **384**, 126721 (2020). https://doi.org/10.1016/j.physleta.2020.126721

[24] A. Biswas, M. Ekici, A. Sonmezoglu, and M. Belic, ”Quiescent optical solitons with nonlinear group velocity dispersion by extended trial function scheme,” Optik, **171**, 529–542, (2018). https://doi.org/10.1016/j.ijleo.2018.06.067

[25] A.H. Arnous, A. Biswas, Y. Yildirim, and A. Asiri, ”Quiescent optical solitons for the concatenation model having nonlinear chromatic dispersion with differential group delay,” Contemp. Math. **4**(4), 877–904 (2023). https://doi.org/10.37256/cm.4420233596

[26] Y. Geng, and J. Li, ”Exact solutions to a nonlinearly dispersive Schrödinger equation,” Appl. Math. Comp. **195**, 420–439 (2008). https://doi.org/10.1016/j.amc.2007.04.119

[27] Z. Yan, ”Envelope compactons and solitary patterns,” Phys. Lett. A, **355**, 212–215 (2006). https://doi.org/10.1016/j.physleta.2006.02.032

[28] Z. Yan, ”Envelope compact and solitary pattern structures for the GNLS(m,n,p,q) equations,” Phys. Lett. A, **357**, 196–203 (2006). https://doi.org/10.1016/j.physleta.2006.04.032

[29] Z. Yan, ”New exact solution structures and nonlinear dispersion in the coupled nonlinear wave systems,” Phys. Lett. A, **361**, 194–200 (2007). https://doi.org/10.1016/j.physleta.2006.07.032

[30] Z. Zhang, Z. Liu, X. Miao, and Y. Chen, ”Qualitative analysis and traveling wave solutions for the perturbed nonlinear Schrödinger’s equation with Kerr law nonlinearity,” Phys. Lett. A, **375**, 1275–1280 (2011). https://doi.org/10.1016/j.physleta.2010.11.070

[31] Z. Zhang, Y.-x. Li, Z.-h. Liu, and X.-j. Miao, ”New exact solutions to the perturbed nonlinear Schrodinger’s equation with Kerr law nonlinearity via modified trigonometric function series method,” Commun. Nonlin. Sci. Num. Simul. **16**, 3097–3106, (2011). https://doi.org/10.1016/j.cnsns.2010.12.010

[32] E.M.E. Zayed, M. El-Shater, A.H. Arnous, Y. Yıldırım, L. Hussein, A.J.M. Jawad, S.S. Veni, and A. Biswas, ”Quiescent optical solitons with Kudryashov’s generalized quintuple-power law and nonlocal nonlinearity having nonlinear chromatic dispersion with generalized temporal evolution by enhanced direct algebraic method and sub-ODE approach,” Eur. Phys. J. Plus, **139**, 885 (2024). https://doi.org/10.1140/epjp/s13360-024-05636-8

[33] N.A. Kudryashov, ”Stationary solitons of the generalized nonlinear Schrödinger equation with nonlinear dispersion and arbitrary refractive index,” Appl. Math. Lett. **128**, 107888 (2022). https://doi.org/10.1016/j.aml.2021.107888

[34] N.A. Kudryashov, ”Quiescent solitons of the model with nonlinear chromatic dispersion and arbitrary refractive index,” Optik, **259**, 168888 (2022). https://doi.org/10.1016/j.ijleo.2022.168888

[35] Z. Yang, and B.Y. Hon, ”An improved modified extended tanh-function method,” Zeitschrift fur Naturforschung A, **61**(3-4), 103–115 (2007). https://doi.org/10.1515/zna-2006-3-401

[36] E.M.E. Zayed, and M.E.M. Alngar, ”Application of newly proposed sub-ODE method to locate chirped optical solitons to Triki–Biswas equation,” Optik, **207**, 164360 (2020). https://doi.org/10.1016/j.ijleo.2020.164360

[37] Z.L. Li, ”Periodic Wave Solutions of a Generalized KdV-mKdV Equation with Higher-Order Nonlinear Terms,” Z. Naturforsch, **65a**, 649-657 (2010). http://www.znaturforsch.com/s65a/s65a0649.pdf

[38] E.M.E. Zayed, Kh.A. Gepreel, M.E.M. Alngar, A. Biswas, A. Dakova, M. Ekici, H.M. Alshehri, and M.R. Belic, ”Cubic–quartic solitons for twin-core couplers in optical metamaterials,” Optik, **245**, 167632 (2021). https://doi.org/10.1016/j.ijleo.2021.167632

[39] Y. Chen, and Z. Yan, ”The Weierstrass elliptic function expansion method and its applications in nonlinear wave equations,” Chaos, Soliton of Fractalas, 29, 948-964 (2006). https://doi.org/10.1016/j.chaos.2005.08.071

[40] Y. Zhen-Ya, ”New Weierstrass semi-rational expansion method to doubly periodic solutions of soliton equations,” Commu. Theor. Phys. **43**, 391-396 (2005). https://doi.org/10.1007/s12596-024-01728-x

# СПОКІЙНІ СОЛІТОНИ В МАГНІТООПТИЧНИХ ХВИЛЕВОДАХ З НЕЛІНІЙНОЮ ХРОМАТИЧНОЮ ДИСПЕРСІЄЮ ТА ФОРМОЮ САМОФАЗОВОЇ МОДУЛЯЦІЇ ЗА КУДРЯШОВИМ, ЩО МАЮТЬ УЗАГАЛЬНЕНУ ЧАСОВУ ЕВОЛЮЦІЮ

**Ельсаєд М.Е. Заєд[1], Мона Ель–Шатер[1], Ахмед Х. Арнус[2,3], Омер Мохаммед Ходаєр Аль-Дулаймі[4], Фараг Махель Мухаммед[5], Ібрагім Зехайтон Чалуб[6], О. Гонзалез–Гаксіола[7], Анджан Бісвас[8,9,10,11], Кармелія Маріана Баланіка Драгомир[10]**

[1]*Кафедра математики, факультет природничих наук, Загазизький університет, Загазиг–44519, Єгипет*
[2]*Кафедра математичних наук, Інженерна школа Савітха, SIMATS, Ченнаї - 602105, Тамілнаду, Індія*
[3]*Науково-дослідний центр прикладної математики, Університет Хазар, Баку, Аризона 1096, Азербайджан*
[4]*Кафедра технічної інженерії зв'язку, Університет Аль-Фарахіді, Багдад–10015, Ірак*
[5]*Аль-Нібрас Університет–Ірак, Тікрит–34001, Ірак*
[6]*Кафедра ділового адміністрування, Коледж адміністрування та економіки, Університет Аль-Есраа, Багдад–10067, Ірак*
[7]*Кафедра прикладної математики та систем, Автономний університет Метрополітану–Куахімальпа, Васко-де-Кірога 4871, 05348 Мехіко, Мексика*
[8]*Кафедра математики & фізики, Державний університет Гремблінга, Гремблінг, Луїзіана 71245–2715, США*
[9]*Кафедра фізики та електроніки, Університет Хазар, Баку, Аризона–1096, Азербайджан*
[10]*Кафедра прикладних наук, Транскордонний факультет гуманітарних, економічних та інженерних наук, Галацький університет Дунареа де Жос, вулиця Домняска, 111, Галац–800201, Румунія*
[11]*Кафедра математики та прикладної математики, Університет медичних наук Сефако Макгатхо, Медунса–0204, Південна Африка*

У статті обговорюється, як запропонована Кудряшовим схема самофазової модуляції та нелінійна хроматична дисперсія спричиняють еволюцію спокійних оптичних солітонів у магнітооптичних хвилеводах. Забезпечується повне розуміння моделі управління; розглядається узагальнена часова еволюція. Для полегшення відновлення таких солітонів використовується модифікований підхід суб-ODE. Це призводить до повного спектру оптичних солітонів та необхідних умов, які повинні бути виконані для існування цих солітонів, які також наводяться.

**Ключові слова:** *солітони; самофазова модуляція; інтегрованість; хроматична дисперсія*

EAST EUROPEAN JOURNAL OF PHYSICS. **4.** 157-163 (2025)
DOI:10.26565/2312-4334-2025-4-13 ISSN 2312-4334

# PARTIAL EXACT SOLUTIONS OF NONLINEAR DISTRIBUTION ONE-COMPONENT ORDER PARAMETER IN EQUILIBRIUM SYSTEMS

**A.R. Shymanovskyi[1]*, V.F. Klepikov[1,2]**
*[1]V.N. Karazin Kharkiv National University, Kharkiv, Ukraine*
*[2]Institute of Electrophysics and Radiation Technologies NAS of Ukraine, Kharkiv, Ukraine*
**Corresponding Author e-mail: andrey.shimanovskii@gmail.com*

Received August 8, 2025; revised September 29, 2025; accepted October 30, 2025

This paper investigates partial exact solutions of a nonlinear fourth-order differential equation arising from the variational principle for a thermodynamic potential with high derivatives. To describe the spatial distribution of the order parameter, the elliptic cosine function of Jacobi is used, which allows reducing the problem to a system of algebraic equations for amplitude, spatial scale, and modulus. The conditions for the existence of physically admissible solutions were obtained, and it was found that periodic solutions expressed in terms of elliptic cosine are relevant for describing first-order phase transitions. Graphs illustrating the dependence of the main parameters of the solution on the characteristics of the system are presented.

**Keywords:** *Nonlinear differential equations; Order parameter; Elliptic Jacobi functions; First-order phase transition; Incommensurate phase*
**PACS:** 64.60.Bd, 64.60.-i 05.70.Jk

## INTRODUCTION

Phase transitions and spatially inhomogeneous states in condensed matter systems remain one of the key areas of research in modern physics. In many physical models — in particular, in the description of ferroelectrics, magnets, alloys, and during spinodal decomposition — the order parameter is a one-component function of the spatial coordinate [1-4]. Their application goes beyond traditional solid-state physics — similar equations also arise in theories of self-organisation of structures in biological, computational, and non-equilibrium systems [5-7]. In such cases, an important task is to find exact or approximate solutions to the corresponding equations that describe the evolution or equilibrium distribution of this parameter.

In the initial stages of phase transitions, when the amplitude of the order parameter is small, linear analytical approximations are often used. However, with increasing nonlinearity of the system, such approaches lose their accuracy. Particularly difficult to describe are cases where strongly nonlinear, periodic or localised distributions are formed — for example, alternating domains with domain walls. [8]

In classical approaches to modelling such structures, harmonic expansion or expansion in terms of the order parameter is widely used. However, the accurate representation of strongly nonlinear profiles, such as bell solitons or modulation structures, requires the inclusion of a large number of terms, which complicates both analytical analysis and numerical investigation.

An alternative approach is to search for partial exact solutions of the variational equation that allow the order parameter to be represented by special functions, in particular Jacobi elliptic functions [9-11]. In particular, the function

$$\varphi = a * cn(bx, k) \tag{1}$$

the elliptic cosine allows us to describe spatial distributions of order parameters that smoothly interpolate between harmonic and bell-soliton behaviour depending on the modulus $k$.

The aim of this work is to construct a class of exact partial solutions in the form of elliptic cosine — Jacobi function — for the fourth-order equation derived from the corresponding variational functional Within the framework of Landau theory, analytical solutions in the form of function (1) are constructed, and the dependence of the distribution parameters on the thermodynamic potential parameters has been investigated.

## CALCULATION ORDER PARAMETER

Let us write down the thermodynamic potential in the form [9]:

$$F = F_0 + \int dx \left[\frac{1}{2}(\varphi'')^2 - \frac{g}{2}(\varphi\varphi')^2 - \frac{\gamma}{2}(\varphi')^2 + \frac{q}{2}\varphi^2 + \frac{p}{4}\varphi^4 + \frac{1}{6}\varphi^6\right], \tag{2}$$

where $g$, γ are material parameters and $q = q_0(T - T_c)/T_c$and $p$ depend on other conditions (e.g. pressure).

The variational equation for functional (1) is the following nonlinear fourth-order differential equation:

---

***Cite as:*** A.R. Shymanovskyi, V.F. Klepikov, East Eur. J. Phys. 4, 157 (2025), https://doi.org/10.26565/2312-4334-2025-4-13

$$\varphi^{(IV)} + g\left[\varphi^2\varphi'' + \varphi\varphi'^2\right] + \gamma\varphi'' + q\varphi + p\varphi^3 + \varphi^5 = 0. \tag{3}$$

Let us represent the order parameter as (1). Substituting (1) into (3) we obtain the following system of equations

$$\begin{cases} a^4 - 3ga^2b^2k^2 + 24b^4k^4 = 0 \\ b^4(20k^2 - 40k^4) + 2ga^2b^2(2k^2 - 1) - 2\gamma b^2k^2 + pa^2 = 0 \\ b^4(16k^4 - 16k^2 + 1) + ga^2b^2(1 - k^2) + \gamma b^2(2k^2 - 1) + q = 0 \end{cases} \tag{4}$$

From the first equation in (4) we can find the parameter $a$:

$$a^2 = 3\frac{g \pm \sqrt{g^2 - \frac{32}{3}}}{2} b^2k^2 = {\acute{a}_{\pm}}^2 b^2k^2 \tag{5}$$

We see that parameter $a$ is valid only when

$$g \geq \sqrt{\frac{32}{3}} \tag{6}$$

Let's look at the limiting case when $k = 0$. From the third equation (4) we obtain

$$b^4 - \gamma b^2 + q = 0 \tag{7}$$

or

$$b^2 = \frac{\gamma \pm \sqrt{\gamma^2 - 4q}}{2} \tag{8}$$

From this, we can see that a second-order phase transition occurs from a highly symmetric phase to a modulated phase at the point $q = \gamma^2/4$.

Now let's look at the limiting case when $k^2 = 1$. We obtain the following system of equations

$$\begin{cases} -20b^4 + 2g\acute{a}^2b^2 - 2\gamma b^2 + p\acute{a}^2b^2 = 0 \\ b^4 + \gamma b^2 + q = 0 \end{cases} \tag{9}$$

From here, we can find an expression for $b^2$:

$$b^2 = \frac{2\gamma - p\acute{a}^2}{2(g\acute{a}^2 - 10)} \tag{10}$$

Parameter b is valid only when either $g\acute{a}^2 > 10$ and $\gamma \geq p\acute{a}^2/2$, or $g\acute{a}^2 < 10$ and $\gamma \leq p\acute{a}^2/2$.

Substitute (5) into the second equation (4):

$$b^2 = \frac{2\gamma - p\acute{a}^2}{2(2k^2 - 1)(g\acute{a}^2 - 10)} = \frac{\xi\sigma}{2(2k^2 - 1)}, \tag{11}$$

where

$$\xi = 2\gamma - p\acute{a}^2, \tag{12}$$

$$\frac{1}{\sigma} = g\acute{a}^2 - 10. \tag{13}$$

Substituting (11) into the third equation (4) we obtain the following expression

$$k^4 - k^2 + \frac{\sigma^2\xi^2 + 2\gamma\sigma\xi + 4q}{(6\sigma^2 - \sigma)\xi^2 + 8\gamma\sigma\xi + 16q} = 0 \tag{14}$$

Let's calculate the discriminant of this equation for $k^2$:

$$D=\frac{(2\sigma^2-\sigma)\xi^2}{(6\sigma^2-\sigma)\xi^2+8\gamma\sigma\xi+16q} \tag{15}$$

The solution to equation (14) will be

$$k^2=\frac{1\pm\sqrt{D}}{2}. \tag{16}$$

It can be seen that these solutions (16) take values either [0, 1/2] or [1/2, 1]. For $k^2$ to take all values, the discriminant (15) must be zero at some point. From (15) it can be seen that at any temperature $D\neq 0$, but at $\xi=0$ (or $p=2\gamma/\acute{a}^2$) – D=0, i.e. we are dealing with first-order transitions.

At $\sigma=0$ or $\sigma=1/2$, we obtain a degenerate solution $k^2=1/2$, which will not be considered further.

A first-order transition occurs at a constant temperature from $0\leq k^2\leq 1$. From (14) we find this temperature:

$$\frac{\sigma^2{\xi_0}^2+2\gamma\sigma\xi_0+4q_0}{(6\sigma^2-\sigma){\xi_0}^2+8\gamma\sigma\xi_0+16q_0}=0 \tag{17}$$

$$q_0=-\frac{\sigma^2{\xi_0}^2+2\gamma\sigma\xi_0}{4}=\frac{\gamma^2}{4}-\frac{(\gamma+\sigma\xi_0)^2}{4} \tag{18}$$

where $\xi_0$ is the initial value of $\xi$ from $p_0$.

Substituting (18) the discriminant (15) can be rewritten as:

$$D=\frac{(2\sigma-1)\xi^2}{(6\sigma-1)\xi^2+8\gamma(\xi-\xi_0)-4\sigma{\xi_0}^2} \tag{19}$$

Expression (11) can be rewritten by substituting (16) and (19):

$$b^2=\frac{|\sigma|}{2}\sqrt{\frac{(6\sigma-1)\xi^2+8\gamma(\xi-\xi_0)-4\sigma{\xi_0}^2}{2\sigma-1}} \tag{20}$$

$\xi$ will take such values that the discriminant (19) takes values from 0 to 1. There is a condition

$$D(\xi_0)=D(\xi_{max})=1 \tag{21}$$

From condition (21) it follows that

$$\xi\in[\xi_0,-\xi_0-2\gamma/\sigma] \tag{22}$$

Expression (11) must be true so we have two cases:

$$\begin{gathered}\xi_0>0\left(p_0<\frac{2\gamma}{\acute{a}^2}\right),\ \sigma<0\\ \xi_0<0\left(p_0>\frac{2\gamma}{\acute{a}^2}\right),\ \sigma>0\end{gathered}. \tag{23}$$

If $\sigma>0$, there are two cases:

$$\begin{gathered}-\xi_0-2\gamma/\sigma>0\rightarrow p_0>\frac{2\gamma}{\acute{a}^2}\left(1+\frac{1}{\sigma}\right)\\ -\xi_0-2\gamma/\sigma<0\rightarrow\frac{2\gamma}{\acute{a}^2}<p_0<\frac{2\gamma}{\acute{a}^2}\left(1+\frac{1}{\sigma}\right)\end{gathered}. \tag{24}$$

In the first case (24) – $0\leq k^2\leq 1$, in the second – $0\leq k^2\leq k^2_{max}<\frac{1}{2}$ where $k^2_{max}$ is found from the extremum condition (19). The extremum itself is equal to

$$\xi_e=2\xi_0+\frac{\sigma\xi_0^2}{\gamma} \tag{25}$$

When $-\xi_0-2\gamma/\sigma=\xi_0$ (or $\xi_0=-\gamma/\sigma$), $k^2_{max}=0$, i.e. the modulated phase is generally not realised.

## RESULTS

Let's move on to the graphs. Let γ = 1 for all graphs.

Let's take $g^2 = 32/3$ or $\sigma = 1/6$. Let's look at the graphs for small values of $p_0$ and we get the following Figure 1.

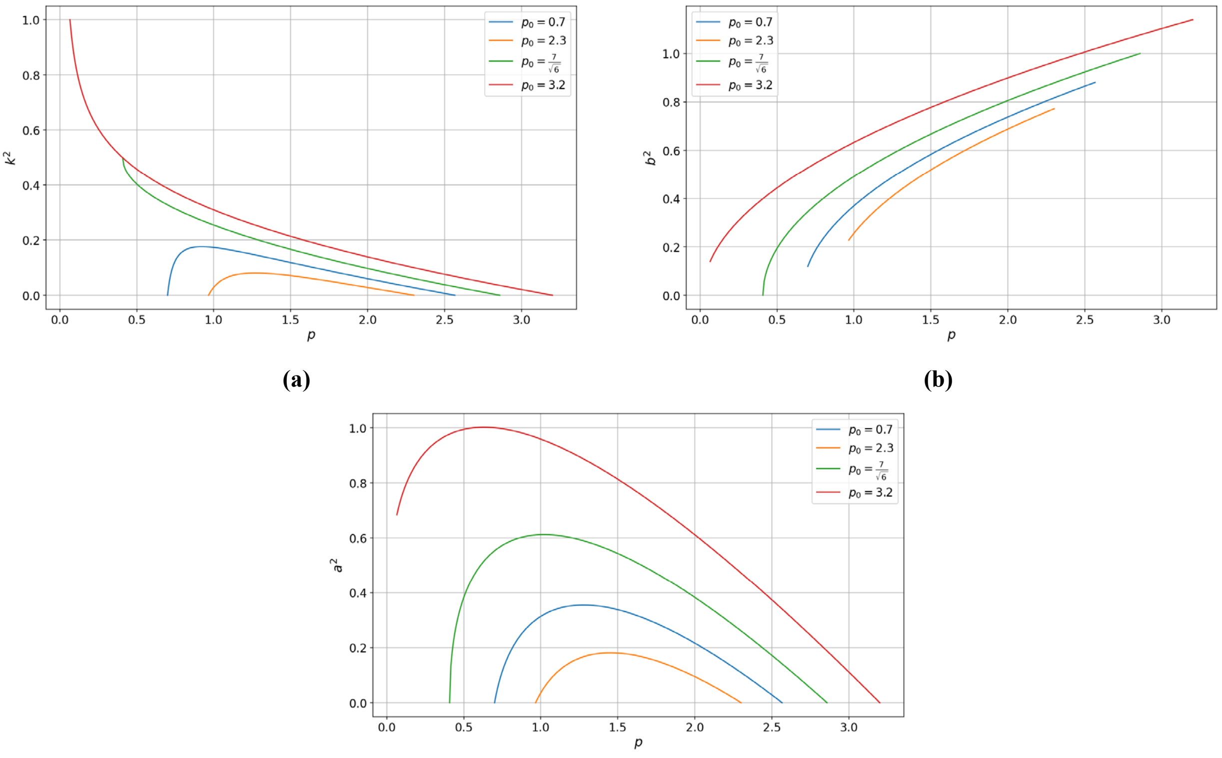

**(a)** **(b)**

**(c)**

**Figure 1.** Graphs of dependence on $p$ at $g^2 = 32/3$ for different initial values of $p_0$ for **(a)** $k^2$ **(b)** $b^2$ **(c)** $a^2$

As can be seen from Fig. 1, there are three types of solutions:

- $\frac{1}{\sqrt{6}} < p_0 < \frac{4}{\sqrt{6}}$ – the parameter p increases and the final phase remains modulated (lock-in transition).
- $\frac{4}{\sqrt{6}} < p_0 \leq \frac{7}{\sqrt{6}}$ – the parameter p decreases and the final phase remains modulated (lock-in transition).
- $p_0 > \frac{7}{\sqrt{6}}$– the parameter p decreases and the final phase transitions to a commensurate phase.

Now let's look at the graphs for larger $p_0$ (Figure 2). As can be seen from Figure 2(b), when $p_0 < \frac{10}{\sqrt{6}}$, the maximum amplitude $a$ is reached at $\xi < \xi_{max}$, in other cases the maximum amplitude $a$ is reached at $\xi = \xi_{max}$.

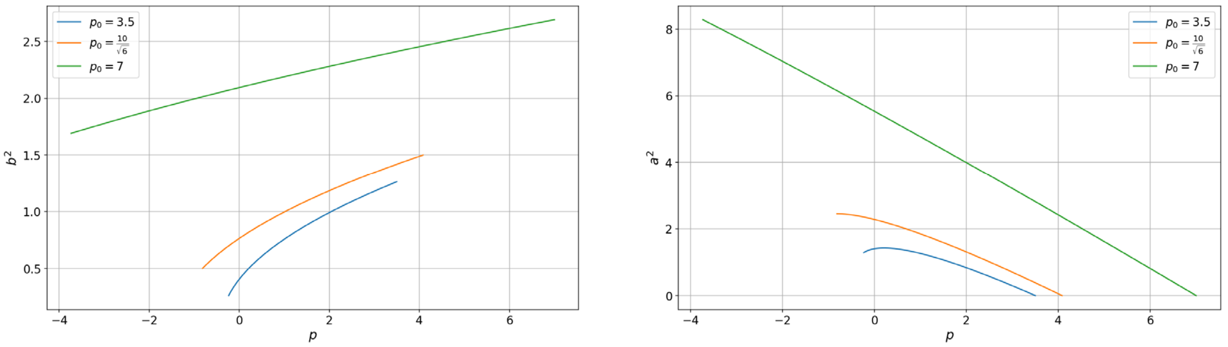

**(a)** **(b)**

**Figure 2.** Graphs of dependence on $p$ at $g^2 = 32/3$ for different initial values of p_0 for **(a)** $b^2$ **(b)** $a^2$

Since in (5) there are two expressions for the amplitude let us consider them separately:

**1.** When $\acute{a}_+$ σ takes the value $(0,1/6)$. The graphs for small $p_0$ will be similar to Figure 1, but for larger $p_0$ ${b_+}^2$ will have a minimum at $\xi < \xi_{max}$, for example, for $g^2 = 11$ we obtain Figure 3.

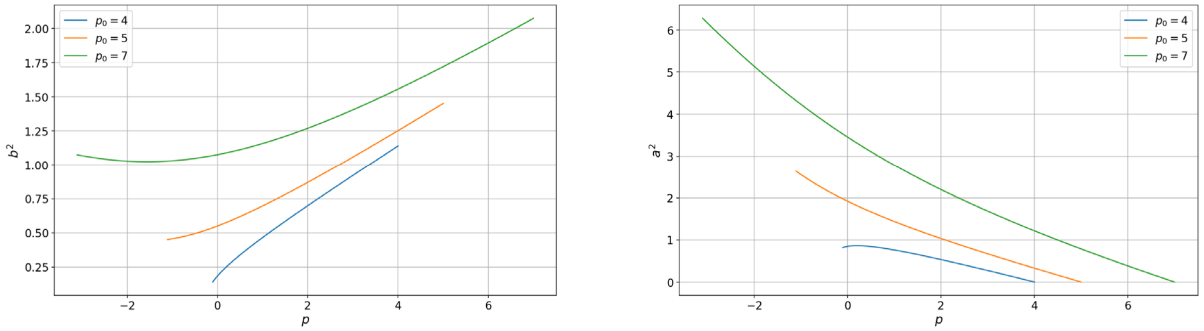

**(a)** **(b)**

**Figure 3.** Graphs of dependence on $p$ at $g^2=11$ for different initial values of $p_0$ for **(a)** $b_+{}^2$ **(b)** $a_+{}^2$

**2.** When $\acute{a}_-$ $\sigma$ takes the values $(1/6,1/2)$, $(1/2,+\infty)$ and $(-\infty,-1/2)$.
For $g^2=11$ (see Figure 4) $b_-{}^2$ i $a_-{}^2$will have a maximum at $\xi<\xi_{max}$.

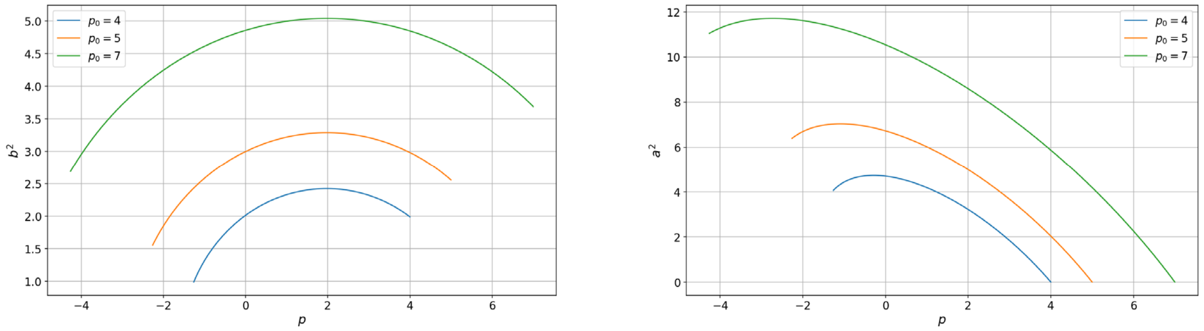

**(a)** **(b)**

**Figure 4.** Graphs of dependence on $p$ at $g^2=11$ for different initial values of $p_0$ for **(a)** $b_-{}^2$ **(b)** $a_-{}^2$

For $\acute{a}_-$ $(g^2>12)$, there are no such values of $p_0$ where $k^2$ took all values from 0 to 1. For $g^2>12$, with an increase in p (see Figures 5-6)

$$k^2 \to \left(1+\sqrt{\frac{(2\sigma-1)}{(6\sigma-1)}}\right)\Big/2 \tag{26}$$

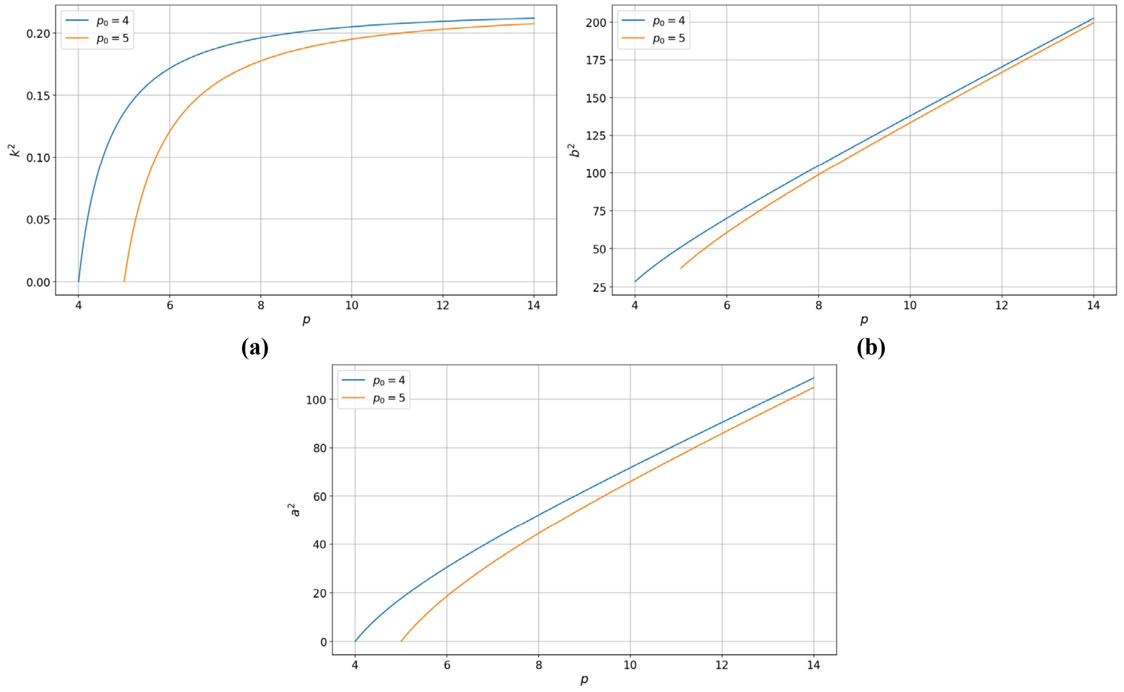

**(a)** **(b)**

**(c)**

**Figure 5.** Graphs of dependence on $p$ at $g^2=16$ for different initial values of $p_0$ for **(a)** $k_-{}^2$ **(b)** $b_-{}^2$ **(b)** $a_-{}^2$

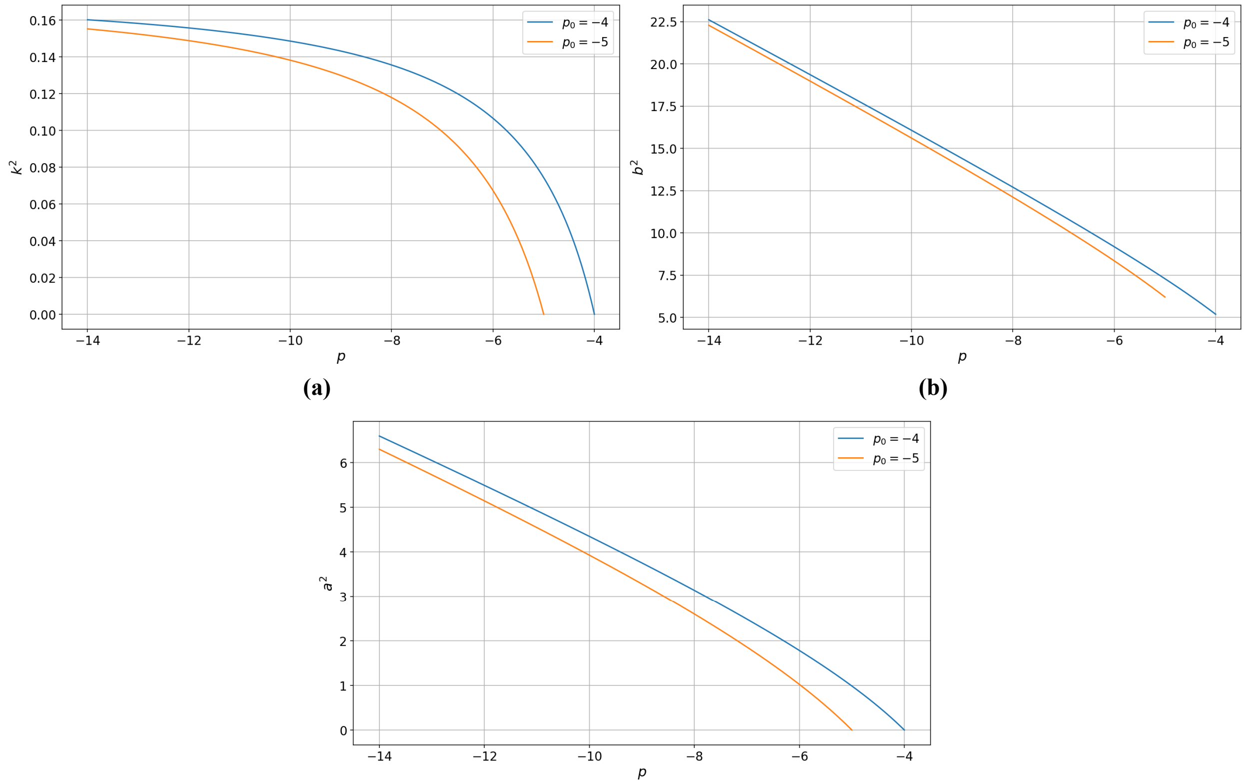

**(a)** **(b)**

**(c)**

**Figure 6.** Graphs of dependence on $p$ at $g^2 = 25$ for different initial values of $p_0$ for **(a)** $k\_^2$ **(b)** $b\_^2$ **(b)** $a\_^2$

## CONCLUSIONS

This paper investigates a nonlinear fourth-order differential equation arising from the variational principle for a thermodynamic potential with high derivatives. For the order parameter, we used a distribution in the form of an elliptic cosine of Jacobi, which allowed us to reduce the problem to a system of algebraic equations for the amplitude, spatial scale, and modulus.

We established conditions for the existence of a physically realisable solution, in particular, a restriction on the parameter $g$, which guarantees the validity of the amplitude. It was found that initially a second-order phase transition occurs from a highly symmetric phase to an incommensurate phase at the point $q = \gamma^2/4$. Further, it was found that solutions based on the elliptic cosine are relevant for describing first-order phase transitions.

Graphs of the dependence of parameters a, b, k on the initial values $p_0$ and $g$ were constructed.

## ORCID

**V.F. Klepikov**, https://orcid.org/0000-0003-0294-7022

## REFERENCES

[1] S. Ghosh, M. Matty, R. Baumbach, E.D. Bauer, K.A. Modic, A. Shekhter, J.A. Mydosh, E.-A. Kim, and B.J. Ramshaw, Sci. Adv., **6**(10), eaaz4074 (2020). http://dx.doi.org/10.1126/sciadv.aaz4074
[2] S. Lee, A.J. Woods, P.F.S. Rosa, S.M. Thomas, E.D. Bauer, S.-Z. Lin, and R. Movshovich, Phys. Rev. Res., **7**(2), L022053 (2025). http://dx.doi.org/10.1103/PhysRevResearch.7.L022053
[3] S.L. Qiu, M. Dutta, H.Z. Cummins, J.P. Wicksted, and S.M. Shapiro, Phys. Rev. B, **34**(11), 7901 (1986). http://dx.doi.org/10.1103/PhysRevB.34.7901
[4] I. Aramburu, G. Madariaga, and J.M. Pérez-Mato, Phys. Rev. B, **49**(2), 802 (1994). http://dx.doi.org/10.1103/PhysRevB.49.802
[5] A.V. Babich, V.F. Klepikov, and E.A. Melyakova, Nanosistemy, Nanomater., Nanotehnologii, **18**(4), 217 (2020). (in Russian)
[6] S.P. Kruchinin, R.I. Eglitis, V.E. Novikov, A.M. Oleś, and S. Wirth, Symmetry,. **15**(9), 1732 (2023). https://doi.org/10.3390/sym15091732
[7] A.R. Shymanovskyi and V.F. Klepikov, *Probl. At. Sci. Technol.*, **157**, 139–141 (2025).
[8] Y. Ishibashi and H. Shiba, *J. Phys. Soc. Jpn.*, **45**(2), 409–413 (1978). http://dx.doi.org/10.1143/jpsj.45.409
[9] S.V. Berezovsky, V.F. Klepikov, V.Y. Korda, and N.A. Shlyakhov, *Int. J. Mod. Phys. B*, **12**(4), 433–447 (1998). http://dx.doi.org/10.1142/s0217979298000284
[10] A.V. Babich, S.V. Berezovsky, V.F. Klepikov, and A.V. Sereda, *Condens. Phys.*, **9**(1), 121 (2006). http://dx.doi.org/10.5488/cmp.9.1.121
[11] V.F. Klepikov, *Low Temp. Phys.*, **44**(12), 1309–1312 (2018). http://dx.doi.org/10.1063/1.5078626

# ЧАСТКОВІ ТОЧНІ РІШЕННЯ НЕЛІНІЙНОГО РОЗПОДІЛУ ОДНОКОМПОНЕНТНОГО ПАРАМЕТРА ПОРЯДКУ В РІВНОВАЖНИХ СИСТЕМАХ

***А.Р. Шимановський*[1], *В.Ф. Клепіков*[1,2]**
[1]*Харківський національний університет ім. В.Н. Каразіна, Україна*
[2]*Інститут електрофізики і радіаційних технологій НАН України, Україна*

У цій роботі досліджено частинні точні розв'язки нелінійного диференційного рівняння четвертого порядку, що виникає з варіаційного принципу для термодинамічного потенціалу з високими похідними. Для опису просторового розподілу параметра порядку використано функцію еліптичного косинуса Якобі, що дало змогу звести задачу до системи алгебраїчних рівнянь для амплітуди, просторового масштабу та модуля. Отримано умови існування фізично допустимих розв'язків та виявлено, що періодичні розв'язки, виражені через еліптичний косинус, релевантні для опису фазових переходів першого роду. Представлено графіки, що ілюструють залежність основних параметрів рішення від характеристик системи.

**Ключові слова:** *нелінійні диференційні рівняння; параметр порядку; еліптичні функції Якобі; фазовий перехід першого роду; несумірна фаза*

East European Journal of Physics. **4**. 164–171 (2025)

DOI: 10.26565/2312-4334-2025-4-14 ISSN 2312-4334

# ON SOLUTIONS OF THE KILLINGBECK POTENTIAL AND CLARIFYING COMMENTS ON A RELATED ANALYTICAL APPROACH

**Fatma Zohra Khaled**[1], **Mustafa Moumni**[2*,3], **Mokhtar Falek**[2,3]

[1]*LPRIM, Department of Physics, University of Batna I, Batna, 05000, Algeria*

[2]*LPPNNM, Department of Matter Sciences, University of Biskra, Biskra, 07000, Algeria*

[3]*Faculty of Technology, University of Khenchela, Khenchela, 40000, Algeria*

[*]*Corresponding Author e-mail: m.moumni@univ-batna.dz*

Received August 10, 2025; revised September 12, 2025; in final form September 15, 2025; accepted September 16, 2025

The work presents analytical solutions to the Schrödinger equation for the Killingbeck potential, a hybrid model combining harmonic, linear, and Coulombic terms, as well as an approximate model of Yukawa-type potentials. The radial Schrödinger equation is solved by means of the series expansion method, thus yielding the exact expressions of both bound-state solutions and eigenfunctions for systems such as quarkonium and confined hydrogen-like atoms in plasma environments. Furthermore, we offer a constructive commentary on the work of Obu et al. (East Eur. J. Phys. 3, 146–157, 2023), with the aim of clarifying a mathematical misstatement utilised in their analytical treatment of analogous systems.

**Keywords:** *Schrödinger equation; Killingbeck potential; Yukawa potential; Series expansion method; Heun equation*

**PACS:** 03.65.-w; 02.30.Gp

## 1. INTRODUCTION

In the domain of quantum mechanics, the accurate modelling of interaction potentials is paramount for the study of particle behaviour in bound states across various scales, ranging from atomic to hadronic systems. The Killingbeck potential is a particularly noteworthy model in this regard, due to its flexibility. The model incorporates a quadratic term, which acts in a manner analogous to a harmonic oscillator, in conjunction with a linear confining term and a Coulomb-like component.

$$V\left(r\right)=-\frac{A}{r}+Br+Cr^{2}. \tag{1}$$

This combination enables the Killingbeck potential to describe both short-range and long-range quantum interactions within a unified analytical framework [1–3]. It has been determined that this subject is of particular value in areas like heavy quarkonium spectroscopy, meson physics, quantum dots and Hydrogen-like systems embedded in a plasma environment, where both confinement and screening effects are present [4–6]. The notable attribute of the Killingbeck potential is twofold: firstly, its inherent solvability, and secondly, its capacity to establish a linkage between disparate potential models. The linear term captures the long-range confining force seen in quark confinement, while the Coulomb term accounts for the dominant one-gluon exchange interaction, which is an essential component of effective QCD potentials [7, 8]. The harmonic term is a useful regulator in hadronic systems, despite its unphysical behaviour at large distances. It facilitates analytic solutions in non-relativistic quantum mechanics, a feature that is frequently advantageous for theoretical research [1, 9].

The Killingbeck potential exhibits noteworthy mathematical and physical affinities with exponential-type potentials, including the Yukawa and its various variants of screened Coulomb forms. These potentials describe interactions involving massive bosons, and which result in short-range forces characterised by exponential decay [10–14]. They also describe the confinement potential of hydrogen-like atoms in plasma [15–17]. When the screening effects are weak, these exponential potentials simplify to the Killingbeck form by employing appropriate series expansions [18–20]. The analogies employed in this context transcend the confines of formalism. They capture a deeper physical intent, with an equilibrium of attraction and screening achieved in quantum confinement models. For systems like quarkonium, where the interplay between asymptotic freedom and confinement is particularly pronounced, these potentials facilitate the calculation of more precise spectral predictions [4, 8, 20]. Furthermore, the employment of various analytical approaches has been demonstrated to be beneficial in this context. The Nikiforov-Uvarov method, the perturbation theory, and the series expansions have all been applied effectively, thereby reinforcing the underlying structural coherence of these potentials [2, 5, 19].

In this work, we present the complete analytical solutions of the Schrödinger equation for the Killingbeck potential using the series expansion method. In addition, we take this opportunity to address a related methodological point in the recent literature (Obu et al. East Eur. J. Phys. 3, 146–157, 2023) [20], where an analytical misstatement affects the interpretation of a series solution in a similar spectral problem.

---

***Cite as:*** F.Z. Khaled, M. Moumni, M. Falek, East Eur. J. Phys. 4, 164 (2025), https://doi.org/10.26565/2312-4334-2025-4-14

## 2. CLARIFYING COMMENT ON THE WORK BY OBU ET AL.

In their recent article, Obu et al. present a "Comparative Study of the Mass Spectra of Heavy Quarkonium System with an Interacting Potential Model" (East Eur. J. Phys. 3, 146–157, 2023) [20]. This study makes a significant contribution to the field of hadronic physics through analytical comparisons by employing the Nikiforov-Uvarov and the Series Expansion Methods (SEM). The authors' approach to solving the Schrödinger equation with Yukawa-type potentials is methodologically rigorous and relevant for charmonium and bottomonium systems.

However, in section 4 of their paper, specifically at equation (62), there is a conceptual misstatement regarding the nature of linear independence in a power series expansion. The authors state the following:

*"Equation (62) is linearly independent implying that each of the terms is separately equal to zero, noting that r is a non-zero function; therefore, it is the coefficient of r that is zero. The coefficients $a_n$ are independent."*

This statement confuses the independence of the functions $r^n$ with the independence of the coefficients $a_n$. The correct interpretation is that the *functions $r^n$* form a linearly independent set in the polynomial on any open interval around $r = 0$. Therefore, for a power series to vanish identically on such an interval, it is necessary that each *coefficient* of these *functions $r^n$* vanishes separately. This structural phenomenon gives rise to recurrence relations between the coefficients, rather than ensuring their independence from each other.

We can see from equation (63) in [20] that it yields the result $L = -\frac{1}{2}(2N + 1)$. This is in direct contradiction to the established definitions of the principal quantum number $N$ and the orbital quantum number $L$ (in the limit where $\alpha_3 = 0$).

Equation (62) in [20] must therefore be expressed as a polynomial given that it is written in [20] as a sum of polynomials. Consequently, a more accurate formulation would be as follows:

*"Since the powers of r are linearly independent, the coefficient of each power must vanish separately. This, in turn, leads to recurrence relations among these coefficients."*

This clarification is important to maintain the mathematical rigour of the derivation and to ensure the educational value of the work for future researchers.

## 3. SCHRÖDINGER ENERGIES FOR THE KILLINGBECK POTENTIAL USING SEM

We will follow the steps outlined in [20] with some adjustments. In [20], the Potential is defined as follows:

$$V(r) = -\frac{a}{r} + \frac{b}{r}e^{-\alpha_I r} - \frac{c}{r^2}e^{-2\alpha_I r}, \tag{2}$$

where $a$,$b$ and $c$ are potential strengths and where the screening parameter is represented by the symbol $\alpha_I$.

By expanding eq.(2) with Taylor series up to order three of $\alpha_I$, the form of the Killingbeck potential is obtained:

$$V(r) = \frac{-\alpha_0}{r} + \alpha_1 r + \alpha_2 r^2 + \frac{\alpha_3}{r^2} + \alpha_4, \tag{3}$$

with:

$$-\alpha_0 = -a + b + 2c\alpha_I; \alpha_1 = \frac{1}{2}b\alpha_I^2 + \frac{4}{3}c\alpha_I^3; \alpha_2 = -\frac{1}{6}b\alpha_I^3; \alpha_3 = -c; \alpha_4 = -b\alpha_I - 2c\alpha_I^2. \tag{4}$$

Here we mention that the parameter $c$ is omitted in the vicinity of the parameter $\alpha_I^3$ in the $\alpha_1$ term in [20].

Due to the spherical symmetry of the interaction, the radial Schrödinger equation is the primary focus:

$$\frac{d^2R(r)}{dr^2} + \frac{2}{r}\frac{dR(r)}{dr} + \left(\frac{2\mu}{\hbar^2}(E - V(r)) - \frac{l(l+1)}{r^2}\right)R(r) = 0, \tag{5}$$

here, $l$ denotes the angular quantum number, while $\mu$ represents the reduced mass for the quarkonium. The variable $r$ is the internuclear separation.

Substituting eq.(3) into eq.(5) gives:

$$\frac{d^2R(r)}{dr^2} + \frac{2}{r}\frac{dR(r)}{dr} + \left(\varepsilon + \frac{A}{r} - Br - Cr^2 - \frac{L(L+1)}{r^2}\right)R(r) = 0, \tag{6}$$

where:

$$\varepsilon = \frac{2\mu}{\hbar^2}(E - \alpha_4); A = \frac{2\mu}{\hbar^2}\alpha_0; B = \frac{2\mu}{\hbar^2}\alpha_1; C = \frac{2\mu}{\hbar^2}\alpha_2, \tag{7}$$

$$L(L+1) = \left(l(l+1) + \frac{2\mu}{\hbar^2}\alpha_3\right). \tag{8}$$

From eq.(8), we get the new "orbital" quantum number $L$

$$L = -\frac{1}{2} + \frac{1}{2}\sqrt{(2l+1)^2 + \frac{8\mu}{\hbar^2}\alpha_3}. \tag{9}$$

Following [20], we write the solution in the form:

$$R(r) = e^{-\left(\alpha r^2+\beta r\right)} F\left(r\right). \tag{10}$$

Substituting eq.(10) into eq.(6) and dividing by $e^{-\left(\alpha r^2+\beta r\right)}$, we obtain:

$$\begin{aligned} &F''\left(r\right) + \left[-4\alpha r - 2\beta + \frac{2}{r}\right] F'\left(r\right) \\ &\left[\left(\varepsilon + \beta^2 - 6\alpha\right) + \frac{\left(A - 2\beta\right)}{r} + \left(4\alpha\beta - B\right) r + \left(4\alpha^2 - C\right) r^2 - \frac{L\left(L+1\right)}{r^2}\right] F\left(r\right) = 0. \end{aligned} \tag{11}$$

We use the parameters $\alpha$ and $\beta$ to simplify the given equation, thereby eliminating the terms in $r$ and $r^2$ in the equation.

$$\begin{cases} 4\alpha^2 - C = 0 \implies \alpha = \frac{\sqrt{C}}{2}, \\ 4\alpha\beta - B = 0 \implies \beta = \frac{B}{2\sqrt{C}}. \end{cases} \tag{12}$$

and we get the new radial equation

$$F''\left(r\right) + \left(-4\alpha r - 2\beta + \frac{2}{r}\right) F'\left(r\right) + \left(\varepsilon + \beta^2 - 6\alpha + \frac{\left(A - 2\beta\right)}{r} - \frac{L\left(L+1\right)}{r^2}\right) F\left(r\right) = 0. \tag{13}$$

We present the solutions of this equation in a polynomial form:

$$F\left(r\right) = \sum_{k=0}^{\infty} a_k r^{k+s}. \tag{14}$$

In this study, the approach taken differs from that of [20] in terms of the chosen polynomial form. Specifically, the latter authors select $F\left(r\right) = \sum_{n=0}^{\infty} a_n r^{2n+L}$ in [20], yet no rationale is provided for the selection of this particular polynomial (it starts at power $r^L$) nor for the choice of an even power of $r$ in the series. We also use the letter $k$ in place of $n$ in the summation, thus ensuring clarity and avoiding any potential confusion with the principal quantum number $n$, which is generally employed in standard textbooks. Putting the solution (14) and its derivatives into the radial equation (13) results in the following equation:

$$\begin{aligned} &\sum_{k=0}^{\infty} \left[\left(k+s\right)\left(k+s+1\right) - L\left(L+1\right)\right] a_k r^{k+s-2} + \sum_{k=0}^{\infty} \left[A - 2\beta\left(k+s+1\right)\right] a_k r^{k+s-1} \\ &+ \sum_{k=0}^{\infty} \left[\varepsilon + \beta^2 - 2\alpha\left(2k+2s+3\right)\right] a_k r^{k+s} = 0. \end{aligned} \tag{15}$$

We rearrange the summation terms to write:

$$\begin{aligned} &\sum_{k=-2}^{\infty} \left[\left(k+s+2\right)\left(k+s+3\right) - L\left(L+1\right)\right] a_{k+2} r^{k+s} + \sum_{k=-1}^{\infty} \left[A - 2\beta\left(k+s+2\right)\right] a_{k+1} r^{k+s} \\ &+ \sum_{k=0}^{\infty} \left[\varepsilon + \beta^2 - 2\alpha\left(2k+2s+3\right)\right] a_k r^{k+s} = 0, \end{aligned} \tag{16}$$

and we get the following form of a single polynomial series:

$$\begin{aligned} &\sum_{k=0}^{\infty} \left[\left[\left(k+s+2\right)\left(k+s+3\right) - L\left(L+1\right)\right] a_{k+2} + \left[A - 2\beta\left(k+s+2\right)\right] a_{k+1} + \left[\varepsilon + \beta^2 - 2\alpha\left(2k+2s+3\right)\right] a_k\right] r^{k+s} \\ &+ \left[\left[\left(s+1\right)\left(s+2\right) - L\left(L+1\right)\right] a_1 + \left[A - 2\beta\left(s+1\right)\right] a_0\right] r^{s-1} + \left[\left[s\left(s+1\right) - L\left(L+1\right)\right] a_0\right] r^{s-2}\} = 0. \end{aligned} \tag{17}$$

Since this relation holds for all values of the variable $r$, each coefficient of the $r^k$-functions must vanish. The following equation therefore holds:

$$\left[\left(k+s-L+2\right)\left(k+s+L+3\right)\right] a_{k+2} + \left[A - 2\beta\left(k+s+2\right)\right] a_{k+1} + \left[\varepsilon + \beta^2 - 2\alpha\left(2k+2s+3\right)\right] a_k = 0, \tag{18}$$

$$\left[\left(s+1\right)\left(s+2\right) - L\left(L+1\right)\right] a_1 + \left[A - 2\beta\left(s+1\right)\right] a_0 = 0, \tag{19}$$

$$\left[s\left(s+1\right) - L\left(L+1\right)\right] a_0 = 0. \tag{20}$$

We impose the condition $a_0 \neq 0$ to ensure that $F(r) \neq 0$; otherwise, it follows from eq.(19) that $a_1 = 0$. Consequently, all $a_k = 0$ from eq.(18). Therefore, from eq.(20), we derive the following result:

$$[s(s+1) - L(L+1)]\, a_0 = 0 \quad \text{and} \quad a_0 \neq 0 \Longrightarrow s = L \quad \text{or} \quad s = -L-1. \tag{21}$$

We reject the solution $s = -L-1$ on the basis of the expressions of $R(r)$ in eq.(10) and $F(r)$ in eq.(14). These expressions imply that $R(r)$ is divergent at the origin of $r$. Therefore, it can be concluded that $s = L$. It is evident here that the minimal power of the polynomial $F(r)$ is $r^L$; this is in contrast to the approach taken in [20], where the rationale for this choice is not provided. Replacing this value in the recurrence relations (18) and (19), we write:

$$a_{k+2} = \frac{2\beta(k+L+2) - A}{(k+2)(k+2L+3)} a_{k+1} + \frac{\varepsilon + \beta^2 - 2\alpha(2k+2L+3)}{(k+2)(k+2L+3)} a_k, \tag{22}$$

$$a_1 = \frac{2\beta(L+1) - A}{2(L+1)} a_0. \tag{23}$$

In the context of the probabilistic interpretation of the wave function, it is imperative to impose the condition that $R(r)$ must be convergent when $r \longrightarrow \infty$ and, consequently, the function $F(r)$ must terminate as a finite polynomial. To accomplish this objective, it is necessary to truncate the series (22).

We can follow the method used in [21] and impose that for some value $k = n_r$, the coefficients of both $a_{n_r}$ and $a_{n_r+1}$ vanish while we have $a_{n_r} \neq 0$ and $a_{n_r+1} \neq 0$:

$$a_{n_r+2} = 0 \quad \text{if} \quad 2\beta(n_r+L+2) - A = 0 \quad \text{and} \quad \varepsilon + \beta^2 - 2\alpha(2n_r+2L+3) = 0. \tag{24}$$

This will give us the energies and a relation between the coefficients $\beta$ and $A$:

$$\varepsilon_{n_r,l} = 2\alpha(2n_r+2L+3) - \beta^2, \tag{25}$$

$$\beta = \frac{A}{2(n_r+L+2)}. \tag{26}$$

These two relations are equivalent to eq.(65) and eq.(68) in [20] when we replace $n_r$ by $2n$, because we have employed a more general expression for $R(r)$.

In order to show that we have a combination of the energies of both a harmonic oscillator and a Coulomb potential, we write the energies as follows:

$$\varepsilon_{n_r,l} = 2\sqrt{C}\left(n_r + L + \frac{3}{2}\right) - \frac{A^2}{4(n_r+L+2)^2}. \tag{27}$$

Upon substituting the expressions of $A$, $C$ and the $\alpha$ terms from relations (4), (6) and (8), we obtain the same energies as in eq.(70) in [20]. It is noteworthy that $2n \longrightarrow n_r$ in the expressions of [20].

$$E_{n_r,l} = \sqrt{-\frac{\hbar^2 b}{12\mu}\alpha_I^3}\left(2n_r + 2 + \sqrt{(2l+1)^2 - \frac{8\mu}{\hbar^2}c}\right) - \frac{2\mu}{\hbar^2}\frac{[a - b - 2c\alpha_I]^2}{\left(2n_r + 1 + \sqrt{(2l+1)^2 - \frac{8\mu}{\hbar^2}c}\right)^2} - b\alpha_I - 2c\alpha_I^2. \tag{28}$$

At this point, it has been demonstrated that the energy spectrum of the Killingbeck potential is obtained by applying rigorously the SEM method and correcting the inaccuracies in the application of this SEM method made by Obu et al. in [20].

In this section, we followed the condition (24) as done in [21] to truncate the series (22). Notwithstanding the utilisation of this condition by the authors of [21] in numerous recent works [22–25], it is imperative to acknowledge that this condition does not guarantee the truncation. An examination of the parameter $a_{n_r+3}$ as depicted from eq.(22) and eq.(24) substantiates this assertion:

$$a_{n_r+3} = \frac{\varepsilon_{n_r,l} + \beta^2 - 2\alpha(2n_r+2L+5)}{(n_r+3)(n_r+2L+4)} a_{n_r+1} = -\frac{4\alpha}{(n_r+3)(n_r+2L+4)} a_{n_r+1}. \tag{29}$$

It is evident that $a_{n_r+3} \neq 0$ and so is all the parameters beside it. The error when employing this method is attributable to the confusion arising from the erroneous identification of the index $k$ of the polynomial coefficients $a_k$ (which is denoted $n$ in [20]), and the index $n_r$ of the energies, which is determined by the level under consideration. Consequently, $n_r$ possesses a fixed value for all the values of $k$ in eq.(22) (A parallel observation concerning this error is documented in [26]). This leads us to consider alternative conditions that could be utilised to truncate the series. A comprehensive discussion of these alternatives will be presented in the subsequent section.

## 4. SCHRÖDINGER ENERGIES FOR THE KILLINGBECK POTENTIAL USING HEUN FUNCTIONS

Now we use the Heun formulation of the Schrödinger equation (6), deriving from the same form of the solutions $R(r)$ in eq.(10) with two additional transformations $F(r) = r^{L+1}g(r)$ and $\rho = \sqrt{2\mu/\hbar^2}r$. This results in the Biconfluent Heun equation (BHE):

$$\rho g''(\rho) + \left(1 + \alpha' - \beta'\rho + 2\rho^2\right) g'(\rho) + \left((\gamma' - \alpha' - 2)\rho - \frac{1}{2}\left(\delta' + \beta'(1 + \alpha')\right)\right) g(\rho) = 0. \tag{30}$$

The parameters of this equation are defined as follows:

$$\alpha' = 2L + 1; \beta' = \frac{B}{\sqrt{C}} C^{-\frac{1}{4}}; \gamma' = \frac{1}{\sqrt{C}}\left(\varepsilon + \frac{B^2}{4C}\right); \delta' = \frac{-2A}{\sqrt{C}} C^{\frac{1}{4}}, \tag{31}$$

where $A$, $B$, $C$, $L$, $\varepsilon$, $\alpha$ and $\beta$ are defined in the relations (7), (8) and (12).

The solution of eq.(30) is given by the biconfluent Heun functions [27]:

$$g(\rho) = H_b(\alpha', \beta', \gamma', \delta', \rho) = \sum_{n \geq 0} a_n \frac{\Gamma(1 + \alpha')}{\Gamma(1 + \alpha' + n)} \frac{\rho^n}{n!}. \tag{32}$$

Thus, we have obtained the radial part $R(r) \propto e^{-\left(\alpha r^2 + \beta r\right)} r^{L+1} g(r)$ of the eigenfunctions of the Schrödinger equation for the Killingbeck potential. The angular part consists of the usual spherical harmonic functions $Y_{L,M}(\theta, \phi)$.

As a consequence of the recurrence relation (22), there exists a value $k = n_r$, for which we have [27]:

$$a_{n_r+2} = 0 \quad \text{if} \quad a_{n_r+1} = 0 \quad \text{and} \quad \left[\text{the coefficient of } a_{n_r}\right] = 0. \tag{33}$$

Equivalently:

$$a_{n_r+2} = 0 \quad \text{if} \quad a_{n_r+1} = 0 \quad \text{and} \quad 4\alpha(n_r + L) - \left(\varepsilon + \beta^2 - 6\alpha\right) = 0. \tag{34}$$

Using the second condition and the relation (12), we obtain the energies as follows:

$$\varepsilon_{n_r,l} = 2\sqrt{C}\left(n_r + L + \frac{3}{2}\right) - \beta^2 = 2\sqrt{C}\left(n_r + L + \frac{3}{2}\right) - \frac{B^2}{4C}. \tag{35}$$

It should be noted that this is analogous to eq.(25), with the exception that eq.(26) is not applicable in this instance.

To determine the value of the $B^2/4C$ term, we use the first condition $a_{n+1} = 0$, which establishes a relationship for each value of the radial quantum number $n_r$.

For instance, when $n_r = 0$, the result obtained from eq.(23) is:

$$a_1 = 0 \Longrightarrow \beta = \frac{A}{2(L + 1)} \Longrightarrow \beta^2 = \frac{B^2}{4C} = \frac{A^2}{4(L + 1)^2}. \tag{36}$$

And we derive the following expression for the corresponding energy levels:

$$\begin{aligned} \varepsilon_{0,l} &= 2\sqrt{C}\left(L + \frac{3}{2}\right) - \frac{B^2}{4C} \\ \Longrightarrow E_{0,l} &= \sqrt{-\frac{\hbar^2 b}{12\mu}\alpha_I^3}\left(2 + \sqrt{(2l + 1)^2 - \frac{8\mu}{\hbar^2}c}\right) - \frac{2\mu}{\hbar^2}\frac{\left[a - b - 2c\alpha_I\right]^2}{\left(1 + \sqrt{(2l + 1)^2 - \frac{8\mu}{\hbar^2}c}\right)^2} - b\alpha_I - 2c\alpha_I^2. \end{aligned} \tag{37}$$

The result obtained here is the same result derived in the previous section in eq.(28) ($n_r = 0$).

In the case of $n_r = 1$, it is necessary to express the value of $a_2$. This is obtained from eq.(22) and eq.(23):

$$a_2 = \frac{2\beta(L + 2) - A}{(2)(2L + 3)} a_1 + \frac{\varepsilon_{1,l} + \beta^2 - 2\alpha(2L + 3)}{2(2L + 3)} a_0. \tag{38}$$

We recall here that:

$$\varepsilon_{1,l} = 2\sqrt{C}\left(1 + L + \frac{3}{2}\right) - \beta^2 \text{ and } \alpha = \frac{\sqrt{C}}{2}.$$

We have the condition $a_2 = 0$, so we write:

$$\Longrightarrow \left[4(L + 2)(L + 1)\right]\beta^2 - \left[2A(2L + 3)\right]\beta + \left[A^2 + 4(L + 1)\sqrt{C}\right] = 0$$

$$\Longrightarrow \beta_{1,2} = \frac{A(2L+3) \pm \sqrt{A^2 - 16(L+2)(L+1)^2\sqrt{C}}}{2(L+2)(L+1)}$$

$$\Longrightarrow \beta^2 = \frac{B^2}{4C} = \left( \frac{A}{2(L+2)(L+1)} \left( (2L+3) \pm \sqrt{1 - 16(L+2)(L+1)^2 \frac{\sqrt{C}}{A^2}} \right) \right)^2 . \tag{39}$$

We have two expressions for the energies, corresponding to the two possible solutions of $\beta$:

$$E^+_{1,l} = \sqrt{-\frac{\hbar^2 b}{12\mu}\alpha_I^3} \left( 2L + 5 + \frac{4}{L+2} \right) - b\alpha_I - 2c\alpha_I^2$$
$$- \frac{2\hbar^2 \left(a - b - 2c\alpha_I\right)^2}{\mu(L+1)^2} \left( 1 - \frac{(2L+3)}{2(L+2)^2} \left( 1 + \sqrt{1 - 16(L+2)(L+1)^2 \frac{\sqrt{-\frac{\hbar^2}{12\mu} b\alpha_I^3}}{(a-b-2c\alpha_I)^2}} \right) \right), \tag{40}$$

$$E^-_{1,l} = \sqrt{-\frac{\hbar^2 b}{12\mu}\alpha_I^3} \left( 2L + 5 + \frac{4}{L+2} \right) - b\alpha_I - 2c\alpha_I^2$$
$$- \frac{2\hbar^2 \left(a - b - 2c\alpha_I\right)^2}{\mu(L+1)^2} \left( 1 - \frac{(2L+3)}{2(L+2)^2} \left( 1 - \sqrt{1 - 16(L+2)(L+1)^2 \frac{\sqrt{-\frac{\hbar^2}{12\mu} b\alpha_I^3}}{(a-b-2c\alpha_I)^2}} \right) \right). \tag{41}$$

It is evident, from the general form eq.(35), that both expressions yield the result obtained in the previous section when $n_r = 1$ in eq.(28), which is similar to the one found by [20], with some corrections in the Coulomb parts of the relations. It is indeed the case that, upon substituting the value of the parameters $\alpha_0 = 0$ and $\alpha_1 = 0$ in the potential from eq. (3), we obtain the standard energies of the harmonic oscillator, and they represent the first contributions observed in both eq.(27) and eq.(28).

We can use the Coulomb limit of these energies to test the validity of the two expressions.

$$\alpha_I \to \infty \implies E^+_{1,l} \to -\frac{2\hbar^2 a^2}{\mu(L+1)^2}, \tag{42}$$

$$\alpha_I \to \infty \implies E^-_{1,l} \to -\frac{2\hbar^2 a^2}{\mu(L+2)^2}. \tag{43}$$

As we can see from eq.(42), that $E^+_{1,l}$ yields a result analogous to that obtained from eq.(37) which is the Coulomb energy of the $n_r = 0$ level. However, it should be noted that this is not the level under consideration in this particular context. Conversely, eq.(43) shows that the limit of $E^-_{1,l}$ corresponds to the Coulomb energy of the $n_r = 1$ level which is the case considered here. This is congruent with the finding of the precedent section, where the energies (28) were employed. Consequently, we conclude that $E^-_{1,l}$ represents the appropriate generalisation of the result previously found in [20].

For $n_r = 2$, we have the condition $a_3 = 0$, which gives us the following algebraic equation for $\beta$:

$$(L+1)(L+2)(L+3)\beta^3 - \left(3L^2 + 12L + 11\right)\frac{A}{\sqrt{2}}\beta^2 - \left[(L+1)(4L+9)\frac{C}{\sqrt{2}} - (L+2)\frac{3A^2}{2}\right]\beta - \frac{A^3}{2\sqrt{2}} = 0. \tag{44}$$

It has been established that the solutions of this equation are real [27–29]. The same procedure as for $n_r = 1$ is employed to write the energies and to check their Coulombian limits, in order to compare with the solutions written in [20].

## 5. CONCLUSION

In this study, we have provided exact analytical solutions to the radial Schrödinger equation for the Killingbeck potential using both the general series expansion method and the biconfluent Heun formalism. The Killingbeck potential, a composite of harmonic, linear, and Coulomb terms, emerges naturally as a limiting case of screened Coulomb potentials, particularly under weak screening conditions relevant for quarkonium and plasma-embedded systems. Through systematic expansion and appropriate transformations, we derived the explicit expressions of both energy eigenvalues and wavefunctions, thus confirming the applicability of the model across various quantum regimes.

A salient feature of the derived solutions is their capacity to interpolate seamlessly between two classical regimes of quantum mechanics. In certain limiting cases, specifically, the vanishing linear and repulsive terms, or the dominant

Coulomb coupling, the spectrum reduces, correspondingly, to that of the harmonic oscillator and the hydrogen-like systems. However, the general expressions go further, capturing a hybrid structure that reflects both screening effects and long-range confinement. This specificity renders the Killingbeck potential a valuable tool for modelling systems where purely Coulombic or harmonic oscillator models fail to capture essential physical features.

We have also revised and clarified a conceptual misinterpretation found in a recent work by Obu et al. [20], related to the treatment of linear independence in power series expansions. Furthermore, a critical re-examination of the analytical approach employed by Guvendi and Mustafa [21] was undertaken, leading to the rectification of a significant mathematical flaw in the truncation conditions for the series. These aforementioned corrections serve a dual purpose; firstly, they ensure the maintenance of the methodology's integrity, and secondly, they serve to enhance the pedagogical and physical insights into spectral problem-solving techniques.

## ORCID

**Fatma Zohra Khaled**, https://orcid.org/0009-0005-2853-2265; **Mustafa Moumni**, https://orcid.org/0000-0002-8096-6280; **Mokhtar Falek**, https://orcid.org/0000-0002-0466-9559

## REFERENCES

[1] J.P. Killingbeck, J. Phys. A: Math. Gen. **14**, 1005 (1981). https://doi.org/10.1088/0305-4470/14/5/020

[2] H. Hamzavi, and A.A. Rajabi, Ann. Phys. **334**, 316 (2013). https://doi.org/10.1016/j.aop.2013.04.007

[3] M. Chabab, A. Lahbas, and M. Oulne, Eur. Phys. J. A, **51**, 131 (2015). https://doi.org/10.1140/epja/i2015-15131-y

[4] O.J. Oluwadare, and K.J. Oyewumi, Chinese Phys. Lett. **34**, 110301 (2017). https://doi.org/10.1088/0256-307X/34/11/110301

[5] M. Hamzavi, A.A. Rajabi, and H. Hassanabadi, Few-Body Syst. **48**, 171 (2010). https://doi.org/10.1007/s00601-010-0095-7

[6] C.Y. Chen, and S.H. Dong, Phys. Lett. A, **335**, 374 (2005). https://doi.org/10.1016/j.physleta.2004.12.062

[7] N. Brambilla, et al., Rev. Mod. Phys. **77**, 1423 (2005). https://doi.org/10.1103/RevModPhys.77.1423

[8] E. Eichten, K. Gottfried, T. Kinoshita, K.D. Lane, and T.-M. Yan, Phys. Rev. D, **17**, 3090 (1978). https://doi.org/10.1103/PhysRevD.17.3090

[9] F. Cooper, A. Khare, and U. Sukhatme, Phys. Rep. **251**, 267 (1995). https://doi.org/10.1016/0370-1573(94)00080-M

[10] H. Yukawa, Proc. Phys. Math. Soc. Jpn. **17**, 48 (1935). https://doi.org/10.11429/ppmsj1919.17.0_48

[11] S. Flügge, *Practical Quantum Mechanics*, (Springer, Berlin, 1999). https://doi.org/10.1007/978-3-642-61995-3

[12] M. Sreelakshmi, and R. Akhilesh, J. Phys. G: Nucl. Part. Phys. **50**, 073001 (2023). https://doi.org/10.1088/1361-6471/acd1a3

[13] A. Kievsky, E. Garrido, M. Viviani, *et al.* Few-Body Syst. **65**, 23 (2024). https://doi.org/10.1007/s00601-024-01893-6

[14] M. Sreelakshmi, and R. Akhilesh, Int. J. Theor. Phys. **64**, 58 (2025). https://doi.org/10.1007/s10773-025-05924-8

[15] N. Mukherjee, C.N. Patra, and A.K. Roy, Phys. Rev. A, **104**, 012803 (2021). https://doi.org/10.1103/PhysRevA.104.012803

[16] Zhan-Bin Chen, Phys. Plasmas, **30**, 032103 (2023). https://doi.org/10.1063/5.0140534

[17] Tong Yan, *et al.*, Phys. Rev. Plasmas, **31**, 042110 (2024). https://doi.org/10.1063/5.0185339

[18] B. Gönül, K. Köksal, and E. Bakir, Phys. Scr. **73**, 279 (2006). https://doi.org/10.1088/0031-8949/73/3/007

[19] A. Arda, and R. Sever, Zeitschrift für Naturforschung A, **69**, 163 (2014). https://doi.org/10.5560/zna.2014-0007

[20] J.A. Obu, E.P. Inyang, E.S. William, D.E. Bassey, and E.P. Inyang, East Eur. J. Phys. (3), 146 (2023). https://doi.org/10.26565/2312-4334-2023-3-11

[21] A. Guvendi, and O. Mustafa, Eur. Phys. J. C, **84**, 866 (2024). https://doi.org/10.1140/epjc/s10052-024-13192-9

[22] O. Mustafa, and A. Guvendi, Int. J. Geom. Methods Mod. Phys. 2550091 (2024). https://doi.org/10.1142/S0219887825500914

[23] O. Mustafa, and A. Guvendi, Eur. Phys. J. C, **85**, 34 (2025). https://doi.org/10.1140/epjc/s10052-025-13779-w

[24] A. Guvendi, and O. Mustafa, Nucl. Phys. B, **1014**, 116874 (2025). https://doi.org/10.1016/j.nuclphysb.2025.116874

[25] A. Guvendi, and O. Mustafa, Ann. Phys. **473**, 169897 (2025). https://doi.org/10.1016/j.aop.2024.169897

[26] F.M. Fernandez, arXiv:2205.07884 https://doi.org/10.48550/arXiv.2205.07884

[27] A. Ronveaux (Ed.), *Heun's Differential Equations*, (Oxford University Press, Oxford, 1995). https://doi.org/10.1093/oso/9780198596950.001.0001

[28] M.S. Child, S-H. Dong, and X-G. Wang, J. Phys. A, **33**, 5653 (2000). https://doi.org/10.1088/0305-4470/33/32/303

[29] P. Amore, and F.M. Fernandez, Phys. Scr. **95**, 105201 (2020). https://doi.org/10.1088/1402-4896/abb252

# ПРО РОЗВ'ЯЗАННЯ ПОТЕНЦІАЛУ КІЛЛІНГБЕКА ТА УТОЧНЮЮЧІ КОМЕНТАРІ ЩОДО ПОВ'ЯЗАНОГО АНАЛІТИЧНОГО ПІДХОДУ

**Фатіма Захра Халед**[1], **Мустафа Мумні**[1,2], **Мохтар Фалек**[2,3]
[1]*LPRIM, Кафедра фізики, Університет Батна I, Батна, 05000, Алжир*
[2]*LPPNNM, Кафедра наук про речовину, Університет Біскри, Біскра, 07000, Алжир*
[3]*Технологічний факультет, Університет Хенчели, Хенчела, 40000, Алжир*

У роботі представлені аналітичні розв’язки рівняння Шредінгера для потенціалу Кіллінгбека, гібридної моделі, що поєднує гармонічні, лінійні та кулонівські члени, а також наближену модель потенціалів типу Юкави. Радіальне рівняння Шредінгера розв’язується методом розкладання в ряд, що дає точні вирази як для розв’язків у зв’язаних станах, так і для власних функцій для таких систем, як кварконій та обмежені воднеподібні атоми в плазмових середовищах. Крім того, ми пропонуємо конструктивний коментар до роботи Обу та ін. (East Eur. J. Phys. 3, 146–157, 2023) з метою уточнення математичної помилки, використаної в їх аналітичному обробці аналогічних систем.

**Ключові слова:** *рівняння Шредінгера; потенціал Кіллінгбека; потенціал Юкави; метод розкладання в ряд; рівняння Гойна*

EAST EUROPEAN JOURNAL OF PHYSICS. **4.** 172-182 (2025)
DOI:10.26565/2312-4334-2025-4-15 ISSN 2312-4334

# ON SYNCHRONIZATION OF AN ENSEMBLE OF OSCILLATORS UNDER SUPERRADIANCE CONDITIONS

**V.M. Kuklin**[1]*, **E.V. Poklonskiy**[2]
[1]*Simon Kuznets Kharkiv National University of Economics. Department of Cybersecurity and Information Technologies, Nauky Ave., 2. 9A. 61165, Kharkiv, Ukraine*
[2]*V.N. Karazin Kharkiv National University, 4 Svobody Square, Kharkiv, 61022, Ukraine*
**Corresponding Author e-mail: volodymyr.kuklin@hneu.net*

Received August 29, 2025; revised September 30, 2025; accepted November 6, 2025

The problems of phase synchronization in an ensemble of oscillators or dipoles, and the mechanisms of coherent field generation in superradiance mode, are discussed. It is shown that an increase in the spread of the initial amplitudes of an ensemble of oscillators suppresses their phase synchronization and reduces the efficiency of field generation. The influence of noise is discussed; it is shown that, below the generation threshold, even an external initiating field cannot synchronize the phases of an ensemble of particles. When the generation threshold is exceeded, the initiating field may not be required. It is shown that the convergence of the oscillator phases with the field phases at the locations of moving oscillators is noticeable only near their exit from the system. At the same time, a complete coincidence of the phases of synchronized oscillators and the field phases in the region of their localization is not observed. Nevertheless, the intensity of the generation field in the superradiance mode is significantly above the spontaneous level, allowing us to speak of induced radiation. The features of the development of the quantum process of superradiance of an ensemble of dipoles are discussed, and a system of equations for its description is given. The features of the quantum analog of superradiance are qualitatively modeled, and the role of the Rabi frequency determining the dynamics of the population inversion is noted. The nutation of the population inversion in the region occupied by the field affects the field intensity not only in this local zone, but also in the subsequent areas of the active zone. This explains the unusual nature of the generation development: the field growth in a particular region of the active zone first stabilizes and then decreases significantly. This decrease in intensity also occurs along the direction of radiation in the peripheral areas of the active zone, despite the large energy reserve there in the form of an unperturbed population inversion.

**Keywords:** *Classical and quantum emitters; Superradiance regime; Phase synchronization conditions in the classical model; Influence of population inversion nutation on field generation*
**PACS**: 03.65.Sq;05.45.Xt; 41.60.–m

## INTRODUCTION

The phenomenon of superradiance, discovered in the well-known work of Dicke [1], was caused by the overlap of the wave functions of many particles collected in a small volume. In this case, the radiation acquired the features of induced radiation, its coherence increased significantly. A similar phenomenon could be observed in the case of phased classical oscillators or emitters collected in a small region, the dimensions of which are significantly smaller than the wavelength of the radiation. Later, works appeared in which the phenomenon of superradiance was discovered for excited quantum emitters distributed in space. An ensemble of such excited emitters in the field of initiating, comparatively weak external radiation also demonstrated effective field generation in the superradiance mode. Initially, this process was associated with spontaneous emission, in which the synchronization of emitters occurred either forcedly or spontaneously, but later it was realized that superradiance is a form of induced emission emission [2].

Interest in superradiance was also associated with the peculiarities of electromagnetic field generation in open resonators and waveguides, the openness of which in the longitudinal direction was due to the energy release and the exit of particles of the active medium, which gave up part of their energy [3]. Previously, it was believed that the proper field of particles (generators and emitters) in the active zone was very small, practically at the level of spontaneous, and all methods for calculating electronic devices were based on the paradigm of the interaction of each of the active particles of the ensemble only with the field of the waveguide or resonator, and the interaction of active particles with each other was neglected. The closed volume of electronic devices also repeatedly amplified their resonant and waveguide fields, which also provided grounds for neglecting the total field of particles interacting with each other in the active zone. The nonlinear theory of such interaction of active particles only with the field of the resonator or waveguide under conditions of neglecting their interaction with each other was first presented in [4], and this approach to describing the amplification and generation modes became traditional. At the same time, works appeared on the description of superradiance, although initially for ensembles of quantum emitters. The study of the behavior of the total summary particle field - the superradiance field both outside and inside open resonators and waveguides in the classical representation showed that in the absence of noise, the same amplitude and random distribution of phases in the ensemble of oscillators, the development of the generation process is similar to the traditional description of the excitation of the resonator and waveguide fields in similar open systems with the same ensemble of emitters, that is, the increments and maximum achievable field amplitudes in these two cases, considered independently, are similar [5].

***Cite as:*** V.M. Kuklin, E.V. Poklonskiy, East Eur. J. Phys. 4, 172 (2025), https://doi.org/10.26565/2312-4334-2025-4-15

Note that in completely open systems (there is no reflection from the ends), only the sum of fields interacting with each other active particles, in fact the superradiance field, can exist if the conditions for its generation are met [6, 7], which will be discussed below [8]. It is obvious that each active particle is capable of emitting only waves for which the medium is transparent, i.e. the eigenwaves of resonators and waveguides formed by the boundary conditions on their lateral surface. However, the field of the resonator or waveguide does not occur in the absence of reflection from its ends. Only the reflection of the field from the ends can form reflected waves, the superposition of which will be the field of the resonator or waveguide. However, if the sum of the field of interacting particles (which always exists) - is large enough, then even its weak reflection from the ends can create reflected waves, the superposition of which will form the field of the resonator or waveguide. This process is discussed in detail in [9,18].

Therefore, the *goal of this study* is to attempt to answer the question of the magnitude of this total field of an ensemble of interacting particles. Outside resonators and waveguides, as well as in similar open systems without reflections from the ends (or with very weak reflections), this field is clearly a superradiance field. Therefore, studying the excitation and synchronization of radiation from an ensemble of active interacting particles, both in free space and in open systems, is of considerable interest, as it may provide an answer to this question.

## FIELD GENERATION BY AN ENSEMBLE OF EXCITED OSCILLATORS

Let us consider the processes of electromagnetic wave generation by a system of oscillators in a one-dimensional case [10]. Let the wave frequency and the oscillator frequency coincide and be equal to $\omega$. The wave vector of oscillations is $\vec{k}=(0,0,k)$, the field components are $\vec{E}=(E,0,0)$, $\vec{B}=(0,E,0)$, and $E=|E|\cdot\exp\{-i\omega t+ikz+i\varphi\}$. The $N$ oscillators are located along the axis $OZ$ in the amount of at the wavelength $2\pi/k$. The mass of the oscillator is equal to $m$, the charge is equal to $-e$, the oscillator frequency coincides with the wave frequency $\omega$. The initial amplitude of the oscillator oscillations is equal to $a$. We will assume that the oscillator moves only in the direction of the axis $OX$. In this case, the influence of the magnetic field of the wave on the oscillator dynamics can be neglected.

The equations describing the excitation of the field by the oscillator current in such a one-dimensional representation $j_x=-ea\omega\cdot\cos(\omega t-\psi)\cdot\delta(z-z_0)$, the coordinates of which can be written as $\vec{r}=(a\cdot\sin(\omega t-\psi),0,z_0)$.

$$\frac{\partial^2 E_x}{\partial z^2}-\frac{1}{c^2}\frac{\partial^2 D_x}{\partial t^2}=\frac{4\pi}{c^2}\frac{\partial J_x}{\partial t}=\frac{4\pi}{c^2}\cdot e\cdot a\cdot\omega_0{}^2\cdot i\cdot\exp\{-i\omega t+i\psi\}\cdot\delta(z-z_0), \tag{1}$$

We will seek a solution for the amplitude of the electric field of the wave in the form $E_x=E\cdot\exp(-i\omega t+ikz)$. For a slowly changing in space amplitude of the radiation field $E$ , the equation is valid

$$\frac{\partial E}{\partial z}=2ea\omega^2\frac{\pi}{c^2k}\cdot\exp\{i\psi+ikz\}\cdot\delta(z-z_0)=\lambda\cdot\delta(z-z_0) \tag{2}$$

the solution of which is

$$E=C+\lambda\cdot\theta(z-z_0), \tag{3}$$

where $\theta(\mathrm{z}<0)=0,\ \ \theta(\mathrm{z}\geq 0)=1$, $C$ – is a constant that should be determined. Since the equation $D(\omega,k)\equiv(\omega^2\varepsilon_0-k^2)=0$, $\varepsilon_0=1$, whose roots are $k_{1,2}=\pm(\omega\mathrm{Re}\,\varepsilon_0/c)(1+i\,\mathrm{Im}\,\varepsilon_0/\mathrm{Re}\,\varepsilon_0)\approx\pm(\omega/c\varepsilon_0)(1+i0)$, are valid for the wave emitted by the oscillator , then for a wave propagating in the direction $z>z_0$ the wave number $k=k_1>0$ and the value of the constant *C* should be chosen equal to zero in order to avoid unlimited growth of the field at infinity. For a wave propagating in the direction $z<z_0$, the wave number $k=k_2<0$ and the value of the constant *C* should be chosen equal to $-\lambda$ for the same reasons. The amplitude of the electric field in this case

$$E_x=2\pi ea\omega_0 M\cdot c^{-1}\exp\{-i\omega t+i\psi\}[\exp\{ik_0(z-z_0)\cdot U(z-z_0)+e\,\mathrm{xp}\{-ik(z-z_0)\cdot U(z-z_0)\}, \tag{4}$$

where $U(\mathrm{z}<0)=0,\ \ U(\mathrm{z}\geq 0)=1$, while $M=n_0 b$, $n_0$ is the density of particles per unit volume, *b* is the length of the space under consideration in the longitudinal direction. For one particle in such a volume of unit cross-section and length *b*, M is numerically equal to unity. In the region $z_j\in 0\div b$ occupied by the ensemble of oscillators, the equations of motion for an individual oscillator take the form

$$\frac{dx_i}{dt}=v_i\,,\ \ \frac{d}{dt}\frac{v_i}{\sqrt{1-\frac{|v_i|^2}{c^2}}}+\omega_0{}^2x_i=-\frac{e}{m}E_x(z_i,t)\,, \tag{5}$$

where $x_i(t)=i\cdot a_i\cdot\exp\{-i\omega t+i\psi\}=iA\cdot\exp\{-i\omega t\},\ \ \ v_{i\perp}=\omega\cdot a_i\cdot\exp\{-i\omega t+i\psi\}=\omega A\cdot\exp\{-i\omega t\}$.
Then the equation of motion describing the change in the amplitudes of the ensemble of oscillators takes the form.

$$\frac{d\,\mathrm{A}_j}{d\tau} = \frac{i\alpha}{2}\cdot\left|\mathrm{A}_j\right|^2 \mathrm{A}_j - \mathrm{E}(Z_j,\tau)\,. \qquad 6)$$

Here, the term proportional to $\alpha$ take into account the weak relativism of the oscillator. By the way, in the theory of cyclotron generators, such nonlinearity, proportional to $\alpha$, is a consequence of the so-called negative mass effect. Taking such nonlinearity into account may be significant, since in [11] it is noted that in a system of linear oscillators the generation efficiency is insignificant. To maintain the field in the volume occupied by the ensemble of oscillators, we will inject them with a random phase from the left edge of the system $z = 0$ and remove them upon reaching the right edge of the system $z = b$, the longitudinal velocity will be considered constant $v_z = Const$.

For the superradiance field of the ensemble of particles, we can write the expression:

$$\mathrm{E}_{sr}(Z,\tau) = \frac{1}{\Theta N}\sum_{s=1}^{N}\mathrm{A}_s\cdot e^{i2\pi|Z-Z_s|}\,. \qquad (7)$$

We can add a second term to (7) $\mathrm{E}_{ex}(Z,\tau) = \mathrm{E}_{0+}\,e^{i2\pi Z} + \mathrm{E}_{0-}\,e^{-i2\pi Z}$ - this is the external initiating field, often necessary to accelerate the process. Dimensionless variables and parameters were used above

$$\mathrm{A} = A/a_0,\quad kz = 2\pi Z,\quad V = kv_z/2\pi\gamma,\quad \gamma_0^2 = \omega_{pe}^2/4 = \frac{\pi n e^2}{m},\quad \gamma = \gamma_0^2/\delta,\quad \gamma t = \tau,\quad kb = 2\pi\bar{b},$$

$$\delta = \frac{c}{b},\quad \Theta = \delta/\gamma_0,\quad E_{01} = \frac{2m\cdot\gamma_0\cdot\omega\cdot a_0}{e},\quad \mathrm{E} = E/E_{01},\quad \alpha = \frac{3\omega}{4\gamma_0}(ka_0)^2.$$

Expression (7) is a slowly changing envelope of the HF oscillations of the field. Due to the short system and the effective removal of energy from it, the accumulation of the field in the volume of the active zone does not occur, as in the case of radiation of a short electron bunch moving in the plasma, considered in [12].

## PHASE SYNCHRONIZATION OF AN ENSEMBLE OF CLASSICAL OSCILLATORS

Let us discuss the possibility of synchronizing oscillators in the superradiance mode. The question arises whether phase synchronization is possible in a system of oscillators, which can ensure the transition to the appearance of sufficiently intense induced radiation? Let us return to equation (6), which can be written differently

$$\frac{d[|\mathrm{A}_j|\exp(i\psi_j)]}{dt} = \frac{i\alpha}{2}\cdot\left|\mathrm{A}_j\right|^2|\mathrm{A}_j|\cdot\exp(i\psi_j) - |\mathrm{E}(Z_j,\tau)|\cdot\exp(i\varphi)\,. \qquad (8)$$

Then the equation for the oscillator phase, which follows from (10), takes the form

$$\frac{d\psi_j}{dt} - \frac{\alpha}{2}\cdot\left|\mathrm{A}_j\right|^2 = -\{|\mathrm{E}(Z_j,\tau)|/|\mathrm{A}_j|\}\cdot\sin(\varphi-\psi_j)\,. \qquad (9)$$

The right-hand side of the last equation is large enough $|\mathrm{E}(Z_j,\tau)/\mathrm{A}_j| >> 1$.. This is what can force the phase of an individual oscillator to synchronize with the phase of the total field of the ensemble $\psi_j(Z_j) \to \varphi(Z_j)$ at the point, where the oscillator is located [13].

For the number of oscillators N=2500, the amplitudes of which are equal to unity, and the phases are randomly distributed, the average integral field $|\mathrm{E}|$ (7) (which can be considered spontaneous in the classical case [2]) is approximately $1/\sqrt{N}$ times smaller than the maximum possible field value in the case when all the phases of the oscillators are close to the phase of the total field at the point where the oscillator is located. That is, for the fields of spontaneous and absolutely coherent induced radiation, the relation is satisfied $(1/N)^{1/2} : 1$. For the squares of the amplitudes $|\mathrm{E}|^2$, this relation takes the form $1/N$. It is not difficult to estimate the last relation; it is enough to take the square of the modulus of the right and left parts of expression (7) at an average over fast oscillations. In Fig. 1, the maximum field amplitude is 0.22, which is an order of magnitude greater than the average amplitude of the spontaneous field and five times smaller than the maximum possible field value in the case when all oscillators are synchronized in phase.

***The influence of the dispersion of the initial amplitudes of the oscillators on the efficiency of their phase synchronization.*** It turns out that the spread of the oscillator amplitudes significantly affects the synchronization process. The squares of the initial amplitudes were randomly distributed so that the average value of the amplitudes at the initial moment was equal to one. The calculations of system (6)–(7) were carried out with the following parameters

$N = 900$, $\alpha = 1$, $A_0 = 1$, $\Delta A^2 = 1; 0.4; 0.65; 0.75; 0.8; 1$. The spread of the oscillator amplitudes with a random distribution of their phases at the initial moment is shown in Fig. 3

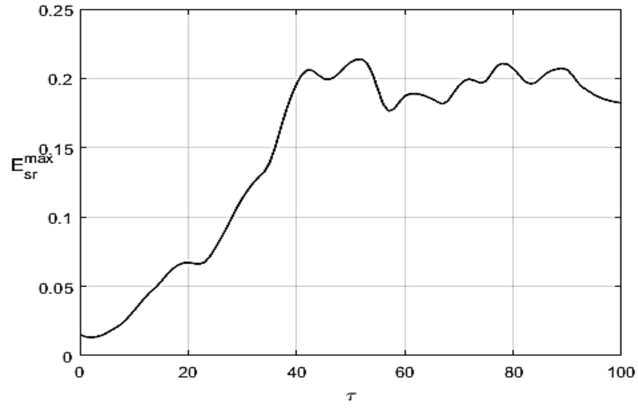

**Figure 1**. Time dependence of the maximum amplitude modulus of the oscillator field for the particle velocity $V = 0.15$ and number of particles N=2500 for $\alpha = 1$ and $\theta = 1$ in the absence of reflection from both ends of the resonator

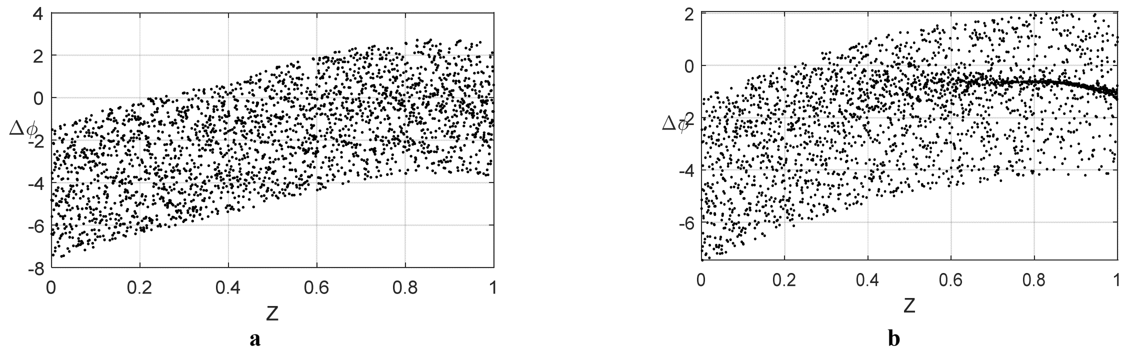

**Figure 2**. Distribution of the phase difference of the oscillators with the phases of the total field of the ensemble at the points where the oscillators were located $\psi_j(Z_j) - \varphi(Z_j)$. a) $\tau = 20$, b) $\tau = 40$ for the velocity $V = 0.15$, the number of particles N=2500, at $\alpha = 1$ and $\theta = 1$ in the absence of reflection from both ends of the resonator

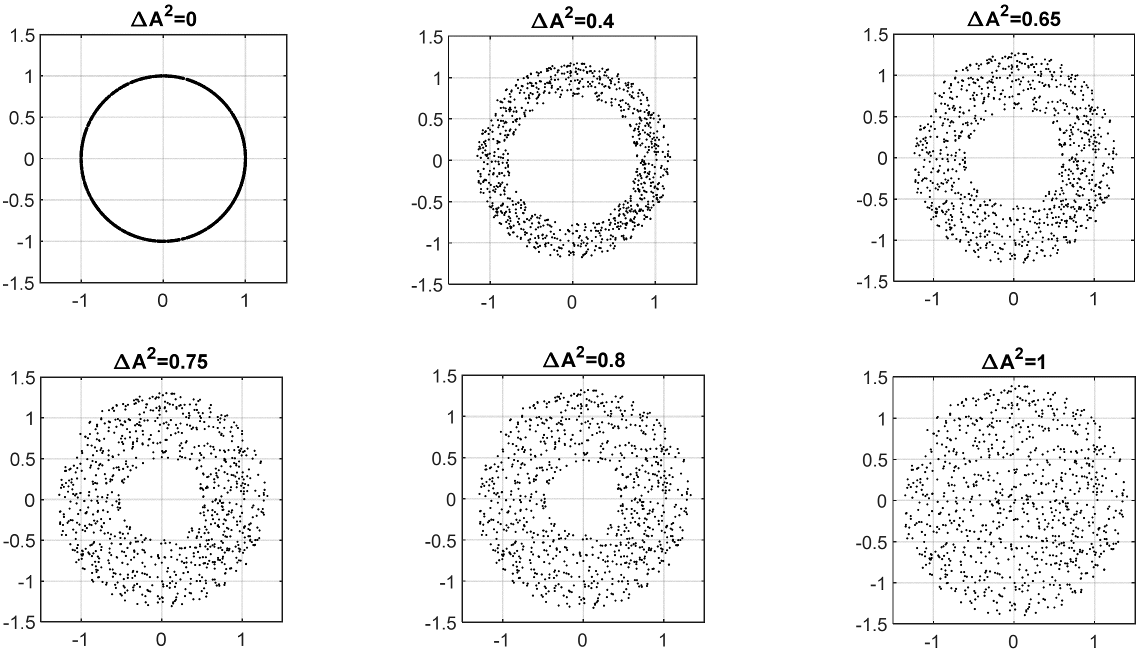

**Figure 3**. Phase planes “amplitude-phase” for different cases of the initial distribution of oscillators

For these cases, we can present the nature of the change in the energy of the oscillator system and the behavior of the field amplitude (see Fig. 4). The influence of the initial oscillator amplitude spread on synchronization efficiency, as noted by V. A. Buts, is related to the oscillator relativism. That is, the initial amplitude spread is equivalent to the frequency spread of the oscillator ensemble. Let us recall that the spontaneous emission level $|E_{sp}|^2 \propto (1/N) \approx 10^{-3}$.

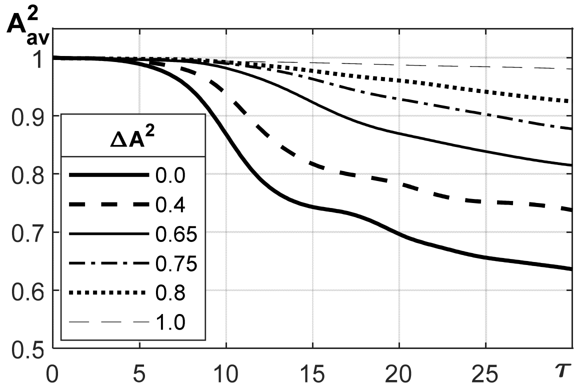

**Figure 4a**. Changes in the energy of the oscillator system $N = 900$, $\alpha = 1$ for different levels of spread of initial amplitudes, $\mathrm{A}_0 = 1$, $\Delta\mathrm{A}^2 = 1; 0.4; 0.65; 0.75; 0.8; 1$.

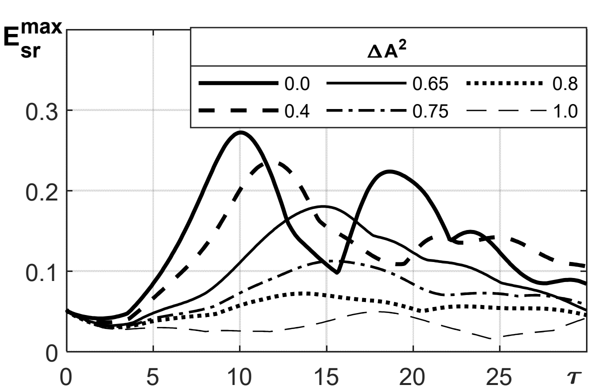

**Figure 4b**. Behavior of the field amplitude for different levels of scatter of initial amplitudes. For each moment of time, the maximum intensity $|E|^2 \propto |E_{\max}|^2$ is selected.

It is evident from Fig. 3 and Fig. 4 that for efficient generation, in particular in the superradiance mode, it is necessary to achieve an insignificant spread of the amplitudes (or energy) of the oscillators. Note that the value $\frac{i\alpha}{2}\cdot|\mathrm{A}_j|^2$, which characterizes the nonlinearity of the oscillator, thereby ensures regularization, that is, some spread of the phase values. With a large spread of the initial amplitudes of the oscillators, it is necessary to use a starting initiating field to accelerate the development of the superradiance process. In this case, the amplitude of such a field should significantly exceed the amplitude of spontaneous emission of an individual oscillator. However, the use of an initiating field not only to accelerate the process, but also to generate coherent superradiance may have another reason, which will be discussed below.

***Conditions for the development of generation in the superradiance mode in the presence of noise*** [8]. The equation describing the change in the complex amplitude of an individual oscillator in the presence of noise takes the form

$$\frac{d\,\mathrm{A}_j}{d\tau}=\frac{i\alpha}{2}\cdot\left|\mathrm{A}_j\right|^2\mathrm{A}_j-\mathrm{E}(Z_j,\tau)+i\cdot\delta\cdot r_j(\tau)\cdot\mathrm{A}_j, \tag{10}$$

where the last term in the right-hand side of (10) is additionally introduced, which takes into account the influence of external noise. Here $r_j(\tau)$ – takes random values from –1 to +1, changing through time intervals $\Delta\tau$ on the selected time scale, $\delta$ – is the maximum value of this effect. Expression (7) is valid for the field. Random effect, switched through intervals $\Delta\tau = 0.4$, leads to weakening of synchronization or even complete phase chaos. The following parameters are used in the calculation results: number of particles $N = 900$, nonlinearity parameter $\alpha = 1$, noise switching interval $\Delta\tau = 0.4$, system length $b = 1$ (one wavelength).

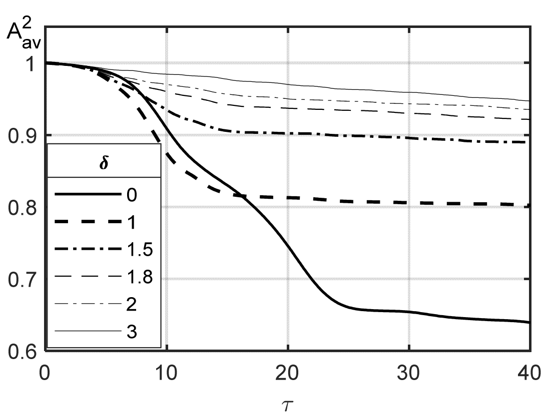

**Figure 5a**. Change in the average value of the square of the amplitude in the system $A^2_{av}=\frac{1}{N}\sum_{s=1}^{N}|\mathrm{A}_s|^2$ over time in the presence of additive noise $\delta$

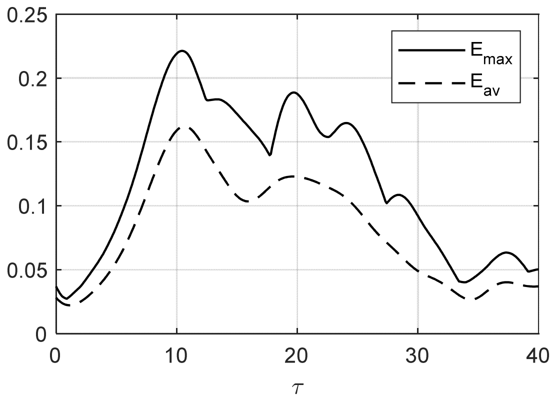

**Figure 5b**. Time dependence of the field amplitude in the system in the absence of noise ($\delta = 0$). Note that for each moment of time the maximum intensity $|E|^2 \propto |E_{\max}|^2$ is selected

Fig. 5a shows the change in the average value of the squared amplitude $A_{av}^2 = \frac{1}{N}\sum_{s=1}^{N}|\mathrm{A}_s|^2$ in the system over time for different values of the external noise level $\delta$. Fig. 5b shows the behavior of the maximum field amplitude $\mathrm{E}_{\max} = \max\limits_{Z\in(0,1)} \mathrm{E}_{sr}(Z)$ and the average field amplitude $\mathrm{E}_{av} = \sqrt{\frac{1}{b}\int_0^b |\mathrm{E}_{sr}|^2\, dZ}$ in the volume in the oscillator system in the absence of noise.

Even from these figures, one can see the existence of a threshold: in case of $\delta = 0$, the value of the field amplitude reaches 0.22 in the selected scale. Below the threshold $\delta_{thr} \propto 1{,}5$, there is practically no field growth, and the energy extraction from the oscillators is weakened (the average energy remains at the level of 96% of the initial). In this case, a turbulent state is formed with an average field value $E_{av}$ close to the spontaneous level of electric field strength of 0.02–0.03. The peak level of fluctuations $E_{\max}$ exceeds the average level by two or more times (see Fig. 6).

Far from the threshold, the average oscillator amplitude values (at $\delta \propto 1.8$, $A_{av}^2 < 0.97$) change slightly, i.e. no noticeable energy extraction from the oscillator system is observed. However, as the threshold is approached, the peak fluctuation values increase (see Fig. 7)

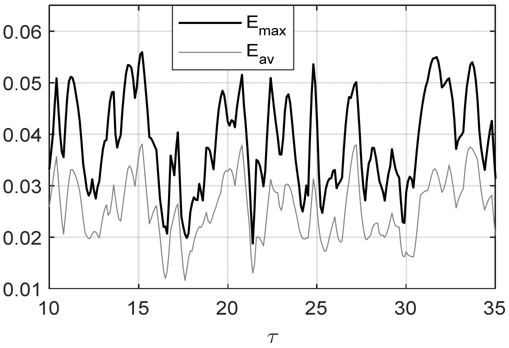

**Figure 6**. Average field values and peak fluctuation values at noise level $\delta = 3$

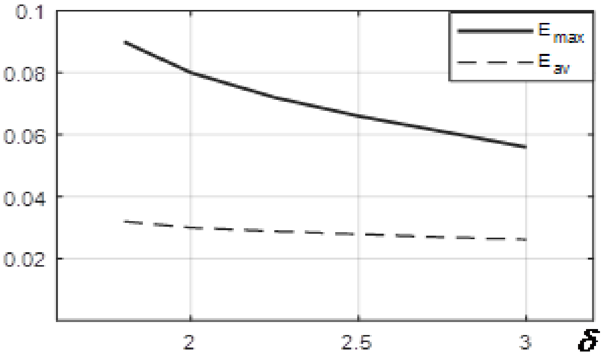

**Figure 7**. Growth of fluctuations when approaching the threshold of generation development under superradiance conditions

Considering the region near and below the threshold, we can find out how the external field affects the occurrence and development of generation under superradiance conditions. The time dependence of the maximum generation field of the oscillator system for different amplitudes of the external field is shown in Fig. 8.

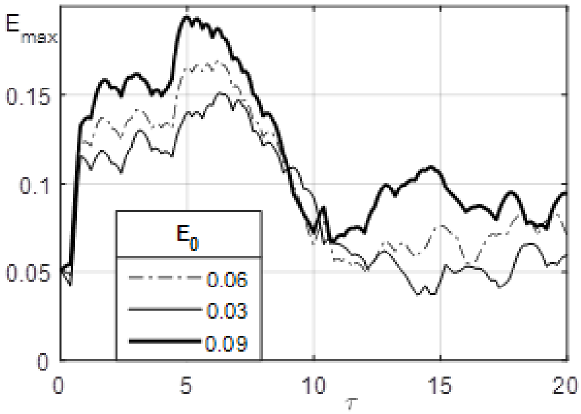

**Figure 8**. Effect of the external initiating field $E_0 = 0.03; 0.06; 0.09$ on generation under superradiance conditions $\delta = 1.8$. Note that in all cases, the maximum intensity $|E|^2 \propto |E_{\max}|^2$.is selected for each time moment

It is evident from Fig.8 that an increase in the amplitude of the external initiating field $E_0 = 0.03; 0.06; 0.09$, even in the case of noise ($\delta \approx 1{,}8$), leads to an increase in the maximum generation field up to values that are realized in the absence of noise. Thus, the noise in the system forms the generation threshold. When this threshold is exceeded, even in the absence of an external initiating field, a significant part of the excited oscillators is capable of generating fields whose maximum amplitudes are comparable with the generation amplitudes in the absence of noise. Below the presented threshold, no field growth is observed.

## ON SYNCHRONIZATION OF QUANTUM EMITTERS

To describe the generation processes of an ensemble of quantum emitters – dipoles, one can use the semiclassical theory, in particular, previously used in the works of Yu. L. Klimontovich [14] and his colleagues.

The system of one-dimensional equations of the semiclassical theory for the amplitudes of the electric field perturbations $E$, polarization $P$ ($E, P = \mathrm{E}, \mathrm{P}\cdot\exp(-i\omega t + ikx)$), $d_{ab}$ is the matrix element of the dipole moment of emitters $\delta$, $\delta\cdot c$ – the temporal and spatial decrements of the field absorption in the medium, describing the excitation of electromagnetic oscillations in a two-level active medium, can be represented in the following form:

$$\frac{\partial^2 E}{\partial t^2} + \delta c\frac{\partial E}{\partial x} - c^2\frac{\partial^2 E}{\partial x^2} = -4\pi\frac{\partial^2 P}{\partial t^2}, \tag{13}$$

$$\frac{\partial^2 P}{\partial t^2} + \omega^2\cdot P = -\frac{2\omega|d_{ab}|^2}{\hbar}\mu E, \tag{14}$$

to which we must add the equation for the slowly changing population inversion with time

$$\frac{\partial\mu}{\partial t} = \frac{2}{\hbar\omega} < E\frac{\partial P}{\partial t} >. \tag{15}$$

***A system of semiclassical equations for a quantum ensemble.*** We will assume that the frequency of the transition between levels corresponds to the field frequency, the line width in the equation for polarization and the relaxation of the inversion due to external causes are neglected, $\delta$ – is the decrement of field absorption in the medium, $d_{ab}$ – is the matrix element of the dipole moment (more precisely, its projection onto the direction of the electric field), $\mu = n\cdot(\rho_a - \rho_b)$ the difference in populations per unit volume, and $\rho_a$ and $\rho_b$ the relative populations of the levels in the absence of a field. The fields are represented as $E = [E(t)\cdot\exp\{-i\omega t\} + E^*(t)\cdot\exp\{i\omega t\}]/2$ and $P = [P(t)\cdot\exp\{-i\omega t\} + P^*(t)\cdot\exp\{i\omega t\}]/2$. In this case $< E^2 >= 2|E(t)|^2 = 4\pi\omega\hbar N.$ For slowly changing amplitudes field $E(t)$ and polarization $P(t)$, the equations are valid

$$\frac{\partial E(t)}{\partial t} + (\delta/2)\cdot E(t) = 2i\pi\omega P(t), \tag{16}$$

$$\frac{\partial P(t)}{\partial t} = |d_{ab}|^2(\mu/\hbar)\frac{E(t)}{i}, \tag{17}$$

$$\frac{\partial\mu}{\partial t} = \frac{2i}{\hbar}[E(t)P^*(t) - E^*(t)P(t)]. \tag{18}$$

From equations (16) – (18) we obtain the law of conservation of energy

$$\frac{\partial N}{\partial t} + 2\delta N + \frac{\partial\mu}{\partial t} = 0. \tag{19}$$

For sufficiently large losses of field energy in the medium $\delta > \gamma$, the equation for the field takes the form

$$\frac{\partial N}{\partial t} + (8\pi\omega\frac{|d_{ab}|^2}{\hbar\delta}\mu)N = 0, \tag{20}$$

from which it follows that for $\delta > \gamma$ the field can increase with an increment $\gamma = \gamma_0^2/\delta$, where the maximum possible increment in the absence of losses $\gamma_0 = \Omega_0 = (\frac{8\pi|d_{ab}|^2\omega\mu_{t=0}}{\hbar})^{\frac{1}{2}} = (\frac{8\pi|d_{ab}|^2\omega\mu_0}{\hbar})^{1/2}$, $N_k = 2|E|^2/4\pi\omega\hbar$ is the number of field quanta per unit volume. In this approximation, the following expressions should be used $\left(\frac{\delta}{2}\right)\cdot E = 2i\pi\omega P$, $\frac{\partial P(t)}{\partial t} = -\frac{|d_{ab}|^2}{i\hbar}\mu E,\ \gamma = \frac{\Omega_0^2}{\delta} = \Omega_0/\theta.$ which are a consequence of the above system of equations, while the equation describing nutations – oscillations of the population inversion is the following

$$\frac{\partial^2\mu}{\partial t^2} + (8\frac{|d_{ab}|^2}{\hbar^2}|E|^2)\mu = 0, \tag{21}$$

where $\Omega_N = [\frac{4|d_{ab}|^2}{\hbar^2}|E|^2]^{1/2}$ – is the Rabi frequency, which has the meaning of the inverse time of the change in inversion and the probability of an induced transition under the influence of the field [15,16]. It is at this frequency that periodic changes in the inversion – nutation occurs, and the conservation law (19) takes the form $2\delta N + \partial\mu/\partial t = 0$.

The increase in the probability of radiation of excited dipoles at each point in space in the semiclassical description occurs under the influence of a growing integral electric field. The transition to the space-time problem transforms (20) into the following equation

$$\frac{\partial N}{\partial x} + \left(8\pi\omega \frac{|d_{ab}|^2}{\hbar\delta c}\mu\right)N = 0, \tag{22}$$

At the initial moment, the field energy density is small, and this initial period corresponds to spontaneous radiation of oscillators, in the developed mode, the radiation of the ensemble of emitters acquires the features of induced radiation $N_k \propto \mu_0 = \mu(t=0)$. To model the process of spatial growth of the field in an inverse medium, we rewrite equations (21) and (22) in dimensionless form. Equation (23) describes the growth of the field in space, equation (24) - oscillations of the population inversion in a local region, taking into account the conservation law in the form (25)

$$\frac{\partial \mathrm{N}}{\partial Z} = \frac{1}{\theta}\mathrm{MN}, \tag{23}$$

$$\frac{\partial^2 \mathrm{M}}{\partial T^2} + \mathrm{MN} = 0, \tag{24}$$

$$2\delta N + \frac{\partial \mu}{\partial t} = 0. \tag{25}$$

where

$\mu/\mu_0 = \mathrm{M}$, $(8\pi\omega \frac{|d_{ab}|^2}{\hbar}\mu_0)^{1/2} t = T$, $\theta = \delta/(8\pi\omega \frac{|d_{ab}|^2}{\hbar}\mu_0)^{1/2}$, $N_k/\mu_0 = \mathrm{N}$, $\mu_0 = \mu(T=0)$,
$\left(8\pi\omega \frac{|d_{ab}|^2}{\hbar}\mu_0\right)^{1/2} x/c = Z/2.$

In the quantum case, when it is impossible to speak about the field phase, synchronization of the ensemble of oscillators-dipoles can be understood only as the transition from spontaneous emission to induced emission. Since the phase of the emitted field in a given quantum system is equal to the phase of the external field, that is, the problem of synchronization in the local sense is removed here. However, the change in the population inversion has an oscillatory character, known as population inversion nutation in an electric field [15, 16]. It is important to note that the Rabi frequency increases proportionally to the magnitude of the increasing external electric field described by equation (20), that is, the rate of change of oscillations of the inversion according to (21) accelerates.

Below, we present the results of numerical modeling of the field growth process in the active zone according to the system of equations (23)–(24). The working region of length $L$ consists of $S$ cells of length $DZ = L/S$. The coordinates of the middle of the cells are $Z_j = DZ \cdot (j - 0.5)$, $j = 1, 2, ..., S$. Each cell is characterized by inversion $\mathrm{M}_j$ and the number of quanta $\mathrm{N}_j$. At the initial moment, a constant value of inversion is specified in all cells $\mathrm{M}_j(T=0) = 1$. The number of quanta is set equal to zero in all cells except the first one $\mathrm{N}_j(T=0) = 0$, $j = 2, 3, ..., S$. Note that the inversion does not change in these cells initially. The first cell, in which a small value of the field is initially set $\mathrm{N}_1 = 0.0001$, is the source of the field's initial growth in the active zone. The active zone expands over time at a given constant speed $c$, i.e., the following cells join the active zone at intervals $DT = DZ/c$. In the model calculation below, the values $DZ = 0.1$, $DT = 0.1$, $c = 1$ were used.

Since the system is open (θ is not small here and is equal to 1), there will be losses of electromagnetic energy from the active zone due to radiation. The field growth occurs due to a decrease in the population inversion. It is the population inversion that generates the field. On the other hand, the inversion, as the field intensity increases, goes into oscillation mode (which is the nutation of the population inversion), and the frequency of these oscillations (the Rabi frequency) increases with increasing field amplitude.

The field growth at the boundary of the active zone (the active zone here is defined by the presence of non-zero values of the population inversion) at a small nutation amplitude acquires an exponential character. However, as the generation front moves, the population inversion value decreases in all regions participating in the generation, both due to the nutation of the population inversion and due to the excitation of field quanta. The field amplitude, in turn, decreases with a decrease in inversion along the entire length of the active generation zone, as well as due to radiation losses (θ =1).

These phenomena lead to stabilization and even to a decrease in the field intensity in the generation region. It is interesting that stabilization and then a decrease in the field intensity first occurs in the region where its maximum was reached and then begins to decrease in the direction of field propagation (see Fig. 9). Although in this direction the population inversion values still remain large. The nature of this stabilization of the field growth is associated not so much with energy losses due to radiation, but to a much greater extent with a decrease in population inversion in the regions located before the point where the maximum radiation was reached, which is illustrated in Fig. 10.

Returning to equation (20), we can understand that the field growth is limited not only by energy losses due to radiation, but also by a decrease in the inversion in the generation region as a whole. Therefore, the development of the superradiance process in the ensemble of quantum dipole emitters passes from a monotonic growth of the field to stabilization and decrease, despite the presence of regions with large values of population inversion ahead.

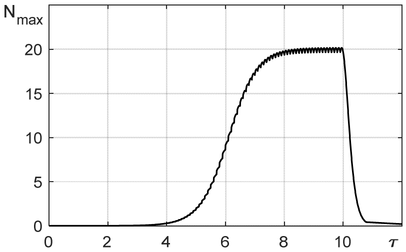

**Figure 9**. Dependence on time of the maximum value of N cells ($N_{max}$=max($N_j$))

Below Fig. 10 is shown diagrams of distribution $N_j$ and $M_j$ by cells and at different moments in time.

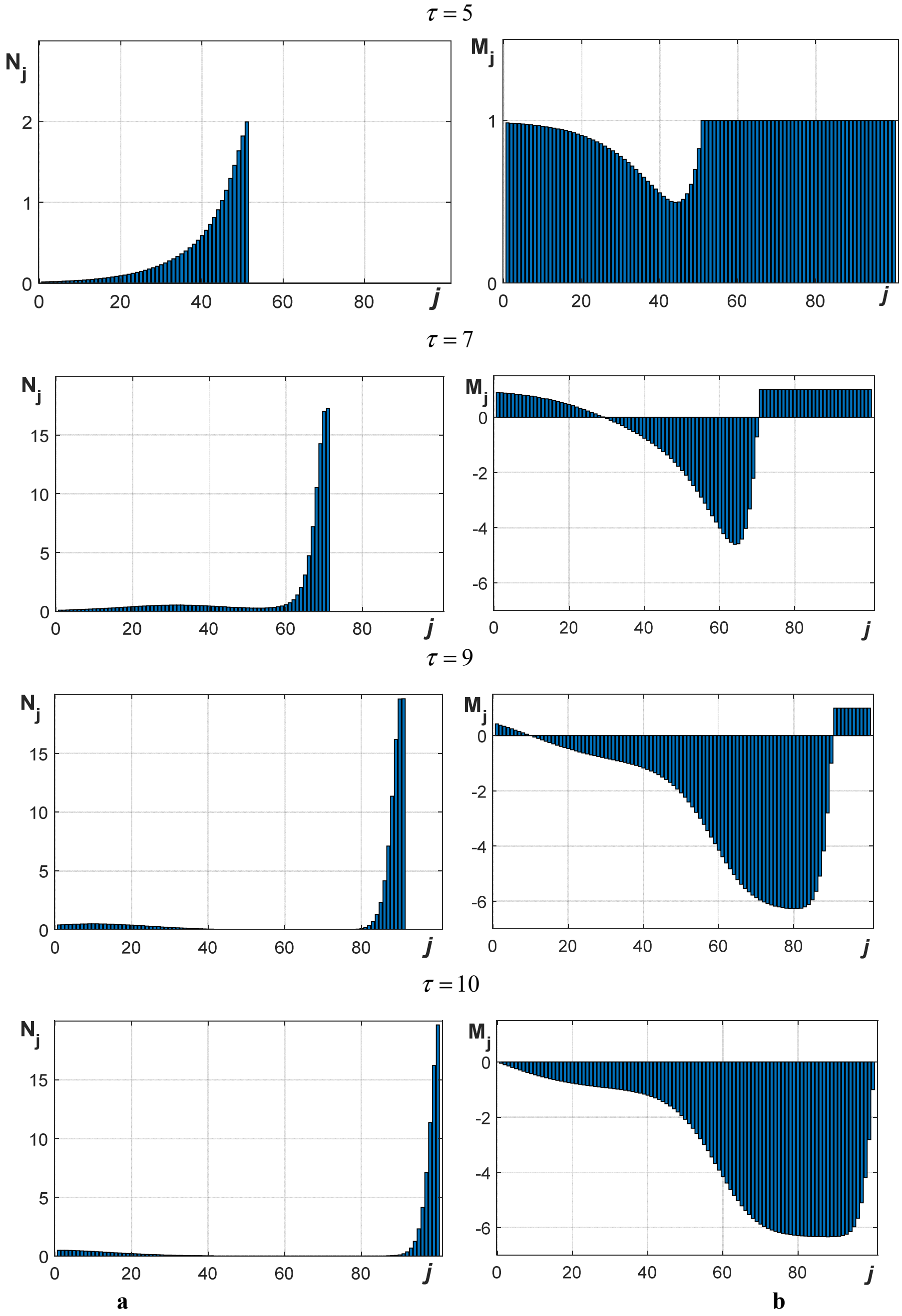

**Figure 10**. Values of $N_j$ and $M_j$ in cells at times 5, 7, 9, 10, 11; a) $N_j$ ; b) $M_j$

$\tau = 11$

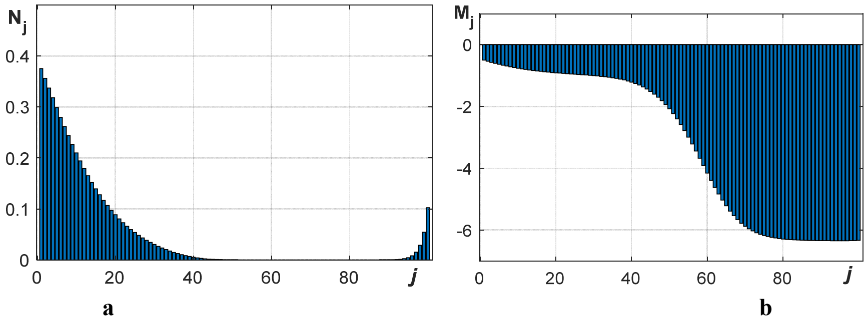

**Figure 10**. Values of $\mathrm{N}_j$ and $\mathrm{M}_j$ in cells at times 5, 7, 9, 10, 11; a) $\mathrm{N}_j$ ; b) $\mathrm{M}_j$ (*continued*)

## CONCLUSIONS

As noted above, the volume of a resonator or waveguide always contains the sum of the fields of interacting oscillators, which corresponds to a superradiance field. It is this type of radiation from an ensemble of active emitter-oscillators, whether in the absence of a resonator or waveguide or in open systems of this type, that is discussed in this article. The role of this type of radiation is quite important, although it has often been overlooked, considered unimportant and spontaneous. Primary attention has been paid to the radiation of resonators and waveguides arising from field reflection from the ends of the system. The interaction of active zone particles with each other was ignored; it was assumed that the particles interact only with the fields of the resonator or waveguide. However, this superradiance, i.e., the sum of the fields of interacting oscillators, even with partial reflection from the ends of the system, is capable of generating reflected waves, the superposition of which always forms a resonant or waveguide field, as demonstrated in [9, 18].

It has been shown that, when the above-mentioned phase-locking conditions are met, the superradiance amplitude can be significant, effectively stimulating the formation of a resonant or waveguide field. With significant reflection from the system ends, the amplitudes of the resonant or waveguide field can significantly exceed the sum of the fields of the interacting oscillators, i.e., the actual superradiance field.

In the classical case, the transition to an induced (and, as noted by K. Townes, largely coherent [17]) radiation regime occurs due to the phase synchronization of some of the oscillator emitters by the integral field. However, the nature of the initial oscillator energy distribution can significantly alter the efficiency of phase synchronization and the rate of growth of the superradiance field. It is also important to consider the presence of a threshold due to noise present in the system. As noted, with a small spread of the initial oscillator amplitudes and under conditions of insignificant external noise, the process of oscillator synchronization and the growth of the superradiance field can develop even in the absence of an external initiating field. If these conditions are violated, an external initiating field is necessary for the formation of the superradiance mode. It is important to note that it is precisely the small spread of the initial oscillator amplitudes and insignificant external noise that make it possible to realize the superradiance mode of gyrotrons, the occurrence of which was noted by the authors of [6] and subsequently studied in detail [18]. It was shown that near the injection region of random-phase oscillators in the superradiance mode, their phase synchronization does not occur. The convergence of the oscillator phases with the field phases at the localization sites of moving oscillators is noticeable only near their exit from the system. Moreover, apparently due to the relativism (nonlinearity) of the oscillator dynamics, a complete coincidence of the phases of synchronized oscillators with the phases of the field in the region of their localization does not occur (i.e., forced regularization of the synchronization process occurs). Nevertheless, the intensity of the generation field in the superradiance mode significantly exceeds the spontaneous level, which indicates the presence of stimulated emission.

In the quantum case of the superradiance regime, phase synchronization of the dipole and the external field occurs locally in accordance with the principles of quantum description [15, 16]. Therefore, the main attention is paid to the nature of the field excitation by the population inversion in the active zone, where the initial values of this inversion are positive and sufficiently large. Since the field acts on the inverted population, causing it to oscillate at the Rabi frequency, this additionally affects the nature of the quantum radiation in this region. Nutations, or the oscillatory behavior of the inverted population in the region occupied by the field, change its intensity not only in this local zone, but also in subsequent regions of the active zone. This explains the unusual nature of the development of the superradiance regime: the growth of the field in a certain region of the active zone first stabilizes and then decreases significantly. Moreover, this decrease in intensity also occurs in the direction of radiation to nearby peripheral regions, despite the large, virtually unused energy reserve in them in the form of an unperturbed population inversion.

### Acknowledgements

In conclusion, the authors express their sincere gratitude to prof. V. O. Buts for valuable comments and attention to the work.

### ORCID

**Volodymyr Kuklin**, https://orcid.org/0000-0002-0310-1582; **Eugen Poklonskiy**, https://orcid.org/0000-0001-5682-6694

## REFERENCES

[1] R.H. Dicke, “Coherence in Spontaneous Radiation Processes,” Phys Rev, **93**(1), 99–110 (1954).
[2] V.L. Ginzburg, “Several remarks on the radiation of charges and multipoles moving uniformly in a medium,” Physics–Uspekhi **45**(3), 341–344 (2002). https://doi.org/10.1070/pu2002v045n03abeh001153
[3] V.A. Flyagin, A.V. Gaponov, M.I. Petelin, and V.K. Yulpatov, “The Gyrotron,” IEEE Transactions on microwave theory and techniques,” MTT, **25**(6), 514–521 (1977).
[4] A. Nordsieck, “Theory of large signal behavior of travelingwave amplifiers.” Proc. IRE, **41**(5), 630–631 (1953). https://doi.org/10.1109/jrproc.1953.274404
[5] V.M. Kuklin, and E.V. Poklonskiy, “Dissipative instabilities and superradiation regimes (classic models),” Problem of Atomic science and Technology, **134**(4), 138–143 (2021). https://vant.kipt.kharkov.ua/ARTICLE/VANT_2021_4/article_2021_4_138.pdf
[6] A.G. Zagorodniy, P.I. Fomin, and A.P. Fomina, “Superradiation of electrons in a magnetic field and a nonrelativistic gyrotron,” NAS of Ukraine, (4), 75– 80 (2004).
[7] P.I. Fomin, and A.P. Fomina, “Dicke Superradiance on Landau Levels,” Problems of Atomic Science and Technology, (6), 45-48 (2001).
[8] E.V. Poklonskiy *et al.* “On the development of super–radiation in noise condition,” Problems of Atomic Science and Technology, (3), 84–86 (2024). https://vant.kipt.kharkov.ua/ARTICLE/VANT_2024_3/article_2024_3_84.pdf
[9] E.V. Poklonskiy, *et al.* “Modeling of superradiance modes and resonator field formation,” Problem of Atomic science and Technology, (4), 45-49 (2025). https://doi.org/10.46813/2025-158-045
[10] V.M. Kuklin, “On the Nature of Coherents in the System of Oscillators,” Problems of Atomic Science and Technology, Series “Plasma Electronics and New Methods of Acceleration”, 4(122), 91–95 (2019).
[11] Yu.A. Il'inskii, and N.S. Maslova, “Classical analog of superradiance in a system of interacting nonlinear oscillators,” Zh. Eksp. Teor. Fiz. **91**(1). 171–174 (1988).
[12] A.V. Kirichok, *et al.* “Modelling of superradiation processes driven by an ultra–short bunch of charged particles moving through a plasma,” Problems of Atomic Science and Technology, series “Plasma Electronics and New Methods of Acceleration”, (4), 255–257 (2015).
[13] V.M. Kuklin, *Selected chapters (theoretical physics)*, (V.N. Karazin KhNU, Kharkiv, 2021). http://dspace.univer.kharkov.ua/handle/123456789/16359
[14] The Statistical Theory of Non–Equilibrium Processes in a Plasma: International Series of Monographs in Natural Philosophy, Vol. 9 [Print Replica] Kindle Edition by Yu L Klimontovich (Author), D. ter Haar (Editor) Format: Kindle Edition. Part of: International series of monographs in natural philosophy (46 books).
[15] A.S. Davydov, *Quantum mechanics*, edited by D. ter Haar. vol.1, (Perg. Press, 1965).
[16] L. Allen, and J. Eberly, *Optical resonance and two–level atoms*, (Witey–lnterscicitce Publication, John Witty and Sons, New York, 1975).
[17] C.H. Townes – Nobel Lecture. NobelPrize.org. Nobel Prize Outreach 2025. Thu. 24 Apr 2025. https://www.nobelprize.org/prizes/physics/1964/townes/lecture/
[18] E. Poklonsky, and V. Kuklin, “On the Features of Open Magnetoactive Waveguides Excitation”, East Eur. J. Phys. (3), 85–92 (2025). https://doi.org/10.26565/2312–4334–2025–3–08

## ПРО СИНХРОНІЗАЦІЮ АНСАМБЛЯ ОСЦИЛЯТОРІВ В УМОВАХ НАДВИПРОМІНЮВАННЯ

**В.М. Куклін[1], Є.В. Поклонський[2]**
[1]*Харківський національний економічний університет імені С. Кузнеця. кафедра кібербезпеки та інформаційних технологій пр. Науки, 2. 9 – А. 61165, Харків, Україна*
[2]*Харківський національний університет імені В. Н. Каразіна, 61022, пл. Свободи, 4, Харків, Україна*

Обговорюються проблеми фазової синхронізації ансамблю осциляторів або диполів та механізми генерації в режимі надвипромінювання. Показано, що збільшення розкиду початкових амплітуд ансамблю осциляторів пригнічує фазову синхронізацію і знижує ефективність генерації поля. Обговорюється вплив шумів, показано, що нижче за поріг генерації навіть зовнішнє ініціююче поле не здатне синхронізувати фази ансамблю частинок. При перевищенні порога генерації ініціююче поле може не знадобитися. Показано, що зближення фаз осциляторів з фазами поля в місцях розташування осциляторів, що рухаються, помітно лише поблизу їх виходу з системи. При цьому повного збігу фаз синхронізованих осциляторів та фаз поля в області їхньої локалізації не спостерігається. Тим не менш, інтенсивність поля генерації в режимі надвипромінювання суттєво перевищує спонтанний рівень, що дозволяє говорити про ознаки індукованого випромінювання. Обговорюються особливості розвитку квантового процесу надвипромінювання ансамблю диполів та наводиться система рівнянь для його опису. Якісно моделюються особливості квантового аналога надвипромінювання, відзначається роль частоти Рабі, що визначає динаміку інверсії населеності. Нутації інверсії населеності в області, що займає поле, впливають на інтенсивність поля не тільки в цій локальній зоні, але і в наступних областях активної зони. Це пояснює незвичайний характер розвитку генерації: зростання поля певної області активної зони спочатку стабілізується, та потім істотно зменшується. Це зменшення інтенсивності відбувається й у напрямку випромінювання в периферійних областях активної зони, незважаючи на великий запас енергії в них у вигляді незбуреної інверсії населеності.

**Ключові слова**: *класичні та квантові випромінювачі; режим надвипромінювання; умови фазової синхронізації у класичній моделі; вплив нутацій інверсії населеності на генерацію поля*

East European Journal of Physics. **4.** 183-191 (2025)
DOI:10.26565/2312-4334-2025-4-16 ISSN 2312-4334

# STIMULATED RAMAN SCATTERING OF HIGH-POWER BEAM IN QUANTUM PLASMA: EFFECT OF RELATIVISTIC-PONDEROMOTIVE FORCE

**Keshav Walia*, Taranjot Singh**
*Department of Physics, DAV University Jalandhar, India*
**Corresponding Author e-mail: keshavwalia86@gmail.com*

Received August 12, 2025; revised September 11, 2025; in final form October 4, 2025; accepted October 8, 2025

The present work explores stimulated Raman scattering of a high-power beam in quantum plasma due to the joint action of relativistic ponderomotive force (RP force). The RP force creates nonlinearity in the plasma's dielectric function. This results in a change in the density profile in a transverse direction to the axis of the pump beam. This change in density profile has a significant impact on all three waves involved in the process, viz., the input beam, the electron plasma beam, and the scattered wave. Second-order ODEs for all three waves, as well as the SRS back-reflectivity expression, are set up and further solved numerically. Impact of well-known laser-plasma parameters, quantum contribution, and combined action of RP force on beam waists of various waves, and also on SRS back-reflectivity are explored.

**Keywords:** *Relativistic-Ponderomotive forces; Back-reflectivity; Electron Plasma Wave; Dielectric function; Scattered Wave*
**PACS:** 52.38.Hb, 52.35.Mw, 52.38.Dx

## 1. INTRODUCTION

Among theoretical/experimental research groups, there has been interest in the interaction of ultra-intense lasers with plasmas, resulting from their applicability to laser-driven fusion [1-3] and the acceleration of charged species [4-9]. During laser-plasma interaction, distinct instabilities are produced, including scattering instabilities, filamentation, self-focusing, modulation instability, and trapping [3, 10-13]. There is a significant reduction in the coupling efficiency of lasers due to these nonlinear phenomena. These instabilities can lead to production of highly energetic electrons. These high-speed electrons preheat the fusion fuel and also cause great reduction in compression rate. Moreover, there is a modification in the irradiance distribution due to these nonlinear phenomena. The transition of lasers through plasmas is mainly controlled by Stimulated Raman Scattering (SRS) process. In fact, it helps in exploring the transmission of energy from lasers to plasmas [14-17]. SRS is a key research topic in laser-plasma interaction for theoretical/experimental researchers [18-22]. In SRS, the pump wave splits up into an electron plasma wave (EPW) and a scattered beam. EPW generates electrons travelling at extremely high speeds, which could, in fact, preheat the target core. A scattered beam helps in identifying the amount of wasted energy. So, Raman reflectivity is very crucial parameter for exploring percentage of useful/wasted energy during laser-plasma interaction. It has already been revealed from literature that mostly research on scattering instabilities is carried out through plane waves. If intensity associated with main beam is kept non-uniform, then self-focusing phenomenon becomes extremely dominant. Self-focusing greatly affects other nonlinear processes, including SRS, SBS, pair production, and harmonic generation [23-31]. So, the inclusion of the self-focusing phenomenon while exploring the SRS process becomes extremely important. Many research groups have explored inter-connection between self-focusing and SRS in the past [32-42]. Most of these studies were explored in classical plasmas. In case of classical plasmas, density is kept low and temperature is kept high. Whenever density is high and temperature is low, we obtain quantum plasmas [43-46]. Theoretical/experimental research groups are motivated to explore quantum plasmas due to their direct connection in diverse fields, including laser-driven fusion, quantum dots, and quantum optics [47-54]. In case of quantum plasmas, $\lambda_d \geq n_0^{-1/3}$ i.e. $n_0\lambda_d^3 \geq 1$. So, de-Broglie Wavelength is greater than or equal to average distance between electrons. For quantum plasmas, $T_f \geq T$. Where $T_f$ and $T$ are Fermi temperature and plasma temperature respectively. There has been keen curiosity of various researchers in exploring instabilities in quantum plasmas due to their relevance in light-matter interaction [55-57]. Also, notable attention has been received by laser-quantum plasmas interaction as a result of its direct involvement in exploring scattering instabilities, inertial fusion and X-ray lasers. Keeping in view these objectives, our aim in the present study is to explore Stimulated Raman Scattering of a laser in quantum plasma due to the joint action of RP force. The main beam $(\omega_0, k_0)$ interacts with EPW $(\omega, k)$ thereby producing a scattered wave $(\omega_0 - \omega,\ k_0 - k)$. Here, we have taken the back-scattering case for $k \approx 2k_0$. The carrier's redistribution takes place due to the joint action of the RP force, thereby causing self-focusing. The dispersion relation associated with EPW gets modified. Moreover, change in phase velocity of EPW is observed. The EPW also gets self-focused under suitable boundary conditions. Irradiance associated with scattered wave is directly proportional to irradiance related with main wave and EPW. So, self-focusing results in improvement in back-scattering.

---

***Cite as:*** K.Walia, T. Singh, East Eur. J. Phys. 4, 183 (2025), https://doi.org/10.26565/2312-4334-2025-4-16

## 2. SOLUTION OF PUMP WAVE IN THERMAL QUANTUM PLASMA

Consider the transition of an intense laser beam having wave number $k_0$ and the angular frequency $\omega_0$ along z-axis in TQP. We are considering the combined influence of RP force in the present investigation. Irradiance distribution for laser beam at $z = 0$ is expressed as

$$E_0 \cdot E_0^* = E_{00}^2 exp\left[-\frac{r^2}{r_0^2}\right] \tag{1}$$

In Eq. (1), $E_{00}$ and $r_0$ represent maximum field amplitude and initial beam width at $z = 0$. Also, $r^2 = x^2 + y^2$. The TQP's dielectric function incorporating the Bohm potential, the Fermi pressure, and quantum involvement can be stated as [53-54].

$$\epsilon = 1 - \frac{\omega_p^2}{\gamma\omega_0^2}\left(1 - \frac{k_0^2 v_f^2}{\omega_0^2} - \frac{\delta q}{\gamma}\right)^{-1} \tag{2}$$

In Eq. (2), $v_f = \sqrt{\frac{2K_B T_f}{m}}$ and $\gamma = (1 + \alpha E_0 E_0^*)^{1/2}$ denote Fermi speed and Lorentz factor respectively and $\delta q = \frac{4\pi^4 h^2}{m^2\omega_0^2\lambda^4}$. If $T_f \text{—>} 0$ is substituted, then cold quantum plasma's (CQP's) dielectric function is obtained. On the other hand, if $T_f \text{—>} 0$, $\frac{h}{2\pi} \text{—>} 0$, then classical relativistic plasma's (CRP's) dielectric function is obtained. Here, $\alpha = \frac{e^2}{m^2c^2\omega_0^2}$ and $\omega_p = \sqrt{\frac{4\pi n e^2}{m}}$ are known as nonlinear coefficient and plasma frequency respectively. The nonlinear ponderomotive force results in change in density of electrons. We can express this changed number density as [53-54]

$$n = n_0 exp\left(-\frac{mc^2}{T}(\gamma - 1)\right) \tag{3}$$

For TQP, one can express generalized dielectric function as

$$\varepsilon = \varepsilon_0 + \Phi\ (E_0 E_0^*) \tag{4}$$

In Eq. (4), $\varepsilon_0 = 1 - \frac{\omega_p^2}{\omega_0^2}$ & $\Phi\ (E_0 E_0^*) = \frac{\omega_p^2}{\omega_0^2}\left[1 - \frac{N_{0e}}{N_0}\right]$ are linear & nonlinear portions for $\varepsilon$ respectively. Including the effect of nonlinear ponderomotive force, we can write nonlinear term $\Phi\ (E_0 E_0^*)$ for TQP as

$$\Phi(EE^*) = \frac{\omega_{p0}^2}{\omega_0^2}\left[1 - \frac{1}{\gamma}\left(1 - \frac{k_0^2 v_f^2}{\omega_0^2} - \frac{\delta q}{\gamma}\right)^{-1} \exp\left(-\frac{mc^2}{T}(\gamma - 1)\right)\right] \tag{5}$$

Where, $\omega_{p0} = \sqrt{\frac{4\pi n_0 e^2}{m}}$.

The field $E_i$ of the pump wave represents wave equation as;

$$\nabla^2 E_i + \frac{\omega_0^2}{c^2}\left[1 - \frac{\omega_p^2}{\omega_0^2}\frac{N_{0e}}{N_0}\right] E_i = 0 \tag{6}$$

One can write the solution for Eq. (6) following the approach [58-60] as

$$E_i = E_0 \exp[i(\omega_0 t - k_0(S_0 + z))] \tag{7}$$

$$E_0^2 = \frac{E_{00}^2}{f_0^2} exp\left[-\frac{r^2}{r_0^2 f_0^2}\right] \tag{8}$$

$$S_0 = \frac{1}{2} r^2 \frac{1}{f_0}\frac{df_0}{dz} + \Phi_0(z) \tag{9}$$

Here, $f_0$ is the pump wave's beam waist satisfying differential equation

$$\frac{d^2 f_0}{dz^2} = \frac{1}{k_0^2 r_0^4 f_0^3} - \frac{\omega_p^2}{\omega_0^2\varepsilon_0}\frac{\alpha E_{00}^2}{2r_0^2 f_0^3}\frac{exp\left(-\frac{mc^2}{T_e}\left[\sqrt{1+\frac{\alpha E_{00}^2}{f_0^2}} - 1\right]\right)}{\left(1+\frac{\alpha E_{00}^2}{f_0^2}\right)^{3/2}\left(1-\frac{k_0^2 v_f^2}{\omega_0^2} - \frac{\delta q}{\sqrt{1+\frac{\alpha E_{00}^2}{f_0^2}}}\right)^2}\left[\left(1 - \frac{k_0^2 v_f^2}{\omega_0^2}\right) + \frac{mc^2}{T_e}\sqrt{1 + \frac{\alpha E_{00}^2}{f_0^2}}\left(1 - \frac{k_0^2 v_f^2}{\omega_0^2} - \frac{\delta q}{\sqrt{1+\frac{\alpha E_{00}^2}{f_0^2}}}\right)\right] \tag{10}$$

Here, the boundary condition used is as follows, $f_0 = 0$ and $\frac{df_0}{dz} = 0$ at $z = 0$.

## 3. EXCITATION OF ELECTRON PLASMA WAVE

The nonlinear interaction between the pump wave and EPW leads to its excitation. For analyzing the excitation of EPW in TQP, the following standard equations are considered;

(a) Continuity Equation

$$\frac{\partial N}{\partial t} + \nabla \cdot (NV) = 0 \tag{11}$$

(b) Equation of motion

$$m\left[\frac{\partial V}{\partial t} + (V \cdot \nabla)V\right] = -e\left[E + \frac{1}{c}(V \times B)\right] - 2\Gamma mV - \frac{\gamma_e}{N}\nabla P \tag{12}$$

(c) Poisson's equation

$$\nabla \cdot E = -4\pi eN \tag{13}$$

In the above equations, the instantaneous electron density, fluid velocity, Landau damping parameter, and pressure term are expressed by $N$, $V$, $\Gamma$, and $P$ respectively. For electron gas $\gamma_e = 3$. Further, by using perturbation analysis and the standard approach, we can obtain the following equation denoting the change in electron density as

$$\frac{\partial^2 n}{\partial t^2} + 2\Gamma\frac{\partial n}{\partial t} - 3v_{th}^2\nabla^2 n + \omega_p^2\frac{N_{0e}}{N_0}n = 0 \tag{14}$$

Following [58-60], the Solution of Eq. (14) can be expressed as

$$n = n_0(r,z)exp[i(\omega t - k(z + S(r,z)))] \tag{15}$$

Here, wave vector, angular frequency, and Eikonal for the EPW are denoted by $k, \omega$ and $S$ respectively. Further, the dispersion relation for EPW is expressed as

$$\omega^2 = \omega_p^2\frac{N_{0e}}{N_0} + 3k^2v_{th}^2 \tag{16}$$

Further, on putting the Eq. (15) in Eq. (14) further separating real and imaginary terms, we have

$$2\frac{\partial S}{\partial z} + \left(\frac{\partial S}{\partial r}\right)^2 = \frac{1}{k^2 n_0}\nabla_\perp^2 n_0 + \frac{\omega_p^2}{3k^2v_{th}^2}\left[1 - \frac{N_{0e}}{N_0}\right] \tag{17}$$

$$\frac{\partial n_0^2}{\partial z} + \frac{\partial S}{\partial r}\frac{\partial n_0^2}{\partial r} + n_0^2\nabla_\perp^2 S + \frac{2\Gamma}{3v_{th}^2}\frac{\omega n_0^2}{k} = 0 \tag{18}$$

Following [58-60], the solution of Eq. (17) and (18) can be expressed as

$$n_0^2 = \frac{n_{00}^2}{f^2}\exp\left(-\frac{r^2}{a^2f^2} - 2k_i z\right) \tag{19}$$

$$S = \frac{1}{2}r^2\frac{1}{f}\frac{df}{dz} + \Phi(z) \tag{20}$$

Here, $k_i$ denotes the damping factor and $'f'$ denotes the beam waist of EPW and 2nd order ODE satisfied by it is expressed as

$$\frac{d^2f}{dz^2} = \frac{1}{k^2a^4f^3} - \frac{\omega_p^2 f}{3k^2v_{th}^2}\frac{\alpha E_{00}^2}{2r_0^2 f_0^4}\frac{exp\left(-\frac{mc^2}{T_e}\left[\sqrt{1+\frac{\alpha E_{00}^2}{f_0^2}}-1\right]\right)}{\left(1+\frac{\alpha E_{00}^2}{f_0^2}\right)^{3/2}\left(1-\frac{k_0^2v_f^2}{\omega_0^2}-\frac{\delta q}{\sqrt{1+\frac{\alpha E_{00}^2}{f_0^2}}}\right)^2}\left[\left(1 - \frac{k_0^2v_f^2}{\omega_0^2}\right) + \frac{mc^2}{T_e}\sqrt{1 + \frac{\alpha E_{00}^2}{f_0^2}}\left(1 - \frac{k_0^2v_f^2}{\omega_0^2} - \frac{\delta q}{\sqrt{1+\frac{\alpha E_{00}^2}{f_0^2}}}\right)\right] \tag{21}$$

Here, the boundary condition used is $f = 0$ and $\frac{df}{dz} = 0$ at $z = 0$.

## 4. STIMULATED RAMAN SCATTERING

The total field vector $E_T$ can be written as addition of fields of main wave $E$ and scattered wave $E_s$. i.e.

$$E_T = E\exp(i\omega_0 t) + E_s\exp(i\omega_s t) \tag{22}$$

Now, the field vector $E_T$ satisfies the following wave equation

$$\nabla^2E_T - \nabla(\nabla \cdot E_T) = \frac{1}{c^2}\frac{\partial^2E_T}{\partial t^2} + \frac{4\pi}{c^2}\frac{\partial J_T}{\partial t} \tag{23}$$

In above Eq., current density is written by $J_T$. Now, further considering scattered frequency terms, we have

$$\nabla^2 E_s + \frac{\omega_s^2}{c^2}\left[1 - \frac{\omega_p^2}{\omega_s^2}\frac{N_{0e}}{\gamma N_0}\right] E_s = \left[\frac{\omega_p^2 \omega_S n^*}{2c^2 \omega_0 N_0}\right] E_i - \nabla(\nabla \cdot E_i) \tag{24}$$

The result of Eq. (24) can be written as

$$E_s = E_{s0}(r,z)e^{+ik_{s0}z} + E_{s1}(r,z)e^{-ik_{s1}z} \tag{25}$$

Where $k_{S0}^2 = \frac{\omega_S^2}{c^2}\left[1 - \frac{\omega_p^2}{\omega_S^2}\right] = \frac{\omega_S^2}{c^2}\epsilon_{S0}$, with $\omega_S = \omega_0 - \omega$ and $k_{S1} = k_0 - k$.

By using Eq. (25) in Eq. (24), we get

$$-k_{S0}^2 E_{S0}^2 + 2ik_{S0}\frac{\partial E_{S0}}{\partial z} + \left(\frac{\partial^2 E_{S0}}{\partial r^2} + \frac{1}{r}\frac{\partial E_{S0}}{\partial r}\right) + \frac{\omega_S^2}{c^2}\left[\epsilon_{S0} + \frac{\omega_p^2}{\omega_S^2}\left(1 - \frac{N_{0e}}{N_0}\right)\right] E_{S0} = 0 \tag{26}$$

$$-k_{S1}^2 E_{S1}^2 + 2ik_{S1}\frac{\partial E_{S1}}{\partial z} + \left(\frac{\partial^2 E_{S1}}{\partial r^2} + \frac{1}{r}\frac{\partial E_{S1}}{\partial r}\right) + \frac{\omega_S^2}{c^2}\left[\epsilon_{S0} + \frac{\omega_p^2}{\omega_S^2}\left(1 - \frac{N_{0e}}{N_0}\right)\right] E_{S1} = \frac{1}{2}\frac{\omega_p^2}{c^2}\frac{n^*}{N_0}\frac{\omega_S}{\omega_0} E_0 exp(-ik_0 S_0) \tag{27}$$

Now, solution of Eq. (27) is expressed as

$$E_{S1} = E_{S1}'(r,z)e^{-ik_0 S_0} \tag{28}$$

Now, putting Eq. (28) in Eq. (27) and further ignoring space derivatives

$$E_{S1}' = -\frac{1}{2}\frac{\omega_p^2}{c^2}\frac{n^*}{N_0}\frac{\omega_S}{\omega_0}\frac{\hat{E}E_0}{\left[k_{S1}^2 - k_{S0}^2 - \frac{\omega_p^2}{c^2}\left(1 - \frac{N_{0e}}{N_0}\right)\right]} \tag{29}$$

Now, solution of Eq. (26) can be written as

$$E_{S0} = E_{S00}e^{ik_{S0}S_c} \tag{30}$$

Now, use Eq. (30) in Eq. (26) and combining the real part and imaginary part separately, we have

$$2\frac{\partial S_c}{\partial z} + \left(\frac{\partial S_c}{\partial r}\right)^2 = \frac{1}{k_{S0}^2 E_{S00}}\left(\frac{\partial^2 E_{S00}}{\partial r^2} + \frac{1}{r}\frac{\partial E_{S00}}{\partial r}\right) + \frac{\omega_p^2}{\epsilon_{S0}\omega_S^2}\left[1 - \frac{N_{0e}}{N_0}\right] \tag{31}$$

$$\frac{\partial E_{S00}^2}{\partial z} + \frac{\partial S_c}{\partial r}\frac{\partial E_{S00}^2}{\partial r} + E_{S00}^2\left(\frac{\partial^2 S_c}{\partial r^2} + \frac{1}{r}\frac{\partial S_c}{\partial r}\right) = 0 \tag{32}$$

Now, following approach of [58-60], Eqs. (31) and (32) have solutions,

$$E_{S00}^2 = \frac{B_1^2}{f_S^2} exp\left[-\frac{r^2}{b^2 f_S^2}\right] \tag{33}$$

$$S_c = \frac{1}{2} r^2 \frac{1}{f_S}\frac{df_S}{dz} + \Phi_S(z) \tag{34}$$

In Eqs. (33) and (34), the initial beam radius for the scattered wave is denoted by $b$ and beam width of the scattered wave is represented by $f_s$ and it satisfies the following 2nd ODE as

$$\frac{d^2 f_s}{dz^2} = \frac{1}{k_{S0}^2 b^4 f_S^3} - \frac{\omega_p^2}{\omega_S^2 \varepsilon_{S0}}\frac{\alpha E_{00}^2 f_S}{2r_0^2 f_0^4}\frac{exp\left(-\frac{mc^2}{T_e}\left[\sqrt{1+\frac{\alpha E_{00}^2}{f_0^2}} - 1\right]\right)}{\left(1+\frac{\alpha E_{00}^2}{f_0^2}\right)^{3/2}\left(1 - \frac{k_0^2 v_f^2}{\omega_0^2} - \frac{\delta q}{\sqrt{1+\frac{\alpha E_{00}^2}{f_0^2}}}\right)^2}\left[\left(1 - \frac{k_0^2 v_f^2}{\omega_0^2}\right) + \frac{mc^2}{T_e}\sqrt{1 + \frac{\alpha E_{00}^2}{f_0^2}}\left(1 - \frac{k_0^2 v_f^2}{\omega_0^2} - \frac{\delta q}{\sqrt{1+\frac{\alpha E_{00}^2}{f_0^2}}}\right)\right] \tag{35}$$

The boundary condition used in the present case is $f_s = 0$ and $\frac{df_s}{dz} = 0$ at $z = 0$.

## 5. BACK-REFLECTIVITY

From Eq. (19), we find that EPW is damped while travelling along the z-axis. So, with a decrease in z, the amplitude of the scattered wave decreases. The boundary condition used is

$$E_s = E_{s0}(r,z)e^{+ik_{s0}z} + E_{s1}(r,z)e^{-ik_{s1}z} = 0 \tag{36}$$

at $z = z_c$. At $z = z_c$, the amplitude for the scattered beam vanishes,

$$B_1 = \frac{\omega_p^2 \omega_s N_{00}}{2c^2 \omega_0 N_0} \frac{E_{00} e^{-ik_i z_c}}{\left[k_{s1}^2 - k_{s0}^2 - \frac{\omega_p^2}{c^2}\left(1 - \frac{N_{0e}}{N_0}\right)\right]} \frac{f_s(z_c)}{f_s(z_c) f(z_c)} \frac{\exp\left(-i(k_0 S_0 + k_{s1} z_c)\right)}{\exp\left(+i(k_{s0} S_c + k_{s0} z_c)\right)} \tag{38}$$

With condition, $\frac{1}{b^2 f_s^2} = \frac{1}{a^2 f^2} + \frac{1}{r_0^2 f_0^2}$ .
Now, SRS back-reflectivity may be derived as,

$$R = \frac{1}{4}\left(\frac{\omega_p^2}{c^2}\right)^2 \left(\frac{\omega_s}{\omega_0}\right)^2 \left(\frac{N_{00}}{N_0}\right)^2 \frac{(L_1 - L_2 - L_3)}{\left[k_{s1}^2 - k_{s2}^2 - \frac{\omega_p^2}{c^2}\left(1 - \frac{1}{\sqrt{1 + \frac{\alpha E_{00}^2}{f_0^2}}}\left[1 - \frac{k_0^2 v_f^2}{\omega_0^2} - \frac{\delta q}{\sqrt{1 + \frac{\alpha E_{00}^2}{f_0^2}}}\right]^{-1} exp\left[-\frac{m_0 c^2}{Te}\left(\sqrt{1 + \frac{\alpha E_{00}^2}{f_0^2}} - 1\right)\right]\right)\right]^2} \tag{39}$$

Where

$$L_1 = \left(\frac{f_s}{f_0 f}\right)_{z=z_c}^2 \frac{1}{f_s^2} exp\left(-2k_i z_c - \frac{r^2}{b^2 f_s^2}\right),$$

$$L_2 = -2\left(\frac{f_s}{f_0 f}\right)_{z_c} \frac{1}{f f_0 f_s} exp\left(-\frac{r^2}{2b^2 f_s^2} - \frac{r^2}{2a^2 f^2} - \frac{r^2}{2r_0^2 f_s^2}\right) exp(-k_i(z + z_c)) Cos(k_{s0} + k_{s1})[z - z_c],$$

$$L_3 = \frac{1}{f^2 f_0^2} exp\left(-\frac{r^2}{a^2 f^2} - \frac{r^2}{r_0^2 f_s^2} - 2k_i z_c\right)$$

## 6. DISCUSSION

Since the analytical results of Eqs. (10), (21), (35), and (39) are not feasible. So, the well-known RK4 method is used for doing numerical calculations of these equations for known laser-plasma parameters;

$$\alpha E_{00}^2 = 2.0, 3.0, 4.0\ ; \frac{\omega_p^2}{\omega_0^2} = 0.15, 0.20, 0.25\ ; T_f = 10^7 K, 10^8 K, 10^9 K$$

Eqs. (10), (21) and (35) contain two terms on RHS with some physical interpretation for each term. The first term on RHS of each equation is the diffractive term, while 2nd one is the focusing term. During the transition of these beams inside, there is a relative competition between these two terms. The dominance of the first term results in the defocusing of beams, whereas the dominance of the second term results in the focusing of beams. When these terms are exactly equal to each other, then the beam neither focuses nor defocuses. Then, a self-trapping case is found.

The alteration of beam waists $f_0$, $f$ and $f_s$ with normalized distance $\eta (= z/k_0 r_0^2)$ at distinct beam intensity $\alpha E_{00}^2$ is shown in Figures 1(a), 1(b) and 1(c) respectively. Here, only the variation of beam intensity is taken, whereas other parameters are kept fixed. Black, green and red curves are for $\alpha E_{00}^2 = 2.0, 3.0$ and $4.0$ respectively. The focusing behavior of all the beams involved is found to get decreased with increase in beam intensity. This is as a result of dominance of diffractive terms over focusing terms with increase in beam intensity.

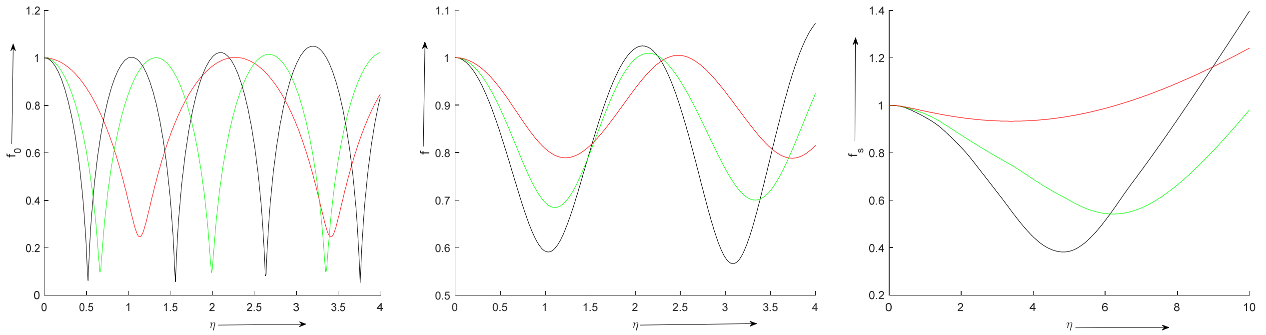

(a) (b) (c)

**Figure 1.** The alteration of beam waists $f_0, f$ and $f_s$ with normalized distance $\eta (= z/k_0 r_0^2)$ at distinct beam intensity $\alpha E_{00}^2$ is shown in figures 1(a), 1(b) and 1(c) respectively. Black, green and red curves are for $\alpha E_{00}^2 = 2.0, 3.0$ and $4.0$ respectively

The alteration of beam waists $f_0$ , $f$ and $f_s$ with normalized distance $\eta (= z/k_0 r_0^2)$ at a distinct plasma density $\frac{\omega_p^2}{\omega_0^2}$ is shown in Figures 2(a), 2(b) and 2(c) respectively. Here, only the variation of plasma density is taken, whereas other parameters are kept fixed. Black, green, and red curves are for $\frac{\omega_p^2}{\omega_0^2} = 0.15, 0.20$ and $0.25$ respectively. The focusing behavior of all the beams is found to get increased with escalation in plasma density. This is due to the dominance of focusing terms over diffractive terms with increase in plasma density.

The alteration of beam waists $f_0$ , $f$ and $f_s$ with normalized distance $\eta(= z/k_0 r_0^2)$ at a distinct Fermi temperature $T_f$ values is shown in Figures 3(a), 3(b) and 3(c) respectively. Here, only the variation of the Fermi temperature is taken, whereas other parameters are kept fixed. Black, green and red curves are for $T_f = 10^7 K, 10^8 K$ and $10^9 K$ respectively. Focusing behavior of all the beams is found to get increased with the rise in Fermi temperature. This is due to supremacy of focusing terms over diffractive terms with increase in Fermi temperature.

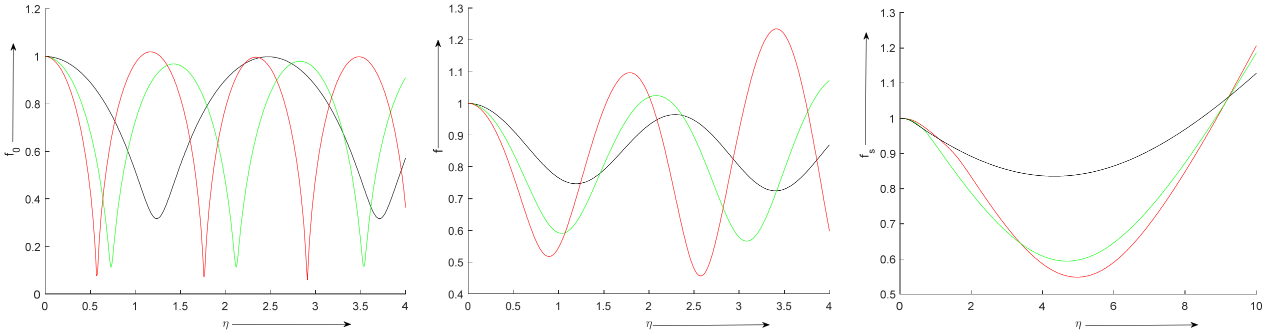

(a) (b) (c)

**Figure 2.** The alteration of beam waists $f_0$, $f$ and $f_s$ with normalized distance $\eta(= z/k_0 r_0^2)$ at distinct plasma density $\frac{\omega_p^2}{\omega_0^2}$ is shown in figures 2(a), 2(b) and 2(c) respectively. Black, green and red curves are for $\frac{\omega_p^2}{\omega_0^2} = 0.15, 0.20$ and $0.25$ respectively

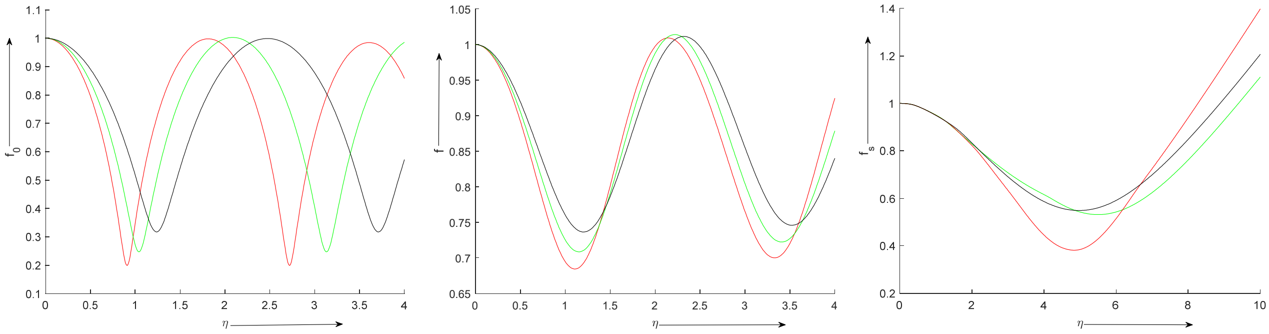

(a) (b) (c)

**Figure 3.** The alteration of beam waists $f_0$ , $f$ and $f_s$ with normalized distance $\eta(= z/k_0 r_0^2)$ at distinct Fermi temperature $T_f$ values is shown in figures 3(a), 3(b) and 3(c) respectively. Black, green and red curves are for $T_f = 10^7 K, 10^8 K$ and $10^9 K$ respectively

The alteration of beam waists $f_0$, $f$ and $f_s$ with normalized distance $\eta(= z/k_0 r_0^2)$ at distinct plasma regimes are given in Figures 4(a), 4(b) and 4(c) respectively. Black, green and red curves are for RPTQP, RPCQP, and RPCRP respectively. From the figures, we find that focusing tendency of all waves involved is maximum in RPTQP system as compared to RPCQP and RPCRP systems respectively. Moreover, focusing tendency of all the waves is found to be more in RQCQP case in comparison to RPCRP case.

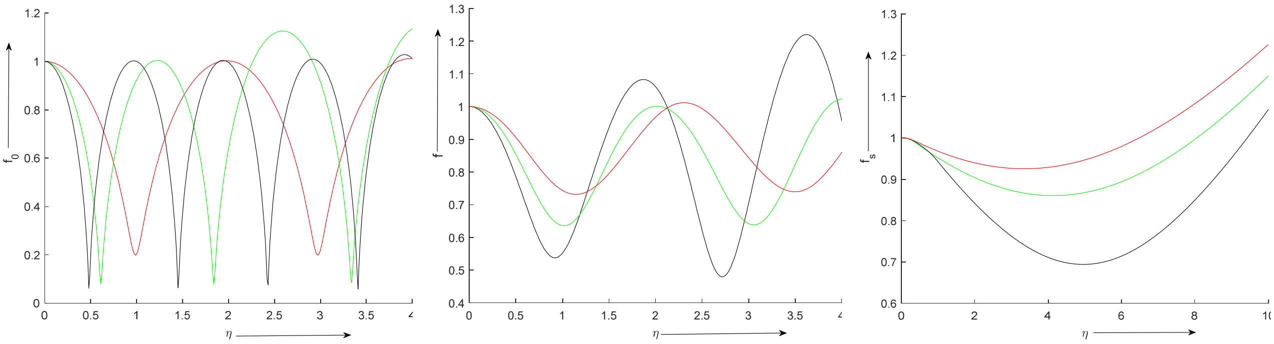

(a) (b) (c)

**Figure 4.** The alteration of beam waists $f_0$, $f$ and $f_s$ with normalized distance $\eta(= z/k_0 r_0^2)$ at distinct plasma regimes are given in figures 4(a), 4(b) and 4(c) respectively. Black, green and red curves are for RPTQP, RPCQP, and RPCRP respectively

The alteration of SRS back-reflectivity R with normalized distance $\eta(= z/k_0 r_0^2)$ at distinct beam intensity $\alpha E_{00}^2$ is shown in Figure 5(a). Red and black curves are for $\alpha E_{00}^2 = 2.0$ and $4.0$ respectively. Increase in laser intensity results in decrease in SRS reflectivity on account of decrease in self-focusing of various waves at increasing beam intensity.

The alteration of SRS back-reflectivity R with normalized distance $\eta(= z/k_0r_0^2)$ at distinct plasma density $\frac{\omega_p^2}{\omega_0^2}$ is shown in Figure 5(b). Red and black curves are for $\frac{\omega_p^2}{\omega_0^2} = 0.15$ and 0.25 respectively. Increase in plasma density results in increase in SRS reflectivity which is due to enhancement in self-focusing of various waves at increasing plasma density.

The alteration of SRS back-reflectivity R with normalized distance $\eta(= z/k_0r_0^2)$ at distinct Fermi temperature $T_f$ is shown in Figure 5(c). Red and black curves are for $T_f = 10^7K$ and $10^9K$ respectively. Increase in plasma Fermi temperature results in increase in SRS reflectivity due to increase in self-focusing of various waves at increasing Fermi temperature.

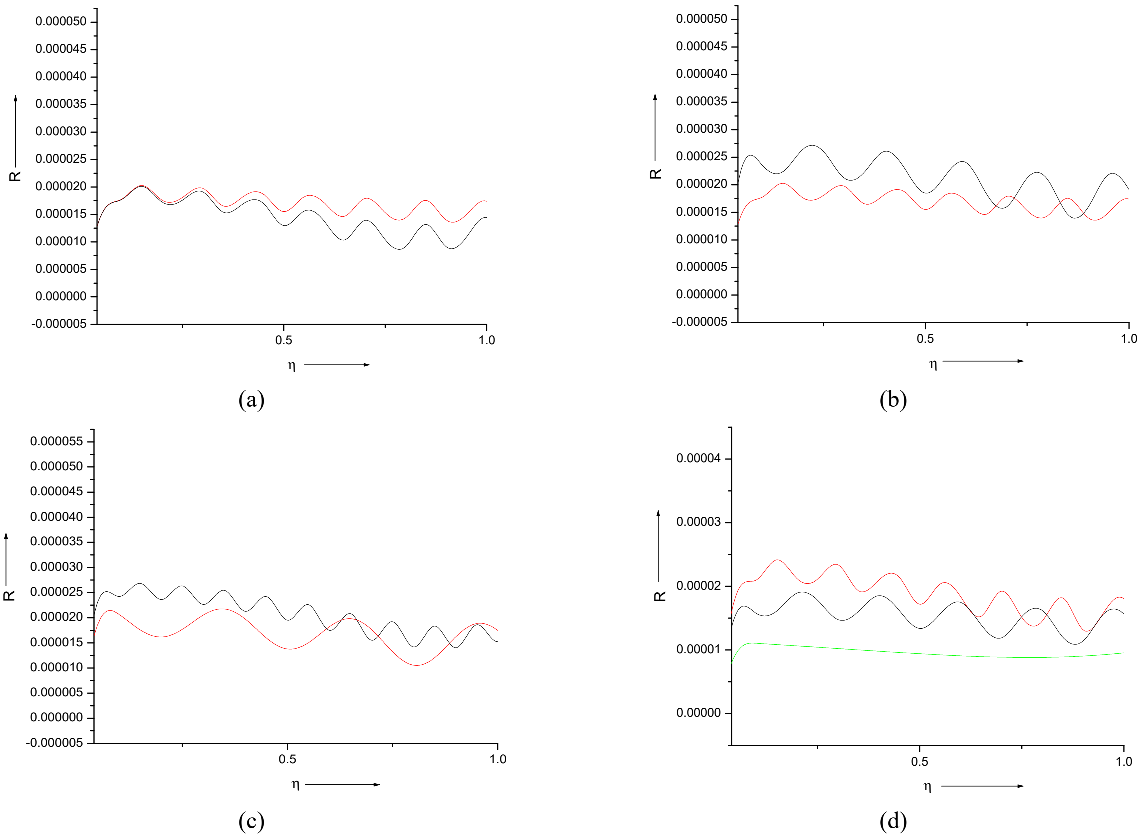

(a) (b)

(c) (d)

**Figure 5.** The alteration of SRS back-reflectivity R with $\eta(= z/k_0r_0^2)$ at (a) distinct beam intensity $\alpha E_{00}^2$. Red and black curves are for $\alpha E_{00}^2 = 2.0$ and 4.0 respectively, (b) distinct plasma density $\frac{\omega_p^2}{\omega_0^2}$. Red and black curves are for $\frac{\omega_p^2}{\omega_0^2} = 0.15$ and 0.25 respectively, (c) distinct Fermi temperature $T_f$. Red and black curves are for $T_f = 10^7K$ and $10^9K$ respectively, (d) distinct plasma regimes. Red, black and green curves are for RPTQP, RPCQP, and RPCRP respectively

The alteration of SRS back-reflectivity R with normalized distance $\eta(= z/k_0r_0^2)$ at distinct plasma regimes is shown in Figure 5(d). Red, black and green curves are for RPTQP, RPCQP, and RPCRP respectively. From the figure it is clear that SRS back-reflectivity is maximum in RPTQP followed by RPCQP and RPCRP. This behavior is exactly in accordance with self-focusing of distinct waves as observed in figures 4(a), 4(b) and 4(c) respectively.

## 7. CONCLUSIONS

The present research deals with the SRS of the laser beam in TQP due to the joint action of RP forces. The results obtained from the present problem are as follows:

(1) Focusing tendency of distinct waves involved is increased with a rise in plasma density, Fermi temperature, and with a decrease in beam intensity.

(2) Inclusion of quantum effects results in an enhancement in the focusing tendency of various waves involved.

(3) There is a rise in SRS back-reflectivity with an increment in density of plasma, Fermi temperature, and with a decrease in beam intensity.

(4) There is an enhancement in SRS back-reflectivity with the inclusion of quantum effects.

These results are really useful in laser-driven fusion.

**ORCID**

**Keshav Walia,** https://orcid.org/0000-0001-9547-3027; **Taranjot Singh,** https://orcid.org/0009-0009-8172-4097

## REFERENCES

[1] M. Tabak, J. Hammer, M.E. Glinsky, W.L. Kruer, S.C. Wilks, J. Woodworth, E.M. Campbell, *et al*., "Ignition and high gain with ultrapowerful lasers," Phys. Plasmas, **1**, 1626–1634 (1994). https://doi.org/10.1063/1.870664

[2] S. P. Regan, D. K. Bradley, A.V. Chirokikh, R. S. Craxton, D. D. Meyerhofer, W. Seka, R. W. Short, *et al*., "Laser-plasma interactions in long-scale-length plasmas under direct-drive National Ignition Facility conditions," Phys. Plasmas, **6**, 2072–2080 (1999). https://doi.org/10.1063/1.873716

[3] D. Batani, V. Maslov, D. Bondar, *et al*., "Smoothing of transverse nonuniformities at the critical density in laser interaction with nonuniform plasmas. Laser part," Beams, **43**, 1-7 (2025). https://doi.org/10.1017/lpb.2025.10003

[4] W.P. Leemans, A.J. Gonsalves, H.-S. Mao, *et al*., "Multi-GeV electron beams from capillary- discharge-guided subpetawatt laser pulses in the self-trapping regime," Phys. Rev. Lett. **113**, 245002 (2014). https://doi.org/10.1103/physrevlett.113.245002

[5] S. Gessner, J. Osterhoff, C.A. Lindstrøm, *et al*. "Design initiative for a 10 TEV pCM wake field collider," arXiv preprint arXiv:2503.20214. 2025. https://doi.org/10.48550/arXiv.2503.20214

[6] D.S. Bondar, I.P. Levchuk, V.I. Maslov, *et al*. "Dynamics of self-injected electron bunches at their acceleration by laser pulse in plasma," Probl. Atom. Sci. Tech. **112**, 76 (2017).

[7] V.I. Maslov, O.M. Svystun, I.N. Onishchenko, *et al*., "Joint wake field acceleration by laser pulse and by self injected electron bunches. Probl. Atom. Sci. Tech. **106**, 144 (2016).

[8] V.I. Maslov, O.M. Svystun, I.N. Onishchenko, *et al*., "Dynamics of electron bunches at the laser–plasma interaction in the bubble regime," Nucl. Instrum. Meth. A, **829**, 422 (2016).

[9] D.S. Bondar, W. Leemans, V.I. Maslov, and I.N. Onishchenko, "Laser-plasma acceleration in a conical plasma channel with longitudinally inhomogeneous plasma profile," Probl. Atom. Sci. Tech. **4**, 56-60 (2025). https://doi.org/10.46813/2025-158-056

[10] H. Schamel, and V. Maslov, "Langmuir Wave Contraction Caused by Electron Holes," Phys. Scr. T. **82**, 122 (1999). https://doi.org/10.1238/physica.topical.082a00122

[11] K. Walia, "Propagation characteristics of a high-power beam in weakly relativistic-ponderomotive thermal quantum plasma," Commun. Theor. Phys. **75**, 095501 (2023). https://doi.org/10.1088/1572-9494/accf82

[12] K. Walia, "Nonlinear interaction of high power beam in weakly relativistic and ponderomotive cold quantum plasma," Optik, **219**, 165040 (2020). https://doi.org/10.1016/j.ijleo.2020.165040

[13] K. Walia, N. Mehra, and S. Pandit, "Propagation Characteristics of q-Gaussian Laser Beam in Cold Collisionless Plasma," J. Contemp. Phys. **59**, 378–385 (2024). https://doi.org/10.1134/s1068337225700203

[14] W.L. Kruer, "Interaction of plasmas with intense lasers," Phys. Plasmas, **7**, 2270–2278 (2000). https://doi.org/10.1063/1.874061

[15] M. Masek, and K. Rohlena, "Stimulated Raman scattering in the presence of trapped particle instability," Commun. Nonlinear Sci. Numer. Simul. **13**, 125-129 (2008). https://doi.org/10.1016/j.cnsns.2007.04.011

[16] E.S. Dodd, and D. Umstadter, "Coherent control of stimulated Raman scattering using chirped laser pulses," Phys. Plasmas, **8**, 3531–3534 (2001). https://doi.org/10.1063/1.1382820

[17] T. Miyakoshi, M.S. Jovanovic, Y. Kitagawa, R. Kodama, K. Mima, A.A. Offenberger, K.A. Tanaka, and T. Yamanaka, "Stimulated Raman back-scattering from a mm-scale inhomogeneous plasma irradiated with ultra-intense laser pulse," Phys. Plasmas, **9**, 3552–355 (2002). https://doi.org/10.1063/1.1491252

[18] T. Tajima, and J.M. Dawson, "Laser electron accelerator," Phys. Rev. Lett. **43**, 267-270 (1979). https://doi.org/10.1103/physrevlett.43.267

[19] D. Umstadter, J.K. Kim, and E. Dodd, "Laser injection of ultrashort electron pulses into wake field plasma waves," Phys. Rev. Lett. **76**, 2073-2076 (1996). https://doi.org/10.1103/physrevlett.76.2073

[20] M. Tabak, J. Hammer, M.E. Glinsky, W.L. Kruer, S.C. Wilks, J. Woodworth, E.M. Campbell, *et al*., "Ignition and high gain with ultrapowerful lasers," Phys. Plasmas, **1**, 1626-1634 (1994). https://doi.org/10.1063/1.870664

[21] E.S. Dodd, and D. Umstadter, "Coherent control of stimulated Raman scattering using chirped laser pulses," IEEE J. Quantum Electron. **8**, 3531 (2001). https://doi.org/10.1063/1.1382820

[22] R.K. Kirkwood, J.D. Moody, C. Niemann, E.A. Williams, A.B. Langdon, O.L. Landen, L. Divol, and L.S. Suter, "Observation of polarization dependent Raman scattering in a large-scale plasma illuminated with multiple laser beams," Phys. Plasmas, **13**, 082703 (2006). https://doi.org/10.1063/1.2215415

[23] T. Singh, and K. Walia, "Second Harmonic Generation of High Power Cosh-Gaussian Beam in Thermal Quantum Plasma: Effect of Relativistic and Ponderomotive Nonlinearity," J. Contemp. Phys. **59**, 244-253 (2024). https://doi.org/10.1134/s1068337224700488

[24] K. Singh, and K. Walia, "Influence of Self-Focused Elliptical Laser Beam on Second Harmonic Generation in Cold Quantum Plasma," J. Contemp. Phys. **59**, 154-164 (2024). https://doi.org/10.1134/s1068337224700300

[25] N. Kant, and A. Sharma, "Effect of pulse slippage on resonant second harmonic generation of a short pulse laser in a plasma," J. Phys. D, **37**, 998 (2004). https://doi.org/10.1088/0022-3727/37/7/007

[26] P. Sprangle, E. Esarey, and A. Ting, "Nonlinear theory of intense laser-plasma interactions," Phys. Rev. Lett. **64**, 2011-2014 (1990). https://doi.org/10.1103/PhysRevLett.64.2011

[27] M.R. Amin, C.E. Capjack, P. Frycz, W. Rozmus, and V.T. Tikhonchuk, "Two dimensional studies of stimulated Brillouin scattering, filamentation, and self-focusing instabilities of laser light in plasmas," Phys. Fluids, **5**, 3748–3764 (1993). https://doi.org/10.1063/1.860845

[28] C.S. Liu, and V.K. Tripathi, "Thermal effects on coupled self-focusing and Raman scattering of a laser in a self-consistent plasma channel," Phys. Plasmas, **2**, 3111-3114 (1995). https://doi.org/10.1063/1.871143

[29] D. Tripathi, T. Singh, A. Vijay, and K. Walia, "Second Harmonic Generation of q-Gaussian Laser Beam in Thermal Quantum Plasma," J. Contemp. Phys. **60**, 171 (2025). https://doi.org/10.1134/S1068337225700574

[30] D. Tripathi, S. Kaur, A. Vijay, and K. Walia, "Nonlinear Dynamics of q-Gaussian Laser Beam in Collisional Plasma: Effect of Linear Absorption," J. Contemp. Phys. **60**, 16-23 (2025). https://doi.org/10.1134/S1068337225700409

[31] T. Singh, and K. Walia, "Impact of High-Power Cosh-Gaussian Beam on Second Harmonic Generation in Collisionless Magnetoplasma," J. Contemp. Phys. **59**, 254-264 (2024). https://doi.org/10.1134/s106833722470049x

[32] S.V. Bulanov, F. Pegoraro, and A.M. Pukhov, "Two-dimensional regimes of self-focusing, wake field generation, and induced focusing of a short intense laser pulse in an underdense plasma," Phys. Rev. Lett. **74**, 710-713 (1995). https://doi.org/10.1103/physrevlett.74.710

[33] K. Walia, and A. Singh,"Effect of self-focusing on stimulated Raman scattering by a gaussian laser beam in collisional plasma: Moment theory approach," J. Nonlinear Opt. Phys. Mater. **22**, 1350030 (2013). https://doi.org/10.1142/s0218863513500306
[34] K. Walia, "Self-focusing of high power beam in unmagnetized plasma and its effect on Stimulated Raman scattering process," Optik, **225**, 165592 (2021). https://doi.org/10.1016/j.ijleo.2020.165592
[35] K. Walia, "Enhanced Brillouin scattering of Gaussian laser beam in collisional plasma: moment theory approach," J. Nonlinear Opt. Phys. Mater. **23**, 1450011 (2014).
[36] A. Singh, and K. Walia, "Stimulated Brillouin scattering of elliptical laser beam in collisionless plasma," Opt. Laser Technol. **44**, 781-787 (2012). https://doi.org/10.1016/j.optlastec.2011.10.028
[37] P. Sharma, and R.P. Sharma, "Suppression of stimulated Raman scattering due to localization of electron plasma wave in laser beam filaments," Phys. Plasmas, **16**, 032301 (2009). https://doi.org/10.1063/1.3077670
[38] P. Sharma, and R.P. Sharma, "Study of second harmonic generation by high power laser beam in magneto plasma," Phys. Plasmas, **19**, 122106 (2012). https://doi.org/10.1063/1.4759014
[39] R.W. Short, and A. Simon, "Collisionless damping of localized plasma waves in laser-produced plasmas and application to stimulated Raman scattering in filaments," Phys. Plasmas, **5**, 4134-4143 (1998). https://doi.org/10.1063/1.873147
[40] D.A. Russell, D.F. Dubois, and H.A. Rose, "Nonlinear saturation of stimulated Raman scattering in laser hot spots," Phys. Plasmas, **6**, 1294-1317 (1999). https://doi.org/10.1063/1.873371
[41] J. Fuchs, C. Labaune, S. Depierreux, V.T. Tikhonchuk, and H.A. Baldis, "Stimulated Brillouin and Raman scattering from a randomized laser beam in large inhomogeneous collisional plasmas," I. Experiment. Phys. Plasmas, **7**, 4659-4648 (2000). https://doi.org/10.1063/1.1312183
[42] K.C. Tzeng, "Suppression of electron ponderomotive blowout and relativistic self-focusing by the occurrence of Raman scattering and plasma heating," Phys. Rev. Lett. **81**, 104-107 (1998). https://doi.org/10.1103/PhysRevLett.81.104
[43] P.K. Shukla, and B. Eliasson, "Novel attractive force between ions in quantum plasmas," Phys. Rev. Lett. **108**, 165007 (2012). https://doi.org/10.1103/PhysRevLett.108.165007
[44] P.K. Shukla, and B. Eliasson, "New aspects of collective phenomena at nanoscales in quantum plasmas," Phys. Usp. **53**, 55 (2010). (in Russian)
[45] P.K. Shukla, and B. Eliasson, "Colloquium: Nonlinear collective interactions in quantum plasmas with degenerate electron fluids," Rev. Mod. Phys. **83**, 885 (2011). https://doi.org/10.1103/revmodphys.83.885
[46] P.K. Shukla, S. Ali, L. Stenflo, and M. Marklund, "Nonlinear wave interactions in quantum magnetoplasmas," Phys. Plasmas, **13**, 112111 (2006). https://doi.org/10.1063/1.2390688
[47] F. Haas, B. Eliasson, and P.K. Shukla, "Relativistic Klein-Gordon-Maxwell multistream model for quantum plasmas," Phys. Rev. E, **85**, 056411 (2012). https://doi.org/10.1103/PhysRevE.85.056411
[48] F.A. Asenjo, V. Munoz, J.A. Valdivia, and S.M. Mahajan, "A hydrodynamical model for relativistic spin quantum plasmas," Phys. Plasmas, **18**, 012107 (2011). https://doi.org/10.1063/1.3533448
[49] M. Marklund, and P.K. Shukla, "Nonlinear collective effects in photon-photon and photon-plasma interactions," Rev. Mod. Phys. **78**, 591-640 (2006). https://doi.org/10.1103/RevModPhys.78.591
[50] S.H. Glenzer, and R. Redmer, "X-ray Thomson scattering in high energy density plasmas," Rev. Mod. Phys. **81**, 1625-1663 (2009). https://doi.org/10.1103/RevModPhys.81.162
[51] S.X. Hu, and C.H. Keitel, "Spin signatures in intense laser-ion interaction," Phys. Rev. Lett. **83**, 4709-4712 (1999). https://doi.org/10.1103/PhysRevLett.83.4709
[52] P.K. Shukla, and L. Stenflo, "Stimulated scattering instabilities of electromagnetic waves in an ultracold quantum plasma," Phys. Plasmas, **13**, 044505 (2006). https://doi.org/10.1063/1.2196248
[53] S. Ali, and P.K. Shukla, "Potential distributions around a moving test charge in quantum plasmas," Phys. Plasmas, **13**, 102112 (2006). https://doi.org/10.1063/1.2352974
[54] S.C. Na, and Y.D. Young, "Temperature effects on the nonstationary Karpman–Washimi ponderomotive magnetization in quantum plasmas," Phys. Plasmas, **16**, 074504 (2009). https://doi.org/10.1063/1.3176616
[55] T. Tajima. "Laser acceleration in novel media," Eur. Phys. J. Spec. Top. **223**, 1037-1044 (2014). https://doi.org/10.1140/epjst/e2014-02154-6
[56] D.S. Bondar, V.I. Maslov, I.P. Levchuk, and I.N. Onishchenko, "Excitation of wakefield by a laser pulse in a metallic-density electron plasma," Probl. Atom. Sci. Tech. **118**, 156 (2018).
[57] V.I. Maslov, D.S. Bondar, and I.N. Onishchenko, "Investigation of the Way of Phase Synchronization of a Self Injected Bunch and an Accelerating Wakefield in Solid-State Plasma," Photonics, **9**, 174 (2022). https://doi.org/10.3390/photonics9030174
[58] S.A. Akhmanov, A.P. Sukhorukov, and R.V. Khokhlov, "Self-focusing and diffraction of light in a nonlinear medium," Sov. Phys. Uspekhi, **10**, 609 (1968). (in Russian)
[59] M.S. Sodha, A.K. Ghatak, and V.K. Tripathi, *Progress in Optics*, (North Holland: Amsterdam, 1976).
[60] M.S. Sodha, A.K. Ghatak, and V.K. Tripathi, *Self Focusing of Laser Beams in Dielectrics, Semiconductors and Plasmas*, (Tata-McGraw-Hill, Delhi, 1974).

## СТИМУЛЬОВАНЕ КОМБІНАЦІЙНЕ РОЗСІЯННЯ ПОТУЖНОГО ПРОМЕНЯ В КВАНТОВІЙ ПЛАЗМІ: ВПЛИВ РЕЛЯТИВІСТСЬКО-ПОНДЕРОМОТОРНОЇ СИЛИ

**Кешав Валья, Таранджот Сінгх**
*Кафедра фізики, Університет DAV, Джаландхар, Індія*

У цій роботі досліджується вимушене комбінаційне розсіювання потужного променя в квантовій плазмі внаслідок спільної дії релятивістської пондеромоторної сили (RP force). RP сила створює нелінійність у діелектричній функції плазми. Це призводить до зміни профілю густини в поперечному напрямку до осі променя накачування. Ця зміна профілю густини має суттєвий вплив на всі три хвилі, що беруть участь у процесі, а саме: вхідний промінь, промінь електронної плазми та розсіяну хвилю. Встановлено та додатково чисельно розв'язано ODE другого порядку для всіх трьох хвиль, а також вираз для зворотного відбиття SRS. Досліджено вплив відомих параметрів лазерної плазми, квантового внеску та комбінованої дії пондемоторної сили на перетяжки пучка різних хвиль, а також на зворотне відбиття SRS.

**Ключові слова:** *релятивістсько-пондеромоторні сили; зворотне відбиття; електронно-плазмова хвиля; діелектрична функція; розсіяна хвиля*

East European Journal of Physics. **4**. 192–211 (2025)

DOI: 10.26565/2312-4334-2025-4-17 ISSN 2312-4334

# EMERGENCE OF LARGE-SCALE MAGNETIC-VORTICES STRUCTURES BY SMALL-SCALE HELICITY IN STRATIFIED MAGNETIZED PLASMA

**Michael I. Kopp**[1*], **Volodymyr V. Yanovsky**[1,2]

[1]*Institute for Single Crystals, NAS Ukraine, Nauky Ave. 60, Kharkiv, 61072, Ukraine*

[2]*V.N. Karazin Kharkiv National University, 4, Svoboda Sq., Kharkiv, 61022, Ukraine*

[*]*Corresponding Author e-mail: michaelkopp0165@gmail.com*

Received September 1, 2025; revised October 25, 2025; accepted November 5, 2025

In this paper, a new type of instability is identified, leading to the generation of vortex motions and magnetic fields in a plasma layer with a constant temperature gradient, subjected to uniform gravity and a vertical magnetic field. The analysis in this study is conducted within the framework of electron magnetohydrodynamics (EMHD), taking into account thermomagnetic effects. A new large-scale instability of the $\alpha$-effect type is identified, which facilitates the generation of large-scale vortex and magnetic fields. This instability arises due to the combined action of an external uniform magnetic field, oriented perpendicular to the plasma layer, and a small-scale helical force. The external force is modeled as a source of small-scale oscillations in the electron velocity field, characterized by a low Reynolds number ($R \ll 1$). The presence of a small parameter in the system allows for the application of the method of multiscale asymptotic expansions, leading to the derivation of nonlinear equations governing the evolution of large-scale vortex and magnetic perturbations. These equations are obtained at third order in the Reynolds number. A new effect associated with the influence of thermal forces (the Nernst effect) on large-scale instability is also discussed. It is shown that an increase in the Nernst parameter reduces the $\alpha$-coefficient and thereby suppresses the development of the large-scale instability. Using numerical analysis, stationary solutions of the vortex and magnetic dynamo equations are obtained in the form of localized helical-type structures.

**Keywords:** *electron magnetohydrodynamics, multiscale asymptotic expansions, small-scale force, $\alpha$-effect, localized structures*

**PACS:** 47.32.C, 47.35.Fg, 52.25.Xz

## 1. INTRODUCTION

The investigation of magneto-vortex structures in plasma is of significant importance for addressing challenges in controlled thermonuclear fusion as well as for understanding the formation of ordered structures in astrophysical plasmas. Magneto-vortex structures represent spatially localized configurations in which magnetic fields are strongly coupled with vortical plasma flows (velocity vortices). Such structures frequently emerge in turbulent plasma environments, where instabilities and nonlinear interactions between electric currents, magnetic fields, and hydrodynamic perturbations play a crucial role. A notable example of these interactions is the generation of magnetic fields by small-scale turbulent plasma motions with non-zero helicity $\overline{\mathbf{v}^T \mathrm{rot}\mathbf{v}^T} \neq 0$ – this process constitutes a dynamo mechanism that is fundamental to explaining the origin of magnetic fields in astrophysical objects such as planets, stars, and galaxies [1]-[6]. Helical turbulence, in this context, typically refers to turbulent states with broken parity symmetry [4]. From a physical standpoint, helical turbulence arises in systems where mirror symmetry is broken, which can occur due to various factors – most notably, the presence of external fields with pseudovector characteristics, such as magnetic fields (Lorentz force) or the Coriolis force.

Despite considerable progress in the theory of magnetic dynamos [5]-[6], several important issues remain insufficiently addressed. One such problem is the lack of a clear connection between the generation of seed magnetic fields and the turbulent dynamo process, since both problems are considered separately. A potential mechanism for the spontaneous generation of seed magnetic fields in plasmas with non-uniform temperature distributions is the Nernst effect [7]. This phenomenon is associated with the formation of a vortex-like electric field disturbance, $\mathbf{E}'_N \sim [\mathbf{B}' \times \nabla T_0]$, which is oriented orthogonally to both the background temperature gradient $\nabla T_0$ and the magnetic field perturbation $\mathbf{B}'$. Under non-dissipative conditions, Maxwell's equations can be employed to estimate the resulting magnetic field fluctuations induced by this effect as

$$\frac{\partial \mathbf{B}^{'}}{\partial t} = -c\,\mathrm{rot}\,\mathbf{E}_N^{'} \;\Rightarrow\; \frac{\partial \mathbf{B}^{'}}{\partial t} \sim \mathrm{rot}[\nabla T_0 \times \mathbf{B}^{'}].$$

Laser-produced plasmas provide a representative example where the Nernst effect plays a significant role. In such systems, intense laser irradiation ionizes and heats the target material, giving rise to a plasma with pronounced temperature gradients. These gradients create favorable conditions for the onset of the Nernst effect. A similar mechanism of magnetic field generation is also expected to operate in astrophysical environments, particularly in the outer layers of hot, massive stars, where strong temperature inhomogeneities are present [8].

---

***Cite as:*** M.I. Kopp, V.V. Yanovsky, East Eur. J. Phys. 4, 192 (2025), https://doi.org/10.26565/2312-4334-2025-4-17

Ref. [9] investigates the spontaneous generation of magnetic fields driven by Rayleigh-Benard convection in a thin plasma layer subjected to a uniform gravitational field. The seed magnetic fields are generated via a mechanism analogous to the Biermann battery effect [10]. However, unlike the classical Biermann mechanism, magnetic field excitation here occurs when temperature perturbations, $T'$, act along a direction misaligned with the background gravitational stratification $\mathbf{g}$. This misalignment gives rise to an eddy-induced electromotive force (EMF):

$$\mathbf{E}^{(i)} = -\frac{m}{e}\frac{T'}{T_0}\mathbf{g},$$

which contributes to magnetic field generation according to

$$\frac{\partial \mathbf{B}'}{\partial t} \approx \mathrm{rot}\mathbf{E}^{(i)} = \frac{mc}{e}\left[\frac{\nabla T'}{T_0}\times\mathbf{g}\right], \Rightarrow \quad B'_y \cong \frac{mc}{e}\frac{T'}{T_0}\frac{g}{\lambda}t_B,$$

where $\lambda$ is the characteristic scale of temperature perturbations, $t_B$ is the characteristic time of magnetic fields generation. Then this initial seed magnetic field acts to induce convective motion of charged particles (electrons and ions) in the stratified plasma. Thus the emergence of positive feedback between the magnetic field and temperature perturbations in the evolution equations is a key condition for the onset of thermomagnetic instability and, as a result, the generation of magnetic field. In a complementary study, Ref. [11] explores magnetic field generation in a fully ionized plasma, both in the presence and absence of an external magnetic field. The analysis incorporates the effects of convective heat transport and thermomagnetic phenomena and establishes criteria for the onset of instabilities that facilitate spontaneous magnetic field growth.

Another unresolved issue is the absence of a fully self-consistent nonlinear theory of the magnetic dynamo. As the magnetic field grows in strength, it begins to influence the plasma flows, thereby limiting the applicability of the kinematic dynamo theory. However, the magnetic fields observed in real astrophysical systems typically exist in a nonlinear regime, highlighting the necessity of developing and studying a nonlinear dynamo theory. The nonlinear theory is commonly formulated as an extension of the mean-field dynamo approach, incorporating nonlinear feedback mechanisms. In the review [6], a phenomenological model of the nonlinear dynamo – referred to as ”catastrophic quenching” – is discussed. This model is grounded in energy balance arguments and posits that the Lorentz force significantly alters the velocity field only when the magnetic energy becomes comparable to the kinetic energy of the turbulent flow. Accordingly, the model introduces a simplified phenomenological framework that includes a nonlinear dependence of the turbulent transport coefficients:

$$\alpha = \frac{\alpha_0}{1 + B_0^2/\mathcal{B}^2}, \quad \eta_T = \frac{\eta_0}{1 + B_0^2/\mathcal{B}^2},$$

where $\alpha_0$ and $\eta_0$ are the values of the transfer coefficients obtained in the kinematic approximation; $\eta_T$ – coefficient of turbulent magnetic viscosity, $B_0^2 = \overline{\mathbf{B}} \cdot \overline{\mathbf{B}}$ – mean field energy, $\mathcal{B}^2$ - kinetic energy of the flow. Reference [5] provides an in-depth analysis of numerical simulation results related to geodynamo and solar dynamo processes. It also introduces a magneto-rotational dynamo mechanism, where turbulence arises as a consequence of magnetohydrodynamic (MHD) instabilities. Furthermore, the review addresses emerging challenges in the theory of magnetic field generation in weakly collisional plasmas, highlighting current gaps and directions for future research. Nevertheless, Ref. [5] does not address regimes where high-frequency, small-scale electron oscillations – such as helicon waves – induce magnetic field restructuring in both space and laboratory plasmas. These rapid, localized processes involve only the electron component, evolving against a quasi-static background of ions. The monograph [3] describes several examples of magnetic field generation driven by Langmuir and ion-acoustic plasma oscillations. In turn, Ref. [12] explores the generation of mean magnetic fields by small-scale turbulence within the framework of electron magnetohydrodynamics (EMHD) with a two and one-half dimensional ($2\frac{1}{2}$D) model. In this approach, while the magnetic field retains all three spatial components, its variation is constrained to two dimensions due to the presence of a strong background field. It is demonstrated that the emergence of large-scale magnetic fields is intimately connected to the statistical properties of turbulence: the breaking of reflectional symmetry gives rise to the $\alpha$-effect, whereas turbulence anisotropy facilitates mechanisms akin to negative dissipation, including negative resistivity and viscosity.

One of the drawbacks of magnetic dynamo theory is that it depends on a simplified approach called the two-scale approximation of mean-field theory, making it harder to create a consistent nonlinear dynamo theory. An alternative approach, based on multiscale asymptotic expansions, was proposed in [13] to describe the generation of large-scale vortex structures (LSVSs) in non-mirror-symmetric turbulence. It was shown that small-scale parity violation due to external forcing leads to a large-scale instability known as the anisotropic kinetic alpha (AKA) effect. Further studies [14] explored the reverse energy cascade and nonlinear saturation of this instability. The effect is interpreted as a parametric instability arising from external periodic forcing $\mathbf{F}_0$, which induces small-scale velocity fluctuations $\mathbf{v}_0$. Their nonlinear interaction with large-scale flow $\mathbf{W}$ modifies the Reynolds stresses, allowing $\delta Tij$ to be expressed as a Taylor series in gradients of $\mathbf{W}$ [15]:

$$\delta T_{ij} = -\alpha_{ijl}W_l - \nu_{ijlm}\nabla_l W_m + O(\nabla^2\mathbf{W}) + \ldots$$

This expansion is valid under the condition of weak large-scale gradients, i.e., for small $\nabla\mathbf{W}$. To ensure the dominance of the first term in the series, one can estimate the tensors $\alpha_{ijl}$ and $\nu_{ijlm}$ using characteristic parameters of the small-scale turbulence. This yields the condition that the gradient scale of the large-scale field, defined as $L_g = (W^{-1}|\nabla \mathbf{W}|)^{-1}$, must be much larger than the turbulence scale $l_0$: $L_g \gg l_0$. The leading term in this expansion corresponds to the anisotropic kinetic $\alpha$-effect (AKA-effect), as described in [13], which accounts for the emergence of large-scale vortex structures (LSVS). Thus, an external force breaking parity at small scales can induce significant modifications in the large-scale flow. In contrast, Ref. [15] analyzed the case where the small-scale forcing is parity-invariant, leading to the suppression of the AKA-effect. In this regime, the interaction between small- and large-scale motions is governed primarily by eddy viscosity.

Using the method of multiscale asymptotic expansions, nonlinear theories of vortex dynamos have been developed for a range of hydrodynamic media, as outlined in Ref. [16]. In particular, Ref. [17] identified a large-scale instability in an electrically conducting, temperature-stratified medium driven by the helicity of small-scale velocity and magnetic fields. This instability gives rise to the simultaneous generation of large-scale vortex and magnetic fields. Building upon these results, Ref. [18] formulated a fully nonlinear, self-consistent theory of the magneto-vortex dynamo for a convective, electrically conducting medium with helical small-scale turbulence. Remarkably, this study demonstrated for the first time the possibility of stationary chaotic large-scale structures forming in both vortex and magnetic fields. The analysis revealed the emergence of stationary magnetic structures, which can be categorized into three distinct types: nonlinear waves, solitons, and kink-type solutions. Furthermore, qualitative estimates of the linear instability stage allowed for a comparison of the characteristic scales and times of the resulting hydrodynamic structures with those observed under solar conditions, as reported in Ref. [19], showing good agreement.

In this work, unlike [20], we investigate the generation of large-scale vortex and magnetic structures driven by small-scale helical forcing (turbulence) in a fully ionized, temperature-stratified plasma subjected to an external vertical magnetic field. The theoretical framework is based on the Braginskii equations for the electron component, with thermomagnetic effects explicitly taken into account. Plasma thermal convection is modeled using the Boussinesq approximation, incorporating an external helical force $\mathbf{F}_0$. Unlike the classical anisotropic kinetic $\alpha$-effect (AKA-effect), our analysis reveals a novel plasma $\alpha$-effect arising in a magnetized plasma with a constant temperature gradient and gravitational field, induced by external helical forcing.

The structure of this paper is as follows. In Section 2, we formulate the problem and derive the governing equations in dimensionless form. Section 3 presents the derivation of the averaged equations for large-scale velocity and magnetic fields in a magnetized, stratified plasma using the method of multiscale asymptotic expansions. The detailed procedure for constructing the asymptotic expansion is provided in Appendix A. The correlation functions appearing in the averaged equations are expressed through the small-scale fields obtained in the zeroth-order approximation with respect to the Reynolds number $R$. The corresponding solutions for the small-scale fields are given in Appendix B. Based on these, the closed-form nonlinear equations describing the vortex and magnetic dynamo are derived in Appendix C. In Section 4, we present the final system of equations governing large-scale velocity and magnetic field perturbations, which describe the hydrodynamic $\alpha$-effect instability. The conditions for the onset of this instability are analyzed as functions of the external magnetic field strength $D$, the Rayleigh number $Ra$, and the Nernst effect parameter. Section 5 provides a numerical investigation of the steady-state nonlinear magneto-vortex dynamo equations, demonstrating the formation of vortex and magnetic structures in the form of helical kink-type solutions.

## 2. PROBLEM STATEMENT AND BASIC EQUATIONS

We consider a fully ionized plasma layer placed in constant gravitational and uniform magnetic fields, denoted by $\mathbf{g}$ and $\overline{\mathbf{B}}$, respectively. The plasma is assumed to possess a steady-state temperature gradient $\nabla\overline{T}$. In the undisturbed state, no fluid motion is present. The development of perturbations is assumed to occur on timescales short enough that ions can be regarded as stationary and thermally inactive. The behavior of the perturbed electron component is analyzed within the framework of the Braginskii equations [21]:

$$\frac{\partial \mathbf{V}}{\partial t} + (\mathbf{V}\nabla)\,\mathbf{V} = -\frac{e}{m}\left(\mathbf{E} + \frac{1}{c}\left[\mathbf{V}\times\mathbf{B}\right]\right) - \frac{1}{m\overline{N}}\nabla P + \frac{1}{m\overline{N}}\left(\mathbf{R}_\nu + \mathbf{R}_T\right) + \frac{\mathbf{F}_\eta}{m\overline{N}} + \frac{\mathbf{F}_g}{m\overline{N}}, \tag{1}$$

$$\frac{\partial T}{\partial t} + (\mathbf{V}\nabla)T = -\frac{2}{3}\frac{\mathrm{div}\mathbf{q}}{\overline{N}}, \quad P = \overline{N}T, \tag{2}$$

$$\mathrm{div}\mathbf{V} = 0. \tag{3}$$

Here $P, \overline{N}, T, \mathbf{V}$ denote the pressure, average density, temperature, and velocities of electrons. In the electron momentum equation (1), several physical effects are taken into account: electron collisions, described by the friction force $\mathbf{R}_\nu$; momentum exchange due to the temperature gradient, represented by the thermal force $\mathbf{R}_T$; viscous effects in the electron fluid, captured by the force $\mathbf{F}_\eta$; and the gravitational contribution $\mathbf{F}_g$. Importantly, the corresponding transport coefficients in the presence of a magnetic field depend on the magnetization parameter $\omega_{Be}\tau$, where $\omega_{Be} = eB/mc$ is the electron gyrofrequency. In the strongly magnetized limit ($\omega_{Be}\tau \gg 1$), the friction and thermal forces, $\mathbf{R}_\nu$ and $\mathbf{R}_T$, respectively, are expressed in specific forms:

$$\frac{\mathbf{R}_\nu}{m\overline{N}} = -0.51\nu\mathbf{V}_\parallel - \nu\mathbf{V}_\perp \tag{4}$$

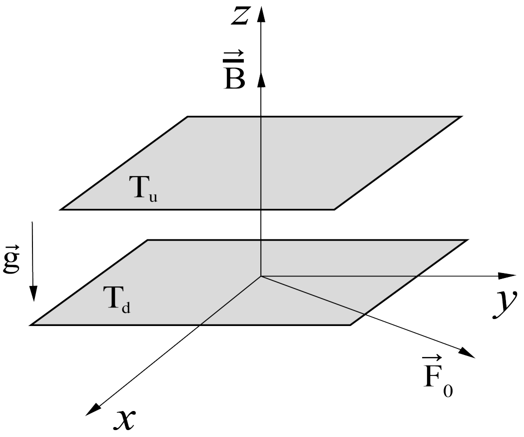

**Figure 1.** The diagram shows a thin layer of plasma with a vertical equilibrium temperature gradient: $T_d > T_u$ (signaling heating from below). The induction vector $\overline{\mathbf{B}}$ of a uniform magnetic field has direction along the $z$-axis, and the external force $\mathbf{F}_0$ is situated in the plane $(x, y)$.

$$\frac{\mathbf{R}_T}{m\overline{N}} = -0.71\frac{\nabla_{\|}T}{m} - \frac{3}{2}\frac{e\nu}{m^2 c\omega_{Be}^2}[\mathbf{B}\times\nabla T] \tag{5}$$

The symbols $\|$ and $\perp$ denote the directional orientation along and across the magnetic field, respectively. The thermal electron flow is similarly composed of two components, denoted as $\mathbf{q} = \mathbf{q}_\nu + \mathbf{q}_T$:

$$\mathbf{q}_\nu = 0.71\overline{N}T\mathbf{V}_{\|} + \frac{3e}{2mc}\frac{\nu\overline{N}T}{\omega_{Be}^2}[\mathbf{B}\times\mathbf{V}] \tag{6}$$

$$\mathbf{q}_T = -3.16\frac{\overline{N}T\tau}{m}\nabla_{\|}T - 4.66\frac{\overline{N}T\nu}{m\omega_{Be}^2}\nabla_{\perp}T - \frac{5}{2}\frac{e\overline{N}T}{cm^2\omega_{Be}^2}[\mathbf{B}\times\nabla T] \tag{7}$$

In expressions (4)-(7), the parameter $\nu \approx \tau^{-1}$ denotes the electron collision frequency. In a fully ionized plasma, the relative velocities involved in electron-electron and electron-ion collisions are of the same order. As a result, the frequency of electron-electron collisions ($\nu_{ee} \approx \tau_e^{-1}$ or $\nu \approx \tau^{-1}$) is comparable to the electron-ion collision frequency ($\nu_{ei} \approx \tau_{ei}^{-1}$).

Next, we supplement the equations (1)-(3) with Faraday's law

$$\mathrm{rot}\mathbf{E} = -\frac{1}{c}\frac{\partial\mathbf{B}}{\partial t}, \tag{8}$$

Ampere's law

$$\mathrm{rot}\mathbf{B} = -\frac{4\pi e\overline{N}}{c}\mathbf{V}, \tag{9}$$

and magnetic field solenoidality equation

$$\mathrm{div}\mathbf{B} = 0. \tag{10}$$

We now formulate the problem, the geometry of which is illustrated in Fig. 1. To describe the dynamics of the electron fluid, we adopt a Cartesian coordinate system with the $Z$-axis oriented vertically upward. The system under consideration is a horizontally extended plasma layer of finite thickness $h$, bounded above and below by free surfaces at $z = h$ and $z = 0$, respectively. The lower boundary at $z = 0$ is maintained at temperature $T_d$, while the upper boundary at $z = h$ is kept at a lower temperature $T_u$, such that $T_d > T_u$, implying that the layer is heated from below. The equilibrium temperature distribution $\overline{T}(z)$ is assumed to vary linearly along the vertical direction:

$$\overline{T}(z) = T_d - \frac{(T_d - T_u)}{h}z.$$

Consequently, the equilibrium temperature gradient is constant and directed downward: $\nabla\overline{T} = \mathrm{const} = -\mathbf{e}(d\overline{T}/dz) = -\mathbf{e}A$, where $\mathbf{e}$ is a unit vector along the $Z$-axis pointing upward, and the gravitational acceleration is given by $\mathbf{g} = -g\mathbf{e}$. Initially, the plasma layer is assumed to be at rest. Convection is triggered by introducing small perturbations to the equilibrium state. All relevant physical quantities appearing in Eqs. (1)-(3) are thus represented as the sum of a stationary background and a small disturbance:

$$\mathbf{V} = \mathbf{V}', \ \mathbf{E} = \mathbf{E}', \ \mathbf{B} = \overline{\mathbf{B}} + \mathbf{B}', \ T = \overline{T} + T', \ P = \overline{P} + P'.$$

The equilibrium electron density is assumed to be uniform throughout the layer, $\overline{N}$ = const, and perturbations in the density, $N'$, are related to temperature perturbations $T'$ via the Boussinesq approximation [22]: $N'/\overline{N} \approx -T'/\overline{T}$. Under this approximation, the gravitational force term in Eq. (1) reduces to a contribution that depends linearly on the temperature perturbation:

$$\frac{\mathbf{F}_g}{m\overline{N}} = \frac{N'}{\overline{N}}\mathbf{g} = -\frac{T'}{\overline{T}}\mathbf{g}. \tag{11}$$

The viscous force $\mathbf{F}_\eta$ in equation (1) can be written as [21]

$$\frac{\eta_e}{m\overline{N}}\nabla^2\mathbf{V}' = 0.73\frac{\overline{T}\tau}{m}\nabla^2\mathbf{V}' = \nu\nabla^2\mathbf{V}',$$

where $\nu$ is the coefficient of kinematic viscosity of the electronic fluid. Below in the text, for convenience, we omit the "prime" sign above the perturbed values $\mathbf{V}, T, P, \mathbf{E}$, and $\mathbf{B}$. In the equilibrium (unperturbed) state, the plasma satisfies the condition of hydrostatic balance:

$$\frac{1}{m}\frac{d\overline{T}}{dz} = g - \frac{0.71}{m}\frac{d\overline{T}}{dz},$$

and no background electric field is present, i.e., $\overline{\mathbf{E}} = 0$. The magnetic field is assumed to be uniform and directed vertically upward, perpendicular to the $(x, y)$ plane: $\overline{\mathbf{B}} = \mathbf{e}\overline{B}$. To model turbulent processes in the plasma, we introduce an external force $\mathbf{F}_0$ into Eq. (1). This force acts as a driver of small-scale, high-frequency oscillations in the electron velocity field, denoted by $\widetilde{\mathbf{v}}_0$, and operates in a regime characterized by a low Reynolds number, $R = \widetilde{v}_0 t_0/\lambda_0 \ll 1$. An analogous dimensionless parameter, the Strouhal number $S = u\tau_c/\lambda_c$ – where $u$ is the turbulent velocity, and $\tau_c$ and $\lambda_c$ are characteristic temporal and spatial correlation scales is commonly used in magnetic dynamo theory [2] to justify the second-order correlation approximation. A relevant physical system in which the condition $R \ll 1$ (or equivalently $S \ll 1$) holds is the solar convective zone. Using observational data on small-scale turbulence in solar granules [2], one obtains:

$$\widetilde{v}_0 \approx 3\cdot 10^2 m/s,\ t_0 \approx 3\cdot 10^2 s,\ \lambda_0 \approx 10^6 m,$$

yielding an estimate of the Reynolds number $R \approx 10^{-1} \ll 1$. Let us consider an external helical force $\mathbf{F}_0$ with the following properties:

1. The vector field $\mathbf{F}_0$ is solenoidal, i.e., it is divergence-free: $\mathrm{div}\mathbf{F}_0 = 0$.
2. The vector field $\mathbf{F}_0$ possesses vorticity: $\mathrm{rot}\mathbf{F}_0 \neq 0$.
3. The helicity of $\mathbf{F}_0$ is nonzero, indicating a helical property: $\mathbf{F}_0\mathrm{rot}\mathbf{F}_0 \neq 0$.

We define the functional form of the external force as

$$\mathbf{F}_0 = f_0\mathbf{F}_0\left(\frac{x}{\lambda_0}; \frac{t}{t_0}\right),$$

where $\lambda_0$ is the characteristic spatial scale, $t_0$ is the characteristic temporal scale, and $f_0$ denotes the typical amplitude of the force. The external force $\mathbf{F}_0$ induces small-scale oscillations in the velocity field, denoted by $\widetilde{\mathbf{v}}_0$, which are characterized by

$$\widetilde{\mathbf{v}}_0 = \widetilde{v}_0\widetilde{\mathbf{v}}_0\left(\frac{\mathbf{x}}{\lambda_0}, \frac{t}{t_0}\right),$$

where $\widetilde{v}_0$ is the characteristic velocity. Assuming that the external force $\mathbf{F}_0$ satisfies the properties listed in (4), it can be explicitly prescribed in the following deterministic form:

$$F_0^z = 0, \quad \mathbf{F}_{0\perp} = f_0\left(\mathbf{e}_x\cos\phi_2 + \mathbf{e}_y\cos\phi_1\right), \tag{12}$$

where the phases $\phi_1$ and $\phi_2$ are defined as

$$\phi_1 = \mathbf{k}_1\mathbf{x} - \omega_0 t, \quad \phi_2 = \mathbf{k}_2\mathbf{x} - \omega_0 t,\ \mathbf{k}_1 = k_0(1,0,1), \quad \mathbf{k}_2 = k_0(0,1,1).$$

The dynamo mechanism operates through the process of energy transfer from small-scale turbulent motions to large-scale flows. The role of the external small-scale force $\mathbf{F}_0$ incorporated into the electron motion equations is to maintain the necessary level of turbulence as a driving source. This force can be specified statistically by defining its correlator:

$$\overline{F_{0i}F_{0m}} = A\delta_{im} + Br_i r_m + H\epsilon_{imn}r_n.$$

However, the statistical approach is considerably more cumbersome, as it requires specifying the functions $A, B$, and $H$, and computing rather complex integrals. When the external force is specified dynamically (as in Eq. 12), averaging over rapid oscillations becomes straightforward, which significantly reduces the computational complexity of the problem.

Let us transform equations (1)-(3) and (9)-(11) into a dimensionless form by introducing the following dimensionless variables

$$\mathbf{x} \longrightarrow \frac{\mathbf{x}}{\lambda_0}, \quad t \longrightarrow \frac{t}{t_0}, \quad \mathbf{V} \longrightarrow \frac{\mathbf{V}}{\widetilde{v}_0}, \quad \mathbf{F}_0 \longrightarrow \frac{\mathbf{F}_0}{f_0}, \quad \mathbf{B} \longrightarrow \frac{\mathbf{B}_1}{b_0}, \quad T \longrightarrow \frac{T_1}{\lambda_0 A}, \quad P \longrightarrow \frac{P_1}{p_0}. \tag{13}$$

Here, $\widetilde{v}0$, $b0$, and $p_0$ are the characteristic values of small-scale fluctuations of velocity, magnetic field, and pressure, respectively. When transitioning to the dimensionless form of equations (1)-(3) and (8)-(10), it is helpful to introduce a set of relations that connect the turbulent parameters $t_0$ and $\lambda_0$ of the medium:

$$t_0 = \frac{\lambda_0^2}{\nu}, \quad f_0 = \frac{\widetilde{v}_0 \nu}{\lambda_0^2}, \quad p_0 = m\overline{N}\frac{\widetilde{v}_0 \nu}{\lambda_0}, \quad \frac{f_0 t_0}{\widetilde{v}_0} = \frac{cE_0 t_0}{\lambda_0 b_0} = 1,$$

$$\frac{\lambda_0^2 m}{0.73\overline{T}\tau^2} = 1, \; \frac{eE_0 t_0}{m\widetilde{v}_0} = \frac{eb_0\lambda_0}{mc\widetilde{v}_0} = \frac{\lambda_0 \widetilde{v}_0 m\omega_{pe}^2}{eb_0 c} = R^2, \; \frac{\lambda_0^2}{r_d^2} = R^4, \tag{14}$$

where $r_d = c/\omega_{pe}$ is the Debye radius, and $\omega_{pe} = \sqrt{4\pi e^2 N_0/m}$ is the electron plasma (Langmuir) frequency. These relations significantly simplify the resulting dimensionless equations, facilitating further mathematical treatment. The first group of relations in (2) is derived from the Navier-Stokes equation (1). The remaining expressions are obtained by applying scaling and dimensional analysis for convenience. The final set of relations is chosen such that a self-consistent system of equations for large-scale perturbations emerges in the leading order of the asymptotic expansion. Upon applying the transformations (13) and (2) to equations (1)-(3), (8)-(10), and introducing a rescaled temperature $T \longrightarrow T/R$, we arrive at the desired system of dimensionless equations:

$$\frac{\partial \mathbf{V}}{\partial t} + R\,(\mathbf{V}\nabla)\,\mathbf{V} = -\nabla P - R^2\mathbf{E} - D[\mathbf{V}\times\mathbf{e}] - R^3[\mathbf{V}\times\mathbf{B}] + \mathbf{e}\widetilde{Ra}T - \mathbf{V}-$$

$$-\widetilde{Ra}\left(\frac{V_{Te}^2}{g\lambda_0}\right)\left(0.71\nabla T + \frac{3}{2}\widetilde{\xi}D[\mathbf{e}\times\nabla T]\right) + \nu\nabla^2\mathbf{V} + \mathbf{F}_0, \tag{15}$$

$$\frac{\partial T}{\partial t} + R(\mathbf{V}\nabla)T - \left(1 + \frac{5}{3}Pr^{-1}\xi R\right)\mathbf{e}\mathbf{V} = 2.1Pr^{-1}\nabla^2 T + \frac{5}{3}Pr^{-1}\xi(\nabla T\mathrm{rot}\mathbf{B}), \tag{16}$$

$$\mathrm{div}\mathbf{V} = 0, \quad \mathrm{div}\mathbf{B} = 0, \tag{17}$$

$$\frac{\partial \mathbf{B}}{\partial t} = -\mathrm{rot}\mathbf{E}, \quad \mathrm{rot}\mathbf{B} = -R^2\mathbf{V}. \tag{18}$$

The equations (2)-(16) have the following notation: $\xi = (\omega_{Be}\tau)^{-1}$ represents the reciprocal of the Hall parameter; $\mathbf{D} = D\mathbf{e}$, $D = (e\overline{B}t_0)/mc = (\omega_{Be}{\lambda_0}^2)/\nu$ is the electron rotation parameter on the scale $\lambda_0$; $\widetilde{Ra} = \frac{Ra}{Pr}$, $Ra = \frac{gA\lambda_0^4}{\overline{T}\nu\chi}$ is the Rayleigh number on the scale $\lambda_0$; $\chi$ is the thermal diffusivity coefficient of electrons; $V_{Te}$ is the thermal velocity of electrons, $Pr = \nu/\chi$ is the Prandtl number; $\widetilde{\xi} = \nu/(\omega_{Be}^2\lambda_0^2\tau)$ is a parameter characterizing the influence of the Nernst effect. As follows, we call $\widetilde{\xi}$ the Nernst parameter.

In this study, we treat the Reynolds number $R = \frac{v_0 t_0}{\lambda_0}$ as a small expansion parameter, assuming $R \ll 1$. The parameters $D$, $\widetilde{Ra}$, and $Pr$ are considered to be of arbitrary magnitude. The smallness of $R$ justifies the application of the method of multiscale asymptotic expansions, as described in [4, 13]. This technique differs from the traditional mean-field approach in that it allows for a consistent description of how perturbations evolve across various spatial and temporal scales at each order of the expansion. At the zeroth order of $R$, small-scale rapidly varying velocity fluctuations $\mathbf{v}_0$ arise due to the action of the external force $\mathbf{F}_0$ on a stationary background. The behavior of these fluctuations is shaped by factors such as vertical stratification and the ambient magnetic field. Although the time-averaged values of these fluctuations are zero, nonlinear effects in higher orders can generate contributions that remain finite upon averaging, thereby influencing the dynamics of the system on larger scales.

The following section outlines the procedure for deriving solvability conditions in the framework of multiscale expansions, which ultimately yield the governing equations for large-scale perturbations.

## 3. EQUATIONS FOR LARGE-SCALE VORTEX AND MAGNETIC FIELDS

To derive the multiscale asymptotic equations, we introduce a set of fast (small-scale) variables $x_0 = (\mathbf{x}_0, t_0)$, alongside slow (large-scale) variables $X = (\mathbf{X}, T)$. For convenience, we denote derivatives with respect to the fast spatial and temporal variables as $\partial_i = \frac{\partial}{\partial x_0^i}$ and $\partial_t = \frac{\partial}{\partial t_0}$, respectively. Correspondingly, the derivatives with respect to the slow (large-scale) spatial and temporal coordinates are written as:

$$\frac{\partial}{\partial X_i} \equiv \nabla_i, \quad \frac{\partial}{\partial T} \equiv \partial_T.$$

The scaling of slow variables relative to the fast ones is chosen as follows:

$$\mathbf{X} = R^2 \mathbf{x}_0, \quad T = R^4 t_0,$$

where $R \ll 1$ is the small expansion parameter introduced earlier. Using these variable transformations, the differential operators in the governing equations (2)–(18) can be rewritten in a form suitable for asymptotic expansion:

$$\frac{\partial}{\partial x_i} \to \partial_i + R^2 \nabla_i, \quad \frac{\partial}{\partial t} \to \partial_t + R^4 \partial_T \tag{19}$$

The physical quantities $\mathbf{V}, \mathbf{E}, \mathbf{B}, P$, and $T$ are expressed as asymptotic expansions in powers of the small parameter $R$:

$$\begin{gathered}
\mathbf{V}(\mathbf{x}, t) = \frac{1}{R} \mathbf{W}_{-1}(X) + \mathbf{v}_0 + R\mathbf{v}_1 + R^2 \mathbf{v}_2 + R^3 \mathbf{v}_3 + \cdots \\
\mathbf{E}(\mathbf{x}, t) = \frac{1}{R} \mathbf{E}_{-1}(X) + \mathbf{E}_0 + R\mathbf{E}_1 + R^2 \mathbf{E}_2 + R^3 \mathbf{E}_3 + \cdots \\
\mathbf{B}(\mathbf{x}, t) = \frac{1}{R} \mathbf{B}_{-1}(X) + \mathbf{B}_0 + R\mathbf{B}_1 + R^2 \mathbf{B}_2 + R^3 \mathbf{B}_3 + \cdots \\
T(\mathbf{x}, t) = \frac{1}{R} T_{-1}(X) + T_0(x_0) + RT_1 + R^2 T_2 + R^3 T_3 + \cdots \\
P(\mathbf{x}, t) = \frac{1}{R^3} P_{-3} + \frac{1}{R^2} P_{-2} + \frac{1}{R} P_{-1} + P_0(x_0) + R(P_1 + \overline{P}_1(X)) + \\
+ R^2 P_2 + R^3 P_3 + \cdots
\end{gathered} \tag{20}$$

In the asymptotic expansions (20), the large-scale components depend solely on the slow variables $X$, whereas the remaining terms involve both the fast variables $x_0$ and the slow variables $X$. We now substitute the expansions (19) and (20) into the system of equations (2)–(18), and collect terms up to and including order $R^3$. The resulting set of equations is rather lengthy and is therefore presented in Appendix A. The main secular equations (solvability conditions), which ensure the consistency of the multiscale asymptotic expansion for the system (2)–(18), are given by:

$$\partial_T W^i_{-1} + \nabla_k \left( \overline{v_0^k v_0^i} \right) = -\nabla_i \overline{P}_1 - \overline{E}^i_1 + \nabla_k^2 W^i_{-1}, \tag{21}$$

$$\partial_T T_{-1} - 2.1 Pm^{-1} \nabla^2 T_{-1} = -1.47 \nabla_k \left( \overline{v_0^k T_0} \right), \tag{22}$$

$$\partial_T B^i_{-1} = -\varepsilon_{ijk} \nabla_j \overline{E}^k_1. \tag{23}$$

Equations (21)–(23) are supplemented by the secular equations derived in Appendix A:

$$-\nabla_i P_{-3} - D\varepsilon_{ijk} W_j e_k + e_i \widetilde{Ra} T_{-1} - W^i_{-1} = 0, \tag{24}$$

$$W^z_{-1} = 0, \ \nabla_i W^i_{-1} = 0, \ \nabla_i B^i_{-1} = 0, \ (\nabla \times \mathbf{B}_{-1})_z = 0 \tag{25}$$

$$\begin{gathered}
W^k_{-1} \nabla_k W^i_{-1} = -\nabla_i P_{-1} - E^i_{-1} - \varepsilon_{ijk} W^j_{-1} B^k_{-1} - \\
-\widetilde{Ra}_1 \left( 0.71 \nabla_i T_{-1} + \frac{3}{2} \tilde{\xi} D \varepsilon_{ijk} e_j \nabla_k T_{-1} \right),
\end{gathered} \tag{26}$$

$$W^k_{-1} \nabla_k T_{-1} = 0, \ \varepsilon_{ijk} \nabla_j E^k_{-1} = 0, \ \varepsilon_{ijk} \nabla_j B^k_{-1} = -W^i_{-1}. \tag{27}$$

The primary secular equations that dictate the development of large-scale vortex and magnetic perturbations are represented by Eqs. (21)-(23). In these equations, the overbar signifies averaging over the rapid variables. The extensive temperature $T_{-1}$ does not influence the dynamics of the extensive velocity field $\mathbf{W}_{-1}$ or the magnetic field $\mathbf{B}_{-1}$. Consequently, our analysis will concentrate on equations (21) and (23). In this paper, we focus on large-scale structures characterized by horizontal dimensions $L_X, L_Y$ that are much greater than the vertical dimension $L_Z$:

$$L_X, L_Y \gg L_Z \gg \lambda_0, \quad \text{or} \quad \varepsilon \cong \left( \frac{L_Z}{L_X}, \frac{L_Z}{L_Y} \right) \ll 1, \quad \frac{\lambda_0}{L_Z} \ll 1, \tag{28}$$

where $\varepsilon$ denotes the scale anisotropy parameter. This scaling relationship clearly indicates that derivatives with respect to $Z$ dominate over those with respect to the horizontal coordinates:

$$\nabla_Z \equiv \frac{\partial}{\partial Z} \gg \frac{\partial}{\partial X}, \frac{\partial}{\partial Y}.$$

Given that the two equations in (25) imply that the large-scale velocity field is two-dimensional and incompressible, and taking into account the scale relations in (28), we assume that all large-scale perturbations depend solely on the vertical coordinate $Z$. Thus, the velocity and magnetic fields are represented as

$$\mathbf{W}_{-1} = \left(W^x_{-1}(Z),\, W^y_{-1}(Z),\, 0\right), \quad \mathbf{B}_{-1} = \left(B^x_{-1}(Z),\, B^y_{-1}(Z),\, 0\right). \tag{29}$$

Then, taking into account the expressions (29), the equations for the large-scale fields (21)-(23) take the following form:

$$\partial_T W_1 + \nabla_Z \left(\overline{v_0^z v_0^x}\right) = -\overline{E}_1^x + \nabla_Z^2 W_1, \quad W^x_{-1} \equiv W_1, \tag{30}$$

$$\partial_T W_2 + \nabla_Z \left(\overline{v_0^z v_0^y}\right) = -\overline{E}_1^y + \nabla_Z^2 W_2, \quad W^y_{-1} \equiv W_2, \tag{31}$$

$$\partial_T B_1 = \nabla_Z \overline{E}_1^y, \quad B^x_{-1} \equiv B_1, \tag{32}$$

$$\partial_T B_2 = -\nabla_Z \overline{E}_1^x, \quad B^y_{-1} \equiv B_2, \tag{33}$$

$$\nabla_Z B_2 = W_1, \quad \nabla_Z B_1 = -W_2. \tag{34}$$

The derivation of the closed form of equations (30)-(31) requires the computation of the Reynolds stress terms $T^{31} = \overline{v_0^z v_0^x}$ and $T^{32} = \overline{v_0^z v_0^y}$. This, in turn, involves determining the small-scale velocity field $\mathbf{v}_0$, as outlined in Appendix B. By substituting equations (32)-(34) into equations (30)-(31), the mean electric field $\overline{E}_1^{x,y}$ is eliminated. As a result, equations (30)-(31) are transformed into a system resembling a nonlinear vortex dynamo:

$$\partial_T(\nabla_Z^2 W_1 - W_1) + \nabla_Z^3 T^{31} = \nabla_Z^4 W_1,$$

$$\partial_T(\nabla_Z^2 W_2 - W_2) + \nabla_Z^3 T^{32} = \nabla_Z^4 W_2. \tag{35}$$

According to Ampere's law (34), large-scale perturbations of the magnetic field are driven by large-scale vortical motions of electrons. Consequently, the nonlinear evolution of large-scale magnetic fields is governed by the following set of nonlinear equations:

$$\partial_T(\nabla_Z^2 B_1 - B_1) - \nabla_Z^2 T^{32} = \nabla_Z^4 B_1,$$

$$\partial_T(\nabla_Z^2 B_2 - B_2) + \nabla_Z^2 T^{31} = \nabla_Z^4 B_2. \tag{36}$$

Appendix C presents the calculation of the Reynolds stresses (6), which enables the closure of system (3), and, consequently, (3). The nonlinear magnetic-vortex dynamo is described by the following set of equations:

$$\partial_T(\nabla_Z^2 W_1 - W_1) - \nabla_Z^4 W_1 =$$

$$= \frac{f_0^2}{8}\nabla_Z^3\left[\frac{D^2}{36(1-W_1)^2 + \left[\frac{D^2}{2} + 9 - (1-W_1)^2\right]^2 + \Xi_1^{(1)} - \widetilde{\xi}\,\Xi_1^{(2)} + \widetilde{\xi}\,\Xi_1^{(3)}}\right] +$$

$$+\frac{f_0^2}{2}\nabla_Z^3\left[\frac{D\left(\frac{3}{2} - \frac{1.05Ra}{17.64+Pr^2(1-1.47W_2)^2}\right)}{36(1-W_2)^2 + \left[\frac{D^2}{2} + 9 - (1-W_2)^2\right]^2 + \Xi_2^{(1)} - \widetilde{\xi}\,\Xi_2^{(2)} + \widetilde{\xi}\,\Xi_2^{(3)}}\right], \tag{37}$$

$$\partial_T(\nabla_Z^2 W_2 - W_2) - \nabla_Z^4 W_2 =$$

$$= \frac{f_0^2}{8}\nabla_Z^3\left[\frac{D^2}{36(1-W_2)^2 + \left[\frac{D^2}{2} + 9 - (1-W_2)^2\right]^2 + \Xi_2^{(1)} - \widetilde{\xi}\,\Xi_2^{(2)} + \widetilde{\xi}\,\Xi_2^{(3)}}\right] -$$

$$-\frac{f_0^2}{2}\nabla_Z^3\left[\frac{D\left(\frac{3}{2} - \frac{1.05Ra}{17.64+Pr^2(1-1.47W_1)^2}\right)}{36(1-W_1)^2 + \left[\frac{D^2}{2} + 9 - (1-W_1)^2\right]^2 + \Xi_1^{(1)} - \widetilde{\xi}\,\Xi_1^{(2)} + \widetilde{\xi}\,\Xi_1^{(3)}}\right], \tag{38}$$

where

$$\Xi_{1,2}^{(1)} = Ra(9 + (1-W_{1,2})^2)\cdot\frac{Pr\widetilde{W}_{1,2}\widetilde{\widetilde{W}}_{1,2} - 12.6 + \frac{Ra}{4}}{17.64 + Pr^2\widetilde{\widetilde{W}}_{1,2}^{\,2}},\ \widetilde{W}_{1,2} = 1 - W_{1,2},\ \widetilde{\widetilde{W}}_{1,2} = 1 - 1.47W_{1,2},$$

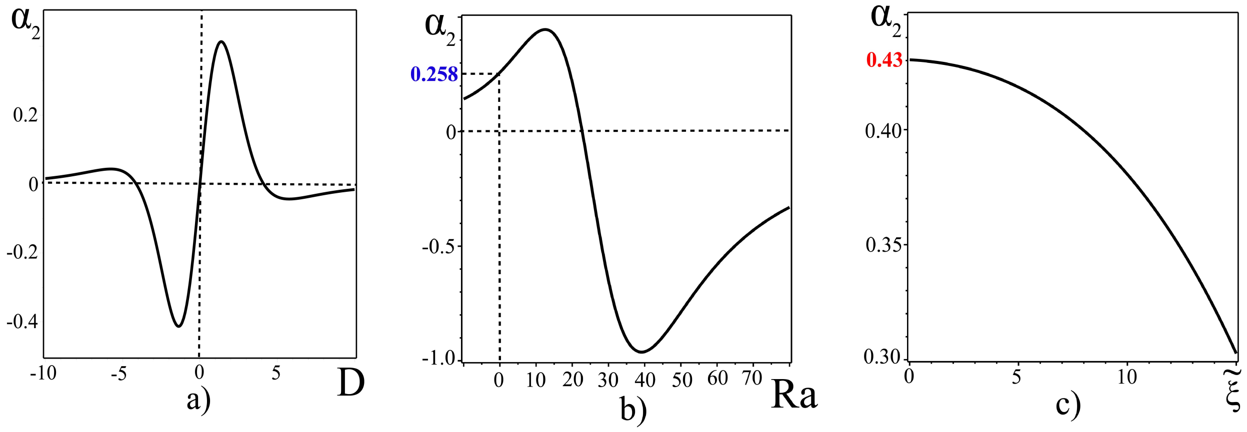

**Figure 2.** The $\alpha$-effect's dependence versus a) magnetic parameter $D$, b) stratification parameter $Ra$, and c) Nernst parameter $\widetilde{\xi}$.

$$\Xi^{(2)}_{1,2} = \frac{3}{2} D^2 Ra_1 \cdot \frac{25.2\widetilde{W}_{1,2} + Pr(9 - \widetilde{W}^2_{1,2})\widetilde{\widetilde{W}}_{1,2}}{17.64 + Pr^2 \widetilde{\widetilde{W}}^2_{1,2}}, \; \Xi^{(3)}_{1,2} = \frac{D^4}{4} \cdot \frac{Ra_1}{17.64 + Pr^2 \widetilde{\widetilde{W}}^2_{1,2}} \left( \frac{9}{4} \widetilde{\xi} Ra_1 - 3Pr \widetilde{\widetilde{W}}_{1,2} \right).$$

As seen from equations (3)-(3), the vortex dynamo effect in a stratified plasma can emerge under the combined influence of an external small-scale helical force and a magnetic field. In the absence of an external magnetic field, even in the presence of turbulence, large-scale perturbations of the electron velocity undergo ordinary viscous damping.

We first address the linear stability of small field perturbations, followed by an analysis of potential stationary structures.

## 4. LARGE-SCALE INSTABILITY

In this section, we address the stability of small-scale perturbations in both the velocity and magnetic fields. By applying expressions (6) to equations (3), we obtain the following set of linear equations describing the vortex dynamo:

$$\partial_T(\nabla^2_Z W_1 - W_1) - \nabla^4_Z W_1 = \alpha_1 \nabla^3_Z W_1 + \alpha_2 \nabla^3_Z W_2,$$
$$\partial_T(\nabla^2_Z W_2 - W_2) - \nabla^4_Z W_2 = \alpha_1 \nabla^3_Z W_2 - \alpha_2 \nabla^3_Z W_1, \tag{39}$$

here,

$$\alpha_1 = \frac{f_0^2}{8} D^2 \alpha, \; \alpha_2 = \frac{f_0^2}{2} D(\alpha\sigma_0 - \alpha_0\sigma_1),$$
$$\alpha_0 = \frac{4}{(D^2+16)^2 + 144 + 40a_0 Ra + 4\widetilde{\xi}(m_0 - c_0)},$$
$$\alpha = \frac{32(20 - D^2 + Ra(a_0 - 5b_0) + \frac{\widetilde{\xi}}{2}(d_0 - n_0))}{\left[(D^2+16)^2 + 144 + 40a_0 Ra + 4\widetilde{\xi}(m_0 - c_0)\right]^2}.$$

The explicit form of the coefficients $\sigma_0, \sigma_1, a_0, b_0, c_0, d_0, m_0, n_0$ can be found in Appendix C. We seek a solution to the linear system of equations (4) in the form of plane waves with a wave vector $K$ aligned along the $Z$-axis, i.e.,

$$W_{1,2} = A_{W_{1,2}} \exp(-i\omega T + iKZ) \tag{40}$$

Substituting expression (40) into the system of equations (4), we obtain the corresponding dispersion relation:

$$\left(i\omega(1+K^2) - K^4 + i\alpha_1 K^3\right)^2 - \alpha_2^2 K^6 = 0 \tag{41}$$

By representing $\omega = \omega_0 + i\Gamma$ in equation (41), we get:

$$\omega_0 = -\frac{\alpha_1 K^3}{1+K^2}, \quad \Gamma_{1,2} = \frac{\mp\alpha_2 K^3 - K^4}{1+K^2}. \tag{42}$$

The solutions given by (42) indicate the presence of unstable oscillatory modes associated with large-scale vortex disturbances. It is important to emphasize that, within the framework of linear theory, the coefficients $\alpha_1$ and $\alpha_2$ are independent

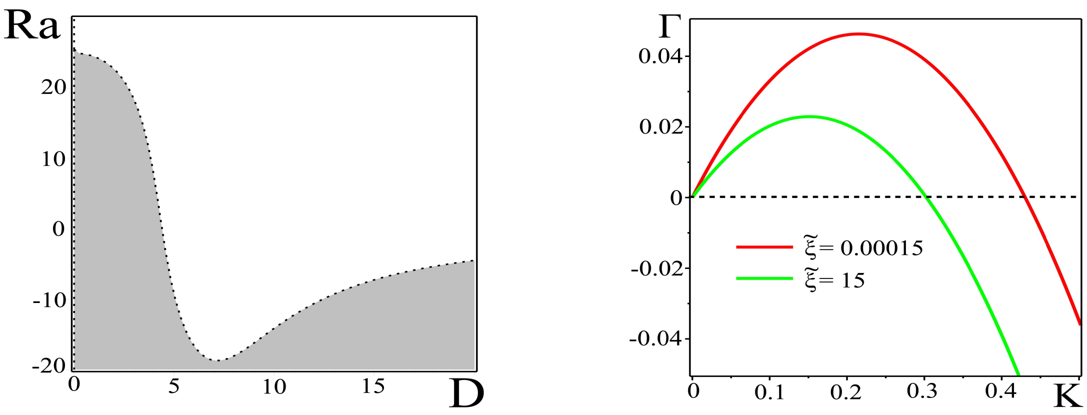

**Figure 3.** Left: instability region in the $(D, Ra)$ plane (gray: $\alpha_2 > 0$, white: $\alpha_2 < 0$). Right: growth rate $\Gamma(K)$ for $\widetilde{\xi} = 0.00015$ and $\widetilde{\xi} = 15$ at $D = 2$, $Ra = 10$.

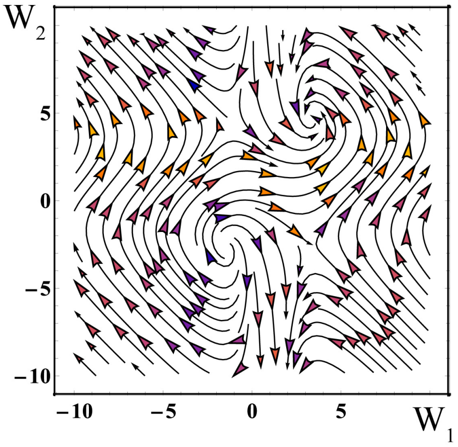

**Figure 4.** Phase portrait of the dynamical system defined by Eqs. (5)-(5) for $C_5 = -0.005$ and $C_6 = 0.005$.

of the velocity field amplitudes; instead, they depend solely on the magnetic rotation parameter $D$, the Rayleigh number $Ra$, the Nernst parameter $\widetilde{\xi}$, and the amplitude of the external forcing $f_0$. Thus, magnetorotational and thermomagnetic effects may play an important role in the development of large-scale instabilities and the emergence of self-organized structures in stratified magnetized plasma.

We consider the effect of an external magnetic field (characterized by the parameter $D$) on the gain $\alpha_2$, which determines the generation of large-scale vortex disturbances. For this analysis, the other parameters are fixed as follows: $f_0 = 10$, $Ra = 5$, $Pr = 1$, $Ra_1 = 0.15$, and $\widetilde{\xi} = 0.15$. Fig. 2a shows that $\alpha_2$ attains a maximum at a certain value of $D$. As $D$ increases further, $\alpha_2$ decreases monotonically, indicating suppression of the $\alpha$-effect by the magnetic field. Interestingly, the $\alpha_2(D)$ curve also demonstrates that vortex generation can be completely inhibited at specific nonzero values of $D$, where $\alpha_2$ vanishes.

Let us now examine how the value of $\alpha_2$ varies with the plasma heating parameter $Ra$, while keeping the other parameters fixed: $D = 2$, $Pr = 1$, $Ra_1 = 0.15$, $\widetilde{\xi} = 0.15$, and the amplitude of the external force $f_0 = 10$. The functional dependence $\alpha_2(Ra)$ is presented in Fig. 2b. For $Ra = 0$, the coefficient $\alpha_2 = 0.258$ corresponds to a plasma without a temperature gradient (i.e., no heating). In this regime, the generation of large-scale vortex structures is driven solely by the external helical small-scale forcing and the Lorentz force. As can be seen from Fig. 2b, the presence of thermal stratification ($Ra \neq 0$) can enhance the value of $\alpha_2$, thereby accelerating the formation of large-scale vortex disturbances compared to the non-stratified case. However, beyond a certain critical value of the stratification parameter $Ra_c$, the generation process is suppressed, as indicated by $\alpha_2 = 0$. For $Ra > Ra_c$, the sign of the gain coefficient $\alpha_2$ reverses. As a result, the previously growing mode becomes damped, and vice versa.

In a similar manner, we can examine the influence of the Nernst parameter $\widetilde{\xi}$ on the gain $\alpha_2$. Fig. 2c clearly shows that the gain coefficient $\alpha_2$ decreases with increasing $\widetilde{\xi}$, starting from $\alpha_2 \approx 0.43$ at $\widetilde{\xi} = 0$. This reduction can be attributed to the Nernst effect, wherein part of the thermal force is directed perpendicular to both the magnetic field vector $\overline{\mathbf{B}}$ and the temperature gradient $\partial_i T_0$. This transverse component of the thermal force impedes the motion of the electron component of the plasma, thereby leading to a suppression of the $\alpha$-effect and a consequent decrease in $\alpha_2$.

The left part of Fig. 3 shows the combined effect of the external magnetic field and thermal stratification in the $(D, Ra)$ plane. The instability region ($\alpha_2 > 0$) is marked in gray. The right part of Fig. 3 shows the dependence of the growth rate $\Gamma$ on the wave number $K$ as given by Eq. (42). As the Nernst parameter increases, the instability increment decreases, reflecting the reduction of $\alpha_2$ with increasing $\widetilde{\xi}$ (see Fig. 2c).

As equations (4) demonstrate, helicity of the small-scale field alone is insufficient for dynamo operation. Efficient generation of large-scale magnetic fields requires some critical parameters to fall within specific ranges, including the external magnetic field parameter $D$ and the thermal driving characterized by the Rayleigh number $Ra$. Additionally, the geometric configuration plays a crucial role, particularly the vertical upward orientation of the external magnetic field vector $\overline{\mathbf{B}}$.

## 5. STATIONARY NONLINEAR STRUCTURES

As the large-scale instability develops, the exponential growth of small perturbations $W_{1,2}$ renders the linear approximation invalid. With increasing disturbance amplitude, nonlinear effects become dominant. This leads to a suppression of the nonlinear $\alpha$-effect coefficients and a transition to a saturated, steady-state regime. In this regime, stable nonlinear vortex and magnetic structures emerge. To identify such stationary structures, we set $\partial_T = 0$ in Eqs. (3)-(3), and perform integration with respect to $Z$. This procedure yields the following set of nonlinear equations:

$$\frac{dW_1}{dZ} = -\frac{f_0^2}{8} \cdot \frac{D^2}{36(1-W_1)^2 + \left[\frac{D^2}{2} + 9 - (1-W_1)^2\right]^2 + \Xi_1^{(1)} - \widetilde{\xi}\Xi_1^{(2)} + \widetilde{\xi}\Xi_1^{(3)}} -$$

$$-\frac{f_0^2}{2} \cdot \frac{D\left(\frac{3}{2} - \frac{1.05Ra}{17.64+Pr^2(1-1.47W_2)^2}\right)}{36(1-W_2)^2 + \left[\frac{D^2}{2} + 9 - (1-W_2)^2\right]^2 + \Xi_2^{(1)} - \widetilde{\xi}\Xi_2^{(2)} + \widetilde{\xi}\Xi_2^{(3)}} + C_1\frac{Z^2}{2} + C_3 Z + C_5, \tag{43}$$

$$\frac{dW_2}{dZ} = -\frac{f_0^2}{8} \cdot \frac{D^2}{36(1-W_2)^2 + \left[\frac{D^2}{2} + 9 - (1-W_2)^2\right]^2 + \Xi_2^{(1)} - \widetilde{\xi}\Xi_2^{(2)} + \widetilde{\xi}\Xi_2^{(3)}} +$$

$$+\frac{f_0^2}{2} \cdot \frac{D\left(\frac{3}{2} - \frac{1.05Ra}{17.64+Pr^2(1-1.47W_1)^2}\right)}{36(1-W_1)^2 + \left[\frac{D^2}{2} + 9 - (1-W_1)^2\right]^2 + \Xi_1^{(1)} - \widetilde{\xi}\Xi_1^{(2)} + \widetilde{\xi}\Xi_1^{(3)}} + C_2\frac{Z^2}{2} + C_4 Z + C_6. \tag{44}$$

Here, the integration constants $C_1, C_2, C_3, C_4, C_5$, and $C_6$ are arbitrary. For the purpose of qualitative analysis of Eqs. (5)-(5), the physical parameters are fixed as follows: $f_0 = 1$, $Ra = 5$, $D = 2$, $Pr = 1$, and $\widetilde{\xi} = Ra_1 = 0.15$. To simplify the analysis, we set $C_1 = C_2 = C_3 = C_4 = 0$ and consider the stationary case by equating the left-hand sides of Eqs. (5)-(5) to zero. Under these conditions, the coordinates of the four fixed points $E_{(1,2,3,4)}$ can be determined numerically:

$$E_1(-1.363, 4.68),\ E_2(3.345, -2.635),\ E_3(3.345, 4.646),\ E_4(-1.358, -2.669). \tag{45}$$

By linearizing the right-hand sides of Eqs. (5)-(5) in the vicinity of the stationary points, we can determine their nature and construct the corresponding phase portrait. This analysis reveals that the system possesses two hyperbolic (saddle) points ($E_1, E_2$), one stable focus ($E_3$), and one unstable focus ($E_4$). The phase portrait of the resulting dynamical system, obtained for the constants $C_5 = -0.005$ and $C_6 = 0.005$, is shown in Fig. 4. The trajectories in the phase space demonstrate characteristic behavior near these points: solutions are repelled from the unstable focus and attracted toward the stable one, while the saddle points form separatrices that partition the phase space into distinct dynamical regions. Physically, these fixed points correspond to stationary nonlinear vortex structures, whose stability or instability determines the long-term evolution of the flow.

The most physically relevant localized solutions correspond to trajectories in the phase portrait that connect stationary points on the phase plane. In particular, the separatrix linking a hyperbolic point to a stable focus represents a solution describing a localized vortex structure, such as a kink with rotational features. An example of such a solution is shown on the left side of Fig. 5, obtained by numerically integrating Eqs. (5)-(5) with the initial conditions $W_1(0) = 3.345$ and $W_2(0) = -2.625$.

Another type of helical kink corresponds to a solution in which the separatrix on the phase plane connects the unstable and stable foci. This solution, shown in the right side of Fig. 5, was obtained by numerically integrating Eqs. (5)-(5) with initial conditions $W_1(0) = 3.345$ and $W_2(0) = 4.63$. All of these solutions – representing large-scale, localized, kink-type vortex structures with rotational features – are generated as a result of the instability mechanisms in the stratified, magnetized plasma with helical force analyzed in this study.

We now turn to the analysis of solutions corresponding to localized magnetic structures. To facilitate this, it is convenient to reformulate the stationary equations for the magnetic field components, Eq. (3), in terms of the current

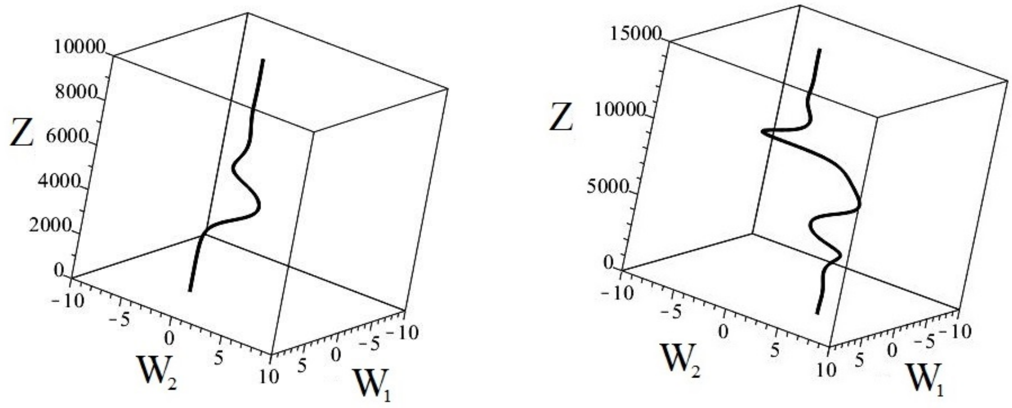

**Figure 5.** Left: kink-type solution corresponding to a separatrix connecting a hyperbolic point to a stable focus. Right: kink connecting an unstable focus to a stable focus, exhibiting an internal helical structure.

components. This can be done using the relation between the current density and the large-scale electron velocity, $\mathbf{J} = -\mathbf{W}$, together with Ampere's law written as:

$$\frac{dB_2}{dZ} = -J_1, \quad \frac{dB_1}{dZ} = J_2.$$

Substituting these expressions into the stationary equations (3) yields the following system for the current components $J_1$ and $J_2$:

$$\frac{dJ_1}{dZ} = \frac{f_0^2}{8} \cdot \frac{D^2}{36(1+J_1)^2 + \left[\frac{D^2}{2} + 9 - (1+J_1)^2\right]^2 + \widetilde{\Xi}_1^{(1)} - \widetilde{\xi}\widetilde{\Xi}_1^{(2)} + \widetilde{\xi}\widetilde{\Xi}_1^{(3)}} +$$

$$+\frac{f_0^2}{2} \cdot \frac{D\left(\frac{3}{2} - \frac{1.05Ra}{17.64+Pr^2(1+1.47J_2)^2}\right)}{36(1+J_2)^2 + \left[\frac{D^2}{2} + 9 - (1+J_2)^2\right]^2 + \widetilde{\Xi}_2^{(1)} - \widetilde{\xi\widetilde{\Xi}}_2^{(2)} + \widetilde{\xi\widetilde{\Xi}}_2^{(3)}} + \widetilde{C}_1 Z + \widetilde{C}_3, \tag{46}$$

$$\frac{dJ_2}{dZ} = \frac{f_0^2}{8} \cdot \frac{D^2}{36(1+J_2)^2 + \left[\frac{D^2}{2} + 9 - (1+J_2)^2\right]^2 + \widetilde{\Xi}_2^{(1)} - \widetilde{\xi\widetilde{\Xi}}_2^{(2)} + \widetilde{\xi\widetilde{\Xi}}_2^{(3)}} -$$

$$-\frac{f_0^2}{2} \cdot \frac{D\left(\frac{3}{2} - \frac{1.05Ra}{17.64+Pr^2(1+1.47J_1)^2}\right)}{36(1+J_1)^2 + \left[\frac{D^2}{2} + 9 - (1+J_1)^2\right]^2 + \widetilde{\Xi}_1^{(1)} - \widetilde{\xi\widetilde{\Xi}}_1^{(2)} + \widetilde{\xi\widetilde{\Xi}}_1^{(3)}} + \widetilde{C}_2 Z + \widetilde{C}_4, \tag{47}$$

where

$$\widetilde{\Xi}_{1,2}^{(1)} = Ra(9 + (1+J_{1,2})^2) \cdot \frac{Pr\widetilde{J}_{1,2}\widetilde{\widetilde{J}}_{1,2} - 12.6 + \frac{Ra}{4}}{17.64 + Pr^2\widetilde{\widetilde{J}}_{1,2}^{2}}, \ \widetilde{J}_{1,2} = 1 + J_{1,2}, \ \widetilde{\widetilde{J}}_{1,2} = 1 + 1.47J_{1,2},$$

$$\widetilde{\Xi}_{1,2}^{(2)} = \frac{3}{2}D^2 Ra_1 \cdot \frac{25.2\widetilde{J}_{1,2} + Pr(9 - \widetilde{J}_{1,2}^2)\widetilde{\widetilde{J}}_{1,2}}{17.64 + Pr^2\widetilde{\widetilde{J}}_{1,2}^{2}}, \ \widetilde{\Xi}_{1,2}^{(3)} = \frac{D^4}{4} \cdot \frac{Ra_1}{17.64 + Pr^2\widetilde{\widetilde{J}}_{1,2}^{2}} \left(\frac{9}{4}\widetilde{\xi}Ra_1 - 3Pr\widetilde{\widetilde{J}}_{1,2}\right).$$

Equations (5)-(5) contain arbitrary integration constants $\widetilde{C}_1$, $\widetilde{C}_2$, $\widetilde{C}_3$, and $\widetilde{C}_4$. To simplify the qualitative analysis, we set $\widetilde{C}_1 = \widetilde{C}_2 = 0$. Under this assumption, we analyze the system by setting the left-hand sides of Eqs. (5)-(5) to zero, which allows us to numerically identify the fixed points and determine their locations in phase space:

$$\widetilde{E}_1(-3.34, 2.635), \ \widetilde{E}_2(1.363, -4.68), \ \widetilde{E}_3(1.358, 2.669), \ \widetilde{E}_4(-3.345, -4.646). \tag{48}$$

As in the case of vortex structures, the system exhibits four stationary points: two hyperbolic points ($\widetilde{E}_1$, $\widetilde{E}_2$), a stable focus ($\widetilde{E}_3$), and an unstable focus ($\widetilde{E}_4$). The corresponding phase portrait of the dynamical system governed by Eqs. (5)-(5), with constants $\widetilde{C}_3 = -0.005$ and $\widetilde{C}_4 = -0.005$, is presented in Fig. 6. Localized magnetic structures naturally correspond to phase trajectories in Fig. 6 that connect equilibrium points in the phase space. The left side of Fig. 7 illustrates such a

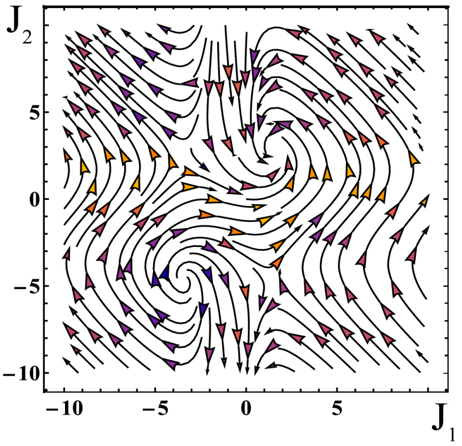

**Figure 6.** The phase plane of the dynamical system equations (5)-(5) with $\widetilde{C}_3 = -0.005$ and $\widetilde{C}_4 = -0.005$.

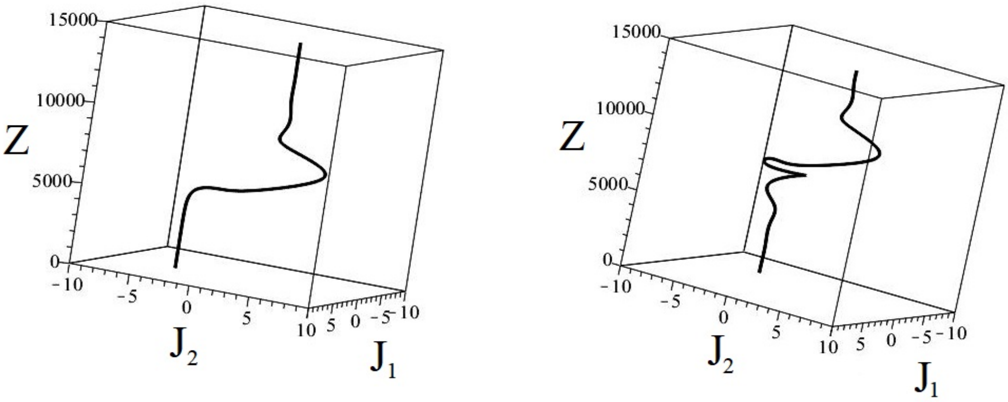

**Figure 7.** Localized magnetic kink structures analogous to vortex kinks in Fig. 6.

structure in the form of a magnetic kink, obtained through numerical integration of Eqs. (5)-(5) with the initial conditions $J_1(0) = 1.363$ and $J_2(0) = -4.68$. This kink represents a separatrix connecting the hyperbolic point $\widetilde{E}_2$ to the stable focus $\widetilde{E}_3$.

Another type of localized magnetic structure – a spiral kink – is obtained by numerically integrating the system of Eqs.(5)-(5) with initial conditions $J_1(0) = -3.345$ and $J_2(0) = -4.65$. This solution corresponds to a separatrix trajectory on the phase plane that connects the unstable focus $\widetilde{E}_4$ to the stable focus $\widetilde{E}_3$, as shown in the right side of Fig. 7.

As a result of numerically solving the stationary equations (5)-(5) and (5)-(5), we identified localized helical structures of both vortex and magnetic nature.

## 6. CONCLUSIONS

In this study, a nonlinear dynamo theory has been developed for a fully ionized, temperature-stratified plasma subjected to an external vertical magnetic field and a uniform gravitational field. The plasma dynamics are considered within the framework of electron magnetohydrodynamics (EMHD), assuming immobile and cold ions. The proposed dynamo mechanism incorporates thermomagnetic effects and is based on the $\alpha$-effect, which arises due to the joint action of a small-scale external helical force and the Lorentz force. The external forcing sustains weak velocity fluctuations in the electron component, forming a low-Reynolds-number turbulence regime ($R \ll 1$). Applying an asymptotic expansion in terms of this small parameter, we derived closed-form equations describing the evolution of large-scale vortex and magnetic perturbations. The linear stage of large-scale instability development was thoroughly analyzed. The regions of instability on the parameter plane $(D, Ra)$, defined by the Lorentz and Rayleigh numbers respectively, were determined. It is shown that the extent and structure of the instability domain are sensitive to the intensity of the small-scale forcing. A key result of this work is the identification of the suppressing role of the Nernst effect on large-scale instability. As the Nernst parameter increases, the growth rate of the instability decreases, owing to the thermomagnetic part of the electron force counteracting the generation process. Conversely, stronger thermal stratification (larger Rayleigh number) enhances the instability until it transitions to convective instability at high values of $Ra$. In the nonlinear regime, as the amplitude of perturbations grows, saturation occurs and the system reaches a stationary state. Numerical integration of the nonlinear equations reveals the formation of localized vortex and magnetic structures in the form of spiral kinks. These coherent structures represent the final stage of nonlinear evolution driven by the large-scale dynamo instability in a stratified magnetized plasma.

## APPENDIX A. ALGEBRAIC STRUCTURE OF THE ASYMPTOTIC EXPANSIONS

Let us present the algebraic structure of the asymptotic expansion for equations (2)-(18) at different orders in $R$, starting with the smallest.

At the $R^{-3}$ order, we have just one equation:

$$\partial_i P_{-3} = 0 \quad \Rightarrow \quad P_{-3} = P_{-3}(X) \tag{49}$$

In order $R^{-2}$ we get the equation:

$$\partial_i P_{-2} = 0 \quad \Rightarrow \quad P_{-2} = P_{-2}(X) \tag{50}$$

Equations (49) and (50) are automatically fulfilled as $P_{-3}$ and $P_{-2}$ solely depend on slow variables.

In order $R^{-1}$ we obtain the system of equations:

$$\begin{gathered}
\partial_t W^i_{-1} + W^k_{-1}\partial_k W^i_{-1} = -\partial_i P_{-1} - \nabla_i P_{-3} + \partial_k^2 W^i_{-1} - D\varepsilon_{ijk} W_j e_k + e_i \widetilde{Ra} T_{-1} - W^i_{-1} + \partial_k^2 W^i_{-1}, \\
\partial_t T_{-1} - 2.1 Pr^{-1}\partial_k^2 T_{-1} = -1.47 W^k_{-1}\partial_k T_{-1} + W^z_{-1} - \frac{5}{3} Pr^{-1}\xi e_i \varepsilon_{ijk}\partial_i B^k_0, \\
\partial_i W^i_{-1} = 0, \qquad \partial_i B^i_{-1} = 0.
\end{gathered} \tag{51}$$

Upon averaging equations (51) over the ”fast” variables, we obtain the secular equations:

$$-\nabla_i P_{-3} - D\varepsilon_{ijk} W_j e_k + e_i \widetilde{Ra} T_{-1} - W^i_{-1} = 0, \quad W^z_{-1} = 0, \tag{52}$$

At zero order $R^0$, we have:

$$\begin{gathered}
\partial_t v^i_0 + W^k_{-1}\partial_k v^i_0 = -\partial_i P_0 - \nabla_i P_{-2} - D\varepsilon_{ijk} v^j_0 e_k + e_i \widetilde{Ra} T_0 - \\
-\widetilde{Ra}_1 \left(0.71 \partial_i T_0 + \frac{3}{2}\tilde{\xi} D\varepsilon_{ijk} e_j \partial_k T_0\right) - v^i_0 + \partial_k^2 v^i_0 + F^i_0,
\end{gathered}$$

where $\widetilde{Ra}_1 = \widetilde{Ra}\left(\frac{V_{Te}}{g\lambda_0}\right)$ is the modified Rayleigh number,

$$\begin{gathered}
\partial_t T_0 - 2.1 Pr^{-1}\partial_k^2 T_0 = -1.47 W^k_{-1}\partial_k T_0 + v^z_0 + \\
+\frac{5}{3} Pr^{-1}\xi \partial_i T_0 \varepsilon_{ijk}\partial_j B^k_0 - \frac{5}{3} Pr^{-1}\xi e_i \varepsilon_{ijk}(\partial_j B^k_1 + \nabla_j B^k_{-1}), \\
\partial_t B^i_0 = -\varepsilon_{ijk}\partial_j E^k_0, \ \varepsilon_{ijk}\partial_j B^k_0 = 0, \ \partial_i v^i_0 = 0, \ \partial_i B^i_0 = 0.
\end{gathered} \tag{53}$$

These equations give secular terms:

$$\nabla P_{-2} = 0 \ \Rightarrow \ P_{-2} = \text{const}, \ (\nabla \times \mathbf{B}_{-1})_z = 0.$$

Let us look at the first-order approximation $R^1$:

$$\begin{gathered}
\partial_t v^i_1 + W^k_{-1}\partial_k v^i_1 + v^k_0 \partial_k v^i_0 + W^k_{-1}\nabla_k W^i_{-1} = -\nabla_i P_{-1} - \\
-\partial_i \left(P_1 + \overline{P}_1\right) - E^i_{-1} - D\varepsilon_{ijk} v^j_1 e_k - \varepsilon_{ijk} W^j_{-1} B^k_{-1} + e_i \widetilde{Ra} T_1 - \\
-\widetilde{Ra}_1 \left(0.71(\partial_i T_1 + \nabla_i T_{-1}) + \frac{3}{2}\tilde{\xi} D\varepsilon_{ijk} e_j (\partial_k T_1 + \nabla_k T_{-1})\right) - v^i_1 + \partial_k^2 v^i_1 + 2\partial_k \nabla_k W^i_{-1}, \\
\partial_t T_1 - 2.1 Pr^{-1}\partial_k^2 T_1 - 4.2 Pr^{-1}\partial_k \nabla_k T_{-1} = -1.47(W^k_{-1}\partial_k T_1 + W^k_{-1}\nabla_k T_{-1} + v^k_0 \partial_k T_0) + v_z + \\
+\frac{5}{3} Pr^{-1}\xi \varepsilon_{ijk}(\partial_i T_0(\partial_j B^k_1 + \nabla_j B^k_{-1}) + \partial_i T_1 \partial_j B^k_0) - \frac{5}{3} Pr^{-1}\xi e_i \varepsilon_{ijk}\partial_j B^k_2, \\
\partial_t B^i_1 = -\varepsilon_{ijk}(\partial_j E^k_1 + \nabla_j E^k_{-1}), \ \varepsilon_{ijk}(\partial_j B^k_1 + \nabla_j B^k_{-1}) = -W^i_{-1}, \\
\partial_i v^i_1 + \nabla_i W^i_{-1} = 0, \quad \partial_i B^i_1 + \nabla_i B^i_{-1} = 0.
\end{gathered} \tag{54}$$

From this system of equations, secular equations are derived in the form

$$W^k_{-1}\nabla_k W^i_{-1} = -\nabla_i P_{-1} - E^i_{-1} - \varepsilon_{ijk} W^j_{-1} B^k_{-1} - \widetilde{Ra}_1 \left(0.71\nabla_i T_{-1} + \frac{3}{2}\widetilde{\xi} D\varepsilon_{ijk} e_j \nabla_k T_{-1}\right), \tag{55}$$

$$\varepsilon_{ijk}\nabla_j E^k_{-1} = 0, \quad \varepsilon_{ijk}\nabla_j B^k_{-1} = -W^i_{-1}, \tag{56}$$

$$W^k_{-1}\nabla_k T_{-1} = 0, \quad \nabla_i W^i_{-1} = 0, \quad \nabla_i B^i_{-1} = 0. \tag{57}$$

At second order $R^2$, we get

$$\begin{gathered}
\partial_t v^i_2 + W^k_{-1}\partial_k v^i_2 + v^k_0 \partial_k v^i_1 + W^k_{-1}\nabla_k v^i_0 + v^k_0 \nabla_k W^i_{-1} + v^k_1 \partial_k v^i_0 = \\
= -\partial_i P_2 - \nabla_i P_0 - E^i_0 - D\varepsilon_{ijk} v^j_2 e_k - \varepsilon_{ijk} v^j_0 B^k_{-1} + e_i \widetilde{Ra} T_2 - \\
-\widetilde{Ra}_1 \left(0.71\partial_i T_2 + \frac{3}{2}\widetilde{\xi} D\varepsilon_{ijk} e_j \partial_k T_2\right) - v^i_2 + \partial^2_k v^i_2 + 2\partial_k \nabla_k v^i_0, \\
\partial_t T_2 - 2.1 Pr^{-1}\partial^2_k T_2 - 4.2 Pr^{-1}\partial_k \nabla_k T_0 = -1.47(W^k_{-1}\partial_k T_2 + \\
+W^k_{-1}\nabla_k T_0 + v^k_0 \partial_k T_1 + v^k_0 \nabla_k T_{-1} + v^k_1 \partial_k T_0) + v^z_2 + \frac{5}{3} Pr^{-1}\xi\varepsilon_{ijk} \times \\
\times(\partial_i T_0 \partial_j B^k_2 + \partial_i T_1(\partial_j B^k_1 + \nabla_j B^k_{-1}) + \partial_i T_2 \partial_j B^k_0) - \\
-\frac{5}{3} Pr^{-1}\xi e_i \varepsilon_{ijk}(\partial_j B^k_3 + \nabla_j B^k_1), \qquad (58) \\
\partial_t B^i_2 = -\varepsilon_{ijk}\partial_j E^k_2, \quad \varepsilon_{ijk}\partial_j B^k_2 = -v^i_0, \\
\partial_i v^i_2 + \nabla_i v^i_0 = 0, \quad \partial_i B^i_2 + \nabla_i B^i_0 = 0.
\end{gathered}$$

The system (6) is averaged over the fast variables, and no secular terms of order $R^2$ are found. Finally, the order $R^3$ is reached, where the equations are

$$\begin{gathered}
\partial_t v^i_3 + \partial_T W^i_{-1} + W^k_{-1}\partial_k v^i_3 + v^k_0 \partial_k v^i_2 + W^k_{-1}\nabla_k v^i_1 + v^k_0 \nabla_k v^i_0 + \\
+v^k_1 \partial_k v^i_1 + v^k_1 \nabla_k W^i_{-1} + v^k_2 \partial_k v^i_0 = -\partial_i P_3 - \nabla_i \left(P_1 + \overline{P}_1\right) - \\
-\left(E^i_1 + \overline{E}^i_1\right) - D\varepsilon_{ijk} v^j_3 e_k - \varepsilon_{ijk} W^j_{-1} B^k_1 - \varepsilon_{ijk} v^j_1 B^k_{-1} + e_i \widetilde{Ra} T_3 - \\
-\widetilde{Ra}_1 \left(0.71(\partial_i T_3 + \nabla_i T_1) + \frac{3}{2}\widetilde{\xi} D\varepsilon_{ijk} e_j (\partial_k T_3 + \nabla_k T_1)\right) - v^i_3 + \partial^2_k v^i_3 + 2\partial_k \nabla_k v^i_1 + \nabla^2_k W^i_{-1}, \\
\partial_t T_3 + \partial_T T_{-1} - 2.1 Pr^{-1}(\partial^2_k T_3 + 2\partial_k \nabla_k T_1 + \nabla^2 T_{-1}) = \\
= -1.47(W^k_{-1}\partial_k T_3 + W^k_{-1}\nabla_k T_1 + v^k_0 \partial_k T_2 + v^k_0 \nabla_k T_0 + v^k_1 \nabla_k T_1 + \\
+v^k_1 \nabla_k T_{-1} + v^k_2 \partial_k T_0) + v^z_3 + \frac{5}{3} Pr^{-1}\xi\varepsilon_{ijk}(\partial_i T_0(\partial_j B^k_3 + \nabla_j B^k_1) + \\
+\partial_i T_1 \partial_j B^k_2 + \partial_i T_2(\partial_j B^k_1 + \nabla_j B^k_{-1}) + \partial_i T_3 \partial_j B^k_0) - \frac{5}{3} Pr^{-1}\xi e_i \varepsilon_{ijk}\nabla_j B^k_2, \qquad (59) \\
\partial_t B^i_3 + \partial_T B^i_{-1} = -\varepsilon_{ijk}(\partial_j E^k_3 + \nabla_j E^k_1), \\
\varepsilon_{ijk}(\partial_j B^k_3 + \nabla_j B^k_1) = -v^i_1, \\
\partial_i v^i_3 + \nabla_i v^i_1 = 0, \quad \partial_i B^i_3 + \nabla_i B^i_1 = 0.
\end{gathered}$$

The fundamental secular equations that describe the development of large-scale disturbances in a stratified plasma with a vertical external magnetic field are obtained by averaging this system of equations over fast variables:

$$\partial_T W^i_{-1} + \nabla_k \left(\overline{v^k_0 v^i_0}\right) = -\nabla_i \overline{P}_1 - \overline{E}^i_1 + \nabla^2_k W^i_{-1}, \tag{60}$$

$$\partial_T T_{-1} - 2.1 Pr^{-1}\nabla^2 T_{-1} = -1.47\nabla_k \left(\overline{v^k_0 T_0}\right), \tag{61}$$

$$\partial_T B^i_{-1} = -\varepsilon_{ijk}\nabla_j \overline{E}^k_1. \tag{62}$$

## APPENDIX B. SMALL-SCALE FIELDS

Let us now examine the zero-order equations in $R$, presented in Appendix A (see Eq. (6)). By introducing the differential operators

$$\widehat{D}_W = \partial_t + 1 - \partial^2 + W^k_{-1}\partial_k, \quad \widehat{D}_T = \partial_t + 1.47W^k_{-1}\partial_k - 2.1Pr^{-1}\partial^2, \tag{63}$$

the system (6) can be conveniently rewritten in the following form:

$$\widehat{D}_W v_0^i = -\partial_i P_0 - D\varepsilon_{ijk} v_0^j e_k + e_i \widetilde{Ra} T_0 - \widetilde{Ra}_1 \left(0.71\partial_i T_0 + \frac{3}{2}\tilde{\xi} D\varepsilon_{ijk} e_j \partial_k T_0\right) + F_0^i \tag{64}$$

$$\widehat{D}_T T_0 = e_k v_0^k \tag{65}$$

$$\partial_i v_0^i = \partial_k B_0^k = \partial_i F_0^i = 0 \tag{66}$$

By substituting Eq. (65) into Eq. (64) and applying the solenoidality condition for the fields (Eq. (66)), we obtain the following expression for the pressure $P_0$:

$$P_0 = \widehat{P}_1 u_0 + \widehat{P}_2 v_0 + \widehat{P}_3 w_0 \tag{67}$$

where

$$v_0^x = u_0, v_0^y = v_0, v_0^z = w_0,$$

$$\widehat{P}_1 = \frac{D\partial_y}{\partial^2}, \ \widehat{P}_2 = -\frac{D\partial_x}{\partial^2}, \ \widehat{P}_3 = \widetilde{Ra}\frac{\partial_z}{\widehat{D}_T \partial^2} - 0.71\frac{\widetilde{Ra}_1}{\widehat{D}_T}.$$

Utilizing the representation given in Eq. (67), the pressure term in Eqs. (64) can be eliminated, yielding the system of equations that governs the velocity fields in the zeroth-order approximation:

$$\begin{cases} \left(\widehat{D}_W + \widehat{p}_{1x}\right) u_0 + \left(\widehat{p}_{2x} + D\right) v_0 + \left(\widehat{p}_{3x} + \widehat{D}_{Rx}\right) w_0 = F_0^x, \\ \left(\widehat{p}_{1y} - D\right) u_0 + \left(\widehat{D}_W + \widehat{p}_{2y}\right) v_0 + \left(\widehat{p}_{3y} + \widehat{D}_{Ry}\right) w_0 = F_0^y, \\ \widehat{p}_{1z} u_0 + \widehat{p}_{2z} v_0 + \left(\widehat{D}_W + \widehat{p}_{3z} - \dfrac{\widetilde{Ra}}{\widehat{D}_T} + \widehat{D}_{Rz}\right) w_0 = 0, \end{cases} \tag{68}$$

where

$$\widehat{D}_{Rx} = \frac{\widetilde{Ra}_1}{\widehat{D}_T}\left(0.71\partial_x - \frac{3}{2}\tilde{\xi} D\partial_y)\right), \ \widehat{D}_{Ry} = \frac{\widetilde{Ra}_1}{\widehat{D}_T}\left(0.71\partial_y + \frac{3}{2}\tilde{\xi} D\partial_x\right), \ \widehat{D}_{Rz} = 0.71\widetilde{Ra}_1 \frac{\partial_z}{\widehat{D}_T},$$

$$\widehat{p}_{1x} = \partial_x P_1, \quad \widehat{p}_{2x} = \partial_x P_2, \quad \widehat{p}_{3x} = \partial_x P_3, \ \widehat{p}_{1y} = \partial_y P_1, \quad \widehat{p}_{2y} = \partial_y P_2, \quad \widehat{p}_{3y} = \partial_y P_3,$$

$$\widehat{p}_{1z} = \partial_z P_1, \quad \widehat{p}_{2z} = \partial_z P_2, \quad \widehat{p}_{3z} = \partial_z P_3.$$

The solution of the system of equations (68) can be obtained by applying Cramer's rule:

$$u_0 = \frac{1}{\Delta}\left(\widehat{d}_1 \cdot F_0^x + \widehat{d}_2 \cdot F_0^y\right), \ v_0 = \frac{1}{\Delta}\left(\widehat{d}_3 \cdot F_0^x + \widehat{d}_4 \cdot F_0^y\right), \ w_0 = \frac{1}{\Delta}\left(\widehat{d}_5 \cdot F_0^x + \widehat{d}_6 \cdot F_0^y\right). \tag{69}$$

where

$$\widehat{d}_1 = \left(\widehat{D}_W + \widehat{p}_{2y}\right)\left(\widehat{D}_W + \widehat{p}_{3z} - \frac{\widetilde{Ra}}{\widehat{D}_T} + \widehat{D}_{Rz}\right) - \widehat{p}_{2z}\left(\widehat{p}_{3y} + \widehat{D}_{Ry}\right),$$

$$\widehat{d}_2 = \left(\widehat{p}_{3x} + \widehat{D}_{Rx}\right)\widehat{p}_{2z} - \left(\widehat{p}_{2x} + D\right)\left(\widehat{D}_W + \widehat{p}_{3z} - \frac{\widetilde{Ra}}{\widehat{D}_T} + \widehat{D}_{Rz}\right),$$

$$\widehat{d}_3 = \left(\widehat{p}_{3y} + \widehat{D}_{Ry}\right)\widehat{p}_{1z} - \left(\widehat{p}_{1y} - D\right)\left(\widehat{D}_W + \widehat{p}_{3z} - \frac{\widetilde{Ra}}{\widehat{D}_T} + \widehat{D}_{Rz}\right),$$

$$\widehat{d}_4 = \left(\widehat{D}_W + \widehat{p}_{1x}\right)\left(\widehat{D}_W + \widehat{p}_{3z} - \frac{\widetilde{Ra}}{\widehat{D}_T} + \widehat{D}_{Rz}\right) - \left(\widehat{p}_{3x} + \widehat{D}_{Rx}\right)\widehat{p}_{1z},$$

$$\widehat{d}_5 = \left(\widehat{p}_{1y} - D\right)\widehat{p}_{2z} - \left(\widehat{D}_W + \widehat{p}_{2y}\right)\widehat{p}_{1z}, \ \widehat{d}_6 = \left(\widehat{p}_{2x} + D\right)\widehat{p}_{1z} - \left(\widehat{D}_W + \widehat{p}_{1x}\right)\widehat{p}_{2z}.$$

Here, the symbol $\Delta$ denotes the determinant of the system of equations (68):

$$\Delta = \left(\widehat{D}_W + \widehat{p}_{1x}\right) \cdot \widehat{d}_1 + \left(\widehat{p}_{2x} + D\right) \cdot \widehat{d}_3 + \left(\widehat{p}_{3x} + \widehat{D}_{Rx}\right) \cdot \widehat{d}_5. \tag{70}$$

All operators involved in (69)-(70) are mutually commutative, which simplifies the evaluation of these expressions. To compute expressions (69)-(70), we rewrite the external force (12) in complex form:

$$\mathbf{F}_0 = \mathbf{i}\,\frac{f_0}{2}\,e^{i\phi_2} + \mathbf{j}\,\frac{f_0}{2}e^{i\phi_1} + c.c. \tag{71}$$

It follows from substituting (71) into (69)-(70) that the operators act on the exponential term from the left, such that $\widehat{p}\exp(i\mathbf{kx} - i\omega_0 t) = \exp(i\mathbf{kx} - i\omega_0 t)p(\mathbf{k}, -\omega_0)$. Therefore, we make use of the following properties of the eigenfunctions $p(\mathbf{k}, -\omega_0)$:

$$\widehat{D}_{W,T}e^{i\phi_1} = e^{i\phi_1}D_{W,T}\left(\mathbf{k}_1, -\omega_0\right),\ \widehat{D}_{W,T}e^{i\phi_2} = e^{i\phi_2}D_{W,T}\left(\mathbf{k}_2, -\omega_0\right),$$

$$\Delta e^{i\phi_1} = e^{i\phi_1}\Delta\left(\mathbf{k}_1, -\omega_0\right),\ \Delta e^{i\phi_2} = e^{i\phi_2}\Delta\left(\mathbf{k}_2, -\omega_0\right). \tag{72}$$

To simplify the formulas, let us set $k_0 = 1$ and $\omega_0 = 1$, introducing new designations:

$$D_W\left(\mathbf{k}_1, -\omega_0\right) = D^*_{W_1} = 3 - i\left(1 - W_1\right),$$

$$D_W\left(\mathbf{k}_2, -\omega_0\right) = D^*_{W_2} = 3 - i\left(1 - W_2\right),$$

$$D_T\left(\mathbf{k}_1, -\omega_0\right) = D^*_{T_1} = 4.2Pr^{-1} - i\left(1 - 1.47W_1\right),$$

$$D_T\left(\mathbf{k}_2, -\omega_0\right) = D^*_{T_2} = 4.2Pr^{-1} - i\left(1 - 1.47W_2\right). \tag{73}$$

$$\Delta\left(\mathbf{k}_1, -\omega_0\right) = \Delta^*_1 = D^*_{W_1}\left(D^*_{W_1}\left(D^*_{W_1} - \frac{\widetilde{Ra}}{2D^*_{T_1}}\right) + \frac{D^2}{2}\left(1 + \frac{3}{2}\tilde{\xi}\frac{i\widetilde{Ra}_1}{D^*_{T_1}}\right)\right),$$

$$\Delta\left(\mathbf{k}_2, -\omega_0\right) = \Delta^*_2 = D^*_{W_2}\left(D^*_{W_2}\left(D^*_{W_2} - \frac{\widetilde{Ra}}{2D^*_{T_2}}\right) + \frac{D^2}{2}\left(1 + \frac{3}{2}\tilde{\xi}\frac{i\widetilde{Ra}_1}{D^*_{T_2}}\right)\right).$$

Here and throughout the text, the superscript $^*$ denotes complex conjugation. Based on formulas (6), we can determine the zeroth-order approximation of the velocity field:

$$u_0 = e^{i\phi_2}\frac{f_0}{2}\frac{A^*_2}{D^*_{W_2}A^*_2 + \frac{D^2}{2}B^*_2} - e^{i\phi_1}\frac{f_0}{2}\frac{D/2}{D^*_{W_1}A^*_1 + \frac{D^2}{2}B^*_1} + c.c. =$$

$$= u_{01}e^{i\phi_1} + u_{02}e^{-i\phi_1} + u_{03}e^{i\phi_2} + u_{04}e^{-i\phi_2}, \tag{74}$$

$$v_0 = e^{i\phi_2}\frac{f_0}{2}\frac{D/2}{D^*_{W_2}A^*_2 + \frac{D^2}{2}B^*_2} + e^{i\phi_1}\frac{f_0}{2}\frac{A^*_1}{D^*_{W_1}A^*_1 + \frac{D^2}{2}B^*_1} + c.c. =$$

$$= v_{01}e^{i\phi_1} + v_{02}e^{-i\phi_1} + v_{03}e^{i\phi_2} + v_{04}e^{-i\phi_2}, \tag{75}$$

$$w_0 = e^{i\phi_1}\frac{f_0}{2}\frac{D/2}{D^*_{W_1}A^*_1 + \frac{D^2}{2}B^*_1} - e^{i\phi_2}\frac{f_0}{2}\frac{D/2}{D^*_{W_2}A^*_2 + \frac{D^2}{2}B^*_2} + c.c. =$$

$$= w_{01}e^{i\phi_1} + w_{02}e^{-i\phi_1} + w_{03}e^{i\phi_2} + w_{04}e^{-i\phi_2}, \tag{76}$$

where

$$A^*_{1,2} = D^*_{W_{1,2}} - \frac{\widetilde{Ra}}{2D^*_{T_{1,2}}},\ B^*_{1,2} = 1 + \frac{3}{2}\tilde{\xi}\frac{i\widetilde{Ra}_1}{D^*_{T_{1,2}}}. \tag{77}$$

The indices $(1, 2)$ in the expressions for $A, B$ are written in accordance with the components $W_1$ and $W_2$. The following relationships are satisfied between the velocity components:

$$u_{02} = \left(u_{01}\right)^*,\ u_{04} = \left(u_{03}\right)^*,\ v_{02} = \left(v_{01}\right)^*,\ v_{04} = \left(v_{03}\right)^*,\ w_{02} = \left(w_{01}\right)^*,\ w_{04} = \left(w_{03}\right)^*.$$

## APPENDIX C. CALCULATIONS OF THE REYNOLDS STRESSES

In order to close the system of equations (30)-(31) governing the evolution of large-scale velocity fields $\mathbf{W}_{-1}$, it is essential to compute correlators of the following form:

$$T^{31} = \overline{w_0 u_0} = \overline{w_{01}\left(u_{01}\right)^*} + \overline{\left(w_{01}\right)^* u_{01}} + \overline{w_{03}\left(u_{03}\right)^*} + \overline{\left(w_{03}\right)^* u_{03}} \tag{78}$$

$$T^{32} = \overline{w_0 v_0} = \overline{w_{01}\left(v_{01}\right)^*} + \overline{\left(w_{01}\right)^* v_{01}} + \overline{w_{03}\left(v_{03}\right)^*} + \overline{\left(w_{03}\right)^* v_{03}} \tag{79}$$

Substituting the expressions for the small-scale velocity fields (6)-(6) into the definitions (78)-(79) yields the following:

$$T^{31} = -\frac{f_0^2}{8}\frac{D(A_2 + A_2^*)}{\left|D_{W_2}A_2 + \frac{D^2}{2}B_2\right|^2} - \frac{f_0^2}{8}\frac{D^2}{\left|D_{W_1}A_1 + \frac{D^2}{2}B_1\right|^2}, \tag{80}$$

$$T^{32} = -\frac{f_0^2}{8}\frac{D(A_1 + A_1^*)}{\left|D_{W_1}A_1 + \frac{D^2}{2}B_1\right|^2} - \frac{f_0^2}{8}\frac{D^2}{\left|D_{W_2}A_2 + \frac{D^2}{2}B_2\right|^2}. \tag{81}$$

Using the expressions given in (77), we derive a set of useful relations for calculating $T^{31}$ and $T^{32}$ as follows:

$$\left|D_{W_{1,2}}\right|^2 = D_{W_{1,2}}D^*_{W_{1,2}} = 9 + (1 - W_{1,2})^2 = 9 + \widetilde{W}^2_{1,2},\ \left|D_{T_{1,2}}\right|^2 = D_{T_{1,2}}D^*_{T_{1,2}} =$$

$$= 17.64Pr^{-2} + (1 - 1.47W_{1,2})^2 = 17.64Pr^{-2} + \widetilde{\widetilde{W}}^2_{1,2},$$

$$\left|A_{1,2}\right|^2 = A_{1,2}A^*_{1,2},\ \left|A_{1,2}\right|^2 = 9 + \widetilde{W}^2_{1,2} + \frac{Ra}{17.64 + Pr^2\widetilde{\widetilde{W}}^2_{1,2}}\left(Pr\widetilde{W}_{1,2}\widetilde{\widetilde{W}}_{1,2} - 12.6 + \frac{Ra}{4}\right),$$

$$\left|B_{1,2}\right|^2 = B_{1,2}B^*_{1,2},\ \left|B_{1,2}\right|^2 = 1 + \frac{\widetilde{\xi}Ra_1}{17.64 + Pr^2\widetilde{\widetilde{W}}^2_{1,2}}\left(\frac{9}{4}\widetilde{\xi}Ra_1 - 3Pr\widetilde{\widetilde{W}}_{1,2}\right),$$

$$A_{1,2} + A^*_{1,2} = 6 - \frac{4.2Ra}{17.64 + Pr^2\widetilde{\widetilde{W}}^2_{1,2}}, \quad \Pi_{1,2} = \left|D_{W_{1,2}}A_{1,2} + \frac{D^2}{2}B_{1,2}\right|^2 =$$

$$= 36(1 - W_{1,2})^2 + \left[\frac{D^2}{2} + 9 - (1 - W_{1,2})^2\right]^2 + \Xi^{(1)}_{1,2} - \widetilde{\xi}\Xi^{(2)}_{1,2} + \widetilde{\xi}\Xi^{(3)}_{1,2},$$

$$\Xi^{(1)}_{1,2} = Ra(9 + (1 - W_{1,2})^2)\cdot\frac{Pr\widetilde{W}_{1,2}\widetilde{\widetilde{W}}_{1,2} - 12.6 + \frac{Ra}{4}}{17.64 + Pr^2\widetilde{\widetilde{W}}^2_{1,2}},$$

$$\Xi^{(2)}_{1,2} = \frac{3}{2}D^2Ra_1\cdot\frac{25.2\widetilde{W}_{1,2} + Pr(9 - \widetilde{W}^2_{1,2})\widetilde{\widetilde{W}}_{1,2}}{17.64 + Pr^2\widetilde{\widetilde{W}}^2_{1,2}},\ \Xi^{(3)}_{1,2} = \frac{D^4}{4}\cdot\frac{Ra_1}{17.64 + Pr^2\widetilde{\widetilde{W}}^2_{1,2}}\left(\frac{9}{4}\widetilde{\xi}Ra_1 - 3Pr\widetilde{\widetilde{W}}_{1,2}\right).$$

Substituting the above relations into (80)-(81), we derive the general form of the Reynolds stress expressions:

$$T^{31} = -\frac{f_0^2}{8}\frac{D^2}{\Pi_1} - \frac{f_0^2}{2}\frac{D}{\Pi_2}\left(\frac{3}{2} - \frac{1.05Ra}{17.64 + Pr^2(1 - 1.47W_2)^2}\right),$$

$$T^{32} = -\frac{f_0^2}{8}\frac{D^2}{\Pi_2} + \frac{f_0^2}{2}\frac{D}{\Pi_1}\left(\frac{3}{2} - \frac{1.05Ra}{17.64 + Pr^2(1 - 1.47W_1)^2}\right). \tag{82}$$

At small $W_{1,2}$, module $\Pi_{1,2}$ can be expanded into a series in $W_{1,2}$:

$$\Pi^{-1}_{1,2} \approx \alpha_0 + \alpha W_{1,2},\ \alpha_0 = \frac{4}{(D^2 + 16)^2 + 144 + 40a_0Ra + 4\widetilde{\xi}(m_0 - c_0)},$$

$$\alpha = \frac{32(20 - D^2 + Ra(a_0 - 5b_0) + \frac{\widetilde{\xi}}{2}(d_0 - n_0))}{\left[(D^2 + 16)^2 + 144 + 40a_0Ra + 4\widetilde{\xi}(m_0 - c_0)\right]^2}, \tag{83}$$

where

$$a_0=\frac{Pr-12.6+Ra/4}{17.64+Pr^2},\;\; b_0=\frac{2.94Pr^2(Pr-12.6+Ra/4)}{(17.64+Pr^2)^2}-\frac{2.47Pr}{17.64+Pr^2},$$

$$c_0=\frac{3}{2}D^2Ra_1\cdot\frac{25.2+8Pr}{17.64+Pr^2},\;\; d_0=\frac{3}{2}D^2Ra_1\cdot\left[\frac{2.94Pr^2(25.2+8Pr)}{(17.64+Pr^2)^2}-\frac{25.2+9.76Pr}{17.64+Pr^2}\right],$$

$$m_0=\frac{D^4}{4}Ra_1\cdot\frac{\frac{9}{4}\tilde{\xi}Ra_1-3Pr}{17.64+Pr^2},\;\; n_0=\frac{D^4}{4}Ra_1\cdot\left[\frac{4.41Pr}{17.64+Pr^2}+\frac{2.94Pr^2\left(\frac{9}{4}\tilde{\xi}Ra_1-3Pr\right)}{(17.64+Pr^2)^2}\right].$$

At small values of $W_{1.2}$, the Reynolds stresses given in (6) take the following form:

$$\begin{gathered}
T^{31}\approx-\frac{f_0^2}{8}D^2(\alpha_0+\alpha W_1)-\frac{f_0^2}{2}D(\alpha_0\sigma_0+(\alpha\sigma_0-\alpha_0\sigma_1)W_2),\\
T^{32}\approx-\frac{f_0^2}{8}D^2(\alpha_0+\alpha W_2)+\frac{f_0^2}{2}D(\alpha_0\sigma_0+(\alpha\sigma_0-\alpha_0\sigma_1)W_1),\\
\sigma_0=\frac{3}{2}-\frac{1.05Ra}{17.64+Pr^2},\;\; \sigma_1=\frac{3.087RaPr^2}{(17.64+Pr^2)^2}.
\end{gathered}\tag{84}$$

Expression (6) for the coefficient of the $\alpha$-effect shows great similarity to the previously obtained results for a rotating viscous fluid [16], the key difference being that the parameter $D$ is due to the Lorentz force rather than the Coriolis force as in Ref. [16].

## ORCID

**Michael I. Kopp**, https://orcid.org/0000-0001-7457-3272; **Volodymyr V. Yanovsky**, https://orcid.org/0000-0003-0461-749X

## REFERENCES

[1] G. Moffatt, *Magnetic Field Generation in Electrically Conducting Fluids*, (Cambridge University Press, Cambridge, 1978).

[2] F. Krauze, and K.H. Rädler, *Mean-field Magnetohydrodynamics and Dynamo Theory*, (Pergamon Press, Oxford, 1980).

[3] Ya. Zeldovich, A. Ruzmaikin, and D. Sokoloff, *Magnetic Fields in Astrophysics*, (Gordon and Breach, New York, 1983).

[4] A. Tur, and V. Yanovsky, *Coherent Vortex Structures in Fluids and Plasmas*, (Springer, New York, 2017).

[5] F. Rincon, ”Dynamo theories,— J. Plasma Phys. **85**, 205850401 (2019). https://doi.org/10.1017/S0022377819000539

[6] S.M. Tobias, ”The turbulent dynamo,” J. Fluid Mech. **912**, P1 (2021). https://doi.org/10.1017/jfm.2020.1076

[7] V. Urpin, ”Nernst effect and generation of magnetic field in radiation-heated plasma,” Plasma Phys. Rep. 45, 366–371 (2019). https://doi.org/10.1134/S1063780X19030103

[8] V. Urpin, ”Thermal generation of the magnetic field in the surface layers of massive stars,” Mon. Not. R. Astron. Soc. **472**, L5–L9 (2017). https://doi.org/10.1093/mnrasl/slx127

[9] M.I. Kopp, A.V. Tur, and V.V. Yanovsky, ”Spontaneous generation of magnetic fields in thin layers of stratified plasma,” Phys. Plasmas, **29**, 042115 (2022). https://doi.org/10.1063/5.0087543

[10] A. Schlüter, and L. Biermann, ”Über den Ursprung der Magnetfelder auf Sternen und im interstellaren Raum,” Z. Naturforsch. A, **5**, 65 (1950). https://doi.org/10.1515/zna-1950-0201

[11] M.I. Kopp, and V.V. Yanovsky, ”Features of generation of spontaneous magnetic fields in fully ionized plasma,” Probl. At. Sci. Technol. 154(6), 25–30 (2024).

[12] V.P. Lakhin, and T.J. Schep, ”On the generation of mean fields by small-scale electron magnetohydrodynamic turbulence,” Phys. Plasmas, **11**, 1424–1439 (2004). https://doi.org/10.1063/1.1645275

[13] U. Frisch, Z.S. She, and P.L. Sulem, ”Large scale flow driven by the anisotropic kinetic alpha effect,” Physica D, **28**, 382–392 (1987). https://doi.org/10.1016/0167-2789(87)90026-1

[14] P.L. Sulem, Z.S. She, H. Scholl, and U. Frisch, ”Generation of large-scale structures in three-dimensional flow lacking parity-invariance,” J. Fluid Mech. **205**, 341–358 (1989). https://doi.org/10.1017/S0022112089002086

[15] B. Dubrulle, and U. Frisch, ”Eddy viscosity of parity-invariant flow,” Phys. Rev. A, **43**, 5355–5364 (1991). https://doi.org/10.1103/PhysRevA.43.5355

[16] M.I. Kopp, and V.V. Yanovsky, ”Vortex Dynamo in Rotating Media,” East Eur. J. Phys. (2), 7–50 (2023). https://doi.org/10.26565/2312-4334-2023-2-01

[17] M.I. Kopp, A.V. Tur, and V.V. Yanovsky, ”Large-scale convective instability in an electroconducting medium with small-scale helicity,” JETP, **120**(4), 733–750 (2015). https://doi.org/10.1134/S1063776115040081

[18] M.I. Kopp, A.V. Tur, and V.V. Yanovsky, ”Nonlinear Dynamo,” arXiv:1612.08860v1 [astro-ph.EP] (2016). https://arxiv.org/abs/1612.08860v1

[19] P.N. Brandt, G.B. Scharmer, S. Ferguson, R.A. Shine, T.D. Tarbell, and A.M. Title, ”Vortex flow in the solar photosphere,” Nature, **335**, 238–240 (1988). https://doi.org/10.1038/335238a0

[20] M.I. Kopp, and V.V. Yanovsky, ”Generation of large-scale magnetic-vortex structures in stratified magnetized plasma by a small-scale force,” Phys. Plasmas, **31**, 082301 (2024). https://doi.org/10.1063/5.0214000

[21] S.I. Braginskii, ”Transport processes in plasma,” in: *Reviews of Plasma Physics*, Vol. 1, edited by M.A. Leontovich, (Consultants Bureau, New York, 1965), pp. 205-311.

[22] G.Z. Gershuni, and E.M. Zhukhovitskii, *Convective Stability of Incompressible Fluids*, (Keter Publishing House, Jerusalem, 1976).

# ВИНИКНЕННЯ ВЕЛИКОМАСШТАБНИХ МАГНІТО-ВИХРОВИХ СТРУКТУР ДРІБНОМАСШТАБНОЮ СПІРАЛЬНІСТЮ В СТРАТИФІКОВАНІЙ ЗАМАГНІЧЕНІЙ ПЛАЗМІ

**М.Й. Копп**[1], **В.В. Яновський**[1,2]

[1]*Інститут монокристаллов, Національна Академія Наук України, пр. Науки 60, 61072, Харків, Україна*

[2]*Харківський національний університет ім. В.Н. Каразіна, майдан Свободи, 4, 61022, Харків, Україна*

В роботі виявлено новий тип нестійкості, що призводить до генерації вихрових рухів та магнітних полів у плазмовому шарі з постійним градієнтом температури під дією однорідної сили тяжіння та вертикального магнітного поля. Аналіз проводиться у межах електронної магнитогидродинамики (ЕМГД) з урахуванням термомагнітних ефектів. Отримано нову великомасштабну нестійкість типу $\alpha$-ефекту, що сприяє генерації великомасштабних вихрових і магнітних полів. Ця нестійкість виникає внаслідок спільної дії зовнішнього однорідного магнітного поля, орієнтованого перпендикулярно до плазмового шару, і маломасштабної спіральної сили. Зовнішня сила моделюється як джерело дрібномасштабних коливань у полі швидкості електронів, що характеризується малим числом Рейнольдса ($R \ll 1$). Наявність малого параметра у системі дозволяє застосувати метод багатомасштабних асимптотичних розкладів. У третьому порядку за кількістю Рейнольдса отримано систему нелінійних рівнянь, що описують еволюцію великомасштабних вихрових та магнітних збурень. Обговорюється також новий ефект, пов'язаний із впливом термосили (ефект Нернста) на великомасштабну нестійкість. Показано, що збільшення параметра Нернста зменшує коефіцієнт $\alpha$ і тим самим пригнічує розвиток великомасштабної нестійкості. За допомогою чисельного аналізу отримано стаціонарні рішення рівнянь вихрового та магнітного динамо у вигляді локалізованих структур спірального типу.

**Ключові слова:** *електронна магнітогідродинаміка; багатомасштабні асимптотичні розкладання; дрібномасштабна сила; $\alpha$-ефект; локалізовані структури*

East European Journal of Physics. **4**. 212–219 (2025)

DOI: 10.26565/2312-4334-2025-4-18 ISSN 2312-4334

# SOLITARY WAVE AND SHOCK WAVE PERTURBATION FOR THE MODIFIED KAWAHARA EQUATION

**Lakhveer Kaur**[1], **Ahmed H. Arnous**[2,3], **Anjan Biswas**[4,5,6*]

[1]*Department of Mathematics, Jaypee Institute of Information Technology, Noida–201304, India*
[2]*Department of Mathematical Sciences, Saveetha School of Engineering, SIMATS, Chennai - 602105, Tamilnadu, India*
[3]*Research Center of Applied Mathematics, Khazar University, Baku, AZ 1096, Azerbaijan*
[4]*Department of Mathematics & Physics, Grambling State University, Grambling, LA 71245–2715, USA*
[5]*Department of Physics and Electronics, Khazar University, Baku, AZ–1096, Azerbaijan*
[6]*Department of Mathematics and Applied Mathematics, Sefako Makgatho Health Sciences University, Medunsa–0204, South Africa*
**Corresponding Author e-mail: biswas.anjan@gmail.com*

Received September 1, 2025; revised October 14, 2025; accepted October 17, 2025

This paper retrieves shock waves and solitary wave solutions to the modified Kawahara equation in the presence of perturbation terms. The generalized $G'/G$–expansion approach is the adopted integration methodology for the model. The parameter constraints naturally emerge during the course of derivation of the solutions which guarantee the existence of such waves.

**Keywords:** *Integrability; $G'/G$–expansion; Parameter constraints*

**PACS:** 02.30.Jr; 05.45.Yv; 02.30.Ik; 47.40.Nm

## 1. INTRODUCTION

There are several popular models in shallow water waves that govern the dynamics of such flows along lake shores and sea beaches. A few such popular models are the Korteweg-de Vries (KdV) equation, the modifies KdV equation, Boussinesq equation, Camassa–Holmes equation [1–15]. Such equations have been studied in detail over the years and their solitary wave solutions as well as shock-like wave solutions have been retrieved. Their conservation laws have also been identified.

One additional model to address shallow water waves, is the Kawahara equation (KE) and the modified KE that predominantly models dispersive shallow water waves [1]. Lately, KE was addressed using the generalized $G'/G$–expansion approach, in presence of perturbation terms [6]. It must be noted that there exists several integration schemes that can recover solirary waves, shock waves and soliton solutions to a wide range of nonlinear evolution equations [16–20]. The current paper is a follow–up of the previous work on KE. The present work addresses the perturbed modified KE and the solitary waves and shock-like wave solutions are recovered with the implementation of the generalized $G'/G$–expansion scheme. The parameter constraints also emerged from this integration scheme during the course of the derivation of the solutions. Such parameter restrictions are an important necessity for the existence of the waves. The details are enumerated and exhibited in the rest of the paper.

The Kawahara and modified Kawahara equations are canonical dispersive models describing shallow-water, plasma, and optical pulse dynamics. Exact tanh- and coth-type solutions have been obtained for unperturbed or standard forms using analytic schemes such as generalized $(G'/G)$, mapping, and bilinear-type methods [21–24]. In contrast, the present study investigates the *perturbed* modified Kawahara equation, where additional Hamiltonian-type and mixed-gradient terms modify the cubic nonlinearity and the fifth-order dispersion. Compared to earlier works, our analysis yields closed-form hyperbolic families constrained by explicit algebraic relations and reveals two distinct regimes $(m = 1)$ and $(m = 2)$ that differ in parameter freedom and tunability. We also examine how the discriminant $(\Theta = \lambda^2 - 4\mu)$ governs wave width and admissible parameter space (see Sections 2–4).

### 1.1. GOVERNING MODEL

An essential model for explaining the propagation of long waves in a variety of physical media, including shallow water, plasma, and nonlinear optical systems, is the modified KE, a dispersive nonlinear evolution equation that incorporates both cubic nonlinearity and higher-order dispersion. Richer wave phenomena, such as oscillatory solitons, non-monotonic wave profiles, and multi-soliton interactions, can be modeled with the modified form of the KE, which takes into account more intricate nonlinear interactions than the conventional version. Recent research has concentrated on achieving exact analytical solutions, such as solitary, periodic, and rational-type waves. Furthermore, the impact of nonlinearities and higher-order effects on the dynamics of wave propagation in realistic settings has been investigated using numerical simulations, modulation theory, and stability analysis.

***Cite as:*** L. Kaur, A.H. Arnous, A. Biswas, East Eur. J. Phys. 4, 212 (2025), https://doi.org/10.26565/2312-4334-2025-4-18

KE is structured as:

$$q_t + a_1 q^2 q_x + a_2 q_{xxx} - a_3 q_{xxxxx} = 0, \tag{1}$$

here $a_1,\ a_2,\ a_3$ represents cubic nonlinear coefficient, third-order and fifth order dispersion coefficient respectively.

By adding physically relevant perturbation terms, we have introduced a perturbed form of the modified KE for the first time in this work. In practical physical contexts, when idealized assumptions are not true, these perturbations take into consideration the impacts of inhomogeneity, dissipation, and external influences. In addition to increasing the model's mathematical complexity, the addition of these components offers a more precise framework for examining the stability, evolution, and interaction of nonlinear dispersive waves in less than ideal circumstances.

The modified KE with perturbation terms is introduced as follows:

$$\begin{aligned} q_t + a_1 q^2 q_x + a_2 q_{xxx} - a_3 q_{xxxxx} &= \theta q_x q_{xx} + \delta q^m q_x + \Lambda q q_{xxx} \\ &+ \nu q q_x q_{xx} + \xi q_x q_{xxx} + \psi q_{xxxxx} + \kappa q q_{xxxxx}, \end{aligned} \tag{2}$$

with $q = q(x,t)$, depicts amplitude of wave with independent variables $t$ and $x$ act as representing temporal and spatial variables.

## 2. MATHEMATICAL ANALYSIS

The perturbed modified KE (2) is investigated herein to find analytical solutions that demonstrate the impact of nonlinearity and higher-order dispersion in the presence of external factors. This analytical framework enables the construction of solitary, periodic, and rational-type solutions, providing deeper insight into how cubic nonlinearity, higher-order dispersion, and perturbative effects jointly influence the stability, amplitude, and velocity of nonlinear wave structures. We have implemented the generalized $G'/G$–expansion technique to model (2) in order to derive its exact solutions.

The considered model with perturbation terms (2) has been reduced to an ordinary differential equation in terms of the new variable $H(\sigma)$ by applying the wave transformation $\sigma = -\chi t + x$ and assuming a solution of the form with $q(x,t) = H(\sigma)$. This transformation simplifies the analysis of wave structures by basically converting the spatiotemporal dynamics into a stationary frame moving with wave speed $\chi$. Consequently, the following ordinary differential equation is reduced from the modified KE (2):

$$\begin{aligned} &(-a_3 - \kappa H(\sigma) - \psi)\, H'''''(\sigma) + (a_2 - \xi H'(\sigma) - \Lambda H(\sigma))\, H'''(\sigma) + (-\nu H(\sigma) - \theta)\, H'(\sigma)\, H''(\sigma) \\ &+ \left(-\chi - \delta\, (H(\sigma))^m + a_1 H(\sigma)^2\right) H'(\sigma) = 0. \end{aligned} \tag{3}$$

A thorough strategic investigation of equation (2) has been done by utilizing the generalized $G'/G$–expansion technique. Then, after it yielded several solitary and shock-like wave solutions, equipped with free parameters. Given the complexity, nonlinearity, and computing demands of the model (2), this study is aimed at $m = 1,\ 2$, resulting into a variety of solutions with structured dynamics.

## 3. SOLITARY AND SHOCK-LIKE (SMOOTH KINK) WAVES

Throughout this section, the term "shock-like" refers to a shock-like smooth kink with a continuous tanh-type core. The steepness, proportional to $\sqrt{\Theta}$, is constraint-limited in Case I and tunable in Case II.

### Case I ($m = 1$): condition ($\Theta > 0$)

Equation (2) has been recasted as follows after considering **m = 1** for find its explicit solutions:

$$\begin{aligned} &(-a_3 - \kappa H(\sigma) - \psi)\, H'''''(\sigma) + (a_2 - \xi H'(\sigma) - \Lambda H(\sigma))\, H'''(\sigma) + (-\nu H(\sigma) - \theta)\, H'(\sigma)\, H''(\sigma) \\ &+ \left(-\chi - \delta H(\sigma) + a_1 H(\sigma)^2\right) H'(\sigma) = 0. \end{aligned} \tag{4}$$

The following solution structure for equation (4) has been generated by appraising the homogeneous balance between its highest order derivative term and extremely nonlinear terms:

$$H(\sigma) = P_0 + P_1 \left(\frac{G'(\sigma)}{G(\sigma)}\right) + P_2 \left(\frac{G'(\sigma)}{G(\sigma)}\right)^2, \tag{5}$$

with $G(\sigma)$ satisfying following auxiliary equation:

$$G''(\sigma) + \lambda G'(\sigma) + \mu G(\sigma) = 0, \tag{6}$$

here, $P_i,\ i = 0, 1, 2$ are arbitrary parameters that need to be determined algebraically in mean computational process. The exact solutions of equation (2) are obtained by inserting the expression from (5) into equation (4), along with auxiliary condition (6) and followed by systematic collection of coefficients of similar powers of $\left(\frac{G'(\sigma)}{G(\sigma)}\right)$. The following parameter values are determined from the collection of algebraic relations, that this technique produced:

$$
\begin{gathered}
\nu = -\tfrac{60\kappa}{P_2},\ \xi = -10\,\kappa\,\sqrt{\Theta},\ P_1 = \left(\lambda + \sqrt{\Theta}\right) P_2, \\
\theta = \tfrac{61\,\kappa\,P_2\lambda^2+24\,\kappa\,P_2\lambda\,\sqrt{\Theta}-168\,\psi-48\,\kappa\,P_0-196\,\mu\,\kappa\,P_2-3\,\Lambda\,P_2-168\,a_3}{2P_2}, \\
a_1 = \tfrac{3(21\,\kappa\,P_2\lambda^2+24\,\kappa\,P_2\lambda\,\sqrt{\Theta}+\Lambda\,P_2-48\,a_3-48\,\psi-48\,\kappa\,P_0-36\,\mu\,\kappa\,P_2)}{{P_2}^2}, \\
a_2 = -52\,\mu^2\kappa\,P_2 - 52\,\mu\,a_3 + \mu\,\Lambda\,P_2 - 52\,\mu\,\psi + 13\,a_3\lambda^2 + \Lambda\,P_0 + 13\,\psi\,\lambda^2 + 39\,\mu\,\kappa\,P_2\lambda^2 + 13\,\kappa\,P_0\lambda^2 - 52\,\mu\,\kappa\,P_0 \\
-13/2\,\kappa\,P_2\lambda^4 - 13/2\,\kappa\,P_2\lambda^3\sqrt{\Theta} + 26\,\mu\,\kappa\,P_2\lambda\,\sqrt{\Theta} - 1/2\,\Lambda\,P_2\lambda^2 - 1/2\,\Lambda\,P_2\lambda\,\sqrt{\Theta}, \\
\delta = -\tfrac{Z_1}{{P_2}^2},\ \ \chi = -\tfrac{Z_2}{2{P_2}^2},\ \ \Theta = \lambda^2 - 4\,\mu,
\end{gathered}
\tag{7}
$$

with

$$
\begin{aligned}
Z_1 = {} & 2\mu\Lambda P_2^2 + \Lambda P_2^2\lambda^2 + 24\psi P_2\lambda^2 - 6\Lambda P_0 P_2 + 24a_3 P_2\lambda^2 - 384\mu\psi P_2 \\
& - 296\mu^2\kappa P_2^2 - 384\mu a_3 P_2 + 61\kappa P_2^2\lambda^4 - 98\mu\kappa P_2^2\lambda^2 - 102\kappa P_0 P_2\lambda^2 \\
& - 168\mu\kappa P_0 P_2 + 84\mu\kappa P_2^2\lambda\sqrt{\Theta} - 288\kappa P_0\lambda P_2\sqrt{\Theta} \\
& + 51\kappa P_2^2\lambda^3\sqrt{\Theta} - 144\psi\lambda P_2\sqrt{\Theta} - 144a_3\lambda P_2\sqrt{\Theta} \\
& + 3\Lambda\lambda P_2^2\sqrt{\Theta} + 288P_0 a_3 + 288P_0\psi + 288P_0^2\kappa,
\end{aligned}
\tag{8}
$$

and

$$
\begin{aligned}
Z_2 = {} & - 13P_2^3\lambda^5\kappa\sqrt{\Theta} - 24\psi\lambda^3 P_2^2\sqrt{\Theta} - 24a_3\lambda^3 P_2^2\sqrt{\Theta} \\
& - \Lambda\lambda^3 P_2^3\sqrt{\Theta} + 552\mu\kappa P_0\lambda P_2^2\sqrt{\Theta} - \Lambda\lambda^4 P_2^3 \\
& - 13P_2^3\lambda^6\kappa + 288P_0^2 a_3 + 288P_0^2\psi + 288P_0^3\kappa + 48\psi P_2^2\lambda^4 + 10\Lambda P_2^3\mu^2 \\
& - 6\Lambda P_0^2 P_2 + 96\mu^2 a_3 P_2^2 + 344\mu^3 P_2^3\kappa + 96\mu^2\psi P_2^2 + 48a_3 P_2^2\lambda^4 \\
& - 340\mu\kappa P_0 P_2^2\lambda^2 + 6\Lambda\lambda P_2^2 P_0\sqrt{\Theta} - 2\Lambda\lambda P_2^3\mu\sqrt{\Theta} \\
& - 432\kappa P_0^2\lambda P_2\sqrt{\Theta} - 288P_0\psi\lambda P_2\sqrt{\Theta} - 288P_0 a_3\lambda P_2\sqrt{\Theta} \\
& + 384\mu a_3\lambda P_2^2\sqrt{\Theta} - 118\mu\kappa P_2^3\lambda^3\sqrt{\Theta} + 248\mu^2\kappa P_2^3\lambda\sqrt{\Theta} \\
& + 78\kappa P_0\lambda^3 P_2^2\sqrt{\Theta} + 384\mu\psi\lambda P_2^2\sqrt{\Theta} - 144\mu\psi P_2^2\lambda^2 \\
& - 144\mu a_3 P_2^2\lambda^2 + 48P_0 P_2\lambda^2 a_3 + 48P_0 P_2\lambda^2\psi - 768P_0\mu a_3 P_2 \\
& - 768P_0\mu\psi P_2 + 170\kappa P_0 P_2^2\lambda^4 - 496\mu^2\kappa P_0 P_2^2 + 418\kappa\mu^2 P_2^3\lambda^2 \\
& - 92\mu\kappa P_2^3\lambda^4 - 78\kappa P_0^2 P_2\lambda^2 - 552\kappa P_0^2 P_2\mu + 2\Lambda P_0 P_2^2\lambda^2 \\
& + 4\mu\Lambda P_0 P_2^2,
\end{aligned}
\tag{9}
$$

equipped with $\psi,\ \Lambda,\ P_0,\ P_2,\ \kappa$ as all free parameters in acquired parameter values.

By replicating (5) using the solution of equation (6) and parameter values found in (7), and then transforming to original variables $x,\ t$, the following solution structure for equation (2) has been retrieved.

The solution structure for equation (2) has been determined as follows:

$$
\begin{aligned}
q\,(x,\ t) = {} & \left(\lambda + \sqrt{\Theta}\right) P_2 \left( \frac{\sqrt{\Theta}\left(w_1 \sinh\left(\frac{1}{2}\,\sigma\,\sqrt{\Theta}\right) + w_2 \cosh\left(\frac{1}{2}\,\sigma\,\sqrt{\Theta}\right)\right)}{2\,w_2 \sinh\left(\frac{1}{2}\,\sigma\,\sqrt{\Theta}\right) + 2\,w_1 \cosh\left(\frac{1}{2}\,\sigma\,\sqrt{\Theta}\right)} - \frac{1}{2}\,\lambda \right) \\
& + P_0 + P_2 \left( \frac{\sqrt{\Theta}\left(w_1 \sinh\left(\frac{1}{2}\,\sigma\,\sqrt{\Theta}\right) + w_2 \cosh\left(\frac{1}{2}\,\sigma\,\sqrt{\Theta}\right)\right)}{2\,w_2 \sinh\left(\frac{1}{2}\,\sigma\,\sqrt{\Theta}\right) + 2\,w_1 \cosh\left(\frac{1}{2}\,\sigma\,\sqrt{\lambda^2 - 4\,\mu}\right)} - \frac{1}{2}\,\lambda \right)^2,
\end{aligned}
\tag{10}
$$

here $w_1,\ w_2$ as arbitrary parameters and $\sigma = x - \chi t$ with $\chi$ given by (7).

**Category–I**: We have set up parameters choices as $w_1$ to zero and $w_2 \neq 0$ in order to find singular solitary wave solutions from the obtained solution (10) for equation (2). The resultant solution offers important information on the behavior of solution structures under particular physical conditions, featuring soliton dynamics.

$$\begin{aligned} q(x,t) &= P_0 + \left(\lambda + \sqrt{\Theta}\right) P_2 \left(\frac{1}{2}\sqrt{\Theta}\coth\left(\frac{1}{2}(x-\chi t)\sqrt{\Theta}\right) - \frac{1}{2}\lambda\right) \\ &+ P_2 \left(\frac{1}{2}\sqrt{\Theta}\coth\left(\frac{1}{2}(x-\chi t)\sqrt{\Theta}\right) - \frac{1}{2}\lambda\right)^2 . \end{aligned} \tag{11}$$

**Category–II**: By taking a particular values into consideration for the parameters $w_1 \neq 0$ and $w_2 = 0$, the shock-like wave solutions are retrieved from the resultant solution (10). This results into a term elimination, making the expression simpler and increases the dominance of nonlinear steepening, as a crucial aspect of shock-like wave production.

$$\begin{aligned} q(x,t) &= P_0 + \left(\lambda + \sqrt{\Theta}\right) P_2 \left(\frac{1}{2}\sqrt{\Theta}\tanh\left(\frac{1}{2}(x-\chi t)\sqrt{\Theta}\right) - \frac{1}{2}\lambda\right) \\ &+ P_2 \left(\frac{1}{2}\sqrt{\Theta}\tanh\left(\frac{1}{2}(x-\chi t)\sqrt{\Theta}\right) - \frac{1}{2}\lambda\right)^2 . \end{aligned} \tag{12}$$

All hyperbolic-type families considered here require $\Theta > 0$. The algebraic consistency relations summarized in (7) tie $\lambda$ and $\mu$ (hence $\Theta$) to the remaining coefficients; therefore $\Theta$ is *not freely tunable* but acts as a constraint on admissible parameter sets. Consequently, the inverse width $\sqrt{\Theta}$—and thus the steepness of the coth/tanh cores in (10)–(12)—is fixed once a feasible coefficient set is chosen.

It is worth noting that the equation (3) results into more computationally demanding analysis and a significantly more complex equation structure due to the higher-order nonlinear term interacting with both third- and fifth-order dispersive effects, as well as the introduced perturbation terms. This enhances the degree of involved computations, leading to larger algebraic systems with multiple coupled nonlinear parameter relations that require higher end symbolic computations. Thus next in this study, equation (2) is analyzed with $m = 2$ for generating new exact solutions.

### Case II ($m = 2$): condition ($\Theta > 0$)

The equation (3) is recited as follows with $m = 2$:

$$\begin{aligned} &(-a_3 - \kappa H(\sigma) - \psi) H''''(\sigma) + (a_2 - \xi H'(\sigma) - \Lambda H(\sigma)) H'''(\sigma) + (-\nu H(\sigma) - \theta) H'(\sigma) H''(\sigma) \\ &+ \left(-\chi - \delta\,(H(\sigma))^2 + a_1 H(\sigma)^2\right) H'(\sigma) = 0. \end{aligned} \tag{13}$$

The homogeneous balancing method is being utilized for equation (13) in order to find a balance between the equation's highest-order linear derivative term and its highest-order nonlinear term. As a result, following solutions structure is being proposed for equation (13):

$$H(\sigma) = P_0 + P_1\left(\frac{G'(\sigma)}{G(\sigma)}\right) + P_2\left(\frac{G'(\sigma)}{G(\sigma)}\right)^2, \tag{14}$$

Here, $G(\sigma)$ is a function that satisfies the auxiliary equation (6), while $P_i,\ i = 0, 1, 2$ are arbitrary parameters that must be found via algebraic calculations. The expression (14) is substituted into equation (13) along with the auxiliary condition (6) and thenafter coefficients of like powers of $\left(\frac{G'(\sigma)}{G(\sigma)}\right)$ are collected, to produce the exact solutions of equation (2). As stated below, this process produces a set of algebraic relations from which the parameter values required for the solutions to exist are derived:

$$\begin{aligned} &\chi = \tfrac{1}{252} P_2 \left(276\,\lambda^4\mu\,\kappa - 312\,\theta\,\lambda^2\mu - 23\,\lambda^6\kappa + 39\,\theta\,\lambda^4 + 624\,\theta\,\mu^2 - 1104\,\lambda^2\mu^2\kappa + 1472\,\mu^3\kappa\right), \\ &\nu = -\tfrac{60\kappa}{P_2},\ \ \psi = -\tfrac{32}{21}\,\kappa\,\mu\,P_2 + \tfrac{8}{21}\,\kappa\,\lambda^2 P_2 - \tfrac{1}{84}\,\theta\,P_2 - a_3, \\ &\xi = -10\,\kappa\sqrt{\Theta}, \Lambda = -\tfrac{1}{3}\,\kappa\,\left(4\,\mu - \lambda^2\right), \\ &\delta = \tfrac{-148\,\lambda^2\kappa + 592\,\kappa\,\mu - 12\,\theta + 7\,a_1 P_2}{7P_2}, \\ &P_0 = -\tfrac{7}{12}\,\lambda^2 P_2 + 4/3\,P_2\mu + \left(\tfrac{1}{2}\,\lambda + \tfrac{1}{2}\sqrt{\Theta}\right) P_2\lambda,\ \ P_1 = \left(\lambda + \sqrt{\Theta}\right) P_2, \\ &a_2 = -\tfrac{1}{252}\,P_2\left(712\,\kappa\,\lambda^4 + 39\,\theta\,\lambda^2 + 11392\,\kappa\,\mu^2 - 156\,\theta\,\mu - 5696\,\kappa\,\lambda^2\mu\right), \end{aligned} \tag{15}$$

accompanied by $P_2,\ a_3,\ a_1,\ \kappa,\ \theta$ as free parameters in obtained parameter values.

The relations reported in (15) allow additional freedom in choosing $\lambda$ and $\mu$, so $\Theta = \lambda^2 - 4\mu$ becomes a *design-tunable* quantity. Accordingly, $\sqrt{\Theta}$ directly controls the front steepness and packet width in the expressions (16)–(18): as $\Theta \downarrow 0^+$ the structures broaden, whereas larger $\Theta$ yields steeper, more localized profiles.

Rewriting (14) using the solution of equation (6) and parameter values (15), we have yielded the following solution structure for equation (2)

$$
\begin{aligned}
q\left(x,\ t\right) = {} & \left(\lambda+\sqrt{\Theta}\right)P_2\left(\frac{\sqrt{\Theta}\left(w_1\sinh\left(\frac{1}{2}\,\sigma\,\sqrt{\Theta}\right)+w_2\cosh\left(\frac{1}{2}\,\sigma\,\sqrt{\Theta}\right)\right)}{2\,w_2\sinh\left(\frac{1}{2}\,\sigma\,\sqrt{\Theta}\right)+2\,w_1\cosh\left(\frac{1}{2}\,\sigma\,\sqrt{\Theta}\right)}-\frac{1}{2}\lambda\right)\\
& +P_0+P_2\left(\frac{\sqrt{\Theta}\left(w_1\sinh\left(\frac{1}{2}\,\sigma\,\sqrt{\Theta}\right)+w_2\cosh\left(\frac{1}{2}\,\sigma\,\sqrt{\Theta}\right)\right)}{2\,w_2\sinh\left(\frac{1}{2}\,\sigma\,\sqrt{\Theta}\right)+2\,w_1\cosh\left(\frac{1}{2}\,\sigma\,\sqrt{\Theta}\right)}-\frac{1}{2}\lambda\right)^2,
\end{aligned}
\tag{16}
$$

here $w_1,\ w_2$ as arbitrary parameters and $\sigma = x - \chi t$ with $\chi$ given by (15).

**Category–I**: The singular solitary wave solutions are recovered from obtained solution (16) for equation (2), by taking into account $w_1 = 0$ and $w_2 \neq 0$ as follows:

$$
\begin{aligned}
q(x,t) = {} & P_0+\left(\lambda+\sqrt{\Theta}\right)P_2\left(\frac{1}{2}\,\sqrt{\Theta}\coth\left(\frac{1}{2}\,(x-\chi t)\,\sqrt{\Theta}\right)-\frac{1}{2}\,\lambda\right)\\
& +P_2\left(\frac{1}{2}\,\sqrt{\Theta}\coth\left(\frac{1}{2}\,(x-\chi t)\,\sqrt{\Theta}\right)-\frac{1}{2}\,\lambda\right)^2.
\end{aligned}
\tag{17}
$$

**Category–II**: Embedding the parameter values as $w_1 \neq 0$ and $w_2 = 0$ in solution (16), we have procured the shock-like wave solutions for equation (2) as described below:

$$
\begin{aligned}
q(x,t) = {} & P_0+\left(\lambda+\sqrt{\Theta}\right)P_2\left(\frac{1}{2}\,\sqrt{\Theta}\tanh\left(\frac{1}{2}\,(x-\chi t)\,\sqrt{\Theta}\right)-\frac{1}{2}\,\lambda\right)\\
& +P_2\left(\frac{1}{2}\,\sqrt{\Theta}\tanh\left(\frac{1}{2}\,(x-\chi t)\,\sqrt{\Theta}\right)-\frac{1}{2}\,\lambda\right)^2.
\end{aligned}
\tag{18}
$$

## 4. RESULTS AND DISCUSSION

In Case I ($m = 1$), perturbation-induced algebraic constraints fix $(\lambda, \mu, \Theta)$, producing specialized localized or kink-type profiles with fixed inverse width ($\sqrt{\Theta}$). In Case II ($m = 2$), $\Theta$ remains tunable, enabling continuous adjustment of front steepness and packet width for a given background level ($P_0$). Physically, Case I corresponds to a calibrated medium with fixed material or flow properties, whereas Case II models a design scenario where front thickness and localization can be engineered.

Now, we interpret the closed–form families obtained in Secs. 3, quantify the parameter regimes under which each family exists, and relate the formulas to their physical content and to limiting or benchmark cases. Throughout we use the traveling coordinate $\sigma = x - \chi t$ with wave speed $\chi$ given by (7) for $m = 1$ and by (15) for $m = 2$, and the discriminant $\Theta = \lambda^2 - 4\mu$. The hyperbolic families discussed below require $\Theta > 0$.

For both $m = 1$ and $m = 2$ we obtained the ansatz

$$
H(\sigma) = P_0 + P_1\left(\tfrac{G'}{G}\right) + P_2\left(\tfrac{G'}{G}\right)^2, \qquad G'' + \lambda G' + \mu G = 0,
$$

with $P_1 = (\lambda + \sqrt{\Theta})P_2$ and $\Theta = \lambda^2 - 4\mu$. When $\Theta > 0$ the auxiliary solution yields the hyperbolic representation (10) (for $m = 1$) and (16) (for $m = 2$). Two canonical parameter selections

$$
(w_1, w_2) = (0,\ w_2 \neq 0), \qquad (w_1 \neq 0,\ 0)
$$

produce, respectively, the singular solitary profiles (11), (17) (with a coth core) and the *shock–type* or kink–like profiles (12), (18) (with a tanh core). A rigid shift $\sigma \mapsto \sigma - \sigma_0$ (absorbed into $w_1, w_2$) relocates the crest or front without altering amplitude or width.

The roles of the key parameters can be summarized as follows in prose. The coefficient $P_2$ scales the overall amplitude of the nonlinear part, while $P_0$ sets the background offset level. The parameter $\sqrt{\Theta}$ controls the inverse width of the wave; larger values of $\sqrt{\Theta}$ yield narrower structures. The sign and magnitude of $\kappa$ couple the field $q$ into the highest–order dispersion and appear explicitly in the algebraic constraints (7) and (15), thereby tuning both the steepening (shock) and localization (solitary) tendencies.

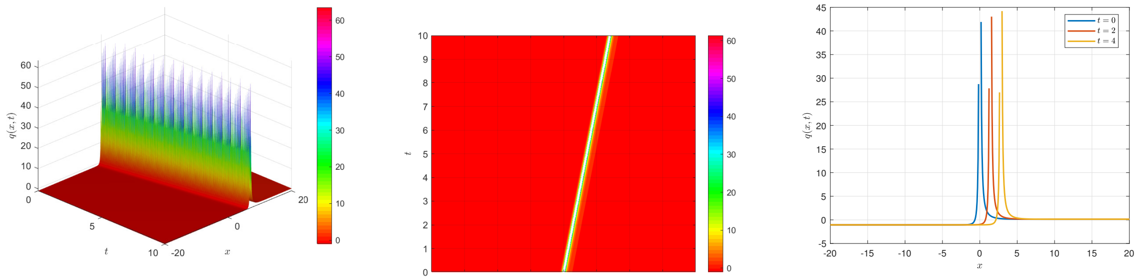

**(a)** Three-dimensional representation of $q(x,t)$.

**(b)** Contour illustration of $q(x,t)$.

**(c)** Cross-sectional profiles at several $t$ values.

**Figure 1.** Category–I singular solitary wave pattern derived from Eq. (11).

Figure 1 illustrates the Category–I singular solitary wave solution of the perturbed modified Kawahara equation. Subfigure 1a shows the three-dimensional structure of $q(x,t)$, highlighting its strongly localized profile with sharp variations in amplitude. The contour plot in Subfigure 1b further emphasizes the persistence of this localized structure across the spatiotemporal domain. Cross-sectional in Subfigure 1c confirm that the wave maintains its shape over time, a defining property of solitary waves. Physically, these solutions represent stable energy packets arising from the balance between higher-order dispersion and cubic nonlinearity, relevant in shallow water dynamics, plasma propagation, and nonlinear optics.

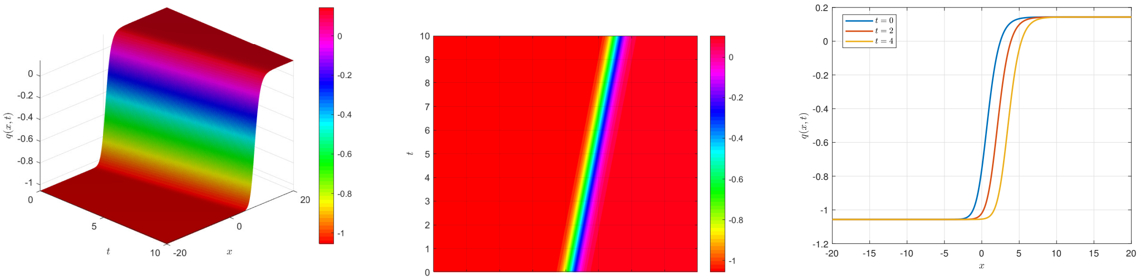

**(a)** Three-dimensional visualization of $q(x,t)$.

**(b)** Contour depiction of $q(x,t)$.

**(c)** Snapshots of wave profiles for multiple $t$ values.

**Figure 2.** Category–II shock-type wave solution corresponding to Eq. (12).

Figure 2 presents the Category–II shock-type wave solution. The three-dimensional visualization in Subfigure 2a reveals the steep front of the shock profile, while the contour map in Subfigure 2b shows the abrupt transitions characteristic of nonlinear steepening. Subfigure 2c illustrate how these sharp wave fronts evolve over time. Physically, such solutions capture the role of strong nonlinearity and perturbative effects that drive shock formation, representing phenomena like breaking waves in hydrodynamics, compression waves in plasmas, and intense pulse propagation in nonlinear optical media. Together, Figures 1 and 2 demonstrate the contrasting interplay of dispersion and nonlinearity: the former yielding localized solitary waves, and the latter producing steep shock fronts under stronger nonlinear dominance. Figures 1 and 2 display the two canonical families for $m = 1$ (the $m = 2$ families have the same functional form with the speed and coefficients given by (15)).

The solution (11) (and (17)) is localized with an algebraic singularity at the center when $\sigma = 0$, reflecting a pole inherited from coth. Physically, this corresponds to a strongly localized structure supported by the balance of cubic nonlinearity and fifth–order dispersion, with the perturbations $(\theta, \delta, \Lambda, \nu, \xi, \psi, \kappa)$ renormalizing the amplitude, width, and speed. The singularity can be shifted off the physical domain by choosing the origin so that $\sigma \neq 0$ in the region of interest.

The solution (12) (and (18)) is a monotone front connecting two asymptotic states determined by $(P_0, P_2, \lambda, \Theta)$. Nonlinear steepening is reinforced by the mixed–gradient terms $(\theta, \nu, \xi)$ and the $q$–dependent highest–order dispersion $(\kappa)$, while fifth–order dispersion ($a_3$ and $\psi$) spreads the front, yielding a finite transition width proportional to $\Theta^{-1/2}$.

To clearly visualize the contrast between both studied regimes, a concise comparative summary is provided in Table titled ”Summary Table: Case I vs. Case II”. This table highlights the algebraic, structural, and physical differences between the two cases, emphasizing how tunability of $\Theta$ and wave localization properties distinguish the calibrated (Case I) and design–oriented (Case II) media.

**Summary Table: Case I vs. Case II**

| **Aspect** | **Case I** ($m = 1$) | **Case II** ($m = 2$) |
|---|---|---|
| Consistency relations | Algebraic constraints summarized near Eq. (7) | Algebraic constraints summarized near Eq. (15) |
| Discriminant $\Theta = \lambda^2 - 4\mu$ | Constrained by coefficients; $\Theta > 0$ restricts admissible sets | Effectively design-tunable (choose $\lambda, \mu$ so $\Theta > 0$) |
| Core profile | coth (singular solitary) Eq. (11); tanh (shock-like) Eq. (12) | coth Eq. (17); tanh Eq. (18) |
| Width / steepness | Fixed by $\sqrt{\Theta}$ (set by constraints) | Tunable via $\sqrt{\Theta}$ (design parameter) |
| Wave speed $\chi$ | Explicit relation from Eq. (7) | Explicit relation from Eq. (15) |
| Physical meaning | Calibrated medium with fixed material/flow properties (restricted set) | Design/tunable medium where front thickness and localization can be engineered |

In the unperturbed limit, setting all perturbations to zero,

$$\theta = \delta = \Lambda = \nu = \xi = \psi = \kappa = 0,$$

reduces (2) to the modified Kawahara equation (1). In this limit the algebraic constraints collapse to the familiar relations for the pure modified KE and the hyperbolic families reduce to the standard tanh and coth profiles reported for the (modified) KE [1].

From (7) (for $m = 1$) and (15) (for $m = 2$), the wave speed $\chi$ is an explicit polynomial in $(\lambda, \mu)$ modulated by $\kappa$ and by the perturbation strengths. Two robust qualitative trends hold. Increasing $\sqrt{\Theta}$, which produces narrower waves, increases $|\chi|$ when the $k^5$ dispersion $(a_3 + \psi)$ reinforces the cubic term (same sign), and decreases $|\chi|$ otherwise. This echoes the linear dispersion balance visible in $\omega(k)$. Moreover, positive $\kappa$, which strengthens the $q$–dependence in $q_{xxxxx}$, increases the magnitude of both steepening (Category–II) and localization (Category–I), manifesting in larger $|\xi|$ and $|\nu|$ via (7) and (15).

For reproducibility it is useful to summarize the most influential controls in narrative form. The wave width is set by $\sqrt{\Theta}$, and choosing $\lambda, \mu$ with $\lambda^2 - 4\mu$ large produces narrow structures. The amplitude scales with $P_2$, while $P_0$ shifts the baseline asymptote. The choice $(w_1, w_2) = (1, 0)$ yields shock–type tanh fronts, while $(0, 1)$ yields singular solitary coth pulses. The high–$k$ tailing is controlled by $a_3 + \psi$, and changing its sign flips the curvature of $\omega(k)$ and the propensity for oscillatory overshoots near the front.

The perturbed terms in (2) also play clear roles. The terms $\theta q_x q_{xx}$ and $\nu q q_x q_{xx}$ enhance local steepening and promote shock formation (Category–II). The couplings $\Lambda q q_{xxx}$ and $\xi q_x q_{xxx}$ mediate nonlinear dispersive effects, modifying the front width and generating mild oscillations depending on the sign of $a_3 + \psi$. The $\psi q_{xxxxx}$ term renormalizes the fifth–order dispersion in the linear limit, directly influencing the selection of $\sqrt{\Theta}$ via the consistency relations. Finally, $\kappa q q_{xxxxx}$ couples amplitude to the highest–order dispersion and provides an additional lever to stabilize or destabilize steep structures without changing the background. These roles align with the contrasting morphologies shown in Figs. 1–2: dispersion versus nonlinearity determines whether energy remains localized (singular solitary waves) or organizes into a persistent transition layer (shock or kink).

## 5. CONCLUSIONS

The current paper recovered singular solitary wave and shock-like wave solutions to the perturbed modified KE. The perturbation terms are of Hamiltonian type which made this retrieval possible. The generalized $G'/G$–expansion scheme has made this retrieval possible along with the parameter constraints that guarantees the existence of such waves. It is visibly obvious of the shortcoming with this integration algorithm. The scheme fails to recover solitary wave solutions to the model. Therefore, later additional integration approaches will be adopted that would recover the solitary wave solutions in addition to the singular solitary waves and shock-like wave solutions. Such studies are under way and the results will be disseminated shortly.

### Acknowledgments

This work of the last author (AB) was supported by Grambling State University for the Endowed Chair of Mathematics. The author thankfully acknowledges this support.

### ORCID

**Lakhveer Kaur**, https://orcid.org/0000-0002-1936-474X; **Ahmed H. Arnous**, https://orcid.org/0000-0002-7699-7068; **Anjan Biswas**, https://orcid.org/0000-0002-8131-6044

## REFERENCES

[1] A. Biswas, Appl. Math. Lett. **22**(2), 208–210 (2009). https://doi.org/10.1016/j.aml.2008.03.011

[2] A. Biswas, J. Vega-Guzman, A. Bansal, A.H. Kara, M. Aphane, Y. Yildirim, and H.M. Alshehri, Proc. Est. Acad. Sci. **72**(1), 17–29 (2023). https://doi.org/10.3176/proc.2023.1.03

[3] L. Kaur, Y. Yildirim, A.R. Adem, L. Moraru, and A. Biswas, Contemporary Mathematics (Wiser Publishers), **6**(2), 1756–1783 (2025). https://doi.org/10.37256/cm.6220256307

[4] L. Kaur, Y. Yildirim, A.H. Arnous, L. Moraru, A.M.K. Al-Dulaimi, A.S. Mahmood, and A. Biswas, Contemporary Mathematics (Wiser Publishers), **6**(3), 3715–3742 (2025). https://doi.org/10.37256/cm.6320256967

[5] L. Kaur, A. Biswas, A.H. Arnous, Y. Yildirim, L. Moraru, and M.J. Jweeg, Contemporary Mathematics (Wiser Publishers), **6**(3), 3743–3762 (2025). https://doi.org/10.37256/cm.6320256903

[6] L. Kaur, A.H. Arnous, I.Z. Chaloob, A.S. Mahmood, A.M.K. Al-Dulaimi, and A. Biswas, Submitted (Solitary waves and shock waves for the perturbed Kawahara equation).

[7] N.A. Kudryashov, and D.I. Sinelshchikov, Acta Appl. Math. **113**(1), 41–44 (2011). https://doi.org/10.1007/s10440-010-9582-6

[8] C.S. Liu, Comput. Phys. Commun. **181**(2), 317–324 (2010). https://doi.org/10.1016/j.cpc.2009.10.006

[9] A.D. Polyanin, and N.A. Kudryashov, Contemporary Mathematics (Wiser Publishers), **5**(4), 5783–5794 (2024). https://doi.org/10.37256/cm.5420245840

[10] X.Y. Tang, and S.Y. Lou, J. Math. Phys. **44**(9), 4000–4025 (2003). https://doi.org/10.1063/1.1598619

[11] A.M. Wazwaz, Chaos, Solitons Fractals, **196**, 116307 (2025). https://doi.org/10.1016/j.chaos.2025.116307

[12] A.M. Wazwaz, S.A. El-Tantawy, L.S. El-Sherif, A.S. Al-Johani, and H.A. Alyousef, Alexandria Eng. J. **123**, 1–16 (2025). https://doi.org/10.1016/j.aej.2025.03.035

[13] K. Manju, and A.M. Wazwaz, Chinese J. Phys. **93**, 515–530 (2025). https://www.sciencedirect.com/science/article/pii/S0577907324004878

[14] A.M. Wazwaz, Int. J. Numer. Model. Electron. Netw. Devices Fields, **38**(3), e70063 (2025). https://doi.org/10.1002/jnm.70063

[15] A.S. Rashed, T.A. Mahmoud, and A.M. Wazwaz, Waves Random Complex Media, **35**(2), 3662–3690 (2025). https://doi.org/10.1080/17455030.2022.2053611

[16] A.J.M. Jawad and M.J. Abu-AlShaeer, Al-Rafidain J. Eng. Sci. **1**(1), 1–8 (2023). https://doi.org/10.61268/sapgh524

[17] N. Jihad, and M.A.A. Almuhsan, Al-Rafidain J. Eng. Sci. **1**(1), 81–92 (2023). https://doi.org/10.61268/0dat0751

[18] A.J.M. Jawad, and A. Biswas, Al-Rafidain J. Eng. Sci. **2**(1), 43–50 (2024). https://doi.org/10.61268/2bz73q95

[19] I.M. Mendez-Zuniga, T.L. Belyaeva, M.A. Aguero, and V.N. Serkin, Transactions in Optics and Photonics, **1**(1), 22–33 (2025). https://ojs.wiserpub.com/index.php/top/article/view/5835

[20] Z. Kasapeteva, Transactions in Optics and Photonics, **1**(1), 58–66 (2025). https://ojs.wiserpub.com/index.php/top/article/view/6639

[21] A.M. Wazwaz, Phys. Lett. A, **360**(4–5), 588–592 (2007). https://doi.org/10.1016/j.physleta.2006.08.068

[22] T. Öziş and İ. Aslan, Appl. Math. Comput. **216**(8), 2360–2365 (2010). https://doi.org/10.1016/j.amc.2010.03.081

[23] A. Bekir, Phys. Lett. A, **372**(19), 3400–3406 (2008). https://doi.org/10.1016/j.physleta.2008.01.057

[24] K.A. Gepreel, J. Partial Differential Equations, **24**(1), 55–69 (2011). https://doi.org/10.4208/jpde.v24.n1.4

# ЗБУРЕННЯ ОДИНОЧНОЇ ХВИЛІ ТА УДАРНОЇ ХВИЛІ ДЛЯ МОДИФІКОВАНОГО РІВНЯННЯ КАВАХАРИ

**Лаквір Каур**[1], **Ахмед Х. Арнус**[2,3], **Анджан Бісвас**[4,5,6]
[1]*Кафедра математики, Інститут інформаційних технологій Джайпі, Нойда–201304, Індія*
[2]*Кафедра математичних наук, Інженерна школа Савітха, SIMATS, Ченнаї - 602105, Тамілнад, Індія*
[3]*Науково-дослідний центр прикладної математики, Університет Хазар, Баку, Аризона 1096, Азербайджан*
[4]*Кафедра математики та фізики, Державний університет Гремблінга, Гремблінг, Луїзіана 71245–2715, США*
[5]*Кафедра фізики та електроніки, Університет Хазар, Баку, AZ–1096, Азербайджан*
[6]*Кафедра математики та прикладної математики, Університет медичних наук Сефако Макгатхо, Медунса–0204, Південна Африка*

У цій статті отримано розв'язки модифікованого рівняння Кавахари на основі ударних хвиль та одиночних хвиль за наявності членів збурень. Узагальнений підхід $G'/G$–розкладу є прийнятою методологією інтегрування для моделі. Обмеження параметрів природно виникають під час виведення розв'язків, які гарантують існування таких хвиль.

**Ключові слова:** *інтегрованість; $G'/G$–розклад; обмеження параметрів*

East European Journal of Physics. **4.** 220-229 (2025)
DOI:10.26565/2312-4334-2025-4-19 ISSN 2312-4334

# STIMULATED RAMAN SCATTERING OF HIGH-POWER BEAM IN COLLISIONAL MAGNETOPLASMA

**Keshav Walia[1]*, Taranjot Singh[1], Anuj Vijay[2], Deepak Tripathi[3]**
*[1]Department of Physics, DAV University Jalandhar, India*
*[2]Department of Physics, GLA University Mathura (U.P.), India-281406*
*[3]Physics Department, USAR, Guru Gobind Singh Indraprastha University, East Delhi Campus, Delhi, India-110032*
**Corresponding Author e-mail: keshavwalia86@gmail.com*

Received August 28, 2025; revised October 5, 2025; accepted October 16, 2025

The present problem investigates Stimulated Raman Scattering of high-power beam in Collisional magnetoplasma. The laser beam has two propagation modes viz. extraordinary and ordinary modes, while its transition along the direction of static magnetic fields. The carrier redistribution affected due to modification in static magnetic field. The carrier redistribution will take place due to non-uniform heating, which results in variation in density profile in a transverse direction to axis of main beam. This density profile further causes modification in all the three waves involved in the process viz. incident beam, electron plasma wave and scattered wave. Here, 2nd order ODE for beam waists of pump beam, EPW and back-scattered wave and also expression for reflectivity will be obtained and further their numerical simulations will be carried out in order to explore impact of change in laser and plasma parameters and also externally applied magnetic field on beam waists of various waves and on SRS back-reflectivity.

**Keywords**: *Stimulated Raman Scattering; Static magnetic field; Non-uniform heating; Scattered Wave; Back-reflectivity*
**PACS:** 52.38.Hb, 52.35.Mw, 52.38.Dx

## 1. INTRODUCTION

New developments in laser technology resulted in generation of laser beams of small duration having peak power up to petawatt range are available [1, 2]. Researchers are interested in exploring lasers interaction with plasma medium as a result of its diverse applications such as particle acceleration, laser driven fusion and new radiation sources [3-8]. Much deeper lasers transition through plasmas is chief concern in accomplishing success in these applications. Further, laser-plasma interaction generates various instabilities such as self-focusing, scattering instabilities, harmonic generation and two plasmon decay [9-22]. The laser energy is not properly transferred to plasma medium due to these instabilities [23]. The coupling efficiency between lasers and plasma can be improved by controlling these instabilities. Self-focusing and Scattering instabilities play crucial role in laser driven fusion. In Self-focusing, laser beam transition through plasmas results in change in plasma's refractive index [24]. The density gradient created in plasmas is main cause behind self-focusing. There is rise in beam's irradiance due to self-focusing. Self-focusing causes variation in beam's angular divergence. [25]. SRS causes the breaking of main beam in to electron plasma wave (EPW) and scattered wave. SRS causes reduction in amount of laser energy transferred to plasma target. Excited EPW due to SRS has phase velocity equivalent to light's speed. It could in fact accelerate electrons that can preheat fusion fuel and reduce implosion efficiency. There is major effect of focusing of beam on SRS back-reflectivity [26]. The reduction in laser-plasma coupling efficiency is found due to both self-focusing and SRS. It is essential to have some control on these instabilities for success of inertial confinement fusion. Researchers have investigated Self-focusing and Scattering instabilities of intense laser pulses in plasmas in the past [27-34]. Barr et al. [35] investigated that SRS growth rate is greatly affected due to self-focusing. Short et al. [36] investigated effect of self-focusing on SRS instability in laser driven plasmas. In their investigation, they find that self-focusing greatly enhances SRS growth rate. The novel method has been proposed for control of SRS and electron production by Dodd and Umstadter [37]. Kalmykova and Shvets have explored SRS of laser radiation in deep plasma channels [38]. They explored that there is great reduction in growth rate of SRS on account of localization of EPW. The impact of beam irradiance and electron temperature on SRS growth rate has been explored with Kirkwood et al. [39]. The impact of filamentation of beam on SRS has been explored using non-paraxial approach by using Sharma et al. [40]. The impact of filamentation of beam on EPW and SRS back-reflectivity has been explored by Purohit et al. [41]. Singh and Walia [42] investigated effect of self-focusing on SRS and observed that focusing tendency of waves involved enhances SRS back-reflectivity. Rawat et al. [43] explored joint action of relativistic-ponderomotive forces on ring rippled beam transition in unmagnetized plasma and its effect on SRS. In their case, SRS back-reflectivity is greatly reduced at larger intensities. Sharma et al. [44] explored SRS of dark hollow Gaussian beam in unmagnetized plasma. They found that there is focusing tendency and scattered power are decreased with increment in hollow Gaussian beam's order. In fact, it has been revealed from the literature that various beam profiles have been used for exploring self-focusing and SRS [45-57]. But, impact of self-focusing on SRS has not been investigated yet in cylindrical Gaussian beams in collisional magnetized plasma. So, in present work, we are investigating for first time impact of self-focusing of Gaussian laser beams in collisional magnetized plasma.

---

***Cite as:*** K. Walia, T. Singh, A. Vijay, D. Tripathi, East Eur. J. Phys. 4, 220 (2025), https://doi.org/10.26565/2312-4334-2025-4-19

EPW $(\omega, k)$ interacts with main beam $(\omega_0, k_0)$ to produce scattered wave $(\omega_0 - \omega, k_0 - k)$. The case of backscattering for $k \approx 2k_0$ is considered in present case. The carrier's redistribution take place due to non-uniform heating thereby causing self-focusing. There is modification in dispersion relation connected with EPW and hence EPW also gets self-focused under suitable boundary conditions. Irradiance associated with scattered wave is directly proportional to irradiance related with main wave and EPW. So, self-focusing results in improvement in back-scattering.

## 2. SOLUTION OF WAVE EQUATION FOR PUMP WAVE

The laser beam having Gaussian profile is assumed to be propagating along z-axis. The direction of static magnetic field is also along z-axis. There are basically two transition modes viz. extraordinary mode and ordinary mode. The RH circularly polarized beam is described by extra-ordinary mode while LH circularly polarized beam is described by ordinary mode.

$$A_1 = E_x + iE_y \tag{1}$$

$$A_2 = E_x - iE_y \tag{2}$$

The field vector $'E'$ of beam obeys following wave equation

$$\nabla^2 E - \nabla(\nabla \cdot E) + \frac{\omega^2}{c^2}\epsilon E = 0 \tag{3}$$

In Component form, we can express Eq. (3) as

$$\frac{\partial^2 E_x}{\partial z^2} + \frac{\partial^2 E_x}{\partial y^2} - \frac{\partial}{\partial x}\left(\frac{\partial E_y}{\partial y} + \frac{\partial E_z}{\partial z}\right) = -\frac{\omega^2}{c^2}(\epsilon E)_x \tag{4}$$

$$\frac{\partial^2 E_y}{\partial z^2} + \frac{\partial^2 E_y}{\partial x^2} - \frac{\partial}{\partial y}\left(\frac{\partial E_x}{\partial x} + \frac{\partial E_z}{\partial z}\right) = -\frac{\omega^2}{c^2}(\epsilon E)_y \tag{5}$$

$$\frac{\partial^2 E_z}{\partial z^2} + \frac{\partial^2 E_z}{\partial y^2} - \frac{\partial}{\partial z}\left(\frac{\partial E_x}{\partial x} + \frac{\partial E_y}{\partial y}\right) = -\frac{\omega^2}{c^2}(\epsilon E)_z \tag{6}$$

Here, we have considered that $(\nabla \cdot E) = 0$ and further we make use of the assumption that alteration in field along z-direction is more rapid.

$$\frac{\partial E_z}{\partial z} = -\frac{1}{\epsilon_z}\left(\epsilon_x \frac{\partial E_x}{\partial x} + \epsilon_x \frac{\partial E_y}{\partial x} + \epsilon_y \frac{\partial E_x}{\partial y} + \epsilon_y \frac{\partial E_y}{\partial y}\right) \tag{7}$$

The term $\pm i$ is multiplied with Eq. (7) and resultant is added to Eq. (4), one can easily get

$$\frac{\partial^2 A_1}{\partial z^2} + \frac{1}{2}\left(1 + \frac{\epsilon_{0+}}{\epsilon_{0z}}\right)\left(\frac{\partial^2}{\partial x^2} + \frac{\partial^2}{\partial y^2}\right)A_1 + \frac{1}{2}\left(-1 + \frac{\epsilon_{0+}}{\epsilon_{0z}}\right)\left(\frac{\partial}{\partial x} + i\frac{\partial}{\partial y}\right)^2 A_2 + \frac{\omega^2}{c^2} \times [\epsilon_{0+} + \phi_+(A_1A_1^*, A_2A_2^*)]A_1 = 0 \tag{8}$$

$$\frac{\partial^2 A_2}{\partial z^2} + \frac{1}{2}\left(1 + \frac{\epsilon_{0-}}{\epsilon_{0z}}\right)\left(\frac{\partial^2}{\partial x^2} + \frac{\partial^2}{\partial y^2}\right)A_2 + \frac{1}{2}\left(-1 + \frac{\epsilon_{0-}}{\epsilon_{0z}}\right)\left(\frac{\partial}{\partial x} - i\frac{\partial}{\partial y}\right)^2 A_1 + \frac{\omega^2}{c^2} \times [\epsilon_{0-} + \phi_-(A_1A_1^*, A_2A_2^*)]A_2 = 0 \tag{9}$$

Eqs. (8) and (9) are coupled with each other, but there exists a very weak coupling between them. So, one of the term can be set equal to zero. Assuming $A_2 \approx 0$. We can write for Eq. (8) as

$$\frac{\partial^2 A_1}{\partial z^2} + \frac{1}{2}\left(1 + \frac{\epsilon_{0+}}{\epsilon_{0z}}\right)\left(\frac{\partial^2}{\partial x^2} + \frac{\partial^2}{\partial y^2}\right)A_1 + \frac{\omega^2}{c^2} \times [\epsilon_{0+} + \phi_+(A_1A_1^*, A_2A_2^*)]A_1 = 0 \tag{10}$$

In Eq. (10), if we substitute $A_1 = A\, exp[i(\omega t - k_+ z)]$ and further make use of WKB approach, one can get

$$-2ik_+\frac{\partial A}{\partial z} + \frac{1}{2}\left(1 + \frac{\varepsilon_{0+}}{\varepsilon_{0zz}}\right)\left(\frac{\partial^2 A}{\partial x^2} + \frac{\partial^2 A}{\partial y^2}\right) + \frac{\omega^2}{c^2}\phi_+(AA^*)A = 0 \tag{11}$$

In Eq. (11), $\varepsilon_{0+} = 1 - \frac{\omega_p^2}{\omega_0(\omega_0 - \omega_c)}$ , $\varepsilon_{0zz} = 1 - \frac{\omega_p^2}{\omega_0^2}$. $\omega_p = \sqrt{\frac{4\pi n_o e^2}{m}}$ is known as plasma frequency. The nonlinear part of the dielectric function for collisional magnetized plasma may be expressed as [58]

$$\varphi_+(|A.A^*|) = \frac{\omega_p^2}{\omega_0\,(\omega_0 - \omega_c)}\left(1 - \frac{2}{2 + \frac{\alpha A.A^*}{\left(1 - \frac{\omega_c}{\omega_0}\right)^2}}\right) \tag{12}$$

In Eq. (12), the nonlinear coefficient $'\alpha'$ is expressed as $\alpha = \frac{8}{3}\left(\frac{M}{m}\right)\alpha_0$ with $\alpha_0 = \frac{e^2}{8m\omega_0^2 K_B T_0}$. Here, electronic mass, ionic mass, Boltzmann constant and plasma equilibrium temperature are expressed as $m$, M, $K_B$ and $T_0$ respectively. Now, following [58-59], Eq. (11) has solution given by

$$A = A_0(r,z)e^{-ik_0 S(r,z)} \tag{13}$$

$$A_0^2 = \frac{E_{00}^2}{f_0^2} exp\left[-\frac{r^2}{r_0^2 f_0^2}\right] \tag{14}$$

$$S = \frac{1}{2}r^2 \frac{1}{\left(1+\frac{\varepsilon_o}{\varepsilon_{ozz}}\right)} \frac{1}{f_0}\frac{df_0}{dz} + \Phi_0(z) \tag{15}$$

$$k_0 = \frac{\omega_0}{c}\sqrt{\varepsilon_0} \tag{16}$$

In Eq. (15), the symbols ' $S$ ' and $\Phi_0(z)$ denote Eikonal of beam and phase shift respectively. The phase shift analysis is not required in current problem. The beam width $f_0$ satisfied the following 2nd order differential equation,

$$\frac{d^2 f}{dz^2} = \left(1 + \frac{\varepsilon_o}{\varepsilon_{Ozz}}\right)^2 \frac{1}{r_0^4 f_0^3 k_0^2} - \left(1 + \frac{\varepsilon_o}{\varepsilon_{Ozz}}\right) \frac{\omega_p^2}{\varepsilon_o \omega_0^2} \frac{\alpha E_{00}^2}{r_0^2 f^3} \left( \frac{\left(1-\frac{\omega_c}{\omega_0}\right)}{\left(2\left(1-\frac{\omega_c}{\omega_0}\right)^2 + \frac{\alpha E_{00}^2}{f^2}\right)^2} \right) \tag{17}$$

In Eq. (17), ‘z’ denotes propagation axis. The boundary condition used in this case is $f = 1$ and $\frac{df}{dz} = 0$ at z=0.

### 3. Electron Plasma Wave Excitation

Nonlinear interaction of EPW and pump wave leads to its excitation. The excitation process of EPW in collisional magnetized plasma can be studied through following standard equations;

(a) Continuity Equation

$$\frac{\partial N}{\partial t} + \nabla \cdot (NV) = 0 \tag{18}$$

(b) Equation of motion

$$m\left[\frac{\partial V}{\partial t} + (V \cdot \nabla)V\right] = -e\left[E + \frac{1}{c}(V \times B)\right] - 2\Gamma m V - \frac{\gamma_e}{N}\nabla P \tag{19}$$

(c) Poisson’s equation

$$\nabla \cdot E = -4\pi e N \tag{20}$$

In above Eqs., instantaneous electron density, fluid velocity, Landau damping parameter and pressure term are expressed by $N$, $V$, $\Gamma$, and $P$ respectively. For electron gas $\gamma_e = 3$. Further, by using perturbation analysis and standard approach, one can obtain the following equation denoting the change in electron density as

$$\frac{\partial^2 n}{\partial t^2} + 2\Gamma\frac{\partial n}{\partial t} - 3v_{th}^2\nabla^2 n + \omega_p^2\frac{N_{0e}}{N_0}n = 0 \tag{21}$$

Following [58-59], Solution of Eq. (21) is shown as

$$n = n_0(r,z)exp[i(\omega t - k(z + S(r,z)))] \tag{22}$$

$$n_0^2 = \frac{n_{00}^2}{f^2}\exp\left(-\frac{r^2}{a^2 f^2} - 2k_i z\right) \tag{23}$$

$$S = \frac{1}{2}r^2\frac{1}{f}\frac{df}{dz} + \Phi(z) \tag{24}$$

$$\omega^2 = \omega_p^2\frac{N_{0e}}{N_0} + 3k^2 v_{th}^2 \tag{25}$$

In above Eqs., $k$, $\omega$ and $S$ are for wave vector, angular frequency and Eikonal for the EPW. Here, $k_i$ is damping factor and $'f'$ denotes beam width of EPW and 2nd order ODE satisfied by it is expressed as

$$\frac{d^2 f}{dz^2} = \frac{1}{k^2 a^4 f^3} - \frac{\omega_p^2 f}{3k^2 v_{th}^2}\frac{\alpha E_{00}^2}{2r_0^2 f_0^4}\left(\frac{\left(1-\frac{\omega_c}{\omega_0}\right)}{\left(2\left(1-\frac{\omega_c}{\omega_0}\right)^2 + \frac{\alpha E_{00}^2}{f^2}\right)^2}\right) \tag{26}$$

Here, the boundary condition used is $f = 0$ and $\frac{df}{dz} = 0$ at $z = 0$

## 4. Stimulated Raman Scattering

The total field vector $E_T$ is expressed as sum of fields of main wave $E$ and scattered wave $E_s$. i.e.

$$E_T = E\exp(i\omega_0 t) + E_s\exp(i\omega_s t) \tag{27}$$

Now, field vector $E_T$ satisfies following wave equation

$$\nabla^2 E_T - \nabla(\nabla\cdot E_T) = \frac{1}{c^2}\frac{\partial^2 E_T}{\partial t^2} + \frac{4\pi}{c^2}\frac{\partial J_T}{\partial t} \tag{28}$$

Here, $J_T$ is known as total current density. One can equate the scattered frequency terms to obtain following differential equation

$$\nabla^2 E_s + \frac{\omega_S^2}{c^2}\left[1 - \frac{\omega_p^2}{\omega_S^2}\frac{N_{0e}}{\gamma N_0}\right]E_s = \left[\frac{\omega_p^2\omega_S n^*}{2c^2\omega_0 N_0}\right]E_i - \nabla(\nabla\cdot E_i) \tag{29}$$

Eq. (29) has solution given by

$$E_s = E_{s0}(r,z)e^{+ik_{s0}z} + E_{s1}(r,z)e^{-ik_{s1}z} \tag{30}$$

Where $k_{S0}^2 = \frac{\omega_S^2}{c^2}\left[1 - \frac{\omega_p^2}{\omega_S^2}\right] = \frac{\omega_S^2}{c^2}\epsilon_{S0}$, with $\omega_S = \omega_0 - \omega$ and $k_{S1} = k_0 - k$.
Now, substituting Eq. (30) in Eq. (29), one can obtain

$$-k_{S0}^2E_{S0}^2 + 2ik_{S0}\frac{\partial E_{S0}}{\partial z} + \left(\frac{\partial^2 E_{S0}}{\partial r^2} + \frac{1}{r}\frac{\partial E_{S0}}{\partial r}\right) + \frac{\omega_S^2}{c^2}\left[\epsilon_{S0} + \frac{\omega_p^2}{\omega_S^2}\left(1 - \frac{N_{0e}}{N_0}\right)\right]E_{S0} = 0 \tag{31}$$

$$-k_{S1}^2E_{S1}^2 + 2ik_{S1}\frac{\partial E_{S1}}{\partial z} + \left(\frac{\partial^2 E_{S1}}{\partial r^2} + \frac{1}{r}\frac{\partial E_{S1}}{\partial r}\right) + \frac{\omega_S^2}{c^2}\left[\epsilon_{S0} + \frac{\omega_p^2}{\omega_S^2}\left(1 - \frac{N_{0e}}{N_0}\right)\right]E_{S1} = \frac{1}{2}\frac{\omega_p^2}{c^2}\frac{n^*}{N_0}\frac{\omega_S}{\omega_0}E_0 exp(-ik_0S_0) \tag{32}$$

Now, solution of Eq. (32) is written as

$$E_{S1} = E_{S1}'(r,z)e^{-ik_0S_0} \tag{33}$$

Now, put Eq. (33) in Eq. (32) and ignoring space derivatives

$$E_{S1}' = -\frac{1}{2}\frac{\omega_p^2}{c^2}\frac{n^*}{N_0}\frac{\omega_S}{\omega_0}\frac{\hat{E}E_0}{\left[k_{S1}^2 - k_{S0}^2 - \frac{\omega_p^2}{c^2}\left(1 - \frac{N_{0e}}{N_0}\right)\right]} \tag{34}$$

Following [58-59], Eq. (31) has solution denoted as

$$E_{S0} = E_{S00}e^{ik_{S0}S_c} \tag{35}$$

$$E_{S00}^2 = \frac{B_1^2}{f_S^2}exp\left[-\frac{r^2}{b^2f_S^2}\right] \tag{36}$$

$$S_c = \frac{1}{2}r^2\frac{1}{f_S}\frac{df_S}{dz} + \Phi_S(z) \tag{37}$$

In Eq. (36), initial beam radius for scattered wave is denoted by $b$ and beam width of scattered wave is represented by $f_s$ and 2nd order ODE satisfies by it is represented as

$$\frac{d^2f_s}{dz^2} = \frac{1}{k_{S0}^2b^4f_S^3} - \frac{\omega_p^2}{\omega_S^2\varepsilon_{S0}}\frac{\alpha E_{00}^2f_S}{2r_0^2f_0^4}\left(\frac{\left(1-\frac{\omega_c}{\omega_0}\right)}{\left(2\left(1-\frac{\omega_c}{\omega_0}\right)^2+\frac{\alpha E_{00}^2}{f^2}\right)^2}\right) \tag{38}$$

The boundary condition used in present case is $f_s = 0$ and $\frac{df_s}{dz} = 0$ at $z = 0$.

## 5. Back-reflectivity

From Eq. (23), we find that EPW is damped as it transits through z-axis. So, scattered wave amplitude is decreased with increase in z. The boundary condition used is

$$E_s = E_{s0}(r,z)e^{+ik_{s0}z} + E_{s1}(r,z)e^{-ik_{s1}z} = 0 \tag{39}$$

at $z = z_c$. At $z = z_c$, scattered wave amplitude becomes zero.

$$B_1 = \frac{\omega_p^2 \omega_s N_{00}}{2c^2 \omega_0 N_0} \frac{E_{00} e^{-ik_i z_c}}{\left[k_{s1}^2 - k_{s0}^2 - \frac{\omega_p^2}{c^2}\left(1 - \frac{N_{0e}}{N_0}\right)\right]} \frac{f_s(z_c)}{f_s(z_c) f(z_c)} \frac{\exp\left(-i(k_0 S_0 + k_{s1} z_c)\right)}{\exp\left(+i(k_{s0} S_c + k_{s0} z_c)\right)} \tag{40}$$

With the condition that $\frac{1}{b^2 f_s^2} = \frac{1}{a^2 f^2} + \frac{1}{r_0^2 f_0^2}$. Now, SRS back-reflectivity is expressed as,

$$R = \frac{1}{4}\left(\frac{\omega_p^2}{c^2}\right)^2 \left(\frac{\omega_s}{\omega_0}\right)^2 \left(\frac{N_{00}}{N_0}\right)^2 \frac{(L_1 - L_2 - L_3)}{\left[k_{s1}^2 - k_{s2}^2 - \frac{\omega_p^2}{c^2}\left(1 - \frac{\left(1 - \frac{\omega_c}{\omega_0}\right)}{\left(2\left(1 - \frac{\omega_c}{\omega_0}\right)^2 + \frac{\alpha E_{00}^2}{f^2}\right)^2}\right)\right]^2} \tag{41}$$

Where

$$L_1 = \left(\frac{f_s}{f_0 f}\right)^2_{z=z_c} \frac{1}{f_s^2} exp\left(-2k_i z_c - \frac{r^2}{b^2 f_s^2}\right),$$

$$L_2 = -2\left(\frac{f_s}{f_0 f}\right)_{z_c} \frac{1}{f f_0 f_s} exp\left(-\frac{r^2}{2b^2 f_s^2} - \frac{r^2}{2a^2 f^2} - \frac{r^2}{2r_0^2 f_s^2}\right) exp(-k_i(z + z_c)) Cos(k_{s0} + k_{s1})[z - z_c],$$

$$L_3 = \frac{1}{f^2 f_0^2} exp\left(-\frac{r^2}{a^2 f^2} - \frac{r^2}{r_0^2 f_s^2} - 2k_i z_c\right).$$

## 6. DISCUSSION

Eqs. (17), (26), (38) and (41) can't be solved analytically. So, RK4 method is used for doing their numerical calculations for the following well-established parameters;

$$\alpha E_{00}^2 = 3.0, 4.0, 5.0\,; \frac{\omega_p^2}{\omega_0^2} = 0.10, 0.15, 0.20\,; \frac{\omega_c}{\omega_0} = 0.04, 0.08 \text{ and } 0.12$$

Eqs. (17), (26) and (38) are the 2nd order ODE representing the focusing/defocusing behavior of main beam, EPW and scattered wave as they transit inside plasma. In each equation, two terms are present on RHS of each equation. 1st term being diffractive term, while 2nd term being nonlinear refractive term. When 1st term is dominating, then defocusing of beams take place. When 2nd term is dominating, then focusing of beam takes place. It must also be noted that there is always change in relative magnitudes of these terms with propagation distance. All the equations have been numerically solved using RK4 method.

Figures 1, 2 and 3 denote variation of beam widths $f_0$ , $f$ and $f_s$ with dimensionless propagation distance $\eta(= z/k_0 r_0^2)$. Here, only change in beam intensity parameter $\alpha E_{00}^2$ is considered whereas other parameters are kept fixed. Here, $\alpha E_{00}^2 = 3.0, 4.0$ and $5.0$ are denoted by Black, Green and Red curves. The focusing tendency of various beams involved is decreased with increase in beam intensity $\alpha E_{00}^2$ as a result of supremacy of divergence term over converging term with rise in $\alpha E_{00}^2$ parameter. The refractive index gets reduced with rise in $\alpha E_{00}^2$ parameter thereby weakening beam focusing.

Figures 4, 5 and 6 denote variation of beam widths $f_0$ , $f$ and $f_s$ with dimensionless propagation distance $\eta(= z/k_0 r_0^2)$. Here, only change in plasma density parameter $\frac{\omega_p^2}{\omega_0^2}$ is considered whereas other parameters are kept fixed. Here, $\frac{\omega_p^2}{\omega_0^2} = 0.10, 0.15, 0.20$ are denoted by Black, Green and Red curves. The focusing tendency of various beams is increased with increase in plasma density $\frac{\omega_p^2}{\omega_0^2}$ as a result of supremacy of converging term over diffraction term with rise in $\frac{\omega_p^2}{\omega_0^2}$ parameter. The refractive index gets enhanced with rise in $\frac{\omega_p^2}{\omega_0^2}$ parameter thereby strengthening beam focusing.

Figures 7, 8 and 9 denote variation of beam widths $f_0$ , $f$ and $f_s$ with dimensionless propagation distance $\eta(= z/k_0 r_0^2)$. Here, only change in cyclotron frequency parameter $\frac{\omega_c}{\omega_0}$ is considered whereas other parameters are kept fixed. Here, $\frac{\omega_c}{\omega_0} = 0.04, 0.08$ and $0.12$ are denoted by Black, Green and Red curves. The focusing tendency of various beams involved is increased with increase in cyclotron frequency $\frac{\omega_c}{\omega_0}$ as a result of supremacy of converging term over diffraction term with rise in $\frac{\omega_c}{\omega_0}$ parameter. The refractive index gets enhanced with rise in $\frac{\omega_c}{\omega_0}$ parameter thereby strengthening beam focusing.

Figure 10 denotes variation of SRS back-reflectivity with dimensionless propagation distance $\eta(= z/k_0 r_0^2)$. Here, only change in beam intensity parameter $\alpha E_{00}^2$ is considered whereas other parameters are kept fixed. Here, $\alpha E_{00}^2 =$

$3.0$ and $5.0$ are denoted by Blue and Red curves. SRS back-reflectivity is found to decrease with increase in laser intensity $\alpha E_{00}^2$. The reason behind it is that SRS back-reflectivity is directly linked with focusing tendency of waves involved. Since, focusing tendency of waves is decreased with rise in laser intensity $\alpha E_{00}^2$. So, SRS back-reflectivity is decreased accordingly.

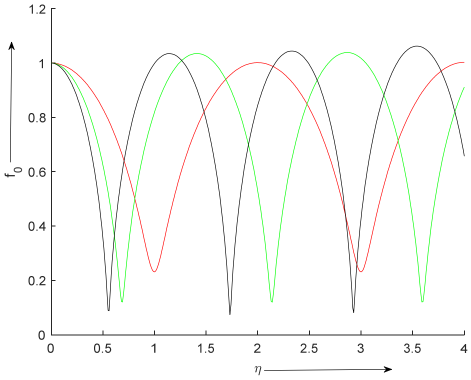

**Figure 1.** Variation of beam width $f_0$ with dimensionless propagation distance $\eta(= z/k_0 r_0^2)$. Here, $\alpha E_{00}^2 = 3.0, 4.0$ and $5.0$ are denoted by Black, Green and Red curves

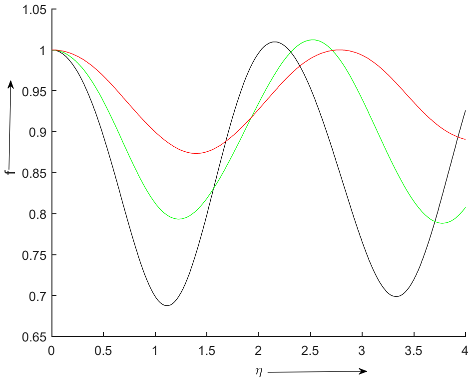

**Figure 2.** Variation of beam width $f$ with dimensionless propagation distance $\eta(= z/k_0 r_0^2)$. Here, $\alpha E_{00}^2 = 3.0, 4.0$ and $5.0$ are denoted by Black, Green and Red curves

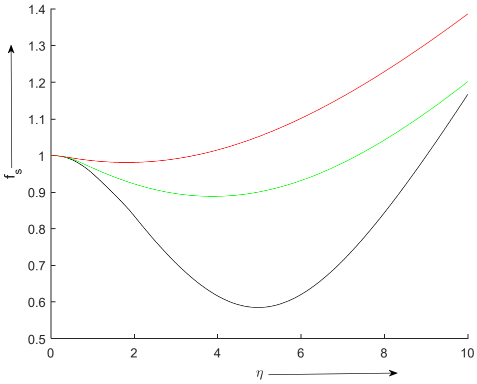

**Figure 3.** Variation of beam width $f_s$ with dimensionless propagation distance $\eta(= z/k_0 r_0^2)$. Here, $\alpha E_{00}^2 = 3.0, 4.0$ and $5.0$ are denoted by Black, Green and Red curves

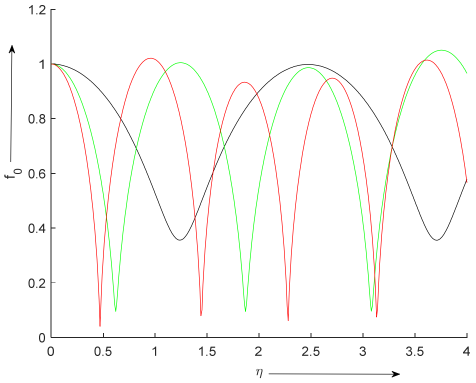

**Figure 4.** Variation of beam width $f_0$ with dimensionless propagation distance $\eta(= z/k_0 r_0^2)$. Here, $\frac{\omega_p^2}{\omega_0^2} = 0.10, 0.15, 0.20$ are denoted by Black, Green and Red curves

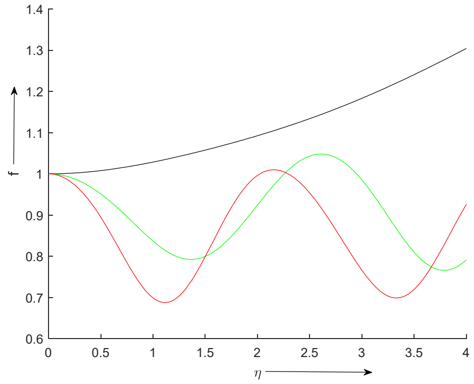

**Figure 5.** Variation of beam width $f$ with dimensionless propagation distance $\eta(= z/k_0 r_0^2)$. Here, $\frac{\omega_p^2}{\omega_0^2} = 0.10, 0.15, 0.20$ are denoted by Black, Green and Red curves

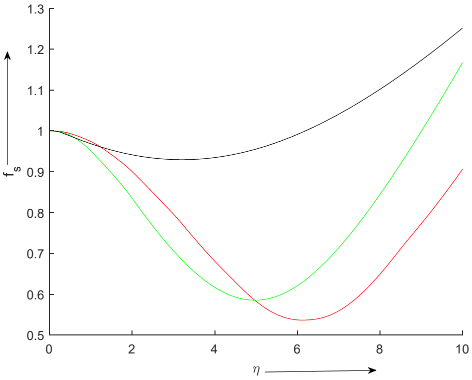

**Figure 6.** Variation of beam width $f_s$ with dimensionless propagation distance $\eta(= z/k_0 r_0^2)$. Here, $\frac{\omega_p^2}{\omega_0^2} = 0.10, 0.15, 0.20$ are denoted by Black, Green and Red curves

Figure 11 denotes variation of SRS back-reflectivity with dimensionless propagation distance $\eta(= z/k_0 r_0^2)$. Here, only change in plasma density $\frac{\omega_p^2}{\omega_0^2}$ is considered whereas other parameters are kept fixed. Here, $\frac{\omega_p^2}{\omega_0^2} = 0.10$ and $0.20$ are denoted by Blue and Red curves respectively. SRS back-reflectivity is increased with rise in plasma density $\frac{\omega_p^2}{\omega_0^2}$. The reason behind it is that SRS back-reflectivity is directly linked with focusing tendency of waves involved. Since, focusing tendency of waves is increased with rise in plasma density $\frac{\omega_p^2}{\omega_0^2}$. So, SRS back-reflectivity is increased accordingly.

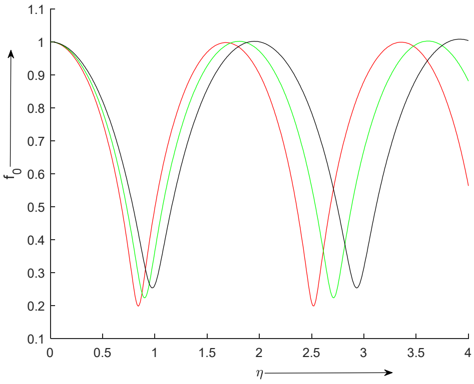

**Figure 7.** Variation of beam width $f_0$ with dimensionless propagation distance $\eta(= z/k_0 r_0^2)$. Here, $\frac{\omega_c}{\omega_0} = 0.04, 0.08$ and $0.12$ are denoted by Black, Green and Red curves

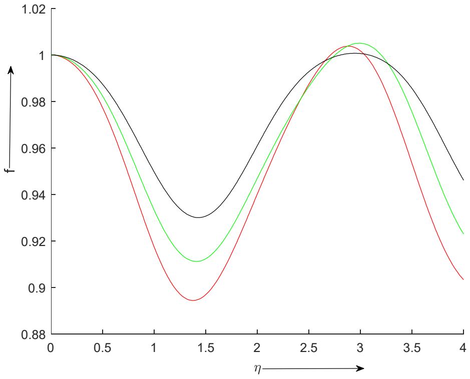

**Figure 8.** Variation of beam width $f$ with dimensionless propagation distance $\eta(= z/k_0 r_0^2)$. Here, $\frac{\omega_c}{\omega_0} = 0.04, 0.08$ and $0.12$ are denoted by Black, Green and Red curves

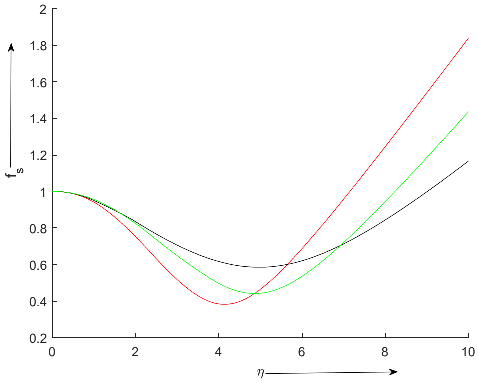

**Figure 9.** Variation of beam width $f_s$ with dimensionless propagation distance $\eta(= z/k_0 r_0^2)$. Here, $\frac{\omega_c}{\omega_0} = 0.04$, 0.08 and 0.12 are denoted by Black, Green and Red curves

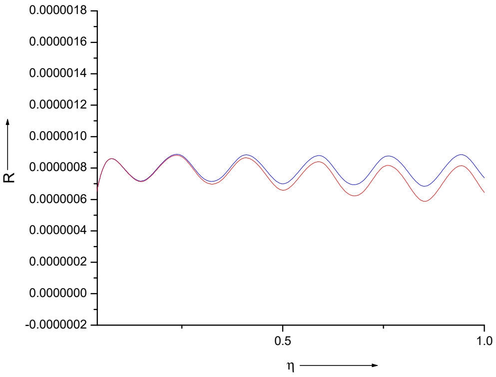

**Figure 10.** Variation of SRS back-reflectivity with dimensionless propagation distance $\eta(= z/k_0 r_0^2)$. Here, $\alpha E_{00}^2 = 3.0$ and $5.0$ are denoted by Blue and Red curves

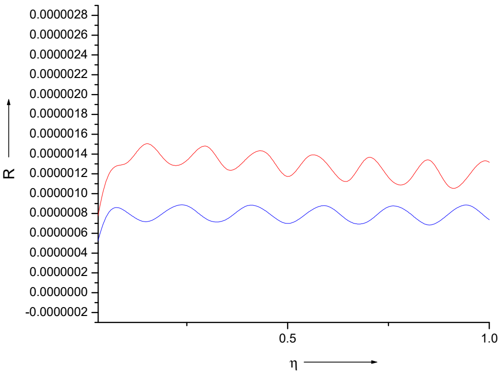

**Figure 11.** Variation of SRS back-reflectivity with dimensionless propagation distance $\eta(= z/k_0 r_0^2)$. Here, $\frac{\omega_p^2}{\omega_0^2} = 0.10$ and $0.20$ are denoted by Blue and Red curves respectively

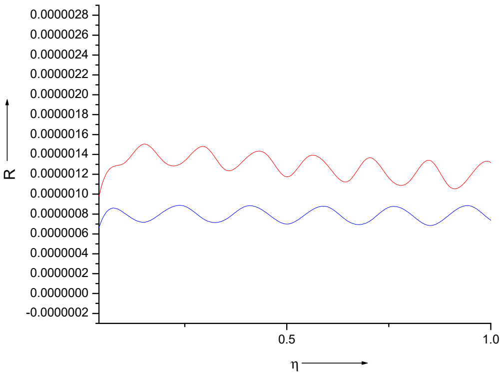

**Figure 12.** Variation of SRS back-reflectivity with dimensionless propagation distance $\eta(= z/k_0 r_0^2)$. Here, $\frac{\omega_c}{\omega_0} = 0.04$ and $0.12$ are denoted by Blue and Red curves respectively

Figure 12 denotes variation of SRS back-reflectivity with dimensionless propagation distance $\eta(= z/k_0 r_0^2)$. Here, only change in cyclotron frequency $\frac{\omega_c}{\omega_0}$ is considered whereas other parameters are kept fixed. Here, $\frac{\omega_c}{\omega_0} = 0.04$ and $0.12$ are denoted by blue and red curves respectively. SRS back-reflectivity is increased with rise in cyclotron frequency $\frac{\omega_c}{\omega_0}$. The reason behind it is that SRS back-reflectivity is directly linked with focusing tendency of waves involved. Since, focusing tendency of waves is increased with rise in cyclotron frequency $\frac{\omega_c}{\omega_0}$. So, SRS back-reflectivity is increased accordingly.

## 7. CONCLUSIONS

The present research deals with SRS of high-power beam in Collisional magnetoplasma. The results obtained from present problem are as follows:

(1) Focusing ability of various waves involved is increased with increase in plasma density, cyclotron frequency and with decrease in laser intensity. This is due to enhancement in net refractive index gradient, which strengthens beam focusing.

(2) SRS back-reflectivity is increased with rise in plasma density, cyclotron frequency and with decrease in beam intensity. This is due to enhancement in net refractive index gradient, which strengthens beam focusing and consequently amplifies SRS back-reflectivity.

Present results are really helpful in knowing physics of laser driven fusion.

## ORCID

**Keshav Walia,** https://orcid.org/0000-0001-9547-3027; **Taranjot Singh,** https://orcid.org/0009-0009-8172-4097
**Anuj Vijay,** https://orcid.org/0000-0001-6610-3844; **Deepak Tripathi,** https://orcid.org/0000-0001-9945-4069

## REFERENCES

[1] M.D. Perry, and G. Mourou, "Terawatt to petawatt subpicosecond lasers," Science, **264**, 917-924 (1994). https://doi.org/10.1126/science.264.5161.917
[2] T. Feder, "Petawatt laser probes nature at Texas University," Phys. Today, **61**, 27 (2008). https://doi.org/10.1063/1.3001859
[3] M. Tabak, J. Hammer, M.E. Glinsky, W.L. Kruer, S.C. Wilks, J. Woodworth, E.M. Campbell, and M.D. Perry, "Ignition and high gain with ultrapowerful lasers", Phys. Plasmas, **1**, 1626–1634 (1994). https://doi.org/10.1063/1.870664
[4] C. Deutsch, H. Furukawa, K. Mima, M. Murakami, and K. Nishihara, "Interaction physics of the fast ignitor concept," Phys. Rev. Lett. **77**, 2483-2486 (1996). https://doi.org/10.1103/PhysRevLett.77.2483
[5] E. Esarey, C.B. Schroeder, and W.P. Leemans, "Physics of laser-driven plasma-based electron accelerators," Rev. Mod. Phys. **81**, 1229-1285 (2009). https://doi.org/10.1103/revmodphys.81.1229
[6] R. Bingham, J.T. Mendonca, and P.K. Shukla, "Topical review: plasma based charged-particle accelerators," Plasma Phys. Controlled Fusion, **46**, R1 (2004). https://doi.org/10.1088/0741-3335/46/1/r01
[7] A. Rousse, "Production of a keV X-Ray Beam from synchrotron radiation in relativistic laser-plasma interaction," Phys. Rev. Lett. **93**, 135005 (2004). https://doi.org/10.1103/physrevlett.93.135005
[8] Z. Zeng, Y. Cheng, X. Song, R. Li, and Z. Xu, "Generation of an extreme ultraviolet supercontinnum in a two-color laser field," Phys. Rev. Lett. **98**, 203901 (2007). https://doi.org/10.1103/physrevlett.98.203901
[9] K. Walia, "Propagation characteristics of a high-power beam in weakly relativistic-ponderomotive thermal quantum plasma," Commun. Theor. Phys. **75**, 095501 (2023). https://doi.org/10.1088/1572-9494/accf82
[10] K. Walia, "Nonlinear interaction of high power beam in weakly relativistic and ponderomotive cold quantum plasma," Optik, **219**, 165040 (2020). https://doi.org/10.1016/j.ijleo.2020.165040
[11] K. Walia, and S. Kaur, "Nonlinear Interaction of Elliptical Laser Beam with Collisional Plasma: Effect of Linear Absorption," Commun. Theor. Phys. **65**, 78 (2016). https://doi.org/10.1088/0253-6102/65/1/78
[12] K. Walia, "Nonlinear Interaction of High Power Elliptical Laser Beam with Cold Collisionless Plasma," J. Fusion Energ. **35**, 446 (2016). https://doi.org/10.1088/0253-6102/65/1/78
[13] K. Walia, "Enhanced Brillouin scattering of Gaussian laser beam in collisional plasma: Moment theory approach," J. Nonlinear Opt. Phys. Mater. **23**, 1450011 (2014). https://doi.org/10.1142/s0218863514500118
[14] T. Singh, and K. Walia, "Second Harmonic Generation of High Power Cosh-Gaussian Beam in Thermal Quantum Plasma: Effect of Relativistic and Ponderomotive Nonlinearity," J. Contemp. Phys. **59**, 244-253 (2024). https://doi.org/10.1134/s1068337224700488
[15] K. Walia, "Self-focusing of high power beam in unmagnetized plasma and its effect on Stimulated Raman scattering process," Optik, **225**, 165592 (2021). https://doi.org/10.1016/j.ijleo.2020.165592
[16] K. Walia, "Stimulated Brillouin Scattering of high-power beam in unmagnetized plasma: Effect of relativistic and ponderomotive nonlinearities," Optik, **221**, 165365 (2020). https://doi.org/10.1016/j.ijleo.2020.165365
[17] K. Singh, and K. Walia, "Influence of Self-Focused Elliptical Laser Beam on Second Harmonic Generation in Cold Quantum Plasma," J. Contemp. Phys. **59**, 154-164 (2024). https://doi.org/10.1134/s1068337224700300
[18] K. Walia, V. Kakkar, and D. Tripathi, "Second harmonic generation of high-power laser beam in cold quantum plasma," Optik, **204**, 164150 (2020). https://doi.org/10.1016/j.ijleo.2019.164150
[19] K. Walia, N. Mehra, and S. Pandit, "Propagation Characteristics of q-Gaussian Laser Beam in Cold Collisionless Plasma," J. Contemp. Phys. **59**, 378-385 (2024). https://doi.org/10.1134/S1068337225700203
[20] V. Nanda, and N. Kant, "Enhanced relativistic self-focusing of Hermite-cosh-Gaussian laser beam in plasma under density transition," Phys. Plasmas **21**, 042101 (2014). https://doi.org/10.1063/1.4870080
[21] N. Kant, M.A. Wani, and A. Kumar, "Self-focusing of Hermite-Gaussian laser beams in plasma under plasma density ramp," Opt. Commun. **285**, 4483-4487 (2012). https://doi.org/10.1016/j.optcom.2012.05.065
[22] M.A. Wani, N. Kant, Investigation of relativistic self-focusing of Hermite-cosine-Gaussian laser beam in collisionless plasma, Optik 127, 4705(2016).

[23] W.L. Kruer, *The Physics of Laser Plasma Interactions*, (Addison-Wesley, Redwood City, 1998).
[24] W.B. Mori, C. Joshi, J.M. Dawson, D.W. Forslund, and J.M. Kindel, "Evolution of self-focusing of intense electromagnetic waves in plasma," Phys. Rev. Lett. **60**, 1298-1301 (1988). https://doi.org/10.1103/PhysRevLett.60.1298
[25] P.M. Lushnikov, and H.A. Rose, "How much laser power can propagate through fusion plasma?" Plasma Phys. Controll. Fusion **48**, 1501 (2006). https://doi.org/10.1088/0741-3335/48/10/004
[26] H.A. Salih, S.T. Mahmoud, R.P. Sharma, and M. Rafat, "Stimulated Raman Scattering of relativistic laser beam in plasmas," Phys. Plasmas **12**, 042302 (2005). https://doi.org/10.1063/1.1856480
[27] C.S. Liu, and V.K. Tripathi, "Consequence of filamentation on stimulated Raman scattering," Phys. Fluids, **29**, 4188-4191 (1986). https://doi.org/10.1063/1.865710
[28] T. Afsar-rad, S.E. Coe, O. Willi, and M. Desselberger, "Evidence of stimulated Raman scattering occurring in laser filaments in long-scale-length plasmas," Phys. Plasmas, **4**, 1301-1322 (1992). https://doi.org/10.1063/1.860086
[29] Y.H. Tang, H. Shen-Sheng, Z. Chang-Xue, W. Yan-Qing, C. Jing, Z. Fang-Chuan, Z. Yu-Zhe, X. Zhi-Zhan, "Stimulated Raman backscattering from an ultrashort laser interacting with underdense plasmas," Chin. Phys. **11**, 50 (2002). https://doi.org/10.1088/1009-1963/11/1/311
[30] R.K. Kirkwood, J.D. Moody, C. Niemann, E.A. Williams, A.B. Langdon, O.L. Landen, L. Divol, and L.J. Suter, "Observation of polarization dependent Raman scattering in a large scale plasma illuminated with multiple laser beams," Phys. Plasmas **13**, 082703 (2006). https://doi.org/10.1063/1.2215415
[31] L. Yin, B.J. Albright, H.A. Rose, K.J. Bowers, B. Bergen, D.S. Montgomery, J.L. Kline, and J.C. Fernandez, "Onset and saturation of backward stimulated Raman scattering of laser in trapping regime in three spatial dimensions," Phys. Plasmas, **16**, 113101 (2009). https://doi.org/10.1063/1.3250928
[32] D. Tripathi, T. Singh, A. Vijay, and K. Walia, "Second Harmonic Generation of q-Gaussian Laser Beam in Thermal Quantum Plasma," J. Contemp. Phys. **60**, 171-180 (2025). https://doi.org/10.1134/s1068337225700574
[33] D. Tripathi, S. Kaur, A. Vijay, and K. Walia, "Nonlinear Dynamics of q-Gaussian Laser Beam in Collisional Plasma: Effect of Linear Absorption," J. Contemp. Phys. **60**, 16-23 (2025). https://doi.org/10.1134/s1068337225700409
[34] K. Singh, and K. Walia, "Impact of High-Power Cosh-Gaussian Beam on Second Harmonic Generation in Collisionless Magnetoplasma," J. Contemp. Phys. **59**, 254-264 (2024). https://doi.org/10.1134/s106833722470049x
[35] H.C. Barr, T.J.M. Boyd, and G.A. Coutts, "Stimulated Raman Scattering in the presence of filamentation in underdense plasmas," Phys. Rev. Lett. **56**, 2256-2259 (1986). https://doi.org/10.1103/PhysRevLett.56.2256
[36] R.W. Short, W. Seka, and R. Bahr, "Stimulated Raman scattering in self-focused light filaments in laser-produced plasmas," Phys. Fluids **30**, 3245-3251 (1987). https://doi.org/10.1063/1.866499
[37] E.S. Dodd, and D. Umstadter, "Coherent control of stimulated Raman scattering using chirped laser pulses," Phys. Plasmas, **8**, 3531-3534 (2001). https://doi.org/10.1063/1.1382820
[38] Y.S. Kalmykov, and G. Shvets, "Stimulated Raman backscattering of laser radiation in deep plasma channels," Phys. Plasmas, **11**, 4686-4694 (2004). https://doi.org/10.1063/1.1778743
[39] R.K. Kirkwood, R.L. Berger, C.G.R. Geddes, J.D. Moody, B.J. Macgowan, S.H. Glenzer, K.G. Estabrook, *et al*., "Scaling of saturated stimulated Raman scattering with temperature and intensity in ignition scale plasmas," Phys. Plasmas, **10**, 2948-2955 (2003). https://doi.org/10.1063/1.1580814
[40] P. Sharma, and R.P. Sharma, "Suppression of stimulated Raman scattering due to localization of electron plasma wave in laser beam filaments," Phys. Plasmas, **16**, 032301 (2009). https://doi.org/10.1063/1.3077670
[41] G. Purohit, P. Sharma, and R.P. Sharma, "Filamentation of laser beam and suppression of stimulated Raman scattering due to localization of electron plasma wave," J. Plasma Phys. **78**, 55-63 (2012). https://doi.org/10.1017/S0022377811000419
[42] A. Singh, and K. Walia, "Self-focusing of Gaussian laser beam in collisionless plasma and its effect on stimulated Raman scattering process," Optik, **124**, 6074-6080 (2013). https://doi.org/10.1016/j.ijleo.2013.07.005
[43] P. Rawat, R. Gauniyal, and G. Purohit, "Growth of ring ripple in a collisionless plasma in relativistic-ponderomotive regime and its effect on stimulated Raman backscattering process," Phys. Plasmas, **21**, 062109 (2014). https://doi.org/10.1063/1.4883221
[44] P. Sharma, "Stimulated Raman scattering of ultra intense hollow Gaussian beam in relativistic plasma," Laser Part. Beams **33**, 489-498 (2015). https://doi.org/10.1017/S0263034615000488
[45] T.W. Huang, C.T. Zhou, A.P.L. Robinson, B. Qiao, H. Zhang, S.Z. Wu, H.B. Zhou, *et al*., "Mitigating the relativistic laser beam filamentation via an elliptical beam profile," Phys. Rev. E, **92**, 053106 (2015). https://doi.org/10.1103/PhysRevE.92.053106
[46] H.S. Brandi, C. Manus, and G. Mainfray, "Relativistic and ponderomotive self-focusing of a laser beam in a radially inhomogeneous plasma. I. Paraxial approximation," Phys. Fluids B, **5**, 3539-3550 (1993). https://doi.org/10.1063/1.860828
[47] H.S. Brandi, C. Manus, G. Mainfray, and T. Lehner, "Relativistic self-focusing of ultraintense laser pulses in inhomogeneous underdense plasmas," Phys. Rev. E, **47**, 3780-3783 (1993). https://doi.org/10.1103/PhysRevE.47.3780
[48] J.F. Drake, P.K. Kaw, Y.C. Lee, G. Schmid, C.S.L. Marshall, and N. Rosenbluth, "Parametric instabilities of electromagnetic waves in plasmas," Phys. Fluids, **17**, 778-785 (1974). https://doi.org/10.1063/1.1694789
[49] M.S. Sodha, G. Umesh, and R.P. Sharma, "Enhanced Raman scattering of a Gaussian laser beam from a plasma," Plasma Phys. **21**, 687 (1979). https://doi.org/10.1088/0032-1028/21/8/002
[50] R.K. Singh, and R.P. Sharma, "Stimulated Raman backscattering of filamented hollow Gaussian beams," Laser Part. Beams, **31**, 387-394 (2013). https://doi.org/10.1017/s0263034613000384
[51] N.S. Saini, and T.S. Gill, "Enhanced Raman scattering of a rippled laser beam in a magnetized collisional plasma," Laser Part. Beams, **22**, 35-40 (2004). https://doi.org/10.1017/S0263034604221073
[52] P. Jha, G. Raj, and A.K. Upadhyaya, "Relativistic and ponderomotive effects on stimulated Raman scattering of intense laser radiation in plasma," IEEE Trans. Plasma Sci. **34**, 922-926 (2006). https://doi.org/10.1109/tps.2006.878144
[53] R.P. Sharma, and M.K. Gupta, "Effect of relativistic and ponderomotive nonlinearities on stimulated Raman scattering in laser plasma interaction," Phys. Plasmas, **13**, 113109 (2006). https://doi.org/10.1063/1.2357895
[54] F. Cornolti, M. Lucchesi, and B. Zambon, "Elliptic Gaussian beam self-focusing in nonlinear media," Optics Comm. **75**, 129-1356 (1990). https://doi.org/10.1016/0030-4018(90)90241-K

[55] S. Konar, and A. Sengupta, "Propagation of an elliptic Gaussian laser beam in a medium with saturable nonlinearity," J. Opt. Soc. Am. B, **11**, 1644-1646 (1994). https://doi.org/10.1364/JOSAB.11.001644
[56] G. Fibich, and B. Ilan, "Self-focusing of elliptic beams: an example of the failure of the aberrationless approximation," J. Opt. Soc. Am. B, **17**, 1749-1758 (2000). https://doi.org/10.1364/JOSAB.17.001749
[57] T.S. Gill, N.S. Saini, S.S. Kaul, and A. Singh, "Propagation of elliptical Gaussian laser beam in a higher order non-linear medium," Optik, **115**, 493-498 (2004). https://doi.org/10.1078/0030-4026-00405
[58] S.A. Akhmanov, A.P. Sukhorokov, and R.V. Kokhlov, "Self-focusing and diffraction of light in nonlinear medium," Sov. Phys. Uspekhi, **10**, 609(1968).
[59] M.S. Sodha, A.K. Ghatak, and V.K. Tripathi, "Self focusing of laser beams in plasmas and semiconductors," Progress in Optics **13**, 169-265 (1976). https://doi.org/10.1016/S0079-6638(08)70021-0

# ВИМУШЕНЕ КОМБІНАЦІЙНЕ РОЗСІЮВАННЯ ПОТУЖНОГО ПУЧКА У МАГНІТОПЛАЗМІ ІЗ ЗІТКНЕННЯМИ

**Кешав Валья[1], Таранджот Сінгх[1], Анудж Віджай[2], Діпак Тріпаті[3]**
[1]*Кафедра фізики, Університет DAV, Джаландхар, Індія*
[2]*Кафедра фізики, Університет GLA, Матхура (У.П.), Індія-281406*
[3]*Кафедра фізики, USAR, Університет Гуру Гобінда Сінгха Індрапрастхи, кампус Східного Делі, Делі, Індія-110032*

У цій задачі досліджується вимушене комбінаційне розсіювання потужного променя в зіткнювальній магнітоплазмі. Лазерний промінь має два режими поширення, а саме: незвичайний та звичайний, під час його переходу вздовж напрямку статичних магнітних полів. Перерозподіл носіїв відбувається через модифікацію статичного магнітного поля. Перерозподіл носіїв відбувається через неоднорідне нагрівання, що призводить до зміни профілю густини в поперечному напрямку до осі основного променя. Цей профіль густини додатково викликає модифікацію всіх трьох хвиль, що беруть участь у процесі, а саме: падаючого променя, електронної плазмової хвилі та розсіяної хвилі. Тут будуть отримані ЗДР 2-го порядку для перетяжок пучка накачування, електроплівкової хвилі та хвилі зворотного розсіяння, а також вираз для відбивної здатності, і далі буде проведено їх числове моделювання, щоб дослідити вплив зміни параметрів лазера та плазми, а також зовнішнього прикладеного магнітного поля на перетяжки пучка різних хвиль та на зворотну відбивну здатність ВКР.

**Ключові слова:** *вимушене комбінаційне розсіювання; статичне магнітне поле; неоднорідний нагрів; розсіяна хвиля; зворотна відбивна здатність*